Civil Engineering Department
Structures

قسم الهندسة المدنية
ألإنشآت

قسم الهندسة المدنية

فرع إلإنشآت والمواد

المحتويات

تسلسل	ألعنوان	رقم ألصفحة
1.	التحلي ألا خطي للكتائف الخرسانية المسلحة العالية المقاومة د. أياد أمجد عبد الرزاق أحمد محمد علي	1
2.	التحليل غير الخطي المعتمد على الزمن بالعناصر المحددة للعتبات والأعمدة الخرسانية المسلحة سعد علي الطعان سمير سعدي يعقوب	14
3.	تطوير نموذج متدني المرونة ثلاثي ألأبعد لتحليل العتبات الصندوقية تحت تأثير ألأحمال ألمركبة أ.د. محمد نجم محمود علي نذير عبد الباقي	25
4.	التحليل غير الخطي بطريقة العناصر المحددة للبلاطات الخراسانية المسلحة جزئيا بالألياف الفولاذية د. أياد أمجد عبد الرزاق نهى حميدي الجبوري	39
5.	الخواص الديناميكية للعتبات المجوفة والمصنوعة من الالياف الزجاجية د. زياد خلف عواد	52
6.	تحليل الانثناء للبلاطات الخرسانية الليفية المسلحة أ. م. د. ازاد محمد أ. د. سعد علي الطعان أ. د. هشام الحسني	60
7.	نموذج الشبكة العصبية الاصطناعية للتنبؤ بالتصرف اللاخطي للصفائح المستطيلة د. سالم طيب يوسف د. اياد امجد اغوان	72
8.	نموذج الشبكات العصبية الاصطناعية لتقدير مقاومة قص العتبات الخرسانية المسلحة التي لا تحتوي على تسليح القص د. سالم طيب يوسف محمد هشام شكر الخفاف	81
9.	فحوصات كتائف خرسانية مسلحة مسبقة التشقق مقوات بشرائط الياف الكاربون البوليمرية د. آزاد عبد القادر محمد كولان ب. حسان	91
10.	سلوك العتبات الخرسانية المسلحة الحاوية على فتحات في منطقة القص المقواة والمعاد تأهيلها بألياف الكاربون البوليمرية تحت تأثير الاحمال التكرارية أ.د.بيار جعفر السليفاني فهد اكرم سعيد الحمداني	99
11.	سلوك مقاومة أنتقال القص في الخرسانة بتأثير درجات الحرارة العالية أ.د.عبد الحكيم حامد احمد بـــان نجيب ميخا	116
12.	تأثير نسب المزج على مقاومة تآكل البري للخرسانة عالية المقاومة علي حسين علي محمد حازم ياسين	130
13.	تقليل نفاذية الخرسانة المستعملة في المنشآت البحرية وألأنفاق أحمد جبير أسيل محمد	142
14.	تأثير الميتاكاؤلين على بعض خواص الخرسانة خفيفة الوزن المتعرضة لتاثير الكبريتات الخارجي الدكتورة شيلان محمود حمه البرزنجي	153
15.	خواص مونة الاسمنت الحاوية على غبار افران الاسمنت أ.م.د. باسل صلاح مهدي م. اسراء يونس حردان محمد شحاذه	164
16.	ألإداء ألحراري لنظام ألمساكن أللإقتصادية الفيروسمنتية أ.د. وائل الرفاعي ليث ابراهيم هشام السامرائي	172

Nonlinear Analysis of High Strength Fibre Reinforced Concrete Corbels

Dr. Ayad A. Abdul-Razzak [a], Ahmed A. Mohammed Ali [b]

[a] *Assistant Professor, Civil Engineering Department, University of Mosul, Mosul, Iraq*
DrAyad_Aghwan@yahoo.co.uk

[b] *Assistant Lecturer, Civil Engineering Department, University of Mosul, Mosul, Iraq*
aaldubony@gmail.com

Abstract:

In the present study, new material constitutive relationships for High Strength Steel Fibre Reinforced Concrete (HSSFRC) has been suggested by means of a regression analysis of many experimental data (from literature) by using SPSS-statistical program. This proposed material constitutive has been employed for formulating the material finite element models to study the behaviour of HSSFRC corbels.

The main focus of this study is developing accurate models to represent the behaviour of HSSFRC matrix used in structural members.

In finite element analysis; eight-node isoperimetric plane stress elements are employed to model the concrete material. An elastic-strain hardening plasticity approach combined with cracking damage is used in modelling the concrete behaviour. The reinforcing bars are treated as embedded elements. Nonlinear tensile stress degradation functions are used to model the tension stiffening. Cracked shear moduli has been used in this study.

The numerical results of proposed material models and corbels behaviour compared with published experimental results showed good agreement..

التحلي ألا خطي للكتائف الخرسانية المسلحة العالية المقاومة

د. أياد أمجد عبد الرزاق أحمد محمد علي

قسم الهندسة المدنية – كلية الهندسة – جامعة الموصل

الملخص:

في هذه الدراسة، تم اقتراح علاقات تكوينية جديدة للخرسانة الليفية المسلحة عالية المقاومة بإجراء عملية التحليل التراجعي على العديد من النتائج العملية (المتوفرة في الدراسات السابقة) باستخدام البرنامج الإحصائي (SPSS)، واستخدمت هذه العلاقات في التحليل غير الخطي للكتائف الخرسانية الليفية المسلحة عالية المقاومة.

تم استخدام العناصر موحدة المتغيرات الثنائية الأبعاد ذات الثماني عقد لتمثيل الخرسانة الليفية، أما حديد التسليح فقد تم تمثيله بعناصر محورية مطمورة في العناصر الخرسانية.

مُثل سلوك الخرسانة الليفية في حالة الانضغاط بوصفها مادة مرنة مع انفعالات لدنة متصلدة بعد الخضوع. شروط الخضوع عبر عنها بدلالة أول متغيرين للإجهاد. تهشم الخرسانة هي ظاهرة محكومة بالانفعال ومنظمة بسطح سحق يشبه سطح الخضوع.

استخدم أسلوب الشق الثابت لتمثيل سلوك الخرسانة المتشققة مع شرط الشد للتنبؤ بحدوث التشقق. اخذ بنظر الاعتبار تأثير صلابة الشد في الخرسانة المتشققة بتطوير نموذج لإجهاد الشد المتناقص، كما اخذ بنظر الاعتبار أيضا مقاومة القص بعد التشقق حيث طورت دالة جديدة لتقليل معامل القص في مناطق التشقق.

لإثبات كفاءة النماذج المقترحة تم تحليل العديد من الأمثلة ، وأظهرت النتائج المستحصلة مثل علاقة (الحمل-الأود)، توزيع الاجهادات، ظهور وانتشار الشقوق و الحمل الأقصى توافقا جيدا مع النتائج العملية المنشورة.

Keywords:

Corbels; Cracked shear modulus; High strength; Steel fibre; Tension stiffening.

Notations:

a	Shear span and constant of regression analysis
b	Width and constant of regression analysis
d	Effective depth
d_f	Diameter of fibre
E_{cf}	Modulus of elasticity of HSSFRC
E_f	Modulus of elasticity of steel fibres
E_s	Modulus of elasticity of steel
F	Fibres reinforcing index
f'_c	Uniaxial compressive strength of plain concrete
f_{cf}	Uniaxial compressive strength of HSSFRC
f'_t	Uniaxial tensile strength of plain concrete
f_{tf}	Uniaxial tensile strength of HSSFRC
f_y	Yield stress of reinforcement
G	Uncracked shear modulus
$\overline{G}$	Cracked shear modulus
G_f	Fracture energy
h_c	Characteristic length
I_1, J_2	Normal and shear stress invariants
l_f	Length of fibre
N	Number of sample
N_f	Effective numbers of fibres per unit cross section area
P	Applied load
R	Reaction
S	Uniaxial compressive to tensile strength ratio (f_{cf} / f_{tf})
V_f	Volume fraction of fibre
α_2	Principal stress ratio (σ_1/σ_2)
α_f, β_f	Stress function parameters
β	Orientation factor of fibres
$\varepsilon_1, \varepsilon_2$	Principal strains
ε_{cuf}	Ultimate crushing strain of HSSFRC
ε_i	Current tensile strain
ε_m	Limiting tensile strain normal to the crack
ε_{pf}	Compressive strain at peak stress of HSSFRC
ε_t	Tensile strain at peak stress of plain concrete
ε_{tf}	Tensile strain at peak stress of HSSFRC
Φ	Reinforcement bar diameter
$\sigma_\circ$	Equivalent effective stress
σ_1, σ_2	Principal stresses
σ_{1p}, σ_{2p}	Ultimate principal tensile and compressive strength respectively in the tension- compression zone of stress

1. Introduction

In the 1970s, (62 MPa) concrete has been produced [1], the use of high strength concrete has increased rapidly because of the demand for higher strength and durability. To be used for high-rise buildings, high strength concrete avoids the unacceptable oversized columns on the lower floors, allowing large column spacing and usable floor space, or increasing the number of possible stories without detracting from lower floors [2]. The major difference between the normal and high strength concrete is that high strength concrete tends to behave as elastic and more brittle material compared with normal strength concrete [3]. However, this brittleness can be overcome by adding fibre[4]. The concept of using fibre was to improve ductility and

avoiding brittle behaviour and enhance the compression, tensile, shear, flexural strengths, toughness, durability and resistant to impact [5].

Corbels are structural members which are build monolithically with columns and its main function is to support precast (beam, slabs…, etc) and transfer of vertical and horizontal forces to principle members (column, wall).

Several studies have been made to investigate experimentally the behaviour of HSSFRC corbels [6,7], and little works have been carried out to study the response of fibre reinforced concrete corbels using nonlinear finite element analysis. An important part of any nonlinear finite element analysis is to model the constitutive material relationships. The constitutive models should correctly describe the behaviour of the material under uniaxial and multiaxial states of loading. Various researchers and numerous proper constitutive relationships have been proposed to simulate the behaviour of HSSFRC [8,9].

In the present research work, many constitutive models are used to simulate the nonlinear behaviour of HSSFRC. In order to demonstrate the validity of the proposed models, many computer programs coded in FORTRAN 90 have been implemented and used for nonlinear finite element analysis of HSSFRC corbels under static loads over the entire range of loading and up to failure.

2. Material Constitutive Relationships

In order to analyze reinforced concrete structure by finite element method, suitable nonlinear material models are required.

2.1 Compressive Behaviour of Concrete

The compressive strength of plain concrete (f_c') will be improved by addition of steel fibre which leads to improve the strain (ε_{pf}) at peak compressive strength of concrete (f_{cf}) and consequently improve the ultimate compressive strain value (ε_{cuf}). The influence of steel fibre content (V_f %) and its length to diameter ratio (l_f / d_f) on compressive strength and strain can be formulated using the experimental data of references [10-13] by performing a regression analysis of this data using SPSS program with the following outcome

$$f_{cf} = f_c' + 0.33.F.f_c'^{0.65} \quad (1)$$

$$\varepsilon_{pf} = 0.00072.f_{cf}^{0.32} + 0.00096.F^{1.77} \quad (2)$$

$$\varepsilon_{cuf} = 1.229.(10^{12}).f_{cf}^{-8.05} + 0.005.F^{0.4} \quad (3)$$

where F, fibres reinforcing index:

$$F = V_f.l_f / d_f \quad (4)$$

Good index of determination which was equal to 99.2%, 97.7%, and 91.5% for equations (1),(2) and (3) respectively.

The plastic behaviour of concrete compression strain can be represented in two models which are perfectly plastic and strain hardening. In the perfectly plastic model, the plastic behaviour will start when the effective stress reaches the value of compressive strength (f_{cf}) and is continued until crushing state occurs. While in strain hardening model the plastic simulation of strain will begins directly at (σ=0.3 f_{cf}), as depicted in Fig. (1). To determine the consecutive expansion of the loading surface during the plastic strain case it is necessary to employ the hardening rule. Nonlinear regression analysis has been done of experimental stress (σ)-strain (ε) data from references [4,11] in SPSS program, equation (5) was

proposed with a very good index of determination of 99.25%. Fig.(2) shows the comparison of proposed model and the experimental results.

$$\sigma = -a.f_{cf}.(\varepsilon/\varepsilon_{pf})[(\varepsilon/b.\varepsilon_{pf})-2] \quad (5)$$

where:

$$a = 0.63 + 1.115.F^2 - 0.997.F^3 \quad (6)$$

$$b = 0.345 + 2.498.F^2 - 2.275.F^3 \quad (7)$$

and ε is the concrete strain, its value is between (0 - ε_{pf}).

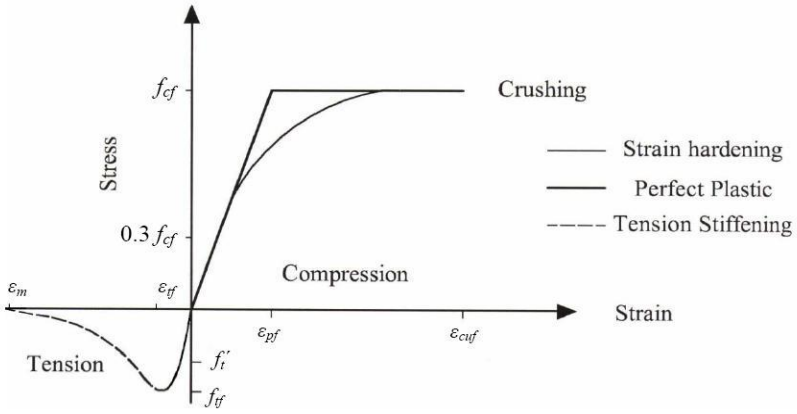

Fig. 1. Compression and tension stress-strain models.

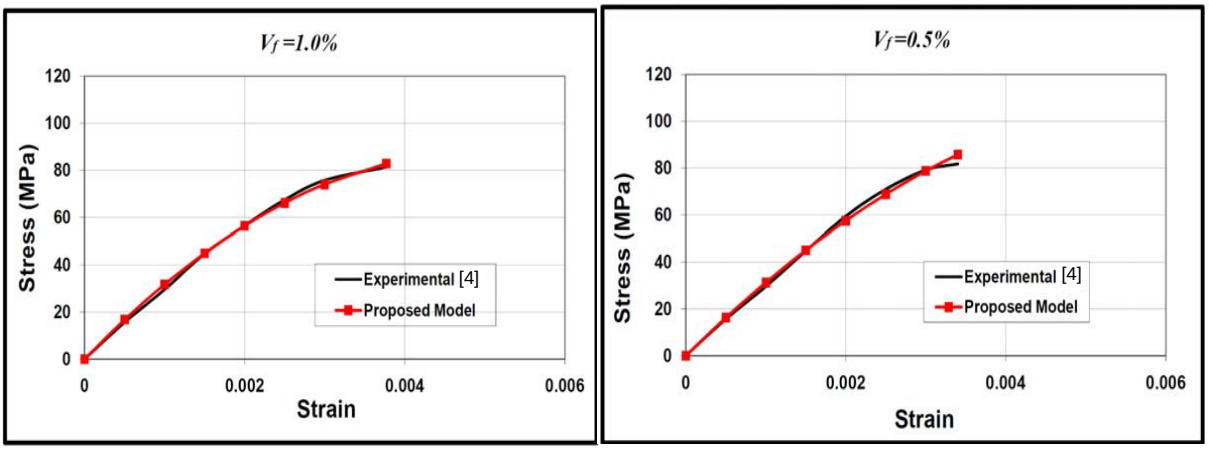

Fig. 2. Comparison of proposed model with experimental data for uniaxial stress-strain curves in compression [4].

2.2 Tensile Behaviour of Concrete

It is a well-known fact that the addition of fibre plays an important role in the improvement of the tensile behaviour of concrete by increasing the tensile strength, controls crack initiation, and increasing in cracking strain value. After cracking point at tensile strength (f_{tf}) the HSSFRC specimens showed smaller cracks width than in the case of plain concrete because of increaser bonding force between concrete components due to the presence of fibre, which consequently increase the resistance to the tensile stresses. So to formulate a tensile stress–strain relationship of fibre concrete, it is better to separate it into two regions,

namely, pre and post-peak regions. For formulating the pre-peak tensile stress–strain relation, a regression analysis was made from many experimental data available in reference [14] and equation (8) was proposed with a good index of determination of (97.8%).

$$f_t = f_{tf}.(\varepsilon / \varepsilon_{tf})^{\eta} \quad (8)$$

$$\eta = 0.683 - 0.118.F \quad (9)$$

Where tensile strength of HSSFRC (f_{tf}) has been obtained by regression analysis depending on numerous experimental data from references [15,16, and 17] and equation (10) was proposed with a good index of determination about (97.0%).

$$f_{tf} = f_t' + 0.0385.N_f + 3.4.F \quad (10)$$

$$N_f = \beta.(4.V_f / \pi.d_f^2) \quad (11)$$

where (β) represents a direction factor of fibre and may be taken to be equal to (0.41) [18].

And tensile strain (ε_{tf}) at tensile strength (f_{tf}) is proposed depending on experimental data available in the reference [14], thus equation (12).

$$\varepsilon_{tf} = \varepsilon_t + 0.00026.N_f.l_f.d_f \quad (12)$$

Good agreement (index of determination=94.0%) was obtained.

Tension stiffening effect in the cracked concrete has been taken into account by adopting a nonlinear tensile stress degradation function with the current tensile strain (ε_i) depending on experimental and fracture energy concept [19], as follows

$$\sigma = f_{tf}[(\varepsilon - \varepsilon_m)/(\varepsilon_{tf} - \varepsilon_m)]^4 \quad (13)$$

where (ε_m) is the limiting tensile strain, and this value is calculated by the area under the stress-strain curve as follows

$$G_f = \int_0^{\delta} \sigma.d\delta = \int_{\varepsilon_{tf}}^{\varepsilon_m} \sigma.h_c.d\varepsilon \quad (14)$$

$$G_f = h_c.f_{tf}.\int_{\varepsilon_{tf}}^{\varepsilon m} [(\varepsilon - \varepsilon_m)/(\varepsilon_{tf} - \varepsilon_m)]^4.d\varepsilon \quad (15)$$

$$G_f = [h_c.f_{tf}.(\varepsilon_m - \varepsilon_{tf})]/5 \quad (16)$$

where

$$\varepsilon_m = [(5.G_f)/(h_c.f_{tf})] + \varepsilon_{tf} \quad (17)$$

and (h_c) is the characteristic length of the Gauss point.

While the estimated amount of fracture energy (G_f) is formulated as equation (18) shows depending on experimental data available in references [20,21, and 22] with index of determination equal to 89.7%.

$$G_f = 3.065(10)^{-5}.f_{cf}^{2.542} + 3.637.F \quad (18)$$

2.3 Biaxial Behaviour of Concrete

A strain hardening plasticity approach is employed to model the compression behaviour of concrete. A hardening role is chosen to describe the growth of yield surface during plastic loading. A yield function depending on the mean normal stress (I_1) and the shear stress invariant (J_2) is used [19,23]

$$f(I_1, J_2) = \sqrt{\alpha_f I_1 + \beta_f (3J_2)} = \sigma_\circ \quad (19)$$

Where (α_f) and (β_f) are material parameters and (σ_o) is an equivalent effective stress, taken as the compressive strength (f_{cf}). The stress function defined in equation (19) may be written in terms of the principal stresses as

$$\beta_f[(\sigma_1^2 + \sigma_2^2 + \sigma_3^2) - (\sigma_1\sigma_2 + \sigma_1\sigma_3 + \sigma_2\sigma_3)] + \alpha_f(\sigma_1 + \sigma_2 + \sigma_3) = \sigma_\circ^2 \quad (20)$$

for the uniaxial compression test

$$\sigma_1 = f_{cf} \qquad \sigma_2 = \sigma_3 = 0 \quad (21)$$

for the biaxial compression test

$$\sigma_1 = \sigma_2 = \omega . f_{cf} \quad (22)$$

Applying regression analysis to the experimental data of reference [24] the following model is adopted taking into account the influence of the stress ratio, fibre aspect ratio and volume fraction, then (ω) (for the range of steel fibres used for practical purpose) becomes equal to

$$\omega = 1.218 + 0.123.F^{0.858} \quad (23)$$

Very good compatibility is found from equation (23) and experimental data (index of determination=98.2%), Fig. (3) shows the comparison of proposed model and the experimental envelope.

The use of equations (21) and (22) in equation (20), (α_f) and (β_f) can be expressed as follows

$$\alpha_f = [(1-\omega^2)/(\omega^2 - 2\omega)]\sigma_\circ \quad (24)$$

$$\beta_f = [(1-2\omega)/(\omega^2 - 2\omega)] \quad (25)$$

And the yield condition can be written in term of the stress components in plane stress problem as

$$f(\sigma) = [\beta_f\{(\sigma_x^2 + \sigma_y^2 - \sigma_x\sigma_y) + 3(\tau_{xy}^2)\} + \alpha_f(\sigma_x + \sigma_y)]^{0.5} = \sigma_\circ \quad (26)$$

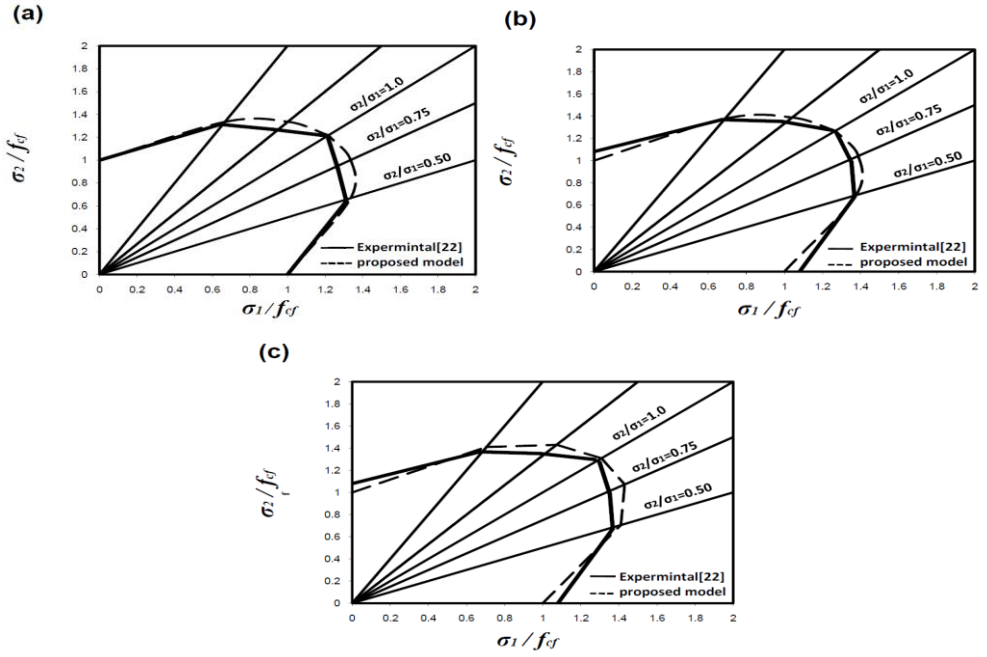

Fig. 3. Comparison of proposed model and experimental envelope [24]. (biaxial compression-compression region): (a) V_f=0.0; (b) V_f=0.5; and (c) V_f=1.0 .

In the case of biaxial tension-compression stress state of concrete, the high strength concrete is supposed to follow the linear behaviour as shown in Fig.(4) [25], therefore, a linear relation of equation (27) has been adopted to predict the ultimate tensile strength

$$S(\sigma_1 / f_{cf}) + (\sigma_2 / f_{cf}) = 1 \quad (27)$$

where

$$S = f_{cf} / f_{tf} \quad (28)$$

Equation (27) can be rewritten to give the peak compressive strength (σ_{2p}) as a function of (f_{cf}), (S) and (α_2) as

$$\sigma_{2p} = f_{cf} /(S.\alpha_2 + 1) \quad (29)$$

And the peak tensile strength as

$$\sigma_{1p} = \sigma_{2p}.\alpha_2 \quad (30)$$

where the values (σ_{1p}) and (σ_{2p}) are the limiting principal tensile and compressive strengths, respectively and (α_2) is the principal stress ratio (σ_1/σ_2).

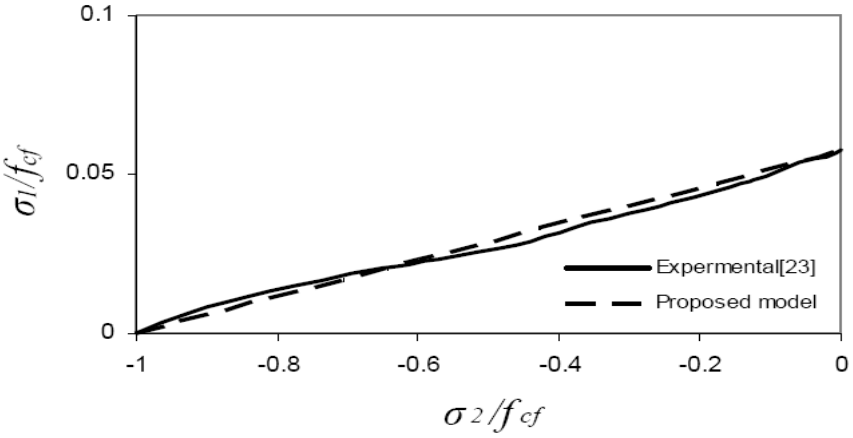

Fig. 4. Comparison of proposed model and experimental data of high strength concrete under biaxial tension-compression [25].

2.4 Modulus of Elasticity of HSSFRC

Equation (31) was derived to represent the modulus of elasticity of HSSERC. Applying regression analysis of many experimental data from reference [15] lead to

$$E_{cf} = 3830.\sqrt{f_{cf}} + 10^5.V_f \quad (31)$$

where (f_{cf}) is in MPa

A suitable index of determination (93.0%) was obtained showing a good agreement with the experimental data.

2.5 Shear Modulus of Cracked Concrete

When a crack is developed in concrete, the surface of the crack is rough and irregular. The majority of the coarse aggregate particles remain embedded in the crack surface. Further movement will be restricted by friction of the aggregate particles, so a certain amount of shear stress will be transferred across the crack interface, this is called aggregate interlock. Also, there is a major shear deformation after tension cracking has occurred, which is an interaction between the reinforcement and concrete. In finite element analysis, the shear stiffness of cracked concrete elements can be calculated by reducing the shear modulus of uncracked concrete, equation (32) was proposed and employed to simulate that

$$\overline{G} = 0.5G[1-\{(\varepsilon-\varepsilon_{tf})/\varepsilon_m\}^{0.5}] \quad (32)$$

where (G) and ($\overline{G}$) are the uncracked and cracked shear modulus respectively.
Poisson's ratio and the modulus of elasticity of concrete are equal to zero after cracking has occurred in the direction perpendicular to the cracked plane.

3. Finite Element Formulation

The eight-node isoperimetric plane-stress element (quadratic element) is used in the present study. Standard Serendipity shape function with two degrees of freedom at each node is adopted. The formulation of this element is mentioned elsewhere [23,26,27].
An embedded bar representation is implemented for steel reinforcement. This approach is similar to that adopted by Ranjbaran [28]. The reinforcing bar is represented by an axial element embedded anywhere within the element as shown in Fig. (5). The failure mode of corbels is often shear failure, shear reinforcement is closed stirrups and for this type of reinforcement, the influence of slip between the concrete and reinforcement steel bar is limited. In addition, many investigators [8,9,29,30,31] assume perfect bond between concrete and steel reinforcement for various types of structures. Therefore, perfect bond is assumed between the reinforcement and surrounding concrete.

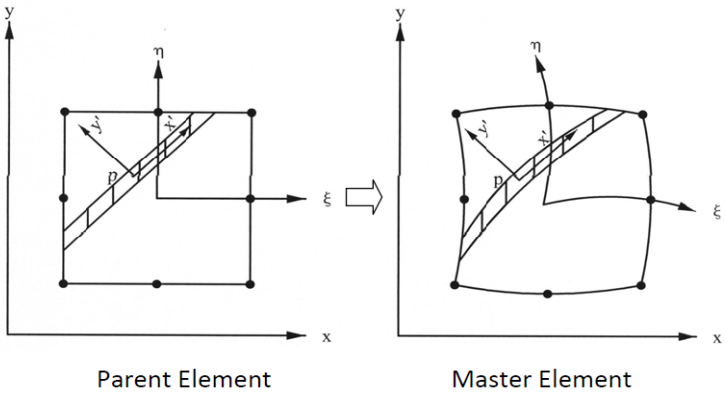

Fig. 5 Embedding reinforcement in reinforced concrete element [28].

4. Numerical Examples

4.1 Description of Test Specimens

HSSFRC corbels were investigated experimentally by Campione et al. [7]. Corbel No.1, V_f =0.5% and Corbel No.2, V_f =1.0% specimens were chosen to carry out the finite element analysis and check the validity of the present material models. The material properties of these corbels are summarized in Table (1), and the dimensions as well as the primary and secondary (stirrups) reinforcement are shown in Fig. (6).

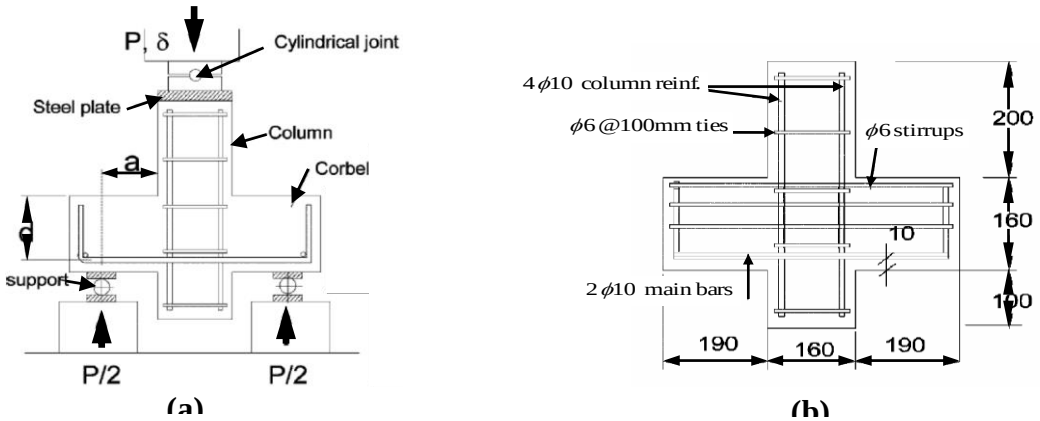

Fig. 6. Test specimen [7]: (a) Loading arrangement; and (b) Dimensions and reinforcement details.

Table 1. Details of corbels [7]

	Corbel No.1	Corbel No.2
Concrete		
Shear Span (a) (mm)	110	110
Width (b) (mm)	160	160
Effective Depth (d) (mm)	140	140
Compressive Strength (f_{cf}) (MPa)	82.0	86.0
Tensile Strength (f_{tf}) (MPa)	7.44	8.66
Modulus of Elasticity* (E_{cf}) (MPa)	35180	36500
Main Reinforcement		
Bar Diameter (Φ) (mm)	2 Φ 10	2 Φ 10
Yield Stress (f_y) (MPa)	488	488
Modulus of Elasticity (E_s) (MPa)	200000	200000
Secondary Reinforcement		
Bar Diameter (Φ) (mm)	4 Φ 6	4 Φ 6
Yield Stress (f_y) (MPa)	445	445
Modulus of Elasticity (E_s) (MPa)	200000	200000
Steel Fibre		
Average Tensile Strength (MPa)	1115	1115
Volume Fraction of Fibre (V_f) (%)	0.5	1.0
Aspect Ratio (l_f / d_f)	60	60

* From equation (31)

4.2 Finite Element Idealization

A computer program coded in FORTRAN 90 was implemented for nonlinear analysis of HSSFRC corbels using finite element modelling, material constitutive relationships were described in the previous sections. Due to symmetry, one-half of the corbel was modelled using 12 eight-node elements, two of these elements were idealized as steel, representing the steel plates as shown in Fig. (7). The simulation of the support has a significant effect on the behaviour of reinforced concrete members[30], therefore, the support was simulated by three points with the outer points carrying some fraction of total reaction (R) (each outer points carrying 0.175 R).

The numerical analysis have been generally carried out using strain hardening model for fibrous concrete in compression and reduced integration (2*2 Gauss points) rule.

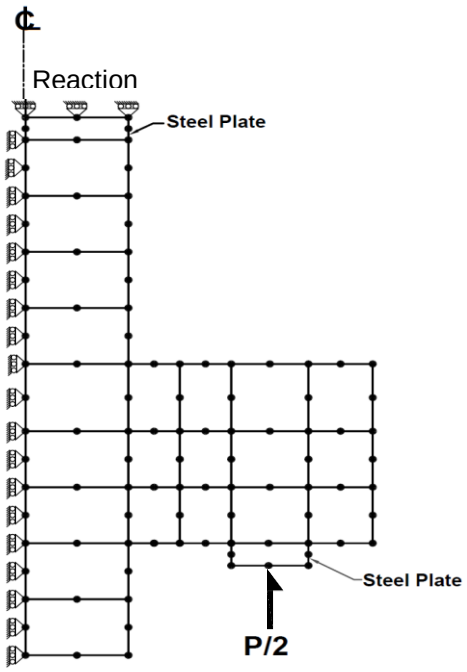

Fig. 7. Finite element mesh and boundary conditions.

4.2 Finite Element Idealization

A computer program coded in FORTRAN 90 was implemented for nonlinear analysis of HSSFRC corbels using finite element modelling, material constitutive relationships were described in the previous sections. Due to symmetry, one-half of the

corbel was modelled using 12 eight-node elements, two of these elements were idealized as steel, representing the steel plates as shown in Fig. (7). The simulation of the support has a significant effect on the behaviour of reinforced concrete members[30], therefore, the support was simulated by three points with the outer points carrying some fraction of total reaction (R) (each outer points carrying 0.175 R).
The numerical analysis have been generally carried out using strain hardening model for fibrous concrete in compression and reduced integration (2*2 Gauss points) rule.

4.3 Analysis of Results

The experimental and numerical load–deflection curves for Corbel No.1 and Corbel No.2 are shown in Fig.(8). This figure shows good agreement for the finite element solution and the proposed constitutive relationships compared with the experimental results. The stiff results at the initial of the load–deflection curve maybe due to the developed models having no concern with the influence of creep. The computed failure loads for all corbels are close to the corresponding experimental collapse load as listed in Table (2).
Crack patterns at ultimate load are shown in Fig.(9), and can be compared with the experimentally observed crack pattern shown in Fig.(10). A good agreement can be observed between the numerical and experimental patterns.

Table 2. Experimental and numerical failure load of corbels

	Corbel No.1	Corbel No.2
Experimental Ultimate Load (kN) [7]	431.5	475.3
Numerical Ultimate Load (kN)(Present Study)	448.8	481.3
Numerical / Experimental	1.04	1.01

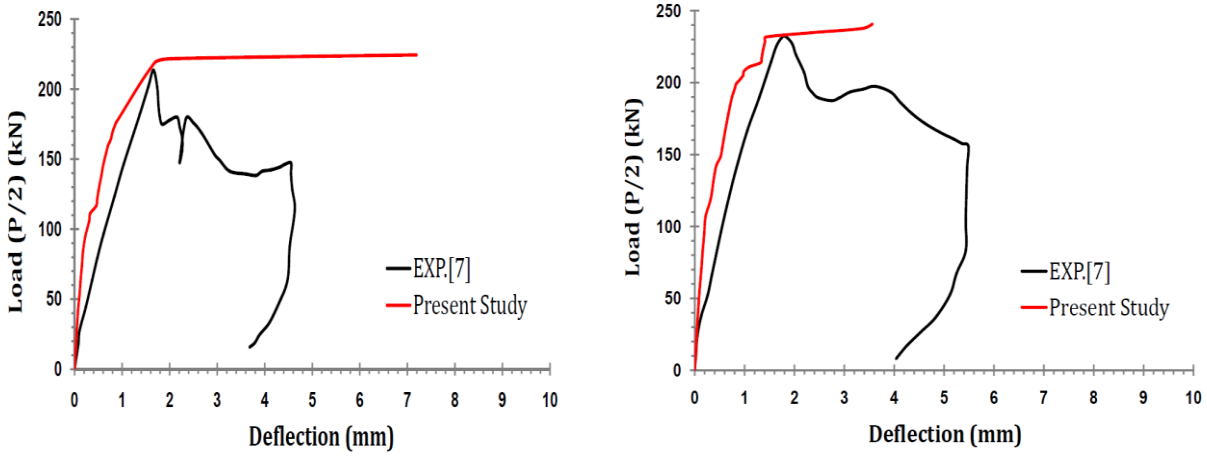

(a)

Fig. 8. Load-deflection curves: (a) Corbel No.1, V_f=0.5; (b) Corbel No.2, V_f=1.0.

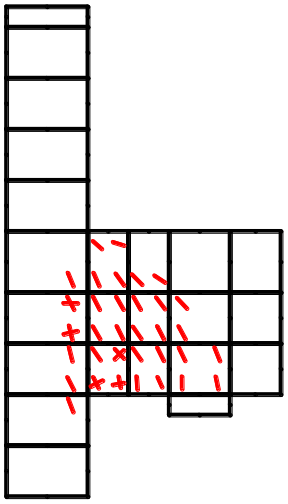

Fig. 9. Numerical crack pattern at ultimate load.

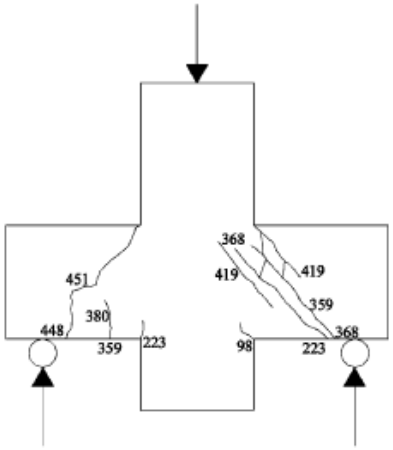

Fig. 10. Experimental Crack pattern[7].

5. Conclusions

Based on the results presented in this study, the following conclusions can be drawn:

1. Many material constitutive relationships for HSSFRC (which contains any type of steel fibres) are adopted. All proposed models showed good agreement with tests data.
2. The developed models proved to give good results for the analysis of HSSFRC corbels subjected to the incremental loading up to failure.
3. The load–deflection curves and crack pattern (location and direction) obtained from the numerical analysis are found to be in a good agreement with the experimental results.
4. The ultimate load of HSSFRC corbels which is obtained from present study are in good agreement with the experimental results.

References

[1] ACI Committee 363, State of the art report on high-strength concrete, Detroit, American Concrete Institute, 1984, pp. 364-411.

[2] Swamy R.N., *"High-strength concrete-material properties and structural behaviours"*, ACI SP-87, Detroit, American Concrete Institute, 1987, pp. 110-146.

[3] Rasmussen L.J., and Baker G., *"Torsion in reinforced normal and high-strength concrete beams-Part1 experimental test series"*, ACI Structural Journal, Vol.92, No.1, 1995, pp. 56-62.

[4] Hsu L.S., and Hsu C.T.T., *"Stress-strain behavior of steel-fiber high-strength concrete under Compression"*, ACI Structural Journal, Vol.9, No.4,1994, pp. 448-457.

[5] ACI Committee 544, State of the art report on fiber reinforced concrete, Detroit, Fiber Reinforced Concrete Int., Symposium, ACI publication, SP-81, 1984, pp. 411-432.

[6] Muhammad A.H., *"Behavior and strength of high-strength fiber reinforced Concrete corbels subjected to monotonic or cyclic (repeated) loading"*, PhD Thesis, University of Technology, Baghdad, Iraq, 1998, 172 pp.

[7] Campione G., and La Mendola L., *"M.L. Mangiavillano, Steel fiber- reinforced concrete corbels: experimental behavior and shear strength prediction"*, ACI Structural Journal,Vol.104, No.5, 2007, pp. 570-579.

[8] Abdul-Razzak A.A., Mohammed Ali A.A., *"Modelling and Numerical Simulation of High Strength Fibre Reinforced Concrete Corbels"*, Applied Mathematical Modelling, Vol.35, No.6, 2011, pp.2901-2915.

[9] Abdul-Razzak A.A., Mohammed Ali A.A., *"Influence of Cracked Concrete Models on the Nonlinear Analysis of High Strength Steel Fibre Reinforced Concrete Corbels"*, Composite structures, Vol.93, No.9, 2011, pp.2277-2287.

[10] Thomas J., and Ramaswamy A., *"Mechanical properties of steel fiber-reinforced concrete"*, ASCE Journal of Materials in Civil Engineering, Vol.19, No.5, 2007, pp. 385-392.

[11] Mansur M.A., Chin M.S., and Wee T.H., *"Stress–strain relationship of high-strength fiber concrete in compression"*, ASCE Journal of Materials in Civil Engineering, Vol.11, No.1, 1999, pp. 21-29.

[12] Ezeldin A.S., and Balaguru P.N., *"Normal- and high-strength fiber reinforced concrete under compression"*, ASCE Journal of Materials in Civil Engineering, Vol.4, No.4, 1992, pp.415-429.

[13] Bencardino F., Rizzuti L., Spadea G., and Swamy R.N., *"Stress–strain behavior of steel fiber reinforced concrete in compression"*, ASCE Journal of Material in Civil Engineering, Vol.20, No.3, 2008, pp. 255-263.

[14] Lin W.T., Huang R., Lee C.L., and Hsu H.M., *"Effect of steel fiber on the mechanical properties of cement-based composites containing silica fume"*, Journal of Marine Science and Technology, Vol.16, No.3, 2008, pp. 214-221.

[15] Ashour S.A., Wafa F.F., and Kamal M.I., *"Effect of the concrete compressive strength and tensile reinforcement ratio on the flexural behavior of fibrous concrete beams"*, Engineering structures, Vol.22, No.9, 2000, pp.1133-1146.

[16] Song P.S., and Hwang S., *"Mechanical properties of high-strength steel fiber-reinforced concrete"*, Construction and Building Materials, Vol.18, No.9, 2004, pp. 669-673.

[17] Koksal F., Altun F., Yigit I., and Sahin Y., *"Combined effect of silica fume and steel fiber on the mechanical properties of high strength concretes"*, Construction and Building Materials, Vol.22, No.8, 2008, pp.1874-1880.

[18] Romualdi J.P., and Mendal J.A., *"Tensile strength of concrete effected by uniformly distributed closely spaced short lengths of wire reinforcement"*, ACI Journal, Vol.61, No.6, 1964 pp.657-671.

[19] Abdul-Razzak A.A., *"Nonlinear finite element analysis of fibrous reinforced concrete structural members"*, Ph.D. Thesis, University of Mosul, Mosul, Iraq, 1996, 237 pp.

[20] Bayramov F., Tasdemir C., and Tasdemir M.A., *"Optimisation of steel fibre reinforced concretes by means of statistical response surface method"*, Cement & Concrete Composites, Vol.26, No.6, 2004, pp. 665-675.

[21] Kurihara N., Kunieda M., Kamada T., Uchida Y., and Rokugo K., *"Tension softening diagrams and evaluation of properties of steel fiber reinforced concrete"*, Engineering Fracture Mechanics, Vol.65, No.2-3, 2000, pp. 235-245.

[22] Bencardino F., Rizzuti L., Spadea G., and Swamy R.N., *"Experimental evaluation of fiber reinforced concrete fracture properties"*, Composites:Part B, Vol.41, No.1, 2010,
pp.17-24.

[23] Hinton E., and Owen D.R.J., *"Finite Element Software for Plates and Shells"*, Pineridge Press, Swansea, U.K., 1984.

[24] Lim D.H., and Nawy E.G., *"Behaviour of plain and steel-fibre-reinforced high-strength concrete under uniaxial and biaxial compression"*, Magazine of Concrete Research, Vol.57, No.10, 2005, pp.603-610.

[25] Hussein A., and Marzouk H., *"Behavior of high-strength concrete under biaxial stresses"*, ACI Materials Journal, Vol.97, No.1, 2000, pp.27-36.
[26] Hinton E., and Owen D.R.J., "*Finite element programming"*, Academic Press INC, London, U.K., 1977.
[27] Zeinkiewicz O.C., and Taylor R.L.,*"Finite element method for solid and structural mechanics"*, Elsevier Butterworth-Heinemann, Sixth Edition, 2005.
[28] Ranjabran A.,*"Embedding of reinforcements in reinforced concrete elements implemented in DENA"*, Computer and Structures, Vol.40, No.4, 1991, pp.925-930.
[29] Mohammed Ali A.A., *"Non Linear Analysis of High Strength Fibrous Reinforced Concrete Corbels Using Plane Stress Elements"*, M.Sc. Thesis, University of Mosul, Mosul, Iraq, 2011, 146 pp.
[30] Al-Ta'an S.A., and Abdul-Razzak A.A., *"Influence of support simulation on the analysis of fibrous reinforced concrete deep beams"*, Al-Rafidain Engineering Journal, Vol.7, No.2, 1999, pp. 70-85.
[31] Haido J.H., Abu Bakar B.H., Abdul-Razzak A.A., and Jayaprakash J., *"Dynamic response simulation for reinforced concrete slabs"*, Simulation Modelling Practice and Theory, Vol.18, No.6, 2010, pp.696-711.

Nonlinear Time Dependent Finite Element Analysis of Reinforced Concrete Beams and Columns

S. A. Al-Ta'an / Professor **S. S. S. Yakoob / Assistant lecturer**
Department of Civil Engineering, Mosul University, IRAQ
Corresponding author, S. A. Al-Ta'an, Email: saad.altaan@yahoo.com

Abstract

Creep and shrinkage of concrete are considered to be the most important factors that affect the long term behaviour of reinforced and prestressed concrete members.
In this study a nonlinear time dependent finite element analysis of reinforced concrete concrete beams and columns is presented. Plane frame element with composite layer system is used to represent the concrete and the reinforcing steel with an additional axial degree of freedom used at the mid length of the frame element to model the strain variation across the element length. An incremental – iterative scheme based on Newton – Raphson's method is used to solve the nonlinear equations of equilibrium depending on the displacement criterion to check the convergence of the solution.
The nonlinear behaviour of concrete in compression, cracking, yielding of steel and geometric nonlinearity were taken into account. Time dependent effects (creep and shrinkage) of concrete were calculated using empirical equations that depends on the creep and shrinkage calculated from ACI Committee (209) recommendations for ordinary concrete. The predicted time dependent deflection using the adopted numerical procedure together with the materials constitutive relationships, showed good agreement with the experimental results of beams and columns made with low, medium and high strength concrete.
Keywords: Beam, column, creep, deflection, finite element, shrinkage.

التحليل غير الخطي المعتمد على الزمن بالعناصر المحددة للعتبات والأعمدة الخرسانية المسلحة

سعد علي الطعان / أستاذ **سمير سعدي يعقوب** / مدرس مساعد
قسم الهندسة المدنية / جامعة الموصل

الخلاصة

زحف وانكماش الخرسانة يعتبران من أهم العوامل التي تؤثر على سلوك الأعضاء الخرسانية المسلحة والمسبقة الجهد. وفي هذه الدراسة تم عرض دراسة تتضمن التحليل غير الخطي المعتمد على الزمن لعتبات وأعمدة خرسانية مسلحة. تم استعمال عناصر هيكلية ذات طبقات لتمثيل الأعضاء الخرسانية المسلحة مع درجة حرية محورية إضافية في منتصف العنصر لتمثيل التغير في الانفعالات على طول العنصر. استعملت طريقة الزيادة والتكرار المستندة على طريقة نيوتن رافسون لحل معادلات التوازن غير الخطية واعتمد معيار الإزاحة لتدقيق تقارب الحل.
سلوك الخرسانة غير الخطي في الانضغاط، التشقق، خضوع حديد التسليح والتغير الشكلي اخذ بنظر الاعتبار عند التحليل. التأثيرات المعتمدة على الزمن (الزحف والانكماش) للخرسانة اعتمدت على المعادلات التجريبية المعدة من قبل لجنة 209 لمعهد الخرسانة الأمريكي للخرسانة الاعتيادية. الأود الطويل الأمد الذي قدر باستعمال الطريقة العددية والعلاقات التكوينية للمواد في هذه الطريقة أظهرت توافقا جيدا مع نتائج عملية لعتبات وأعمدة مصنعة من خرسانة قليلة، متوسطة وعالية المقاومة.

Introduction

The present trend towards using higher strength concrete, reinforcing steel and the strength design method since the early sixties of the last century resulted in shallower sections of reinforced concrete members. For this reason, the problem of predicting and controlling deflections of reinforced concrete flexural members during the service conditions has become increasingly important since then. Excessive deflection can cause either aesthetic or functional problems, may results in damage of either structural or non-structural elements and may cause discomfort to occupants where dynamics effects occur due to insufficient stiffness [1]. However, long term deflection is more important than the short term one and in most cases it is much more than the short term deflection [2,3].

Concrete is one of the materials whose properties change with time like the compressive strength, tensile strength and elastic modulus. Other important properties which are also time-dependent are shrinkage and creep. These changing properties affect the internal strain and stress distribution and lead to a redistribution of the internal forces that results in values different from those induced at the initial time of loading. The effect of creep and shrinkage on reinforced and prestressed concrete members can be summarized as follow [2]:

1- The shrinkage strains usually create tensile stresses in concrete leading to cracking,
2- In flexural members, the deflection and the stresses in the compression steel increase with time,
3- In columns the relaxation of concrete stresses cause an increase in the longitudinal compressive steel stresses,
4- Redistribution of forces in highly stressed regions and
5- In prestressed members, the prestressing force decreases with time and thus reducing the effectiveness of prestressing.

Predicting short and long term deflections was the concern of engineers and researchers long time ago. For more than four decades, the American and Australian codes [4,5] have used Branson's equation to determine an effective second moment of area I_{eff} for the span which is then used to estimate the short term deflections. Bischoff [6] proposed a modified version of Branson's equation that provide a better prediction of immediate deflection. Gilbert and Kilpatrick [7] proposed a simple empirical equations for predicting long term deflections of flexural members using the age-adjusted effective modulus method. The method takes into account the long-term creep and shrinkage- induced changes in curvature of reinforced concrete members. The predicted long term deflections correlate well with measured deflections of beams and one-way slabs.

Since the late seventies of the last century, nonlinear time-dependent finite element analysis is used also to predict the long term behavior of reinforced concrete columns, arches, plain frames and shells taking into account the shrinkage and creep of concrete [8-10].

The object of this study is to develop a time-dependent nonlinear finite element analysis of reinforced concrete beams and columns and to validate the accuracy of the proposed method by comparing the numerical results with published experimental deflection – time relationships for beams made with low and high strength concrete and columns made with medium strength concrete.

Materials Constitutive Relationships

Concrete in compression

The equation proposed by Carreira and Chu for plain concrete in uniaxial compression [11] is used in this investigation:

$$\frac{f_c}{f_c^{'}} = \frac{\beta(\varepsilon_c / \varepsilon_o)}{\beta - 1 + (\varepsilon_c / \varepsilon_o)^{\beta}} \tag{1}$$

where f_c is the stress at strain ε_c, $f_c^{'}$ is the cylinder compressive strength of concrete, ε_o is the strain at peak stress and proportional to the compressive strength and usually taken equal to 0.002 and β is a variable that depends on the concrete strength as given in Equation (2):

$$\beta = (\frac{f_c^{'}}{32.4})^3 + 1.55 \tag{2}$$

Concrete in tension

In this investigation the following equation which was developed for reinforced concrete in uniaxial tension by Carreira and Chu, [12] is used in this investigation:

$$\frac{f_t}{f_t^{'}} = \frac{\beta(\varepsilon_t / \varepsilon_t^{'})}{\beta - 1 + (\varepsilon_t / \varepsilon_t^{'})} \tag{3}$$

where f_t is the stress at strain ε_t, β is the variable defined in Eq. (2) , $f_t^{'}$ is the tensile strength and $\varepsilon_t^{'}$ is the corresponding strain and ranges between 100-130 μs. In the absence of test data $f_t^{'}$ for normal strength concrete, can be taken as [4]:

$$f_t' = 0.5\sqrt{f_c'} \tag{4}$$

For high strength concrete, the tensile strength of concrete can be taken as follow [13]:

$$f_t' = 0.58\sqrt{f_c'} \tag{5}$$

Elastic modulus of concrete

The equation recommended by the ACI Committee [4] for normal weight concrete is used in this investigation:

$$E_c = 4730\sqrt{f_c'} \tag{6}$$

For high strength concrete, the following equation which was proposed by Carraquillo et al. [14] is used:

$$E_c = 3320\sqrt{f_c'} + 6900 \tag{7}$$

Time dependent strains

The ACI Committee 209 recommendations [15] are used for predicting the shrinkage and creep strains with the corresponding correction factors for mixes with properties other than the following values; the relative humidity (≤ 40%), thickness of the member (≤ 150 mm), slump (≤ 130 mm), fine aggregate percentage by weight (40-60%), cement content (279 – 445 kg/m^3), air content (≤ 6%) and age when the member is loaded (7 days) for moist cured concrete. The ultimate shrinkage strain is taken equal to 780 μs and the ultimate creep coefficient equal to 2.35.

Finite Element Formulation

Since the shear deformation is not dominant in reinforced concrete members with the usual dimensions, a plane frame element with a composite layer system is used to represent the analyzed beams and columns in this study. At each node there are three degrees of freedom (two translations and one rotation). An additional mid-length axial degree of freedom is imposed to simulate the variation of strain along the element length making the element stiffness matrix (7×7). This additional degree of freedom is eliminated latter on using static condensation leaving the size of the stiffness matrix of the element (6×6). The additional mid-length axial degree of freedom is calculated then using the original stiffness (7×7) matrix and the displacements at the external nodes of the element. The derivation of the shape function, stiffness matrix and the solution procedure is mentioned elsewhere [16-18]. An iterative scheme based on Newton-Raphson's method is employed for the nonlinear solution algorithm. A displacement criterion is used to check the convergence of the nonlinear solution. The average modified absolute value is used as follow:

$$\frac{1}{N}\sum_{i=1}^{N}\left|\frac{\Delta r_i}{r_{i,ref.}}\right| \le Tol. \qquad (8)$$

N=total degrees of freedom of the member, Δr_i= change in the degree of freedom (i) between the previous and the current iteration,

$r_{i,ref.}$ = reference displacement which represent the largest value of a certain displacement component and

Tol. = a prescribed value for the tolerance which varied in this study between (0.8-2.5%) depending on the required accuracy [17].

The time interval used in the analysis depend on the problem, but in general an interval of 5 days is used in the early ages due to the relatively rapid increase of shrinkage and creep strains and increased latter on to 25 days after the first 100 days. However for the high strength concrete beams of example 2 below, the time interval in the early ages was 3 days.

RESULTS AND DISCUSSION

EXAMPLE 1

Washa and Fluck [19] have tested a series of reinforced concrete beams under sustained uniformly distributed load. The beam B3 which was simply supported on an effective span of 6.096 m and uniformly loaded with a sustained load of 1.561 kN/m (at the age of 14 Days) is

chosen in this study for the analysis. The beam has the following properties: b = 152.4 mm, h = 203 mm, d = 157mm, A_s = 396 mm^2, $f_c^{'} = 23.6$ MPa, $f_y = 324$ MPa and E_s = 22972 MPa. The properties of the concrete mix and other relevant data are given in Table (1).

Table (1) Mix properties of concrete for Example 1 [19]

t_o (Days)	Relative Humidity (%)	Slump (mm)	Air Content (%)	Thickness (mm)	Cement Content (kg/m^3)	Fines (%)
7	47.5	152	4	203.2	333.3	37

The span is divided into 48 elements and each element into 24 layers besides the steel layers. The variations of the measured and numerical values of the deflection with time are shown in Figure (1) and it may be seen that very good agreement is obtained. The Figure shows also that the long term deflection due to creep and shrinkage increase with time at a reduced rate similar to the increase in creep and shrinkage strains of concrete.

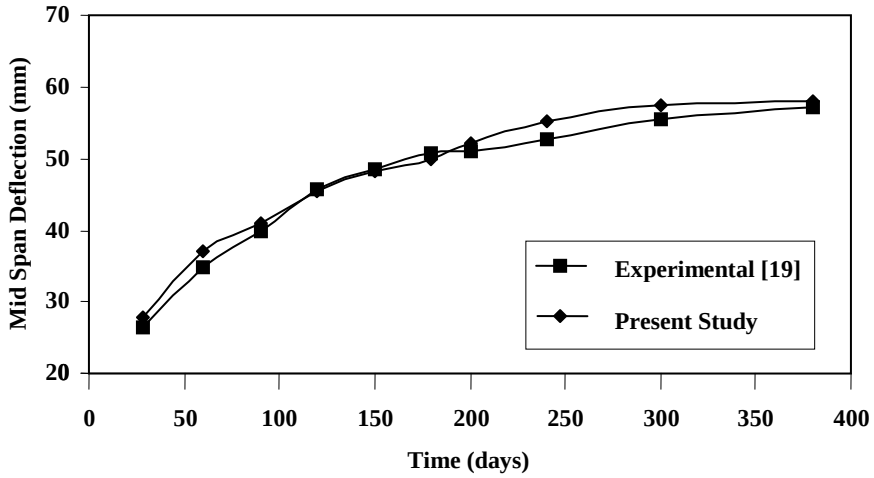

Figure (1) Variation of the deflection with time, beam B3 [19]

EXAMPLE 2

A series of high strength concrete beams with and without steel fibres were tested by Ashour et al. [20] under long term loading, the beams without steel fibres were chosen for the analysis in this study. Figure (2) and Table (2) show the geometry and the reinforcing detail. The beams were divided into six elements in the shear spans and four elements in the constant bending moment region (a total of 16 elements) and each element was divided into 12 layers in addition to the steel layers. The beams were loaded by 6 kN (2×3 kN) which is about 50% of the ultimate load. The loads were sustained for a period of 180 Days. The correction factors for the concrete mix and other parameters are shown in Table (3). The creep coefficient is taken as 60% of the value for normal strength concrete, since the creep in high strength concrete is about (50-75%) of that for normal strength concrete as mentioned by Ngab et al. [21].

Figures (3-5) show the variation of the deflection with time for the three beams whose details are shown in Tables (2-3). The good agreement between the numerical and the measured deflection is clear from the three Figures. It is well known that the compression steel reduce the long term deflection due to creep and shrinkage. Figure (6) show that when the compression steel equal to 50 and 100% of the tension steel the total long term deflection at the age of 180 days reduced by 19 and 28% respectively relative to that of the singly reinforced beams.

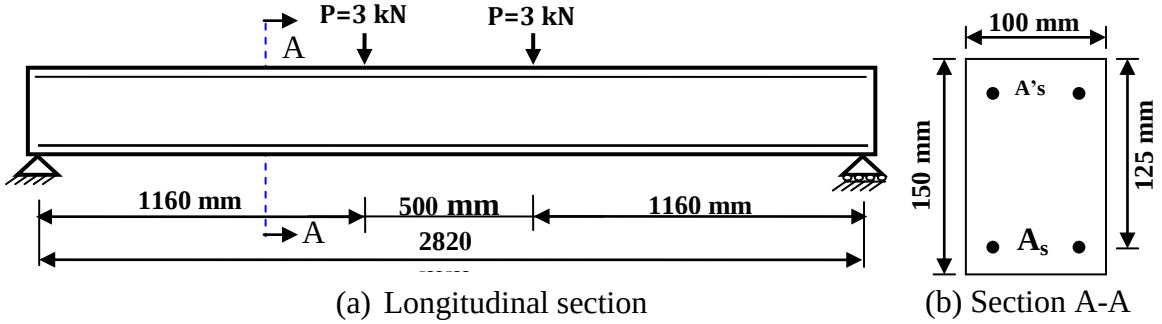

(a) Longitudinal section (b) Section A-A

Figure (2): Geometry and reinforcement details of Beams (BS), (a) Longitudinal section, (b) Section A-A [20]

Table (2) Details of the beams tested by Ashour's et al. [20]

Beam Designation	Longitudinal Reinforcement		f'_c (MPa)
	Tension	Compression	
BS-0.0	2ϕ10	-----	80.19
BS-0.5	2ϕ10	1ϕ10	80.19
BS-1.0	2ϕ10	2ϕ10	80.19

Table (3) Properties of the Concrete mix for Example (2)

t_o (Days)	Relative Humidity (%)	Slump (mm)	Air Content (%)	Thickness (mm)	Cement Content (kg/m^3)	Fines (%)
3	80	45	*	150	548	*

* Not specified and the correction factor assumed = 1.0

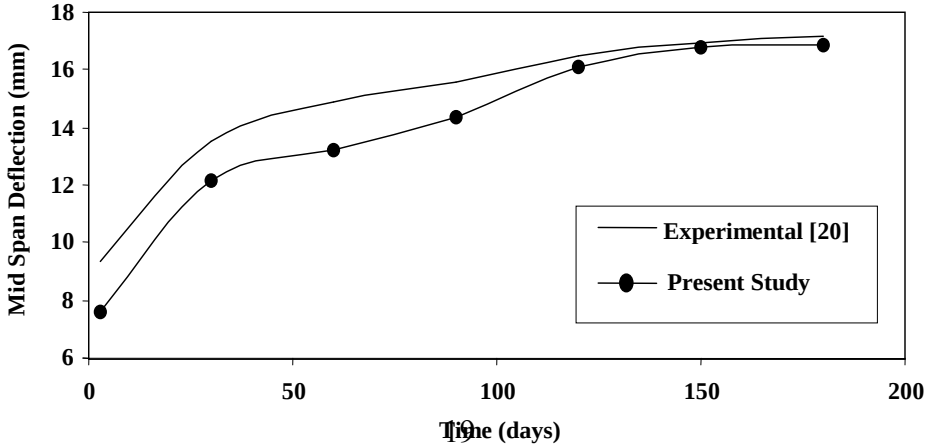

Figure (3) Variation of the deflection with time for beam BS-0.0 ($A'_s/A_s = 0$)

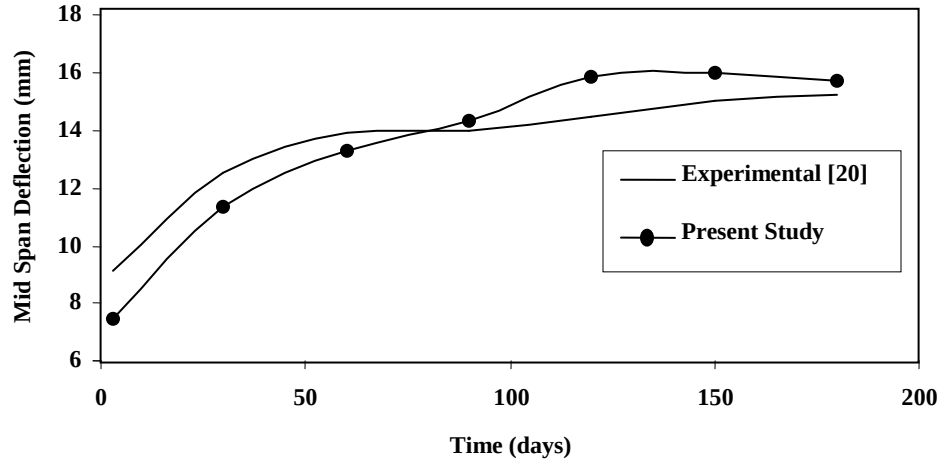

Figure (4) Variation of the deflection with time for beam BS-0.5 (A'_s/A_s=0.5)

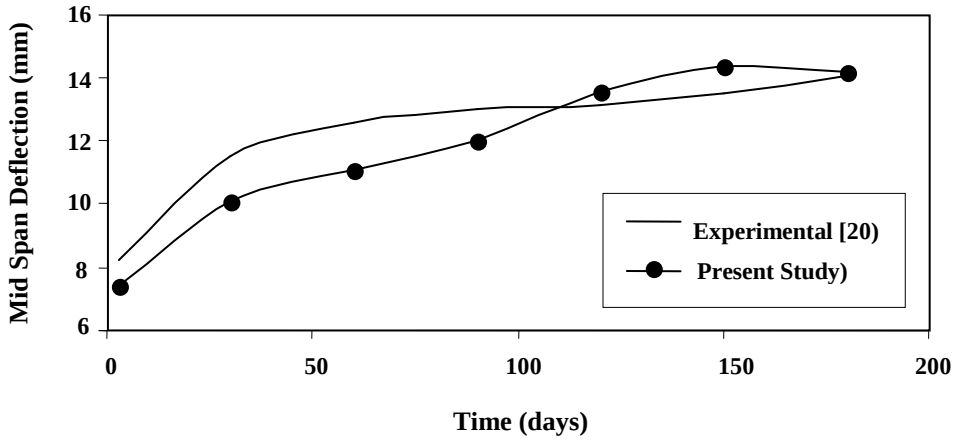

Figure (5) Variation of the deflection with time for beam BS-1.0 (A'_s/A_s=1.0)

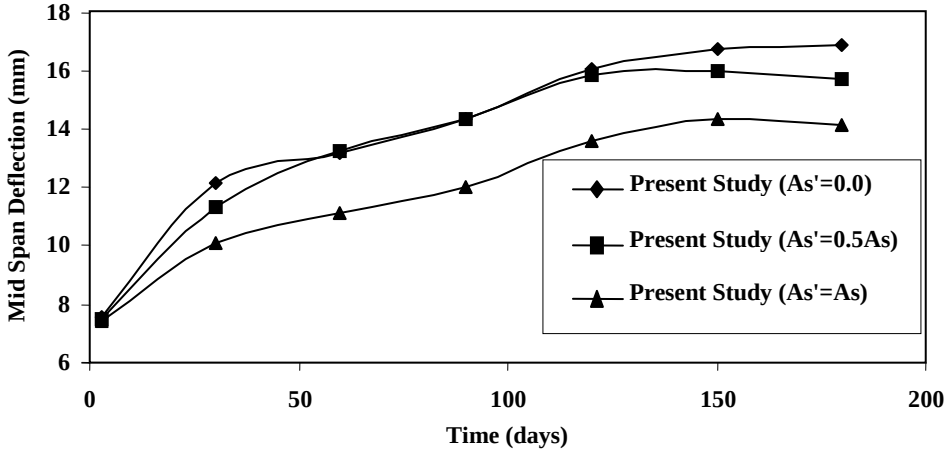

Figure (6) Influence of the compression steel on the calculated long term deflection

EXAMPLE 3

A series of columns have been tested by Behan and Connor [22] as shown in Figure (7) with an initial crookedness (deflection y_o) under short and long term loading. The initial deflection is represented in this study by a parabolic relationship as shown in the following equation:

$$y = \frac{4y_o}{l}.x - \frac{4y_o}{l^2}.x^2 \qquad (9)$$

Where y_o = initial deflection at the mid height of the column.

Two columns (L110 and L111) with 1220 mm long each have been tested under long term loading are chosen for the analysis. The columns were reinforced with two layers of steel (3 # 4.04) and the distance between the two layers is 28 mm. The cross-section and the reinforcement detail are shown in Figure (7) and Table (4). The yield strength of the bars = 231 MPa and the elastic modulus = 206 GPa. Due to symmetry, half of the column was analyzed. Half of the column is represented by 10 finite elements and each element with 18 layers in addition to the steel layers. The two columns were subjected to the sustained loads given in Table (4).

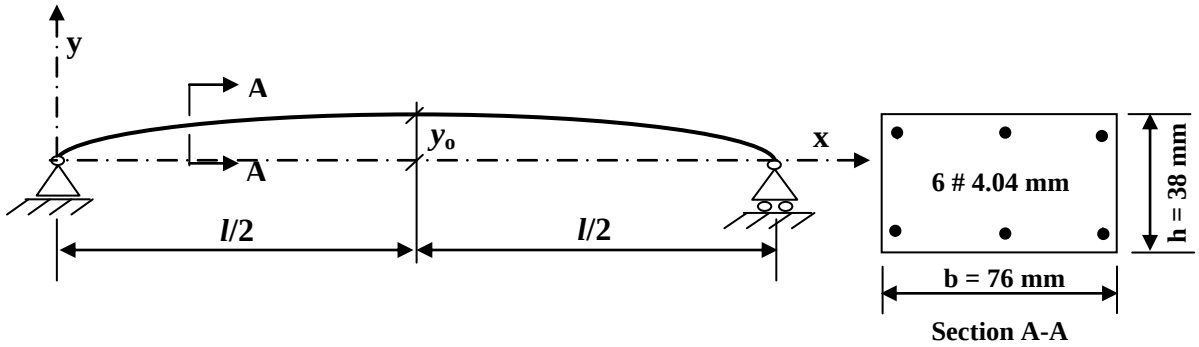

Figure (7) Column centerline and cross-section of Example 3 [22]

Table (4) Details of the columns of example 3 [22]

Column Number	Column Height (mm)	Slenderness Ratio (***l/h***)	Initial Central Deflection (mm)	Sustained axial load (kN)	f'_c (MPa)
L 110	1220.0	32	2.591	32.04	42.1
L 111	1220.0	32	2.057	26.7	41.9

The variation of the measured and calculated deflections with time for the two columns is shown in Figures (8-9), a good agreement can be noticed between the two variations with time.

A relationship is drawn between the age and the sustained loads for the two columns (having the same slenderness ratio), the load that can be sustained at the age of 10000 Days (27.4 years) is found from this relationship and called the creep capacity [22]. A good agreement can be noticed in Table (5) and Figure (10) between the experimental and predicted values of the column lives and creep capacities of the two columns. Table (5) show that the creep capacity of the analyzed reinforced concrete columns inversely proportional with the eccentricity and applied sustained load.

Table (5) Experimental and predicted column life and creep capacity for columns L110 and L111

Column number	Column life (Days)		Creep Capacity at 10000 Days (kN)	
	Experimental	Present Study	Experimental [22]	Present Study
L 110	16	13	20.915	19.384
L 111	277	288		

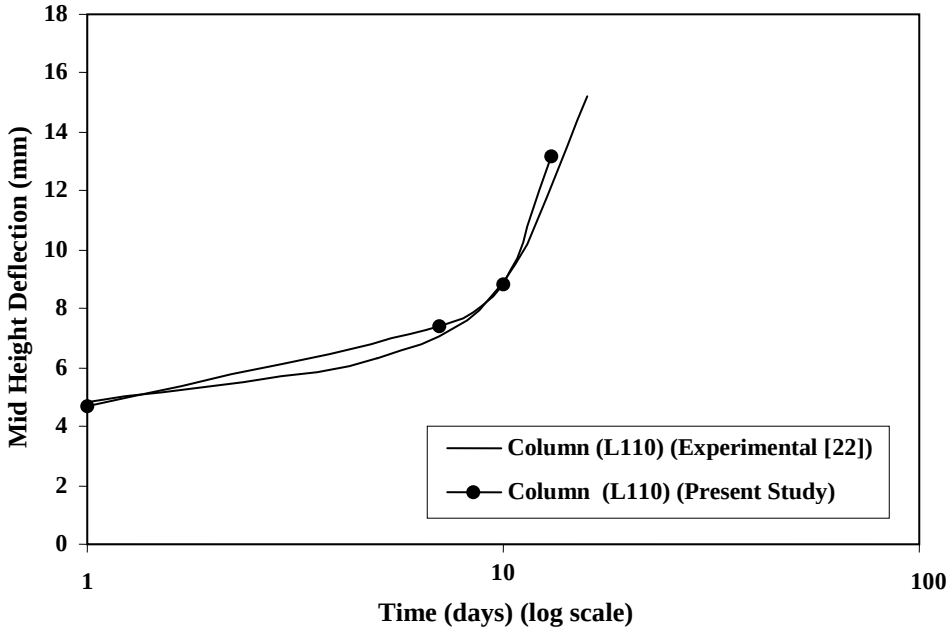

Figure (8) Variation of the deflection with time for column L110 [22]

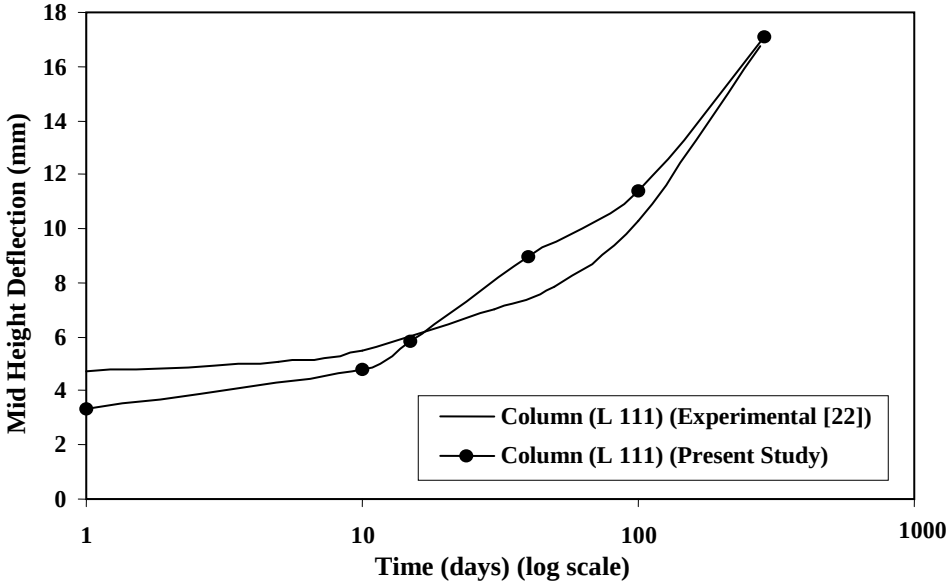

Figure (9) Variation of the deflection with time for column L111[22]

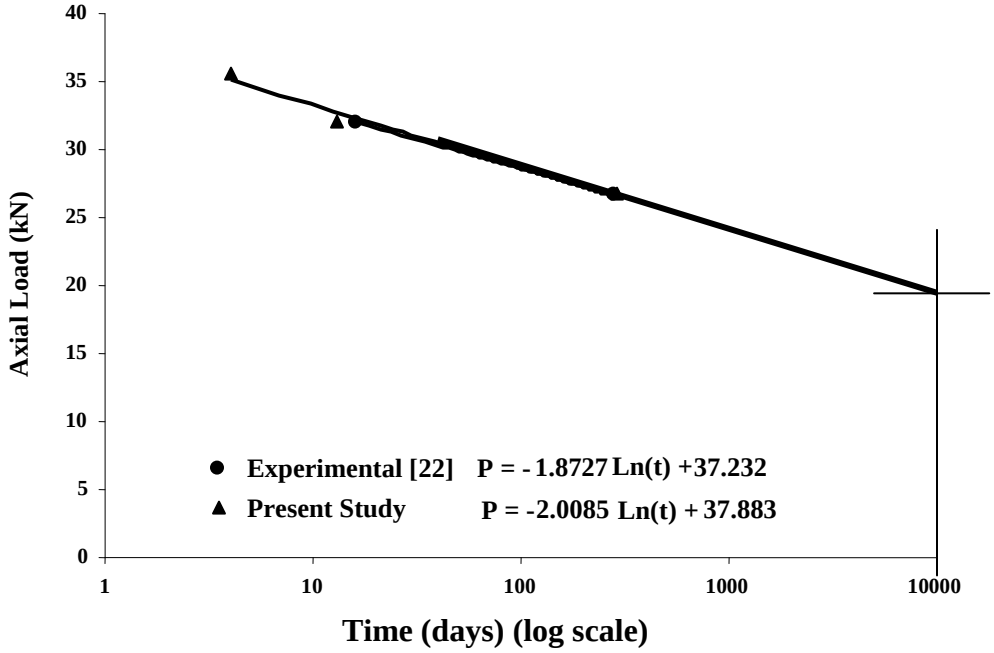

Figure (10) Variation of the Axial Load with time for columns L110, L111[22]

Conclusions

1- The chosen plane frame element with the composed layer system, the solution strategy and the adopted materials constitutive relationships is capable of tracing the time dependent behaviour of normal, medium and high strength reinforced concrete beams and columns.
2- The compression steel reduces the long term deflection by as much as 28% relative to that of the singly reinforced beams.
3- The time dependent behaviour of reinforced concrete columns like the column life and creep capacity is also predicted reasonably good using the adopted type of the finite element together with the materials constitutive relationships.
4- The creep capacity of the reinforced concrete columns inversely proportional with the eccentricity and applied sustained load.
5- The long term behaviour should be taken into account during the design of reinforced concrete members and the proposed procedure for calculating the column life and creep capacity can be used as a design guide.

References

1- Gilbert, R. I.," Shrinkage, Cracking and Deflection- the Serviceability of Concrete Structure", Electronic Jour. of Structural Engineering, Vol. 1, No. 1, 2001, pp. 2-14
2- Branson, D. E.," Deformation of Concrete Structures", McGraw – Hill Book Company, 1977, pp. 111-340.
3- Ghali, A., Favre, R. and Elbadry, M., " Concrete Structures: Stresses and Deformation", Third Ed., Spon Press, 2002, 584 pp.

4- ACI Committee (318-11), " Building Code Requirements for Structural Concrete", ACI 318-11, American Concrete Institute, Farmington Hills, MI., 2011, 369 pp.
5- Australian Standard, " Concrete Structures" , 3600 – 1988, Standards Association of Australia, 108 pp.
6- Bischoff, P. H., "Reevaluation of Deflection Prediction for Concrete Beams Reinforced with Steel or FRP Bars", Jour. Of Structural Engineering, ASCE, Vol. 131, No. 5, 2005, pp. 752-767.
7- Gilbert, R. I. and Kilpatrick, A., " Improved Predictions of the Long Term Deflections of Reinforced Flexural Members", Proceedings of *fib* Symposium PRAGUE 2011, pp. 1-9.
8- Aldstedt, E., and Bergan, P.G., " Nonlinear Time–Dependent Concrete – Frame Analysis", Journal of Structural Division, Proceeding of ASCE, Vol. 104, No. ST7, July 1978, pp. 1077-1092.
9- Kang, Y.J., and Scordelis, A.C., " Non – Linear Analysis of Reinforced and Prestressed Concrete Frames", Journal of The Structural Division, Proceeding of ASCE, Vol. 106, No. ST2, Feb. 1980, pp. 445 – 461.
10- Chan, E., " Nonlinear Geometric Material and Time – Dependent Analysis of Reinforced Concrete Shells with Edge Beams", UC – SEMS, Report No.82/8, California University, Berkeley, Dec. 1982.
11- Carreira, D.J. and Chu, K.H., " "Stress-Strain Relationship for Plain Concrete in Compession", ACI Journal, Proceedings, Vol. 82, No.6, June 1985, pp. 797-804.
12- Carreira, D.J. and Chu, K.H., " Stress-Strain Relationship for Reinforced Concrete in Tension", ACI Journal, Proceedings, Vol. 83, No.1, Jan.-Feb. 1986, pp. 21-28.
13- ACI Committee (363-1997), " State-of-Art-Report of High Strength Concrete", ACI Manual of Concrete Practice, 1997, 55 pp.
14- Carraquillo, R.L., Nilson, A.H. and Slate, F.O., " Properties of High Strength Concrete Subjected to Short Term Loads", ACI Journal, Proceedings, Vol. 78, No. 8, May-June 1981, pp.171-178.
15- ACI Committee 209 (1997), " Prediction of Creep, Shrinkage, and Temperature Effects in Concrete Structures", ACI Manual of Concrete Practice, (ACI 209R-92), (Re approved 2002), 47 pp.
16- Ezzadeen, N.A.," Nonlinear Geometric and Material Finite Element Analysis of Reinforced Fibrous Concrete Frames", MSc. Thesis, University of Mosul, Iraq, 1991.
17- Yakoob, S. S. S.," Nonlinear Time Dependent Finite Element Analysis of Fibrous Reinforced Concrete Frames", M.Sc. Thesis, Mosul University, Iraq, 2005, 130pp.
18- Cook, R.D., " Concepts and Applications of Finite Element Analysis", Second Edition, John, Wiley and Sons, Inc., USA, 1981, 537 pp.
19- Washa, G.W. and Fluck, P.G., " Effect of Compressive Reinforcement on the Plastic Flow of Reinforced Concrete Beams", ACI Journal, Proceedings, Vol. 49, No. 2, October 1952, pp. 89-108.
20- Ashour, S.A., Mahmood, K., and Wafa, F.F., " Long-term Deflection of High-Strength Fiber Reinforced Concrete Beams", International Journal of Structural Engineering and Mechanics, Vol.8, No.6, December 1999, pp.531-546.
21- Ngab, A.S., Nilson, A.H. and Slate, F.O., " Shrinkage and Creep of High Strength Concrete", ACI Journal, Vol. 78, No. 4, July-August 1981, pp.255-261.
22- Behan, J.E. and O'Connor, C., " Creep Buckling of Reinforced Concrete Columns", Journal of the Structural Division, Proceeding of ASCE, Vol. 108, No. ST.12, December 1982, pp. 2779-2818.

Development of 3D Hypoelasticty Model for Combined Loading Analysis of Box Beams

Mohamad N. Mahmood **Ali N. Abdul Baki**
Professor **Assistant Lecturer**
Civil Engineering Department/ College of Engineering-Mosul University/ Mosul-Iraq

Abstaract

This paper represents the applicability, ability and accuracy of a modified hypoelasticty model in simulating the concrete behavior under three dimensional loading state. The model is based on orthotropic approach and the concept of equivalent uniaxial strain. The model was adopted for the nonlinear analysis of reinforced concrete box beams under combined torsion and bending loading. The 8-node isoparametric brick elements are used to model the concrete, while the reinforcing bars are idealized by 3D truss axial members connected to the nodes of concrete element assuming perfect bond between the concrete and steel bars. The principal stress axes are assumed to be parallel to the material orthotropic axes. Cracking of concrete was modeled by smeared cracks model with fixed orientation. Tension stiffening model are used to represent the post-cracking behavior of concrete. The validity of the concrete material model and the accuracy of the developed computer program for the nonlinear analysis of box beams under combined torsion and flexural loadings are checked by comparing the predicted results with that of the experimentally tested beams. The predicted results showed good agreement with the published experimental results.

Keywords: Box beams**,** Finite Element, Hypoelasticity, Reinforced concrete.

تطوير نموذج متدني المرونة ثلاثي ألأبعد لتحليل العتبات الصندوقية تحت تأثير ألأحمال ألمركبة

أ.د. **محمد نجم محمود** علي نذير عبد الباقي
قسم الهندسة المدنية / كلية الهندسة / جامعة الموصل

الخلاصة

يتضمن البحث عرض قابلية ودقة نموذج متدني المرونة المطور في تمثيل تصرف الخرسانة تحت تاثير الأحمال ثلاثية الأبعاد. يعتمد النموذج على مبدأ التعامد والأنفعال الأحادي المكافئ. استخدم النموذج في التحليل غير الخطي للأعتاب الخرسانية الصندوقية المسلحة تحت تأثير الأحمال المركبة اللي-العزم. استخدمت العناصر الطابوقية موحدة المعلمية ثمانية العقد لتمثيل الخرسانة بينما تم تمثيل قضبان حديد التسليح بأستخدام عنصر القضيب ثلاثي الأبعاد بافتراض ترابط تام بين الخرسانة وحديد التسليح وذلك بربط عقد عناصر القضيب بعقد العنصر الطابوقي. تم تمثيل نموذج التشقق بافتراض حالة الشقوق المنتشرة الثابتة الأتجاه واستخدم نموذج تصلب الشد لتمثيل حالة الخرسانة مابعد مرحلة التشقق. تم التحقق من دقة النموذج وقابلية البرنامج المطور في التحليل غير الخطي للأعتاب الخرسانية الصندوقية المسلحة تحت تاثير الأحمال المركبة لي-عزم وذلك بمقارنة النتائج المستحصلة من التحليل مع النتائج العملية لأعتاب مفحوصة مختبرياً. النتائج المستحصلة اظهرت توافق جيد مع النتائج العملية المنشورة.

1. Introduction

Concrete is a non-homogeneous, anisotropic material with nonlinear response even under small stress levels. Furthermore, concrete exhibits a different behavior under tension and compression stresses. In compression, the response hardens up to a peak stress value that depends on the level of lateral confinement. The post peak behavior depends in general on the level of lateral confinement, while under low confinement; the post-peak response is brittle softening. By increasing confinement stresses, the response of concrete changes to ductile hardening [1, 2]. Under tensile stresses concrete cracks and eventually loses its strength in the direction of crack. The complex nonlinear behavior of concrete makes it difficult material to model. In spite of the widespread interest in modeling of concrete under three-dimensional states of stresses, few models are available for immediate and simple numerical implementation in finite element method. Models developed to date range from very sophisticated laws based on plasticity theory that rely on the definition of a plastic flow rule and on the separation of the deformation into plastic and elastic components, to a simpler models based on phenomenological rules [3]. Concrete model should be able to simulate the most important characteristics of the monotonic and cyclic response of concrete under triaxial state of stresses, while maintaining a certain computational simplicity to allow analyses of structural elements with reasonable computational efforts.Predicting the nonlinear response of reinforced concrete box beams under combined action of torsion and bending is one of complex 3D problems which required a reliable material model.

2. Research Significance

The main emphases of the present study are to develop and check the accuracy of the hypoelastic orthotropic model which is used to simulate the concrete behavior under combined action of stresses, and to check it's applicability in the nonlinear analysis of reinforced concrete box beams.

3. Finite Element Formulation

In this study, concrete is modeled by using isoparametric 8-node brick element which is shown in Fig. (1), each node of this element has three transitional degrees of freedom, full details of both theory and performance of the brick element are given in references [4, 5].

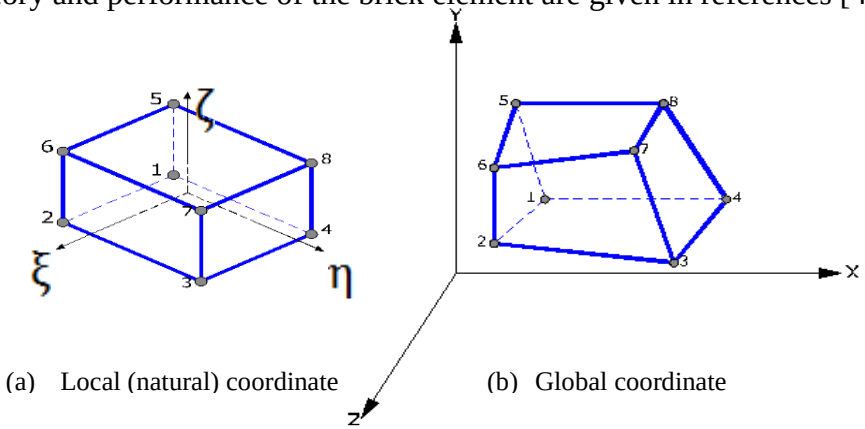

(a) Local (natural) coordinate (b) Global coordinate

Figure (1) 8-node isoparametric brick element (4)

In the present study the discrete bar elements (three dimensional space truss elements) are used to model the reinforcing bars. This element has two nodes with three degrees of freedom (translations) at each node.

4. Three Dimensional Concrete Model

4.1 Hypoelasticity Based Model with Orthotropic Approach

The hypoelasticity approach is based on nonlinear elasticity in which the orthotropic concept is employed to predict the concrete behavior. A hypoelastic models have the ability to capture shear dilatation, non-proportional loading and cyclic response of concrete [1]. The developed hypoelastic model is based on the concept of equivalent uniaxial strain [6]. The principal stress axes are assumed to coincide with the material orthotropic axes.

4.1.1 Triaxial Stress-Strain Relations

It is commonly accepted that concrete was considered as an initially isotropic material that exhibits deformational anisotropy during loading [7, 8, 9]. Consequently, in structures where the stress state at every point is defined by three principal stresses, concrete can be characterized during loading as a nonlinear orthotropic medium with the directions of orthotropy coincident with the principal stress directions [8]. The incremental stress-stain relation of concrete with respect to the orthotropic axes (1, 2, and 3) can be written as,

$$\{d\sigma\} = [\mathrm{C}_\circ]\{d\varepsilon\} \qquad \dots\dots(1)$$

Where $d\sigma$ and $d\varepsilon$ are the vectors of stress and strain increments respectively and $\mathrm{C}_\circ$ is the material matrix which has the following form [8].

$$[C_0] = \frac{1}{\varphi}\begin{bmatrix} E_1(1-\mu_{32}^2) & \sqrt{E_1E_2}(\mu_{13}\mu_{32}+\mu_{12}) & \sqrt{E_1E_3}(\mu_{12}\mu_{32}+\mu_{13}) & 0 & 0 & 0 \\ & E_2(1-\mu_{13}^2) & \sqrt{E_2E_3}(\mu_{12}\mu_{13}+\mu_{32}) & 0 & 0 & 0 \\ & & E_3(1-\mu_{12}^2) & 0 & 0 & 0 \\ & & & G_{12}\varphi & 0 & 0 \\ & symmetrical & & & G_{13}\varphi & 0 \\ & & & & & G_{23}\varphi \end{bmatrix} \qquad \dots\dots(2)$$

in which,

E_i : is the secant modulus of elasticity,$(i = 1,2,3)$.

G_{ij}: is the shear modulus,$(i,j = 1,2,3)$.

μ_{ij} : is the equivalent Poisson's ratio,$(i,j = 1,2,3)$, which is evaluated from the relationships.

$$\left.\begin{aligned} \mu_{12}^2 &= v_{12}v_{21} \\ \mu_{32}^2 &= v_{32}v_{23} \\ \mu_{13}^2 &= v_{13}v_{31} \end{aligned}\right\} \qquad \dots\dots(3)$$

v_{ij} : is the Poisson's ratio of concrete material,$(i,j = 1,2,3)$.

$$\varphi = 1 - \mu_{12}^2 - \mu_{32}^2 - \mu_{13}^2 - 2\,\mu_{12}\,\mu_{32}\,\mu_{13}\,, \text{ and} \varphi > 0 \qquad \dots\dots(4)$$

$$\left.\begin{aligned} G_{12} &= \frac{1}{4\varphi}\left[E_1 + E_2 - 2\mu_{12}\sqrt{E_1E_2} - (\sqrt{E_1}\mu_{23} + \sqrt{E_2}\mu_{13})^2\right] \\ G_{13} &= \frac{1}{4\varphi}\left[E_1 + E_3 - 2\mu_{13}\sqrt{E_1E_3} - (\sqrt{E_1}\mu_{23} + \sqrt{E_3}\mu_{12})^2\right] \\ G_{23} &= \frac{1}{4\varphi}\left[E_2 + E_3 - 2\mu_{23}\sqrt{E_2E_3} - (\sqrt{E_2}\mu_{13} + \sqrt{E_3}\mu_{12})^2\right] \end{aligned}\right\} \quad \ldots\ldots (5)$$

In the finite element implementation, incremental stress-strain relation with respect to the orthotropic axes must be rotated into the global reference system. This is done by using the transformation matrix[T], which contains the direction cosines of the orthotropic axes with respect to the global reference system [10, 11]:

$$[D_c] = [T]^T[C_0][T] \quad \ldots\ldots (6)$$

$[D_c]$:is the material matrix in the global reference system.

4.1.2 Equivalent Uniaxial Strain

The equivalent uniaxial strain is a fictitious strain with no physical meaning except in uniaxial loading case. It is used to trace the deformation history and determine the hysteric behavior of concrete, similar to the effective strain concept that was used in the plasticity theory. It is used to de-couple the three dimensional material law into three equivalent uniaxial constitutive laws. This concept has been first developed by *Darwin and Pecknold* [8]. For a given principal stresses σ_{pi}, the equivalent uniaxial strains $\varepsilon_{ui}$are the strains that would induce the same stresses on the equivalent uniaxial stress-strain curves. The material parameters that define the equivalent uniaxial stress-strain curves depend on the current stress ratio. The equivalent uniaxial strains ε_{ui} are typically derived from the following incremental law.

$$d\varepsilon_{ui} = \frac{d\sigma_{pi}}{E_i} \quad \ldots\ldots (7)$$

where,

$d\sigma_{pi}$: is the increment of the principal stresses.

E_i : is the secant modulus.

The total equivalent uniaxial strain is defined as the sum of the incremental strains $d\varepsilon_{ui}$

$$\varepsilon_{ui} = \int d\varepsilon_{ui} \approx \sum d\varepsilon_{ui} \quad \ldots\ldots (8)$$

They are fictitious strains defined in the current principal stress directions and accumulated in the principal stress directions. This does not mean accumulation about fixed direction but about continuously changing principal stress directions [3].

4.1.3 Incremental Secant Modulus, E_i

In the tensile field, a linear elastic model prior to cracking is used, after cracking the tension-stiffening model based on exponential function is used as shown in Fig. (2), reference [7]

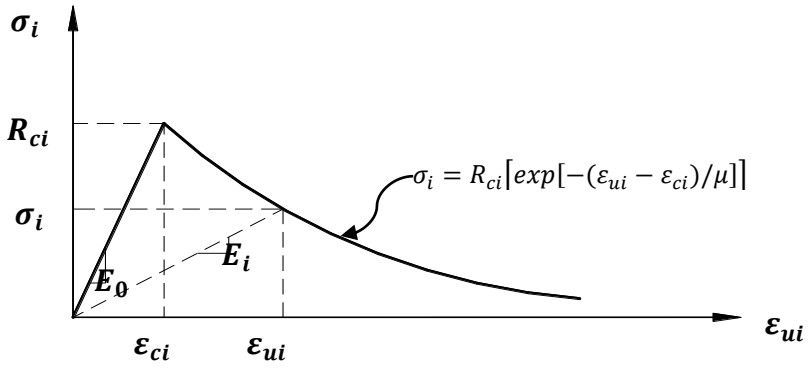

Figure (2) Tensile stress-strain relationship

In the compression field, the proposed expression for the incremental secant modulus is modified from an equation developed by*Elwi and Murray* [8].

$$E_i = \frac{E_\circ}{1 + A_i\left(\frac{\varepsilon_{ui}}{\varepsilon_{ci}}\right) + B_i\left(\frac{\varepsilon_{ui}}{\varepsilon_{ci}}\right)^2 + C_i\left(\frac{\varepsilon_{ui}}{\varepsilon_{ci}}\right)^3} \quad (i = 1,2,3) \qquad \ldots\ldots (9)$$

However, in place of the *"equivalent uniaxial strain"*, the incremental secant modulus E_i is expressed as a function of a strain indicator ε_{si} proposed by *Tho, et al.* [12].

$$E_i = \frac{E_\circ}{1 + A_i\left(\frac{\varepsilon_{si}}{\varepsilon_{ci}}\right) + B_i\left(\frac{\varepsilon_{si}}{\varepsilon_{ci}}\right)^2 + C_i\left(\frac{\varepsilon_{si}}{\varepsilon_{ci}}\right)^3} \quad (i = 1,2,3) \qquad \ldots\ldots (10)$$

where, $E_\circ$ is the initial elastic modulus and the coefficients $(A_i, B_i \text{and} C_i)$ are evaluated as follows:

$$\left.\begin{aligned} A_i &= C_i + K_i - 2 \\ B_i &= 1 - 2C_i \\ C_i &= K_i\frac{(K_{\sigma i} - 1)}{(K_{\varepsilon i} - 1)^2} - \frac{1}{K_{\varepsilon i}} \end{aligned}\right\} \qquad \ldots\ldots (11)$$

$$\left.\begin{aligned} K_i &= E_\circ\frac{\varepsilon_{ci}}{R_{ci}} \\ K_{\varepsilon i} &= \frac{\varepsilon_{fi}}{\varepsilon_{ci}} \\ K_{\sigma i} &= \frac{R_{ci}}{R_{fi}} \end{aligned}\right\} \qquad \ldots\ldots (12)$$

Eq. (12) needs the values at two control points to be defined. These are the stress and corresponding strain at failure$(R_{ci}, \varepsilon_{ci})$, and an arbitrary point on the descending branch of the stress-strain curve, $(R_{fi}, \varepsilon_{fi})$ as shown in Fig. (3) [8], and the determination of the stresses and the corresponding strains at failure $(R_{ci}, \varepsilon_{ci})$ are discussed following sub-sections. The value of the control point $(R_{fi}, \varepsilon_{fi})$ is taken to be$(0.25R_{ci}, 4.0\ \varepsilon_{ci})$ [2,7,8,9].

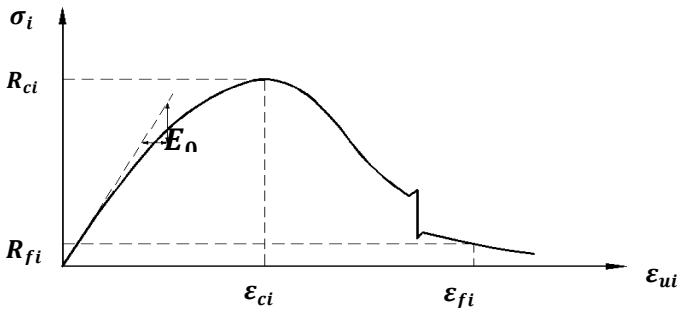

Figure (3) Concrete Compressive stress-strain relationship

4.1.4 Determination of Strain Indicator,ε_{si}

The strain indicator in Eq. (10) defines the extent to which the concrete is loaded in each principal direction. Since principal stresses act independent of each other, the stress-equivalent strain relationship in each direction [8] may be expressed as a function of ε_{si} as follows:

$$\sigma_i = R_{ci}\frac{K_i\left(\frac{\varepsilon_{si}}{\varepsilon_{ci}}\right)}{1 + A_i\left(\frac{\varepsilon_{si}}{\varepsilon_{ci}}\right) + B_i\left(\frac{\varepsilon_{si}}{\varepsilon_{ci}}\right)^2 + C_i\left(\frac{\varepsilon_{si}}{\varepsilon_{ci}}\right)^3} \quad (i = 1,2,3) \qquad \ldots\ldots (13)$$

where $(A_i, B_i \text{and} C_i)$: are coefficients defined in Eq. (11).

After substituting the values of the principal stresses for the current load state into Eq. (13), strain indicator ε_{si} can be evaluated by solving the equation for each direction of orthotropy. Because of the non-linearity of Eq. (13), a numerical solution based on the Newton-Raphson method is adopted to determine ε_{si} [12]. Since the selection of an initial approximation is critical to the rate of convergence of the solution, an initial approximation of ε_{si} is suggested as follows [12]:

$$\varepsilon_{si} = \frac{2\ \sigma_i}{E_0 + E_{sc}} \qquad \ldots\ldots (14)$$

where, E_0 is the initial elastic modulus and $E_{sc} = \frac{R_{ci}}{\varepsilon_{ci}}$.

4.2 Ultimate Surfaces

To calculate the incremental secant modulus in Eq. (10), it is necessary to determine the stresses and the corresponding strains at failure $(R_{ci}, \varepsilon_{ci})$.

4.2.1 Failure Strength Surface

A new unified five-parameter failure surface which is depicted in Fig. (4) has been presented by *Seow and Swaddiwudhipong*[13], to be used for normal strength (NC), high strength (HSC), and steel fiber-reinforced (SFRC) concrete under biaxial and triaxial loading.

Due to the six-fold symmetry of the surface, Eqs. (15) to (17) describeρ_t, ρ_c, and $\rho(\xi, \theta)$, are sufficient to define the entire failure surface:

$$\frac{\xi}{f_{cu}} = a_2(\frac{\rho_t}{f_{cu}})^2 + a_1\left(\frac{\rho_t}{f_{cu}}\right) + a_\circ \quad \ldots\ldots (15)$$

$$\frac{\xi}{f_{cu}} = b_2(\frac{\rho_c}{f_{cu}})^2 + b_1\left(\frac{\rho_c}{f_{cu}}\right) + b_\circ \quad \ldots\ldots (16)$$

$$\rho(\xi,\theta) = \frac{2\rho_c({\rho_c}^2 - {\rho_t}^2)\cos\theta + \rho_c(2\rho_t - \rho_c)[4({\rho_c}^2 - {\rho_t}^2)cos^2\theta + 5{\rho_t}^2 - 4\rho_t\rho_c]^{\frac{1}{2}}}{4({\rho_c}^2 - {\rho_t}^2)cos^2\theta + (\rho_c - 2\rho_t)^2} \quad \ldots\ldots (17)$$

where, $\cos\theta = \left[\frac{(2\sigma_1 - \sigma_2 - \sigma_3)}{3\sqrt{2}\tau_{oct}}\right]$ for $\sigma_1 \geq \sigma_2 \geq \sigma_3$ …… (18)

$$\sigma_{oct} = \frac{\sigma_1 + \sigma_2 + \sigma_3}{3} \text{ (Octahedral normal stress)} \quad \ldots\ldots (19)$$

$$\tau_{oct} = \frac{1}{3}\sqrt{(\sigma_1 - \sigma_2)^2 + (\sigma_2 - \sigma_3)^2 + (\sigma_3 - \sigma_1)^2} \quad \text{(Octahedral shear stress)} \quad \ldots\ldots (20)$$

$\sigma_i (i = 1\ to\ 3)$ is the principal normal stress in the i^{th} direction, tension is positive.

$$\xi = \sqrt{3}\sigma_{oct} \quad \ldots\ldots (21)$$

$$\rho = \sqrt{3}\tau_{oct} \quad \ldots\ldots (22)$$

where,

f_{cu}:is the uniaxial compressive strength of concrete cube.
$a_\circ, a_1, a_2$: coefficients of tensile meridian.
$b_\circ, b_1, b_2$:coefficients of compression meridian.

The determination of tensile and compressive meridians,ρ_t,ρ_c in Eqs.(15), (16) respectively depends on the constant values $(a_\circ, a_1, a_2, b_\circ, b_1, b_2)$. The coefficients $a_\circ$ and $b_\circ$ are the point of intersection of the tensile and compressive meridians with the hydrostatic axis. At this point, concrete is subjected to equal triaxial tension(f_{ttt}). Due to the difficulty in conducting triaxial tension experiments, there exists only few conclusive experimental findings available for predicting f_{ttt}. Some studies showed that taking $f_{ttt}$to be equal to f_t' (where$f_t' \approx 0.1 f_c'$) , results in a closer fit to the experimental data for normal concrete (NC) and high strength concrete (HSC). Thus, $a_\circ$ and $b_\circ$ are defined by

$$a_\circ = b_\circ = \frac{\sqrt{3}f_{ttt}}{f_c} = 0.1732 \quad \ldots\ldots (23)$$

The values of the remaining coefficients, a_1, a_2, b_1 and b_2, are determined through regression analysis conducted by *Seow and Swaddiwudhipong* [13] on (296) experimental data points of NC and HSC cubes and cylinders for concrete strengths ranging from (20 - 132) MPa, subjected to triaxial loads and failing on ρ_t and ρ_c .

$$\left.\begin{array}{l} a_2 = -0.1597\ , a_1 = -1.455 \\ b_2 = -0.1746\ , b_1 = -0.778 \end{array}\right\} \quad \ldots\ldots (24)$$

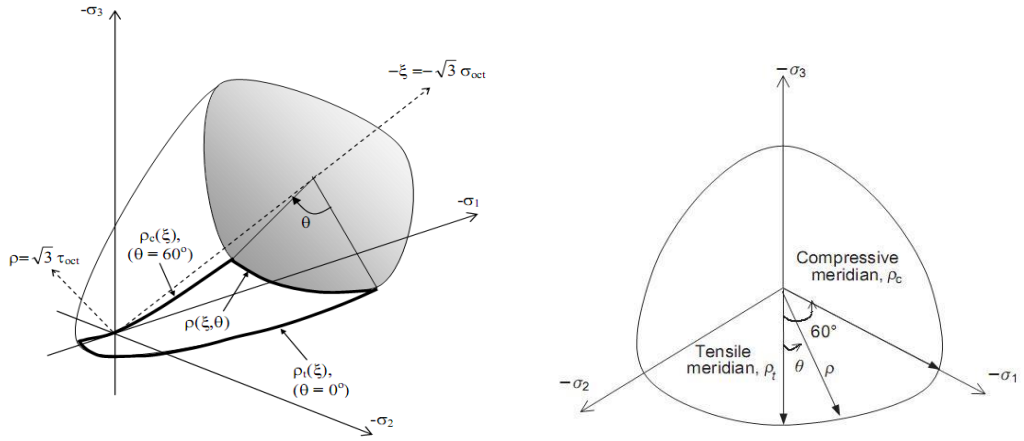

(a) General view of failure surface *(b) Deviatoric view of failure surface*

Figure (4) Unified Failure Surface [13]

4.2.2Ultimate Strain Surface

Unlike the stresses at failure, it is difficult to accurately measure and predict the actual strains in the vicinity of the failure stresses of concrete [14]. A set of modified equations are used in the constitutive model to predict the compressive strains in concrete under multi-axial compression [6].

$$\varepsilon_{ci} = |\varepsilon_0|\left[1.6\left|\frac{R_{ci}}{f_{cu}}\right|^3 - 2.25\left|\frac{R_{ci}}{f_{cu}}\right|^2 - 0.35\left|\frac{R_{ci}}{f_{cu}}\right|\right] when \left|\frac{R_{ci}}{f_{cu}}\right| \leq 1.0 \quad \ldots\ldots (25)$$

$$\varepsilon_{ci} = -|\varepsilon_0|\left[3.0\left|\frac{R_{ci}}{f_{cu}}\right| - 2.0\right] when \left|\frac{R_{ci}}{f_{cu}}\right| > 1.0 \quad \ldots\ldots (26)$$

where,

ε_0 : is the strain at peak compressive stress of concrete.
f_{cu} : is the uniaxial compressive strength of concrete cube.

In case of tensile strain, the prediction of ultimate strain ε_{ci} is based on linear relation shown in Fig. (4), between the ultimate stress R_{ci} and the initial modulus of concrete E_0 as follows [19]:

$$\varepsilon_{ci} = \frac{R_{ci}}{E_0} \quad \ldots\ldots (27)$$

4.3 Modeling of Ordinary Steel Reinforcement

The elastic perfectly plastic model is introduced by assigning a zero value for the elasto-plastic Young's modulus(E_{ep}).

5. Model Verification

5.1Karayannis and Chalioris Beam (Ra)

A series of (12) plain concrete beams with rectangular, non-rectangular, L and T cross-section were tested under a pure torsion by *Karayannis and Chalioris*[15]. The selected beam (Ra) is a plain concrete beam with rectangular cross-section of $(100 \times 200$ mm) and (1.6 m) length which is divided into three parts: two reinforced end parts and one plain concrete middle part. The beam is mounted on two roller supports to ensure that the tested beam was

free to rotate and elongate longitudinally at both ends. The load was applied at the ends of two steel arms, fixed at the end parts of the beam, through a steel spreader as shown in Fig. (5). The effective length of the tested beam under pure torsion is (0.6m) as described in the experimental test.

Experimental testing procedure and applying loads and supporting conditions allow making use of symmetry, therefore, only one half of the beam is idealized by (48) brick elements as shown in Fig. (6), the boundary conditions are described in Fig. (7), the material properties of the beam are given in Table (1).

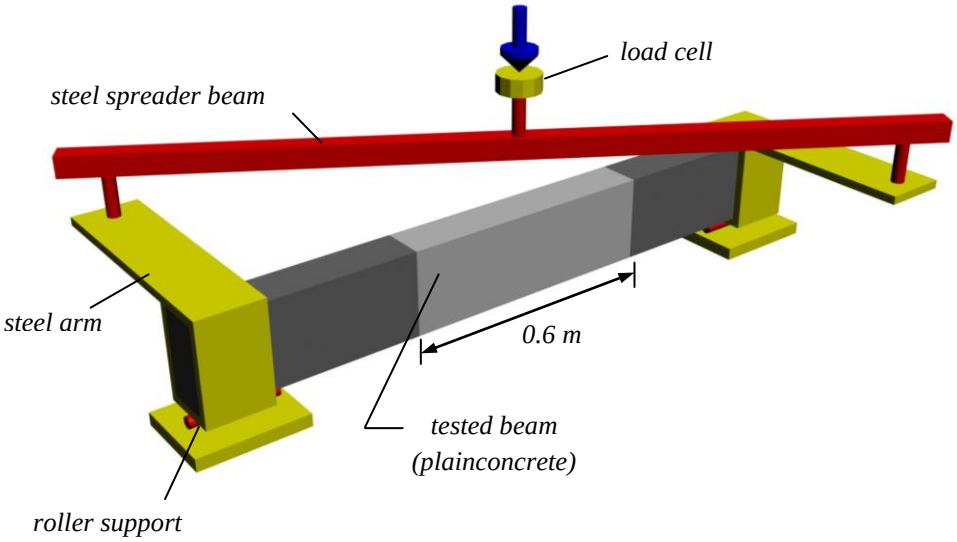

Figure (5) Experimental test setup of beam (Ra)

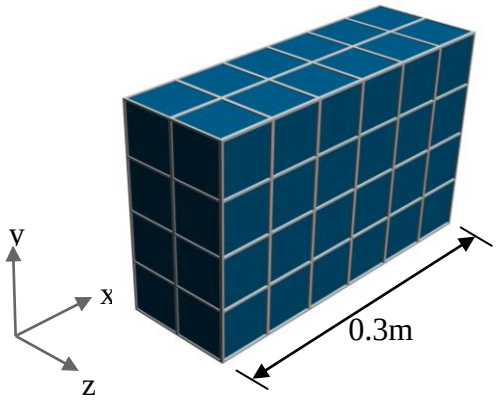

Figure (6) Finite elements mesh of beam (Ra)

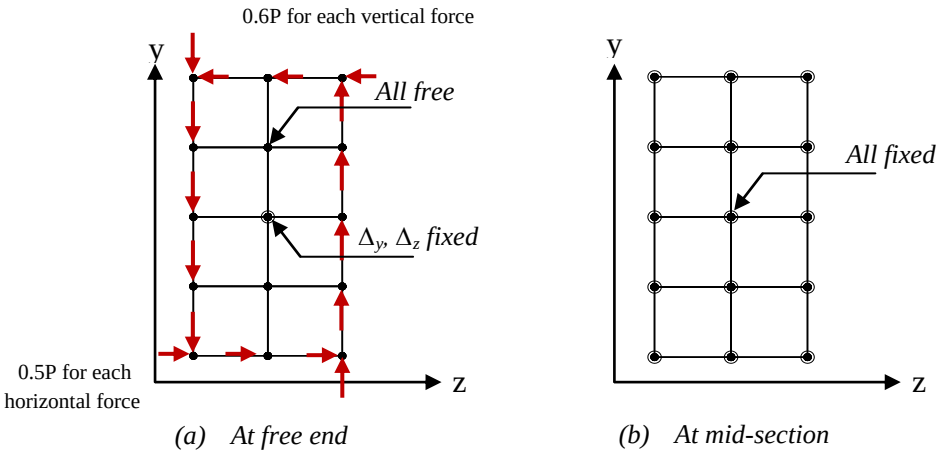

Figure (7) Boundary conditions and the applied nodal forces of beam (Ra)

Table (1) Material properties of beam (Ra)

Concrete	
Compressive strength, f_c'	20.96 MPa
Young's modulus, E_c	21518 MPa*
Poisson's ratio, $v_\circ$	0.2 **
Tensile strength, f_t'	2.89 MPa

* $E_c = 4700\sqrt{f_c'}$ [28], **Assumed value

The torque-twist angle curve shows a good agreement with the experimental results as demonstrated in Fig. (8). The predicted results at failure in terms of ultimate torque and angle of twist from finite element method are equal to (2.02 kN.m) and (0.00873 rad/m), respectively; while the ultimate torque and angle of twist from the experimental work were equal to (1.93 kN.m) and (0.00834 rad/m), respectively, which indicate a good matching between the two results.

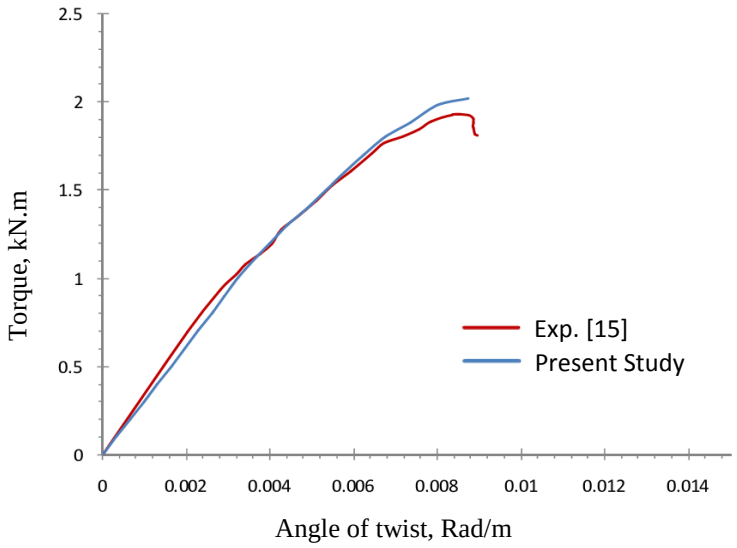

Figure (8) Torque-twist angle curves for the beam (Ra)

5.2 Onsongo Beam (TBO3)

Onsongo[16] tested three series of beams under a wide range of (T/M) ratios. All tested beams were subjected to a uniform bending moment and torque along their lengths, and were tested to failure. The selected beam (TBO3) is of rectangular hollow cross-section as illustrated in Fig. (9), with (2.286 m) tested span length and loaded with a torque to moment ratio equal to (0.7).

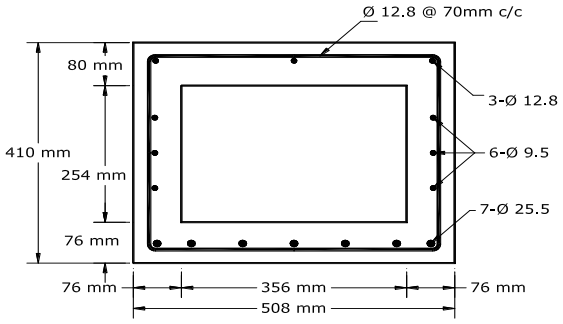

Figure (9) Cross-section details of (TBO)

A schematic representation of testing rig is shown in Fig. (10), the steel extension beams were connected to the ends of the concrete specimens and the torsion arms were clamped to the specimen. The tested beam was supported at the ends of the steel extension beams.

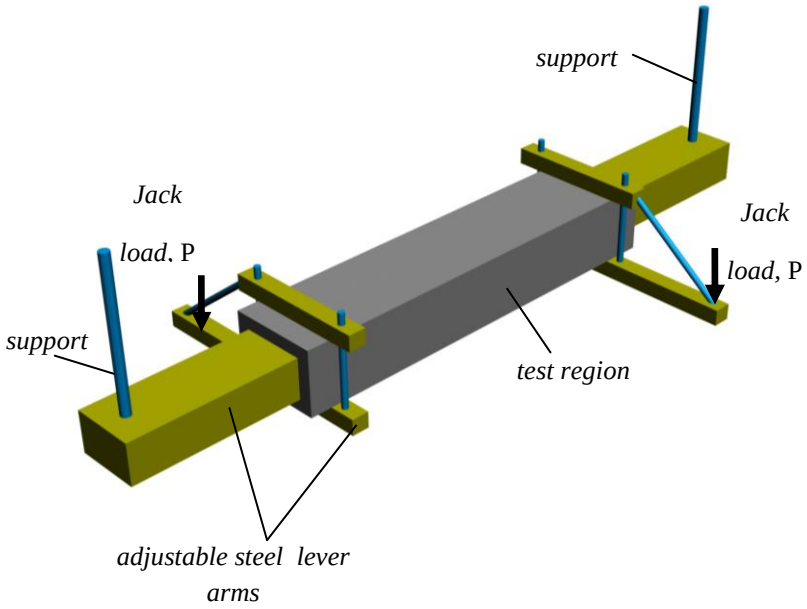

Figure (10) Schematic representation of testing rig

Making advantage of symmetry, only one-half of the beam is idealized with (1968) brick elements as shown in Fig. (11). To apply the torque and moment loads steadily and to avoid local failure and also to satisfy the boundary conditions, a subsidiary concrete brick elements with stiff elastic material properties were added to both ends of the beam.

The tested beam (TBO3) subjected to constant moment and torque along their length. To obtain the constant moment, the nodal loads were applied to determine a uniform compressive stress in the top flange and a uniform tensile stress in the bottom flange. The nodal loads for torque were applied in two opposite directions having the same value. The boundary conditions are described in Fig. (12), and the material properties of the beam are given in Table (2).

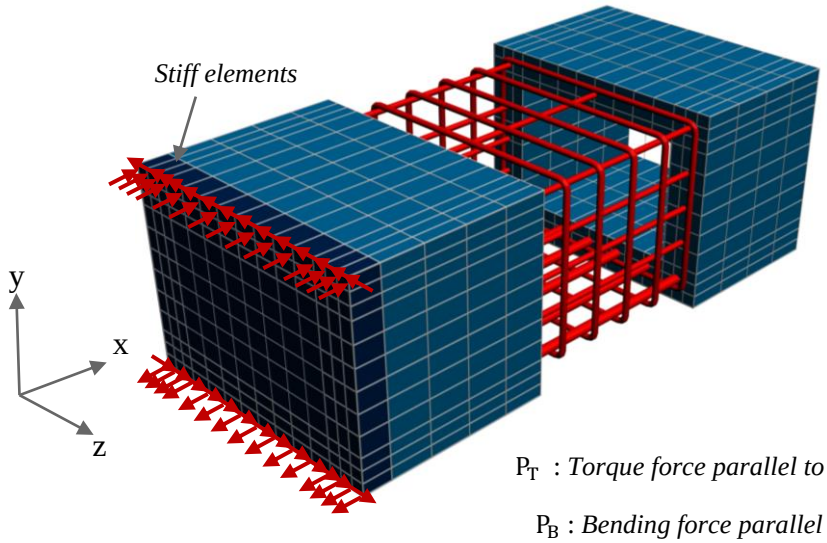

Figure (11) Finite elements mesh and the applied nodal forces of beam TBO3

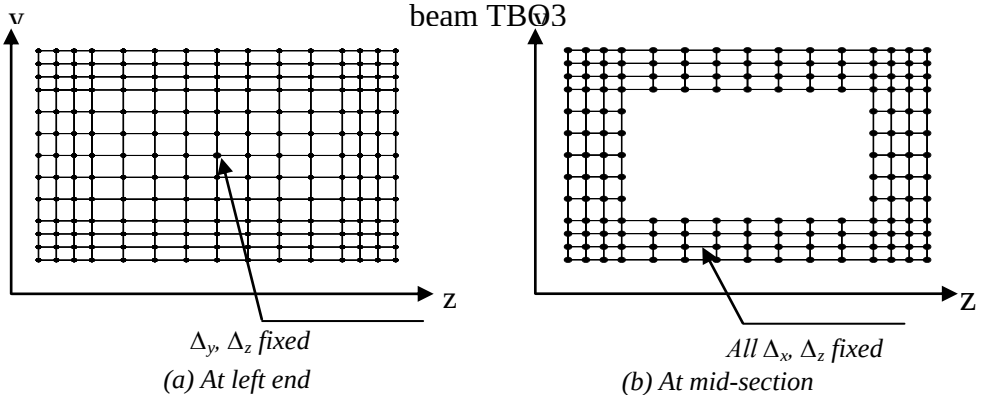

Figure (12) Boundary conditions of beam TBO3

Table (2) Material properties of beam (TBO3)

Concrete		
Compressive strength, f_c'		19.1 MPa
Young's modulus, E_c		20541 MPa*
Poisson's ratio, v		0.2 **
Tensile strength, f_t'		1.44 MPa
Steel		
Bar dia.	Area	Yield stress f_y
9.5 mm	71.0 mm^2	401.0 MPa
12.8 mm	129.0 mm^2	393.0 MPa
25.5 mm	510.0 mm^2	436.0 MPa
Young's modulus, E_s		200000.0 MPa**

* $E_c = 4700\sqrt{f_c'}$[28], ** Assumed value

The experimental results [16], numerical results of present study and numerical results of Ref. [17] in terms of torque-twist angle curves of beam (TBO3) are given in Fig. (13). This figure indicates a good agreement between the predicted results with the experimental results and also indicate a good matching that given by Ref. [30]. The predicted ultimate torque and corresponding angle of twist from present study are equal to (143.27 kN.m) and (0.016954 rad/m), respectively; while the ultimate torque and angle of twist from the experimental work were equal to (144.4 kN.m) and (0.017926 rad/m) respectively which are in very good matching with the predicted values.

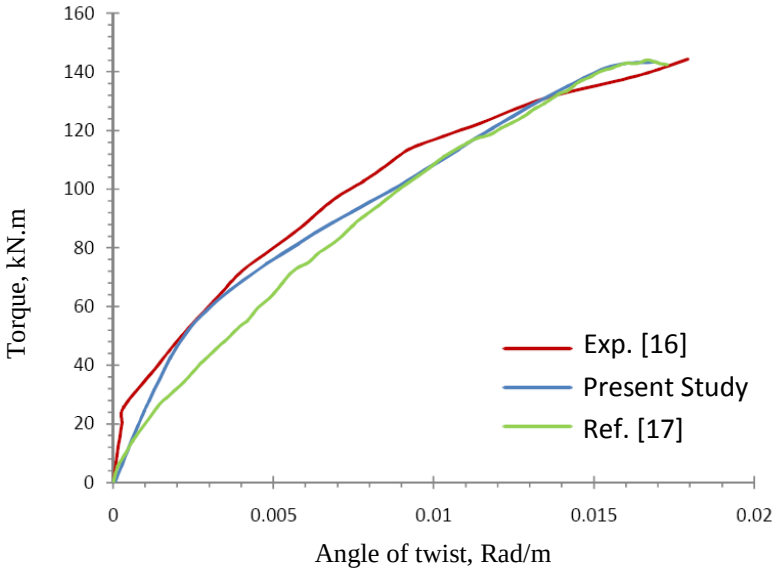

Figure (13) Torque-twist angle curves for the beam (TBO3)

6.Conclusions

From the present numerical investigation of reinforced concrete box beams, the following conclusions can be drawn:

The hypoelastic model with orthotropic approach adopted in the present work is suitable to predict the behavior of plain and reinforced concrete members subjected to different types of loading.

REFERENCES

1. Kwon, M., "*Three Dimensional Finite Element Analysis of Reinforced Concrete Members*", Ph.D. dissertation, Department of Civil, Environmental, and Architectural Engineering, University of Colorado, Boulder, 2000.
2. Saenz. L.P., "*Discussion of Equation for The Stress-Strain Curve of Concrete by Desayi and Krishman*", ACI Structural Journal, Vol.61, No.3, 1964, pp.1229-1235.
3. Balan, T.A., Spacone, E. and Kwon, M. "*A 3D hypoplastic model for cyclic analysis of*

concrete structures", Engineering Structures, Vol.23, No.4, 2001, pp.333-342.

4. Zienkiewicz, O.C., and Taylor, R.L., "*The Finite Element Method for Solid and Structural Mechanics*", Sixth Edition, Elsevier Butterworth-Heinemann, U.K., 2005.
5. Liu, G.R., and Quek, S.S., "*The Finite Element Method: A Practical Course*", Elsevier Butterworth-Heinemann, U.K., 2003.
6. Darwin, D. and Pecknold, D.A., "*Nonlinear Biaxial Stress-Strain Law for Concrete*", Journal of Engineering Mechanics Division, ASCE, Vol.103, No.2, 1977, pp.229-241.
7. Jing, J.J., "*Finite Element Techniques for Static Analysis of R.C. Structures*", Invited Paper at Int. Conf. Computer-Aided Analysis and Design of Concrete Structures, Split, Yugoslavia, September 1984.
8. Elwi, A. A., and Murray, D. W., "*A 3D Hypoelastic Concrete Constitutive Relationship*", Journal of Engineering Mechanics Division, ASCE, Vol.105, No.4, 1979, pp.623-641.
9. Chen, W.F., "*Plasticity in Reinforced Concrete*",J. Ross Publishing, U.S.A., 2007.
10. Balan, T.A., Filippou, F.C. and Popov, E.P., "*Constitutive Model for 3D Cyclic Analysis of Concrete Structures*", Journal of Engineering Mechanics Division, ASCE, Vol. 123, No.2, 1997, pp. 143-153.
11. Lekhnitskii SG. In: Brandstatter JJ, editor. "*Theory of Elasticity of An Anisotropic Elastic Body*", San Francisco, CA: Holden Day, Inc., 1963.
12. Tho, K.K., Seow, P.E. and Swaddiwudhipong, S.," *Numerical Method for Analysis of Concrete Under Multi-axial Loads*", Magazine of Concrete Research, Vol.55, No.6, 2003, pp.537-547.
13. Seow, P.E. and Swaddiwudhipong, S., "*Failure Surface for Concrete under Multiaxial Load A-Unified Approach*", Journal of Materials in Civil Engineering, ASCE, Vol. 17, No. 2, 2005.
14. Swaddiwudhipong, S., Lu, H. R. and Wee, T. H., "*Probabilistic Model For Tensile Strain Capacity of Concrete*". Proceedings of the 3rd International Conference on Concrete Under Severe Conditions, The University of British Columbia, Vancouver, Canada, 2001, pp. 1602-1609.
15. Karayannis, C.G. and Chalioris C.E.," *Experimental validation of smeared analysis for Effective in the beams with rectangular cross-section than in the Plain concrete in torsion*", Journal of Structural Engineering, ASCE, Vol.126, No.6, 2000, pp.646-653.
16. Onsongo, W. M., "*The Diagonal Compression Field Theory for Reinforced Concrete Beams Subjected to Combined Torsion, Flexure, and Axial Load*," Ph.D. thesis, Department of Civil Engineering, University of Toronto, Toronto, Ontario, Canada, 1978.
17. Vecchio, F.J. and Selby, R.G.," *Toward Compression-Field Analysis of Reinforced Concrete Solids*", Journal of Structural Engineering, ASCE, Vol. 117, No. 6, June 1991, pp. 1740-1757.

Nonlinear Finite Element Analysis of Fibrous Reinforced Concrete Slabs Reinforced with Partial Steel Fiber

Dr. Ayad A. Abdul-Razzak **Nuha H. Al-Jubory**
Assist. Professor **Lecturer**
College of Engineering/ Mosul University, Mosul-Iraq

Abstract

In the present work, the finite element method is utilized to investigate the behavior of fiber reinforced concrete slabs, at pre and post-cracking levels up to ultimate load. The slabs are partially fiber reinforced at tension zone and other zone are normal reinforced concrete. A tension stiffening model has been suggested using a regression analysis of the experimental results, with index of determination (90.61%). Assumed strain and Heterosis elements are employed in the analysis. A layered approach is adopted to discretize the concrete through the thickness. Two shear modulii of cracked fiber concrete are used and it is concluded that the shear crack approach G2 gives better results than G1 approach as compared to experimental results. Several examples of published experimental results are analyzed using the proposed models, the outcome results showed good agreement with experimental results.

Keywords: Assumed Strain Element, Finite Element Method, Heterosis Element, Partial Steel Fiber Reinforced Concrete, Slab, Tension Stiffening Model.

التحليل غير الخطي بطريقة العناصر المحددة للبلاطات الخراسانية المسلحة جزئيا بالألياف الفولاذية

د. أياد أمجد عبد الرزاق نهى حميدي الجبوري
قسم الهندسة المدنية / كلية الهندسة / جامعة الموصل

ألخلاصة

في هذا البحث تم إجراء التحليل غير الخطي بطريقة العناصر المحددة لبحث أداء البلاطات الخرسانية الليفية المسلحة في مرحلة ما قبل التشقق وبعدها إلى الحمل الأقصى. إن البلاطات التي تم تحليلها تحتوي على الخرسانة الليفية في منطقة الشد وما تبقى هو خرسانة عادية. ولغرض تمثيل تأثير صلابة الشد في الخرسانة المتشققة تم اقتراح نموذج بعمل تحليل تراجعي للنتائج العملية وقد أعطى هذا النموذج معامل توافق (90.61%). استخدم نوعين من العناصر ، العناصر ذات الانفعال المفروض وعناصر هيتروسز . كما استخدم أسلوب تقسيم السمك إلى طبقات لتمثيل الخرسانة خلال السمك. استخدم نموذجان لتمثيل مقاومة القص بعد التشقق واظهر النموذج G2 نتائج أفضل مقارنة بالنموذج G1 . تم تحليل عدة أمثلة وأظهرت توافقا جيدا عند مقارنتها مع النتائج العملية.

Notations

d_f Equivalent diameter of fiber.
E_c Concrete elastic modulus.
E_{cf} Modulus of elasticity of SFRC.
E_i Initial modulus of elasticity of concrete.
E_s ,E_s' Initial and second modulus of elasticity for steel.
f Yield function.
f'_{cmax} Maximum compressive strength in the direction parallel to the crack.
f_c' Uniaxial compressive strength of plain concrete.
f_{cf}' Uniaxial compressive strength of SFRC.
f_t' Uniaxial tensile strength of matrix.
f_{tf} Uniaxial tensile strength of composite.
f_u Average tensile stress of fibers crossing the cracked section.
G_f Fracture energy of SFRC.
h Characteristic length of Guass points.
l_f Length of fiber.
N_f Effective number of fibers per unit cross section area
V_f Volume fraction of fiber.
ε_1 ,ε_2 Strain in principal direction 1 and 2 respectively.
ε_{cuf} Ultimate crushing strain of SFRC.
ε_m Limiting tensile strain normal to the crack.
ε_{pf} Compressive strain at peak stress of SFRC.
ε_t Tensile strain at peak stress of matrix.
ε_{tf} Tensile strain at peak stress of composite.
σ_o Equivalent effective stress.
σ_t Tensile stress
τ_u Average characteristic bond strength.
ν Poisson's ratio.

Introduction

Heterosis elements are a 9-node quadrilateral which employs serendipity shape function for the transverse displacement, and Lagrange shape function for the rotations[1].

The principal reason for incorporating fibers into a cement matrix is to increase the toughness and tensile strength and improve the cracking and deformation characteristics of the composite. The fibers appear to has two important roles in reinforced concrete:[2]

- Fibers may permit the post-cracking (or residual) strength of the fiber reinforced concrete to be used in design, since the fiber reinforced matrix can continue to carry a considerable amount of load after cracking has occurred, over a wide range of deflection (unlike plain concrete).
- Fibers enhance the bond between the matrix and the reinforcing steel, by inhibiting crack growth emanating from the bar deformations.

Huang [3] used an artificial method for the elimination of shear locking by interpolating new shear strain fields from the strain values at the sampling points which are appropriately located in individual elements.

Proper constitutive models were introduced to simulate the nonlinear behaviors of reinforced concrete and FRP. The finite element program ABAQUS was used to perform the nonlinear failure analysis of the discussed problems. The validity of proposed material models was verified with experimental data and some strengthening schemes were discussed in detail for engineering applications. It had been shown that the use of fiber-reinforced

plastics can significantly increase the stiffness as well as the ultimate strengths of reinforced concrete slabs[4].

Finite element simulation was used to analyze the normal reinforced concrete and steel fiber reinforced concrete slab due to different percentage of volume fraction with 1%,1.5%,2%,2.5% and 3%.through this simulation. The results of the analysis indicated that, by using and adding steel fiber into the conventional reinforced concrete, it will influence the ductility, toughness, energy absorption and strength of concrete [5].

New constitutive models for High Strength Steel Fiber Reinforced Concrete (HSSFRC) had been formulated by means of a regression analysis of many experimental data (from literature) by using SPSS-statistical program. The proposed constitutive models had been employed for formulating the material finite element models to study the behavior of HSSFRC corbels [6]. These models are used to analyze (HSSFRC) corbels [7] and showed good agreement with experimental results.

Behavior of Fibrous Concrete in Uniaxial Compression

The addition of fiber to the concrete increased the compressive strength and the strain at peak stress as defined below [8]:

$$f_{cf}^{`} = f_{c}^{`} + 3.6\frac{V_f l_f}{d_f} \quad (1)$$

$$\varepsilon_{pf} = 0.0021 + 0.0007\frac{V_f l_f}{d_f} \quad (2)$$

where $f_{cf}^{`}, f_{c}^{`}$ are the compression strength of standard cylinder for plain and fibrous reinforced concrete (MPa).

V_f is fiber by volume.

l_f, d_f is fiber length and diameter.

The modulus of elasticity of fiber reinforced concrete calculated using the following equation [9]:

$$E_{cf} = 0.43E_s V_f + E_c(1 - V_f) \quad (3)$$

E_s, E_c are modulus of elasticity of fibers and concrete respectively.

The ultimate strain in compression calculated using the following equation [10]:

$$\varepsilon_{cuf} = 3011 + 2295V_f \quad (\mu_s) \quad (4)$$

The Behavior of Fibrous Concrete in Uniaxial Tension

a. The ascending part:

A simple expression is used for defining uniaxial tensile stress-strain curve up to the peak stress value of plain concrete [11]. This model takes the effect of fiber reinforced concrete parameters [12]. The comparison between experimental [13] and numerical model is shown in Fig.(1):

$$\sigma_t = f_{tf}\left[1 - \left(1 - \frac{\varepsilon}{\varepsilon_{tf}}\right)^A\right] \quad (5)$$

σ_t : Tensile stress at tensile strain ε_{tf}

$$f_{tf} = f_t^{'}(1+0.016N_f^{1/3}+0.05\pi\ d_f l_f N_f) \qquad (6)$$

where N_f is the number of fibers crossing a unit area

$$N_f = 1.64\ V_f / \square\ d_f^2 \qquad (7)$$

$$A = E_i \frac{\varepsilon_{tf}}{f_{tf}} \qquad (8)$$

(E_i): initial tangent modulus.

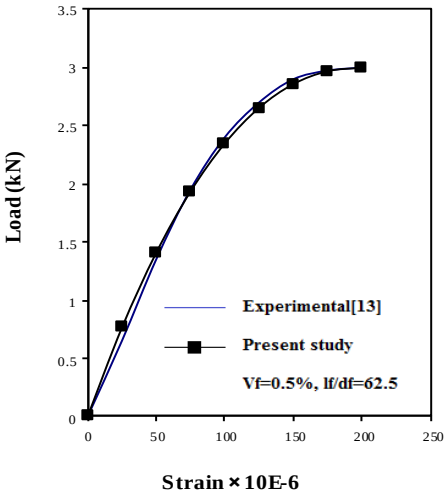

Fig.(1) The ascending part of tension model

b. The descending part:

Using regression analysis of the experimental results of references [14 and 15], the following model is adopted to express the relationship between post-peak stress and strain, the comparison between experimental and numerical model is shown in Fig.(2), (with index of determination=90.61%):

$$\sigma_t = f_{tf} e^{-f_{tf} S\left(\frac{\varepsilon}{\varepsilon_{tf}}-1\right)^R} \qquad (9)$$

S and R : constants depend on fiber volume fraction V_f and aspect ratio $\frac{l_f}{d_f}$.

where

$$S = 0.66875 - 0.48842\left(V_f \frac{l_f}{d_f}\right) + 0.1125\left(V_f \frac{l_f}{d_f}\right)^2 \qquad (10)$$

$$R = 6.26513\left(\frac{l_f}{V_f . d_f}\right)^{-0.50327} \qquad (11)$$

After crack initation the elastic modulus and Poisson's ratio are reduced to zero in the direction perpendicular to the crack and a reduced shear modulus is employed to simulate aggregate interlock. Two different approaches are used to calculate the reduced shear modulus:

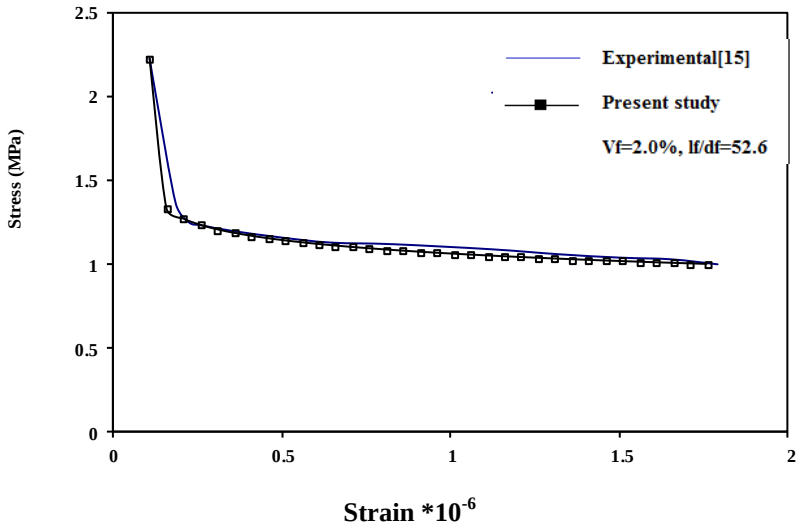

Fig.(2) Descending part of tension model

(i) Approach designated G1: This approach was initially proposed by Al-Mahaidi [16] and modified by many investigators [17 and 18]. The shear modulus of cracked concrete G can be calculated as follows:

$$G^{`} = \frac{0.4G}{(\varepsilon_1 / \varepsilon_t)} \qquad (12)$$

(ii) Approach designated G2: This approach was initially proposed by Abdul-Razzak [10] According to this approach, for concrete cracked in direction 1:

$$G_{12}^{`} = 0.25G\left[\frac{\varepsilon_1 - \varepsilon_m}{\varepsilon_{tf} - \varepsilon_m}\right]^2 \quad \text{for} \quad \varepsilon_1 < \varepsilon_m$$

$$= 0 \quad \text{for} \quad \varepsilon_1 > \varepsilon_m \qquad (13)$$

where:

$$\varepsilon_m = \frac{3G_f}{h.f_u} + \varepsilon_{tf} \qquad (14)$$

$$G_f = 0.04592\frac{V_f l_f^2}{d_f} \qquad (15)$$

$$f_u = 0.41V_f \tau_u l_f / d_f \qquad (16)$$

$$\tau_u = 2.62 - 0.0036N_f \qquad (17)$$

Material modeling of Plain Concrete:

Based on the flow theory of plasticity, the nonlinear compressive behavior of concrete is modeled. Adopting Kupfer's results [19] the yield condition for the plate can be written in terms of the stress components as:

$$f(\sigma)=\{1.355\ [(\sigma_x^2+\sigma_y^2-\sigma_x\sigma_y)+3\ (\tau_{xy}^2+\tau_{xz}^2+\tau_{yz}^2)]+0.355\ \ \sigma_\circ(\sigma_x+\sigma_y)\}^{1/2}=\sigma_\circ \qquad (18)$$

where ($\sigma_\circ$) is the equivalent effective stress taken as compressive strength ($f_c^{'}$) which is obtained from uniaxial test. This model is used in many investigations [20 - 23].

Both perfect plastic and strain hardening plasticity approaches are employed which are illustrated in Fig. (3).

The crushing type of concrete is a strain-controlled phenomenon. A simple way is by converting the yield criterion directly in terms of the strain; thus the crushing condition can be expressed in terms of the total strain components as:

$$1.355\ [(\varepsilon_x^2+\varepsilon_y^2-\varepsilon_x\varepsilon_y)+0.75\ (\gamma_{xy}^2+\gamma_{xz}^2+\gamma_{yz}^2)]+0.355\ \ \varepsilon_u(\varepsilon_x+\varepsilon_y)=\varepsilon_u^{\ 2} \qquad (19)$$

When equation (19) is satisfied, the strain (ε_u) reaches the crushing surface, and the concrete is assumed to lose all its characteristics of strength and stiffness.

The response of concrete in tension is assumed to be linearly elastic until the fracture surface is reached. Cracks are assumed to form in planes perpendicular to the direction of maximum principal tensile stress if the maximum stress reaches the specified concrete tensile strength. After cracking has occurred, a gradual release of concrete stress component normal to cracked plane is adopted according to a tension stiffening diagram illustrated in Fig. (4). The process of loading and unloading of cracked concrete is also shown in Fig.(4). A reduced shear modulus taken as a function of the current tensile strain is used to simulate aggregate interlock and dowel action.

The tensile cracks produce damage to concrete with the transverse strain having a degrading effect not

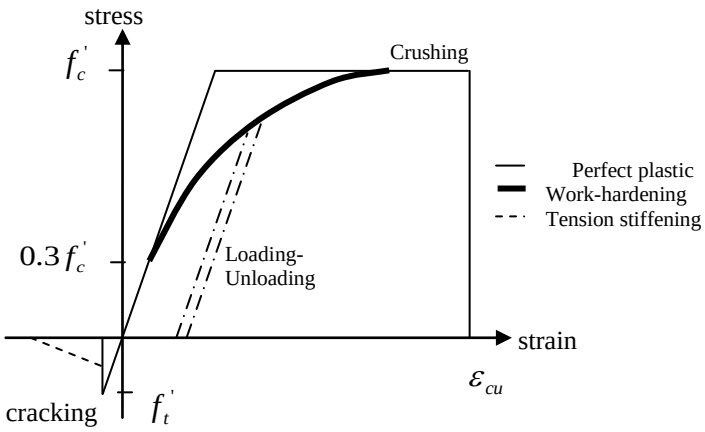

Fig.(3) Uniaxial representation of the concrete constitutive model

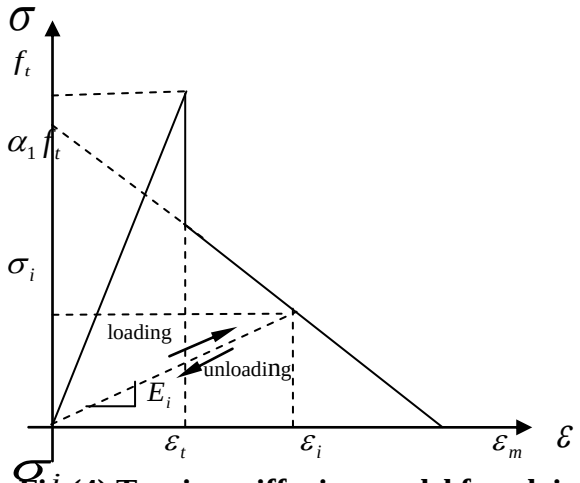

Fig.(4) Tension stiffening model for plain concrete after cracking

only on the compressive strength but also on the compressive stiffness, so that the concrete in the case becomes softer and weaker than that in a standard cylinder test. In the present study the relationship suggested by Belarbi and Hsu [24] is adopted.

$$f'_{c\max} = \frac{0.9 f'_c}{\sqrt{1+400\varepsilon_1}} \qquad (20)$$

where (f'_c) is the concrete cylinder compressive strength and (ε) is the average principal tensile strain of concrete in direction (1).

Numerical Application

Example 1.

A simply supported square slab was tested by Swamy and Ali [25]. The test specimen is (1800*1800)mm with (125)mm thickness and an effective depth of (100)mm to steel reinforcement. The fibers are distributed at the center of slab on a distance of 450 mm in both sides. The material properties of the tested slab are summarized in Tables (1) and (2). Due to the symmetry of the slab, only are quarter of the slab is analyzed. The slab is modeled using four elements, four steel layers are used to represent the reinforcement and eight concrete layers are found to be enough for the analysis. All dimensions and details of the slab are shown in Fig.(5), and the
finite element mesh is shown in Fig.(6).

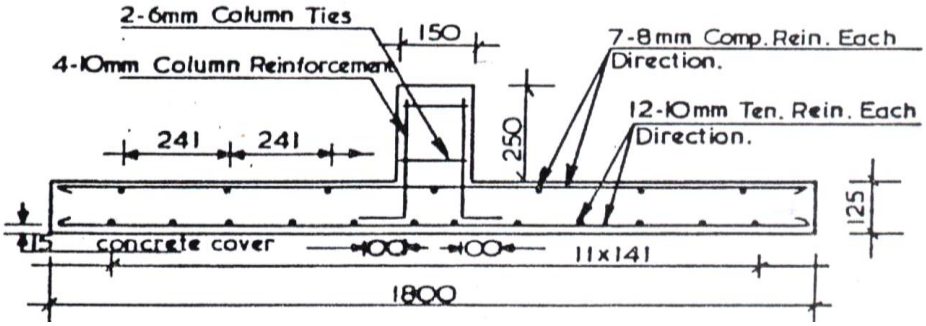

Fig.(5) Dimensions and details of slabs No.(S-5) and (S-6)

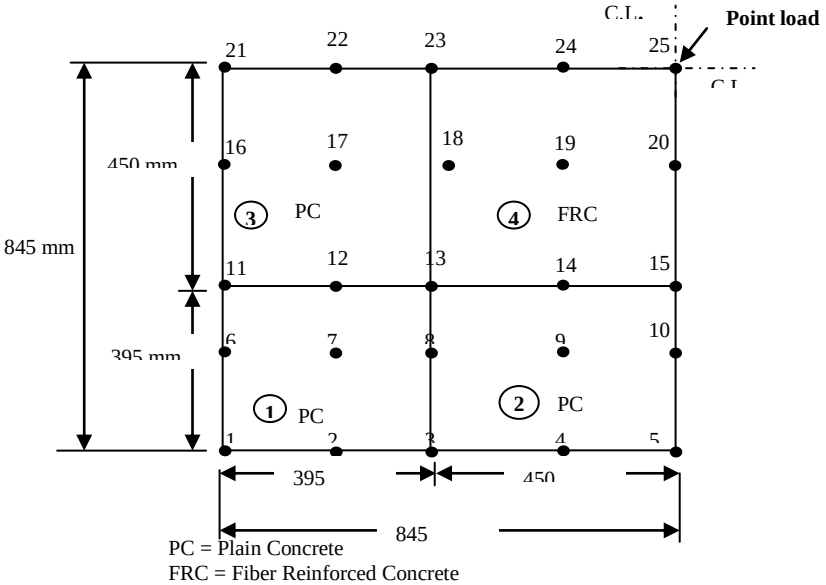

Fig.(6) Finite element mesh used for slabs No.(S-5) and (S-6)

Table (1) Details of fibrous concrete of slab (S-5) [25].

Slab No.	E_{cf} MPa	E_s MPa	V_f^* %	$f`_{cf}$ MPa	f_{tf} MPa	fy MPa	$\frac{l_f}{d_f}$	As` Bar	As Bar	ε_{cuf} $\times 10^{-3}$
S-5	39360	204000	0.9	37.5	4.18	460	100	7-Φ8	12-Φ10	5.08

ν_c =0.15 ., *Crimped steel fiber 0.5*50 mm

Table (2) Details of plain concrete of the slab (S-5) [25].

Slab No.	E_c MPa	ν_c	ε_u	α	ε_m	$f`_c$ MPa	$f_t`$ MPa
S-5	33290	0.19	0.003	0.6	0.002	38.1	3.33

Fig. (7) shows a comparison between two models of cracked shear modulus G1 and G2. These two models give good agreement compared with experimental results. However, G1 model give ultimate load less than G2 model for both the assumed and heterosis elements. Both of G models give ductile results as compared to experimental results.

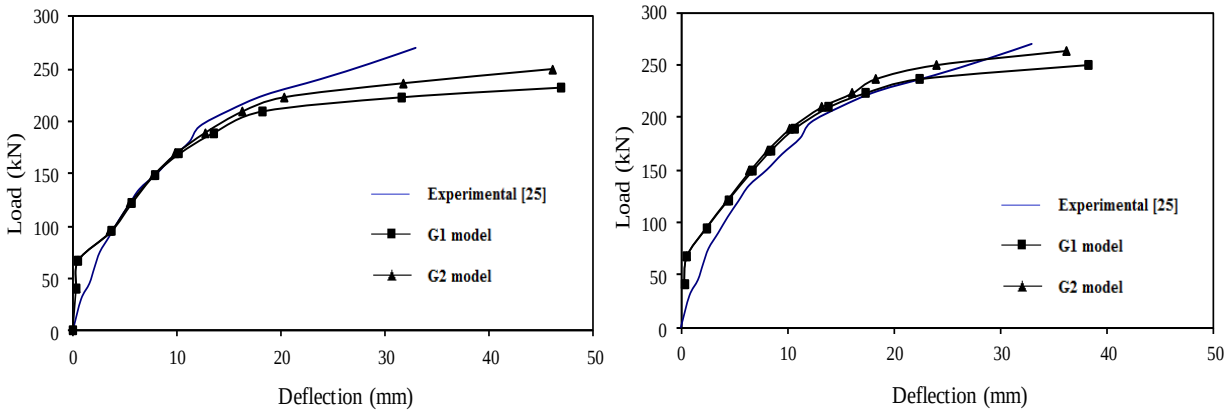

a. Assumed strain elements **b. Heterosis elements**

Fig.(7) Effect of G1 and G2 model on load deflection curves.

Fig.(8) shows a comparison between the assumed strain element and 9-node Lagrangian degenerate elements. The use of 9-node Lagrangian degenerate element shows stiff results and higher in ultimate load, this is due to shear locking that happened in 9-node Lagrangian degenerate element.

Fig.(9) shows a comparison between the assumed strain element and heterosis element. The use of two elements shows good response compared with experimental results.

Fig.(10) shows the relation between stress and strain in steel reinforcement in tension and compression zones using assumed strain and heterosis elements. It is clear from this figure that the numerical results have good agreement with the experimental values especially when heterosis element is used.

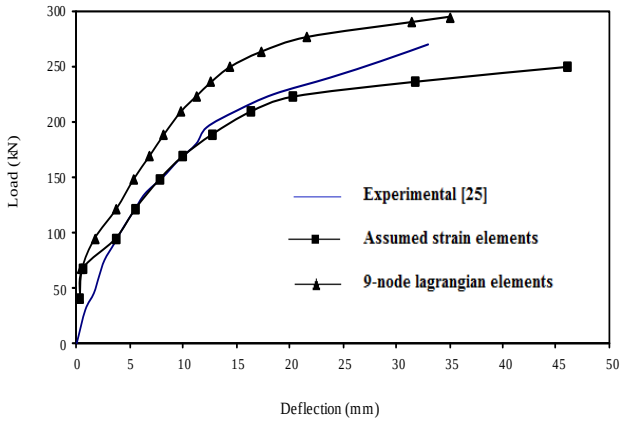

Fig.(8) Comparison between assumed and Lagrangian element on load deflection curves of G1 model.

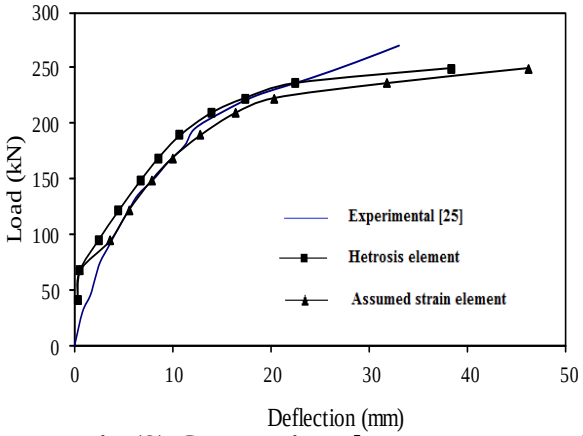

Fig.(9) Comparison between assumed strain and heterosis elements on load deflection curves of G1 model.

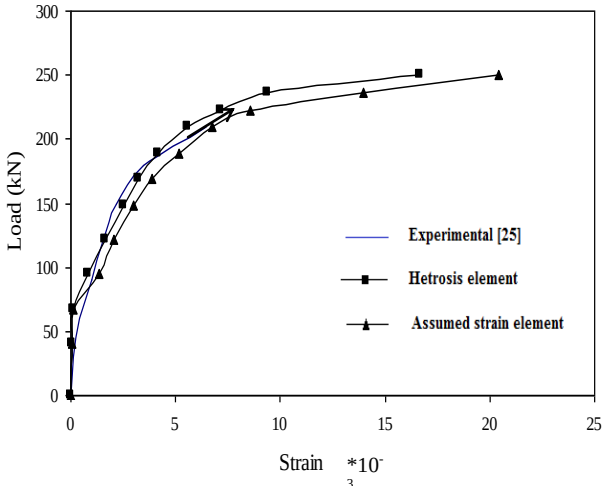

a. In tension zone

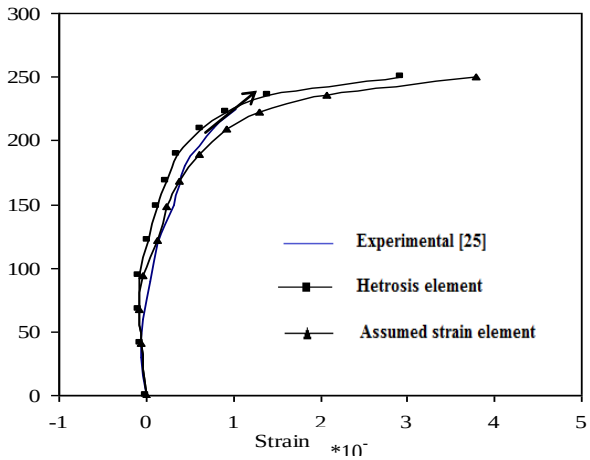

b. In compression zone

Fig. (10) Strains of steel reinforcement in Example 1

Example 2.

A simply supported square slab (S-6 tested by Ali [26]. The test specimen is (1800*1800)mm with (125)mm thickness and an effective depth of (100)mm to steel reinforcement. The slab included steel fiber 60 mm from the total thickness measured from tension face. The material properties of tested slab are summarized in Tables (1) and (2). The slab is modeled by four elements. Due to the symmetry

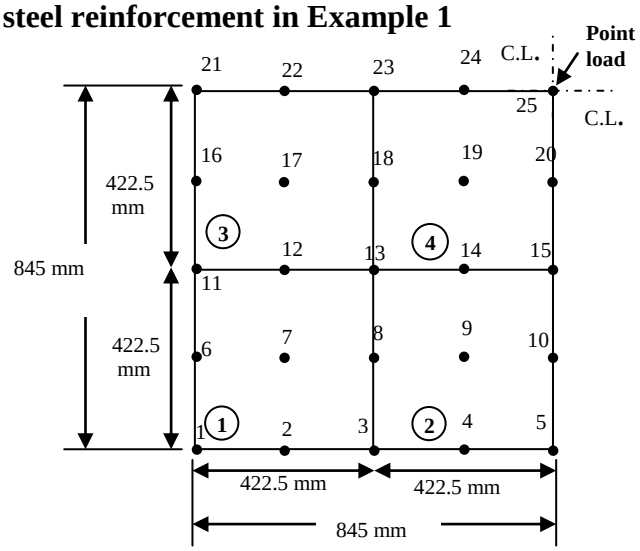

Fig. (11) Finite element mesh used for slab (S-6)

of the slab, only are quarter of the slab is analyzed. Four steel layers are used to represent the reinforcement and eight concrete layers are found to be enough for the analysis. All dimensions and details of the slab shown in Fig.(5), and finite element mesh shown in Fig.(11).

Fig. (12) shows a comparison between the two models of cracked shear modulus G1 and G2 models. These two models give good agreement compared with experimental results. However, G1 model gives ultimate load less than G2 model for both the assumed and heterosis elements. Both of G models give ductile results compared to experimental results.

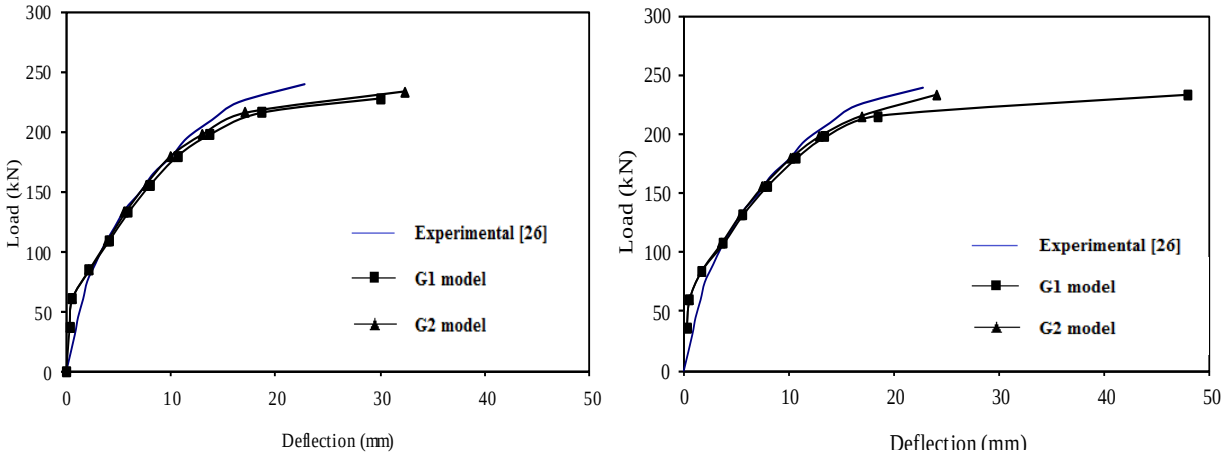

a. Assumed strain element **b. Heterosis elements**

Fig.(12) Effect of G1 and G2 models on load deflection curves.

Fig.(13) shows a comparison between the assumed strain element and 9-node Lagrangian degenerate element. The use of 9-node Lagrangian degenerate element shows stiff results and higher in ultimate load. This is because of shear locking that happened in 9-node Lagrangian degenerate element.

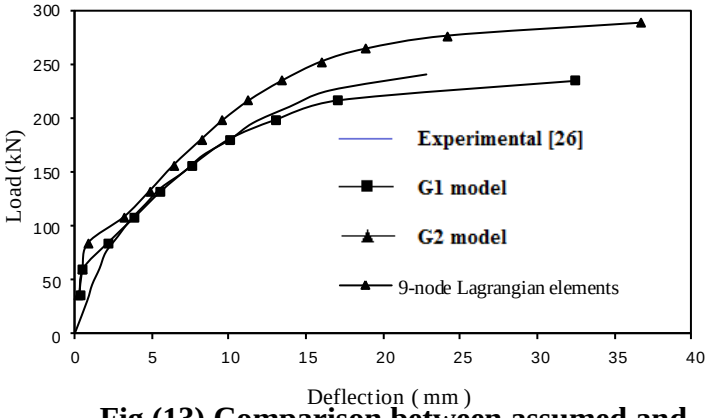

Fig.(13) Comparison between assumed and Lagrangian element on load deflection curves of G1 model.

Fig.(14) shows a comparison between the assumed strain element and heterosis element. The use of two elements show good agreement with experimental results.

Fig.(15) shows the relations between stress and strain in steel reinforcement in tension and compression zones near mid span for the experimental and numerical results, using assumed strain and heterosis elements. It is clear from Fig.(15-a) that the numerical results have good agreement with the experimental values especially in the cracking stage load. Fig. (15-b) shows compression steel stresses-strain curves, it is shown that below a load level of about 200 kN, the strain is compression after that the neutral surface is rising up and the steel becomes in the tension zone. A fair agreement is found between numerical and experimental

results.

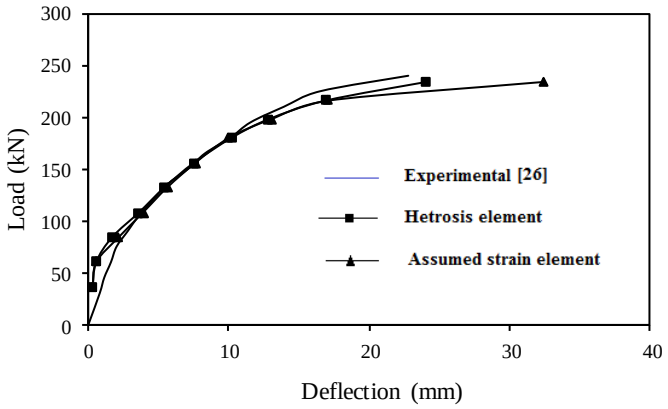

Fig.(14) Comparison between assumed strain and heterosis elements on load deflection curves of G1 model.

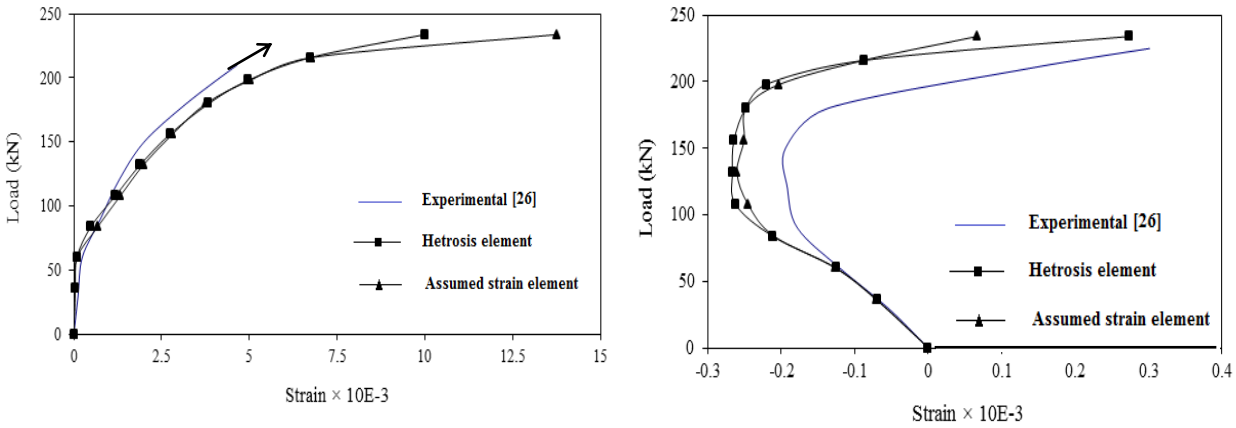

a. In tension zoon **b. In compression zone**

Fig. (15) Strain of steel bars for Example 2

Conclusions

1. The strain hardening plasticity and tension stiffening developed models of the fiber concrete proved to give satisfactory results for the analysis of reinforced concrete slabs subjected to incremental loading up to failure.
2. Two shear moduli of cracked fiber concrete are used and it is concluded that the shear crack approach G2 gives better results than G1 approach as compared to experimental results.
3. The assumed strain and heterosis elements proved to be efficient for nonlinear analysis of fibrous reinforced concrete slabs, and no locking was detected in those types of elements.

References

1. Hughes, T.J.R., and Cohen, M., " The heterosis finite element for plate bending ", J. of Computers and Structures Vol. 9, 1978, pp. 445 – 480.

2. Mindess, S., "Fiber Reinforced Concrete: Challenges and Prospects," FiberReinforced Concrete, edited by N. Banthia and S. Mindess, Second University-Industry Workshop on Fiber Reinforced Concrete and other Advanced Composites, Toronto, Canada, March 26-29, 1995.
3. Huang, H.C., "Static and Dynamic Analysis of Plates and Shells theory, Software and Applications", Springer, Verlag, Berlin, Heidelberg 1989.
4. Fu-Ming Lin, and Hsuan-Teh Hu, "Strengthening of Square Reinforced Concrete Plates with Fiber Reinforced Plastics", Proceedings of The Fourteenth (2004) International Offshore and Polar Engineering Conference, Toulon, France, May 23-28, 2004.
5. Shahidan, Sh., "Behavior of Steel Fiber Reinforced Concrete Slab Due to Volume Fraction of Fiber", MSc. Thesis, University Putra Malaysia, December 2009.
6. Abdul-Razzak, A. A., and Mohammed Ali A. A., "Modelling and Numerical Simulation of High Strength Fiber Reinforced Concrete", Applied Mathematical Modelling, Vol.35, No.6, 2011, pp. 2901-2915.
7. Abdul-Razzak, A. A., and Mohammed Ali A. A., "Influence of Cracked Concrete on The Nonlinear Analysis of High Strength Fiber Reinforced Concrete Corbels", Composite Structures, Vol.93, 2011, pp. 2277-2287.
8. Soroushian, P., and Lee, C. D., "Constitutive modelling of steel fiber reinforced concrete under direct tension and compression", Proc. of the Inter. conf. on recent developments in fiber reinforced cements and concrete, 18-20 Sept. 1989, Cardiff (U.K.), Eds. Swamy and Barr, Elsevier Applied Science, pp. 363-377.
9. Patton, M.E., and Whittoker, W.L., " Effects of fiber content and damaging load on steel fiber reinforced concrete stiffness ", ACI J. Vol. 80, No. 2, January – February 1983, pp. 13 – 16.
10. Abdul-Razzak, A.A., " Nonlinear finite element analysis of fibrous reinforced concrete structural members " .Ph.D. Thesis, University of Mosul, Iraq, Aug. 1996, 233 pps.
11. Gopalaratnam, V.S. and Shah, S.P., " Softening response of plain concrete in direct tension ", ACI J. Vol. 82, No. 27, May – June 1985, pp. 310 – 323.
12. نهى حميدي الجبوري،"التحليل غير الخطي بطريقة العناصر المحددة للبلاطات الخرسانية الليفية المسلحة. اطروحة ماجستير، جامعة الموصل ، تشرين الثاني 2002.
13. Shah, S.P., and Gopalatnam, V.S., " Micromechanical and model for the tensile fracture of stell fiber reinforced concrete ", in RILEM Symp. on Developments infiber Reinforced Cementand Concrete (Eds. R.N. Swamy, and R.L. Wagstaffe and D.R. Sakley), University of Sheffield Press, 13 – 17 July 1986, Sheffield, pp. 17 – 26 .
14. Mansur, M.A., Nagataki, S., Lee, S.H., and Oosumimoto, Y., " Torsional response of reinforced fibrous concrete beams ", ACI Structural Journal, Vol. 86, No. 1, Jan – Feb 1989, pp. 36 – 44.
15. Lim, T.Y., Paramasivam, P., Mansur, M.A., and Lee, S.L., " Tensile behaviour of steel `fiber reinforced concrete composites ", Proceedings, 3rd RILEM International Symposium on Developments in fiber Reinforced Cement and Concrete, University of Sheffieid Press, 13-17 July 1986, Sheffield, pp. 7 – 15.
16. Al-Mahaidi, R.S.H., " Nonlinear finite element analysis of reinforced concrete deep members ", Ph. D. Thesis, Dept. of Structural Engineering, Cornell University, Ithaca, New York, May 1978, 374 pps.

17. Al-Ta'an, S.A. and Abdul-Razzak, A.A., "Nonlinear finite element analysis of fibrous reinforced concrete corbels", AL-Rafidain Engineering Journal, Vol. 11, No. 1, 2003, pp. 34-46.
18. Abdul-Razzak, A.A. and Al-Ta'an, S.A., "Nonlinear finite element analysis of fibrous reinforced concrete deep beams", AL-Rafidain Engineering Journal, Vol. 11, No. 1, 2003, pp. 47-62.
19. Kupfer's, H., Hilsprof, K.H., and Rush, "Behaviour of concrete under biaxial stresses" , proceedings ACI, Vol. 16, No. 8, 1969, pp. 656-666.
20. Abdul-Razzak, A.A. and Abdulah, S.M., "Nonlinear analysis of reinforced concrete plates", SIGMA, Majalah Sains Dan Teknologi Vol. 5, No. 1, Jan 2002, pp. 9-18.
21. Abdul-Razzak, A.A., "geometric And Material Nonlinear Analysis Of Reinforced Concrete Slabs Using Assumed Strain Elements", Mu'tah Lil-Buhuth wad-Dirasat, Vol. 17, No. 3, 2002, pp. 139-155.
22. Abdul-Razzak, A.A. and Abdulah, S.M., "The Influence Of Tension Stiffening Models On The Nonlinear Analysis Of Reinforced Concrete Shells", Tikrit Jour. Of Eng. Sci., Vol. 9, No. 2, July 2002, pp. 49-70.
23. Mahmood, K.S., Abdul-Razzak, A.A., and Kasim, M.K., "Nonlinear Dynamic Analysis Of Reinforced Concrete Slabs ", Tikrit Jour. Of Eng. Sci., Vol. 13, No. 3, October 2006, pp. 121-142.
24. Belarbi, A., and Hus, TH. T. C., "Constitutive laws of softened concrete in biaxial tension compression", ACI Structural Journal, Vol. 92, No. 5, 1995, pp. 562-573.
25. Swamy, R.N., and Ali, S.A.R., " Punching shear behaviour of reinforced concrete slab – column connections made with steel fibers concrete ", ACI J. Proceedings, Vol. 78, No. 5, Sept. – Oct. 1981, pp. 395 – 405 .
26. Ali, S.A.R., " Effect of fiber reinforcement on the punching shear of flat plates", Ph.D. Thesis, University of Sheffield, UK, April 1979, 241 pps.

Investigation of Frequency Characteristics of GFRP Pultrusion Composite Beams

Ziad K. Awad
Civil Engineering Department, Faculty of Engineering,
University of Mosul, Iraq
e-mail: drziadawad@gmail.com, drziadawad@uomosul.edu.iq

Abstract

This research was carried out to study the dynamic characteristics of a new GFRP pultruded beam. As a part of the project, the natural frequency behavior of such fiber composite beam has been investigated by experimental tests and numerical simulation. The GFRP composite beam was developed for civil engineering applications. This beam was used in several applications such as; beams, pedestrian bridge, bridge decks, girders, and piles. The GFRP beam is made from multi-layers glass fiber with resin. This beam was manufactured in automated pultrusion machine. The experimental analysis was conducted to find the GFRP beam natural frequency behavior under simply supported condition. The experimental results were then compared with the Finite Element (FE) numerical analysis. In addition, the experimental results were compared with the existing analytical equation. It was found that the FE analysis showed a good agreement with the existing experimental results.
Keywords: beam; composite; GFRP; finite element; natural frequency.

الخواص الديناميكية للعتبات المجوفة والمصنوعة من الالياف الزجاجية

د. زياد خلف عواد
قسم الهندسة المدنية – كلية الهندسة – جامعة الموصل

مستخلص

تم اجراء هذا البحث لدراسة الخواص الديناميكية للعتبات المجوفة والمصنوعة من الالياف الزجاجية. كجزء من متطلبات البحث فقد تم دراسة سلوك العتب تحت تأثير الاهتزازات بالطرق العملية والعددية. هذا النوع من الاعتاب تم تطويره ليفي بمتطلبات اعمال الهندسة المدنية وقد استخدم هذا النوع في جسور المشاة، الجسور الاعتيادية، الاعتاب الرئيسة في الجسور، بلاطة الجسور واعمال الركائز. المواد المركبة تصنع من الالياف الزجاجية مع المواد الصمغية وتكون على شكل طبقات. صنعت الاعتاب بواسطة السحب في مصنع أتوماتيكي. وتم فحص الاعتاب عمليا وتم قياس التردد تحت تأثير اسناد بسيط لطرفي العتب. تمت مقارنة النتائج العملية مع النتائج العددية لطريقة العناصر المحددة والطرق التحليلية. وتم الاستنتاج بان طريقة العناصر المحددة أعطت أفضل النتائج مقارنةً بالنتائج العملية.

1. **Introduction**

FRP composite pultrusions are now been considered by the structural engineers as a most attractive application. Glass fiber (GFRP) is well known today in the markets and represents the most versatile industry materials. The available glass fiber is made from compositions containing silica. Glass fiber has some benefits such as; high tensile strength, fire resistance, chemical resistance, hardness, moisture resistance [1, 2] and low cost compared to carbon fiber [3]. The FRP pultrusion might be used in the sport stadiums, clubs, shopping centers, offices and houses. Highway bridge girder and deck represent the well-known composite pultrusion applications because it solves several problems related to the decking system [4, 5]. In addition, there are many applications for pultrusions in the constructions of columns and piles [6].

An Australian manufacturer has fabricated a new structural GFRP pultrusion for civil engineering applications such as beams, girder bridge, piles, cross ties, and bridge deck [7] as shown in Fig. a-1. The pultrusion is made from E-CR glass fiber with 9-plies in 0^o and $\pm 45^o$ orientations as shown in Fig. b-1. This product has a density equal to 1970 kg/m^3. The GFRP pultrusion beam offers many benefits such as; ability to carry high flexural load, high strength to weight ratio, moisture resistance and termite resistance [8]. The properties of the GFRP pultrusion beam are shown in Table 1 as it is given by manufacturer.

Most current design studies are concerned in avoiding structural failure and excessive vibration problems [9]. Many design formulae do not consider the frequency of the load as a design parameter. However, many researchers believe that the natural frequency is important to control the human-induced vibration. Murphy [10] presented a numerical formula to find the natural frequency of a simply supported beam. This formula showed a good agreement with the analytical solution. Murphy equation is shown below:

$$f^2 = 2.467 * \frac{E.I.L}{\rho.S^4} \qquad (1)$$

where f is the frequency, E is the elastic modulus, I is the moment of inertial, L is the total length, S is the span and ρ is the density.

The analysis of a free vibration of fiber composite beam is more complicated than the normal homogenous beam section. The fiber composite beam is usually made from many layers in different orientations. The behavior of the fiber composite material is more complicated due to anisotropic composition. Nilsson and Nilsson [11] used the six order differential equation to simulate the free vibration of the sandwich beam depending on the Hamilton's principle. The conclusion was made that shear effect is dominant in the lightweight composite sandwich beam. Żak et al [12] studied the free vibration of multi-layered beam with delamination effects. Their work showed that the natural frequency decreased with the delamination length. Epaarachchi [13] studied the vibration behavior of FRP composite beam under the effect of fatigue and fracture. It was found that the fundamental frequencies of the beam have been changed significantly due to fatigue cycling.

This product was used in the fabrication of 9 m girder bridge [14] as shown in Fig. 2. This girder was used in the replacement of degraded timber girder. Therefore, understanding the behavior of this kind of product is more essential.

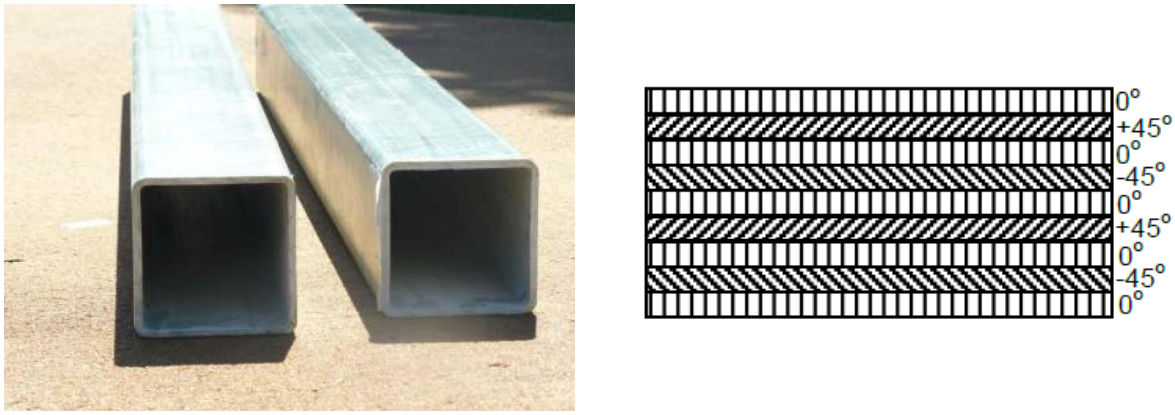

a. Square pultrusion b. Section plies configuration

Figure 1 GFRP pultrusion

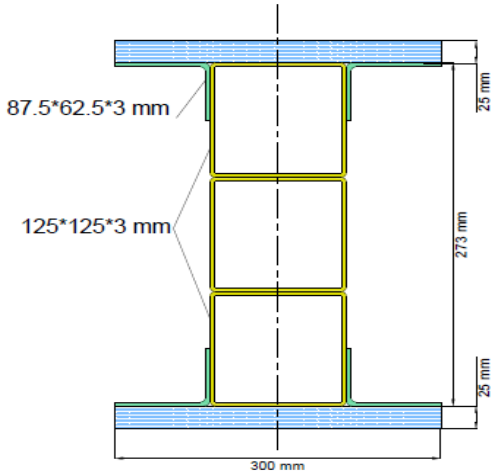

Figure 2 GFRP girder bridge

Table 1 Mechanical property by manufacturer

Property	Longitudinal	Transfers
Density (kg/m^3)	1970	
Tensile strength (MPa)	650	41
Compression strength (MPa)	550	104
Shear strength (MPa)	84	84
Modulus of Elasticity (MPa)	35400	12900

2. **Experimental Test**

The fiber composite beam was prepared by cutting a sample of 1500 mm in length and clear span is equal to 1400 mm. The beam cross section dimensions were 100 x 100 x 5.25 mm. Simple supported hollow beam was tested as shown in Fig. 3. The experimental test was done by using the LMS Test-lab instrument. The experimental model is shown in Fig. 3. Two-channel data reading was used; one for the sensor and the second for the impact hammer as shown in Fig. 4. Sensor was fixed in three positions; mid-span, quarter span and 1/6 of the beam span to pick-up three different modes.

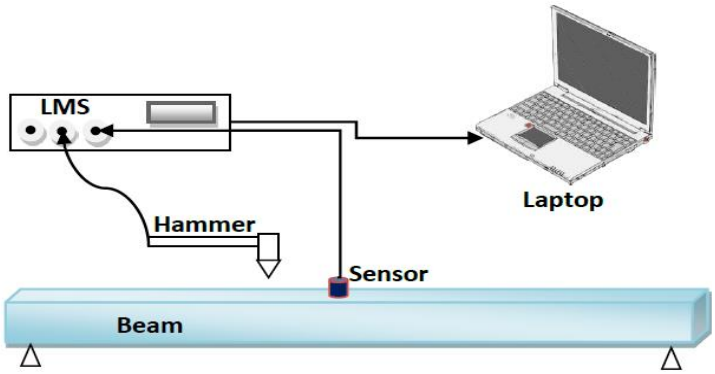

Figure 3. Experimental model

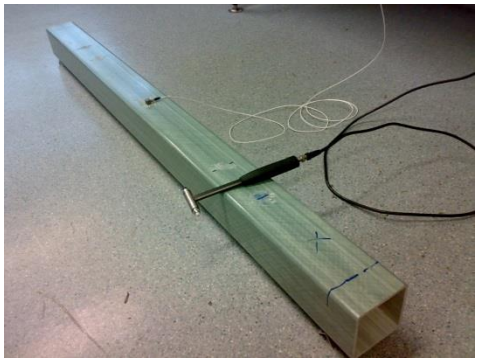

Figure 4 Experimental setup

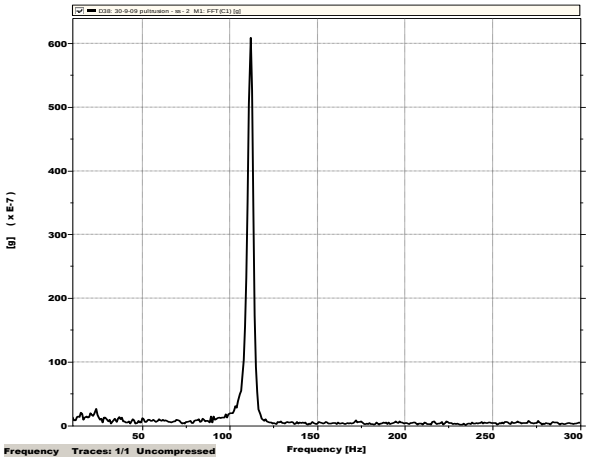

a-First mode

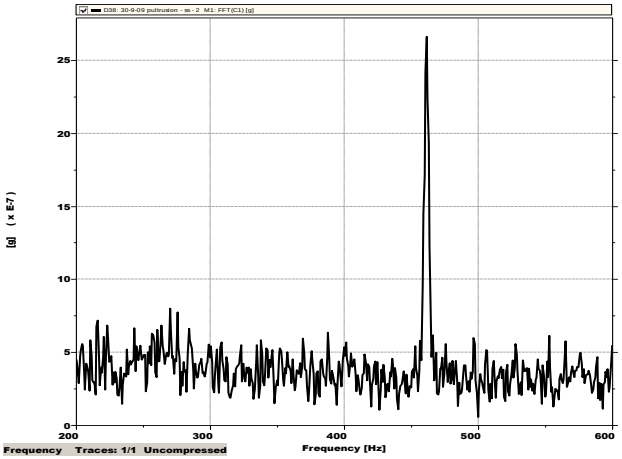

b-Second mode

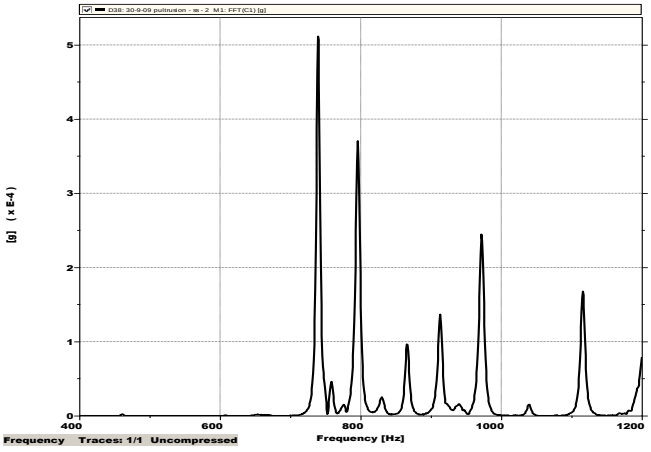

c-Third mode

Figure 5 Experimental free vibration results

The results of the free vibration test are shown in Fig. 5. The first, second, and three modes are 111.7 Hz, 461.0 Hz, and 739 Hz respectively. The sensor was fixed in the mid-span to pick-up the first natural frequency. The frequency spectrum is shown in Fig. a-5, and the peak gives the first natural frequency value which is equal to 111.7 Hz. The frequencies spectrums for the second and third modes are shown in Figs. b-5 and c-5 respectively.

3. **Analytical Solution**

There are few existing formulae suggested for the calculation of the natural frequency of homogenous beams section. Most of these equations depend on the section rigidity, mass and the span of the beam. The Euler-Bernoulli beam model represents one of the analytical solutions for the free vibration analysis of beams. The Euler-Bernoulli beam model can be applied for different type of boundary conditions. The general equation of Euler-Bernoulli beam is described below [15].

$$w = \left(\frac{a_n}{L}\right)^2 * \sqrt{\frac{EI}{\rho A}} \tag{2}$$

where, A is the cross section area and a_n is the boundary conditions parameters. The analytical values of the present FRP sandwich beam are calculated by using equations 2 are listed in Table 2.

It can be seen that the results of the Euler-Bernoulli equation gives a higher estimation than the experimental results, especially for the third mode. This is mainly attributed to the effect of shear deformation, which is not included in Euler-Bernoulli equation.

4. **FE Simulation**

The FE simulation is formulated for the analysis fiber composite pultrusion beam and conducted using ABAQUS commercial software. FE method is regarded as efficient method to predict the natural frequency of sandwich structures [16]. The beam wall was formulated using a C3D20R (20- node quadratic brick element, reduced integration) as shown in Fig, a-6. Composite plies were modeled as well as shown in Fig. b-6. First order shear deformation theory (FSDT) is used for the formulation of the 3D solid element used in the simulation. The formulation of FSDT needs only C_o continuity and it is the most common in FE analysis. The FE analysis results are shown in Table 2, with the predicted mode shape. FE method shows a better prediction than the analytical equation.

Table 2 Analytical, FE, and experimental results

		f_1	f_2	f_3
Frequency (Hz)	Analytical	131.36	131.36	1182.2
	FE	126.23	469.7	758.0
	Frequency (Hz)	111.7	461.0	739.0
Mode Shape	mode	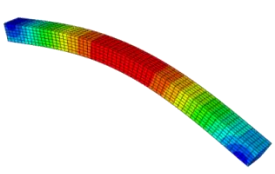	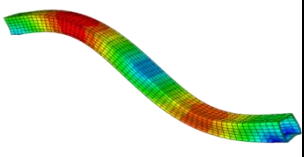	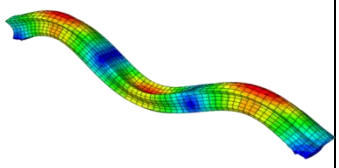

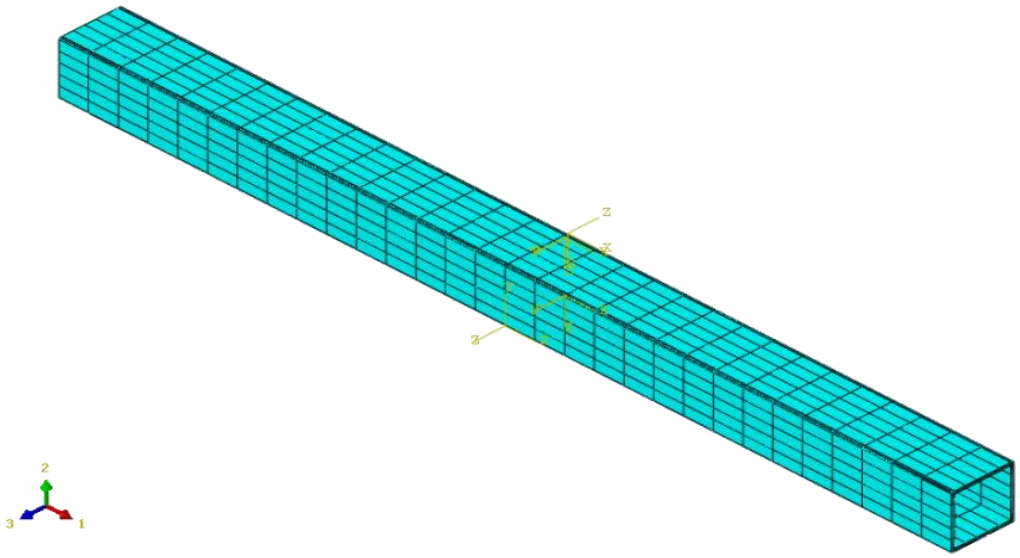

a- Beam mesh

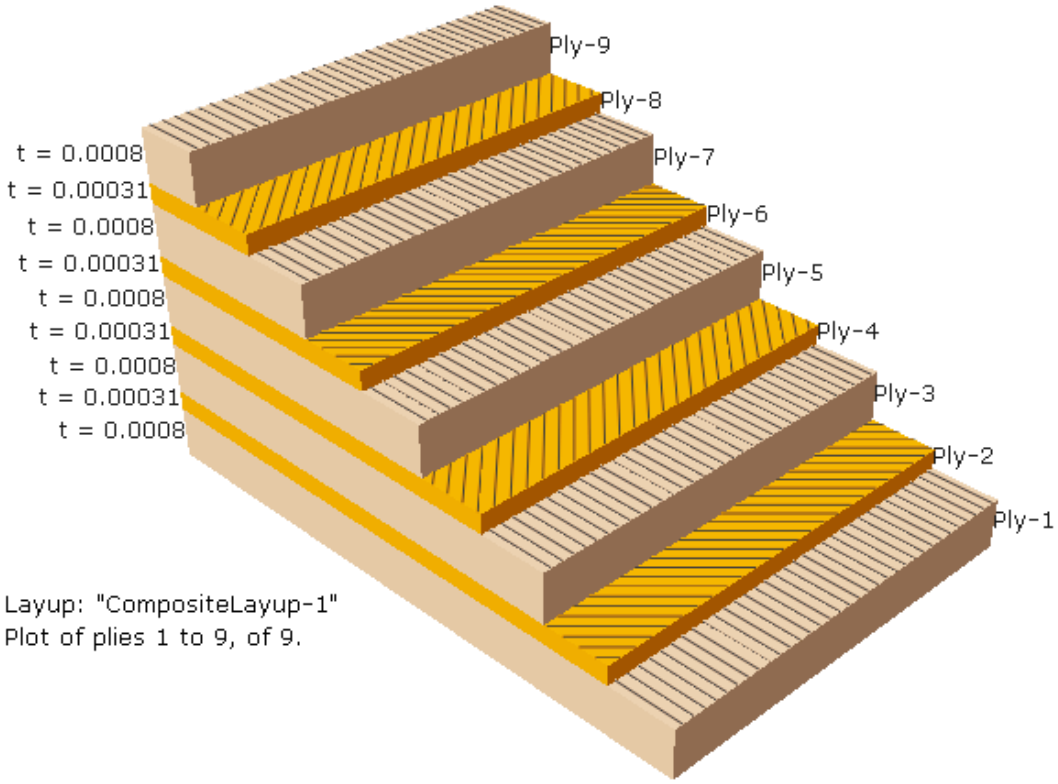

b- Plies structure

Figure 6 FE model

5. GFRP Beam Damping

Damping is very important in the structural design. The damping properties of the structure effect on the long fatigue life of the structure. Structure with high damping might have longer life than the structure with low damping ratio. Fiber glass usually has low damping ratio with less than 2% [17]. A half power method was used to calculate the damping ratio of fiber composite beam. The damping ratio (ξ) is calculated from the equation below and the explanation of this method is shown in Fig. 7.

$$\xi = \frac{w_2 - w_1}{2w_r} \tag{3}$$

where, w_r is the resonance frequency. w_1 and w_2 are the left and right frequencies at 3dB below the resonance amplitude as shown in Fig. 7 (dB is decibel).

The damping ratio for the simply supported beam is calculated and shown in Table 3.

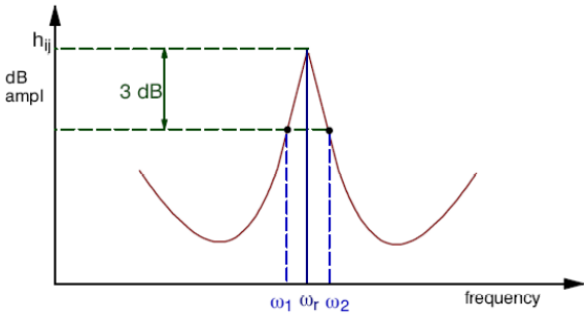

Figure 7 Half power (3dB) method for damping estimation

Table 3 Damping ratio calculation

Beam support type	w_r (Hz)	w_1 (Hz)	w_2 (Hz)	Damping %
Simply supported	111.7	110.8	112.2	1.2

6. Results Discussion

The results of the above three sections show the prediction of natural frequency of the glass fiber composite pultrusion. The first three natural frequencies are calculated by experimental, analytical and numerical approaches for the composite pultrusion. The results show that there are differences between the numerical, analytical and experimental results. These differences due to the effect of shear deformation. The FE results are more accurate than the analytical results, because the shear deformation is considered in the simulation. However, the FE method is overestimates the results because the FSDT gives over-estimation for the transfers shear stiffness. The damping ratio of the GFRP composite beam was calculated and it is equal to 1.2 %. The damping ratio is much lower than the damping ratio of other materials such as steel (damping ratio 2 - 5%) and concrete (damping ratio 3 - 6%).

7.Conclusions

An experimental investigation of the natural frequency of a GFRP composite beam was carried out for three modes. The experimental results were compared with the FE method and it showed a good agreement. The analytical equation required a correction factor to consider the shear deformation effect. Damping ratio was calculated from the experimental test and it showed a low value compared to traditional materials.

8.References

[1] Knox, C.E. *"Fiberglass Reinforcement. In: Handbooks of Composites"*, Lubin, G. Ed., VAN NOSTRAND REINHOLD, New York, 1982, pp. 136-59.

[2] Frederick, T., Wallenberger, Watson, J.C., Li, H. *"Glass Fibers. In: ASM Handbook: Composite"*, Miracle, D.B., Donaldson, S.L. Eds., 2001, Vol. 21.

[3] Lavoie, J.A. *"Scaling effects on damage development, strength and stress- rupture life of laminated composite in tension"*. Virginia, PhD thesis: Virginia Polytechnics Institute and State University; 1997.

[4] Davalos, J.F., Qiao, P., Ramayanam, V., Shan, L., Robinson, J. *"Torsion of honeycomb FRP sandwich beams with a sinusoidal core configuration"*. Composite Structures. 2009, Vol. 88, 97-111.

[5] O'Connor, J.S. *"GRP bridge decks and superstructures in the USA"*. Reinforced Plastics. 2008, Vol. 52, pp. 26-31.

[6] Gay, D., Hoa, S., Tsai, S. *"Composite Materials: Design and Applications"*. Florida, CRC Pr I Llc, 2003.

[7] Guades, E., Aravinthan, T., Islam, M., Manalo, A. *"A review on the driving performance of FRP composite piles"*. Composite Structures. 2012, Vol. 94, pp. 1932-42.

[8] Van Erp, G., Rogers, D. *"A Highly Sustainable Fibre Composite Building Panel"*. In: Sustainable Procurement Conference, Brisbane, 2008.

[9] Ebrahimpour, A., Sack, R.L. *"A review of vibration serviceability criteria for floor structures"*. Computers & Structures. 2005, Vol. 83, pp. 2488-94.

[10] Murphy, J. *"Transverse vibration of a simply supported beam with symmetric overhang of arbitrary length"*. Journal of Testing and Evaluation. 1997, Vol. 25, pp. 522-4.

[11] Nilsson, E., Nilsson, A.C. *"Prediction and measurement of some dynamic properties of sandwich structures with honeycomb and foam cores"*. Journal of Sound and Vibration. 2002, Vol. 251, pp. 409-30.

[12] Zak, A., Krawczuk, M., Ostachowicz, W. *"Numerical and experimental investigation of free vibration of multilayer delaminated composite beams and plates"*. Computational Mechanics. 2000, Vol. 26, pp. 309-15.

[13] Epaarachchi, J. *"Change of dynamic response of pultruded composite components used in advanced composite structures due to fatigue and fracture"*. In: Proceedings of the 20th Australasian Conference on the Mechanics of Structures and Materials (ACMSM 20), Taylor & Francis (CRC Press), 2009, pp. 759-63.

[14] Awad, Z.K., Aravinthan, T., Zhuge, Y., Gonzalez, F. *"A review of optimization techniques used in the design of fibre composite structures for civil engineering applications"*. Materials & Design. 2012, Vol. 33, pp. 534-44.

[15] Han, S., Benaroya, H., Wei, T. *"Dynamics of transversely vibrating beams using four engineering theories"*. Journal of Sound and Vibration. 1999, Vol. 225, pp. 935-88.

[16] Reddy, J. *"Mechanics of laminated composite plates and shells: theory and analysis"*. London, CRC, 2004.

[17] Berthelot, J.-M., Sefrani, Y. *"Longitudinal and transverse damping of unidirectional fibre composites"*. Composite Structures. 2007, Vol. 79, pp. 423-31.

Flexural Analysis of Reinforced Fibrous Concrete Slabes

Azad Mohammed [1], Sa'ad Al-Ta'an [2] , Hisham Al-Hassani[3]

[1] Assistant professor, Faculty of Engineering, University of Sulaimaniah, Kurdistan Region, Iraq, E-mail:azada1971@yahoo.com.
[2] Professor, College of Engineering, University of Mosul, Iraq, Email: saadaltaan@yahoo.com
[3] Professor, Building and Construction Department, University of Technology, Baghdad, Iraq.

Abstract

Flexural analysis of fibrous concrete rectangular slabs with or without skeletal steel reinforcement was carried out in this study. The analysis depends on simple calculation steps for deriving moment– curvature relationship utilizing the idealized stress-strain relations in compression and in tension for the constitutive slab materials. The load–deflection relationship is then calculated based on the classical plate theory results for the case of orthotropic simply supported rectangular slab. Comparison of the calculated and the experimental load-deflection curves showed good agreement.

Keywords: Curvature, Deflection, Moment, Slab, Steel fibres.

تحليل الانثناء للبلاطات الخرسانية الليفية المسلحة

أ. م. د. ازاد محمد[1] أ. د. سعد علي الطعان[2] أ. د. هشام الحسني[3]

1- أستاذ مساعد / هيئة الهندسة / جامعة السليمانية / العراق
2- أستاذ / كلية الهندسة / جامعة الموصل / العراق
3- أستاذ / قسم هندسة البناء وألإنشآت / الجامعة التكنلوجية / العراق

الخلاصة

في هذا البحث تم القيام بتحليل بلاطات خرسانية ليفية مسلحة مستطيلة الشكل مع أو بدون تسليح رئيسي. التحليل اعتمد على حسابات بسيطة باشتقاق علاقة العزم- التقوس باستعمال علاقات مثالية للإجهاد- الانفعال في الانضغاط والشد للمواد المكونة للبلاطات. علاقة الحمل الأود حسبت بالاعتماد على النظرية التقليدية للبلاطات البسيطة الاستناد والمتعددة الخواص. مقارنة منحنيات الحمل - الأود المحسوبة والعملية أظهرت توافقا جيدا.

Introduction

Fibrous concrete is greatly applied in the area of slabs, bridge decks, airport pavements, parking locations and erosion environments. In bridge decks, wearing surfaces have been the most common application. For seven bridge deck rehabilitation projects in USA latex-modified fiber reinforced concrete was used successfully. Steel fiber reinforced concrete slab-on-grade project was an experimental highway overlay project in Green County, Iowa, USA and it is considered as the most well mentioned one. Due to its improved flexural properties, steel fiber reinforced concrete is often used in aircraft pavements and warehouse floors. Twenty- three airports using slabs and four experimental test slabs for aircraft type loading have been reported [1].
With regard the fibrous concrete slab analysis and design Saib [2] studied the applicability of the yield line theory for predicting the ultimate load through testing nine square slabs having 960×960×33 mm dimensions, simply supported on four columns at corners and exposed to a central concentrated load. The main variables tested were the aspect ratio, fiber volume and fiber orientation. A relationship between ultimate moment and fiber volume was obtained via a relationship which combines the influences of aspect ratio fiber volume and fiber orientation with the ultimate moment. The results indicate that fibrous concrete slabs can be analyzed accurately by using the yield line theory.

Ghalib[3] used an analytical approach based on experimental results to determine the cracking moment and ultimate capacity of small fibrous concrete slabs. From a cracking load the cracking moment was calculated and by applying the simple elastic bending formula the cracking stress was determined.

Extensive experimental works were carried out by Agha [4] in order to test the applicability of yield line theory for fibrous concrete slab analysis. The research contains test results on a total of thirty four square slabs having dimensions of 800×800×30mm. In addition to plain concrete a fiber volume of 0.75 percent was used, but six fiber aspect ratios have been tested. The ratio of test / theoretical load using yield line theory was found to vary from 1.01 to 1.28.

The finite element method was used by Abdul-Razzak and Al-Jubory [5] for the nonlinear analysis of square and circular fibrous reinforcced concrete slabs. Assumed strain and heterosis elements are used to represent the slabs and a layered approach is used to discretize the concrete through the thickness. The nonlinear behaviour in compression, tension and the shear retension of the fibrous concrete were taken into account. The numerical results showed good agreement with published experimental test results.
In this research an attempt was made to calculate the complete load- deflection relationship for fibrous concrete slabs with or without steel bars in which the material nonlinear behavior was included in the analysis. The analysis is based on deriving moment- curvature relationship and using the deflection equation of elastic slab for calculating the complete load- deflection relationship. Based on the proposed model for analysis a stress distribution for the ultimate load capacity can be drawn for fibrous concrete slab with or without sketetal steel reinforcement.

Materials Behaviour and Idealization

Behaviour of Fibre Concrete in Compression

Although the equations derived below are limited to steel fiber concrete, they can also be used for other types of fibers but with some modifications by using appropriate fiber-concrete parameters. The model presented by Soroshian and Lee [6] for the compressive stress- strain relationship shown in Figure (1) consists of a parabolic ascending part followed by a bilinear descending one is adopted in the present analysis. The parabolic ascending portion of the relationship is given by the following expression:

$$f_c = f'_{cf}\,\frac{\varepsilon}{\varepsilon_{pf}}\left(2-\frac{\varepsilon}{\varepsilon_{pf}}\right) \qquad \text{for } \varepsilon \le \varepsilon_{pf} \tag{1}$$

Where f_c is the compressive stress, f'_{cf} is peak compressive stress, ε is the compressive strain, and ε_{pf} is compressive strain at peak compressive stress. A bilinear descending portion is given by the fllowing equation [6]:

$$f_c = z + (\varepsilon - \varepsilon_{pf}) + f'_{cf} \quad \ge f_o \tag{2}$$

In the absence of the experimental test for f_{cf}' it can be calculated from the following relationship [6]:

$$f'_{cf} = f'_c + 3.6 V_f l_f / d_f \tag{3}$$

where f'_c is the compressive strength of plain concrete, V_f , l_f and d_f are the fibers volume fraction, length and diameter respectively and ε_{pf} is the strain at peak stress of fibrous concrete and it is given by [6]:

$$\varepsilon_{pf} = 0.0021 + 0.0007 V_f l_f / d_f \tag{4}$$

The slope of the descending portion z and the residual stress f_o are respectively given by the following two equations [6]:

$$z = -343 f'_c (1 - 0.66\sqrt{V_f . l_f / d_f}) \tag{5}$$

$$f_o = 0.12 f'_{cf} + 14.8 V_f l_f / d_f \tag{6}$$

Behaviour of Fibre Concrete in Tension

Among many proposed stress strain relationships in tension which are available in literature the simplified relationship proposed by Lim, Paramasivam, and Lee [7] is adopted. Figure (1) shows this idealized tensile stress– strain relationship of steel fiber concrete. The value of the modulus of elasticity for fibrous concrete in tension is given by

$$E_{ct} = E_{mt}(1 - V_f) + \eta_l . \eta_o E_f V_f \tag{7}$$

where E_{mt} and E_f are the elastic moduli of concrete in tension and fibers respectively. E_{mt} can be calculated by the equation given by ACI 318M-11 [8] as follows:

$$Emt = 4700\sqrt{f'_c} \tag{8}$$

The cracking strain, ε_{cr}, is calculated as follows:

$$\varepsilon_{cr} = \eta_o \eta_l V_f (\varepsilon_{pf} - \varepsilon_{mp}) + \varepsilon_{mp} \quad (9)$$

where ε_{mp} is cracking strain of the matrix = modulus of rupture divided by the elastic modulus of concrete in tension and ε_{pf} is strain at proportionality limit.

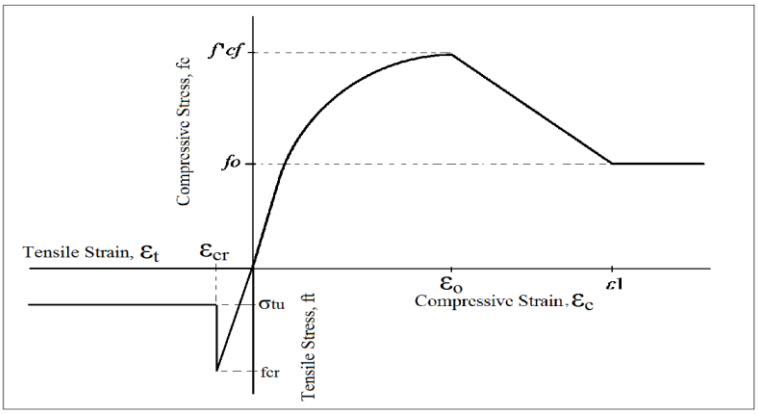

Figure (1) Idealized fibrous concrete stress- strain relationship [6]

The residual strength at the onset of matrix cracking, σ_{tu}, can be calculated using the general relationship given by Swamy and Al-Ta'an [9] based on pullout manner at failure:

$$\sigma_{tu} = 2\tau \eta_o \eta_l \mu_b V_f l_f / d_f \quad (10)$$

η_o is the orientation factor, η_l is the length efficiency factor and $\mu_b \geq 1.0$ is the bond efficiency factor that depends on the surface roughness of the fibres. A constant value for the product of $\eta_o \eta_l$ which is 0.41 is used in this study was proposed by Patton and Whittaker [10] based on experimental tests carried out to study the stiffness of fibrous concrete. The value of the dynamic bond stress τ ,can be taken from experimental tests. In this study τ = 3.5 MPa recommended by Lok and Pei [11] is used.

Behaviour of Steel Bars under Compression and Tension

The stress – strain relationship of steel reinforcement in both compression and tension can be represented by the idealized elastic fully plastic relationship.

Further Assumptions

The analytical model adopted in the present investigation is based on fundamental assumptions that are commonly used in the theories of shallow reinforced concrete members:

a- Plane section before bending remains plane after bending so that the strain distribution across the thickness of the slab is always linear even at ultimate stage of loading,

b- Time dependent effects of shrinkage and creep are neglected and

c- The steel bars and the surrounding concrete are perfectly bonded together so that no bond slip occurs.

Moment- Curvature Relationship of Reinforced Fibrous Slabs

In the present analysis, a procedure is followed to derive the moment-curvature relationship for a reinforced fibrous concrete slab section for the pre and post cracked stages [12]. Effects of concrete cover, *d'*, and compression steel area A'_s are taken into account in such derivation. The concrete cover in the two orthogonal directions of the slab is taken to be one-sixth of the slab thickness which is an approximate value range in full scale slabs. The resulting expressions of the moment – curvature relationship differ from those derived by Lim, Paramasivam and Lee [7] who neglected the effect of concrete cover, *d'*, and restricted their derivation to singly reinforced concrete beams.

Behaviour of Slabs under Loading

Elastic Uncracked Stage

A slab strip of unit width reinforced with top and bottom reinforcement is shown in Figure (2). The stress and strain distribution in the elastic pre-cracked stage, caused by pure bending, are as illustrated in Figure (2a). The location of the neutral axis will be defined by:

$$\mu = h_t / h_c \tag{11}$$

where h_t and h_c represent the depth of tensile and compressive zones, respectively. Taking d' as one sixth of the slab thickness, μ can be obtained by setting equilibrium of forces acting on the slab section which gives:

$$a_1\mu^3 + a_2\mu^2 + a_3\mu + a_4 = 0 \tag{12a}$$

where

$$a_1 = E_{ct}.h^2/2 + E_s.h(5A_s + A_s^{'})/6 \tag{12b}$$

$$a_2 = E_{ct}.h^2/2 + E_s.h(3A_s - A_s^{'})/2 \tag{12c}$$

$$a_3 = -f_{cf}^{'}.h^2/\varepsilon_{pf} + E_s.h(A_s - 3A_s^{'})/2 \tag{12d}$$

$$a_4 = E_{ct}.h^3.\phi_e/(3\varepsilon_{pf}^2) - f_{cf}^{'}.h^2/\varepsilon_{pf} - E_s.h(A_s + 5A_s^{'})/6 \tag{12e}$$

where Φ_e is the curvature in the elastic stage, f'_{cf} and ε_{pf} are given by Eqs. (3 and 4), respectively. E_{ct} can be calculated from Eq. (7). E_s is the modulus of elasticity of steel and taken as 200 kN/mm^2 and h is the overall depth of the slab strip. The above equations are applicable till the limiting case is reached when the extreme fiber of the tension zone cracks. The corresponding value of the curvature then becomes:

$$\phi_{cr} = \varepsilon_{cr}(1+\mu)/(\mu.h) \tag{13}$$

The flexural moment is given by the following Equation:

$$M_e = \int_{-h_c}^{0} \frac{f_{cf}^{'}}{\varepsilon_{pf}}(2\phi_e.\beta^2 - \frac{\phi_e^2.\beta^3}{\varepsilon_{pf}})d\beta + \int_{0}^{h_t} \phi_e.E_{ct}.\beta^2 d\beta + T_s(h_t - d^{'}) + T_s^{'}(h_c - d^{'}) \tag{14}$$

in which T_s and T'_s are the forces in the tension and compression reinforcement, respectively. Substituting the values of T_s, $T_s^{'}$, h_c and h_t in Eq. (14) and integrating the tensile and compressive stresses, the following Equation is obtained:

$$M_e = \frac{\phi_e.h^3}{12(1+\mu)^4}\left\{\frac{f_{cf}^{'}}{\varepsilon_{pf}}[(1+\mu)+\frac{3\phi_e.h}{\varepsilon_{pf}}]+4E_{ct}.\mu^3(1+\mu)\right\}+ \\ E_s.\phi_e[(\frac{\mu.h}{1+\mu}-\frac{h}{6})^2 A_s+(\frac{h}{1+\mu}-\frac{h}{6})^2 A_s^{'}] \quad (15)$$

Cracking Stage (1)

The stress and strain distributions for this stage are illustrated in Figure (2b). Equilibrium of forces lead to an equation similar to Eq. (12). Constants a_1, a_2, a_3 and a_4 are given by:

$$a_1 = \sigma_{tu}.\varepsilon_{cr}/\phi_c^2 - \sigma_{tu}.h/\phi_c - E_s.h(5A_s+A_s^{'})/6 - E_{ct}.\varepsilon_{cr}^2/(2\phi_c^2) \quad (16a)$$

$$a_2 = 3\sigma_{tu}.\varepsilon_{cr}/\phi_c^2 - 2\sigma_{tu}.h/\phi_c - E_s.h(A_s-3A_s^{'})/2 - 3E_{ct}.\varepsilon_{cr}^2/(2\phi_c^2) \quad (16b)$$

$$a_3 = f_{cf}^{'}.h^2/\varepsilon_{pf} + 3\sigma_{tu}.\varepsilon_{cr}/\phi_c^2 - \sigma_{tu}.h/\phi_c + E_s.h(3A_s-A_s^{'})/2 - 3E_{ct}.\varepsilon_{cr}^2/(2\phi_c^2) \quad (16c)$$

$$a_4 = f_{cf}^{'}.h^2/\varepsilon_{pf} + \sigma_{tu}.\varepsilon_{cr}/\phi_c^2 - \phi_c.f_{cf}^{'}h^3/(3\varepsilon_{pf}^2) + E_s.h(5A_s+A_s^{'})/6 - E_{ct}.\varepsilon_{cr}^2/(2\phi_c^2) \quad (16d)$$

The above equations are applicable until the tension reinforcement yields. The corresponding value of the curvature is given by:

$$\phi_{c1} = 6.\varepsilon_{sy}(1+\mu)/(h(5\mu-1)) \quad (17)$$

During this stage the flexural moment is given by the following Equation:

$$M_e = \int_{-h_c}^{0}\frac{f_{cf}^{'}}{\varepsilon_{pf}}(2\phi_c.\beta^2-\frac{\phi_c^2.\beta^3}{\varepsilon_{pf}})d\beta + \int_{0}^{h_t}\phi_c.E_{ct}.\beta^2 d\beta + \int_{h_y}^{h_t}(\phi_c.E_{ct}.\beta^2-\sigma_{tu}.\beta)d\beta + \\ T_s(h_t-d^{'})+T_s^{'}(h_c-d^{'}) \quad (18)$$

Substituting the values of T_s, $T_s^{'}$, h_c and h_t in Eq. (18) and integrating the tensile and compressive stresses, the following Equation is obtained:

$$M_{c1} = \frac{\phi_c.h^2}{(1+\mu)^3}\left\{\frac{f_{cf}^{'}}{\varepsilon_{pf}}(\frac{2h}{3}+\frac{\phi_c.h^2}{4\varepsilon_{pf}(1+\mu)})+\frac{\sigma_{tu}.\mu^2}{2\phi_c}(1+\mu)(1-\lambda^2)+\frac{E_{ct}.h.\lambda^3.\mu^3}{3}\right\}+ \\ E_s.\phi_c[(\frac{\mu.h}{1+\mu}-\frac{h}{6})^2 A_s+(\frac{h}{1+\mu}-\frac{h}{6})^2 A_s^{'}] \quad (19)$$

where λ is given by

$$\lambda = h_y/h_t = \varepsilon_{cr}(1+\mu)/(\phi_c.\mu.h) \quad (20)$$

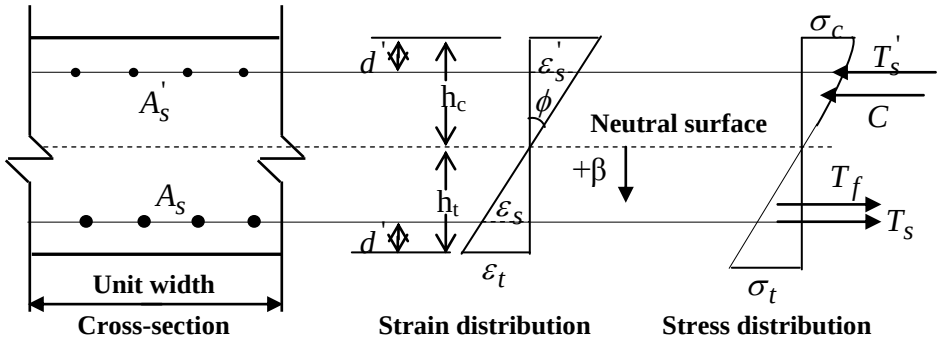

(a) Elastic Uncracked Stage $0 \leq \Phi \leq \Phi_{cr}$

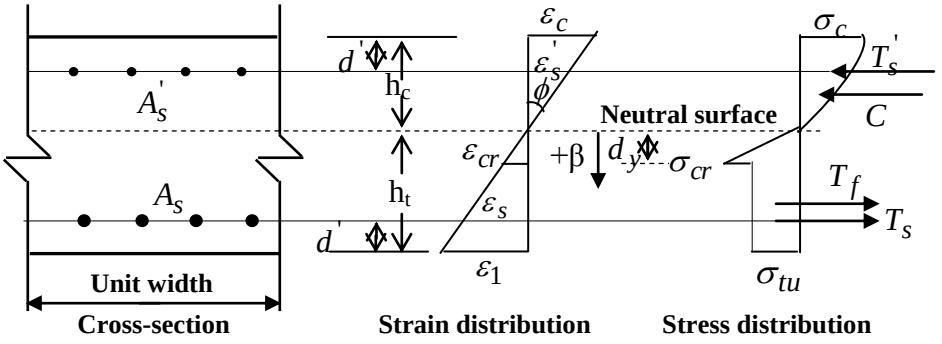

(b) cracked Stage (1) $\Phi_{cr} \leq \Phi_c \leq \Phi_{c1}$

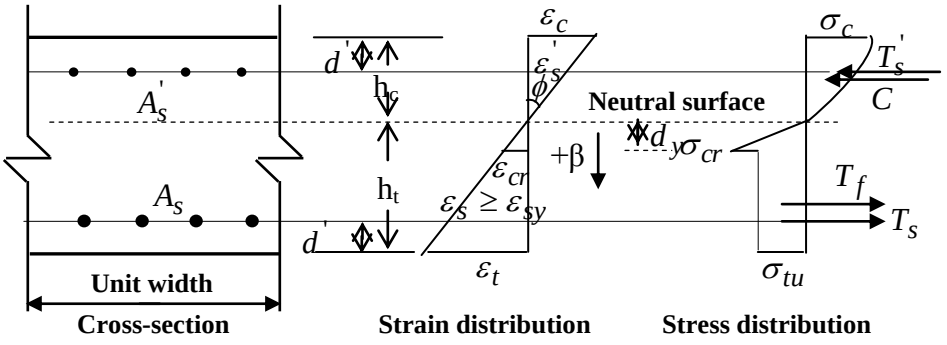

(c) cracked Stage (2) $\Phi_{c1} \leq \Phi_c \leq \Phi_{c2}$

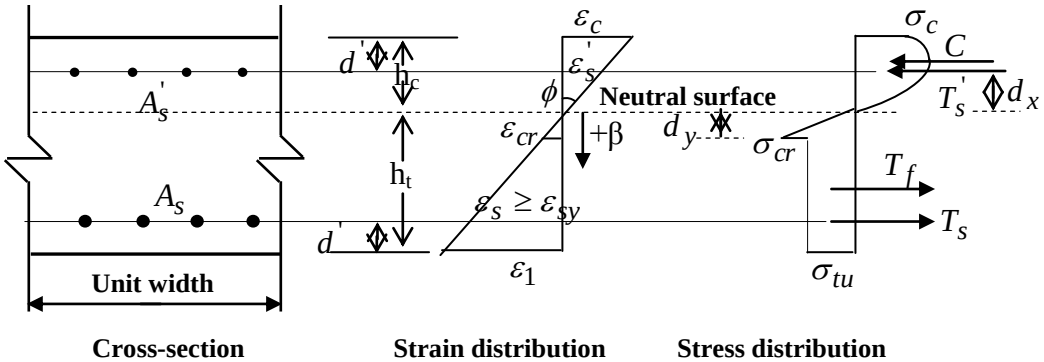

(d) cracked Stage (3) $\Phi_{c2} \leq \Phi_c \leq \Phi_{c3}$

Figure (2) Stress and Strain Distribution across the Slab Section [12]

Cracking Stage (2)

This stage starts, at the yielding of the tension reinforcement , and continues until the strain, ε_c, at the extreme fiber of the compression zone reaches the limiting value, ε_{pf}, given by Eq. (4). The stress and strain distribution during this stage are shown in Figure (2c). Equilibrium of forces lead to an equations similar to Eq. (12). The constants a_1, a_2, a_3 and a_4 are given by:

$$a_1 = \sigma_{tu}.\varepsilon_{cr}/\phi_c - \sigma_{tu}.h - A_s.f_y - E_{ct}.\varepsilon_{cr}^2/(2\phi_c) - A_s^{'}.E_s.\phi_c.h/6 \quad (21a)$$

$$a_2 = 3\sigma_{tu}.\varepsilon_{cr}/\phi_c - 2\sigma_{tu}.h - 3A_s.f_y - 3E_{ct}.\varepsilon_{cr}^2/(2\phi_c) + A_s^{'}.E_s.\phi_c.h/2 \quad (21b)$$

$$a_3 = 3\sigma_{tu}.\varepsilon_{cr}/\phi_c - \sigma_{tu}.h - 3A_s.f_y - 3E_{ct}.\varepsilon_{cr}^2/(2\phi_c) + 3A_s^{'}.E_s.\phi_c.h/2 + f_{cf}^{'}.\phi_c.h^2/\varepsilon_{pf} \quad (21c)$$

$$a_4 = \sigma_{tu}.\varepsilon_{cr}/\phi_c - A_s.f_y - E_{ct}.\varepsilon_{cr}^2/(2\phi_c) + A_s^{'}.E_s.\phi_c.h/6 + (f_{cf}^{'}.\phi_c.h^2/\varepsilon_{pf})[1-\phi_c.h/(3\varepsilon_{pf})] \quad (21d)$$

The above equation terminates when ε_c becomes equal to ε_{pf}, and when this limit is reached the corresponding curvature becomes:

$$\phi_{c2} = \varepsilon_{pf}(1+\mu)/h \quad (22)$$

The flexural moment for this stage is given by the following equation:

$$M_{c2} = \int_{-h_c}^{0} \frac{f_{cf}^{'}}{\varepsilon_{pf}}(2\phi_c.\beta^2 - \frac{\phi_c^2.\beta^3}{\varepsilon_{pf}})d\beta + \int_{0}^{h_t} \phi_c.E_{ct}.\beta^2 d\beta - \int_{h_y}^{h_t} (\phi_c.E_{ct}.\beta^2 - \sigma_{tu}\beta)d\beta + T_s(h_t - d^{'}) + T_s^{'}(h_c - d^{'}) \quad (23)$$

Or

$$M_{c2} = \frac{f_{cf}^{'}\phi_c.h^3}{\varepsilon_{pf}(1+\mu)^3}[\frac{2}{3} + \frac{\phi_c.h}{4\varepsilon_{pf}(1+\mu)}] + \frac{\varepsilon_{cr}^2}{\phi_c^2}(\frac{E_{ct}.\varepsilon_{cr}}{3} - \frac{\sigma_{tu}}{2}) + \frac{\sigma_{tu}.\mu^2.h^2}{2(1+\mu)^2} + A_s.f_y.h.(\frac{\mu}{1+\mu} - \frac{1}{6}) + A_s^{'}.E_s\phi_c.h^2(\frac{1}{1+\mu} - \frac{1}{6})^2 \quad (24)$$

Cracking Stage (3)

This stage covers all values of compressive strain ε_c between ε_{pf} and ε_1, the later is the ultimate strain at which the descending branch of the compressive – strain relationship terminated as shown in Figure (1). Strain and stress distribution during this stage is shown in Figure (2d). Equilibrium of forces lead to the following relationship for calculating μ:

$$a_1\mu^2 + a_2\mu + a_3 = 0 \quad (25)$$

where

$$a_1 = \sigma_{tu}.\varepsilon_{cr}/\phi_c - \sigma_{tu}.h - E_{ct}.\varepsilon_{cr}^2/(2\phi_c) - f_{cf}^{'}.\varepsilon_{pf}/(3\phi_c) + z.\varepsilon_{pf}^2/(2\phi_c) - \phi_c.h.E_sA_s^{'}/6 - A_s.f_y \quad (26a)$$

$$a_2 = 2\sigma_{tu}.\varepsilon_{cr}/\phi_c + (f_{cf}^{'} - \sigma_{tu})h - E_{ct}.\varepsilon_{cr}^2/\phi_c - 2f_{cf}^{'}.\varepsilon_{pf}/(3\phi_c) + z.\varepsilon_{pf}^2/\phi_c - 2\phi_c.h.E_s.A_s^{'}/3 - 2A_s.f_y - z.\varepsilon_{pf}/h \quad (26b)$$

$$a_3 = \sigma_{tu}.\varepsilon_{cr}/\phi_c + f_{cf}^{'}.h - E_{ct}.\varepsilon_{cr}^2/(2\phi_c) - f_{cf}^{'}.\varepsilon_{pf}/(3\phi_c) + z.\varepsilon_{pf}^2/(2\phi_c) + 5\phi_c.h.E_s.A_s^{'}/6 - A_s.f_y + z.h(\phi_c.h/2 - \varepsilon_{pf}) \quad (26c)$$

The above equation is usefull for all ε_c smaller than ε_1. It should be noted that ε_1 is usually larger than 0.003 recommended by ACI318M-11 [8] as ultimate compressive strain. The corresponding curvature related to strain equal to ε_1 is given by:

$$\phi_{c3} = [\varepsilon_{pf} + (f_o - f_{cf}^{'})/z](1+\mu)/h \quad (27)$$

The flexural moment during this stage is given by the following equation:

$$M_{c3} = \int_{-h_x}^{0} \frac{f_{cf}^{'}}{\varepsilon_{pf}}(2\phi_c.\beta^2 - \frac{\phi_c^2.\beta^3}{\varepsilon_{pf}})d\beta + \int_{-h_c}^{h_x}(f_{cf}^{'}.\beta + z.\phi_c.\beta^2 - z\varepsilon_{pf}.\beta)d\beta + \int_{0}^{h_t}\phi_c.E_{ct}.\beta^2 d\beta - \int_{h_y}^{h_t}(\phi_c.E_{ct}.\beta^2 - \sigma_{tu}.\beta)d\beta + T_s(h_t - d^{'}) + T_s^{'}(h_c - d^{'}) \quad (28)$$

or

$$M_{c3} = \frac{\phi_c.h_2}{(1+\mu)^3}[\frac{f_{cf}^{'}}{\varepsilon_{pf}}(\frac{2h}{3} + \frac{\phi_c h^2}{4\varepsilon_{pf}(1+\mu)}) + \frac{\sigma_{tu}\mu 2}{2\phi_c}(1+\mu)(1-\lambda^2) + \frac{E_{ct}h\lambda^3\mu^3}{3}] + E_s\phi_c[(\frac{\mu h}{1+\mu} - \frac{h}{6})^2 A_s + (\frac{h}{1+\mu} - \frac{h}{6})^2 A_s^{'}] \quad (29)$$

For the case when the compression reinforcement exists there is an additional cracking stage starting from $\varepsilon_c = \varepsilon_1$ and terminating at the limit when the compression reinforcement begins to yield. This stage is, however, not important because slab sections are usually singly reinforced.

Load – Deflection Relationship for Reinforced Fibrous Concrete Slab

In deriving the load – deflection relationship a single function is determined to be employed in both the elastic and plastic stages since the value of such function can simplify the problem drastically. The deflection surface w(x,y) can be expressed by a double sine series, which satisfies the boundary conditions for a simply supported plate without in-plane restraints [13] as follows:

$$w(x,y) = \sum_{m=1,3,..}^{\infty}\sum_{n=1,3,..}^{\infty}\frac{16q}{\pi^2.m.n.D}\sin\frac{m\pi x}{L_x}\sin\frac{n\pi y}{L_y} \quad (30)$$

For orthotropically reinforced concrete slabs the value of D can be found as follows [13]:

$$D = \frac{D_x \pi^4 m^4}{L_x^4} + \frac{2\sqrt{D_x D_y}\,\pi^2 m^2 n^2}{L_x^2 L_y^2} + \frac{D_y \pi^4 n^4}{L_y^4} \tag{31}$$

where D_x is flexural rigidity in x-direction and D_y the flexural rigidity in y-direction. L_x and L_y is the slab length in the x and y directions respectively. The curvature in x-direction can be obtained by differenting Eq. (30) two times:

$$\Phi_x = \frac{16q}{\pi^4 L_x{}^2} \sum_{m=1,3,..}^{\infty} \sum_{n=1,3,..}^{\infty} \frac{m \sin\frac{m\pi x}{L_x} \sin\frac{n\pi y}{L_y}}{n\left(\frac{D_x m^4}{L_x{}^4} + \frac{2\sqrt{D_x D_y}\, m^2 n^2}{L_x{}^2 L_y{}^2} + \frac{D_y n^4}{L_y{}^4}\right)} \tag{32}$$

The curvature in y-direction is related to that in x-direction by the following equation:

$$\phi_y = R.\phi_x \tag{33}$$

where

$$R = \frac{\sum_{m=1,3,..}^{\infty} \sum_{n=1,3,..}^{\infty} n.\sin\frac{m\pi x}{L_x} \sin\frac{n\pi y}{L_y} / (m.D.L_y^2)}{\sum_{m=1,3,..}^{\infty} \sum_{n=1,3,..}^{\infty} m.\sin\frac{m\pi x}{L_x} \sin\frac{n\pi y}{L_y} / (nDL_x^2)} \tag{34}$$

The method of analysis is based on an incremental procedure in which the curvature in the x-direction is incremented in steps. The procedure for obtaining the total lateral load q and the deflection ω for a given curvature Φ_x is as follows:

a- for a given curvature Φ_x find value of μ by trial and error using the corresponding stress - strain relatioships and the equilibrium equation,
b- calculate the moment M_x and divide by Φ_x to obtain the flexural rigidity in x-direction (i.e. D_x),
c- assume Φ_y and compute μ and M_y as above, and then find D_y,
d- compute the value of R from Eq. (34) and a new value of Φ_y,
e- repeat the steps of c and d until the value of Φ_y converges,
f- having the last value of D_y, compute the load using Eq. (32).
g- compute the deflection using Eq. (30) and
h- return to step a for another increment of Φ_x value.

Validity of the Analysis

A series of fibrous concrete square slabs reinforced with or without steel reinforcement was tested under uniformly distributed load by Agha [4]. From the slab properties, load –deflection relationship was calculated based on the analysis procedure presented in the previous sections. Results of load-deflection for two slabs are taken in order to make a comparison with predicted load-deflection relationship.

The first slab designated as S32, has a dimensions of 800×800 mm and 30 mm thick, reinforced by 0.25 % steel wires and 0.75 % volume of fiber having the aspect ratio of 62.5. The analysis was extended to the deflection value reached by testing slab S32 which is about 0.6 times the

slab thickness. Figure (3) shows the test and theoretical load –deflection relationship for slab S32. It is shown that both the load-deflection relationship and the ultimate load predicted by the theoretical analysis are in good agreement with that of tested slab S32. The test ultimate load for this slab is 37.19 kN and the corresponding deflection is about 18 mm. At the later value of deflection the predicted load is 34 kN, while at the terminating point of the cracking stage (2) such value of load becomes 36.6 kN. It should be noted that the theoretical load predicted by applying yield line theory is 31.82 kN. Therefore the predicted ultimate load using the present approach offer better results compared with that predicted by yield line theory.

Those fibrous concrete slabs which are free from steel reinforcement slab (S14) have been chosen and the load-deflection relationship for this slab is shown in Fig.4. The load-deflection relationship based on the analysis is also shown in the same figure for comparison sake. It is shown that for the range where the test load-deflection relationship exists a good agreement between the two curves was obtained. The test ultimate load is 29.5 kN while the theoretical one is 26.7 kN and these two values is close to each other. Calculating the theoretical ultimate load using yield line theory was not tackled by Agha [4].

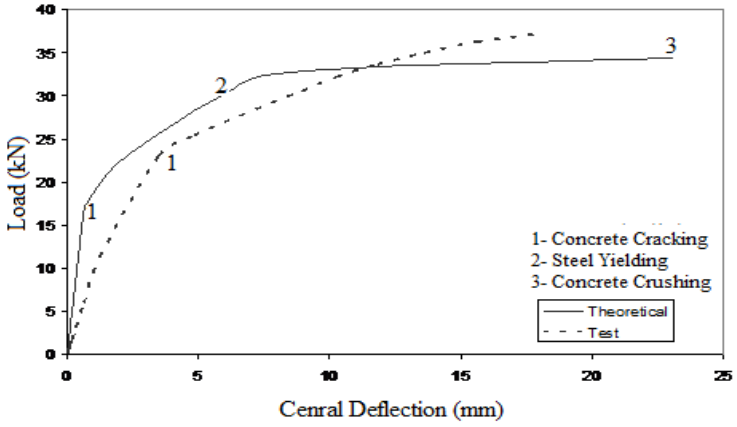

Fig.3 Theoretical and test load- deflection relationship of reinforced fibrous slab S32 [4]

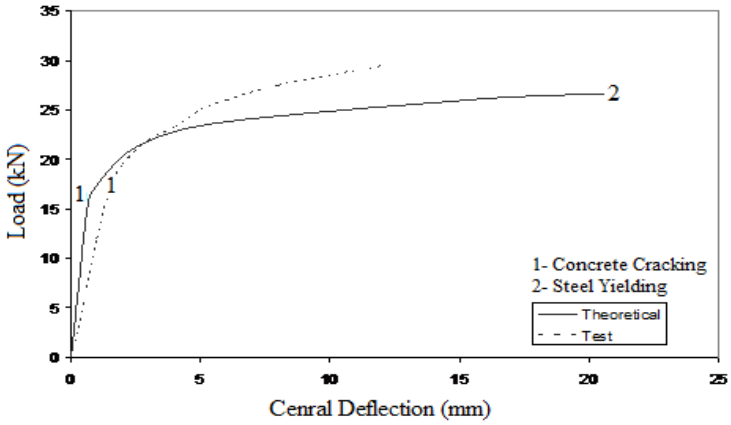

Fig.4 Theoretical and test load- deflection relationship of reinforced fibrous slab S14 [4]

Conclusions

From the present work on the analysis of reinforced fibrous concrete slabs, the following conclusions can be drawn:

1. The adopted materials consititutive relationships together with the method of nonlinear analysis of fibrous concrete slabs with or without top and bottom reinforcement presented in this study can be followed as a design guide for fibrous reinforced concrete slabs.
2. The calculated ultimate load capacity of reinforced fibrous concrete slab was found to be more accurate than that obtained using the yield line theory.
3. The change in stress distribution with the load across the depth can be traced easily.
4. Slabs with other boundary conditions can be analysed by modifying the governing equations controlling the bounary conditions.

References

[1] ACI Committee 544; *Design of Steel Fiber Reinforced Concrete*. Manual of Concrete Practice, Part 5, 1995.

[2] Saib, I. A.; *Yield Line Theory for Steel Fiber Reinforced Concrete Slabs*. MSc. Thesis, University of Baghdad, 1977.

[3] Ghalib, M. A.; *Moment Capacity of Steel Fiber Reinforced Small Concrete Slabs*. ACI Journal, Vol. 77, No. 4, April 1980, pp. 247-257

[4] Agha, A. Z. S.; *Ultimate Flexural Strength of Reinforced Fibrous Concrete Slabs Subjected to Uniformly Distributed Load*, MSc Thesis. University of Salah-Addin, 1988: 117pp.

[5] Abdul-Razzak, A. A. And Al-Jubory, N. H.; Nonlinear Analysis of Fibrous Reinforced Concrete Slabs by Assumed Strain and Heterosis Elements. AlRaffidain Engineering Jour., Vol. 18, No. 5, Oct. 2010, pp. 14-23.

[6] Soroushian, P. and Lee, C. D.; *Constitutive Modeling of Steel –Fiber Reinforced Concrete Under Direct tension and Compression*. Fiber Reinforced cements and Concretes. R.N. Swamy and Barr. eds. Elsevier Applied Science, New York, 1989: 363-377.

[7] Lim, T. Y., Paramasivam, P. and Lee, S. L.; *Behaviour of Reinforced Steel Fiber Concrete Beams in Flexure*. ASCE Structural Journal, 1987, 113(10): 2439-2458

[8] ACI Committee 318M-11; *Building Code Requirements for Structural Concrete*. American Concrete Institute. Farmington Hill MI, USA, 2011, 503 pp.

[9] Swamy , R. N. and Al-Ta'an , S. A.; *Deformation and Ultimate Strength in Flexure of Reinforced Concrete Beams Made with Steel Fiber Concrete*. ACI Journal, 1981, 78(5): 395 - 405.

[10] Patton, and Whittaker, W. L.; *Effect of Fiber Content and Damaging Load on Steel Fiber Reinforced Concrete Stiffness*. ACI Journal, 1983, 80(1): 13-16.

[11] Lok, T. and Pei, J.; *Flexural Behaviour of Steel Fiber Reinforced Concrete*. ASCE, Journal of Materials in Civil Engineering, 1998, 10(2):86-97.

[12] Mohammed, A. A., "Behaviour of Restrained Reinforced Fibrous Concrete Slabs allowing for Membrane Action", Ph.D. Thesis, Dept. Of Buildings and Structures, University of Technology, Iraq, Dec. 2003.

[13] Timoshenko, S. P. and Woinowsky-Krieger, S.; *Theory of Plates and Shells*, 1959, 580 pp.

Artificial neural networks model for predicting nonlinear response of rectangular plates

Dr. Salim T. Yousif
College of Engineering,
University of Mosul
E-mail styousif59112@uomosul.edu.iq

Dr. Ayad A. Abdul-Razzak
College of Engineering,
University of Mosul
E-mail: Drayad_aghwan@yahoo.co.uk

Abstract

This study illustrates the application of the artificial neural networks to build model for predicting the nonlinear response of plates with uniformly distributed load and different ductile material properties, plate size and boundary conditions. The data were collected using 2240 runs of nonlinear finite element analysis with Huber-Mises failure criterion. The input data for the model were: Load, thickness of plate, breadth of plate, aspect ratio (length /breadth), elastic modulus, plastic modulus, yield stress and boundary condition, while the output of the model was central deflection response, which consists of eight deflection values. The Levenberg-Marquardt (LM) techniques built in MATLAB used to construct the neural network model. The results show that artificial neural network has strong potential as a feasible tool for predicting the structural properties of plate within the range of input parameters considered.

Keywords: Artificial neural networks, Nonlinear finite elements, Plates, Modelling

نموذج الشبكة العصبية الاصطناعية للتنبؤ بالتصرف اللاخطي للصفائح المستطيلة

د. سالم طيب يوسف
كلية الهندسة/جامعة الموصل

د. اياد امجد اغوان
كلية الهندسة/جامعة الموصل

الخلاصة:

البحث يبين تطبيق الشبكات العصبية الاصطناعية في تكوين نموذج التنبؤ بالتصرف اللاخطي للصفائح المحملة باحمال منتظمة و مكونة من مواد ذات خصائص لدنة مختلفة و كذلك ذات ابعاد و ظروف محيطة مختلفة. البيانات جمعت باستخدام 2240 من مخرجات التحليل اللاخطي بطريقة العناصر المحددة و المتضمنة معيار(Huber-Mises) للفشل. مدخلات النموذج كانت: الحمل. سمك الصفيحة، عرض الصفيحة، نسبة العرض الى الارتفاع، معامل المرونة، معامل اللدونة، اجهاد الخضوع و الظروف المحيطة، بينما كانت استجابة الانحراف المركزي هي مخرج النموذج، و التي تضمنت ثمانية قيم للانحراف. استخدمت تقنية ((The Levenberg-Marquardt (LM) المتضمنة في برنامج MATLAB في بناء نموذج الشبكات العصبية الاصطناعية. اظهرت النتائج ان الشبكات العصبية الاصطناعية لديها امكانات قوية كأداة مجدية للتنبؤ بالخصائص الانشائية للصفائح ضمن حدود بيانات الادخال المستخدمة في تكون النموذج.

الكلمات الدالة: الشبكات العصبية الاصطناعية، العناصر المحددة الاخطية، الصفائح، النمذجة

Introduction

Traditional research efforts in structural analysis and design that have evolved in the literature during the past few decades generally aimed at developing mathematical models to predict structure behaviour under different loading conditions. These mathematical models, however, focused generally upon determining the behaviour of individual structural elements, which could not be generalized to describe the behaviour of other elements. Also, the models require the calculation of several equations to arrive at predictions for more than one parameter. The structural behaviour of plates is affected by many factors such as material properties, geometric properties, load and boundary conditions. Mathematical models have been used to describe aspects of this behaviour, but they fall short in considering a large number of variables simultaneously. This paper investigates the use of Artificial Neural Networks (ANN) as a preliminary alternative to mathematical modelling or experimental testing for quick prediction of the nonlinear response of elasto-plastic plates. Such predictions could be utilized by a structural engineer on a preliminary basis to determine the initial suitability of a particular plate analysis and design. The present study explore the use of ANN modelling of the elasto-plastic plates in conjugation with finite element method (FEM). The model is constructed through the use of the neural network design (NND) toolbox in MATLAB from the MathWorks[1,2].

Neural network [3,4]

Neural networks are an information processing techniques based on the way biological nervous systems, such as the brain, process information. The fundamental concept of neural networks is the structure of the information processing system. Composed of a large number of highly interconnected processing elements or neurons, a neural network system uses the human-like technique of learning by example to solve problems. The neural network is configured for a specific application, such as data classification or pattern recognition, through a learning process called training. Just as in biological systems, learning involves adjustments to the synaptic connections that exist between the neurons. Neural networks can differ on the way their neurons are connected; the specific kinds of computations their neurons do; the way they transmit patterns of activity throughout the network; and the way they learn including their learning fate. Neural networks are being applied to an increasing large number of real world problems. Their primary advantage is that they can solve problems that are too complex for conventional technologies; problems that do not have an algorithmic solution or for which an algorithmic solution is too complex to be defined. The multi-layer perceptron is the most widely used type of neural network. It is both simple and based on solid mathematical grounds. Input quantities are processed through successive layers of ‘‘neurons’’. There is always an input layer, with a number of neurons equal to the number of variables of the problem, and an output layer, where the perceptron response is made available, with a number of neurons equal to the desired number of quantities computed from the inputs. The layers in between are called ‘‘hidden’’ layers. Each neuron of a layer other than the input layer computes first a linear combination of the outputs of the neurons of the previous layer, plus a bias. The coefficients of the linear combinations plus the biases are called the weights. Neurons in the hidden layer then compute a non-linear function of their input. Generally, the non-linear function is the sigmoid function. Once the networks are considered to be trained, testing data are presented to it and outputs are compared with the experimental or observed results. In this study, a multi-layer feed-forward neural network is used. In a multi-layer feed-forward neural network, the artificial neurons are arranged in

layers, and all the neurons in each layer have connections to all the neurons in the next layer. Associated with each connection between these artificial neurons, a weight value is defined to represent the connection weight. Fig.(1) shows architecture of a multi-layer feed-forward neural network with an input layer, an output layer, and one hidden layer. The operation of the network consists of a forward pass through the network. A number of learning rules are available. The back propagation learning algorithm is used in this study.

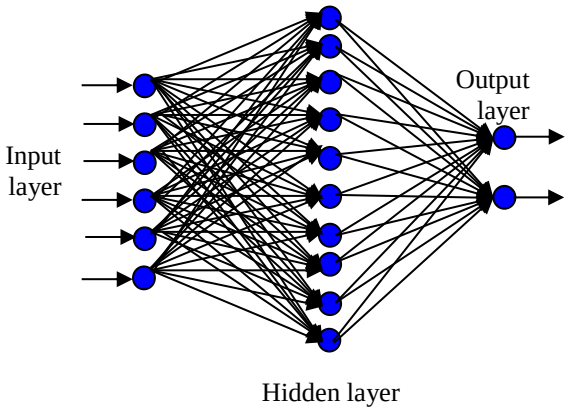

Figure 1 Architectural graph of multilayer perceptron with one hidden layer

Neural network design and training

Rectangular plates with different parameters and uniform distributed loads were used to generate the 2240 set of finite element outputs [5]. variables used in the ANN models are given in Table 1. The boundary supports were clamped or simple. To train the ANN models, first the entire training data file was randomly divided into training and testing data sets. 2130 sets were used to train the different network architectures. The remaining 110 patterns were used for testing to verify the prediction ability of each trained ANN model. The multi-layer feed forward back-propagation technique is implemented to develop and train the neural network of current research where the sigmoid transform function [2] is adopted. The connection weights are modified during the training until the ANN yields a force response that satisfactorily agrees with the correct FE simulation results. The term back propagation refers to the training algorithm, where the observed difference in the force output, ANN vs FE, is used to modify the connection weights. The term "ANN prediction" is reserved for ANN response for cases that were not used in the pre-training stages. This is used in order to examine the ANN's ability to associate and generalize a true physical response that has not been previously "seen." A good prediction for these cases is the ultimate verification test for the ANN models. These tests have to be applied for (input and output) response within the domain of training. Pre-processing of data by scaling was carried out to improve the training of the neural network. To avoid the slow rate of learning near the end points specifically of the output range due to the property of the sigmoid function, the input and output data were scaled between the interval 0.1 and 0.9. The scaling of the training data sets was carried out using the following equation:

Table 1. The range of input data

	Minimum	Maximum
Thickness mm	10	200
Length(a) m	0.5	2
Breadth(b) m	0.5	2
Elastic modulus MPa	150000	220000
Plastic modulus MPa	7000	12000
Yielding stress MPa	300	525
b/a	1	2

$$y = (0.8/\Delta)x + (0.9 - 0.8x_{\max}/\Delta) \quad (1)$$

Where $\Delta = x_{\max} - x_{\min}$

It should be noted that any new input data should be scaled before being presented to the network and the corresponding predicted values should be un-scaled before use. The back-

propagation learning algorithm was employed for learning in the MATLAB program [2]. Each training "epoch" of the network consisted of one pass over the entire 2130 training data sets. The 110 testing data sets were used to monitor the training progress.

Training stage of neural network

Different training functions available in MATLAB [2] were experimented for the current application. The Levenberg-Marquardt (LM) techniques built in MATLAB [1] proved to be efficient training functions, and therefore, is used to construct the NN model. This training function is one of the conjugate gradient algorithms that start training by searching in the steepest descent direction (negative of the gradient) on the first iteration. The LM algorithm is known to be significantly faster than the more traditional gradient descent type algorithms for training neural networks. It is, in fact, mentioned as the fastest method for training moderately sized feed-forward neural network [2]. While each iteration of the LM algorithm tends to take longer than each iteration of the gradient descent algorithm used previously, the LM algorithm yields far better results using far less iteration, leading to a net saving in computer processor time over the previous method. One concern, however, is that it may over fit the data. The network should be trained to recognize general characteristics rather than variations specific to the data set used for training.

Neural network model

The network architecture or topology is obtained by identifying the number of hidden layers and the number of neurons in each hidden layer. There is no specific rule to determine the number of hidden layers or the number of neurons in each hidden layer. The network learns by comparing its output for each pattern with a target output for that pattern, then calculating the error and propagating an error function backward through the neural network. The capacity of the network to learn the patterns on the training set is called convergence and the capacity to respond correctly to new patterns is known as generalization. The process of defining the network architecture is a compromise between generalization and convergence [6, 7, and 8]. To use the trained neural network, new values for the input parameters are presented to the network. The network then calculates the neuron outputs using the existing weight values developed in the training process.

The training of the neural network is carried out using the training data set. Testing and monitoring of the developed neural network during the training stage is performed by computing the mean squared error over all training data sets. After each training iteration, the obtained weights are used to predict the corresponding output to the input parameters of the training data sets. The mean squared error was calculated for each pattern as the difference between the outputs obtained from the trained neural network and the corresponding target.

Every stage of any ANN project requires a number of trial and error to establish a suitable and stable network for that project. Trial and error may be extended to build several networks, stopping and testing the network at different stages of learning and initializing the network with different random weights. Each network must be tested, analysed and the most appropriate network must be chosen for a particular project. The choice hidden layer size is mainly problem specific and to some extent depends on the number and the quality of training patterns. The number of neurons in a neural network must be sufficient for the correct modelling of the problem, but it should be sufficiently low to ensure generalization

[2]. Table 2 shows the properties (architectures and parameters) of model related to rectangular plates under uniform distributed load. 2130 sets of the data formation the input matrix for training the forward models. The output of the model was central deflection response, which consists of eight deflection values corresponding to the following increment of the load [0.3750, 0.5625, 0.6250, 0.6875, 0.7875, 0.8625, 0.9375 and 1.0000]. 110 sets of unseen data were used to exam the trained models

Table 2 Properties of forward problem model

Architecture	8-18-18-18-8
Activation Function	Log sigmoid
Learning Algorithm	LM
Number of Epochs	500
Mean Squared Error (MSE) for scaled data	0.0000206

Figure 2 shows load-deflection relation of plate. It can be seen that at the beginning of load increment (linear part of relations) the ANN predicted values are matching to that of FEM values with less errors, the major differences appear at final incremental loads (nonlinear part of relations), the largest difference is at maximum loading, hence the percentage errors for incremental 1 and 0.375 of loads for all 110 sets were plotted in Figures 3-6. The Figures show that most of the predicted results have error less than 10%, this is clear from Figure 4 and 6 which indicate that 71% and 98% of predicted result has error less than 10% for incremental 1 and 0.375 of maximum loads respectively. On the other hand Figure 7 shows that the correlation coefficient (r) of 89% of the results is more than 0.998 and only 2% are less than 0.98. Depending upon these results, it can be said that the ANN approach shows good agreements with elasto-plastic nonlinear finite element results in predicting the nonlinear response of uniformly loaded rectangular plates. Because the weight of the BPNN cannot be easily understood in the form of a numeric matrix, they may be transformed into coding values in the form of a percentage by dividing the weights by the sum for all the input parameters, which gives the relative importance for each input parameter to output parameter. The relative importance for various input parameters are shown in Figure 8. As the figure indicates, the material properties (E (2.58%), Es (0.68%) and fy (3.4%)) has less importance than other properties of plate, while the geometry (t (14.5%), b (31.25%) and a/b (13.88%)) has significant importance on predicting the response of plates, on other hand the load record importance of 19.62% which is more than boundary importance (14.10%). These results agree with the formula citation by Timoshenko[9]

$$defl_{\max} = \alpha \frac{p b^4}{D} \qquad (2)$$

where α factors depend upon the aspect ratio a/b and the boundary conditions and $D = \frac{E t^3}{12(1-\nu)}$.

This formula shows that the maximum deflection in uniformly loaded rectangular plates is depending mainly on the breadth of plate, while other factors are less importance.

Conclusions

The study conducted in this paper shows the feasibility of using the artificial neural networks in building the models for predicting the nonlinear response of plates with uniform distributed load and different ductile material properties, plate size and boundary conditions. The data were collected using 2240 runs of nonlinear finite element analysis with Huber-Mises failure criterion. The model was used successfully for predicting the response of plate.

The test of the model by un-used data within the range of input parameters, shows that the correlation coefficient (r) of 89% of the results is more than 0.998 and only 2% are less than 0.98. The parametric study shows that the material properties has less importance than other properties of plate, while the geometry has significant importance on predicting the response of plates, These results agree with the formula citation by Timoshenko.

The neural network approach was adopted in an attempt to overcome significant limitations with traditional analytical methods such as FEM. Compared to similar works using the FEM, the neural network approach does not require a new model to be developed for each new problem.

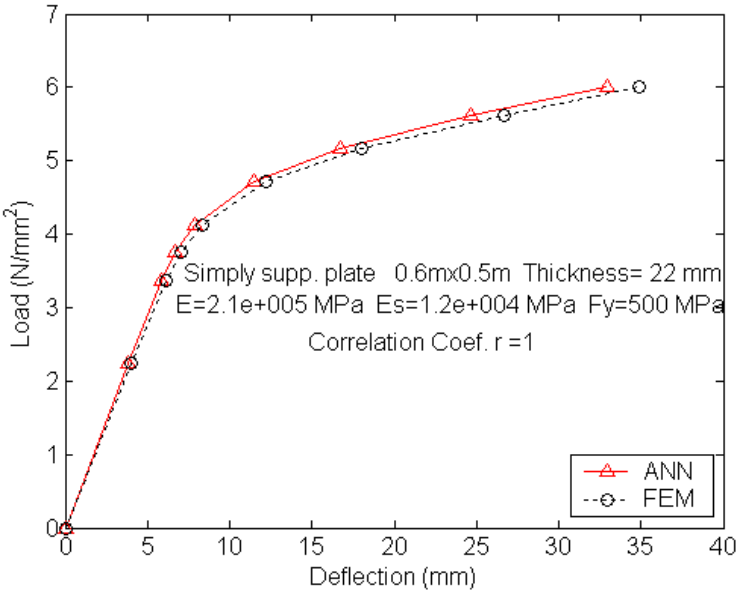

Figure 2 Central load-deflection response for Nonlinear finite elements and ANN results.

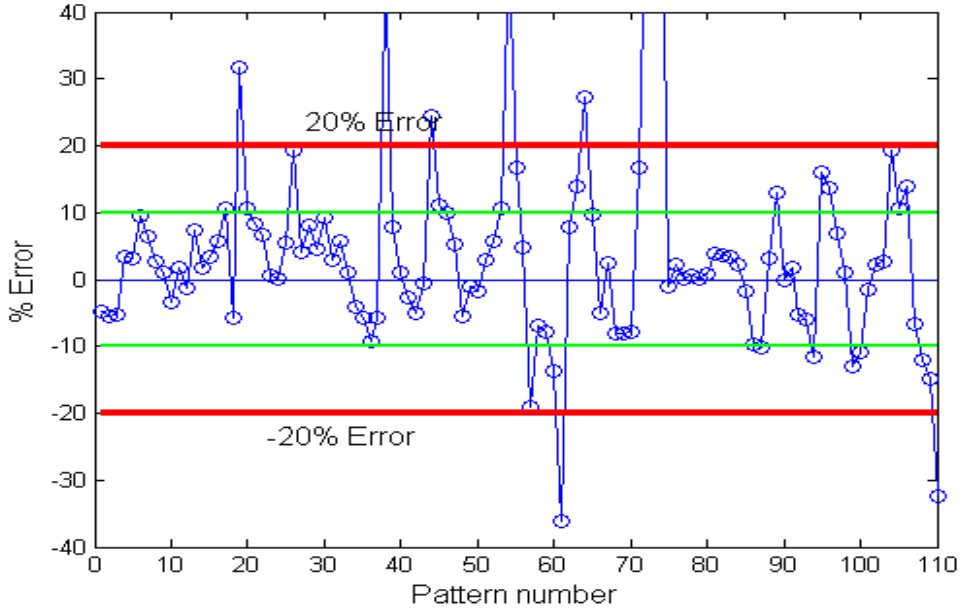

Figure 3 Percentage errors of maximum deflections at load increment 1 with pattern number.

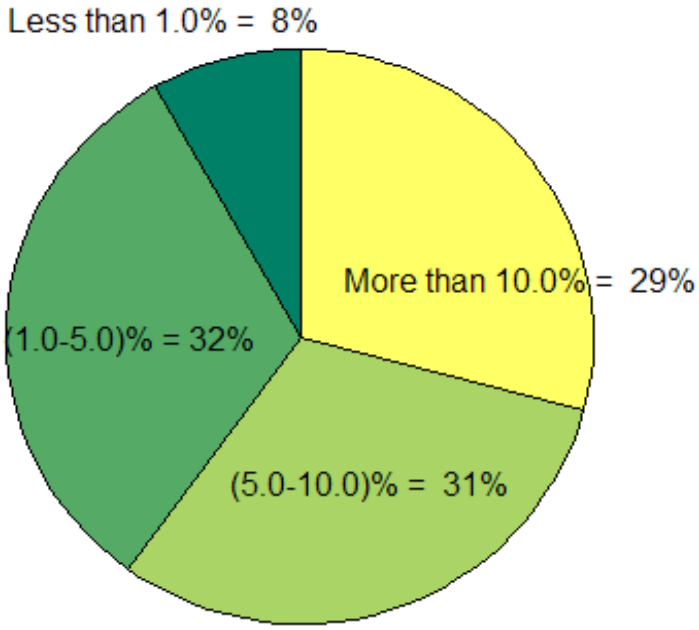

Figure 4. Pie chart of percentage errors of maximum deflections at load increment 1.

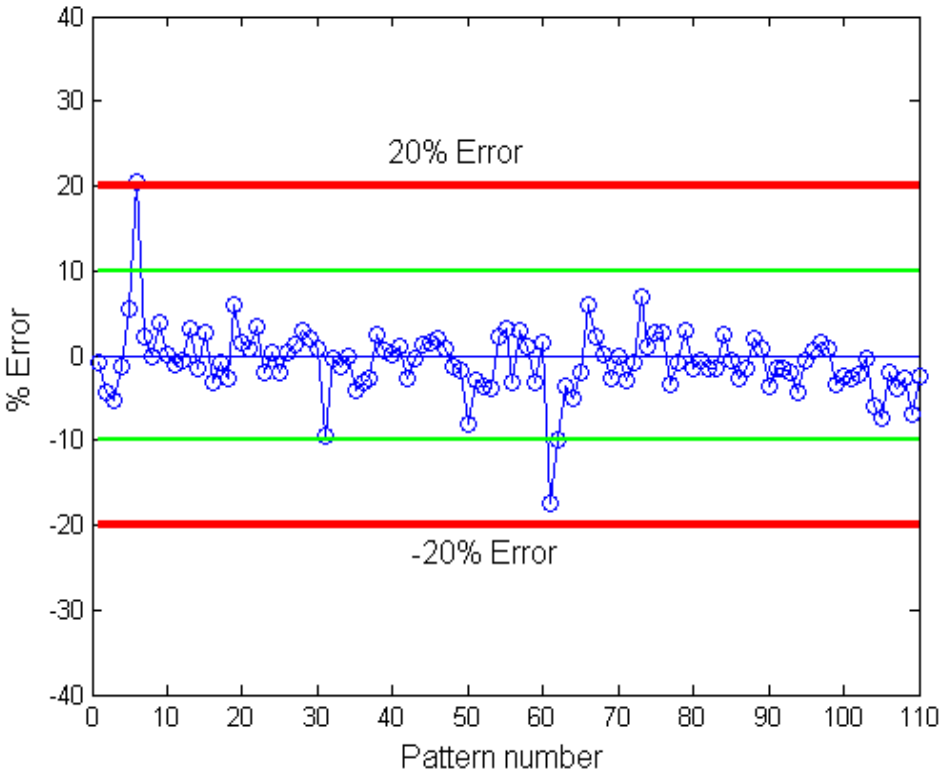

Figure 5 Percentage errors of deflections at 0.375 of maximum loads with pattern number.

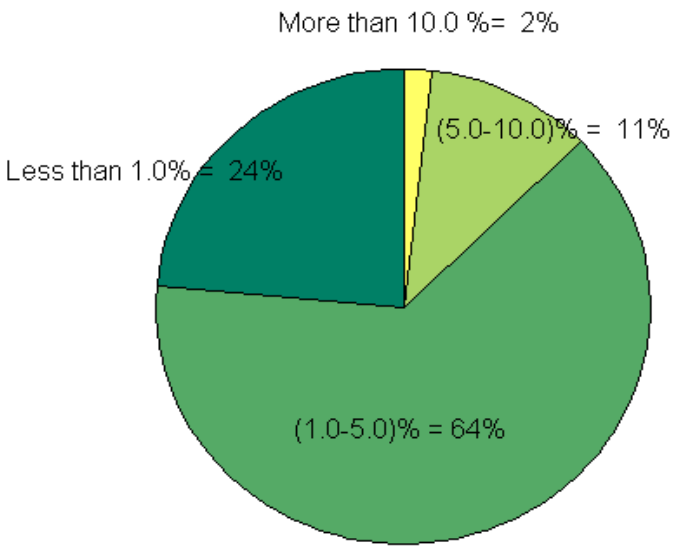

Figure 6 Pie chart of Percentage errors at 0.375 of maximum loads.

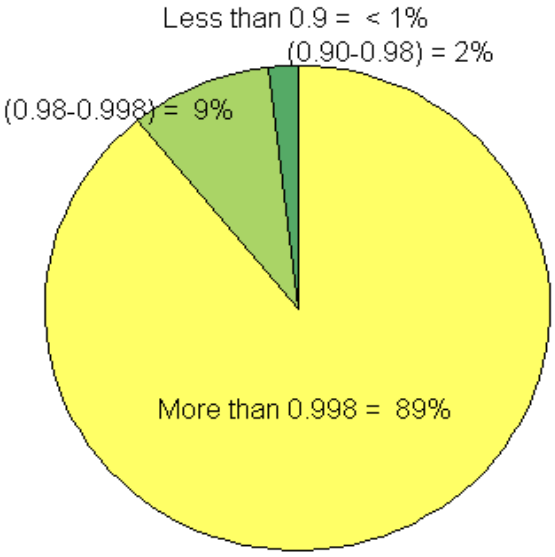

Figure 7 Pie chart of correlation coefficients.

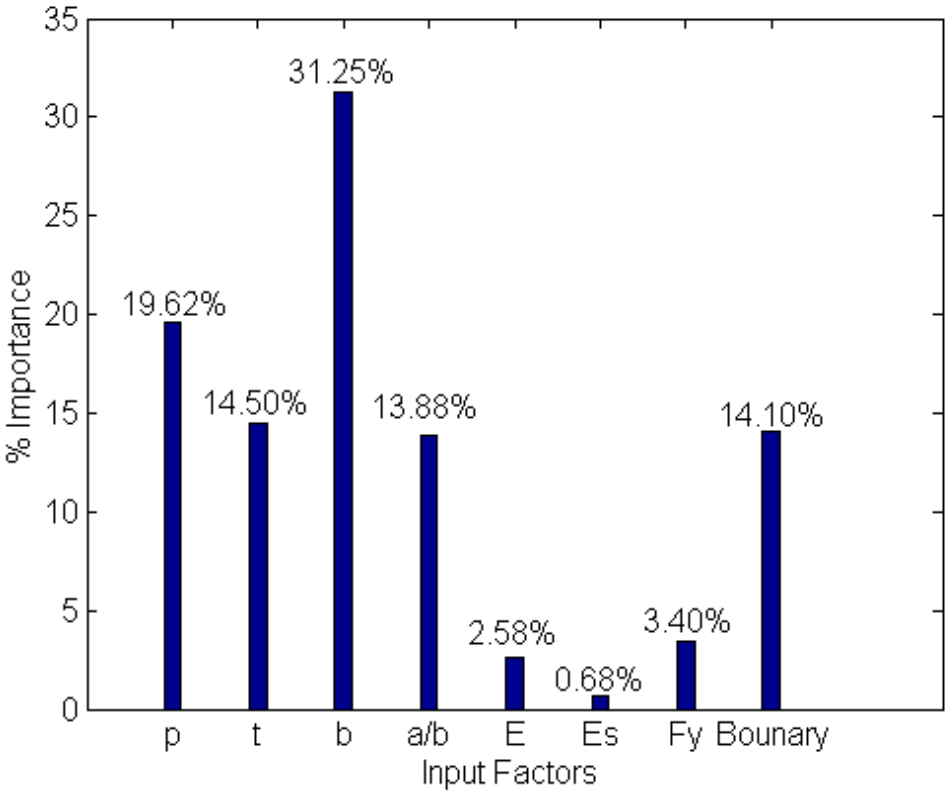

Figure 8 Relative importance of input parameters to prediction of output.

References

1 The math works, MATLAB V6.5, 24 Prime way, Natick, MA 01760-1500, USA, 2002.
2 Howard, D., and Mark, B. Neural network toolbox for use with MATLAB, User's Guide, Version 4. the Math works, Inc 2002.
3 Simon Haykin, Neural networks a comprehensive foundation. 2nd ed., Prentice Hall, New Jersey, 1999.
4 Vanluchene R. D., and Sun R. Neural Networks in Structural Engineering. Microcompter in Civil. Engineering, 1990 (5); 207-215.
5 Hou-Cheng Huang, "Static and Dynamic Analyses of Plates and Shells", pringer-Verlag. UK., 1989
6 D. Maity and A. Saha, "Damage assessment in structure from changes in static parameter using neural networks", Sadhana, Vol. 29, Part 3, pp 315-327, June, 2004.
7 Özgür Sariyar, " Evaluation of soil-structure interactions by using Neural Network methodology", M.Sc. Thesis, Istanbul Technical University, Institute of Science and Technology, Istanbul, pp 1-205, 2005.
8 M.T. Hagan, H. B. Demuth, and M. H. Beale, "Neural network design", Boston, MA: PWS Publishing, 1996.
9 S. Timoshenko S. and Woinowsky-Krieger, S.,"Theory of plates and shells", 2nd ed., McGraw. Hill, New Yourk, Ltd, 1959.

نموذج الشبكات العصبية الاصطناعية لتقدير مقاومة قص العتبات الخرسانية المسلحة التي لا تحتوي على تسليح القص

د. سالم طيب يوسف
استاذ مساعد
كلية الهندسة/ جامعة الموصل
styousif59112@uomosul.edu.iq

محمد هشام شكر الخفاف
مدرس مساعد
كلية الهندسة/ جامعة الموصل
Email: memo_civil@yahoo.com

الخلاصة

توضح هذه الدراسة استخدام تقنية الشبكات العصبية الاصطناعية (ANNs) في تكوين نموذج لتقدير قيم تحمل القص للعتبات الخرسانية المسلحة والتي لا تحتوي على تسليح القص، تم اخذ نتائج فحص (385) عتبة من الدراسات السابقة، وتم الاعتماد على هذه البيانات في تكوين نماذج تقدير القص من خلال إدخال المتغيرات المؤثرة على مقاومة القص (عرض العتبة، عمق العتبة، مقاومة انضغاط الخرسانة، نسبة فضاء القص الى عمق العتبة، نسبة حديد التسليح الطولي)، أظهرت نتائج مقارنة النموذج مع المدونات العالمية إمكانية استخدام الشبكات العصبية الاصطناعية كطريقة معتمدة لتقدير قيم تحمل العتبات لقوى القص، كما ان نسبة فضاء القص\عمق العتبة ونسبة حديد التسليح الطولي هما اهم عاملان في التنبؤ بقيمة تحمل القص للعتبات الخرسانية المسلحة التي لا تحتوي على تسليح القص، وبينت دراسة العوامل المؤثرة على تحمل القص ان تأثير الزيادة في قيمة نسبة فضاء القص الى عمق العتبة (a/d) يكون قليلا او معدوما عند قيم التسليح الطولي (ρi) العالية، وان تأثير عمق العتبة يزداد مع زيادة نسبة التسليح الطولي(ρi)، ويلاحظ ايضا ان تأثير قيمة التسليح الطولي (ρi) يزداد كلما قل عرض المقطع.

الكلمات الدالة:
العتبات الخرسانية المسلحة، مقاومة القص، النمذجة، الشبكات العصبية الاصطناعية.

Artificial Neural Network Model to Estimate the Shear Strength of Reinforced Concrete Beams without Shear Reinforcements

Dr. Salim T. Yousif
Assistant Prof.
College of Engineering

Mohammed H. Sh. ALkhafaf
Assistant lecturer
College of Engineering

University of Mosul

Abstract

This study explains the ability of using Artificial Neural Networks to predict the shear strength of reinforced concrete beams, In the present study the results of (385) tested beams have been taken from previous studies, these results have been used to create the shear prediction model. The study parameters are beam width, beam depth, compressive strength of concrete, shear distance/beam depth ratio, longitudinal reinforcement ratio.

The results showed the validity of using the Artificial Neural Networks as a depended method for predicting shear strength of beam.

Relative importance analysis was used to determine the relative importance of various inputs into predicting the shear strength value of beams without shear reinforcement. The longitudinal reinforcement ratio and shear distance / beam depth ratio have the most importantly. The effectiveness study on beams shear strength that doesn't included shear reinforcement showing that the increasing value is little or nearly vanished on the shear strength at the high longitudinal reinforcement ratio. Increasing the effectiveness of beam depth in shear strength when increasing the longitudinal reinforcement ratio and the study also showed that the effectiveness of increase when beam width decrease.

Keywords: Reinforced concrete beams, Shear strength Modeling and Artificial neural networks.

المقدمة:

تُعدّ العتبات من الأجزاء المهمة في المنشأ حيث أنها تتحمل الأحمال وتعمل على نقلها وتوزيعها على الأعمدة والمساند، وهناك عدة أشكال لفشل العتبات، الفشل في القص هو أحد أشكال الفشل في العتبات.

أن سلوك العتبات الخرسانية يتأثر بالعديد من العوامل مثل خواص الخرسانة، خواص ونسبة حديد التسليح، أبعاد المقطع، نسبة فضاء القص\ عمق العتبة ونوع الأحمال المسلطة وتوزيعها، هناك العديد من الطرائق التي تحسب قيمة تحمل العتبة لقوى القص، وهي مدونات الخبرة العالمية وبعض المعادلات التي توصل إليها الباحثون وفي هذه الدراسة سيتم استخدام الشبكات العصبية الاصطناعية (ANN) للتنبؤ بقيم تحمل العتبات لقوى القص.

الشبكات العصبية الاصطناعية [1] هي معالج مكثف موزع بالتوازي تتكون من وحدات معالجة بسيطة لها ميل طبيعي لتخزين المعرفة من التدريب وجعلها متاحة للاستخدام، الدراسة الحالية ستشرح كيفية تكوين نماذج الشبكات العصبية الاصطناعية للتنبؤ بتحمل القص للعتبات الخرسانية المسلحة من خلال استعمال صندوق أدوات (MATLAB).

القص في العتبات الخرسانية:

يمثل فشل القص بصيغة الشق القطري أو بمجموعة الشقوق القطرية التي تحدث بزاوية مع محور العتبة، الشقوق القطرية تحدث نتيجة الشد القطري في العتبات الخرسانية المسلحة، ان فشل القص هو فشل فجائي لذا يوصى بأن تكون مقاومة القص التصميمية عالية واكبر من مقاومة العتبات، إن أهمية فشل القص في العتبات الخرسانية المسلحة جاءت من تعقيد ميكانيكية مقاومة القص، وخلال السنوات الاخيرة تم أجراء العديد من البحوث لإيجاد طريقة نظرية تحليلية لتصميم القص، ان صعوبة ايجاد طريقة نموذجية لحساب قوة القص تأتي من كون فشل القص يحدث نتيجة مجموعة قوى.

إجهادات القص في بعض المدونات العالمية:

على الرغم من أن العديد من المدونات العالمية تتناول مفاهيم متشابهة حول التعامل مع قوى القص لكن كل من هذه المدونات يعطي نتائج مختلفة عن الأخر.

المدونة الأمريكية ((ACI Standard (ACI318-08)):[2]

إن المعادلات المعتمدة لحساب قوى القص في العتبات الخرسانية بدون تسليح القص هي:

$$v_c = 0.17\sqrt{f_c'}.b_w.d \quad (1)$$

$$v_c = \left(0.16\sqrt{f_c'} + 17\rho_i.\frac{Vu.d}{Mu}\right) \quad (2)$$

b_w: عرض العتبة (m).

d: العمق الفعال للعتبة (m).

f_c': مقاومة انضغاط الخرسانة (MPa).

ρ_i: نسبة التسليح الطولية.

V_u, M_u: تمثل قوى العزوم والقص في المقطع الحرج $(kN.m, kN)$.

المدونة الكندية ((CSA_Design of concrete structures (A23.3-04)):[3]

لحساب قوى القص في حالة العتبات الخرسانية بدون تسليح القص فان مقاومة القص تساوي (v_c) وتحسب كما في المعادلة التالية:

$$v_c = 0.2\ Øc\sqrt{f_c'}.bw.d \quad (3)$$

وعندما تكون قيمة $(Øc = 0.6)$ فان المعادلة ستصبح كالاتي:

$$v_c = 0.12\ \sqrt{f_c'}.bw \quad (4)$$

المدونة الأوربية ((European Standard (2002):-[4]

يتم حساب مقاومة القص للعتبات الخرسانية المسلحة بدون تسليح القص حسب المدونة الأوربية (Eurocode 2) كالآتي:

$$v_{Rd,c} = \left[\frac{0.18}{\gamma_c}.K(100.\rho_i.f_{ck})^{\frac{1}{3}} + 0.15.\sigma_{cp}\right].b_w.d \quad (5)$$

وحددت المدونة أقل قيمة لمقاومة القص بالمعادلة التالية:

$$v_{Rd,min} = \left[0.035.(k)^{\frac{3}{2}}.(f_{ck})^{\frac{1}{2}}\right].b_w.d \quad (6)$$

$$\rho_i = \frac{A_{sl}}{b_w.d} \leq 0.02\sigma_{cp} \quad (7)$$

$$K = 1 + \sqrt{(\frac{200}{d})} \leq 2.0 \ , \ d:(mm) \quad (8)$$

$$\sigma_{cp} = \frac{N_{Ed}}{A_c} < 0.2f_{cd} \quad (9)$$

v_{Rd} : مقاومة القص التصميمية (kN) .
N_{Ed} : القوى المحورية على المقطع(kN).
A_c : مساحة المقطع الخرساني (mm^2).
f_{cd} : مقاومة الانضغاط الخرسانة التصميمية (MPa).
A_{sl} : مساحة حديد تسليح الشد (mm^2).
f_{ck} : مقاومة انضغاط الخرسانة بوحدة (MPa) . $f_{ck} \leq 100\ (MPa)$
b_w: أقل عرض للعتبة في منطقة الشد (mm).

المنظمة الأمريكية للطرق والنقل (AASHTO LRFD 2005)[5]:

لحساب مقاومة القص للعتبات الخرسانية المسلحة بدون تسليح القص حسب مدونة (AASHTO LRFD) فان مقاومة القص تساوي (v_c)، حيث إن:

$$v_c = 0.083\ \beta\sqrt{f_c'}\ bv.dv \quad (10)$$

bv: عرض الوترة (m).
dv : العمق الميكانيكي ويؤخذ كنسبة (0.9d) من العمق الفعال (d).
β : تحسب من جداول خاصة في المصدر **[5]**

الشبكات العصبية الاصطناعية:

تعرف الشبكات العصبية الاصطناعية بأنها نظام حسابي يتكون من عدد كبير من عناصر المعالجة (Processing Elements) المترابطة مع بعضها وتتصف بطبيعتها الديناميكية والمتوازية في معالجة البيانات الداخلة إليها. وتسمى الشبكات العصبية الاصطناعية كونها بنيت لمحاكاة الشبكات العصبية في الكائنات الحية وتسمى الشبكات العصبية الاصطناعية أحيانا بالحاسوب الحي وأحيانا بالدماغ الإلكتروني ،كما يمكن صياغة تعريف آخر لها على أنها مجموعة القواعد والأساليب المتعلقة بأنظمة معالجة البيانات المكيفة وغير المبرمجة.

ذكر المهندس علام زكي [6] أن الباحثان (McCulloch - Pitts) صمما المفهوم العام لأول الشبكات العصبية عام1943، واستخدمت أنواع عديدة من الشبكات والخوارزميات وتطورت بعد ذلك، ففي عام 1982 [6] تم اكتشاف الشبكات العصبية المتعددة الطبقات من قبل الباحث(Barker) والباحث (Rumhart) في عام1985، ولقد تطورت الشبكات العصبية بوصفها امثلة رياضية معتمدة على طريقة التفكير البشري وكيفية معالجة الاعصاب للمعلومات، ان الشبكة العصبية الاصطناعية تتكون من عدد من عناصر المعالجة تدعى عصبونات او (وحدات ، خلايا ، عقد) ،كل عصبونة ترتبط مع العصبونات الاخرى بأداة ربط مباشرة، كل اداة ربط ترفق بوزن معين، هذه الاوزان تمثل المعلومات التي ستبدأ بها حل المشكلة.

صمم العصب الاصطناعي [7] ليقلد أولا الخصائص الأساسية للخلية البيولوجية وتطبق مجموعة من المدخلات (والتـــي تقابل الزوائد التشـــجيرية في الخليـــة البيولوجية) والتي تمثل المخرج لعصب آخر، كل إدخال يضرب بما يوافقه أو يطابقه من وزن أي كل إدخال يضرب بالوزن الخاص به ، والوزن يناظر العقد التي تربط الخلايا مع بعضها ، كل الإدخالات الموزونة يتم جمعها حتى تحدد مستوى التأثير (الفاعلية) للخلية العصبية.

معالجة المعلومات في الشبكات العصبية تقسم إلى طورين أساسيين [6] الطور الاول هو تدريب الشبكات العصبية الاصطناعية و التدريب في الشبكات العصبية الاصطناعية هو عملية تحديث الاوزان الخاصة بكل عصبونة في كل دورة وفقا لخوارزمية معينة لحين الحصول على اوزان تنتج مخرجاً قريباً من قيمة المخرج الحقيقي، في الشبكات العصبية الاصطناعية يكون التدريب إما مراقباً أو غير مراقب. الطور الثاني لمعالجة المعلومات في الشبكة العصبية الاصطناعية

هو طور الاسترجاع إذ يطبق المدخل المعطى مع الأوزان الناتجة من أول طور أي من طور التدريب للشبكة العصبية وبخطوة واحدة نحصل على المخرج المطلوب . طور الاسترجاع هو ذو تغذية أمامية فقط.

استخدمت الشبكات العصبية [8] الاصطناعية في عدة مجالات ومنها الهندسة المدنية وكذلك استخدمت في أنظمة السيطرة ومجال الطب ومجال الأعمال وتمييز الأصوات والصور والعينات ومجال معالجة الإشارة وفي السنوات الماضية ازداد استخدام الشبكات العصبية الاصطناعية في العديد من مجالات الهندسة، وقد استخدمها العديد من الباحثين في مجال الهندسة المدنية بفروعها كافة وفيما يلي ذكر لبعض بحوث وتطبيقات الشبكات العصبية الاصطناعية في مجال الهندسة الإنشائية:

قام الباحث (Tully) [9] بالتنبؤ بسلوك السقوف الخرسانية المسلحة لأربع حالات مختلفة وتكوين اربعة نماذج للتنبؤ ومن خلال النماذج الأربعة استنتج الباحث بان انسب صيغ الشبكات العصبية للتنبؤ بسلوك السقوف المسلحة هي تقنية الانشار الخلفي (Back Progration Techniques) وان الشبكات العصبية تعطي افضل النتائج عندما يكون عدد المخرجات قليلاً، كما استنتج ايضا انه يمكن اعتماد نتائج التنبؤ بسلوك العتبات الخرسانية بدون الحاجة الى التجارب العملية المكلفة.

قام الباحث (Nandy) [10] بتكوين نماذج للتنبؤ بسلوك حديد التسليح الخارجي للعتبات الخرسانية المسلحة ، وقد وجد أن الشبكات العصبية الاصطناعية لها القابلية على اعطاء قيم دقيقة لتنبؤ بسلوك حديد التسليح كما قام بتكوين ثلاثة نماذج للتنبؤ بقيم الهبوط من خلال دراسة ثلاث متغيرات هي (مساحة المقطع العرضي لحديد تسليح الشد ، موقع حديد التسليح الخارجي ، وقيمة الحمل المسلط)، وقد أعطت جميع النماذج نتائج جيدة وبدقة تجاوزت (85%).

واجرى الباحث (Hadi) [8] دراسة لمناقشة تطبيقات الشبكات العصبية في مجال الهندسة الإنشائية وبالأخص في مجال التصميم ، بالاعتماد على نتائج التطبيقات وجد ان الشبكات العصبية الاصطناعية ملائمة جدا للاستخدام في هذا المجال وذلك لدقة نتائجها ولسهولة استخدامها وتطبيقها وكذلك مرونتها العالية في التعامل مع المشكلات المختلفة.

وطور الباحث (Oreta) [11] نموذجاً للشبكات العصبية الاصطناعية باستخدام بيانات عملية سابقة على فشل القص للعتبات الخرسانية المسلحة بدون حديد تسليح القص. وهذا النموذج للشبكة العصبية يحتوي على خمس عقد إدخال والتي تمثل مقاومة انضغاط الخرسانة، عرض العتبة، العمق الفعال، نسبة فضاء القص ونسبة التسليح الطولي. والتي مثلت بخمس طبقات مخفية وطبقة واحدة للإخراج والتي تمثل مقاومة القص العظمى, إن هذا النموذج يعطي نتائج تنبوء جيدة مقارنة بالنتائج العددية والنظرية ومعادلات التصميم في المدونات العالمية، إن اخذ تأثير عدة متغيرات وحساب تأثيراتها يبين قدرة الشبكات العصبية الاصطناعية في العلاقات الإنشائية ذات المتغيرات المتعددة للعمليات الفيزيائية المعقدة.

وقام الباحث (Mansour) وآخرون [12] بدراسة تطبيق الشبكات العصبية الاصطناعية للتنبؤ بمقاومة القص العظمى للعتبات الخرسانية المسلحة والمسلحة بالاتجاه العرضي أيضا. حيث قاموا بإنشاء نموذج للشبكة العصبية الاصطناعية وقاموا بتجريبها وفحصها باستخدام بيانات لـ (176) عتبة خرسانية مسلحة تم تجميعها من دراسات سابقة، وتم ترتيب النموذج المستخدم باستخدام تسعة محددات إدخال والتي تشمل مقاومة انضغاط الخرسانة، مقاومة الخضوع لقضبان التسليح الطولية والعرضية، نسبة فضاء القص الى العمق الفعال، نسبة الفضاء إلى العمق الفعال، إبعاد مقطع العتبة (الطول-العرض)، ونسب التسليح الطولي والعرضي. وان نموذج الشبكات العصبية الاصطناعية المختار أظهر تنبأ جيداً لإجهاد القص الأعظم من خلال محددات الإدخال التي أخذت بنظر الاعتبار، إن متوسط القيمة العملية للتنبؤ بنسب مقاومة القص وجد أنها مساوية لـ (1.003)، واظهر النموذج نتائج جيدة عند مقارنها مع النتائج العملية والمدونات العالمية.

وقام الباحث (Yousif) [13] بتكوين (16) نموذج للتنبؤ بسلوك الصفائح تحت تأثير أحمال مختلفة وقد أظهرت النتائج انه بإمكاننا استخدام الشبكات العصبية الاصطناعية في التنبؤ والتصميم حيث أظهرت نتائج جيدة وبدقة عالية لكلتا الحالتين (التنبؤ والتصميم)، كما اوصى الباحث باستخدام الشبكات العصبية الاصطناعية في مجال الامثلية (Optimization).

كما قام الباحثان (Yousif و Abdullah) [14] باستخدام تقنية الشبكات العصبية الاصطناعية للتنبؤ بمقاومة انضغاط الخرسانة اعتمادا على مكونات المزجة ، الحجم الأكبر للركام و هبوط الخرسانة الطرية.

تصميم نموذج الشبكات العصبية وتدريبها:

تحدد معمارية الشبكات العصبية [15, 16, 17] اعتمادا على عدد الطبقات المخفية وعلى عدد العصبونات في كل طبقة مخفية حيث انه لا يوجد اي قانون لتحديد عدد الطبقات المخفية أو لتحديد عدد العصبونات في كل طبقة، الشبكة العصبية تُعلم نفسها من خلال مقارنة مخرجاتها مع القيم المطلوبة إلى أن تصل إلى قيمة خطأ قليلة ضمن الحدود المقبولة، إن قابلية الشبكة على التعلم في طور التدريب تسمى التقارب (convergence) وقابلية الشبكة للاستجابة الصحيحة للأنماط الجديدة التعميم (generalization). يتم تدريب نموذج الشبكات العصبية من خلال استخدام مجموعة بيانات للتدريب، ويتم مراقبة وفحص أداء نموذج الشبكات العصبية المطورة أثناء مرحلة التدريب من خلال حساب متوسط مربع الخطأ (MSE). بعد كل مرحلة تدريب تستخدم الأوزان الناتجة من التدريب للتنبؤ بقيمة المخرج المصممة الشبكة لإنتاجه. و يتم تكوين كل نموذج عن طريق عدد من المحاولات واعتماد طريقة الصح والخطأ للوصول للنموذج المناسب للشبكة العصبية ويتم فحص وتحليل نتائج كل نموذج لمعرفة مدى ملائمة النموذج لإنتاج الهدف المطلوب. ويعد اختيار حجم [18] الشبكة العصبية الاصطناعية من المشاكل المهمة والصعبة وقد يتم اختيارها اعتمادا على عدد ونوع المدخلات وطريقة التدريب ، كما أن عدد عصبونات الشبكة العصبية يجب إن يكون كافيا لإنتاج نموذج صحيح ودقيق في حساب المخرجات

لاستعمال نموذج الشبكات العصبية المدربة تغذى ببيانات إدخال جديدة والتي تمثل مدخلات نموذج الشبكة العصبية، بعدها سيحسب النموذج المخرج الذي دُرب لإنتاجه باعتماد قيمة الأوزان الناتجة من تدريب الشبكة العصبية. لقد جمعت البيانات المستخدمة في هذه الدراسة من الدراسات العملية السابقة [19, 20, 21, 22] وبعد جمع البيانات تم تقسيمها الى

بيانات تدريب وبيانات فحص، بيانات التدريب تستخدم لحساب وتقدير أوزان الشبكة بينما بيانات الفحص تستخدم لفحص الشبكة والتأكد من صلاحيتها.

طبقة المدخلات تعطي البيانات المدخلة وطبقة المخرجات تعطي الإجابة، ونحتاج الى طبقة أو أكثر من الطبقات المخفية لخزن النموذج الناتج خلال فترة التدريب، كل عصبون في الطبقة المخفية يرتبط مع كل عصبون في الطبقة المجاورة ولكن لا يرتبط مع العصبونات التي في طبقته وكل ارتباط له وزن يستخدم لإيجاد المخرجات. في التدريب يتم تغيير هذه الأوزان الى أن يتم الوصول الى النتيجة الصحيحة، إذا لم يتم التوصل الى تدريب جيد للشبكة العصبية معناها أن الشبكة بحاجة الى بيانات أكثر، إما إذا كان التدريب جيداً ولكن نتائج الفحص غير منطبقة أو قريبة من القيم الحقيقية معناها أن الشبكة بحاجة الى المزيد من التدريب أو بحاجة الى إعادة تقسيم البيانات.

نموذج الشبكات العصبية المكون:

تم تكوين نموذج الشبكة العصبية بالاعتماد على البيانات العملية التي تم جمعها وكانت (385) بيان للتدريب وفحص النموذج وقسمت البيانات على قسمين، بيانات إدخال وعددها (347) بيان وبيانات فحص وعددها (38) بياناً، وكان المخرج المطلوب هو مقاومة القص (Vu)، الجدول (1) يوضح مدخلات النموذج والجدول (2) يوضح مواصفات النموذج المكون.

الجدول (1) مدخلات النموذج

المدخل	الرمز	الوحدة
عرض العتبة	bw	mm
عمق العتبة	d	mm
مقاومة انضغاط الخرسانة	f_c'	Mpa
نسبة حديد التسليح الطولي	ρi	_
(فضاء القص\عمق العتبة)	(a/d)	_

الجدول (2) يوضح مواصفات النموذج المكون

أسم النموذج	OFM
البنية المعمارية للشبكة	18-18-18-1
عدد التكرارات	51
متوسط مربع الخطأ (MSE)	0.00092

يوضح الشكل (1) العلاقة بين قيمة مقاومة القص المحسوبة من قبل نموذج الشبكات العصبية مع النتائج العملية (النتائج الحقيقية) لبيانات التدريب، ومن الملاحظ إن قيمة معامل الانحدار (R=0.968) وهذا يدل على إن النموذج قد تم تدريبه بصورة جيدة حيث ان هنالك تقارب بين القيم المحسوبة و القيم العملية .

كما يوضح الشكل (2) العلاقة بين قيمة مقاومة القص المحسوبة باستخدام نموذج الشبكات العصبية مع النتائج العملية لبيانات الفحص، حيث إن النموذج أعطى دقة عالية للتنبؤ بقيم بيانات الفحص و كان معامل الانحدار (R=0.970)، وهذا يدل على مدى دقة النموذج المصمم وقدرته على التنبؤ بقيم القص.

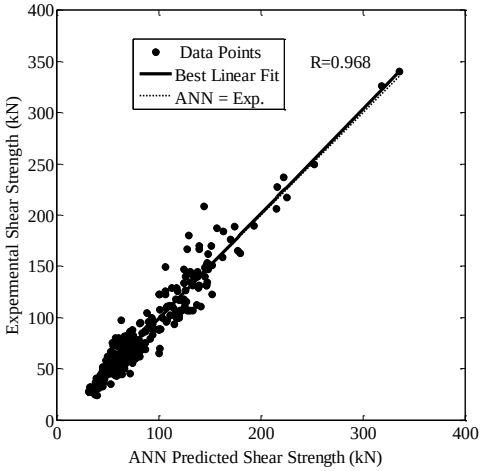

الشكل (1) العلاقة بين قيم التحمل المقدر للقص وقيم القص العملية (مجموعة بيانات التدريب)

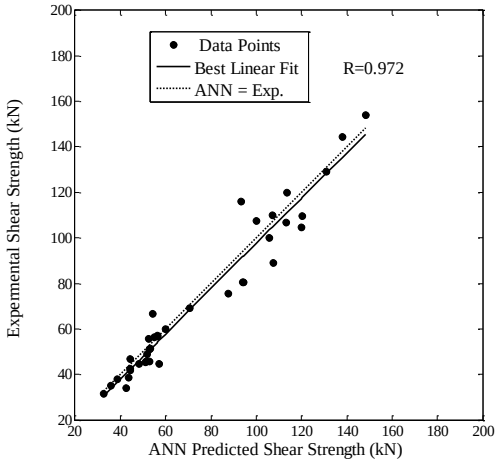

الشكل (2) العلاقة بين قيم التحمل المقدر للقص وقيم القص العملية (لمجموعة بيانات الفحص)

لصعوبة فهم أوزان الشبكة العصبية بصيغتها العددية من الممكن تحويلها إلى نسبة مئوية وذلك بتقسيم وزن كل مدخل على مجموع أوزان المدخلات وبالتالي الحصول على الأهمية النسبية لكل مدخل في إنتاج المخرج والشكل (3) يوضح أهمية المدخلات في حساب المخرج.

من خلال الشكل يلاحظ إن قيمة كل من نسبة حديد التسليح الطولي (ρi) (38.607%)، ونسبة فضاء القص\عمق العتبة (a/d) (36.796%) لهما أهمية كبيرة في حساب قيمة تحمل القص. ويلاحظ إن باقي العوامل تكون ذات أهمية اقل في حساب تحمل القص حيث كانت أهمية عرض المقطع (bw) (8.094%)، وأهمية عمق المقطع (d) (7.777%) وكذلك أهمية مقاومة انضغاط الخرسانة (f_c') (8.762%).

إن الخطأ في التنبؤ بقيم تحمل القص لبيانات الفحص تم حسابه وتوضيحه بالشكل (4)، من خلال ملاحظة الشكل نرى أن اغلب القيم لها نسبة خطأ اقل من (10%) .

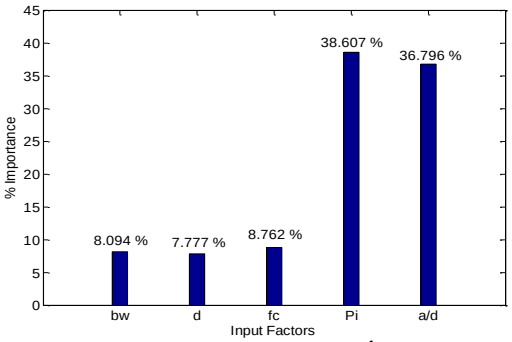

الشكل (3) أهمية المدخلات في التنبؤ بقيم مخرجات

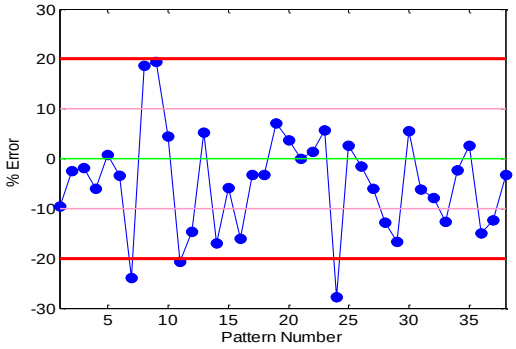

الشكل (4) الخطأ بقيم تحمل القصلبيانات

مقارنة نتائج النموذج المكون مع النتائج التي اعطتها المواصفات العالمية:

الأشكال (5)، (6)، (7) و (8) توضح العلاقة بين قيم تحمل القص التي تنبئ بها نموذج الشبكات العصبية وقيم القص المحسوبة من المدونات العالمية [(ACI – 08) ، (AASHTO – 05) ، (CSA - 04) ، (EURO - 02)] وقيمة معامل الانحدار بين القيم العملية والمحسوبة من المدونات.

من خلال ملاحظة هذه الإشكال ومقارنة قيم معامل الانحدار (R) نرى إن أفضل معامل للانحدار هو معامل انحدار نموذج الشبكة العصبية حيث كان (R=0.97) بينما معامل الانحدار للمدونة الأوربية (EURO - 02) يساوي (R=0.855)، ولمدونة (AASHTO – 05) يساوي (R=0.834)، ولمدونة (ACI – 08) يساوي (R=0.826)، ولمدونة (CSA - 04) يساوي (R=0.825).

من خلال مناقشة نتائج النموذج (OFM) نستنتج انه من الممكن استخدام طريقة الشبكة العصبية الاصطناعية (ANN) للتنبؤ بقيم تحمل القص للعتبات الخرسانية المسلحة التي لا تحتوي على تسليح القص.

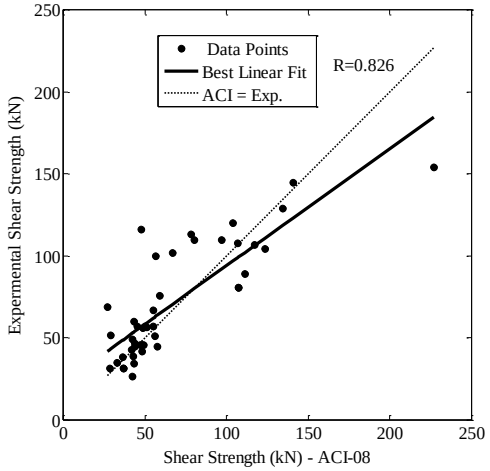

الشكل (5) العلاقة بين قيم تحمل القص العملية وقيم القص المحسوبة من مدونة (ACI-08)

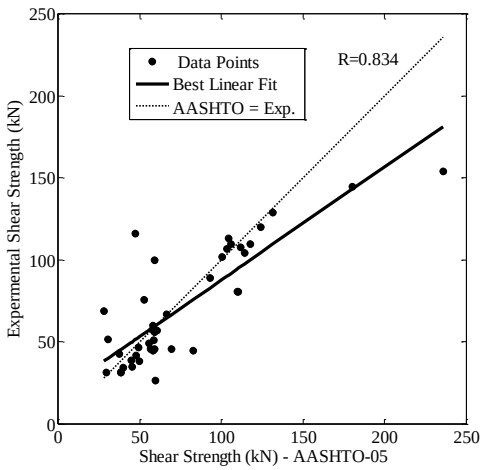

الشكل (6) العلاقة بين قيم تحمل القص العملية وقيم القص المحسوبة من مدونة (AASHTO-05)

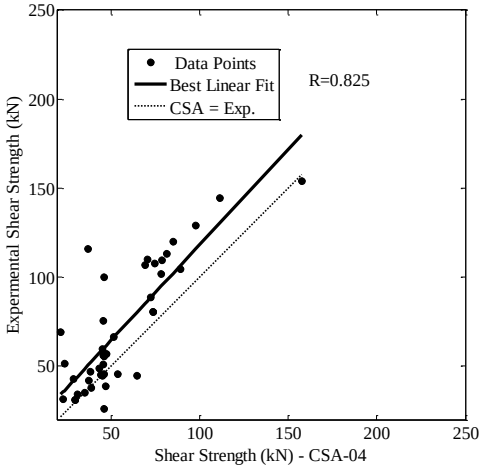

الشكل (7) العلاقة بين قيم تحمل القص العملية وقيم القص المحسوبة من مدونة (CSA-04)

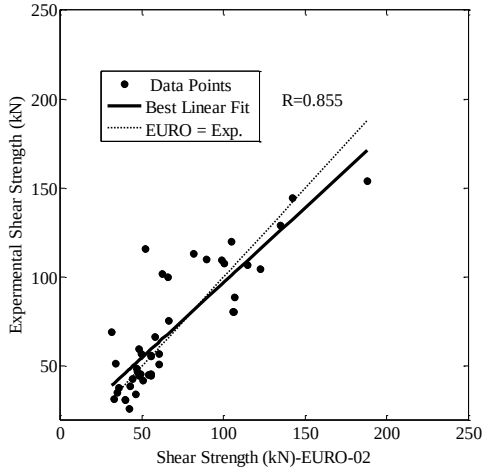

الشكل (8) العلاقة بين قيم تحمل القص العملية وقيم القص المحسوبة من مدونة (EURO-02)

دراسة العوامل المؤثرة على مقاومة القص باستخدام الشبكات العصبية الاصطناعية:

يبين الشكل (9) تأثير قيمتي كل من نسبة حديد التسليح الطولي (ρi) وقيمة (فضاء القص\عمق العتبة) (a/d)على قيمة تحمل القص في العتبات، ونلاحظ انه بزيادة قيمة (ρi) فأن تحمل القص سوف يزداد حيث تتغير قيمة تحمل القص من (65kN) إلى (180kN) عند تغيير قيمة (ρi) من (0.5%) إلى (7.5%) وعند قيمة (a/d=4)، وكما نلاحظ انخفاض قيمة تحمل القص عند زيادة قيمة (a/d)، حيث انخفضت قيمة تحمل القص من (215kN) إلى (160kN) عند زيادة قيمة (a/d) من (2 إلى 8) وعند قيمة (ρi=%7.5)، وكذلك عند تغير قيمة (a/d) من (6-8) عند قيمة (ρi=%7.5) فان قيمة تحمل القص تبقى ثابتة ولا تنخفض مما يدل على انه عند زيادة قيمة (a/d) فان تأثيرها يكون قليلا أو معدوما عند قيم (ρi) العالية، بينما عند قيمة (a/d) (2 و 4) فأن تأثير (ρi) العالية يكون واضحاً وذلك ناتج من تداخل العزم مع القص.

يظهر الشكل (10) تأثير قيمتي كل من نسبة حديد التسليح الطولي (ρi) وعرض المقطع (bw) على قيمة تحمل القص في العتبات ، ونرى إن زيادة عرض المقطع تزيد من تحمل العتبة لقوى القص، حيث ازداد التحمل من (148kN) إلى (236kN) عندما ازداد عرض المقطع من (150mm) إلى (300mm) عند قيمة (ρi=%7.5)، وهذه النتيجة متوافقة لما ورد في جميع المدونات حيث إن تحمل القص يتناسب طرديا مع عرض المقطع، نرى إن زيادة نسبة حديد التسليح الطولي تعمل على زيادة قيمة تحمل العتبة لقوى القص، حيث ازداد التحمل إلى أكثر من الضعف من (104kN الى 236kN)، عندما ازدادت نسبة التسليح من (0.5- 7.5%) وعند قيمة (bw =300mm) .

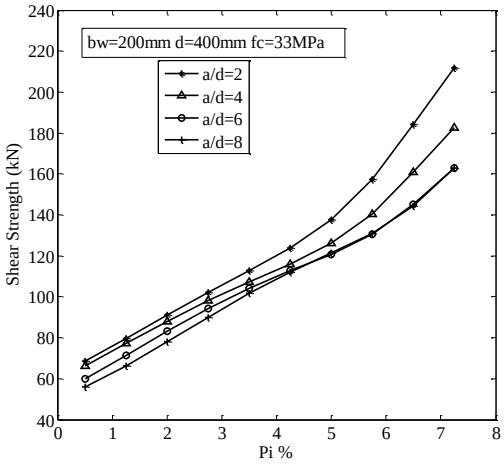

الشكل (9) دراسة تأثير قيمتي كل من(ρi) و(a/d) على قيمة تحمل القص

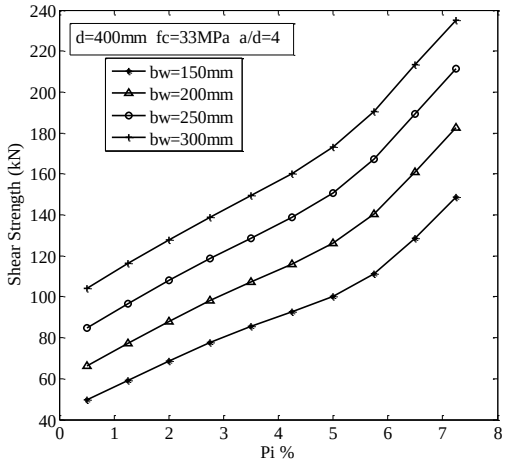

الشكل (10) دراسة تأثير قيمتي كل من(ρi) و(bw) على قيمة تحمل القص

الشكل (11) يوضح تأثير قيمتي كل من نسبة حديد التسليح الطولي (ρi) وعمق المقطع (d) على قيمة تحمل القص ، وهو يشابه الشكل (10) حيث انه عند زيادة كل من قيمة نسبة حديد التسليح الطولي وعمق المقطع فان تحمل العتبة لقوى القص سوف يزداد، فقد ارتفعت قيمة تحمل العتبة من (70kN) إلى (198kN) عند زيادة (ρi) من (0.5%) إلى (7.5%) وقيمة (d =450mm)، كما ارتفعت قيمة تحمل العتبة من (142kN) إلى (198kN) عند زيادة قيمة (d) من (300mm) إلى (450mm) وعند قيمة (ρi=%7.5)، ونلاحظ ان تأثير عمق العتبة يزداد مع زيادة نسبة التسليح الطولي(ρi).

يوضح الشكل (12) تأثير قيمتي كل من نسبة حديد التسليح الطولي (ρi) و قيمة مقاومة انضغاط الخرسانة (f_c') على قيمة تحمل القص، ومن خلال مشاهدة الشكل نرى إن الزيادة بقيمة (f_c') تعمل على زيادة تحمل العتبة لقوى القص ولكن هذه الزيادة تكون قليلة وبحدود (5kN) عندما ترتفع قيمة (f_c') بمقدار (4 Mpa)، حيث ارتفعت قيم تحمل القص من (54) إلى (59) ،(64) و(70) عندما ازدادت قيمة (f_c') من (24 Mpa) إلى (28)،(32) و(36) على التوالي عند قيمة (ρi=%0.5) ويلاحظ أن تأثير قيمة مقاومة الانضغاط (f_c') لا تتأثر بقيمة (ρi) حيث ان المنحنيات تكون متوازية، كما إن الزيادة بقيمة (ρi) تعمل على زيادة التحمل العتبة للقص حيث ارتفعت قيمة التحمل من (70kN) إلى (185kN) عند زيادة (ρi) من (0.5%) إلى (7.5%) وعند قيمة (f_c'=36 Mpa).

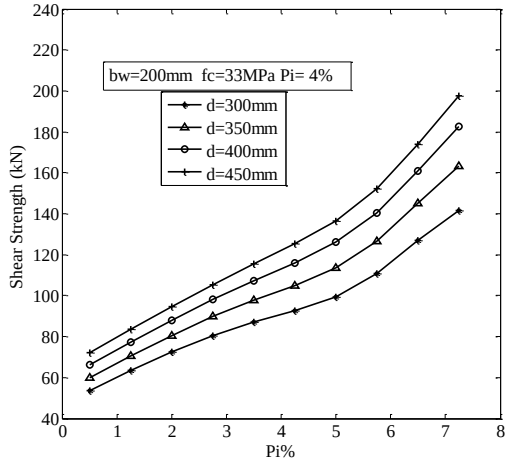

الشكل (11) دراسة تأثير قيمتي كل من(ρi) و(d) على قيمة تحمل القص

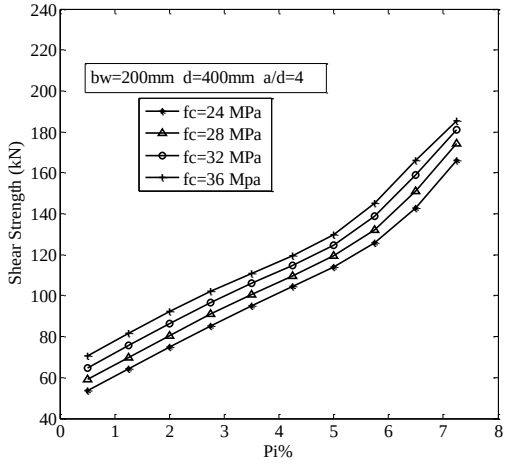

الشكل (12) دراسة تأثير قيمتي كل من(ρi) و(f_c) على قيمة تحمل القص

الشكل (13) يبين تأثير قيمتي كل من قيمة (فضاء القص\عمق العتبه) (a/d) وعرض العتبه (bw) على قيمه تحمل القص في العتبات، من الشكل نلاحظ انه بزيادة عرض العتبة ستزداد قيمة تحمل القص ،حيث ازداد تحمل القص من (111kN) إلى (186kN) عند زيادة قيمة (bw) من (150mm) إلى (300mm) وعند قيمة (a/d=3)، ويلاحظ أيضا نقصان قيمة تحمل القص عند زيادة قيمة (a/d) حيث انخفضت قيمة تحمل القص من (186kN) إلى (161kN) عندما ارتفعت قيمة (a/d) من (3) إلى (7.5) عند قيمة (bw =300mm)، ولكن هذا النقصان يتوقف عند حد معين (a/d=5) أو قد يصبح النقصان قليلا. يبين الشكل (14) تأثير قيمتي كل من (فضاء القص\عمق العتبة) (a/d) وقيمة مقاومة انضغاط الخرسانة (f_c') على قيمة تحمل القص.

ومن خلال ملاحظتنا للشكل نرى أنه بزيادة قيمة (f_c') فان مقاومة القص سوف تزداد ، حيث ازدادت قيمة تحمل القص من (164kN) إلى (194kN) عندما ازدادت قيمة (f_c') من (24 Mpa) إلى (f_c'=36Mpa) وعند قيمة (a/d=3) وان تأثير مقاومة الانضغاط (f_c') لا يتأثر بزيادة قيمة (a/d) حيث أن المنحنيات تكون متوازية ونرى انه كلما زادت قيمة (a/d) فان تحمل القص سوف يتناقص إلى حد قيمة (a/d=4.5) بعدها يتوقف النقصان ويبدأ بالزيادة ولكنها زيادة قليلة وغير مؤثرة.

يستنتج مما سبق أن نسبة فضاء القص\عمق العتبة (a/d) تكون مؤثرة الى حد 5 بعدها تكون غير مؤثرة على قيمة تحمل القص، كذلك فأن تغيير قيمة مقاومة الانضغاط (f_c') تكون ذات تأثير قليل مقارنة مع تأثير تغير قيم (bw)، (d)، (ρi) على قيمة تحمل القص.

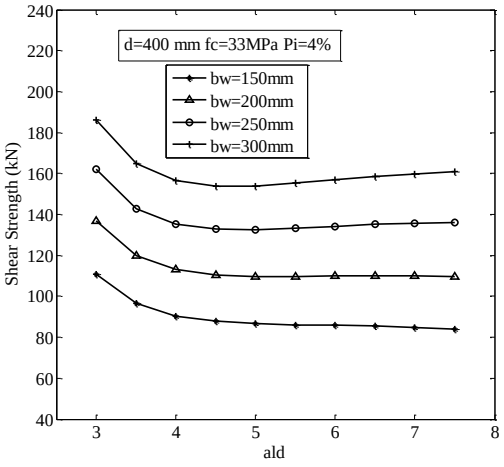

الشكل (13) دراسة تأثير قيمتي كل من(a/d) و(bw) على قيمة تحمل القص

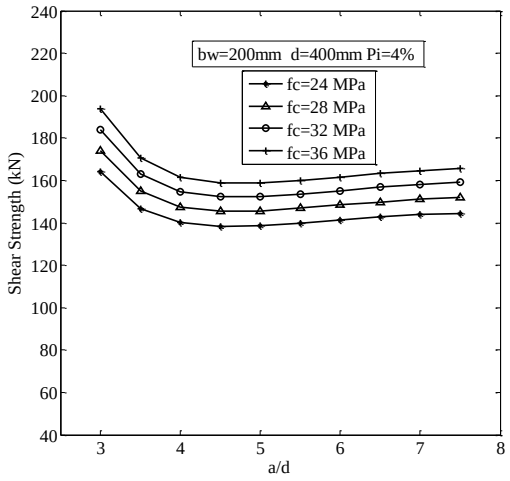

الشكل (14) دراسة تأثير قيمتي كل من(a/d) و($f_{c\backslash}$) على قيمة تحمل القص

الاستنتاجات:

اعتماداً على النتائج التي اعطاها نموذج الشبكات العصبية الاصطناعية المُدرب والمفحوص نستنتج ما يلي:

1. امكانية اعتماد تقنية الشبكات العصبية الاصطناعية لتقدير قيم تحمل القص للعتبات الخرسانية المسلحة التي لا تحتوي على تسليح القص.
2. ان نسبة فضاء القص\عمق العتبة ونسبة حديد التسليح الطولي هما اهم عاملان في تقدير قيمة تحمل القص للعتبات الخرسانية المسلحة التي لا تحتوي على تسليح القص.
3. عند قيم التسليح الطولي (ρi) العالية يكون تأثير الزيادة في قيمة (a/d) على تحمل القص قليلا او معدوما، وان تأثير عمق العتبة على تحمل القص يزداد مع زيادة نسبة التسليح الطولي(ρi)، ويلاحظ ايضا ان تأثير نسبة التسليح الطولي (ρi) على تحمل القص يزداد كلما قل عرض المقطع.
4. بعد التدريب فأن نموذج الشبكات العصبية الاصطناعية يعطي النتائج بزمن قياسي إذا ما قورنت بطرق التحليل التقليدية.

المصادر:

1. Haykin S., "Neural Networks A Comprehensive Foundation", Preatic Hall, 2nd Edition, New Jersey, 1999, pp.842 .
2. ACI Committee 318-08, Building Code Requirements for Reinforced Concrete (ACI 318-08) and commentary-ACI 318 RM-08, American concrete Institute, Detroit, 2008.
3. Canadian Standards Association, Design of Concrete Structures A23.3-04, Canadian Standards Association, Rexdale, Ontario, 2004.
4. European Committee for Standardization, Euro code 2: Design of Concrete Structures, Part 1: General rules and rules for buildings, Revised Final Draft, pp. 226, April 2002.
5. AASHTO LRFD Bridge Design Specifications and Commentary. Second Edition, (2005), American Association of State Highway Transportation Official, Washington D.C., 2005
6. "الشبكات العصبية الصناعية ، البنية الهندسية ،الخوارزميات ، التطبيقات"علام زكي عيسى، شعاع للنشر والعلوم ، سوريا. حلب، 2000
7. أل فليح ، مها عبد الرحمن عبد المجيد ، "تطبيقات الشبكات العصبية الصناعية في تحديد القدرة المتفاعلة التعويضية في شبكات التوزيع" ، أطروحة جامعة الموصل ، 2004.

8. An-Najjar H.M., " Prediction of Ultimate Shear Strength of Reinforced Concrete Deep Beams Using Artificial Neural Networks", M.Sc. Thesis, Department of Civil / Structural Engineering, Islamic University, Gaza, 2005.
9. Tully S.H., "A Neural Network Approach for Predicting the Structural Behavior of Concrete Slabs", M.Sc. Thesis, Faculty of Engineering and Applied Science, University of Newfoundland, Canada, 1997.
10. Nandy S., "Assessing External Reinforcement on Reinforced Concrete Beams Using Neural Networks", M.Sc. Thesis, Department of Civil Engineering, University of Florida, 2001.
11. Oreta A.W. C., "Simulating Size Effect on Shear Strength of R.C. Beams Without Stirrups Using Neural Networks", Engineering Structures, Vol. 26, 2004, pp. 681-691.
12. Mansour M. Y., Dicleli M., Lee J.Y., and Zhang J., "Predicting the Shear Strength of Reinforced Concrete Beams using Artificial Neural Networks", Engineering Structures Vol. 26, 2004, pp. 781-799.
13. Yousif S. T., "Artificial Neural Networks Modeling of Elasto_Plastic Plates", Ph.D. Thesis, Department of Civil Engineering, University of Mosul, Iraq, 2007.
14. Yousif, S. T. and Abdullah, S. "Artificial neural networks model for predicting compressive strength of concrete.", Tikrit Journal of Eng. Sciences,Vol.16, No.3, September 2009, pp.55 - 63.
15. Xu Y.G., Liu G.R., Wu Z.P., and Huang X.M., "Adaptive Multilayer Preceptron Networks For Detection of Cracks In Anisotropic Laminated Plates", International Journal of Solid Structures, Vol. 38, 2001, pp. 5625-5645.
16. Ahn Y., Nieholson D. W., Wang M. C., and Ni P., "Inverse Method for Identifying The Underlying Crack Distribution In Plates With Random Strengths", Acta Mechanical, Vol. 144, 2000, pp. 137-154.
17. Chang C.C., and Zhou L., "Neural Network Emulation of Inverse Dynamics For A Magneto Rheological Damper", Journal of Structural Engineering, ASCE, Vol. 128, No.2, 2002, pp. 231-239.
18. Araujo A.L., Soares C.M., Herskovits M.J., and Pedersen P., "Parameter Estimation in Active Plate Structures Using Gradient Optimization and Neural Networks", Inverse Problems, Design and Optimization Symposium, Rio de Janeiro, Brazil, 2004.
19. Ghadhban H.N., "Shear Strength Prediction of Reinforced Concrete Beams", M.Sc. Thesis, Department of Building and Construction of the University of Technology, Iraq, 2005.
20. Bazant Z.P., and Sun ,H.H., "Size Effect in Diagonal Shear Failure: Influence of Aggregate Size and Stirrups", ACI Materials Journal, Vol.84, No.4, 1987, pp. 259 - 272.
21. AL-Musawi J.M.S., "Shear Capacity of High Strength Concrete Beams with Web Reinforcement", M.Sc., Thesis, University of Technology, Baghdad, Iraq, 1989, pp. 121.
22. Bunni Z.K., "The Effect of the Shear Span to Depth Ratio on Shear Strength of the High-Strength Concrete Beams", M.Sc. Thesis, University of Technology, Baghdad, 1994, pp. 120.

Tests On Precracked Reinforced Concrete Corbels Strengthened With Cfrp Sgeets

Azad A. Mohammed **Gulan B. Hassan**
Civil Engineering Dept, Faculty of Engineering
University of Sulaimani **University of Duhok**
Sulaimani, Iraq **Duhok, Iraq**
e-mail: azada1971@yahoo.com **e-mail: gulan1980@yahoo.com**

Abstract

This paper outlines tests on six reinforced concrete corbels subjected to preloading then strengthened with CFRP sheets externally bonded to the corbel. Test results indicate that high strength reinforced concrete corbels subjected to moderate and severe cracking can be repaired for a load capacity higher than that of control corbel. Results also indicate that corbel steel and CFRP materials suffer from high deformations before collapse. Strengthening compression zone of the corbel with steel plate was found to be not useful for more load enhancement.

Keywords: Corbel, Cracking, Preloading, Repairing, Strengthening.

فحوصات كتائف خرسانية مسلحة مسبقة التشقق مقوات بشرائط الياف الكاربون البوليمرية

د. آزاد عبد القادر محمد **كولان ب. حسان**
قسم الهندسة المدنية / هيئة الهندسة
جامعة السليمانية / العراق **جامعة دهوك / العراق**

الخلاصة

يتضمن البحث الحالي نتائج فحوصات اجريت على ست كتائف خرسانية مسلحة تعرضت الى تحميل ثم تم تقويتها بربط طبقات خارجية من صفائح الياف الكاربون البوليمرية. اظهرت النتائج بأن الكتائف الخرسانية المسلحة المصنوعة من خرسانة عالية المقاومة و المتعرضة الى تحميل مسبق بشكل معتدل و بشكل كبير يمكن صيانتها لتحمل قوى اكبر من تحمل الكتائف الأصلية. اظهرت النتائج أيضا بأن مادة الحديد والصفائح البوليمرية للكتائف تعرضتا الى تشوهات كبيرة قبل الفشل النهائي. وجد بأن تقوية منطقة الانضغاط للكتائف بصفائح الحديد ليس لها دور مهم لتحمل احمال اضافية.

1- Introduction

Reinforced concrete corbels likewise other structural members may subject to cracking as a result of many reasons. Any cracked corbels must be strengthened or repaired before that the full collapse of the component takes place. For different types of structural members, different strengthening techniques and materials were used. Different types of fiber reinforced polymers as an alternative of steel were used for strengthening. Such new materials have a promised future due to their high efficiency and ease of application.

With regard the reinforced concrete corbels different methods for strengthening were followed and test results in this context can be found in the literature. Test results on strengthening reinforced concrete corbels using steel plate were reported by Heidayet et al.[1]. Strengthening reinforced concrete corbels using prestressing bars were done by Nagrodzka-Godycka[2]. Other tests were carried out by Campione et al.[3] on corbels made from normal strength concrete and wrapped completely with CFRP at side faces. They found that the overall behavior of the corbels was quite similar in terms of maximum load and mode of failure. It is also observed that the compressive rupture was consequent to the failure of CFRP wraps in tension.

More recently, tests were carried out by Mohammed and Hassan[4] to check the suitability of strengthening or repairing reinforced concrete corbels made from normal strength concrete using CFRP sheets. Test results indicated that the efficiency of strengthening reinforced concrete corbels made from normal strength concrete using CFRP sheets is low. Using the best strengthening configuration, load enhancement did not exceeded 14.6%. They also found that there is a good chance to repair fully damaged corbels using CFRP sheets, in which the ultimate load capacity was found to be 83.4% of that of concrete corbel. Other research work by Mohammed and Hassan[5] on the behavior of high strength concrete corbels, strengthened with CFRP sheets, indicated that using best strengthening configuration, load enhancement did not exceeded 28.3%. Results also indicated that strengthening is useful for those corbels lightly reinforced with flexure or shear reinforcements.

In the present research the efficiency of strengthening pre-cracked corbels, sufficiently reinforced for flexure, made from high strength concrete was studied through casting and testing six corbels. Such study is important to know the efficiency of CFRP sheets for repairing damaged corbels occurred by cracking, to avoid the complete collapse of the structure.

2- Experimental Work

2-1 Materials

The cement used in this investigation was ordinary Portland cement (Type I ASTM). The fine aggregate used was clean river rounded shape. For the fine aggregate used, apparent specific gravity was equal to 2.61 and fineness modulus equal to 2.28. Natural gravel used as coarse aggregate of rounded shape river gravel and maximum size equal to 14 mm. For the natural gravel used, apparent specific gravity was found to be 2.7. Test results indicated that compacted dry density of the natural gravel is equal to 1680 kg/m^3. A high range water reducer (super plasticizer) of Glenum type (GLENUM ACE 30) of constant dosage (by weight of cement) equal to 1.1% was used in high strength concrete mix. Deformed bar of 12 mm diameters was used for the main tension reinforcement in corbels and as longitudinal reinforcement in the column. It is also used as cross bars to anchor the main steel at the ends of the corbels. Three specimens for each bar were tested in tension. Deformed bars of

diameter 10 mm were used for shear reinforcement in the corbel, and as tie in the column and used as framing bars to support the stirrups. Test results of steel reinforcements properties are shown in Table 1.

Laminates of CFRP of Sikawrap-230c type were used as strengthening materials. The laminates consist of fibers arranged in one direction (main direction) [i.e. unidirectional laminate] bonded together in a shape of woven fabric. CFRP laminate was of 600 mm width and 1 mm thickness per layer was supplied in rolls of 50 m length. Based on the manufacturer report elastic modulus in tension for CFRP material was found to be 238000 MPa, tensile strength was 4300 MPa, ultimate elongation was 1.8% and density was 1.76 gm/cm^3. The epoxy resin used for bonding the laminates to the concrete was of Sikadur-330 type consisting of two components of resin and hardener (A:B) ratio of 1:4. Elastic modulus in tension for epoxy was found to be 3800 MPa and tensile strength was 30 MPa.

2-2 Mix Details And Mixing

Mix proportion for production of high-strength concrete requires more quality control compared with normal strength concrete. The mix proportion selected from suitable ingredients of concrete with relative quantities in order to have a concrete of high compressive strength with suitable workability. Different mix proportions were used as trial mixes. The mix of higher compressive strength at 28 days was chosen for casting high strength concrete corbels. The mix proportion was found to be 1 : 1.25 : 1.75 (cement: fine aggregate: coarse aggregate) by weight. For mixing procedure, a rotary mixer of 0.25 m^3 capacity was used. The interior surface of the mixer was moistened before placing the materials. First, the fine and coarse aggregates were poured in the mixer, followed by 25% of the mixing water to wet them and then left to mix for a period of two minutes. Afterwards, the cement was added and finally, the remaining 75% of the mixing water was added gradually to the mixture, and the mixing operation continued for another three minutes until homogenous concrete was obtained.

2-3 Corbel dimensions and reinforcement details

Fig.1 shows details of corbel dimensions and reinforcement cage. The corbel width is constant for all corbels and equal to 180 mm. Fig.2 shows the position of corbel at testing and strain gage position in steel reinforcement and CFRP sheet for strain measurements.

Table (1): Properties of steel reinforcement

Nominal diameter (mm)	Yield stress (N/mm^2)	Ultimate tensile stress (N/mm^2)	Elongation (%)	Location of using
10	518.5	617.3	21.2	Shear reinforcement, ties and framing bar
12	449.6	530.0	22.3	Flexural and column reinforcements

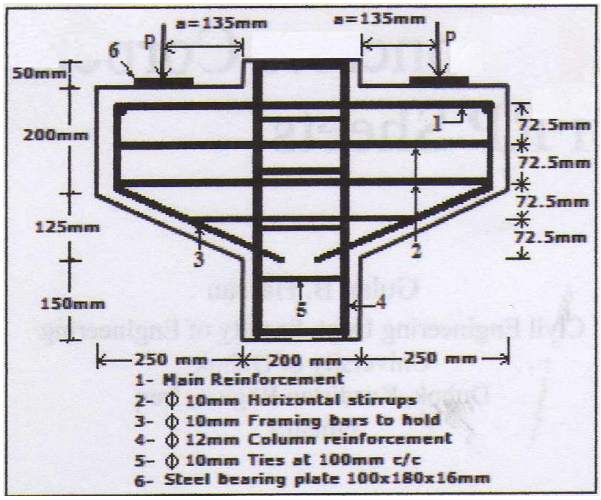

Fig. (1): Details of corbel dimensions and reinforcement

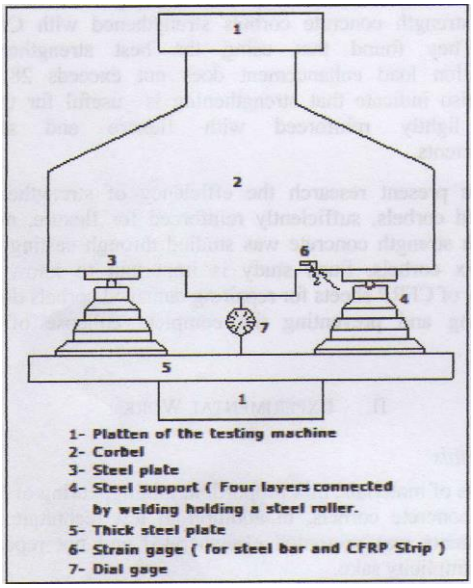

Fig. (2): Details of corbel support and measurement tools

2-4 Corbel Strengthening Configuration

Different CFRP strengthening configuration was followed for repairing the pre-cracked corbels. Details of strengthening configuration for corbels can be found in Table 2 and also in Figs.3 and 4. Before strengthening, the surfaces of the concrete corbel were cleaned by airbrushing to remove dust or debris and fine particles and to obtain a uniform surface. Later, a uniform 2 mm thin layer of the mixture of epoxy resin was applied by palette knife to the surface of the concrete corbel thoroughly.

The CFRP strips were then placed in the given location according to the configuration shown in Figs.3 and 4 on the concrete surface and pressed on the epoxy to ensure a good bond with concrete. A uniform pressure was applied along the entire length of the strips. A CFRP strips were placed with the direction of fibers perpendicular to the expected cracking pattern. In order to ensure that failure does not occur in the column the upper portion of the column (150 mm height) was confined with one layer of CFRP for the strengthened corbels. For Corbels C4 and C6 steel plate of 2 mm thickness and 180 mm width (equal to width of the corbel) was provided to the compression face of the corbel bonded with epoxy to the corbel and the wrapped with CFRP sheets. The aim of this procedure is to control slippage of the outer cracked portion of the corbel and to improve the strength of the compression zone**.**

Table (2): Corbels reinforcement and strengthening configuration

Corbel	Flexural Reinforcement	Shear Reinforcement	Strengthening Configuration
C1	4Φ12 mm	3Φ10 mm	-
C2	4Φ12 mm	3Φ10 mm	-
C3[a]	4Φ12 mm	3Φ10 mm	One horizontal strip of 10mm width for flexure and fully wrapped with diagonal strips.
C4[a]	4Φ12 mm	3Φ10 mm	One horizontal strip of 10mm width for flexure, compression strut strengthened with steel plate and fully wrapped with diagonal strips.
C5[b]	4Φ12 mm	3Φ10 mm	Similar to corbel C3
C6[c]	4Φ12 mm	3Φ10 mm	Similar to corbel C4

a Subjected to 60% preloading
b Corbel C2 tested and then repaired
c Corbel C1 tested and then repaired

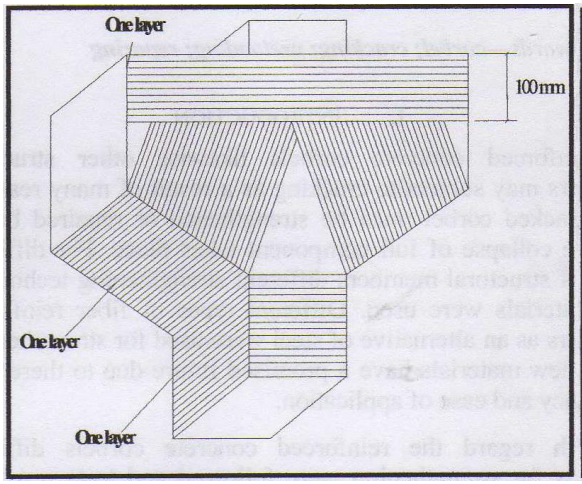

Fig.(3): Strengthening configuration of corbels C3 and C5

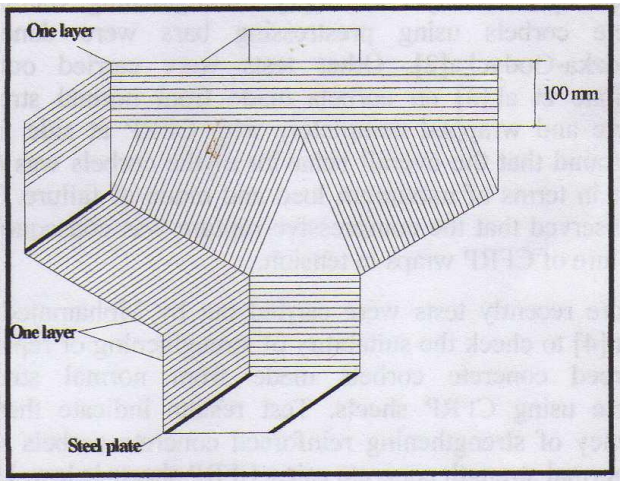

Fig.(4): Strengthening configuration of corbels C4 and C6

3-Results And Discussion

Measurements for cube compressive strength of each corbel concrete material were made, from which the cylinder compressive strength was calculated and the test results are given in Table 3. Ultimate load capacity of tested corbels and the load percentages are given in the same table. Fig.5 shows load- deflection relationship of tested corbels. Results of Table 3 indicate that the load capacity of all strengthened corbels is higher than that of control corbels. Such experimental observation indicates that any reinforced concrete corbels suffered from damages of moderate and severe cracking can be reasonably repaired using CFRP sheets, following the strengthening configuration shown in Fig.3 or Fig.4. Load percentage of corbel C4 is higher than that of corbel C3 as shown from results of Table 3. This observation

Table (3): Results of concrete compressive strength and ultimate load capacity of corbels

Corbel	Concrete compressive strength (MPa)[a]	Ultimate load capacity (kN)	Ultimate load percentage
C1	61.28	478.0	100
C2	59.44	462.8	100
C3[a]	62.56	581.85	123.69[b]
C4[a]	60.27	602.75	128.14[b]
C5	59.44	606.85	131.13
C6	61.28	554.75	116.06

a Subjected to 60% preloading
b Based on the average of ultimate load capacity of control corbels.

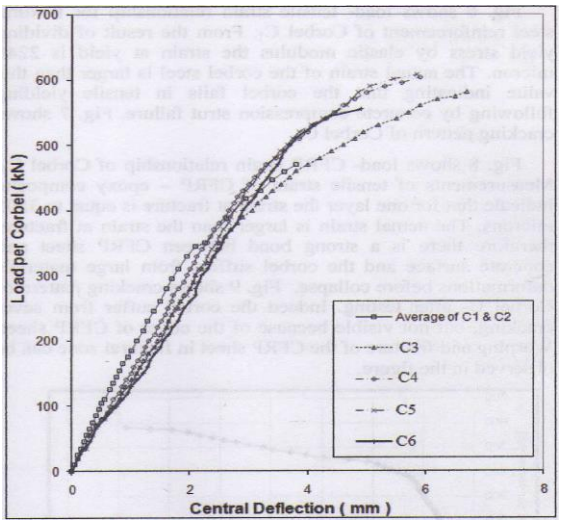

Fig. (5): Load- deflection relationship of tested corbels

indicates that using steel plate with CFRP sheets is better for those corbels moderately damaged by cracking (subjected to 60% preloading). For those corbels subjected to full damage of cracking using steel plate beside CFRP sheets is not helpful to obtain more load enhancement.

According to the measured load- deflection relationship given in Fig.5 the maximum deflection is larger in strengthened corbels compared with control corbels. The role of preloading is not important on such behavior. Such behavior can be considered to be useful because the corbel after strengthening will fail in larger deflection value and providing more ductile behavior before collapse. Previous test data[5] on high strength reinforced concrete corbels also indicate that strengthened corbels suffered from high steel and CFRP materials deformation before collapse.

Fig.6 shows load- tensile strain relationship for flexural steel reinforcement of corbel C1. From the results of dividing yield stress by elastic modulus the strain at yield is 2248 microns. The actual strain of the corbel steel reinforcement is larger than this value indicating that the corbel failed in tensile yielding following by concrete compression strut failure. Fig.7 shows cracking pattern of corbel C1.

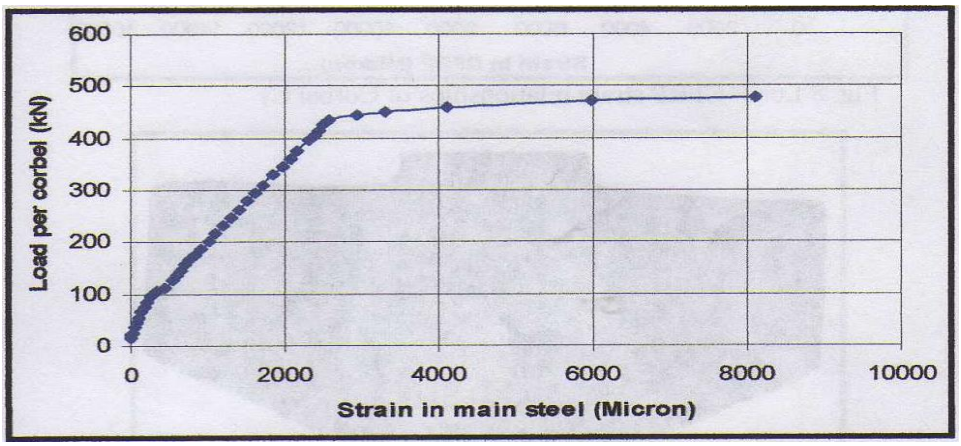

Fig. (6): Load- steel tensile strain relationship for corbel C1

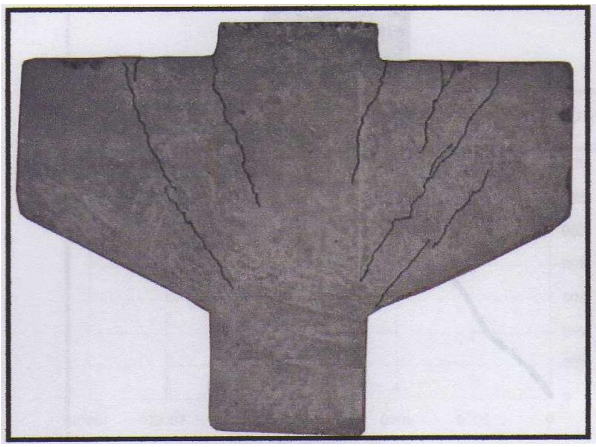

Fig.(7): Cracking pattern of corbel C1

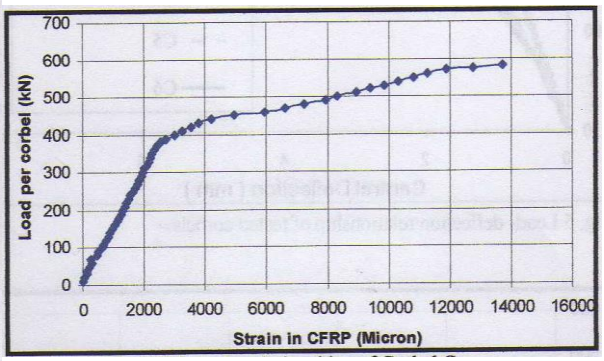

Fig. (8): Load CFRP strain relationship of corbel C3

Fig. (8): Shows load- CFRP strain relationship of corbel C3. Measurements of tensile strain of CFRP- epoxy composite indicate that for one layer the strain at fracture is equal to 3505 microns. The actual strain is larger than the strain at fracture, therefore there is a strong bond between the CFRP sheet and concrete surface, and the corbel suffers from large materials deformations before collapse. Fig.9 shows cracking pattern of corbel C3 after testing. Indeed the corbel suffer from sever cracking but not visible because of the cover of CFRP sheet. Warping and fracture of CFRP sheet in flexural zone can be observed in the figure.

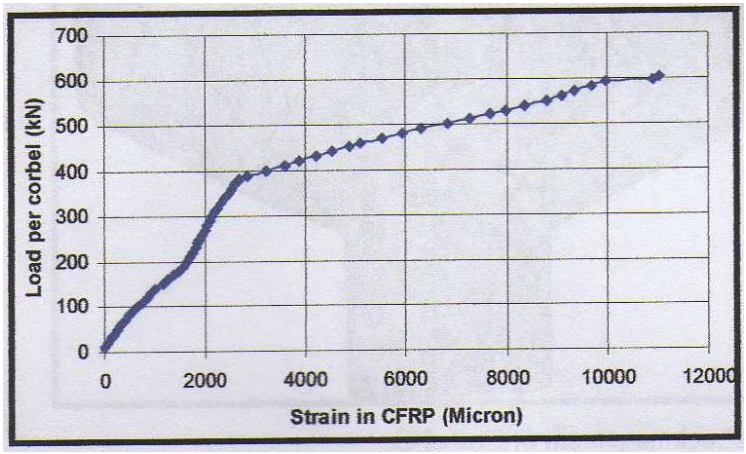

Fig.(9): Cracking pattern of corbel C3

Fig.10 shows load- CFRP strain relationship of corbel C4. The behavior of this corbel is similar to that of corbel C3. Therefore the role of providing steel plate to compression zone on the CFRP deformation is not important. Fig.11 shows cracking pattern of the corbel after testing. Cracking behavior of this corbel is not differ widely from that of corbel C3. Therefore, the role of steel plate on cracking behavior of the strengthened corbel is not important.

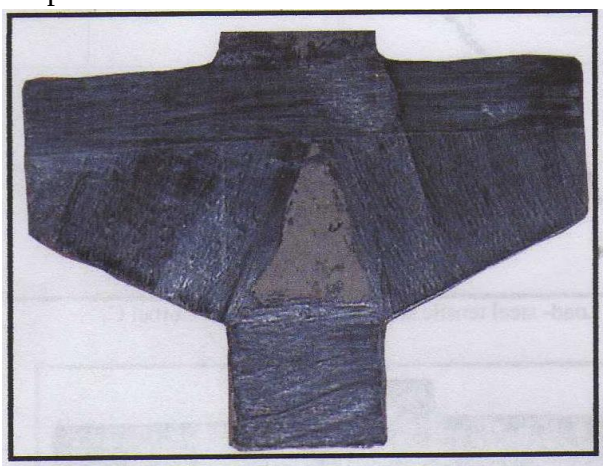

Fig. (10): Load- CFRP strain relationship of corbel C4

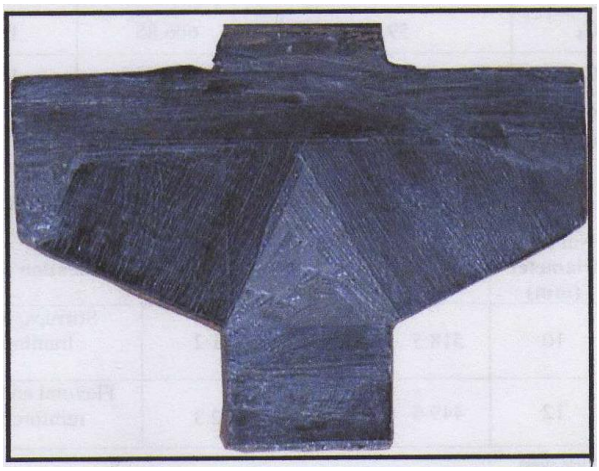

Fig. (11): Cracking pattern of corbel C4

Fig.12 shows load- CFRP strain relationship of corbel C5. The behavior of this corbel is similar to that of other corbels indicating that the extension and propagation of cracks has less importance on the deformation of flexural steel reinforcement of repaired corbel using CFRP sheets. Fig.13 shows cracking pattern of corbel C5 after testing. Cracking behavior of this corbel is not differ widely from that of other strengthened corbels.

Deformation and cracking pattern of corbel C6 were found to be similar to corbel C5 indicating that the role of providing steel plate to the full damaged corbels in companion with CFRP wraps is not important.

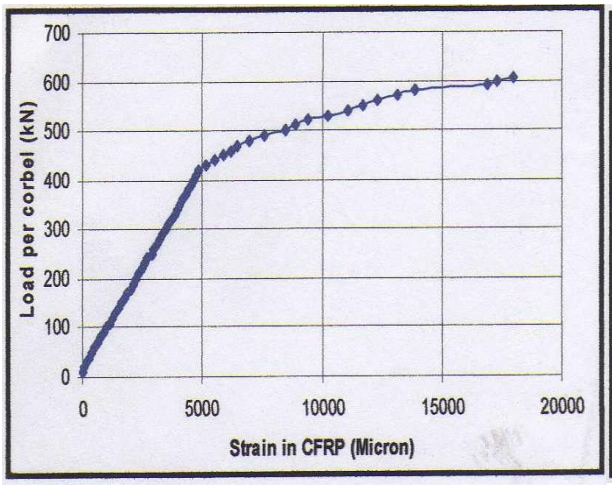

Fig. (12): Load - CFRP strain relationship of corbel C5

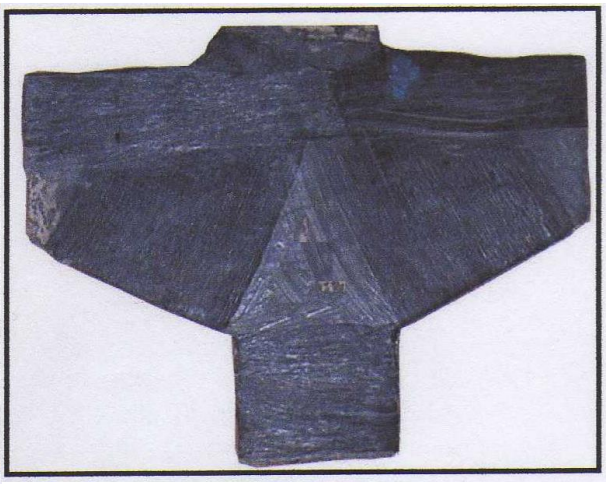

Fig. (13): Cracking pattern of corbel C5

4- Conclusions

From the experimental test results presented in this paper the following conclusions can be drawn

a- Reinforced high strength concrete corbels subjected to moderate and full cracking can be repaired for a load capacity of 116.06% to 128.14% of control corbel. Therefore damaged corbels can be repaired successfully using CFRP sheets.

b- For cracked corbels strengthened with CFRP sheets, corbel materials suffer from high deformations and maximum deflection of repaired corbel is higher than that of control corbel.

c- Using externally bonded steel plate for strengthening compression zone of the damaged corbel was found to be not useful for more load enhancement of repaired corbel.

References

[1] Heidayat, A., Ramadhan, A., and Aziz O. Q., " *Repairing of Damaged Reinforced Concrete Corbels by Externally Bonded Steel Plate*," The Scientific Journal University of Salahaddin University-Erbil, Iraq, V. 16, No. 1, 2004.

[2] Nagrodzka-Godycka, K., "*Behavior of Corbels with External Prestressing Bars-Experimental Study*," ACI Structural Journal, Vol. 96, No. 6, November- December, 1999, pp.1033-1040.

[3] Campione, G., Mendola, La. L. and Papia, M. ," *Flexural Behavior of Concrete Corbels Containing Steel Fiber or Wrapped with FRP Sheets*", Material and Structures Vol. 38, July 2005, pp. 617-625.

[4] Mohammed, A. A. and Hassan, G. B.," *Tests on Normal Strength Reinforced Concrete Corbels Wrapped with CFRP Sheets*," Accepted for publication, International conference held at Bangkok, March 5-6, 2013.

[5] Mohammed, A. A. and Hassan, G. B.," *Tests on High Strength Reinforced Concrete Corbels Wrapped with CFRP Sheets*," Accepted for publication, World E-conference of engineering, June 12-13, 2013.

[6] Hassan, Gulan B., "*Behavior of High Strength Reinforced Concrete Corbels Wrapped with Carbon Fiber Reinforced Polymer (CFRP) Sheets*," MSc thesis, University of Duhok, Iraq, 2009, p. 92.

سلوك العتبات الخرسانية المسلحة الحاوية على فتحات في منطقة القص المقواة والمعاد تأهيلها بألياف الكاربون البوليمرية تحت تأثير الاحمال التكرارية

أ.د.بيار جعفر السليفاني استاذ
فهد اكرم سعيد الحمداني مهندس
جامعة الموصل /كلية الهندسة/قسم المدني

الخلاصة

يهدف البحث إلى دراسة السلوك الإنشائي للعتبات الخراسانية المسلحة التي تحتوي على فتحات في وسط منطقة القص المقواة والمعاد تأهيلها تحت تأثير الأحمال التكرارية. اذ تضمن البرنامج العملي للدراسة الحالية فحص (9) عتبة خرسانية مسلحة بأبعاد (200x350x2400 mm) وقسمت هذه العتبات على ثلاث مجاميع، المجموعة الاولى تتألف من ثلاث عتبات ذات فتحات دائرية في وسط منطقة القص وبقطر (150 mm) ،أما المجموعة الثانية فتتألف من ثلاث عتبات خرسانية ذات فتحات مربعة بأبعاد (133*133 mm) ،المجموعة الثالثة تتألف من ثلاث عتبات ذات فتحات مستطيلة بأبعاد (200*88mm)،وبعد تحليل النتائج لوحظ أن وجود الفتحات في العتبات الخرسانية قد سبب انحدارا في مقاومة العتبات الخرسانية بنسبة تتراوح بين (19-50)% وعند دراسة تأثير الشكل وجد ان العتبات ذات الفتحات المستطيلة لها قابلية تحمل اعلى من قابلية تحمل العتبات ذات الفتحات المربعة بنسبة (20.4%) والدائرية بنسبة (38.77%) ، ووجد ايضا بعد فحص العتبات المقواة بالياف الكاربون ان في عتبات المجموعة الأولى ذات الفتحات الدائرية كان مقدار الزيادة في مقاومة القص للعتبة هو (51-62%) وفي عتبات المجموعة الثانية ذات الفتحات المربعة كان مقدار الزيادة في مقاومة القص للعتبة (15-23.6%) أما في عتبات المجموعة الثالثة ذات الفتحات المستطيلة كان مقدار الزيادة بمقاومة القص للعتبة (8.6-16.7%)،

Behavior Of Reinforced Concrete Beams with Openings in Shear Zone Strength and rehabilitated with CFRP under Repeated Loading

Dr. Bayar J. Al-Sulayfani / Professor **Fahad Akram Al-Hamdani**

Abstract

This research work aims at studying the structural behavior of reinforced concrete strengthened and rehabilitated beams with openings at the middle of shear zone under repeated loads. The experimental program of the current study includes testing a reinforced beams (200x350x2400mm) divided into 3 groups. The 1st one consists of 3 beams with circular openings at the middle of shear zone having a diameter (150mm),while the 2nd group consisted of 3 reinforced beams with a square openings of (133x133mm).the 3rd group consisted of beams with rectangular openings of (200x88mm).When the results were analyzed , it was noticed that the presence of openings in the beams caused a reduction in the R.C beams strength a mounting to a ratio between (14-50)%,When the effect of shape was studied , it was found that the beams with rectangular openings had a higher strength than the ones with square openings by(20.4)% and (38.77)% than those of circular openings.

It was also found that when the carbon fiber strengthened beams of the circular openings were tested they showed an increase of shear strength between (51-62%) and an increase of (15-23.6 %) for the strengthened beams with square openings , while the increase was (8.6-16.7 %) for the strengthened beams with rectangular openings .

المقدمة:-

يعد نظام البلاطات والعتبات من أكثر النظم المستخدمة في انشاء الأرضيات والسقوف الخرسانية، وفي معظم هذه المنشآت تكون بلاطة الأرضيات والسقوف جزءا متكاملا (Integral Part) من العتبة الحاملة .

ان استحداث الفتحات في العتبات الخرسانية هو لغرض تسهيل مرور شبكة الأنابيب والقنوات اللازمة من خلالها أو استحداثها لأسباب اقتصادية[1]، يؤدي وجود هذه الفتحات إلى تقليل مقاومة هذه العتبات، وتعد عملية تغليف الأعضاء الخرسانية باستخدام ألياف البوليمر الكربونية إحدى الطرائق المتبعة للحد من ضعف مقاومة العتبات فضلا عن إعادة تأهيل الأعضاء الخرسانية من حيث زيادة مقاومتها لإجهادات القص والانثناء واللّي.[3] [2]

بما أن وجود الفتحات في العتبات يؤدي إلى تقليل مقاومتها لذا استخدم عدد من الباحثين ألياف البوليمر fiber reinforcement polymer (FRP) في تقوية العتبات الخرسانية المسلحة والاعمدة والسقوف وقد نجحت هذه الطريقة بزيادة مقاومة القص والانثناء والانضغاط [4]

وفي عام(2003)قام الباحث [5] [Abdalla] وآخرون. بدراسة سبل تقوية العتبات الخرسانية المسلحة باستخدام ألياف البوليمر الحاوية على فتحات ،أذ تضمن البحث تقوية الفتحات في العتبات الخرسانية باستخدام ألياف البوليمر للسيطرة على التشققات التي تنتج من تسليط الاحمال على العتبات الحاوية على هذه الفتحات ،واستخدمت عتبات بأبعاد (100X250)ملم وطول 2000ملم واستنتج الباحث أن مقدار الحمل المسلط على العتبة ذات الفتحات بأبعاد(200x100) ملم اقل بمقدار 50% من الحمل المسلط على العتبة الصلدة واستنتج أيضا أن وجود الفتحات يزيد من مقدار الاود الناتج واستنتج أن تقوية الفتحات باستخدام ألياف البوليمر لتقوية الفتحات له تأثير واضح في مقدار الأود الناتج والشكل (1) يوضح ذلك

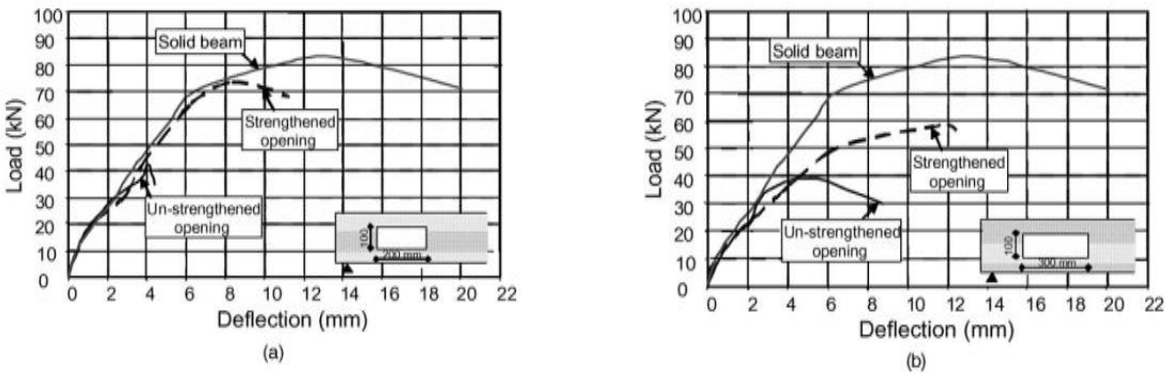

الشكل (1) تاثير التقوية بالياف البوليمر على علاقة الاود- الحمل للعتبات[3]

الهدف من البحث :-

1- معرفة التغير الحاصل في مقاومة القص بعد تقوية هذه الفتحات باستخدام ألياف البوليمر.
2- التعرف على دور ألياف الكاربون في مجال تقوية العتبات
3- التعرف على دور الياف الكاربون في مجال إعادة التأهيل للعتبات المتضررة

البرنامج العملي:_

جهزت (9) عتبات خرسانية بأبعاد (2400*350*200mm) سلحت هذه العتبات في منطقة الشد بثلاثة قضبان من حديد التسليح بقطر (16mm) من الاسفل وفي منطقة الانضغاط بقضيبين بقطر (12mm) من الاعلى وبحلقات بقطر (8mm) بمسافة بين منتصف حلقة واخرى (150mm) مع الغاء الحلقات التي تمر بالفتحات والشكل (2) يوضح تفاصيل حديد التسليح للعتبات المستخدمة في البحث.

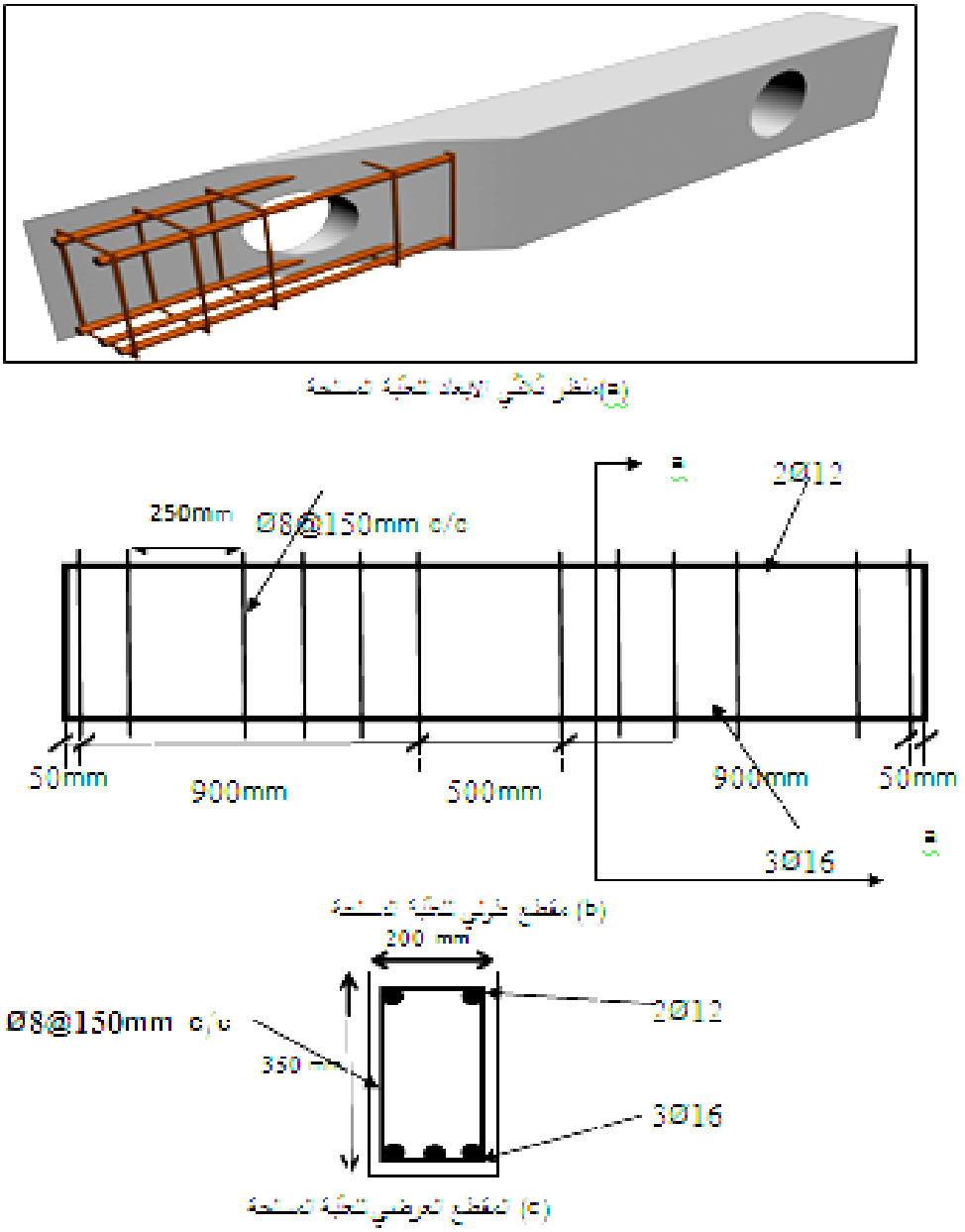

الشكل(2) تفاصيل حديد التسليح للعتبات المستخدمة في البحث

وتم فحص العتبات تحت اربعة احمال متمركزة مستندة الى اربعة صفائح حديدية بابعاد (200*120*20mm) والشكل (3) يوضح ذلك.

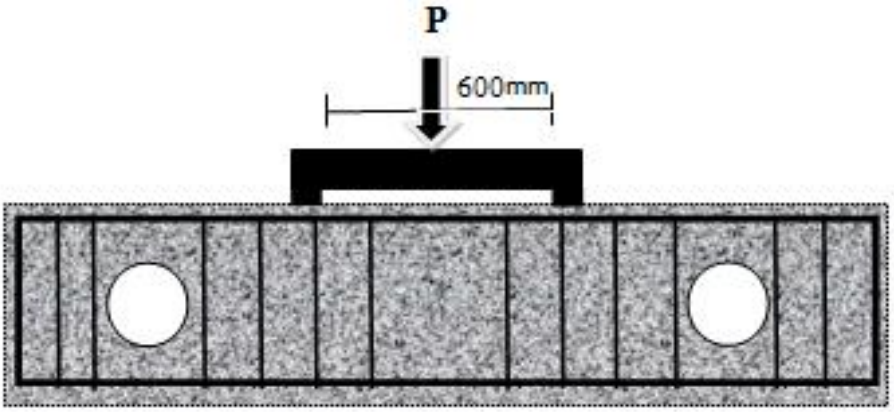

الشكل(3): مناطق استناد العتبة والاحمال

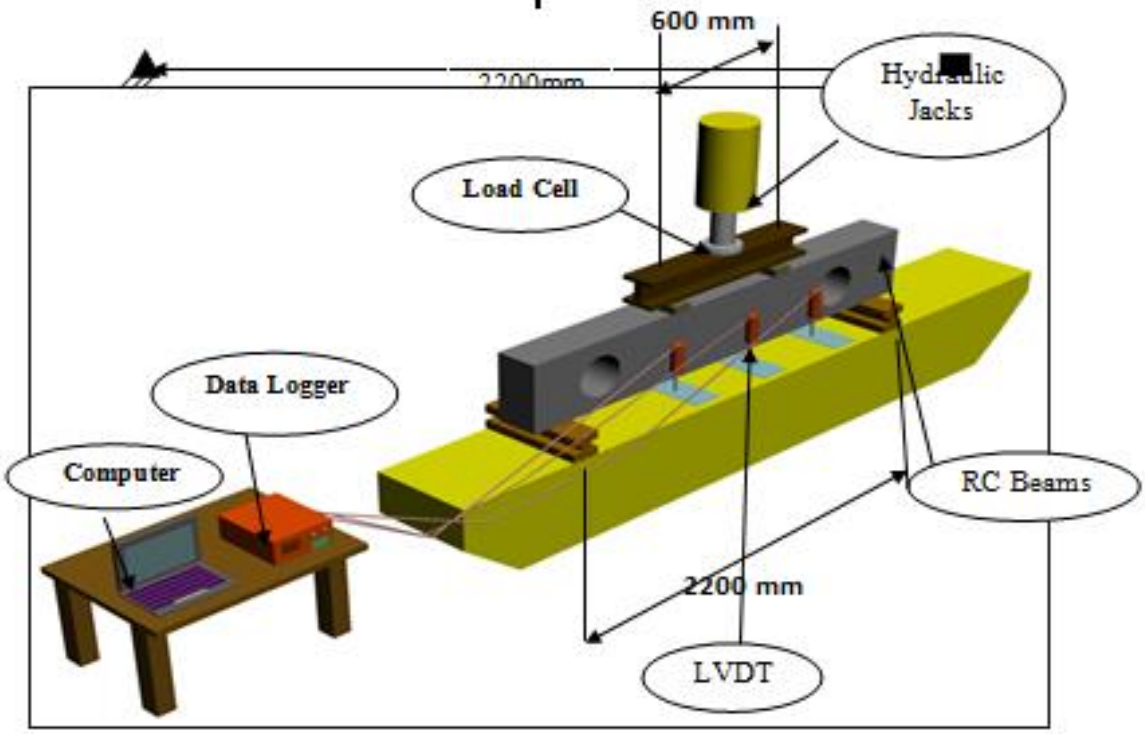

الشكل(4): تفاصيل عملية فحص نماذج الأعتاب الخرسانية.

وصف آلية تسليط الأحمال المتكررة (Repeated Load):-

تفحص العتبات الخرسانية المستخدمة في البحث تحت تأثير الأحمال التكرارية وهذه الأحمال تختلف عن الأحمال الساكنة في آلية تسليطها ،والأحمال التكرارية هي أقرب إلى الأحمال المسلطة على المنشأ في الواقع ،وتم فحص العتبات بزيادة الحمل (3) اطنان لكل دورة تحميل الى فشل العتبة، وتم اختيار هذا المقدار للزيادة بعد فحص عتبة تحت تأثير أحمال ساكنة ومعرفة حمل الفشل للعتبة ويمكن الاستفادة من الأحمال المتكررة في معرفة مقدار الأود النهائي الذي اكتسبته العتبة من تأثير تسليط الأحمال التكرارية ،

النتائج

دراسة تقوية الفتحات في العتبات الخرسانية باستخدام شرائط الألياف الكاربونية :-
أُجريت هذه الدراسة على تسع عتبات خرسانية مسلحة بأبعاد(2400*350*200)mm.وكانت هذه العتبات مقسمة على ثلاث مجموعات كل مجموعة تتكون من ثلاث عتبات خرسانية إحدى هذه العتبات لم يتم تغليفها استخدمت كعتبة مرجعية .المجموعة الاولى ذات فتحات دائرية،المجموعة الثانية ذات فتحات مربعة والمجموعة الثالثة ذات فتحات مستطيلة الشكل،تم تغليف العتبة الاولى بالياف الكاربون على شكل شرائط مائلة بزاوية 45والثانية على شكل حرف (U).وأن الغرض من اجراء هذه الدراسة هو معرفة دور ألياف الكاربون في تقوية العتبات الخرسانية خارجياً ذات الفتحات وتم فحص العتبات جميعها في هذا الجزء من الدراسة تحت تأثير الأحمال التكرارية ، والجدول (1) والشكل(4) يوضحان النتائج المستحصلة من فحص عتبات هذا الجزء من الدراسة.

الجدول(1): فحص العتبات قبل عملية التقوية وبعدها.

Group	Beams	Failure Load (kN)	%Increasing in Failure Load With Respect to Control Beams
Group1 (circle)	BOC150R(Control)	150	.....
	BOC150SRR(1)	227	51
	BOC150SUR(2)	243	62
Group2 (square)	BOS133*133R	195	.....
	BOS133^{2}SRR(1)	224	15
	BOS133^{2}SUR(2)	241	23.6
Group3 (Rectangular)	BOR200*88R	245	.....
	BOR200*88SRR(1)	266	8.6
	BOR200*88SUR(2)	286	16.7

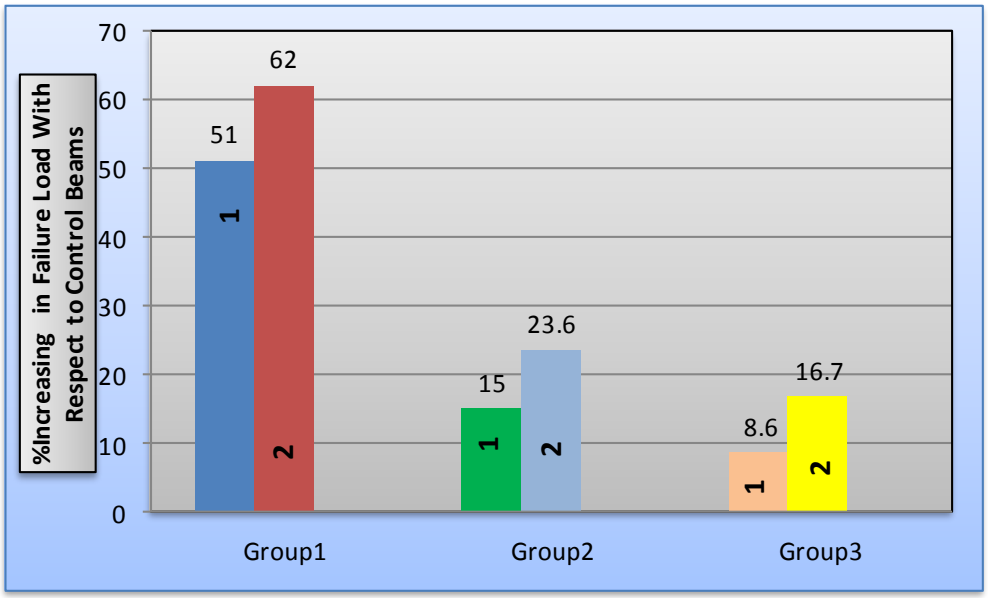

الشكل(4): الزيادة بمقاومة العتبات المقواة المستحصلة من فحص عتبات هذا الجزء من الدراسة.

من ملاحظة النتائج بالجدول (1) المستحصلة من الفحص وجد ان في عتبات المجموعة الأولى ذات الفتحات الدائرية كان مقدار الزيادة في مقاومة القص للعتبة (51-62%) وفي عتبات المجموعة الثانية ذات الفتحات المربعة كان مقدار الزيادة

في مقاومة القص للعتبة (15-23.6%) أما في عتبات المجموعة الثالثة ذات الفتحات المستطيلة كان مقدار الزيادة بمقاومة القص للعتبة (8.6-16.7%)،وحيث ان التغليف للعتبات في كل مجموعة يكون على شكل شرائط مائلة للعتبة رقم واحد وعلى شكل حرف (U) للعتبة الثانية، ومن خلال هذه النتائج المستحصلة من الفحص يتبين ان استخدام الياف الكاربون لتقوية الفتحات له تأثير واضح في زيادة مقاومة القص للعتبات المقواة، وتعزى زيادة مقاومة العتبات إلى مقاومة ألياف الكاربون لقوى الشد المتولدة في العتبات نتيجة تسليط الأحمال التكرارية إذ يلاحظ بأن ألياف الكاربون قد أسهمت بصورة واضحة في زيادة حمل الفشل للعتبات بنسبة تتراوح بين (8.6-62%)،وأن دور الياف الكاربون في تقوية العتبات ذات الفتحات الدائرية كانت ذات كفاءة أكبر من غيرها وذلك يعود إلى أن كفاءة التقوية بألياف الكاربون يزداد في العتبات التي تكون مقاومتها قليلة لاجهادات القص، أن التغليف على شكل حرف (U) يعمل على حصر الخرسانة حول الفتحة من الوجهين فضلاً عن أسفل الفتحة إذأن شكل الفشل في حالة التغليف على شكل حرف (U) يكون فجائياً مع تهشم منطقة ما حول الفتحات، وهذا يثبت حصره للخرسانة حول الفتحة وهو افضل من التغليف على شكل شرائط مائلة بزاوية 45 والشكل (5) يوضح صور أشكال الفشل للعتبات المقواة بعد الفحص.

الشكل (5) صور أشكال الفشل للعتبات المقواة بعد الفحص

والاشكال(6)(7)(8)(9)(10)(11) توضح منحنيات (الحمل_الأود) لعتبات هذه الدراسة قبل عملية التقوية وبعدها.

الشكل(6) منحني (الحمل_الأود)وشكل الفشل للعتبة ذات الفتحة الدائرية قبل التقوية وبعدها المغلفة على شكل شرائط مائلة.

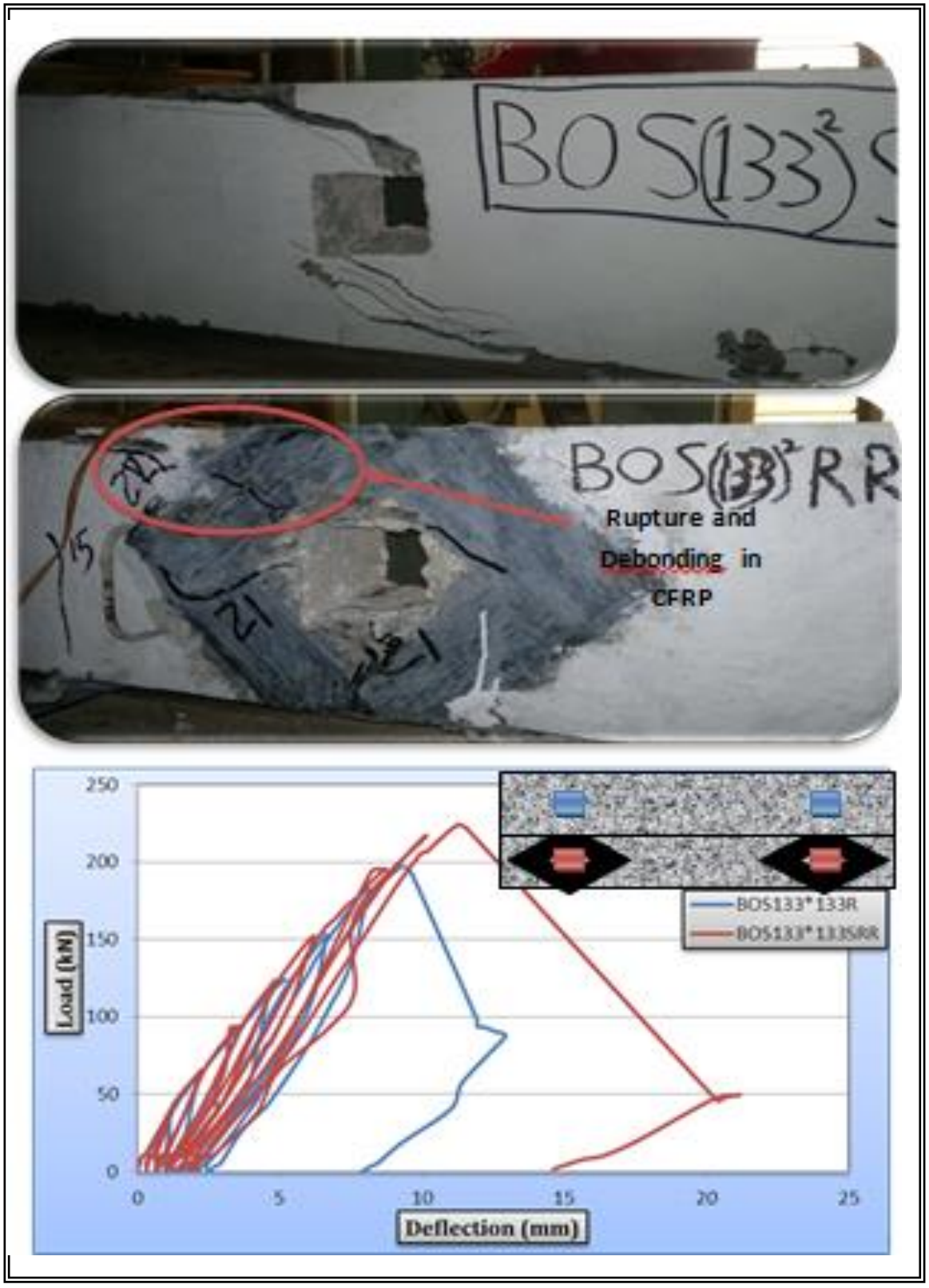

الشكل(7) منحني (الحمل-الأود) وشكل الفشل للعتبات ذات الفتحات الدائرية قبل التقوية وبعدها المغلفة على شكل حرف (U).

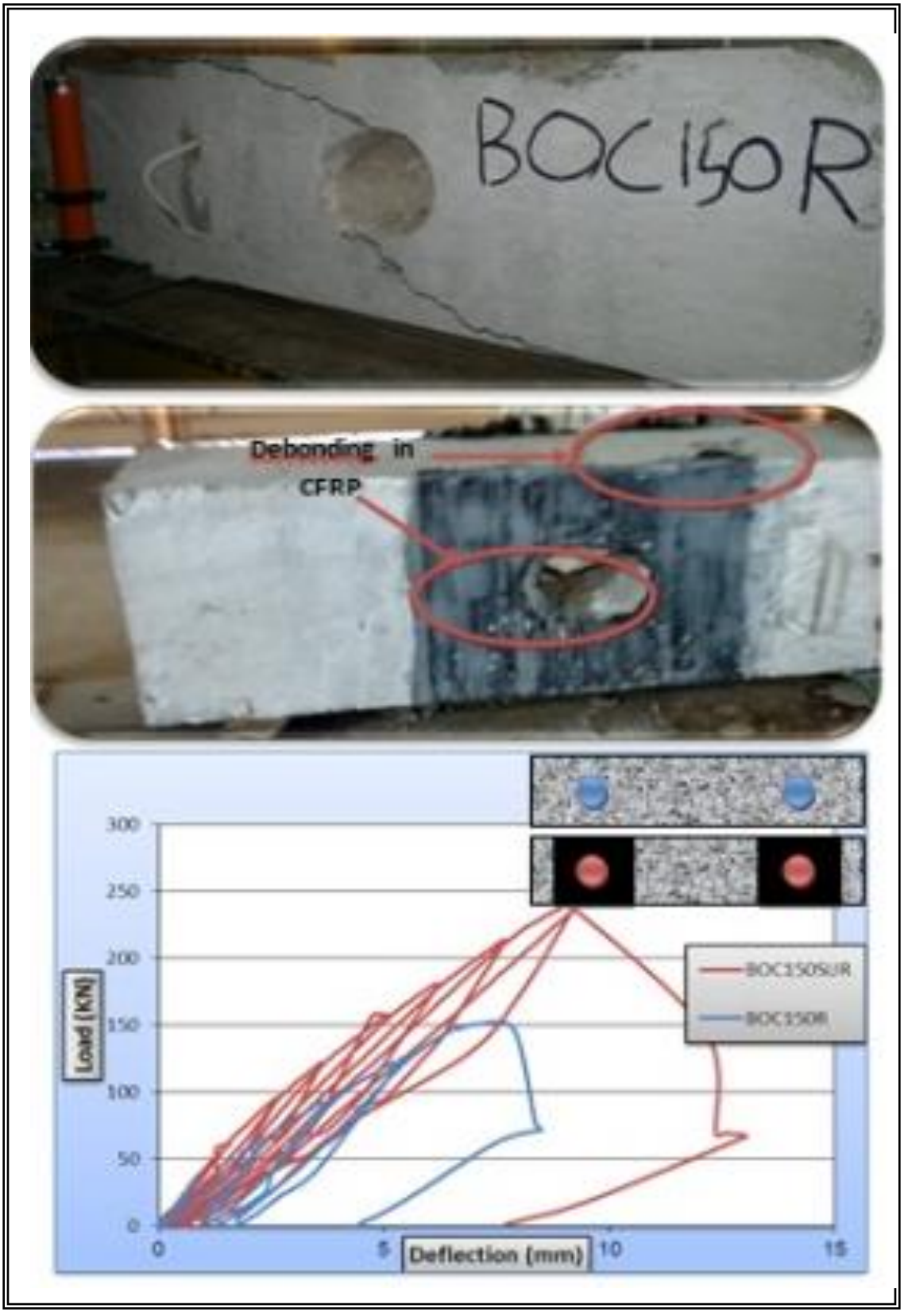

الشكل(8) منحني (الحمل-الأود)وشكل الفشل للعتبات ذات الفتحات المربعة قبل التقوية وبعدها المغلفة على شكل شرائط مائلة..

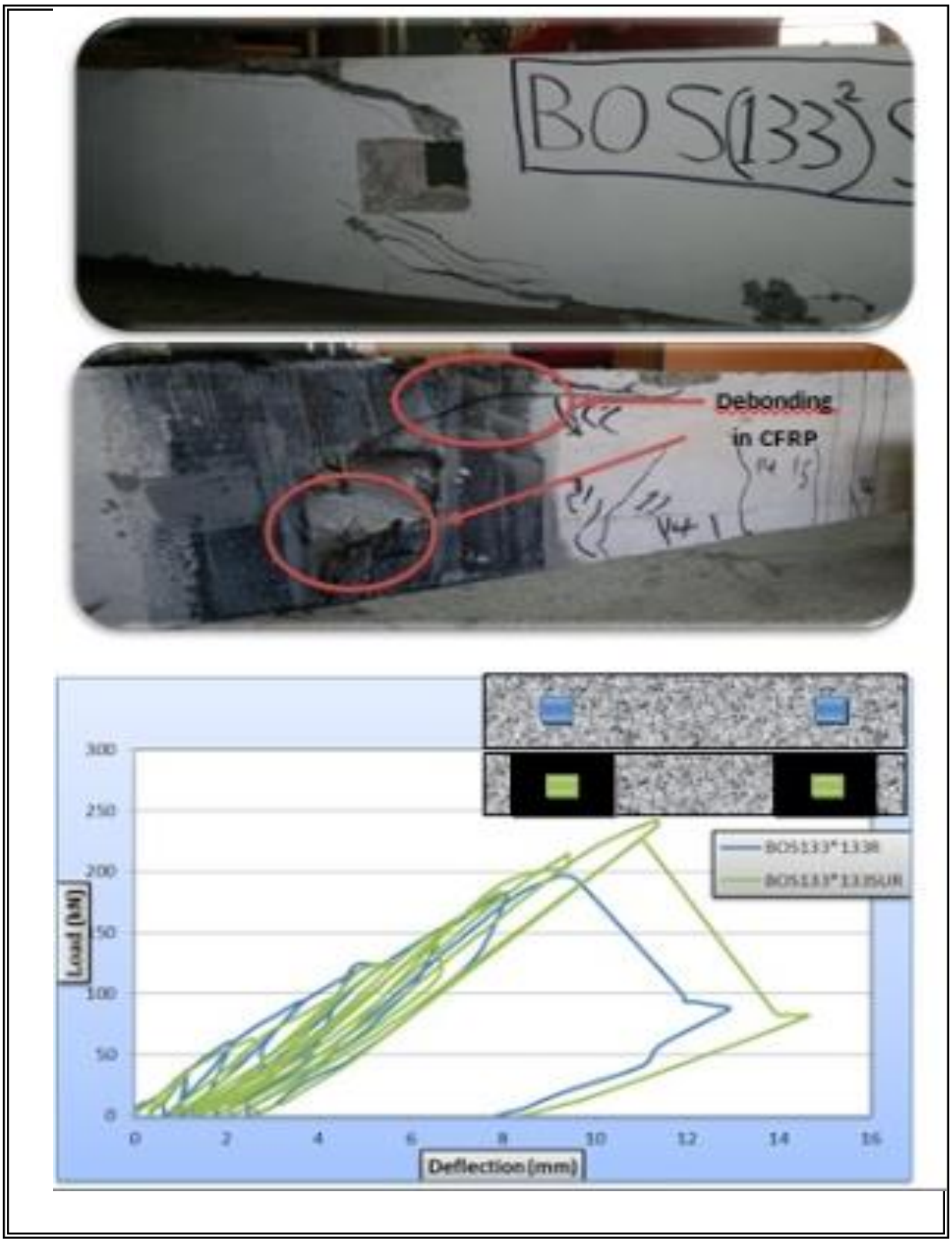

الشكل(9):منحني (الحمل-الأود)وشكل الفشل للعتبات ذات الفتحات المربعة قبل التقوية وبعدها المغلفة على شكل حرف (U).

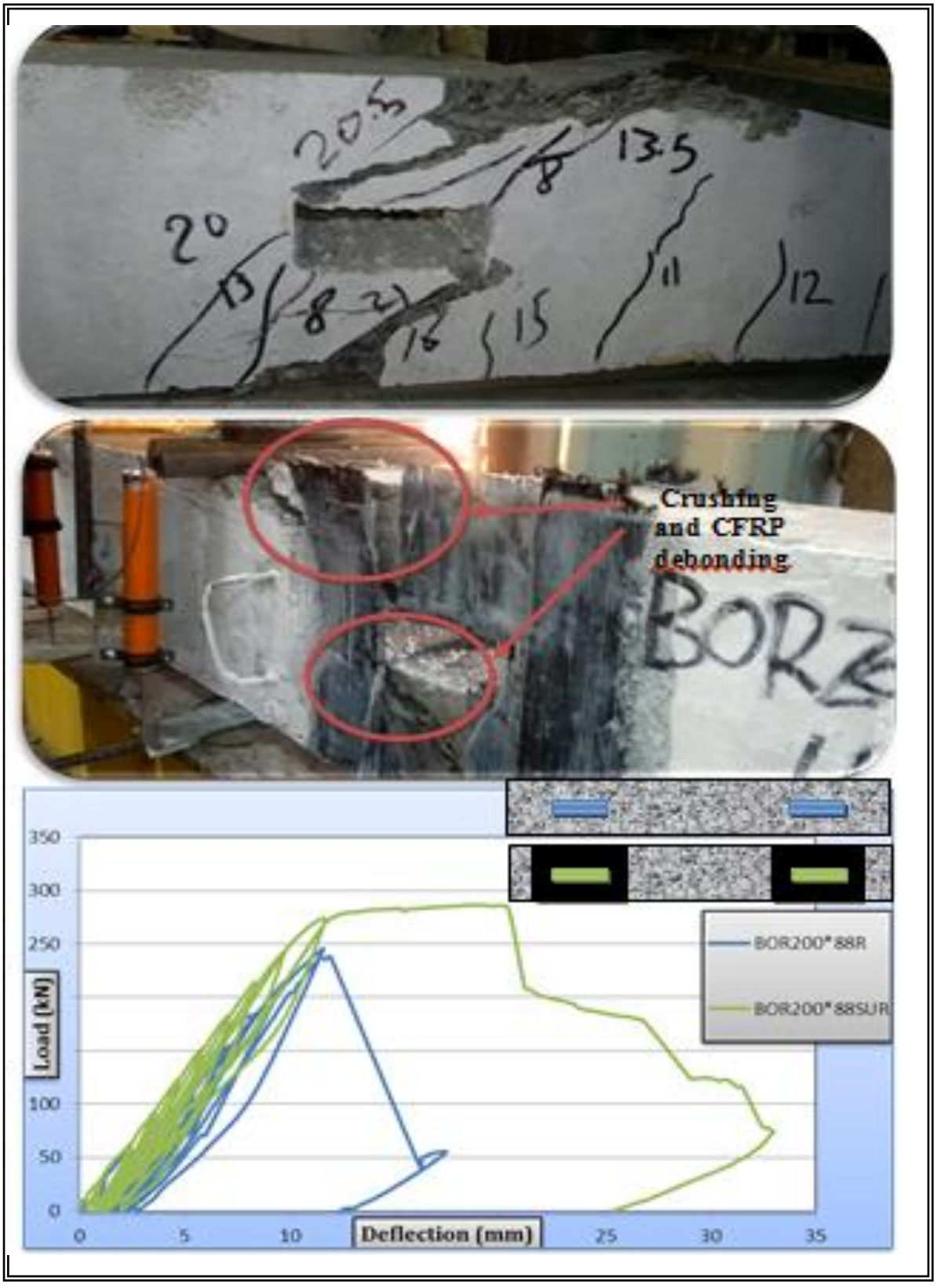

الشكل(10) منحني (الحمل-الأود)وشكل الفشل للعتبات ذات الفتحات المستطيلة قبل التقوية وبعدها المغلفة على شكل حرف (U).

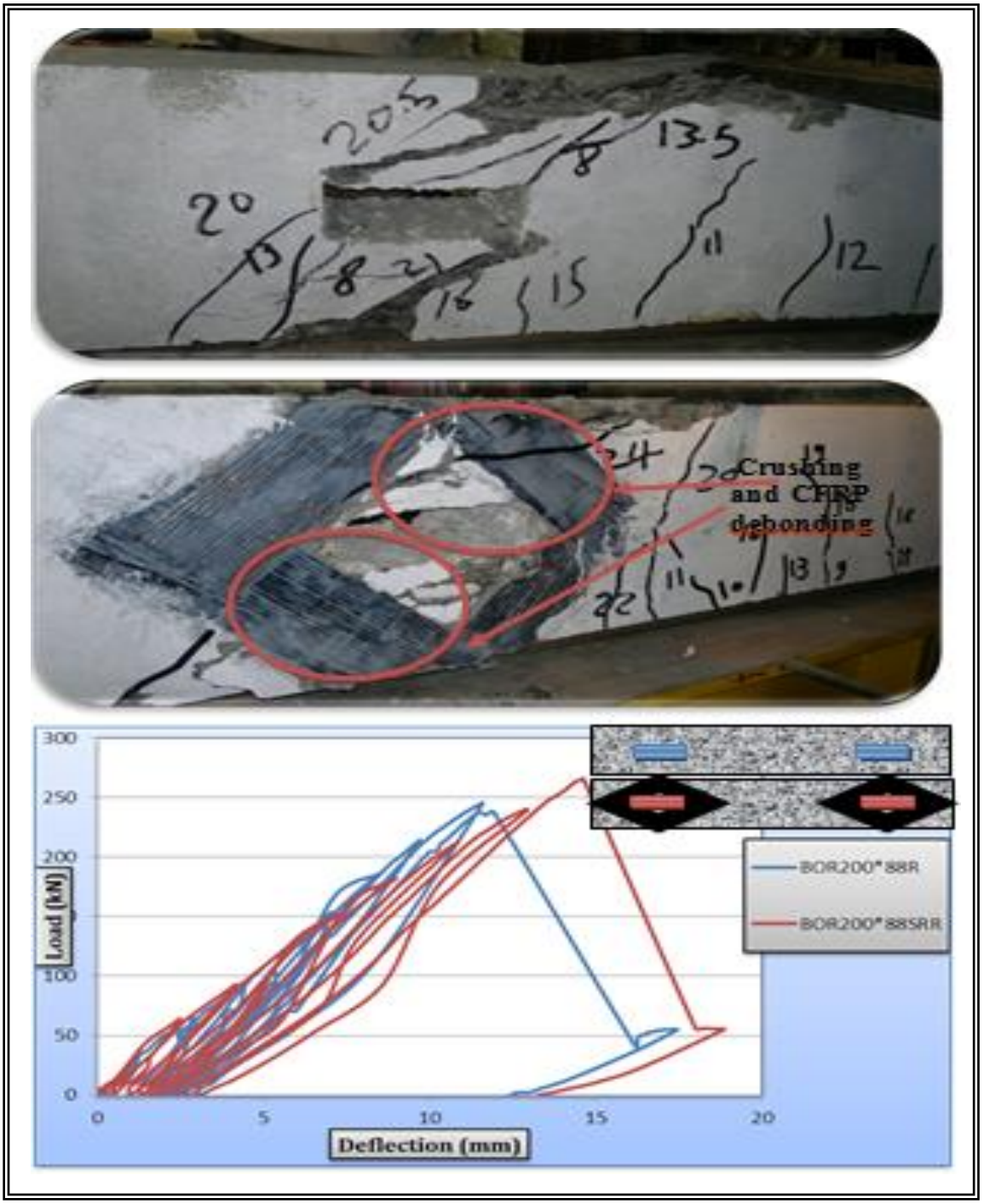

الشكل(11) منحني (الحمل-الأود)وشكل الفشل للعتبات ذات الفتحات المستطيلة قبل التقوية وبعدها المغلفة على شكل شرائط مائلة.

الجدول (2) يبين مقدار الاود للعتبات قبل التقوية وبعدها عند الحمل (150kN)، إن التغليف بألياف الكاربون كان له تأثير واضح في التقليل من مقدار أود المنتصف الحاصل في نماذج الأعتاب الحاوية على فتحات، و الجدول ايضاً يبين قيم النقصان ونسبه في الأود للعتبات المقواة مقارنة بالأود الحاصل في العتاب المرجعية وتعتمد هذه النسب على شكل التغليف بألياف الكاربون المستخدمة في تقوية كل عتبة وتراوحت نسب النقصان في الأود في وسط العتبات بين (2.9%-34.3%)، والسبب في ذلك يعود لكون ألياف الكاربون قد قوت المنطقة الضعيفة حول الفتحة وتحملت قوة الشد المتولدة مما أدى إلى تقليل مقدار الأود الناتج للعتبات المقواة، والجدول (2) والشكل (12) يوضحان ذلك.

الجدول (2) مقدار الاود للعتبات قبل التقوية وبعدها عند الحمل (150kN).

Group	Beams	Deflection(mm) at mid-span at load 150 (kN)	% Decreasing in deflection With Respect to Control Beams
Group1 (circle)	BOC150R(Control)	7	……..
	BOC150SRR(1)	4.6	34.3
	BOC150SUR(2)	4.77	31.8
Group2 (square)	BOS133*133R (Control)	6.8	……
	BOS133*133SRR(1)	6	11.7
	BOS133*133SUR(2)	6.5	4.4
Group3 (Rectangular)	(BOR200*88R Control)	6.9	……..
	BOR200*88SRR(1)	6.7	2.9
	BOR200*88SUR(2)	5.75	16.7

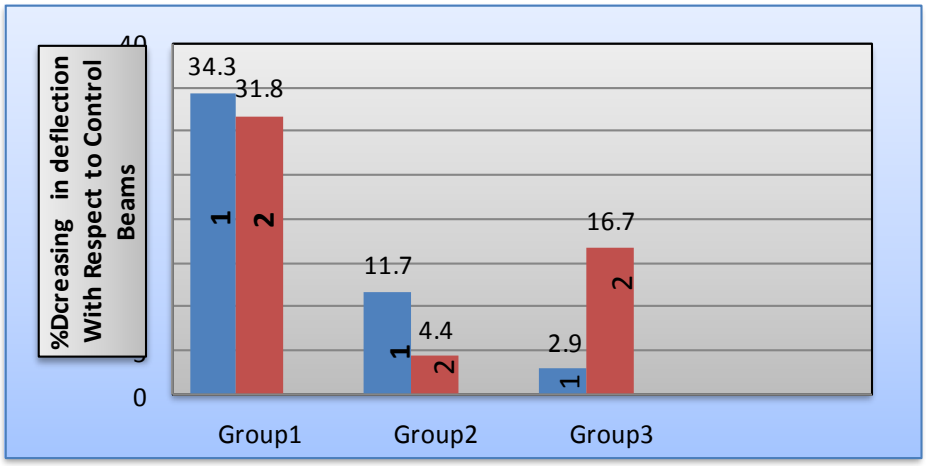

الشكل (12): نسبة النقصان بالأود بعد تقوية العتبات نسبة للعتبات المرجعية

لوحظ بعد فحص نماذج هذا الجزء من الدراسة بأن دور ألياف الكاربون لايقتصر على زيادة قوة تحمل العتبات الحاوية على فتحات مع النقصان في الأود، وإنما تعمل ألياف الكاربون على زيادة جساءة العتبات المقواة ، ويمكن ملاحظة الزيادة في جساءة العتبات الحاوية على فتحات في الجدول(3) والشكل(13) يوضحان مقدار الزيادة بالجساءة بالمقارنة مع العتبات المرجعية غير المقواة.

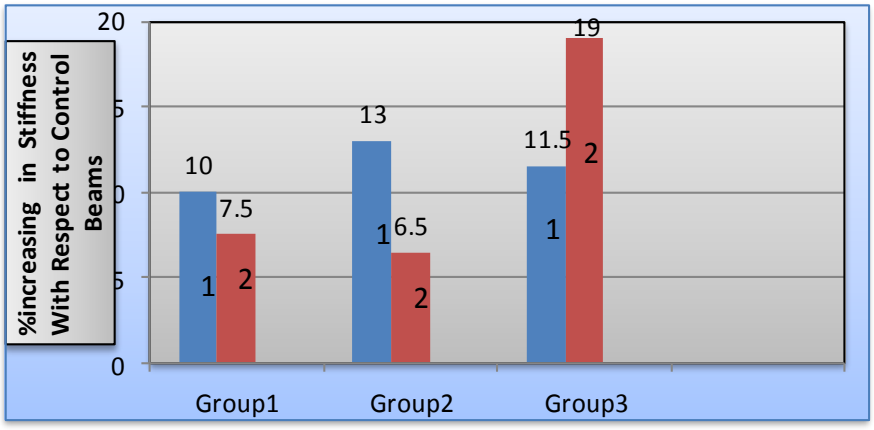

الشكل(13): مقدار الزيادة بالجساءة بالمقارنة مع العتبات المرجعية غير المقواة.

الجدول(3) مقدار الزيادة بالجساءة بالمقارنة مع العتبات المرجعية غير المقواة.

Group	Beams	Stiffness at load (50kN) (kN/mm)	%increasing in Stiffness With Respect to Control Beams
Group1 (circle)	BOC150R(Control)	28	.....
	BOC150SRR(1)	44	57
	BOC150SUR(2)	43	53.5
Group2 (square)	BOS133*133R (Control)	31	.....
	BOS133*133SRR(1)	35	13
	BOS133*133SUR(2)	33	6.5
Group3 (Rectangular)	BOR200*88R(Control)	26	.....
	BOR200*88SRR(1)	29	11.5
	BOR200*88SUR(2)	31	19

إن ألياف الكاربون لاتؤثر فقط في زيادة جساءة العتبات المركبة، وإنما في زيادة طاقة الامتصاص للعتبات المقواة بألياف البوليمر الكاربوينة أي قابليتها على امتصاص الطاقة وتبديدها، ويمكن حساب طاقة الامتصاص من حساب المساحة تحت منحني (الحمل-الأود) للعتبات المقواة، والجدول (4) يبين قيم طاقة الامتصاص المحسوبة ونسب الزيادة فيها للعتبات المقواة مقارنة بألاعتاب المرجعية والشكل (14) يوضح العلاقة بين نسب الزيادة في طاقة الامتصاص بالمقارنة مع ألعتبات المرجعية، ويعود سبب زيادة طاقة الامتصاص للعتبات المقواةإلى ألياف الكاربون التي تعمل على التقليل من الأود الحاصل في العتبات مع زيادة في الحمل مما يؤدي إلى زيادة المساحة تحت المنحني أي تزداد قابلية العتبة على امتصاص الطاقة المتولدة من تسليط الحمل.

الجدول(4): طاقة الامتصاص للعتبات قبل التقوية وبعدها.

Group	Beams	Toughness (kN.mm)	%Increasing in Toughness with Respect to Control Beams(kN.mm)
Group1 (circle)	BOC150R(Control)	557	.....
	BOC150SRR	685	23
	BOC150SUR	928	66.6
Group2 (square)	BOS133*133R (Control)	1026	.....
	BOS133*133SRR	1498	46
	BOS133*133SUR	1526	48.7
Group3 (Rectangular)	BOR200*88R (Control)	1831	.....
	BOR200*88SRR	2150	17
	BOR200*88SUR	3812	108

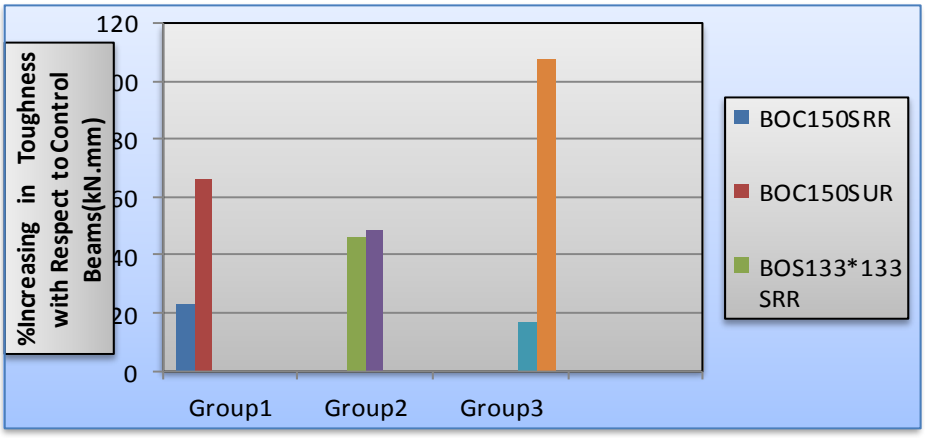

الشكل (14) : العلاقة بين نسب الزيادة في طاقة الامتصاص بالمقارنة مع العتبات المرجعية

6-4: إعادة تأهيل العتبات الخرسانية المسلحة الحاوية على فتحات باستخدام ألياف البوليمر تحت تأثير الاحمال التكرارية:

أُجريت الدراسة على عتبتين خرسانيتين ذات فتحات دائرية بقطر mm (150) بأبعاد mm(2400*350*200)وتم إعادة تأهيل النماذج باستخدام شرائط ألياف البوليمر على المنطقة المتضررة من العتبة بعرض (600)وفحصت العتبات تحت تاثير الاحمال التكرارية والجدول (5) يوضح النتائج المستحصلة من هذه الدراسة

الجدول(5):نتائج فحص العتبات المعاد تأهيلها

النماذج	حمل الفشل قبل إعادة التأهيل(kN)	حمل الفشل بعد إعادة التأهيل(kN)	%قابلية التحمل بعد إعادة التأهيل بالنسبة للعتبة قبل إعادة تأهيلها
BOC150RRe1	**150**	**152**	**101**
BOC150RRe2	**150**	**131**	**87**

ومن خلال النتائج المبينة بالجدول(5) نرى أن دور ألياف البوليمر في مجال إعادة التأهيل هو أكبر من دورها في مجال التقوية ويرجع إلى كفاءة الياف الكاربون التي تكون كبيرة بالنسبة للعتبات التي تكون مقاومتها قليلة، ففي العتبات المتضررة تكون المقاومة معدومة قبل إعادة التأهيل أي إن ألياف الكاربون مع المادة الرابطة هي التي تتحمل القوى التي يتعرض لها الأنموذج بعد إعادة التأهيل والشكل (15) يوضح شكل الفشل للعتبات المعاد تأهيلها،وكان الفشل بالنماذج هو تمزق ألياف الكاربون وحدوث الفشل في مكان الفشل نفسه قبل إعادة التأهيل.

الشكل (15) شكل الفشل للعتبات المعاد تأهيلها.

الشكل (16)(17) يوضح منحني (الحمل-الاود) للعتبات قبل اعادة التاهيل وبعدها.

الشكل (16) يوضح منحني (الحمل-الاود) للعتبات قبل إعادة التأهيل للعتبة الاولى وبعدها.

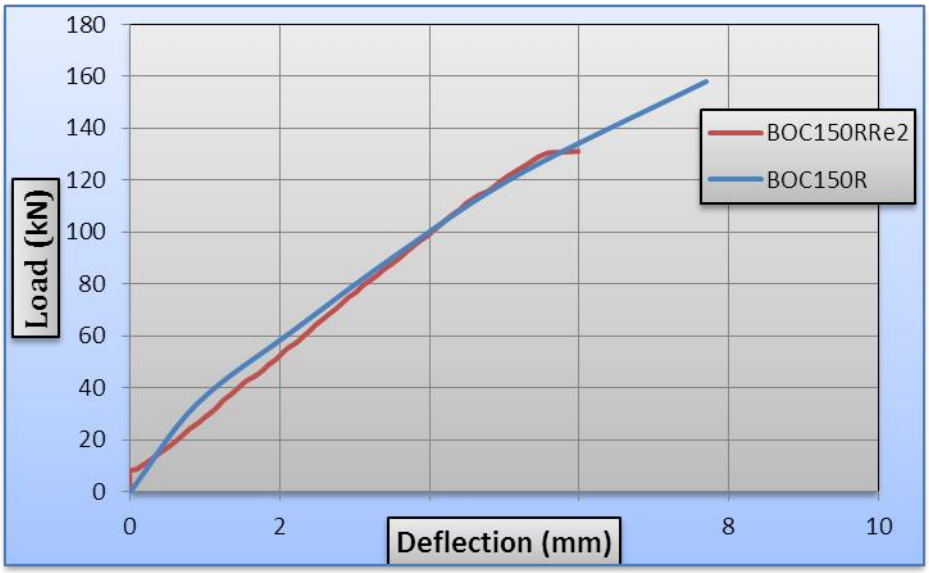

الشكل (17) يوضح منحني (الحمل-الاود) للعتبات قبل إعادة التأهيل للعتبة الثانية وبعدها.

ومن خلال منحني (الحمل-الأود) للعتبات المعاد تأهيلها يلاحظ ان هذه العتبات تكون جساءتها ومتانتها اقل من العتبات غير المتضررة ويرجع السبب في ذلك إلى وجود التشققات في العتبات المعاد تأهيلها قبل الفحص،ويلاحظ ايضاً أن منحني (الحمل-الأود) للعتبات المعاد تأهيلها خطياً ويرجع السبب في ذلك إلى ان دور ألياف الكاربون يظهر في بداية تسليط الاحمال على العتبة الى حين حصول الفشل على الرغم من طلس الشقوق بمادة الايبوكسي.

6-5:الاستنتاجات

من خلال الفحوصات المختبرية واستنادا إلى النتائج العملية

1- أن استحداث الفتحات في العتبات الخرسانية في وسط منطقة القص له تأثير واضح في مقاومة إجهادات القص للعتبات إذ ادى وجود هذه الفتحات الى نقصان في مقاومة العتبات لإجهادات القص بنسب متفاوتة تتراوح بين (14%-50.5) اعتماداً على شكل الفتحات المستخدمة وحجمها، وكانت أكبر نسبة نقصان للعتبات ذات الفتحات الدائرية ومن ثم العتبات ذات الفتحات المربعة والمستطيلة على التوالي.
2- أدى وجود الفتحات في العتبات إلى زيادة مقدار الأود المقاس في منتصف العتبات وبنسب متفاوتة تتراوح بين (25.5%-39.2) اعتماداً على شكل الفتحات المستخدمة وحجمها وهذه الزيادة في مقدار الأود أدت إلى نقصان في جساءة العتبات ومتانتها.
3- استنتج أن تقوية الفتحات باستخدام ألياف الكاربون أدى إلى زيادة مقاومة القص للعتبات وبنسب تتراوح بين (8.6%-62) وفق نوع الفتحات وشكل التغليف .
4- إن تقوية الفتحات باستخدام ألياف الكاربون أسهمت في تقليل الأود المقاس في منتصف العتبات وعند مستوى حمل ثابت قدرة (150kN) وبنسب تتراوح بين (2.9%-35.2%) بالمقارنة مع أعتاب السيطرة وتختلف القيم باختلاف شكل التغليف ونوع الفتحات وهذا النقصان أدى إلى زيادة في جساءة العتبات.
5- إن اسلوب وطريقة التقوية للفتحات له دور واضح على مقاومة القص للعتبات الحاوية على فتحات إذ لوحظ أن التقوية على شكل حرف (U) أسهمت في زيادة مقاومة القص بنسب تتراوح بين (16.7%-62) وهذه النسبة أعلى من التقوية باستخدام شرائط مائلة بزاوية 45 التي اسهمت بزيادة مقاومة القص بنسب تتراوح بين (8.6%-51) .

6- إن إعـــادة تأهيـــل العتبـــات الخرســـانية المســـلحة الحاويـــة علـــى فتحـــات فـــي منطقـــة القـــص المتضـــررة باســـتخدام شـــرائط الألـيـــاف الكربونيـــة أدى وبشـــكل كبيـــر إلـــى إعـــادة تحملهـــا ومقاومتها للإجهادات المعرضة لها.

المصادر

1. Mansur, M. A., "Design of Reinforced Concrete Beams with Web Openings", Proceedings of The 6th Asia-Pacific Structural Engineering and Construction Conference, Malaysia, September, 2006, pp.104-120.
2. Buyukozturk, O., and Hearing, B., "Failure behavior of Precracked Concrete Beams Retrofitted with FRP", Journal of Composites for Construction, Vol. 13, No. 4, August, 1998, pp. 138-144.
3. Nanni,A.,‘‘ Fiber Reinforced Polymer Composites for Infrastructure Strengthening - From Research to Practice", *University of Missouri – Rolla and University of Naples Federico*, Vol.2,No.15, June,2005,pp.1-7.
4. Uomoto,T., "Test Methods for FRP Materials ", FRPRCS-8 ، University of Patras,Greece,Vol.1,No.3,(16-18) July,2007,pp.1-9.
5. Abdalla,H., Torkey,A. and Haggag , H.. Design against cracking at openings in reinforced concrete beams strengthened with composite sheets. Cairo : Journal Of Composite Structures, Vol. 60, No. 3.(2003), pp 197–204

سلوك مقاومة أنتقال القص في الخرسانة بتأثير درجات الحرارة العالية

أ.د.عبد الحكيم حامد احمد بـــان نجيب ميخا
جامعة الموصل / كلية الهندسة / قسم الهندسة المدنية

الخلاصة

تم في هذا البحث دراسة تأثير درجات الحرارة على سلوك اجهادات القص في الخرسانة ألإعتيادية المتصلبة. تم صب نماذج الفحص (نماذج الدفع) بأبعاد (300x158x500mm)، حيث تم تسليح النموذج بالاتجاه العمودي باستخدام حديد تسليح عدد (4) قطر (12mm) لمقاومة قوى الانضغاط مع حلقات تسليح في منطقة القص قطر (8mm) ولأربع حالات تتمثل (بدون تسليح ، التسليح بحلقة واحدة وحلقتان وثلاث حلقات).
استخدمت نماذج خرسانية قطر .150mm وارتفاع .300mm لدراسة تأثير درجات الحرارة على كل من مقاومة ألإنضغاط ومقاومة ألإشطار ومعامل المرونة للخرسانة.
تم تعريض النماذج المتصلبة، بعمر (28) يوم لدرجات حرارة عالية تشمل (20,200,400,600℃) ولمدة ساعة واحدة من التسخين في الفرن الكهربائي ومن ثم فحصها بعمر (29) يوم بعد تركها لمدة 24 ساعة للوصول ألى درجة حرارة المختبر .
من خلال دراسة إجهادات انتقال القص في النماذج الخرسانية وقياس مقدار الانزلاق. تبين أن اجهادات القص تتأثر بتغيير درجات الحرارة حيث أن نسبة النقصان في مقاومة انتقال القص للنماذج غير المسلحة في منطقة القص كان بنسبة (9.1%، 16.6%، 51.7%) عند زيادة درجات الحرارة إلى (200℃،400℃،600℃) نسبة الى مثيلتها في درجة حرارة المختبر. وهذا السلوك يتغير بتغيير نسبة حديد التسليح في منطقة القص حيث أن النسب أعلاه أصبحت (3.8%، 8.3%، 18.7%) عند استخدام حلقة واحدة بقطر(.mm 8) و (3.1%، 4.7%، 12.5%) عند استخدام حلقتين و (5.4%،11.7%، 23.2%) عند استخدام ثلاث حلقات. كان مقدارألإنزلاق في النماذج غير المسلحة قليل جدا" هع حدوث فشل فجائي، أما للنماذج المسلح فيتراوح مقدار ألإنزلاق بين 0.096 عند درجة الحرارة 20℃ وتسليح بحلقة واحدة ليصل الى 2.062 عندما يكون التسليح بثلاث حلقات ودرجة حرارة .600℃
وهذه النتائج تشير ألى أن وجود حديد التسليح القص يساعد في تقليل تأثير درجات الحرارة العالية على مقاومة القص في المقطع .

الكلمات الدالة:ـ خرسانة، مقاومة أنتقال القص ، درجات الحرارة العالية، الانزلاق في الخرسانة

Behavior of concrete shear transfer strength at high temperature

Dr. A.H. Ahmad (prof.) **Ban Najeeb Mikha**
Civil Engineering Dept. / College of Engineering / University of Mosul

Abstract

In this research study, the effect of high temperature on the behavior of the shear transfer stresses of ordinary hardened concrete was investigated. Push-off samples (500x300x158mm.) were casted and reinforced with (8.0mm) diameter shear reinforcement (single, double and triple two legs ties). The samples also reinforced in the vertical direction with ($4\varphi 12mm$) reinforcement to provide the compressive strength.

A cylindrical concrete samples (150x300mm.) were used to study the effect of high temperature on compressive strength, splitting strength and modulus of elasticity.

The samples exposed to different high temperature (20,200,400,600℃) for a period of (1 hr.) in an electrical oven at the age of (28 days) then tested at room temperature (20℃) after (24 hrs.) at room temperature.

From the results of the shear transfer stresses in the concrete models at different high temperature, and measuring the slips and crack widths. It is found that the shear transfer strength varied with the variation of temperature. For specimen without shear reinforcement the shear strength reduced by (9.1 , 16.6 , 51.7 %) at temperatures of (200,400,600℃), and for single, double and triple ties the shear strength reduced as (3.8 , 8.3 , 18.7 %) , (3.1 , 4.7 , 12.5 %) and (5.4 , 11.7 , 23.2 %) respectively, the relative to shear strength at (20℃) for each condition of reinforcement . A very small slip found in the unreinforced samples due to sudden shear failure, for reinforced samples the slip ranged between 0.096mm. at 20℃ with single stirrup to 2.062mm. at 600℃ with three stirrups.

These results point out that the shear reinforcements have a valuable effect to reduce the effect of high temperature on shear strength.

Key word: Concrete, Shear transfer strength, High Temperature, Concrete.

المقدمة :-

يعتمد تأثير درجات الحرارة العالية على خصائص الخرسانة بصورة مباشرة وعلى نوع الخرسانة. فالخرسانة ذات المقاومة الاعتيادية تتأثر بشكل مغاير عن الخرسانة ذات المقاومة العالية وهذا يعني أن مقاومة الانضغاط تتأثر بتعرض الخرسانة للحرارة العالية ومن ثم مقاومة القص والتي كانت الدراسة بصددها ، كما أن مكونات الخرسانة لها دور في سلوك الخرسانة أثناء وبعد تعرضها لدرجات الحرارة العالية مثل نوع السمنت المستعمل ، نوع الركام ، نسب المزج ، نسبة (الماء/ السمنت) ونوع المواد المضافة .

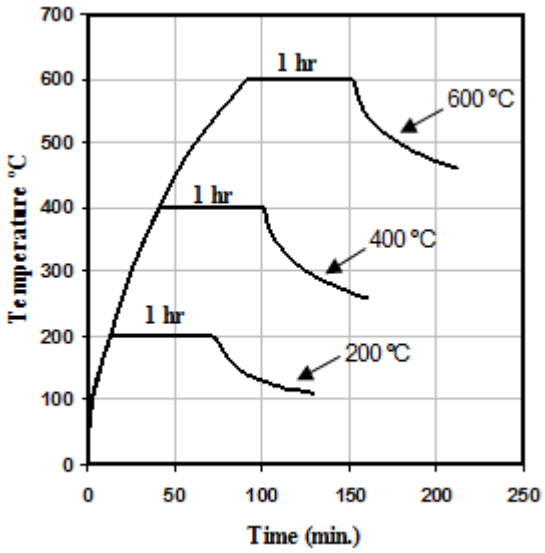

الشكل (1) آلية التسخين المعتمدة [2]

وعليه فإن دراسة بعض الخصائص الهندسية التي تتضمن مقاومة الانضغاط ، الشد الانشطاري ، معامل المرونة وعلاقة (الإجهاد – الانفعال) [1] للخرسانة الاعتيادية ومدى تأثير درجات الحرارة العالية عليها سيكون جزءاً من الدراسة الحالية الخاصة بتأثير درجات الحرارة العالية على مقاومة القص في الخرسانة الاعتيادية.

أخذت مستويات متعددة من درجات الحرارة العالية ، ويلاحظ من الدراسات السابقة عدم التطرق الى درجات حرارة أقل من (200°C) لأن تأثير التسخين يكون محدوداً، لذا فقد استخدمت أربعة مستويات حرارية (20,200,400,600°C) [2] والشكل رقم (1) يوضح آلية التسخين المعتمدة. حيث اعتمد ترك النموذج في الفرن لمدة ساعة واحدة بعد وصول درجة حرارة الفرن الى الحرارة المطلوبة.

وتعتبر إجهادات القص من الخصائص المهمة للخرسانة التي تتأثر بتغيير درجات الحرارة العالية والتي تؤخذ بنظر الاعتبار في تصاميم المنشآت الخرسانية، وهذه تحددها المواصفات العالمية الخاصة في تصميم المنشآت الهندسية، غير ان هذه المواصفات تعتمد الخصائص الهندسية للخرسانة في ظروف درجات الحرارة الاعتيادية، علماً أن المواصفات الخاصة بتأثير درجات الحرارة على الخرسانة [3] ACI 216R-89 لم تتطرق لسلوك إجهادات القص بعد التعرض لدرجات حرارة عالية.

تعرف إجهادات القص في مستوي قص محدد بانتقال القص ، ويمكن لإجهادات القص في الخرسانة أن تسبب تشققات مائلة خلال العنصر الإنشائي ، كذلك من المحتمل أن تسبب إجهادات القص فشل انزلاقي.

ميكانيكية انتقال القص:-

تتمثل ميكانيكية انتقال القص بالعوامل التالية:

1- تحمل المقطع الخرساني .
2- تحمل حديد التسليح.
3- تداخل الركام .

الدراسات السابقة :-

درس الباحثان (**Mattock and Hawkins**) [4] عام (1972) العوامل المؤثرة على مقاومة انتقال القص في الخرسانة العادية وخصائص مستوي القص ونسبة التسليح وإجهادات القص المباشر. حيث تم فحص نماذج الدفع وتم تعديل نماذج الدفع والسحب واختيار النماذج غير المتشققة ، وأستنتج أن التغيرات في مقاومة الخرسانة وحجم ومسافات حديد التسليح يؤثر بصورة مباشرة على مقاومة انتقال القص .

عام (1987) قام الباحثون (**Swamy, R., N.**) وآخرون [5] بدراسة مقاومة انتقال القص في الخرسانة الليفية والعادية وكانت الخرسانة الليفية في نماذج القص مسلحة بنسب حجمية مختلفة من الألياف الفولاذية ، أظهرت النتائج إن وجود الألياف الفولاذية يعزز من قوة انتقال القص ويقلل من عرض التشقق في الخرسانة . وأقترح معادلات الانحدار الخطي التي تتعلق بمقاومة انتقال القص:

$$V_u = 4.03 + 0.85\,(\rho f_y) \qquad for\ ordinary\ \ concrete$$

$$V_u = 5.1 + 0.85\ (\rho f_y + \sigma_{tu}) for\ fibrous\ concrete$$

حيث أن:

ρ = نسبة حديد التسليح.

f_y = الخضوع للحديد

σ_{tu}= إجهاد الشد في الخرسانة الليفية.

عام (1998) قام الباحث (**Al-Obidi**) [6] بدراسة مقاومة القص المباشر للخرسانة ذات المقاومة العالية مع الألياف الفولاذية، بناء على نتائج الفحص تم تطوير المعادلة التجريبية لمقاومة انتقال القص المباشر للخرسانة العادية وذات المقاومة العالية في حالة وجود الالياف الفولاذية أو عدم وجودها وكانت المعادلة المقترحة هي..

$$V_u = \varphi\ (0.7\sqrt{fc'} + 0.86\,\rho_v\,f_y + 8.8\,F)$$

حيث أن :

$$\varphi = 0.85$$

$$\rho_v = {A_{vf}}/{bh}$$

$$F = \left(\frac{L_f}{D_f}\right) V_f\, B_f$$

A_{vf} =مساحة حديد تسليح القص

bh = مساحة المقطع

B_f= معامل الألياف الفولاذية وتساوي (0.5) للألياف ذات المقطع الدائري و (0.75) للألياف المعكوفة

ρ_v=مساحة حديد التسليح العمودي على مقطع القص

V_f= حجم للألياف

$\frac{L_f}{D_f}$ = نسبة طول الليف إلى القطر.

قام الباحث (حسن) [7] عام (2002) بدراسة تأثير التسخين المتناوب على الصفائح الخرسانية المسلحة السميكة ، ودراسة خواص الخرسانة (مقاومة الانضغاط ، مقاومة الشد الانشطاري ، معامل المرونة والانفعال الاقصى) وتضمن وضع نموذج رياضي لتصرف الصفائح الخرسانية المسلحة السميكة تحت تأثير التسخين المتنوب ، حيث أستنتج بأن الصفائح الخرسانية المسلحة تتأثر بالتعرض للتسخين المتكرر الى حد كبير نتيجة لتأثر خواص المواد المكونة للصفيحة ، وأشار الباحث انه لم يطرأ أي تغيير على خواص الحديد (مقاومة الخضوع والمقاومة القصوى ومعامل لمرونة والانفعال الاقصى) نتيجة التعرض لعدد من دورات التسخين والتبريد ، سوى بعض التغييرات الطفيفة جداً بعد الدورة الاولى ، حيث أن قيمة مقاومة الخضوع للحديد كانت بنسبة %(102, 107.12, 104.3) عند درجات حرارة ℃(600 400, 200)على التوالي من القيمة الاولية لها قبل التسخين.

قام الباحث (**Vinayagam**) [8] عام (2004) بدراسة انتقال القص في الخرسانة ذات المقاومة العالية مع الألياف الفولاذية (HSFRC) ، بناء على نتائج الاختبارات التي أجريت على نماذج القص، فقد اقترح معادلة تجريبية للتنبؤ عن قوة القص المباشر .

$$V_u = 0.575\left(\frac{\rho_v\,f_y + \sigma_{tu}}{fc'}\right)^{0.5} * fc'$$

حيث أن :

σ_{tu}= أجهاد الشد في الخرسانة الليفية

$$\sigma_{tu} = \eta_1 \eta_\circ V_f \frac{l_f}{2r} \tau_u\, \eta$$

η_1=معامل كفاءة الطول ، $\eta_\circ$ =معامل أتجاه الألياف، V_f = حجم للألياف .

l_f= طول الليف، r = نسبة المقطع إلى المحيط للألياف و τ_u= مقاومة الأرتباط

عام (2005) أجري الباحث (**Peng**) [9] وآخرون دراسة ظاهرة التشظي المتفجر والخواص الميكانيكية المتبقية للخرسانة عالية الأداء مسلحة بالألياف الفولاذية عند تعرضها للحرارة العالية ، وتم دراسة مقاومة الأنضغاط ، مقاومة الشد الأنشطاري وطاقة الكسر لخلطات خرسانية مسلحة بالألياف الفولاذية أو بأليـاف البوليمير أو كلاهما معاً، وبعد تعريض النماذج الخرسانية لحرارة عالية تراوحت بين (200-800)°C ، بينت النتائج وعلى الرغم من تناقص المقاومة المتبقية للنماذج بعد تعرضها لحرارة تجاوزت (400°C) إلا أن طاقة الكسر المتبقية للنماذج أصبحت أعلى مما عليه قبل التسخين ، وأن وجود الألياف قد حسن من مقاومة الخرسانة للتشظي المتفجر .

عام (2006) أجرت الباحثة (**AL-Feel**) [10] دراسة عملية ونظرية لانتقال إجهادات القص المباشرة في الخرسانة المسلحة الحاوية على الياف فولاذية حيث كانت نماذج الفحص التي استخدمت من نوع الدفع والسحب لتمثيل إجهادات الشد والانضغاط العمودي على مستوي القص، أظهرت النتائج أن الألياف الفولاذية تزيد من اجهادات التشقق الاولية والنهائية لنماذج الدفع والسحب وكانت هذه الزيادة أكثر في النماذج التي تحتوي على تسليح القص ، بناء على هذه النتائج تم تطوير معادلة تجريبية لمقاومة انتقال القص

$$V_u = 0.766\sqrt{fc'} + 0.612\,\rho_v\,f_y + 0.96\,\sigma_{\mathrm{tu}} + 1.66\,\mathrm{V_f}\frac{l_f}{d_f} \qquad \text{R=0.993}$$

أجري الباحث (**Husem**) [11] عام (2006) دراسة مقارنة لمقاومة الانضغاط والانثناء بين نوعين من الخرسانة خرسانة أعتيادية بمعدل مقاومة (34MPa) وخرسانة عالية الاداء ذات معدل مقاومة (71MPa) وتضمنت الدراسة كذلك المونة المكونة لكل من الخلطتين تحت تأثير مستويات مختلفة من درجات الحرارة تراوحت بين (20-1000)°C مع أختلاف طرق التبريد التي تضمنت التبريد بالماء والهواء. أظهرت النتائج أن مقاومة الخرسانة تقل بأرتفاع درجات الحرارة وأن الانخفاض في مقاومة الخرسانة عالية الاداء كان أكبر من الانخفاض في المقاومة للخرسانة الاعتيادية ، كما أن التشظي المتفجر (Explosive Spalling) لم يحدث في الخرسانة الاعتيادية بينما حدث لبعض النماذج للخرسانة عالية الاداء عند درجات الحرارة المتراوحة بين (400-500) °C كذلك ظهر تأثير أختلاف أسلوب التبريد على المقاومة المتبقية إذ أن التبريد بالماء يسبب أنخفاض أكبر خاصة مع أرتفاع الحرارة المؤثرة .

قامت الباحثة (**الشهواني**) [12] عام (2007) بدراسة عملية لبعض الخصائص الميكانيكية للخرسانة التي تضمنت مقاومة الانضغاط ، الشد الانشطاري و معامل المرونة وعلاقة (الإجهاد – الانفعال) للخرسانة المسلحة بالألياف الفولاذية ومدى تأثير الحرارة العالية عليها ومقارنة النتائج مع الخرسانة الاعتيادية . وكانت استنتاجاتها :

1- تتأثر خواص الخرسانة بصورة سلبية عند تعرضها لدرجات الحرارة العالية ويزداد تأثرها مع ارتفاع درجات الحرارة ، وأكثر الخواص تأثراً بالحرارة خاصتي هي مقاومة الشد الانشطاري ومعامل المرونة.
2- أنخفض معامل المرونة ومقاومة الشد الانشطاري ومقاومة الانضغاط للمزجات الخرسانية بشكل عام وبنسب مختلفة بعد التعرض لدرجات الحرارة العالية ، وكانت مقاومة الشد للخرسانة الليفية أعلى من الخرسانة الاعتيادية عند كافة درجات الحرارة .
3- سببت درجات الحرارة العالية انخفاضاً في سعة امتصاص الطاقة لجميع الخلطات الخرسانية وزيادة الانفعال الذي يتناسب طردياً مع ارتفاع درجات الحرارة وبازدياد الإجهاد وكان الانفعال أكبر في حالة استعمال نسبة الياف أعلى .

أجري الباحث (**AL-Owaisy**) عام (2007) [13] دراسة حول تأثير التعرض للحرارة العالية لحد (500°C) على مقاومة أنتقال القص للخرسانة عملياً بأستخدام نماذج دفع بأبعاد (100mm × 440 ×200) ، النماذج مقسمة الى ثلاثة مجاميع تتكون كل منها من أربع نماذج . تم تعريض نموذج من كل مجموعة الى (150°C) والثاني الى (350°C) والنموذج الثالث تم تعريضه الى (500°C) ، وتم فحصه النموذج الرابع كنموذج مرجعي في درجة الحرارة ألإعتيادية. تختلف المجاميع الثلاثة عن بعضهما بكمية حديد القص الذي يقطع مستوي القص كانت التسليح بحلقة واحدة وحلقتان بقطر (10mm) وبدون تسليح قص .

نتائج هذه الدراسة تبين أن مقدار النقص الحاصل بمقاومة أنتقال القص يتراوح تقريباً بين (42% - 18) وان مقاومة انتقال القص وبعد التعرض لكل درجات الحرارة ، بقيت أعلى للنماذج ذات كمية تسليح القص الأكبر من نلك ذات كمية تسليح القص الاقل . كما تم في هذا البحث مقارنة تصرف مقاومة انتقال القص بعد التعرض الى درجات الحرارة العالية مع تصرف مقاومة الانضغاط والشد للخرسانة وتبين ان تصرف انتقال القص اقرب لتصرف مقاومة انضغاط الخرسانة منها لمقاومة شد الخرسانة .

عام (2012) قامت الباحثة **(Ridha)** وآخرون [14] بدراسة مقاومة الخرسانة عالية الأداء المسلحة بالألياف الفولاذية تحت تأثير القص المباشر ، وذلك بإجراء دراسة عملية وتحليلية ، في الدراسة العملية تم فحص ثمانية نماذج من الخرسانة العالية الأداء المسلحة بالألياف الفولاذية تحت قوى القص المباشر وتم استعمال نوعين من الألياف الفولاذية، المستقيمة والمعقوفة النهايات ، وكانت نسبة حجوم الألياف (0.5, 1.0, 1.5, 2.0) % . أما في الدراسة التحليلية فتم اشتقاق معادلة لإيجاد مقاومة القص المباشر، وذلك بالاعتماد على النتائج العملية لهذا البحث وبحوث سابقة ولمقاومة انضغاط تتراوح بين MPa(107-40) . المتغيرات التي تم اعتمادها بالمعادلة كانت معامل الألياف (F) ومساحة حديد التسليح العمودي على مقطع القص $(\rho v f y)$ ومقاومة الأنضغاط للخرسانة $(f c')$، حيث أستنتجت أن زيادة حجم الألياف الفولاذية يقلل من الازاحة العمودية في المراحل المبكرة من الحمل.

البرنامج العملي والمواد المستخدمة:-

1- المواد المستخدمة في الدراسة العملية ، وتشمل :-

أ)- الأسمنت المستخدم سمنت تركي اعتيادي (أورغني) .

ب)- ماء شرب اعتيادي .

ج)-الركام الناعم (الرمل) : الرمل المستخدم هورمل نهري (كنهش) ، بعد إجراء التحليل المنخلي له وجد أنه ضمن الحد العام للمواصفة البريطانية [15] (B.S 882:1992) ، وبمعامل نعومة (3.1%) ونسبة مواد طينية (2.1%) ، الجدول رقم (1) يبين نتائج التحليل المنخلي وموضحة في الشكل (2).

الجدول (1) التحليل المنخلي للرمل المستخدم مع حدود المواصفات البريطانية [15](B.S.882:1992)

مقاس المنخل (mm)	النسبة المئوية المارة المتجمعة				
	الحدود القياسية	النسبة المارة للرمل المستخدم	حدود مناطق التدرج		
			خشن C	متوسط M	ناعم F
4.75	100-89	100	-	-	-
2.36	100-60	84	100-60	100-65	100-80
1.18	100-30	68	90-30	100-45	100-70
0.6	100-15	24	54-15	80-25	100-55
0.3	70-5	9	40-5	48-5	70-5
0.15	15-0	5	-	-	-

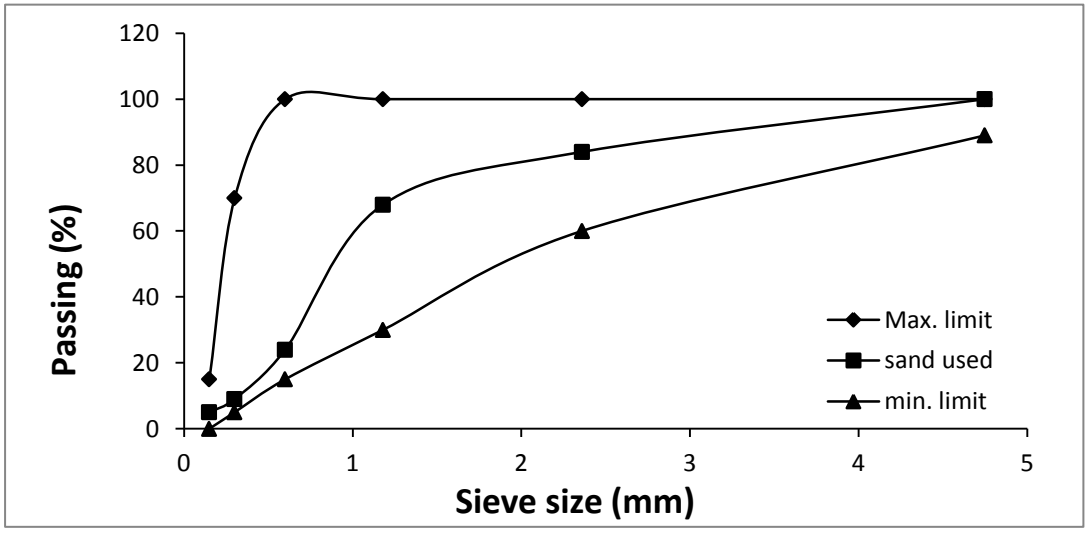

الشكل (2) : التحليل المنخلي للركام الناعم

د)- الركام الخشن (الحصى) :حصى نهري ذ و نهايات مدورة (rounded aggregate) مطابق للمواصفة البريطانية (B.S 882 :1992) [15] والمقاس الأقصى للركام (M.A.S) (10 mm).

2- الخرسانة الطرية :-

تم اختيار نسب المواد في الخلطة الخرسانية للحصول على مقاومة انضغاط بحدود (35MPa) وهطول (130mm) ، وتم تصميم الخلطة حسب الطريقة البريطانية (D.O.E) [16]. النسب الوزنية للخلطة الخرسانية هي (1:2.52:1.65/0.52). وتم صب أسطوانات قياسية ($150\times 300mm$) عدد 3 لكل مرحلة تسخين لإيجاد مقاومة ألإنضغاط ومعامل المرونة. وثلاث اسطوانات اخرى لإيجاد مفاومة الشد ألإنشطاري. كما تم صب 16 نموذج دفع خاص بفحص انتقال القص المباشر بأبعاد ($500mm \times 158 \times 300$)، شكل (3). أهم المتغيرات التي أخذت بنظر الاعتبار هي نسبة التسليح في منطقة القص حيث تم استخدام أربع نسب تسليح (بدون حلقات، حلقة واحدة Ø8mm-1، حلقتان Ø8mm-2، وثلاث حلقات Ø8mm-3) كما تم تعريض النماذج (ألأسطوانات ونماذج فحص القص) الى أربع درجات حرارة مختلفة كما موضح في الجدول رقم (2) . يلاحظ من الجدول التغيير في مقاومة الانضغاط بتغيير درجة الحرارة.

جدول رقم (2) يمثل ترميز النماذج والمتغيرات

رقم النموذج	(f_c') مقاومة الانضغاط (MPa)	عدد وقطر حلقات تسليح القص	درجات الحرارة (°C)
NA0	38.33	_____	20
NA1	38.33	1-φ 8mm	20
NA2	38.33	2-φ 8mm	20
NA3	38.33	3-φ 8mm	20
NB0	37.38	-------	200
NB1	37.38	1-φ 8mm	200
NB2	37.38	2-φ 8mm	200
NB3	37.38	3-φ 8mm	200
NC0	33.62	-------	400
NC1	33.62	1-φ 8mm	400
NC2	33.62	2-φ 8mm	400
NC3	33.62	3-φ 8mm	400
ND0	27.18	-------	600
ND1	27.18	1-φ 8mm	600
ND2	27.18	2-φ 8mm	600
ND3	27.18	3-φ 8mm	600

3- تهيئة النماذج الخرسانية وطريقة المعالجة:-

قبل أجراء عملية الصب تم تنظيف القوالب الخاصة بفحص القص المباشر وذلك بدهن القوالب من الداخل لتسهيل إخراج النماذج من القوالب. ثم وضع حديد التسليح المُعد للنموذج داخل القالب وكان تسليح القص بحلقات قطر (8mm) لأربع حالات (بدون حلقة ، حلقة واحدة ، حلقتان ، ثلاث حلقات) . كما تم تسليح النموذج بالاتجاه العمودي باستخدام حديد تسليح قطر (12mm) كما في الشكل (3) وذلك لضمان عدم فشل النموذج بتأثير قوى الانضغاط. الجدول رقم (3) يوضح اجهاد الخضوع ومقاومة الشد والاستطالة لحديد التسليح العمودي والحلقات. وتم استخدام قطع بلاستيكية (spacers) لتحديد الغطاء الخرساني .mm(25) لقضبان حديد التسليح (Concrete Cover). بعد ذلك مزجت المواد المكونة للخلطة الخرسانية باستخدام الخباطة بإضافة المواد الجافة أولا وأضافه الماء تدريجياً وبعد المزج يتم التأكد من مقدار الهطول باستعمال مخروط الهطول وكان مقدار الهطول يتراوح بين mm (140-120) وبعدها وضعت الخرسانة داخل القوالب واستخدمت المنضدة الهزازة لغرض ضمان خروج الفقاعات ورص الخرسانة بصورة جيدة ومتجانسة. وتم تسوية سطح القوالب وتركها لمدة 24 ساعة في المختبر بعدها تم فتح القوالب، وتم المعالجة في أحواض الماء بصورة مستمرة لمدة

(14) يوم وبعدها تم اخراجها وتغطيتها بالجنفاص الرطب إلى عمر (27) يوم ليتم تركها في المختبر بدرجـــــــةحـــرارة (20± 2°C) قبل تسخينها بعمر (28) يوم بالفرن الكهربائي لدرجة الحرارة المطلوبة.

الجدول (3) مواصفات حديد التسليح المستخدم

قطر حديد التسليح (mm)	اجهاد الخضوع (fy)(MPa)	مقاومة الشد القصوى (fu)(MPa)	الاستطالة (Elongation)
8	614	710	10.5%
12	691	591	11.05%

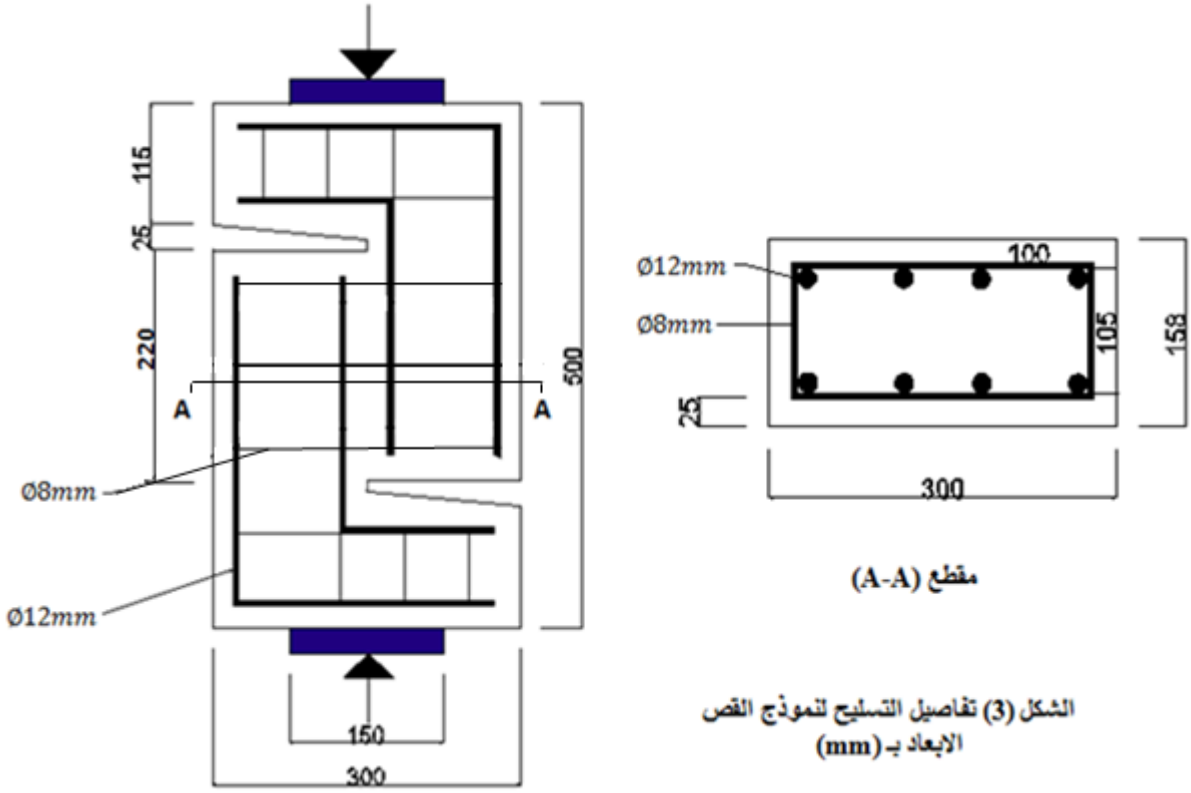

الشكل (3) تفاصيل التسليح لنموذج القص
الابعاد بـ (mm)

4- تسخين النماذج الخرسانية :-

تم تسخين النماذج الخرسانية الى المستويات المحددة من درجات الحرارة بأستعمال فرن كهربائي ذو حجرة واسعة مهواة تصل درجة حرارته القصوى الى (600°C) كما في الشكل (4)، تم وضع النموذج بالفرن وتثبيت درجة الحرارية المطلوبة ولحين الوصول لهذه الدرجة يترك النموذج لمدة ساعة داخل الفرن في درجة الحرارة الثابتة ، بعدها يترك النموذج داخل الفرن مع أيقاف التسخين وفتح البوابة لمدة 24 ساعة بدرجة حرارة المختبر بعد ذلك يتم فحص النماذج.

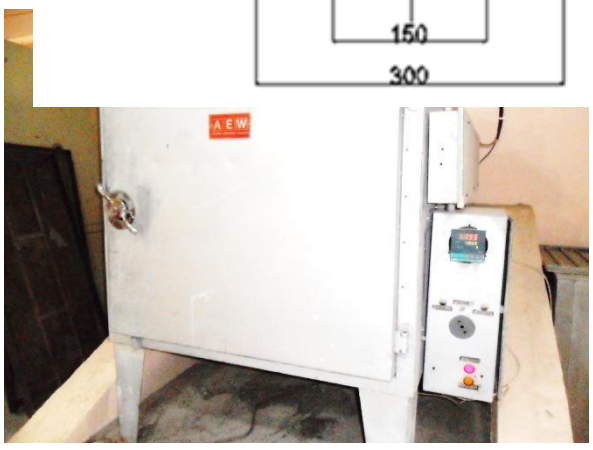

الشكل (4) الفرن الكهربائي المستخدم للتسخين

5- تـــهيئة نـــماذج للفحص :-

بعد انهاء المعالجة وتسخين النماذج وتبريدها تم وضع نموذج القص على جهاز الفحص وضبط استقامة النموذج باستخدام الوزان وتحديد موقع مركز النموذج مع مركز تسليط الحمل على النموذج بوساطة الشاقول لضمان توزيع الحمل على

النموذج أثناء الفحص بصورة متجانسة. توضع صفائح حديدية سمك (25mm) فوق وتحت النموذج بأبعاد (150*158mm) لنقل الحمل على اقل مساحة ممكنة لمنطقة القص المباشر على طول مستوي القص. تم تهيئة (16) نموذج للفحص والشكل (5) يوضح تهيئة النماذج للفحص، حيث تم تثبيت قطعتي زجاج عمود على مستوي القص الاولي في أسفل وأعلى مستوي القص لنقل الانزلاق الناتج عن مستوي القص وتم قياس ذلك باستعمال (Transducers) مثبت بين قطعتي الزجاج، يتم قراءة مقدار الانزلاق لمراحل الحمل المسلط باستخدام جهاز (Data logger) متصل بجهاز الحاسوب والذي يسجل الأود مع الزيادة التدريجية للحمل الى مرحلة حصول الفشل وبعد انتهاء الفحص تحول نتيجة الفحص الى برنامج (Excel) لرسم العلاقة بين الحمل ومقدار الانزلاق ومن ثم تحليل النتائج، كما تم تثبيت (Strain gauge Rosette) في منتصف مستوي القص لقياس الإزاحة العمودية والأفقية مع زيادة الحمل تدريجياً إلى حين حصول الفشل،ومن معرفة الإزاحة الأفقية يمكن معرفة حمل التشقق وقياس عرض التشقق خلال مستوي القص وذلك عند زيادة عرض التشقق عن مقدار انفعال الشد في الخرسانة.

الشكل (5). يوضح آلية تهيئة النماذج للفحص

6- النتائج :-

اشتملت نتائج البحث على قياس مقدار الإزاحة العمودية والانحراف بعد حصول التشقق في مستوي القص إضافة إلى مقدار الإزاحة الافقية مع عرض التشقق لكافة مراحل الحمل المسلط .

الاشكال (6-9) تمثل العلاقة بين (الحمل- الازاحة) لكافة حالات التسليح (بدون حديد قص ، بحلقة واحدة وحلقتين وثلاث حلقات) ولجميع مراحل التسخين (20,200,400,600°C) مع زيادة الاحمال .

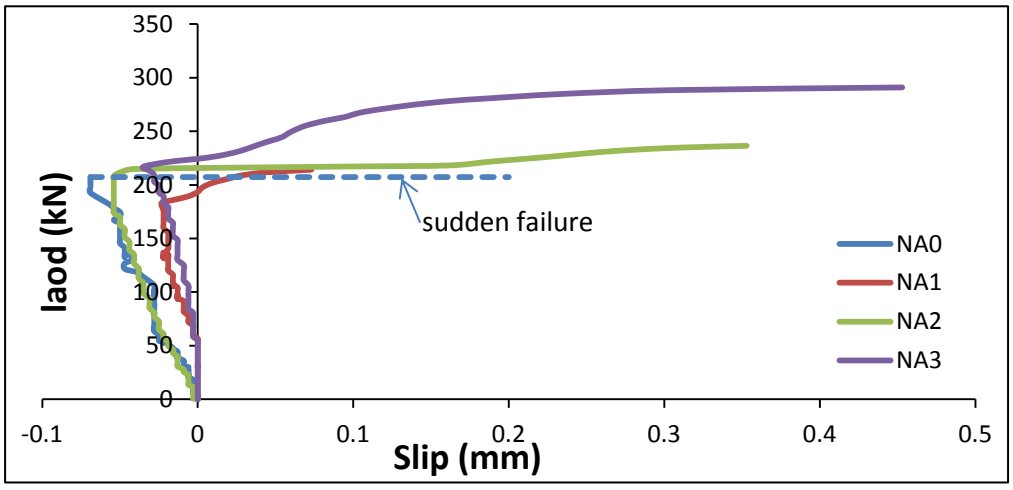

شكل (6) علاقة (الحمل _الازاحة) للخرسانة الاعتيادية لدرجة حرارة 20

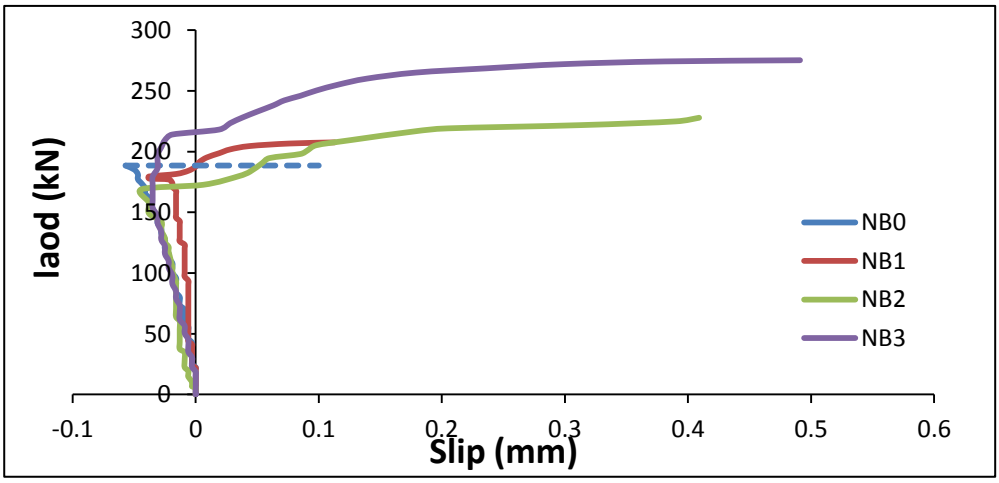

شكل (7) علاقة (الحمل _الازاحة) للخرسانة الاعتيادية لدرجة حرارة 200

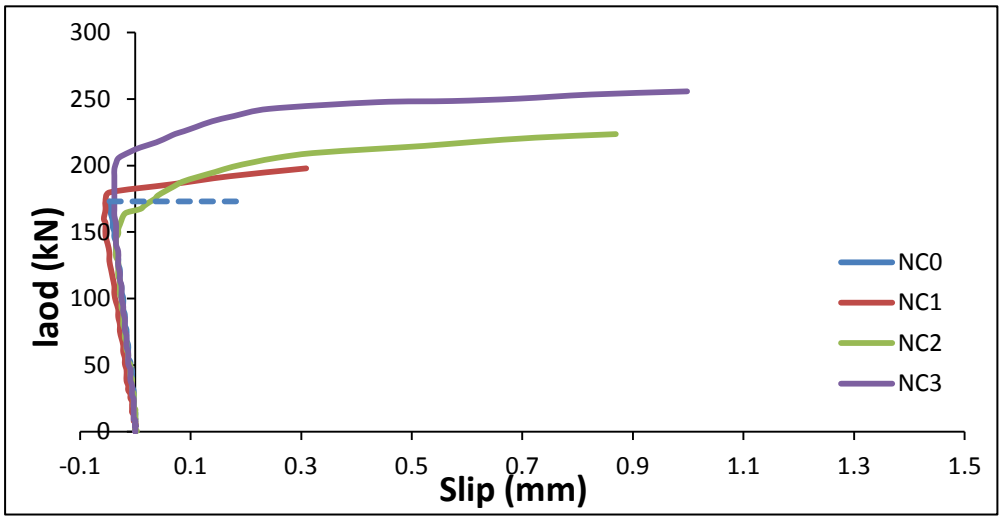

شكل (8) علاقة (الحمل - الازاحة) للخرسانة الاعتيادية لدرجة حرارة 400

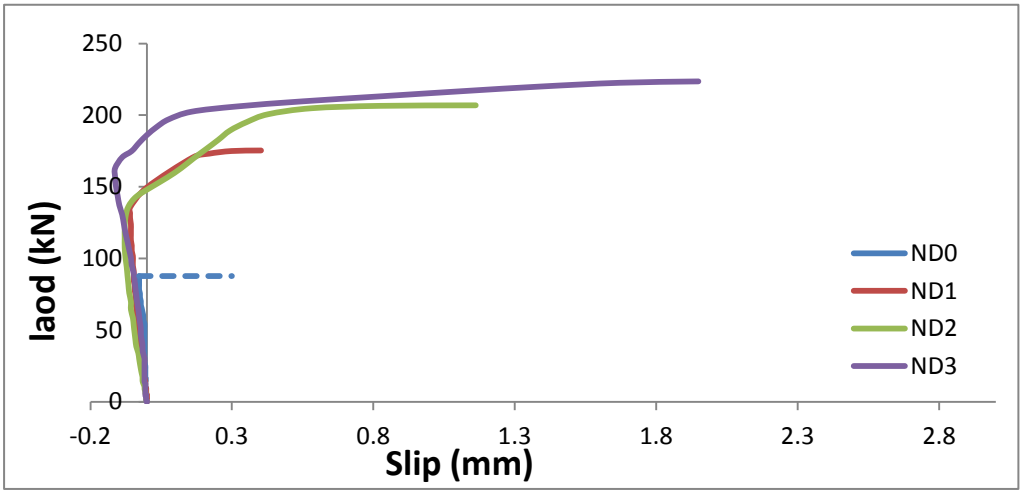

شكل (9) علاقة (الحمل - الازاحة) للخرسانة الاعتيادية لدرجة حرارة 600°C

الجدول (4) نتائج التغيير في اجهاد القص والزحف بتعيير درجة الحرارة اضافة لتغيير خصائص الخرسانة

رقم النموذج	درجة الحرارة (°C)	مقاومة انتقال القص (MPa) (f_v)	مقدار الانزلاق (mm)	fc' (MPa)	ft (MPa)	(f_v/f'_c) %
NA0	20	5.96	0.069	38.33	3.92	15.5
NB0	200	5.42	0.057	37.38	3.5	14.5
NC0	400	4.97	0.047	33.62	2.92	14.78
ND0	600	2.52	0.028	27.18	1.35	9.27
NA1	20	6.2	0.096	38.33	3.92	16.17
NB1	200	5.96	0.151	37.38	3.5	15.94
NC1	400	5.69	0.366	33.62	2.92	16.92
ND1	600	5.04	0.466	27.18	1.35	18.54
NA2	20	6.8	0.407	38.33	3.92	17.74
NB2	200	6.59	0.426	37.38	3.5	17.63
NC2	400	6.48	0.904	33.62	2.92	19.27
ND2	600	5.95	1.241	27.18	1.35	21.89
NA3	20	8.36	0.488	38.33	3.92	21.81
NB3	200	7.91	0.522	37.38	3.5	21.16
NC3	400	7.39	1.036	33.62	2.92	21.98
ND3	600	6.42	2.062	27.18	1.35	23.62

يتضح من الأشكال اعلاه أن هناك انفعال سالب (انضغاط) في المراحل الأولى (قبل التشقق) لتسليط الحمل إلى مرحلة حدوث الشق الاولي تبدأ بعدها مرحلة الانزلاق في مستوي القص إلى مرحلة حصول الفشل .
كما يلاحظ أن هناك فشل فجائي في النموذج الخالي من تسليح القص وانتقال الانفعال من المقدار السالب إلى مرحلة الفشل أما الحالات الاخرى (وجود تسليح القص) فيلاحظ أن الحمل الاقصى يزداد بازدياد نسبة حديد القص ويقل بازدياد درجات الحرارة . حيث أن هذه الزيادة تتمثل
الجدول (4) يوضح أن مقدار الانزلاق يتناقص بازدياد درجات الحرارة للنماذج غير المسلحة بحديد التسليح مما يشير إلى تحول الخرسانة إلى خرسانة قصيفه (Brittle) ، في الوقت الذي يزداد فيه مقدار ألإنزلاق بازدياد درجات الحرارة في النماذج المسلحة بحديد القص إضافة إلى ازديادها مع زيادة نسبة التسليح مما يشير إلى فعالية حديد التسليح في مقاومة تأثير درجات الحرارة.
ويلاحظ من الجدول (5) أهمية استخدام حديد تسليح القص في الخرسانة المعرضة لدرجات حرارة عالية، حيث أن الخرسانة غير المسلحة تفقد نسبة عالية من تحمل قوى القص عند تعرضها لدرجات حرارة عالية تمثلت (9.1, 16.6, 57.7 %) عند درجات الحرارة ($200,400,600C^0$) على التوالي. في الوقت الذي تتغير فيه هذه النسب بشكل واضح عندما تكون الخرسانة مسلحة. و الجدول (5) يوضح نسب التغيير نسبة الى مقاومة القص في النموذج غير المسلح عند درجة الحرارة $20C^0$.

الجدول (5) النسبة المئوية للزيادة والنقصان في قوى القص مع تغيير درجات الحرارة نسبة إلى درجة الحرارة 20°C وبدون تسليح *النموذج المرجعي

النموذج	درجات الحرارة			
	20	**200**	**400**	**600**
بدون تسليح* $\rho=0.0$	——	-9.1	-16.6	-57.7
التسليح بحلقة واحدة $\rho=0.289\%$	+4.0	0.00	-4.53	-15.4
التسليح بحلقتين $\rho=0.578\%$	+14.09	+10.57	+8.72	-0.16
التسليح بثلاث حلقات $\rho=0.867\%$	+40.27	+32.72	+24.0	+7.72

الشكل رقم (10) يبين العلاقة بين التغيير في مقدار مقاومة انتقال القص مع نسبة حديد تسليح القص لمختلف درجات الحرارة ، ويتضح أن دور حديد التسليح يكون أكبر عند درجات الحرارة الأعلى (600°C) مع وجود زيادة واضحة في درجات الحرارة الأخرى وهذا التغيير واضح ايضا" في الشكل رقم (11) ، وقد تم مقارنة نتائج تغيير مقاومة أنتقال القص مع تغيير درجات الحرارة لنماذج بدون تسليح وكانت القيم متقاربة الى حد ما [13].

تم اقتراح المعادلة التالية لإيجاد مقدار مقاومة القص عند درجات حرارة تتراوح بين 20-600C^{o} و لمقاومة انضغاط بين 27-38 MPa ونسبة تسليح القص بين 0.0-0.867%

$$f_v = -0.10-2.65*10^{-4*}T+3.167*\rho+0.144*f'c \qquad R^2=0.90$$

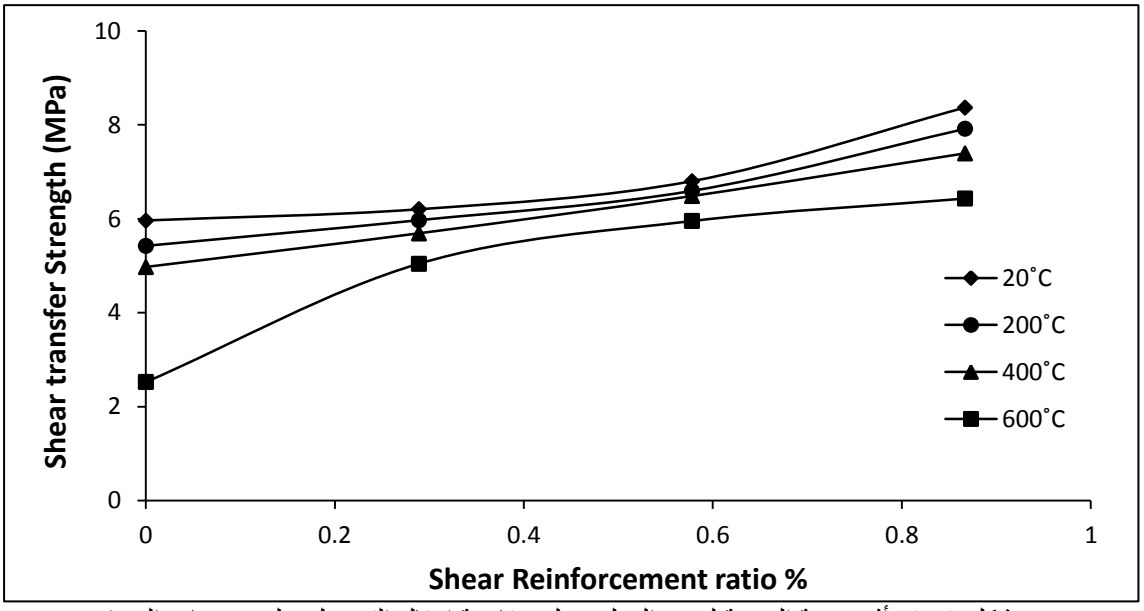

شكل (10) تأثير نسبة المئوية لحديد التسليح على مقاومة انتقال القص لمختلف درجات الحرارة

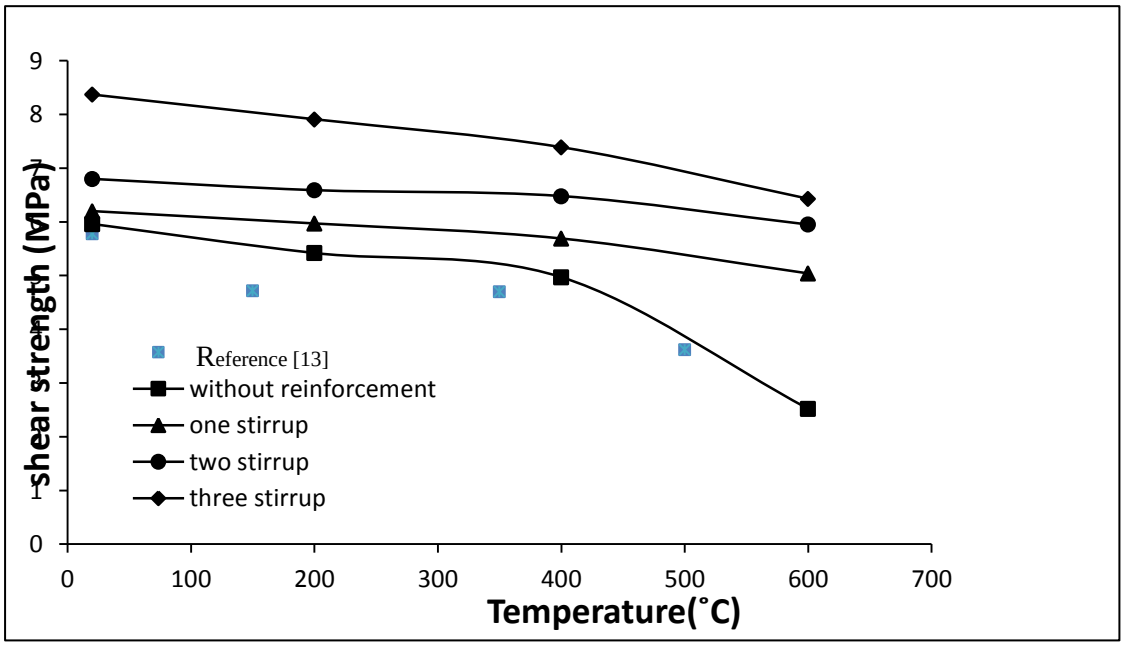

الشكل رقم (11) : مقاومة انتقال القص في الخرسانة الاعتيادية تحت تأثير درجات الحرارة كافة

كما يتضح وجود علاقة مباشرة بين مقدار اجهادات القص واجهادات الانضغاط لمختلف درجات الحرارة كما في الشكل رقم (12) حيث أن نسبة مقاومة القص تمثل حوالي (15%) من مقاومة الانضغاط عند درجات الحرارة

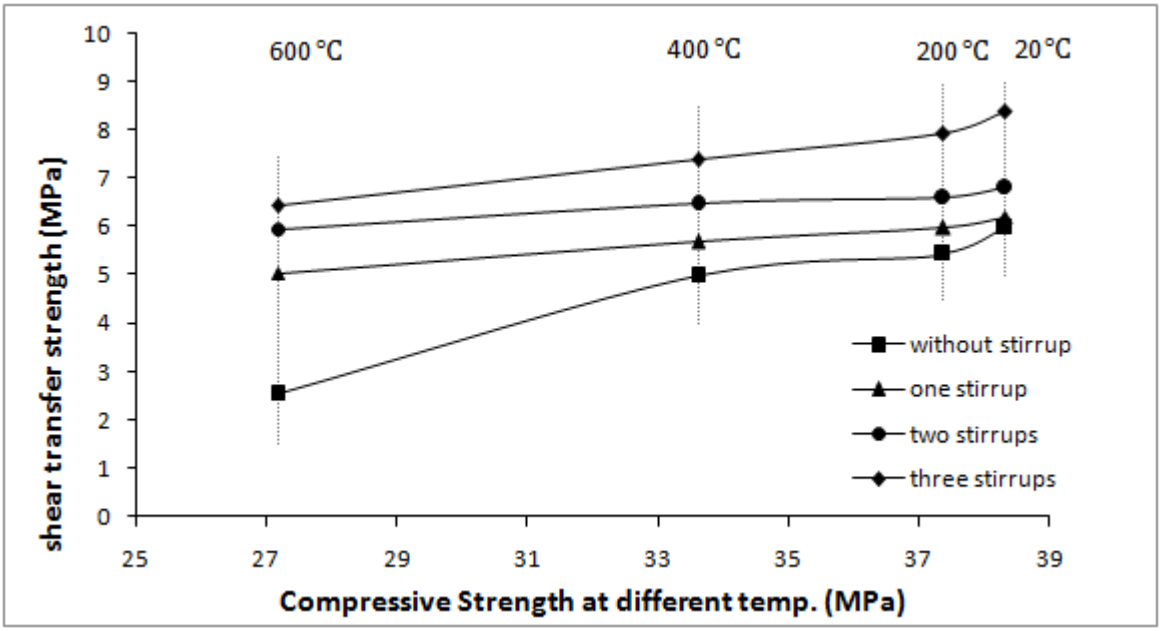

(20,200,400°C) وهذه النسبة تقل إلى حوالي (9.3%) في درجة الحرارة (600°C) في النماذج غير السلحة كما موضح في الجدول (4) ، و تزداد بزيادة حديد التسليح حيث أنها تتراوح بين (16%) إلى (23%) اعتمادا على عدد حلقات التسليح . يستنتج من ذلك أن حديد التسليح يساعد على زيادة مقاومة اجهادات القص في الخرسانة المسلحة .

الشكل (12) : علاقة (مقاومة انتقال القص - مقاومة الانضغاط) لمختلف درجات الحرارة

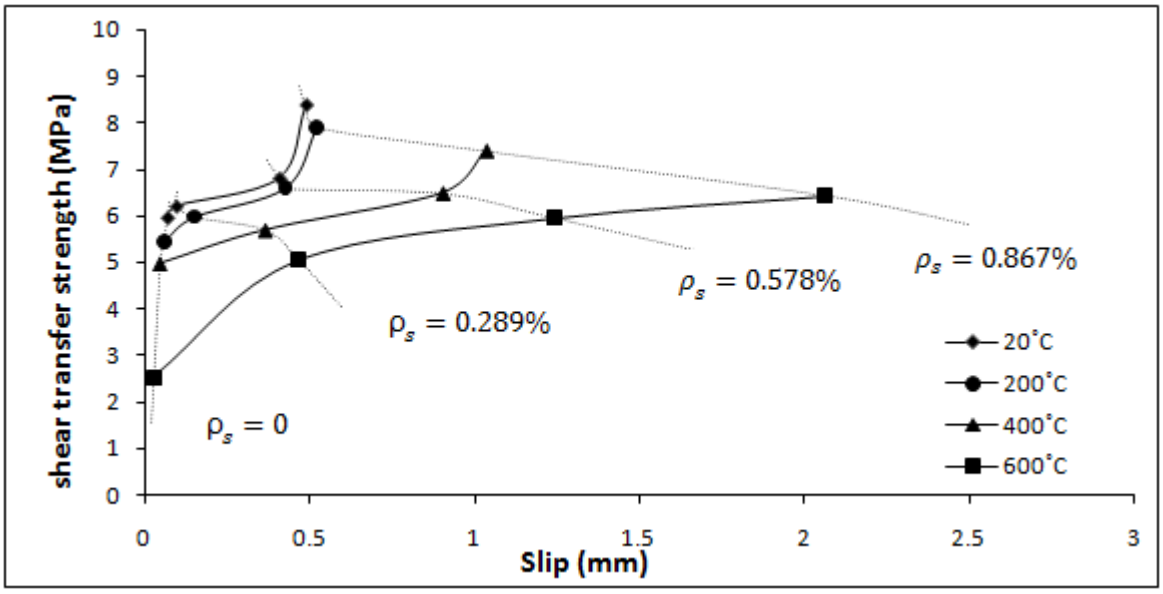

أما العلاقة بين مقدار الانزلاق ومقاومة القص بتأثير درجات الحرارة، فيتضح من الشكال (13,14) أن مقدار الانزلاق يعتمد بصورة مباشرة على مقدار درجة الحرارة ونوع التسليح المستعمل ففي حالة عدم وجود حديد التسليح (ρ=0.0) فإن مقدار الانزلاق يكون محدوداً جداً لكافة قيم اجهادات القص ويتراوح مقدار الانزلاق بين (0.069mm) إلى (0.028mm)

عند تغيير درجات الحرارة من (20˚C) إلى (600˚C) مع زيادة في مقاومة القص تمثل حوالي 4%. اما في حالة وجود حديد التسليح فإن هذه القيم تزداد بشكل واضح بازدياد درجات الحرارة ونسبة حديد التسليح نظراً لكون حديد التسليح يوفر للنموذج مرونة أكبر في تحمل درجات الحرارة ، وكان مقدار الانزلاق (0.096mm) عند درجة الحرارة (20˚C) ولحلقة واحدة من التسليح ليصل إلى (2.062mm) عند درجة الحرارة (600˚C) والتسليح بثلاث حلقات ترافقها زيادة في مقاومة القص بنسبة 7.71% كما موضح في الجدول (4).

الشكل (13): علاقة (مقاومة انتقال القص - الانزلاق) للخرسانة الاعتيادية بدرجات حرارة مختلفة

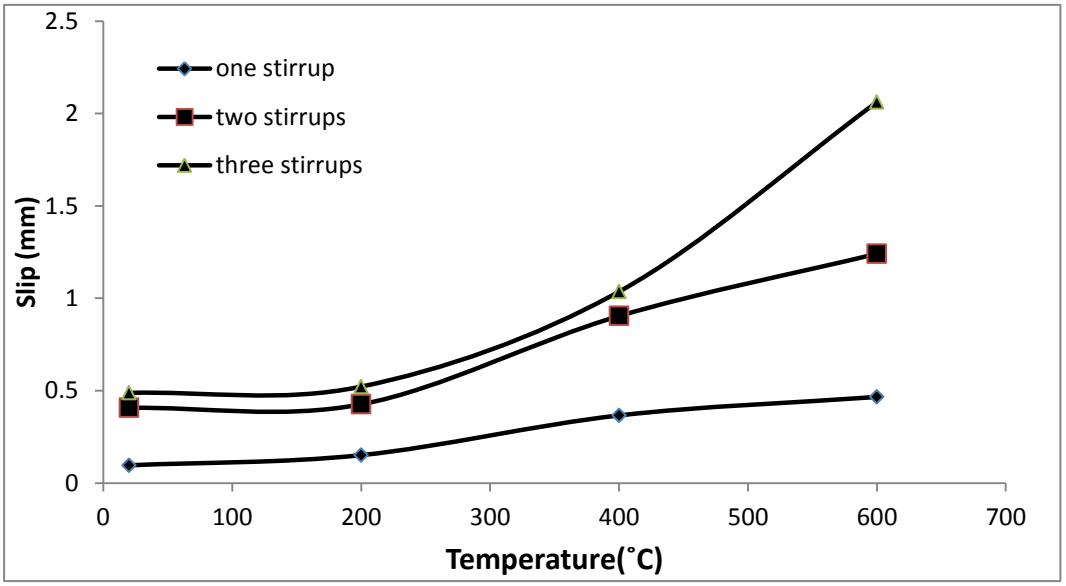

الشكل (14) تغيير مقدار أكبر أنزلاق مع تغيير درجات الحرارة المختلفة وتأثير نسبة التسليح

7- الاستنتاجات :-

إعتماداً على النتائج المتوفرة يمكن الوصول إلى الاستنتاجات التالية :-

1. أن خصائص الخرسانة ومن ضمنها مقاومة انتقال القص تتأثر بارتفاع درجات الحرارة وبشكل واضح ، حيث أن مقاومة انتقال القص تقل بأرتفاع درجات الحرارة ، وجد أن مقاومة القص للنماذج غير المسلحة تتراوح القيم بين (5.96-2.52 MPa) عند تغيير درجة الحرارة بين ˚C(600-20) ، وفي النماذج المسلحة بثلاث حلقات تسليح قص تراوحت هذه القيم بين (8.36-6.42 MPa) .
2. يساهم حديد التسليح في تقليل التدهور الحاصل في اجهادات القص نتيجة لتأثير درجات الحرارة ، حيث ان قيم مقاومة انتقال القص كانت (5.96, 6.2, 6.8, 8.36) عند تغيير نسبة حديد تسليح القص (ثلاث حلقات، حلقتان، حلقة واحدة، بدون تسليح القص) على التوالي في درجة حرارة 20°C وعند درجة حرارة 600°C تمثلت هذه القيم (2.52, 5.04, 5.95, 6.42) عند تغيير نسبة حديد تسليح القص ب(ثلاث حلقات، حلقتان، حلقة واحدة، بدون تسليح القص) على التوالي.
3. هناك علاقة مباشرة بين اجهادات القص ومقاومة الانضغاط للخرسانة. حيث ان نسبة اجهادات القص تزداد بازدياد نسبة حديد التسليح . تراوحت بين (15%) الى (9.3%) في النماذج غير المسلحة ، بينما تتراوح هذه القيم بين (16%) إلى (23%) في النماذج المسلحة بحديد قص من واحد الى ثلاث حلقات.
4. يتأثر مقدار الانزلاق عند مقاومة انتقال القص القصوى بشكل واضح بتغيير درجات الحرارة ونسبة حديد التسليح ففي الخرسانة غير المسلحة يكون الفشل بشكل مفاجئ ومقدار انزلاق قليل جداً ، أما في حالة وجود التسليح فيزداد مقدار الانزلاق بإزدياد نسبة التسليح وبأرتفاع درجات الحرارة وذلك لكون حديد التسليح أكثر مطاوعة من الخرسانة. حيث ان مقدار الانزلاق عند درجة الحرارة (20˚C) ولحلقة واحدة من التسليح كان بمقدار(0.096mm) ليصل إلى (2.062mm) عند درجة الحرارة (600˚C) والتسليح بثلاث حلقات.

8- المصادر :-

[1]Cheng, F., Kodur, V.K.R and Wang, T., " Stress-Strain Curves forHigh Strength Concrete at Elevated Temperatures ", Journal of Materialsin Civil Engineering, Vol.16,No.1, February, 2004, pp.84-90.

[2]يمان حذيفة النعمة ، " تأثير درجات الحرارة العالية على الخصائص الميكانيكية ومقاومة سحب الحديد من الخرسانة مقصودة الهواء " ،أطروحة ماجستير، وزارة التعليم العالي والبحث العلمي ، جامعة الموصل ،2012 .

[3]ACI 216R-89 " Guide for Determining the Fire ' Endurance of Concrete Elements" Reported by ACI Committee 216. USA. (Reapproved 1994)

[4] Mattock , A.H. and Hawkins, N.M. 1972. " Shear Transfer in Reinforced Concrete, Recent Research " PCI jour., Vol. 17 , No. 2, pp.55-75.

[5] Swamy, R.N., Jones, R. and Chiam, T. 1987. " Shear Transfer in Steel Fiber Reinforced Concrete ", ACI Special Publication, Detroit, SP-105,, Fiber Reinforced Concrete Properties and Applications, pp.565-592.

[6] Al-Obidi, L., " Direct Shear of High Strength Concrete with Fibers " , MSc Thesis , University of Technology , Baghdad , 1998 , 121 PP.

[7]حسن محمد أحمد حسن ، " تأثير التسخين المتناوب على الصفائح الخرسانية المسلحة السميكة " ،أطروحة ماجستير، وزارة التعليم العالي والبحث العلمي ، جامعة الموصل ،2002 .

[8] Vinayagam, Th., " Shear Transfer in High Strength Concrete " , PhD. Thesis , National University of Singapore, 2004, 218 PP.

[9] Peng, G., Yang, W., Zhao, J., Liu, Y., Bian, S. and Zhao, L., "Explosive Spalling and Residual Mechanical Properties of Fiber-Toughened " , Cement and Concrete Research , 2005 , pp.1-5.

[10] AL-Feel, J., R., "Experimental and Numerical Investigation of Shear Transfer with Direct Stress in Steel Fiber Reinforced Concrete", PhD.Thesis, University of Mosul, 2006.

[11] Husem , M. , "The Effect of High Temperature on compressive and Flexural strengths of Ordinary and High performance Concrete " , Fire Safety Journal , Vol. 41 , 2006 , pp. 155-163.

[12] رنا برهان عبدالرحمن الشهواني ، " تأثير دراسة الحرارة العالية على خواص الخرسانة المقصودة بالهواء والمسلحة بالألياف الفولاذية " ، أطروحة ماجستير ، وزارة التعليم العالي والبحث العلمي ، جامعة الموصل ،2007 .

[13] Al-Owaisy, S., R., " Effect of High Temperatures on Shear Transfer Strength of Concrete" , Journal of Engineering and Development, Vol. 11, No. 1, March (2007).

[14] Maha M.S. Ridha , Nagham T. Hamad, Kaiss F. Sarsam, " Predicting the Strength of Fiber Reinforced High Performance Concrete Based on Push-Off Tests ", Building and Construction Engineering Department, University of Technology / Baghdad, Eng. & Tech. Journal. Vol.30, No.7, 2012.

[15] BS 882 – 1992 , " Aggregate from Natural Source for Concrete " , British Standard Institution , 1992 .

[16] Neville, A. M. (2002), Properties of Concrete , 3rd Edition , Pitman Publishing Ltd ,

تأثير نسب المزج على مقاومة تآكل البري للخرسانة عالية المقاومة

علي حسين علي
أستاذ مساعد/ الكلية التقنية/الموصل

محمد حازم ياسين
طالب ماجستير/ الكلية التقنية/الموصل

الخلاصة

تم عمل خلطات تجريبية لدراسة تأثير نسب الخلط على مقاومة الانضغاط ومقاومة البري للخرسانة عالية المقاومة. اثنا عشر خلطة خرسانية تتضمن كالاتي: خلطة مرجعية (C1)، اربعة خلطات خرسانية (C2,C3,C4,C5) بإضافة كميات مختلفة من الملدنات الفائقة كنسب مئوية من وزن السمنت، اربعة خلطات خرسانية (C6,C7,C8,C9) بتقليل وتثبيت نسبة الماء الى السمنت مع استعمال السليكا فيوم واضافة كميات مختلفة من الملدنات الفائقة كنسب مئوية من وزن السمنت، وثلاث خلطات خرسانية(C10,C11,C12) بتثبيت نسبة الملدنات الفائقة واستعمال نسب ماء الى السمنت بكميات مختلفة. النتائج بينت ان الخلطة الخرسانية (C11) والتي تحتوي 1,5% من الملدنات الفائقة و 15% سليكافيوم ادت الى 90,3% زيادة بمقاومة الانضغاط وتحسين مقاومة تأكل البري بنسبة205,2% مقارنة مع الخلطة المرجعية ،كما لوحظ ان جميع نسب المزج للخلطات الخرسانية بإضافة الملدنات الفائقة والسلكافيوم ادت الى زيادة مقاومة الانضغاط ومقاومة تآكل البري.

Influence of Mix Proportions on the Abrasion Resistance of High Strength Concrete

Ali Hussain Ali
Assistant Professor
Technical College / Mosul

Mohammed Hazim Yasin
M.Sc. Student
Technical College / Mosul

Abstract

Trial laboratory batches were used to study the effect of mix proportions on the compressive strength and abrasion resistance of high strength concrete. A series of twelve different concrete mixtures including: normal concrete mixture (C1) as a reference mix, four concrete mixtures (C2, C3, C4, C5) prepared with different amounts of superplasticizers used as a percentage of cement content, four concrete mixtures (C6 , C7 , C8, C9) prepared by reducing and fixing (w/c) ratios and using silica fume and different amount of superplasticizers (as a percentage of cement content), and three concrete mixtures (C10, C11, C12) prepared by similar amount of super- plasticizers and using different (w/c) ratios. Results show that Mixture C11, prepared with (1.50%) addition of super plasticizers and (15%) addition of silica fume resulted in (90.3%) increase in the compressive strength and records a significant improvement in the abrasion resistance by (205.2%) as compared with the reference mix. All of the mix proportions, with super-plasticizers and silica fume additions leads to an increase in both compressive strength and abrasion resistance.

Keywords: Concrete Mix Proportions, Abrasion Resistance, Compressive Strength, Superplasticizers, Depth of Wear, High Strength Concrete (HSC).

1. Introduction:

1.1. Scope:

Abrasive wear is known to occur in pavements, floors, or other surfaces upon which friction forces are applied due to relative motion between the surfaces and moving objects. The resistance of concrete to abrasion is influenced by variables such as strength, aggregate properties, surface finish, and type of hardeners or toppings. It is well established that concrete abrasion resistance increases with increasing compressive strength**[1]**. The factors that affect concrete strength can also influence abrasion resistance.

In general, hardened cement paste possesses low resistance to abrasion. In order to develop concrete with high abrasion resistance, it is desirable to use hard surface material, aggregate, and paste having low porosity and high strength**[1,2,3]**.

The parameters such as cementitious materials content, water to cementitious materials ratio, air content, type of finish, and curing are known to affect the characteristics of the concrete surface layer including abrasion resistance. The abrasion resistance of concrete is of importance in various types of concrete construction. For example, in pavements, floors and hydraulic structures such as tunnels and dam spillways, the concrete should withstand destructive wearing forces, which may include abrasion and impact**[2]**. The abrasive wear of concrete is described with the change in mass decrement or the depth of the cavity in function of its material qualities (as compressive strength)**[3]**.

1.2. Literature Review:

Data on the abrasion resistance of concrete is needed to determine appropriate mixture proportions in order to manufacture abrasion resistant concrete, limited amount of published work is available on abrasion resistance of concrete.

Several investigators**[4,5]** have substantiated that compressive strength is the most important factor governing the abrasion resistance of concrete. Witte and Backstrom**[6]** reported that for equal strengths, abrasion resistance of air-entrained concrete is similar to that of non-air-entrained concrete. Abrasion resistance of concrete is mainly dependent upon abrasion resistance of its constituent materials, coarse aggregates and mortar**[7]**.

Researches used many types of surface finishing techniques and curing practices to have a strong influence on abrasion resistance of concrete**[6-13]**.

Nanni**[13]** indicated that, compressive strength is a poor parameter to evaluate abrasion because of the influence of surface finishing and curing conditions. In general, proper finishing and curing practices are one of considerable factor to enhance the abrasion resistance of concrete considerably.

1.3. Aim of the research:

In this investigation, the abrasion resistance of concrete incorporating with chemical and mineral admixture will be discussed.

2. Experimental investigation:

The experimental work of this investigation included ***two*** categories:

2.1. Manufacturing the apparatus:

The apparatus, which was used in measuring the abrasion resistance, was manufactured with all its accessories in accordance to the requirement of ASTM C 944**[14]** at the Technical College of Mosul. This apparatus consists of a series of dressing wheels mounted on a rod that is attached to a press drill. This press drill is used to apply a constant force on the surface of the specimen and to rotate a cutter at 200 revolution / minute; this test determines the abrasion resistance by measuring the amount of concrete abraded of a surface by a rotating cutter in a given period at time. Figure (2.1) shows the apparatus with its dressing wheels

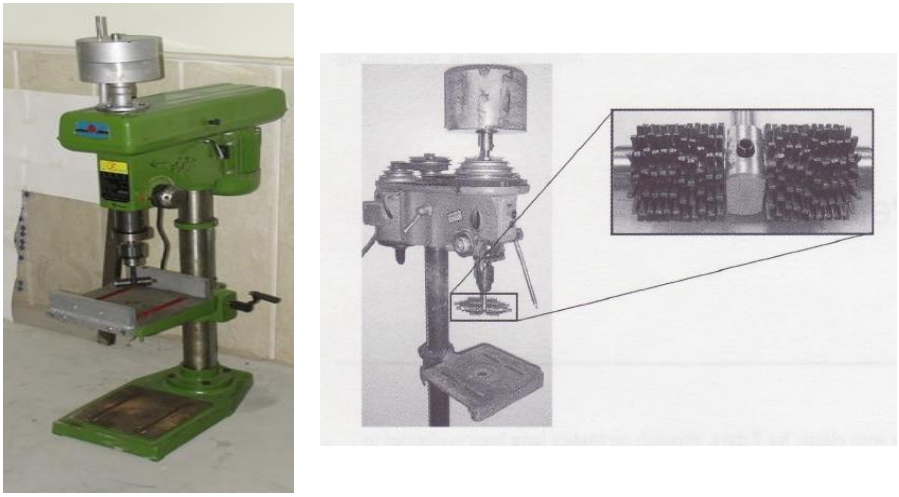

Fig. (2.1): Rotating-cutter press drill with dressing

*A set of dressing wheels replaced periodically (for each concrete mixture).

2.2. Practical Work:

This part of the investigation includes preparation of all the concrete mixes as well as the tests performed on the concrete specimens.

2.2.1. Materials:

2.2.1.1. Cement:

Sulfate–resistance cement obtained from Hammam-Al-Alil was used. Physical and chemical properties of the used cement were carried out in accordance to Iraqi specifications No.5/1984**[15]**, test results are given in Tables (2.1 and 2.2).

Table (2.1): Physical properties of Sulfate–resistance cement

Physical properties	Test results of Sulfate-resistance cement	Iraqi specifications No. 5/1984[15]
Specific surface area by Blain method, m^2/kg	280	≥ 230
Initial setting time (hrs : min)	1 : 30	≥ 45 minute
Final setting time (hrs: min)	3 : 18	≤ 10 hours
Compressive strength, MPa 3 days 7 days	 21 29	 ≥ 15 ≥ 23

Table (2.2): Chemical compositions of Sulfate–resistance cement

Chemical analysis Oxides and compounds	Test results of Sulfate-resistance cement (%)	Iraqi specifications No. 5/1984 (% by weight)[15]
MgO	1.9	≤ 5.0
SO_3	2.3	≤ 2.5
CaO	62.92	-
SiO_2	20.3	-
Fe_2O_3	5.4	-
Loss on Ignition	1.1	≤ 4.0
Insoluble Residue	0.85	≤ 1.5
C_3A	2.3	≤ 3.5
C_3S	58.9	-
C_2S	13.6	-

2.2.1.2. Coarse aggregate:

Coarse aggregate of maximum aggregate size of (10) mm., obtained from Mosul city was used. Its sieve analysis is shown in Table (2.3).

Table (2.3): Sieve analysis of the used coarse aggregate

Sieve size (mm)	Cumulative passing (%)	Iraqi specification No.45/1984[16]
14	100	100
10	94.6	85-100
5	4.8	0-25
2.36	0	0-5

2.2.1.3. Fine aggregate:

Fine aggregate (sand) obtained from Mosul city was used. Its sieve analysis is shown in Table (2.4).

Table (2.4): Sieve analysis of the used fine aggregate

Sieve size (mm)	Cumulative passing (%)	Limits of Iraqi specification No.45/1984[16]
4.75	98.4	90-100
2.36	94.6	85-100
1.18	92	75-100
0.60	66	60-79
0.30	40	12-40
0.15	10	0-10

Main properties of the used coarse and fine aggregates are shown in Table (2.5).

Table (2.5): Main properties of coarse and fine aggregates[16]

Property	Coarse aggregate	Fine aggregate
Dry sp. Gravity	2.63	2.59
S.S.D. sp. Gravity	2.64	2.65
App. sp. Gravity	2.66	2.79
Absorption capacity (%)	0.5	2.9
Rodded unit weight (kg/m^3)	1716	1765
Fineness modulus	6.55	2.61

2.2.1.4. Chemical admixtures:

Sika Visco Crete-5930, is a third generation of superplasticizers for concrete and mortar, was used. It meets the requirements for superplasticizers according to ASTM C 494 Types G and F**[17]**.

2.2.1.5. Water:

Tap water was used in preparing all concrete mixtures.

2.2.1.6. Silica fume:

Silica fume is specified under ASTM C1240. Physical and chemical properties of the used silica fumes are given in Table (2.6 and 2.7).

Table (2.6): Typical properties of silica fumes

Form	Powder
Colour	Grey
Bulk density	550 Kg/m3
Chloride content	< 0.1 %
Dosage	15 % by weight of cement.

Table (2.7): Chemical properties of silica fume.

Chemical composition	Percentages (by weight)
MgO	1.47
K_2O	0.9
CaO	0.5
SiO_2	90.7
Al_2O_3	0.68
Fe_2O_3	2.2
Na_2O	0.86
L.O.I.	2.5

2.2.2. Mix design of normal-strength concrete (NSC):

Mix proportions used in this investigation were obtained using three methods (ACI, British, and Road Note No. 4) methods **[18]**, as shown in Table (2.8).

Table (2.8): Mix proportions

Mix design method	Mix proportions	(A/C) Ratio
ACI	1 : 2.245 : 2.012 , w/c = 0.61	4.257
British	1 : 1.861 : 1.861 , w/c = 0.5	3.722
Road Note No. 4	1 : 1.957 : 2.419 , w/c = 0.45	4.376

Since all methods of concrete mix design shown in Table (2.8) give the same compressive strength 25 MPa, therefore, the mix proportions obtained by the (Road Note No.4) was chosen because it gives (A/C) ratio higher than the other two methods and this will be the best mix design method from economical as point of view.

2.2.3 Mix design of high-strength concrete (HSC):

Mix proportions were selected from a number of trial laboratory batches to obtain HSC as follows:

2.2.3.1. By fixing (w/c) ratio and using different amount of super plasticizers as a percentage of cement content, as shown in Table (2.9).

Table (2.9): Mix proportions for trial mixes

Mix Code	Mix Proportions	Cement content (kg)	Silica fume (kg)	Super-plasticizers (kg)	Fine aggregate (kg)	Coarse aggregate (kg)	(w/c) ratio	28-day Compressive strength (MPa)
C1	**1 : 1.957 : 2.419**	**420**	**0**	**0.00**	**822**	**1016**	**0.45**	**33.1**
C2	**1 : 1.957 : 2.419**	**420**	**0**	**1.05**	**822**	**1016**	**0.45**	**33.3**
C3	**1 : 1.957 : 2.419**	**420**	**0**	**2.10**	**822**	**1016**	**0.45**	**35**
C4	**1 : 1.957 : 2.419**	**420**	**0**	**3.15**	**822**	**1016**	**0.45**	**36.6**
C5	**1 : 1.957 : 2.419**	**420**	**0**	**4.20**	**822**	**1016**	**0.45**	**39.6**

2.2.3.2. By using silica fume and different amount of superplasticizers as a percentage of cement content as shown in Table (2.10).

Table (2.10): Mix proportions for trial mixes

Mix Code	Mix Proportions	Cement content (kg)	Silica fume (kg)	Super-plasticizers (kg)	Fine aggregate (kg)	Coarse aggregate (kg)	(w/c) ratio	28-day Compressive strength (MPa)
C6	1 : 1.957 : 2.419	357	63	5.25	822	1016	0.30	53.7
C7	1 : 1.957 : 2.419	357	63	6.30	822	1016	0.30	57.4
C8	1 : 1.957 : 2.419	357	63	7.35	822	1016	0.30	55.8
C9	1 : 1.957 : 2.419	357	63	8.40	822	1016	0.30	53.2

2.2.3.3. By fixing amount of superplasticizers and using different (w/c) ratios as shown in Table (2.11).

Table (2.11): Mix proportions for trial mixes

Mix Code	Mix Proportions	Cement content (kg)	Silica fume (kg)	Super-plasticizers (kg)	Fine aggregate (kg)	Coarse aggregate (kg)	(w/c) ratio	28-day Compressive strength (MPa)
C10	1 : 1.957 : 2.419	357	63	6.3	822	1016	0.40	52.6
C11	1 : 1.957 : 2.419	357	63	6.3	822	1016	0.29	62.9
C12	1 : 1.957 : 2.419	357	63	6.3	822	1016	0.27	49.9

2.2.4. Preparation and casting of specimens:

All batches of concrete were cast in the laboratory using a drum mixer. Mixing, casting, and curing was conformed to ASTM C192**[19]**. Each batch was used to cast 6 (100*100*100) mm cubes, and 6(150*75)mm cylinders. to perform both the compressive strength and abrasion resistance tests. The mixing procedures were performed according to the following sequences:

(a) The fine and coarse aggregates were placed in the mixer, and mixed for two minutes.

(b) The cement was added to the mixed aggregate, and mixed for another two minutes also.

(c) Two-third of the mixing water was mixed with half the quantity of the superplasticizers and added to the mixer, for another two minutes.

(d) The rest quantity of water and superplasticizers were added to the mixer and the mixing continue till there are no dry balls of cement and the mixture have a slump of (120 - 180mm)**[20]**.

(e) Molds were oiled and placed on the vibration table while the concrete was poured. The cylinder specimens were cast in three layers and each layers compacted by the vibrator until no further air bubbles appeared on its surface, while the cubes specimens were casted in two layers and compacted as the same manner.

(f) After completing the compaction operation, the top of the specimen was smooth finished by a trowel.

(g) The specimens were demolded after (24 ± 2) hrs, and subjected to the standard moist curing by immersing them in the curing tank water at (23^{o}C) till testing time at 28 days.

2.2.5. Specimens tests:

2.2.5.1. Compressive strength test:

The cube specimens were taken out from the curing tank, and the compressive strength of the specimens was determined in accordance with BS 1881: Part 116 : 2003**[21]**.

2.2.5.2. Abrasion resistance test:

The cylindrical specimens were taken out from the curing tank, and the abrasion resistance of concrete was measured in compliance with ASTM C 944.

Readings were taken every two minutes for 12 minutes or 1.0 mm. depth wear, whichever occurred first.

The testing procedure of the abrasion resistance was carried out as follows:

(a) Determine the mass of the specimen to the nearest 0.1 gram.

(b) Fasten the specimen securely in the abrasion device by put piece of wood around the specimen to restrict the specimen and then fasten the piece of wood by bolt, so that the bottom face of the concrete cylinder is placed upwards and normal to the press drill shaft.

(c) Mount the special rotating cutter device (dressing wheels) in the press drill shaft.

(d) Start the motor and lower the rotating cutter shaft slowly until just in contact with the surface of the concrete cylinder.

(e) Continue abrasion operation with applying a normal load of (10 kg) on the surface of the specimen for two minutes after contact between the press drill cutter and the surface. At the end of each two-minute abrasion period, remove the test specimen from the device and clean surfaces with compressed air. Determine the specimen mass after test to the nearest 0.1 gram.

(f) The depth of wear shall be checked up with the average thickness loss of specimen obtained by the following equation:

$$t = \frac{(W_1 - W_2)\, V_1}{W_1 \times A}$$

where:

t = loss in thickness, mm.,

W_1 = initial mass of the specimen, gm,

W_2 = final mass of the abraded specimen, gm,

V_1 = initial volume of the specimen, mm^3,*

A = surface area of the specimen, mm^2.

*****All of the dimensions of specimens measured by digital vernea.

3. Results and Discussions:

Results of the existing investigation were tabulated in Table (3.1), and illustrated in Figures (3.1 to 3.7).

Table (3.1): Test results of compressive strength and abrasion resistance

Mixture Code	Type of Concrete	28-day Compressive strength (MPa)	Percentage increase in compressive strength (%)	Depth of abrasion (t) (mm)	Abraded materials (gm)	Percentage increase in abrasion resistance (%)
C1 (Reference)	_	33.06	_	0.355	14.80	_
C2	NSC	33.34	0.85	0.311	13.38	10.61
C3	NSC	34.97	5.78	0.305	13.12	12.80
C4	NSC	36.61	10.74	0.299	12.85	15.17
C5	NSC	39.62	19.84	0.264	11.35	30.39
C6	HSC	53.66	62.32	0.178	7.65	93.46
C7	HSC	57.36	73.50	0.142	6.12	141.83
C8	HSC	55.76	68.67	0.168	7.23	104.70
C9	HSC	53.23	61.01	0.181	7.80	89.74
C10	HSC	52.64	59.21	0.195	8.40	72.72
C11	HSC	62.91	90.29	0.113	4.85	205.15
C12	HSC	49.90	50.92	0.210	9.00	64.44

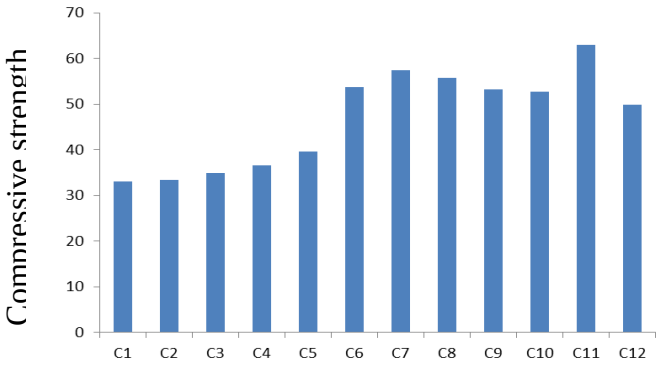

Fig. (3.1): 28-day compressive strength results

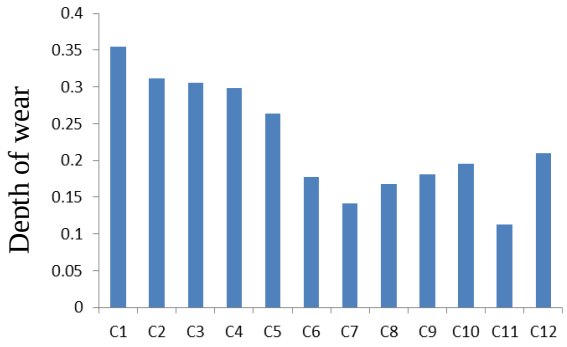

Fig. (3.2): Depth of wear results results

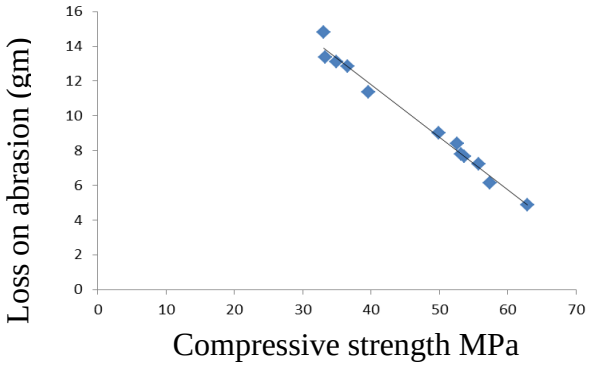

Fig. (3.3): Effect of compressive strength on abrasion resistance of concrete

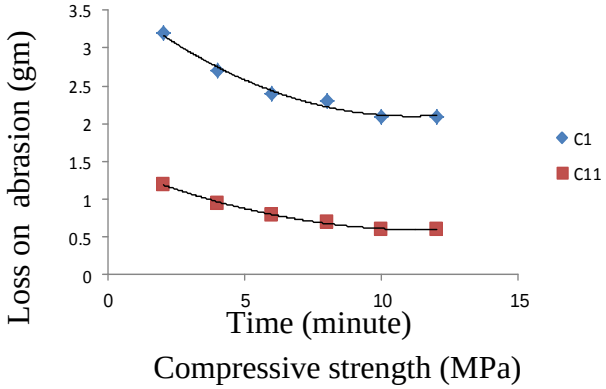

Fig. (3.4): Loss on abrasion versus time for Mixtures C1 and C11

Fig.(3.5): Cylinder specimens before abrasion test.

Fig.(3.6): Cylinder specimens after abrasion test.

The following parameters may be discussed, as follows:

3.1. Effect of mix proportions on the compressive strength of concrete:

It was clear from Table (3.1) and Figure (3.1) that, the maximum compressive strength value was 62.91 MPa (90.3% increase), is recorded for Mixture C11 (HSC) with (1.5%) super plasticizers and (15%)silica fume, whilst the minimum compressive strength value is 33.34 MPa (0.85% increase), which is obtained with the (0.25%) super plasticizers in Mixture C2 (NSC).

3.2. Effect of mix proportions on the abrasion resistance of concrete:

It is clear from Table (3.1) that, the addition of (0.25%) of superplasticizers leads to an increasing in the abrasion resistance by (10.61%) for Mixture C2 (NSC), while the increasing in the abrasion resistance is (205.15%) with the addition of (1.5%) superplasticizers and (15%) of silica fume for Mixture C11 (HSC).

On the other hand, figures (3.2 and 3.3) show that the compressive strength is an important factor affecting the abrasion resistance of concrete mixture. Loss on abrasion decreased linearly as compressive strength increased.

Figure (3.4) show that, the loss on abrasion of concrete mixtures decreased with time.

However, all mixtures with and without admixture exhibited high resistance to abrasion under the actions of applied abrasive forces (i.e., much less than 1.0 mm. depth of wear).

4. Conclusions:

The data collected in this investigation led to the following conclusions:

1. Compressive strength increases for all dosage of chemical and mineral admixture than normal concrete. The high early age strength achieved with the addition of micro-silica may be attributed to its finer particle size, resulting in an increased hydration rate. This is due to confinement provided by admixture bonding characteristics of concrete increases and improving the interfacial zone, reducing the potential stress concentration between the aggregate and the cement paste. Such an increase achieved by reducing the water-to-cement ratio.
2. The compressive strength for NSC and HSC mixtures at 28 days vary according to admixture. The highest compressive strength is achieved by mixture C11 followed by mixtures C7 and C8 for both seven and 28 days.
3. The28-day compressive strengths for mixture C12 are considerably lower than the compressive strength for mixture C11,where the w/c ratio for mixtures C12, and C11 are (0.27, and 0.29) respectively, we expect that, reducing in w/c ratio with high percentage in super plasticizers may cause in complete in hydration.
4. All mixtures exhibited substantially higher rates of abrasion resistance gain as compared with the reference mixture C1.
5. All mixtures with and without admixture show a high abrasion resistance .
6. Concrete abrasion resistance was proportional to compressive strength, i.e, abrasion resistance increase with the increasing in the compressive strength.
7. The effect admixtures on hardened concrete properties were significant.

Recommendation for future work:

In this study sulfate resistance cement (Type V) was used, the effect of other types of Portland cement with other additives may be also studied.

References:

1.T.R.Naik;S.S.Singh; and B.W. Ramme, "*Effect of source of Fly Ash on abrasion resistance of concrete*", Journal of Materials in Civil Engineering, Sep.-Oct.pp.0899-1561(2002).

2.Şemsi Yazici, and G.İ. Sezer, "*Abrasion resistance estimation of high strength concrete*", Journal of Engineering Sciences, Vol.13, pp.1-6, (2007).

3.ACI Committee 201 Report, "*Guide to durable concrete*", ACI Manual of Concrete Practice, ACI 201.2R-01, American Concrete Institute, (2000).

4.Mehta, P.K., and Monteiro, P.J.M., "*Concrete Structure, Properties and Materials*", Prentice-Hall Inc., Englewood Cliff, New Jersey, Second Edition, 548 pages, (1993).
5.Hadchti, K. M. and Carrasquillo, R.L., "*Abrasion resistance and scaling resistance of concrete containing Fly Ash*", Center for Transportation Research, Bureau of Engineering Research, University of Texas at Austin, Research Report: 481-3, August 1988, 185 pages.
6.Witte, L. P. and Backstrom, J. E., "*Some properties affecting the abrasion resistance of Air-entrained concrete*", ASTM Proceedings, Vol. 51, pp.1141-1155, (1951).
7.Ytterburg, R.F., "*Wear-resistant industrial floors of Portland cement concrete*", Civil Engineering – ASCE, Vol. 41, No. 1, pp. 68-71, (1971).
8.Nanni, A."*Curing of Roller Compacted Concrete and Strength Development*", Journal of Transportation Engineering, ASCE, Vol. 114, No. 6, pp.684-694, (1988).
9.Fentress, B, "*Slab construction practice compared by wear tests*", ACI Journal, Proceedings Vol. 70, No.7, pp. 486-491, (1973).
10.Kettle, R., and Sadegzadah, M., "*The influence of construction procedures on abrasion resistance*", ACI Special Publication No. SP-100, American Concrete Institute, Detroit, pp.1385-1410, (1987).
11.Senbetta, E., and Malchow, G., "*Studies on Control of Durability of Concrete Through Proper Curing*", Proceedings of the Katharine and Bryant Mather Intl. Conference on Concrete Durability, ACI Special Publication No. SP-100, American Concrete Institute, Detroit, Vol. 1, pp.73-87, (1987).
12.Sadeyzadeh, M., Page, C.L., and Kettle, R.J., "*Surface microstructure and abrasion resistance of concrete*", Cement and Concrete Research, Vol. 17, No. 4, pp.581-590, (1987).
13.Nanni, A."*Abrasion Resistance of Roller Compacted Concrete*", ACI Materials Journal, Vol. 86, No. 5, pp.559-565, November – December 1989.
14.ASTM C 944/C 944M– 99 (Reapproved 2005), "*Standard Test Method for Abrasion Resistance of Concrete or Mortar Surfaces by the Rotating-Cutter Method*", The American Society for Testing and Materials, Philadelphia, (2004).
15.Iraqi specification No.5/1984, "*Standard specifications for Portland cement*".
16.Iraqi specification No.45/1984, "*Aggregates from natural sources for concrete*".
17.ASTM C494/C494 M, "*Standard Specifications for Chemical Admixtures for Concrete*", The American Society for Testing and Materials, Philadelphia, (2004).
18.A.M. Neville, and J.J. Brooks "*Concrete Technology*", Second Edition, (2010).
19.ASTM C192/C192 M, "*Standard Practices for Making and Curing Concrete Test Specimens in the Laboratory*", The American Society for Testing and Materials, Philadelphia, (2004).
20.ASTM C143/C143M–08,"Standard Test Method for Slump of Hydraulic-Cement Concrete", The American Society for Testing and Materials, Philadelphia, (2008).
21.BS 1881 : Part 116, "*Method for determination of compressive strength of concrete*", (2003).

Reduce the Permeability of Concrete Used In Marine Structures and Tunnels

Ahmed A. Jubair **Aseel M. Mohammed**
Lecturer – College of Engineering
Anbar University

Abstract:

This research aims to find a solution to the problem of seepage occurring in oil interchange facilities and tunnels. Recently, real instances of the problem occurred at Al-Anbar province of Iraq. The impact of this phenomenon seriously erodes the concrete and thus reduces the life span of affected structures.

The presented work investigates the effect adding the admixture plastocrete-N to concrete as a partial replacement of cement weight in order to reduce seepage and improve the strength of concrete. Plastocrete-N was added by (0.25, 0.5, 0.75,and 1) % of cement weight. Five mixes were selected, four of them contained plastocrete-N and one reference concrete sample was left without any admixtures for the ages 7, 14 and 28 days. Compressive strength, flexural strength and porosity as an empirical indicator of permeability were tested. The test results indicated that the use of plastocrete-N led to significant increase in concrete strength and decrease in porosity with the increase of plastocrete-N. For example at 28 days, the compressive strength of reference concrete (A) was 44.96 MPa, while the compressive strength of (B,C,D,E) samples containing (0.25 , 0.5,0.75 and 1)% plastocrete-N were (48.22 , 51.02 ,52.41 and 56.45) MPa respectively. The modulus of rapture of reference concrete (A) was 5.8 MPa, while the modulus of rapture of the (B,C,D,E) samples which contained (0.25 , 0.5,0.75, 1)% plastocrete-N were (6.44,7.38,8 and 8.37) MPa respectively. The porosity of reference concrete (A) was 6.92% ,while that of the (B,C,D,E) samples which contained (0.25 , 0.5,0.75 and 1)% plastocrete-N were (2.101 , 2 , 0.862 , 0.182) % respectively.

Keywords:Compressive strength , Flexural strength , Permeability , Porosity.

تقليل نفاذية الخرسانة المستعملة في المنشآت البحرية وألأنفاق

أحمد جبير أسيل محمد
كلية الهندسة / جامعة ألأنبار

الخلاصة :

يهدف البحث الى ايجاد حل لمشكلة التسرب الحاصل في مجسر ونفق الزيوت في محافظة الانبار والذي هو قيد الانشاء وهذه الظاهرة تؤدي الى اضعاف الخرسانة وتقليول العمر الافتراضي للمنشا حيث تمت دراسة تأثير اضافة المضاف (بلاستوكريت – ن) على الخرسانة كجزء من وزن الاسمنت وقد اضيف المضاف (بلاستوكريت – ن) بنسب (0,25 ، 0,5 ، 0,75 ، 1)% من وزن الاسمنت . تم استخدام خمس خلطات اربعة منها تحتوي على المضاف (بلاستوكريت – ن) وواحدة خلطة مرجعية بدون اي مضاف لأعمار (7 ، 14، 28) يوم . تم اجراء فحوصات مقاومة الانضغاط ، مقاومة الانثناء وفحص المسامية كمقياس غير مباشر للنفاذية . نتائج الفحص بينت بان استخدام مضاف (بلاستوكريت – ن) يؤدي الى زيادة في مقاومة الخرسانة وتناقص في مساميتها مع ازدياد نسبة المضاف (بلاستوكريت – ن) المستخدمة ، على سبيل المثال بعمر 28 يوم كانت مقاومة الانضغاط للخرسانة المرجعية (A) 44,96 ميكا باسكال بينما كانت مقاومة الانضغاط للخلطات (B,C,D,E) الحاوية على المضاف(بلاستوكريت – ن) بنسب (0,25 ، 0,5 ، 0,75 ، 1) % (48,22 ، 51,02 ، 52,41 ، 56,45) ميكا باسكال على التوالي و كانت مقاومة الانثناء للخرسانة المرجعية (A) 5,8 ميكا باسكال بينما كانت مقاومة الانثناء للخلطات (B,C,D,E) الحاوية على المضاف(بلاستوكريت – ن) بنسب (0,25 ، 0,5 ، 0,75 ، 1) % (6,44 ، 7,38 ، 7,8 ، 8,37) ميكا باسكال على التوالي . و كانت مسامية الخرسانة المرجعية (A) 6,92% بينما كانت مسامية الخلطات (B,C,D,E) الحاوية على المضاف(بلاستوكريت – ن) بنسب (0,25 ، 0,5 ، 0,75 ، 1) % (2,101 ، 2، 0,862 ، 0,182) %على التوالي .

الكلمات المفتاحية : مقاومة الانضغاط ، مقاومة الانثناء ، النفاذية ، المسامية .

1- Introduction:

Concrete can be a highly durable construction material as long as care and quality control are enforced at all stages of the design, production and construction processes. However, experience has demonstrated that its potential long-term durability is not always achieved, leading to early failure of reinforced concrete structures. [1] It should be recognized that concrete is intrinsically a porous material, despite the improvements on its formulation and quality control to the best possible extent, it is not possible to prevent completely the ingress of potentially harmful agents into it. Micro-cracks and macro-pores will always exist on the concrete surface, providing a path for the transportation of aggressive ions into the interior of concrete [2]. It is now accepted that the durability of the reinforced concrete depends mainly on the composition and properties of the concrete surface layer [3] This layer, sometimes with a thickness close to the cover of the reinforcement, is most of the times the only responsible for the corrosion protection of the reinforcement. Surface treatments act as a barrier between the environment and the concrete. They prevent or retard the entry of harmful substances such as water, chlorides, etc.[4] Permeability is an important property for durability of concrete. Improper mix proportioning may lead to permeable concrete that tends to deteriorate in marine environment. This is due to the fact that the hydration products of Portland cement becomes unstable in certain aggressive salt ion component present in sea water. [5] Pedro M. Moreira1, José B. Aguiar2, Aires Camões3 [6] evaluate the influence of cement; two types of cement were used: Portland Type I 42.5R and Type IV/A (V) 32.5R. Crushed granite with a density of 2566 kg/m3, water absorption of 2.1% and a maximum size of 9.53 mm was used as a coarse aggregate, while crushed sand with a density of 2477 kg/m3 and water absorption of 1.36 % was used as a fine aggregate in the preparation of concrete specimens.

Concrete coatings were selected to represent the following three generic types:

i. Silicone varnish (S);

ii. Acrylic coatings (A);

iii. Epoxy resin coatings (E).

Cylinder concrete specimens 110 mm in diameter and 230 mm in eight (ø110 x 230) were cast to evaluate the absorption by capillarity of the selected concrete coatings. Cubic concrete specimens 100x100x100 mm3 were cast to evaluate the absorption by immersion of the selected concrete coatings. Disk concrete specimens 50 mm in diameter and 40 mm in thickness (Ø50 x 40) were cast to evaluate the permeability to oxygen, the permeability to water and the porosity of the selected concrete coatings.

The concrete specimens were proportioned for an effective water-to-cementations materials ratio of 0.60 and a cement content of 320 kg/m^3.

Figure (1) show that the use of the selected coatings decreases the permeability to water, specially the epoxy and acrylic resins.

Product B of epoxy resins proved to be impermeable to the penetration of

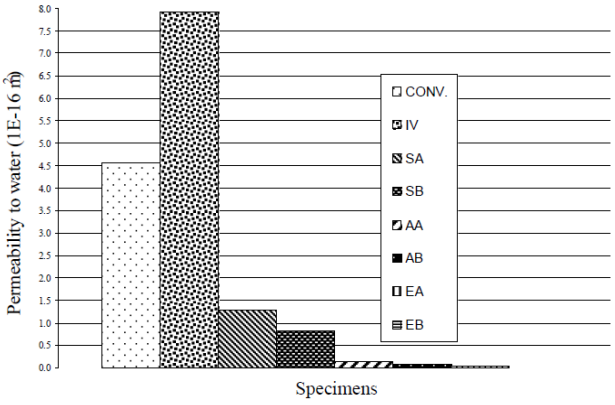

Figure (1) Water permeability in the coated and uncoated specimens

water. Product A had a very good performance reducing the permeability to water in 99.5% to the uncoated specimens with conventional cement and 99.7% to the uncoated specimens with Type IV cement. In the test were used pressures of 5.5 to 5.8 bar in product B and 5.3 to 5.6 bar in product A.

The acrylic resins had the best performance next to the epoxy resins reducing, in the case of product B, the permeability in 98.5% to the uncoated specimens with conventional cement and 99.2% to the uncoated specimens with Type IV cement. In the test were used pressures of 5.2 to 5.98 bar in product B and 4.6 to 5.4 bar in product A.
The varnishes of silicone had the worst results reducing (for product B) the permeability in 81.9% to the uncoated specimens with conventional cement and 89.5% to the uncoated specimens with Type IV cement, which indicates that this material is still effective protecting the concrete from water.
The uncoated specimens with Type IV cement had a permeability 42.4% bigger than the uncoated specimens with conventional cement, due to its bigger porosity, despite having the same cement content, the same water-to-cementitious materials ratio and addictions.
Md. Moinul Islam, Md.Saiful Islam, Bipul Chandra Mondal and Mohammad Rafiqul Islam [7] investigate the performance of slag concrete exposed to artificially made seawater. Concrete specimens of 100 mm cubical size were cast and cured for 30 days in water before the exposure to different seawater environments. Physical aspects regarding the deterioration of OPC and slag concrete of cement slag mix ratio 85:15, 70:30 and 55:45 have been studied in plain water and seawater of salt concentration 1N, 3N and 5N over the periods of 1, 3, 6 and 12 months. The specimens were taken out periodically and subjected to compressive strength and ultrasonic pulse velocity tests. From the investigation, it has been revealed that slag concrete of cement slag mix ratio 70:30 has better resistance against strength deterioration for all curing conditions and curing ages. It is primarily due to high fineness of slag, which after hydration markedly reduce the permeability of concrete that restrict the penetration of sea salt. Slag concrete of mix ratio 70:30 with water cementations ratio 0.4 and 30 days pre-curing is found to be the most effective in resisting the adverse effect of sea water.

According to S.A. Barbhuiya, J.K. Gbagbo, M.I. Russell, P.A.M. Basheer [8] Figs. 2 and 3 show the air permeability and the sorptivity indices of the different mixes. From Fig. 2, it can be seen that the air permeability of concrete containing hydrated lime and silica fume decreased at 30% fly ash content and remained the same at 50% fly ash content when compared to the fly ash concretes without the additions. The addition of hydrated lime and silica fume also improved the sorptivity of fly ash concretes at both the replacement levels (Fig. 3). As highlighted for the compressive strength, these improvements are considered to be due to: (i) the early hydration of fly ash particles when the hydrated lime was added and (ii) the high pozzolanic reactivity and pore filling effects of the silica fume. For concrete containing 20% fly ash, with the addition of hydrated lime a decrease in porosity was observed by Mira et al.[9] . The authors attributed this to the acceleration of pozzolanic activity in presence of hydrated lime. An additional explanation for the improved transport properties in lime-activated fly ash systems is the formation of flocs inside the matrix due to lime hydration. These flocs reduce the effective voids and, hence, the interconnectivity of the pores, leading to a denser microstructure.

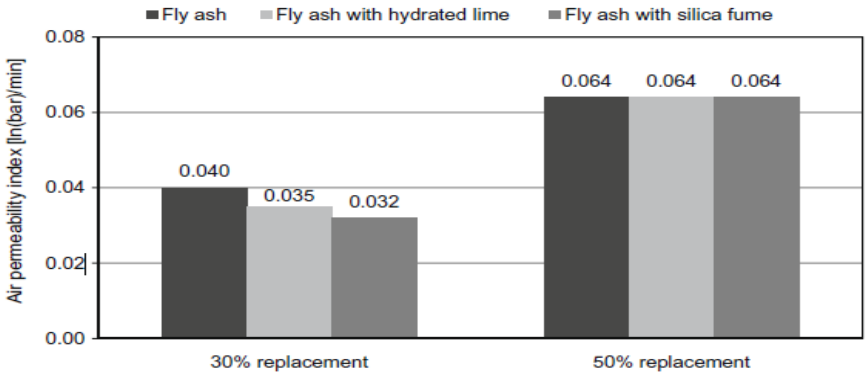

Figure (2) Air permeability of Concrete

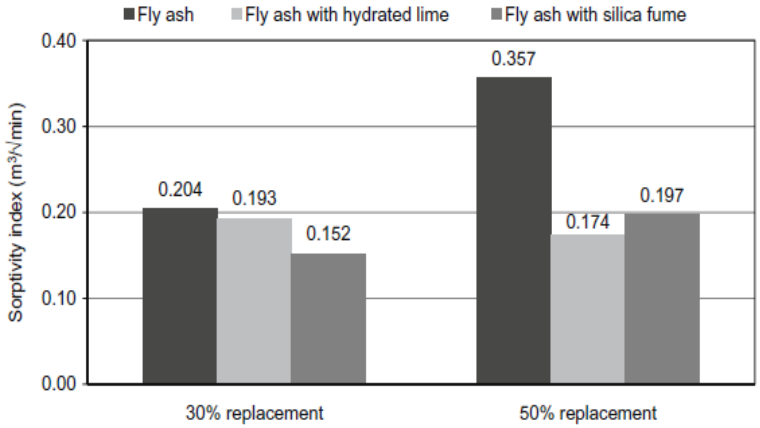

Figure (3) Sorptivity of Concrete

2- Experimental Work :

2-1 Materials :

2-1-1 Cement :

Sulfate resistance Portland cement produced by Al-Rajhi cement plant was used throughout this work . The physical and chemical test results of the used cement are given in Table (1) and Table (2) . It conforms to Iraqi specification No.5/1984 [10].

Table (1): Physical properties of cement.

Physical properties	**Test result**	**Limits of Iraqi spec. No.5/1984**
Specific surface area Blaine Method , m^2/kg	365	≥ 230 m^2/kg
Setting time, Vicats method: Initial setting (min.) Final setting hrs : min.	 130 3:45	 $\geq$ 45 min. $\leq$ 10 hours
Soundness	0.3%	$\leq$ 0.8%
Compressive strength of mortar, N/mm^2: 3 – day 7 – day	 18 26	 ≥ 15 N/mm^2 ≥ 23 N/mm^2

Table (2): chemical properties of cement

Chemical components	Percent(%)	Limits of Iraqi spec. No. 5 /1984
CaO	62	-
SiO_2	22	-
Al_2O_3	4.5	-
Fe_2O_3	5.12	-
MgO	2.33	$\leq 5\%$
SO_3	2.22	$\leq 2.5\%$
Loss of ignition	0.81	$\leq 4\ \%$
Insoluble residual	1.07	$\leq 1.5\%$
Lime saturation factor	0.83	0.66-1.02
C_3S	42.84	-
C_2S	30.36	-
C_3A	2.56	$\leq 3.5\%$
C_4AF	15.41	-

2-1-2 Fine Aggregate :

Sand of 4.75mm maximum size was used in this investigation. The specific gravity, absorption and sulfate content were (2.65 , 0.67 % , 0.15%) respectively . The grading of fine aggregate is given in Table (3).It conforms to limits of Iraqi specification No.45/1984 [11].

Table (3) : The grading of fine aggregate

Sieve size (mm)	A cumulative passing (%)	Limits of Iraqi spec. No.5/1984 for zone (3)
4.75	100	90-100
2.36	91.6	85-100
1.18	80.1	75-100
0.6	70.8	60-100
0.3	24	12-40
0.15	7.6	0-10

2-1-3 Coarse Aggregate:

The washed coarse aggregate used was 10 mm maximum size. The sieve analysis of this aggregate is given in table (4). It conforms to Iraqi specification No.45/1984 [11]. The specific gravity, absorption and sulfate content were (2.68, 1.07% and 0.07%) respectively.

Table (4) : The grading of coarse aggregate

Sieve size (mm)	A cumulative passing (%)	Limits of Iraqi spec. No.5/1984
12.5	100	100
9.5	99	85-100
4.75	15	10-30
2.36	3	0-10
1.18	0	0-5

2-1-4 Mixing Water:
Potable water was used for mixing and curing purposes.

2-1-5 Plastocrete – N :
Added liquid plasticizer highly efficient agent to reduce the permeability of concrete conformity with the American specifications ASTM C 494 – 81 type A .
Color : Broun liquid .
Density : 1.09 Kg/L.

3- Types of Specimens:
Steel molds were used throughout this work . The control specimens used in all tests were as follow:

1- For compressive strength and porosity cubes of (100*100*100) mm were used.
2- For flexural strength, prisms of (100*100*500) mm were used.

4 -Concrete mixture:
The details of the mixes used through this study are given in Table (5).

T able (5) : Details of the experimental program

Mix. Designation	Cement content Kg/m^3	Sand Content Kg/m^3	Gravel Content Kg/m^3	W/C ratio%	Plastocrete – N (%)
A	**420**	**818**	**985**	**0.45**	**0**
B	**420**	**818**	**982**	**0.38**	**0.25**
C	**420**	**818**	**980**	**0.35**	**0.5**
D	**420**	**818**	**980**	**0.3**	**0.75**
E	**420**	**818**	**980**	**0.28**	**1**

5- Mixing of Concrete:
A mechanical mixer of (0.1) m^3 capacity was used to mix concrete to obtain the required homogeneity. The interior surface of the mixer was cleaned and moistened before place the materials.
First the cement, coarse and fine aggregate were mixed. Then water with admixture (Plastocrete-N) were added and the ingredients mixed and the mixing was continued for suitable time (until the concrete becomes homogenous and consistency).

6- Casting, Compaction and Curing:
The molds were coated with mineral oil before use, according to ASTM C 192-88 [12], concrete casting was carried out in different layer each layer of 50 mm. Each layer was compacted by using a vibrating table for (15-30) second until no air bubbles emerged from the surface of the concrete and the concrete is leveled smoothly to the top of molds. After that the specimens marked and immersed in water until the age of test. The specimens were tested at age of 7, 14 and 28 days.

7- Testing of Hardened Concrete:

7-1 Compressive Strength:

The compressive strength was determined according to B.S.1881.part 4, 1970 [13]. The average of compressive strength of three cubes was recorded for each testing age (7, 14 and 28) days.

7-2 Flexural Strength :

The flexural strength was determined according to ASTM C 192-88 (14). The average of flexural strength of two prisms was recorded for each testing age (7, 14 and 28) days. The ultimate flexural strength (modulus of rupture) was calculated using the following equation:

$$Fr = P*L / b*d^2 \quad (1)$$

Where :
Fr : Modulus of rupture(MPa).
P : Maximum applied load (N).
L : Span length (mm).
b : Average width of specimen (mm).
d : Average depth of specimen (mm).

7-3 Porosity :

The vacuum equipment shown in fig (4) used in this test where the specimens placed in oven with temperature (105-110)c for 24 hrs and they were weighted after draying .After that they were placed in vacuum equipment with water for 24 hrs and the saturated and immersed weight were measured . Porosity was calculated from this equation :

Fig. (4) : Vacuum equipment

$$\text{Porosity } \% = (w_{saturated} - w_{dry} / w_{saturated} - w_{immersed})*100 \quad (2)$$

Where :
$w_{saturated}$:saturated weight w_{dry}: dry weight $w_{immersed}$: immersed weight
This method was taken as indirect measure to test permeability because the permeability test is not available.

8- Results and Discussion :

8-1 Compressive Strength:

Table (6) shows the results of compressive strength test of this study . Fig. (4) shows the relationship between compressive strength and age . From this figure it can be seen that the compressive strength increase with time. The compressive strength of specimens increases with increasing of the percentage of Plastocrete – N . From the results, it can be noted that the increasing of compressive strength of (B,C,D,E) comparing with A at 28 days are equal to (6.76,11.87,14.21,20.35)% for (B,C,D,E) respectively . From this figure it can be noticed

that, adding of Plastocrete – N to concrete with these percentages leads to improve the compressive strength of concrete . This may be due to the effect of the Plastocrete – N to reduce w/c ratio due to lesser-entrapped air voids and delay the unstable development of micro cracking , as well as limitation the propagation of these micro-crack .

Table (6) : Average compressive strength results

Mix. Design	**Cement content Kg/m^3**	Plastocrete – N **(%)**	**Compressive Strength (MPa) at 7 days**	**Compressive Strength (MPa) at 14 days**	**Compressive Strength (MPa) at 28 days**
A	**420**	**0**	23.22	38.98	44.96
B	**420**	**0.25**	28.33	41.6	48.22
C	**420**	**0.5**	38.24	44.56	51.02
D	**420**	**0.75**	40.22	44.73	52.41
E	**420**	**1**	40.6	46.27	56.45

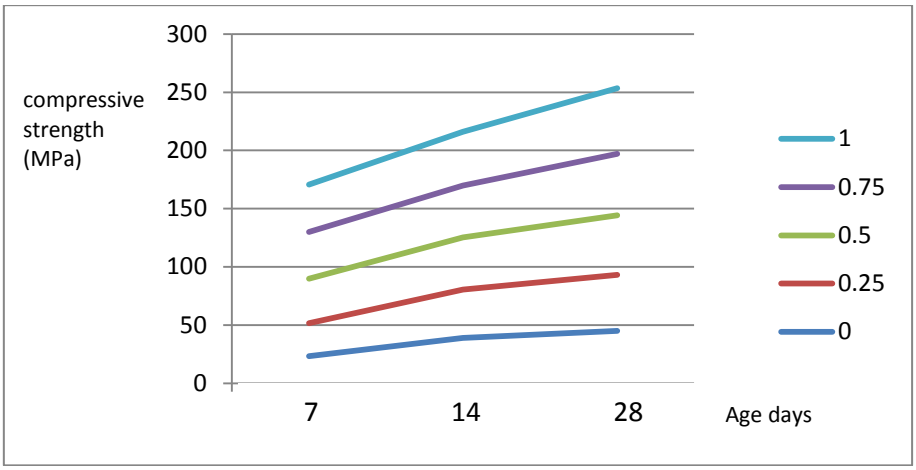

Fig. (4) : Relationship between compressive strength and age .

8-2 Flexural strength:

Table (7) shows the results of flexural strength test of this study . Fig. (5) shows the relationship between flexural strength and age . From this figure it can be seen that the flexural strength increase with time. The flexural strength of specimens increases with increasing of the percentage of Plastocrete – N . From the results, it can be noted that the increasing of flexural strength of (B,C,D,E) comparing with A at 28 days are equal to (9.93,21.41,27.5,30.7)% for (B,C,D,E) respectively . It is appearing that adding of Plastocrete – N with these percentages lead to good improve in flexural strength of concrete and and this increasing relatively with an increasing in Plastocrete – N percentages . These increasing in flexural strength might be due to the bridging the cracks , the development of bonding property of Plastocrete – N on the surface of concrete and the interface with other material which lead to an increase in the tensile strength of concrete and hence its flexural strength.

Table (7) : Average flexural strength results

Mix. Design	Cement content Kg/m^3	Plastocrete – N (%)	Flexural Strength (MPa) at 7 days	Flexural Strength (MPa) at 14 days	Flexural Strength (MPa) at 28 days
A	**420**	**0**	4.53	5.2	5.8
B	**420**	**0.25**	5.9	6.77	6.44
C	**420**	**0.5**	6.91	7.14	7.38
D	**420**	**0.75**	7	7.35	8
E	**420**	**1**	7.22	7.69	8.37

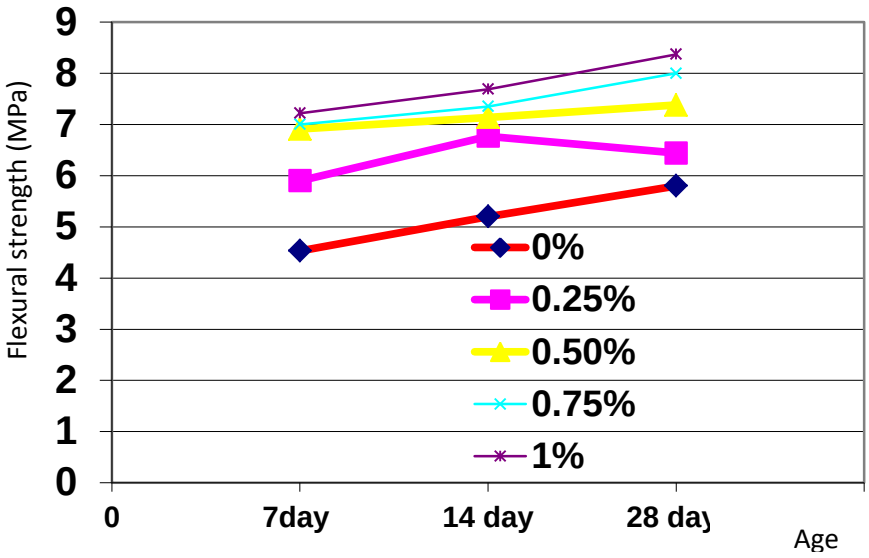

Fig. (5) : Relationship between flexural strength and age .

8-3 Porosity:

Table (8) shows the results of porosity test of this study . Fig. (6) shows the relationship between porosity and Plastocrete – N percentages. From this figure it can be seen that the porosity decreased with Plastocrete – N percentage. The porosity of specimens decreases with increasing of the percentage of Plastocrete – N. From the results, it can be noted that the decreasing of porosity of (B,C,D,E) comparing
with A at 28 days are equal to (69.63,71.1,87.54,97.36)% for (B,C,D,E) respectively. This decreasing in porosity refers to fill the voids in concrete mixtures with admixture used (Plastocrete – N) and this leads to increase in compressive and flexural strength.

Table (8) : Porosity results

Plastocrete – N percentage%	Porosity%
0	**6.92**
0.25	**2.101**
0.5	**2**
0.75	**0.862**
1	**0.182**

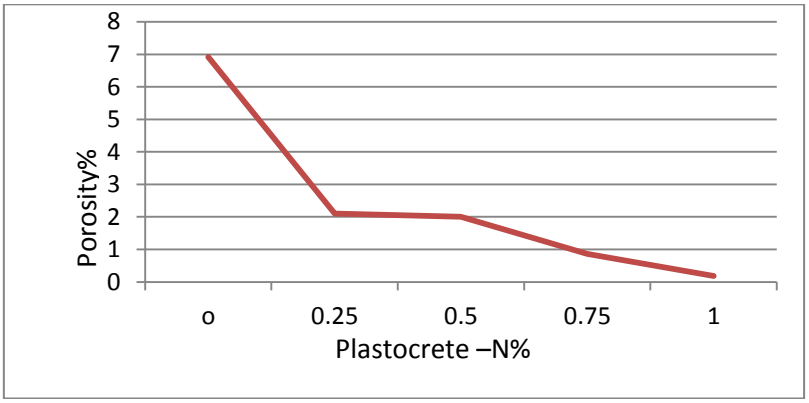

Fig. (6) : Relationship between porosity and Plastocrete –N%.

9- Conclusions:

Depending on the results of this investigation , the following conclusions can be drown:

1- The compressive strength of all specimens increases with time .
2- The compressive strength of all specimens increases with the percentage of Plastocrete – N.
3- The flexural strength of all specimens increases with time .
4- The flexural strength of all specimens increases with the percentage of Plastocrete – N.
5- The porosity decreases with increasing the percentage of Plastocrete – N.

10 – References :

1- Rodrigues, M. P. M. C., Costa, M. R. N., Mendes, A. M. and Marques, M. I. E., "Effectiveness of surface coatings to protect reinforced concrete in marine environments", *Materials and Structures*, Vol. 33, December (2000).

2- Swamy, R. N., Suryavanshi, A. K. and Tanikawa, S.," Protective ability of an acrylic-based surface coating system against chloride and carbonation penetration into concrete", *ACI Materials Journal*, March-April, (1998).

3- Kreijger, P. C.," The skin of concrete. Composition and properties", *Materials and. Structures* 17**,** (1984).

4- Pfeifer, D.W., Scali, M.J.," Concrete Sealers for Protection of Bridge Structures", *Department of Transportation*, NCHRP 244, Washington D.C., (1981).

5- Sujjavanich, S., Sida, V., and Suwanvitaya, P., Chloride Permeability and Corrosion Risk of High-Volume Fly Ash Concrete with Mid-Range Water Reducer, ACI Materials Journal, V.102, No.3, May-June, 2005.

6- Pedro M. Moreira1, José B. Aguiar2, Aires Camões3, **Systems for superficial protection of concretes,** *University of Minho, Department of Civil Engineering Azurém, Guimarães, Portugal.*

7- Md. Moinul Islam, Md.Saiful Islam, Bipul Chandra Mondal and Mohammad Rafiqul Islam, Strength behavior of concrete using slag with cement in sea water environment ,

Department of Civil Engineering, Chittagong University of Engineering and Technology, Chittagong-4349, Bangladesh Received 27 June 2010 .
8- Mira P, Papadakis VG, Tsimas S. Effect of lime putty addition on structural and durability properties of concrete. Cem Concr Res 2002.
9- Pandian NS, Balasubramonian S. Permeability and consolidation behavior of fly ashes. J Test Eval 1999.
10- . 1999، بغداد ، المواصفات العراقية / 5 " الاسمنت البورتلاندي " الجهاز المركزي للتقييس والسيطرة النوعية
11-)المواصفة القياسية العراقية رقم (45) لسنة 1984 (ركام المصادر الطبيعية المستخدم في الخرسانة والبناء
12- - ASTM C 192-88 " Standard Practice for Making and Curing Test Specimens in the Laboratory" , Annual book of ASTM Standard , Philadelphia,Vol.04-02 , 1989.
13- - British Standard Institution " Methods of Making and Curing Concrete Test Specimens" , B.S.1881 , part 3 , 1970 , London.
14- ASTM "Standard Test Method for Flexural Strength of Concrete (Using Simple Beam with Third – Point Loading)", Annual Book of ASTM Standards , American Society for Testing and Materials . Vol.04.02 1994.

تأثير الميتاكاؤلين على بعض خواص الخرسانة خفيفة الوزن المتعرضة لتاثير الكبريتات الخارجي

الدكتورة شيلان محمود حمه البرزنجي / مدرس
كلية الهندسة/جامعة الانبار drsheelan@yahoo.com

الخلاصة

الهدف الاساسي من هذه الدراسة هو البحث في تاثير الكبريتات الخارجي على مقاومة الخرسانة خفيفة الوزن وامكانية تحسين مقاومتها لتاثير الكبريتات باستخدام مواد بوزلانية. اجريت الفحوصات على الخلطات الاتية: 1. خرسانة خفيفة الوزن معالجة في ظروف عادية (خلطة مرجعية) 2. خرسانة خفيفة الوزن معرضة لتاثير الكبريتات الخارجي 3. خرسانة خفيفة الوزن مضاف اليها ميتاكاؤلين (خلطة مرجعية) 4. خرسانة خفيفة الوزن مضاف اليها ميتاكاؤلين معرضة لتاثير الكبريتات الخارجي. وقد تم دراسة الخصائص التالية: الكثافة، مقاومة الانضغاط ومعايير الكسر (مقاومة الانثناء) وبمقارنة مع الخلطة المرجعية فان الخرسانة خفيفة الوزن المعرضة للتاثير الكبريتات الخارجي ابدت نقصانا بالكثافة يتراوح من 0.44% الى 23.04% - للأعمار من 7 الى 120 يوم بعد تعرضها لتاثير الكبريتات . اما النماذج الحاوية على الميتاكاؤلين ابدت نقصانا بالكثافة يتراوح من 0.32% - الى 20.52% – للأعمار من 7 الى 120 يوم بعد تعرضها لتاثير الكبريتات . اما التغير في مقاومة الانضغاط للخرسانة خفيفة الوزن مقارنة بالمرجعية فكانت من 1.59% الى 35.40% – للأعمار من7الى 120 يوم بعد تعرضها لتاثير الكبريتات ، اما للحاوية على الميتاكاؤلين كانت: من 2.44% الى 12.18% –للأعمار 7 الى 120 يوم بعد تعرضها لتاثير الكبريتات . اما التغير في معايير الكسر للخرسانة خفيفة الوزن مقارنة بالمرجعية تراوح من 8.70% - الى 48.63% - للأعمار7 الى 120 يوم بعد تعرضها لتاثير الكبريتات ، اما الحاوية على الميتاكاؤلين كانت: 2.22% الى 35.71% – للأعمار7 الى 120 يوم بعد تعرضها لتاثير الكبريتات .

الكلمات الدالة: بورسلينايت، خرسانة خفيفة الوزن، ميتاكاؤلين و تاثير الكبريتات.

The effect of metakaolin on some properties of lite weight concrete affected by external sulfate

Sheelan Al-Barazangi
College of Engineering / Anbar University

Abstract

The goal of this work is to investigate the effect of sulfate effect on some properties of lightweight concrete and the chance to improve sulfate resistance of lightweight concrete using pozalanic material like metakaolin. Tests were made on these mixes: 1. Lightweight concrete curing in tap water (as reference mix) 2. Lightweight concrete subjected to sulfate effect 3. Lightweight concrete contain metakaolin curing in tap water (as reference mix) and 4. Lightweight concrete contain metakaolin subjected to sulfate effect. Density, compressive strength and modulus of rupture (flexural strength) are studied. With comparison to reference mix the decrease in density of the lightweight concrete subjected to sulfate effect are: -0.44% to -23.04% after 7 to 120 day from subjected to sulfate effect. While the decrease in density of the one contain metakaolin subjected to sulfate effect are: -0.32% to -20.52% after 7 to 120 day from subjected to sulfate effect. The change in compressive strength of the lightweight concrete subjected to sulfate effect are as compared to reference one are: 1.59% to 35.40% after 7 to 120 day from subjected to sulfate effect. While the change in compressive strength of the one contain metakaolin are: -2.44% to -12.18%. And the change in modulus of rupture of the lightweight concrete subjected to sulfate effect are as compared to reference one are: -8.7% to 34.62% and -48.63% after 7 to 120 day. While the change in modulus of

rupture of the one contain metakaolin are: - 2.22% to – 35.70% after 7 to 120 day from subjected to sulfate effect.

المقدمة

التآكل هو التفتت الناتج عن تفاعل مادتين أو أكثر أو مكوناتهما في وجود وسط مساعد كالحرارة والرطوبة والأملاح ، كما أنه إفساد للمادة أو خواصها نتيجة تفاعلها مع المؤثرات الخارجية أو الداخلية بحيث يفقد المنشأ مواصفاته التصميمية والغرض من استخدامه .إن الخسائر الاقتصادية الكبيرة التي يسببها تآكل الخرسانة، قد جعلت منها المشكلة الكبرى للبنية التحتية في الدول الصناعية، وخلال العقود الثلاثة الماضية بلغت هذه المشكلة نسبًا مقلقة، أدت إلى تكاليف إصلاح عاليةٍ سواء إن كان في الخرسانة أو في حديد التسليح الذي يتآكل نتيجة التفاعلات الكيميائيةً بسبب نفاذية الخرسانةً، وهذه التكاليف تجاوزت تكاليف الإنشاء الأولية، تفاديًا لانهيار المنشآت في حالات خاصة [1,2,3]. عندما تصمم وتنفذ المنشآت الخرسانية بشكلٍ صحيح، يجب ان تكون جودة الخرسانة، والغطاء الخرساني لحديد التسليح كافية لتحقيق الديمومة المطلوبة، لكن بعيدًا عن أخطاء التصميم الإنشائية فإنه يمكن أن تحدث خلال التنفيذ بعض النواقص أو مواضع الخلل التي يمكن أن يكون لها عواقب على الديمومة، مثل نفاذية عالية للخرسانة نتيجة الإنضاج غير الصحيح علاوة على ذلك فإن الخرسانة يمكن أن تتعرض لظروف عدوانية جدًا، منها على سبيل المثال :الاستعمال المتكرر لأملاح إذابة الجليد، والتعرض لماء البحر أو للأوساط الحامضية أو الكبريتية... الخ. [2,3] تعد مشكلة مهاجمة أملاح الكبريتات للخرسانة من المشاكل الإنشائية الكبيرة التي أثارت اهتمام الباحثين والمهندسين خلال القرن الماضي ولا تزال تثير الاهتمام نفسه في الوقت الحاضر وخاصة بعد إن ظهر تأثير تلك المشكلة على الكثير من المنشآت المهمة حول العالم [4] . وبصورة عامة فان هناك مصدرين أساسيين للأملاح الكبريتية التي تهاجم الخرسانة وهما الأملاح الموجودة في المياه الجوفية والسطحية او في التربة المحيطة بالخرسانة وهذا ما يعرف بالأملاح الخارجية .والأملاح الموجودة ضمن المواد الداخلة في إنتاج الخرسانة كالرمل والحصى والسمنت والماء والمضافات وهذا ما يعرف بالأملاح الداخلية [3]. أما محليا فتبدو هذه المشكلة واضحة من خلال مظاهر التآكل المتفاقم في كثير من المنشآت والمباني سواء في خرسانة الصب الموقعي أو الوحدات الخرسانية الجاهزة الصب ويرجع السبب في ذلك الى ارتفاع نسبة الأملاح الكبريتية في الرمال العراقية والمياه الجوفية . فقد أشار السامرائي [5] إلى إن تفتت الخرسانة بتأثير الأملاح يعتبر من أهم المشاكل التي تواجه المهندس في العراق والى ان الأملاح توجد في تربة العراق ومياهه الجوفية وهي منتشرة سطحا وعمقا وخصوصا في المنطقة الوسطى. بين الربيعي [6] في دراسته لمقاومة الخرسانة عالية الأداء المعرضة لتاثير الكبريتات الداخلية والخارجية والتي تم فيها إضافة الجبس الطبيعي كإحلال جزئي من وزن الرمل وبنسب تراوحت بين (0.5 - 2.5)% إن اتاثير الضار للكبريتات الداخلية يظهر في الأعمار المبكرة ابتدءا من 7 أيام ويزداد مع تقدم العمر خلافا لتاثير الكبريتات الخارجية التي لا يظهر تأثيرها السلبي في الأعمار المبكرة .

الخرسانة خفيفة الوزن

أدى التطور الكبير في تكنولوجيا مواد البناء خاصة في حقل إنتاج الخرسانة الى ظهور أنواع متعددة من الخرسانة منها الخرسانة خفيفة الوزن ذات كثافة قليلة ($< 1800\ kg/m^3$) مقارنة بالخرسانة الاعتيادية. و يتم إنتاج هذه الخرسانة بطرق عديدة منها استخدام الركام خفيف الوزن. الخرسانة ذات الركام خفيف الوزن عادة"يتم اختيارها للأغراض الإنشائية . إذ إن استخدامها يؤدي إلى تقليل كلفة الإنشاء الكلية بالمقارنة مع الخرسانة الاعتيادية ، كما إن الخرسانة خفيفة الوزن لها أهمية كبيرة في المنشات العصرية في الوقت الحاضر، وهي تستعمل في إنشاء الأبنية السكنية و الجدران القاطعة و السقوف القشرية والألواح العائمة والجسور، وكذلك تستخدم في إنتاج الكتل بنائية خفيفة لها أهمية كونها ذات حراري جيد مقارنة بالكتل الخرسانية الاعتيادية إضافة إلى خفة وزنها بحيث لا تضيف أحمال كبيرة للمنشأ، مما يجعلها اقتصادية في الاستعمال لما توفره من استهلاك في الطاقة اللازمة للتدفئة والتبريد مما يعطي أهمية لدراسة خصائص هذا النوع من الخرسانة [8,7]. توسعت البحوث في العراق في حقل تكنولوجيا المواد من ضمنها دراسة خواص الخرسانة خفيفة الوزن باستخدام ركام طبيعي. استخدام البورسلينايت كركام خفيف الوزن في إنتاج خرسانة إنشائية يتطلب العديد من الدراسات لفهم وتحسين خواصها لتصبح مناسبة للتطبيقات العملية. الكثير من البحوث عن خرسانةِ البورسلينايت خفيفة الوزن تم التطرق إليها في العديد من الجامعات العراقية ، وعلى الرغم من الأهمية العملية لهذا النوع من الخرسانة في تطبيقات كثيرة في مجالات الإنشاء، إلا إن هذه البحوث لم تتطرق إلى السلوك الطويل الأمد لهذه الخرسانةِ عن تعرضها للتأثير الكبريتات الداخلي أو الخارجي. لذا أصبح من الضروري معرفة خواص وسلوك هذه الخرسانة في هذه الظروف. في هذا العمل تم التحري عن سلوك الخرسانة خفيفة الوزن عند تعرضها لتاثير الكبريتات الخارجي.

المواد المستخدمة و طرق الفحص

1-السمنت:

استعمل السمنت المقاوم المحلي، إنتاج معمل سمنت القائم والمبينة خواصهما الكيميائية و الفيزيائية في جداول (1) و (2) وهي مطابقة للمواصفات العراقية الخاصة بالسمنت البورتلندي م.ق.ع 1984/5 [9] .

جدول (1) : الخواص الكيمائية للإسمنت المقاوم

المركبات الكميائية	نتائج الفحص الكميائي	حدود المواصفة العراقية م.ق.ع 1984/5
CaO	62.72	–
SiO2	21.83	
MgO	2.22	(الحد الاقصى) 5%
SO3	2.18	(الحد الاقصى) 2.8
Fe2O3	5.0	–
Al2O3	3.70	–
L.O.I	2.0	(الحد الاقصى) 4%
المركبات الاساسية (معادلات Bogue's)		
C3S	42.84	–
C2S	30.36	–
C3A	2.56	–
C4AF	15.41	–

جدول (2) : الخواص الفيزيائية للإسمنت المقاوم

الخواص الفيزيائية	نتائج الفحص	حدود المواصفة العراقية م.ق.ع 1984/5
النعومة (كغم/م3)	365	(الحد الادنى) 230
زمن التجمد		
زمن التجمد الابتدائي (دقيقة)	129	(الحد الادنى) 45
زمن التجمد النهائي (ساعة)	3.47	(الحد الاقصى) 10
مقاومة الانضغاط مكعبات مونة الاسمنت (ميكا باسكال)		
3 يوم	17.4	(الحد الادنى) 15
7 يوم	25.2	(الحد الادنى) 23

2-الركام

2-1-الركام الناعم (الرمل): استعمل الركام الناعم مصدره مقلع (كيلو 35) في محافظة الانبار وتم إيجاد تدرجه حسب المواصفة العراقية الخاصة بالركام م.ق.ع 1984/45[10]. و كما هو موضح في جدول (5). جدول (6) يوضح الخواص الفيزيائية والكيمائية للرمل المستخدم.

جدول (5) : التحليل المنخلي للركام الناعم (الرمل).

مقاس المنخل (ملم)	نسبة العابر %	حدود المواصفة العراقية م.ق.ع 1984/45 (Zone No. 1) نسبة العابر%
10	100	100
4.75	90	100–90
2.36	75	95–60
1.18	56	70–30
0.6	30	34–15
0.3	13	20–5
0.15	6	10–0

جدول (6) : الخواص الفيزيائية والكيمائية للرمل

خواص الرمل المستخدم	نتائج الفحص	حدود المواصفة العراقية م.ق.ع 1984/45
الوزن النوعي	2.5	–
% الامتصاص	2.2	–
الكثافة الجافة (كغم/م3)	1600	–
محتوى الكبريتات (SO3)%	0.25	0.5 (max.)

2-2-الركام خفيف الوزن (البورسلينايت):

استعمل الركام الخشن من الحجر البورسلينايت المكسر مقاس أقصى 12.5 مصدره مقلع (التريفية -رطبة) في محافظة الانبار وتم إيجاد تدرجه حسب المواصفة الأمريكية (ASTM 330-05) [11] وكما هو موضح في جدول (7). جدول (8) و جدول (9) يوضح الخواص الفيزيائية والكيمائية لحجر البورسلينايت المستخدم.

جدول (7) : التحليل المنخلي للركام البورسلينايت

(ملم) حجم المنخل	نسبة العابر %	ASTM C330–05 [11] نسبة العابر%
12.5	100	100
9.5	83	80–100
4.75	36	5–40
2.36	10	0–20
1.18	0.7	0–10

جدول (8) : الخواص الفيزيائية لحجر البورسلينايت

الخواص	النتائج	المواصفات
الوزن النوعي	2.0316	ASTM C127–84 [12]
% الامتصاص	46.249	ASTM C127–84 [12]

جدول (9) : التحليل الكيميائي لحجر البورسلينايت

الاكاسيد	% النسبة المئوية
SiO2	71.15
Fe2O3	0.92
Al2O3	3.2
TiO2	7.31
CaO	5.5
MgO	0.16
SO3	0.08
L.O.I	9.65

3-المـــاء: استعمل ماء الشرب الاعتيادي لمدينة الرمادي لمعالجة جميع النماذج لحد عمر 28 يوم وبعدها ابقيت النماذج المرجعية في ماء المعالجة العادي لحين وقت الفحص، اما النماذج المتعرضة لتاثير الكبريتات الخارجي فقد تم استكملت معالجتها في الماء الجوفي. الجدول (10) يبين التحليل الكيميائي للماء الشرب و الماء الجوفي لمدينة الرمادي.

جدول (10) : الخواص الكيميائية لماء الشرب وماء الجوفي لمدينة الرمادي

الخواص	ماء الشرب	الماء الجوفي
PH	7.300	8.340
Na+1%	0.003	4.980
Cl-1%	0.008	0.017
Ca+2%	0.010	0.037
Mg+2%	0.008	0.045
SO3%	0.031	0.301
K+1%	0.0002	0.003

* تم الفحص في مختبر كلية الزراعة

4- الميتاكاؤلين:

الميتاكاؤلين المستخدم في هذا البحث تم الحصول عليه من حرق الكاؤلين بدرجة ^{o} 700 لمدة ساعة واحدة ، جدول (11) يبين التحليل الكيميائي لهذه المادة.

جدول (11) : التحليل الكيميائي لميتاكؤلين

الاكاسيد	% من الوزن
SiO_2	52.38
Al_2O_3	37.31
Fe_2O_3	1.21
CaO	1.68
MgO	0.3
K_2O	0.44

5- الملدن الفائق:

الملدن الفئق المستخدم في هذه الدراسة هو Sikament –163 (مقلل للماء عالي المدى نوع F)، جدول (12) يبين خواص هذه المادة.

جدول (12) : خواص الملدن الفائق

الخواص	الوصف
الوظيفة	تقليل الماء وانتاج خرسانة ذات جودة عالية في الاجواء الحارة
الجرعة	0.6% – 2.5% من وزن السمنت
المظهر	سائل
اللون	FKD
الوزن النوعي	1.2 كغم/لتر
قيمة PH	10 ± 1.0

6- القوالب المستخدمة:

تم استخدام قوالب حديدية بابعاد (100×100×100) ملم للحصول على مكعبات خرسانية استخدمت في فحوصات مقاومة الانضغاط ، واستخدام قوالب حديدية بابعاد (100×100×500) ملم للحصول على مواشير خرسانية استخدمت في فحوصات معايير الكسر.

7- الخلطات المستخدمة:

استخدمت الخلطات الخرسانية و الموضحة كميات المواد الاولية المستخدمة لإنتاج متر مكعب واحد من تلك الخلطات في الجدول أدناه .

جدول (13) :كميات المواد الأولية المستخدمة لإنتاج متر مكعب واحد

الخلطة		الكميات (كعم/م3)				w/c	SP نسبة من وزن) %السمنت)	مقاومة الانضغاط بعمر 28 يوم (ميكا باسكال)
		السمنت	ميتاكاؤلين (15% من وزن السمنت)	رمل	بورسلينايت			
LWP	RIV	500	0	520	550	0.38	2.5	18.6
	EIV	500	0	520	550	0.38	2.5	18.9
LWPCM	RIVM	500 (C+MK)	75	520	550	0.38	2.5	32.0
	EIVM	500 (C+MK)	75	520	550	0.38	2.5	32.8

الملدن الفائق :SP ,نسبة الماء/السمنت :w/c ,ميتاكاؤلين :MK

8- عملية خلط و رص الخرسانة:

للسيطرة على كمية ماء الخلط تم تنقيع البورسلينايت ليوم واحد ثم نشر في الهواء لغرض الحصول على ركام مشبع جاف السطح. تم إنجاز عملية خلط الخرسانة داخل مختبر الخرسانة في قسم الهندسة المدنية في كلية الهندسة/جامعة الانبار. باستخدام خلاطه الحوضية ذات سعة (0.07) متر مكعب. بعد تحضير الأوزان المطلوبة لكل خلطة يتم إضافة الركام الخشن و الناعم و الأسمنت ووضعها في الخلاطة القدرية ومن ثم تم خلط هذه المواد و هي جافة و لمدة نصف دقيقة للحصول على خلطة متجانسة القوام. بعد ذلك تم صب الخرسانة في القالب المكعبة والمواشير ، بعد دهن السطح الداخلي للقوالب، على شكل طبقات حيث تم رص كل طبقة بواسطة هزازة كهربائية و لمدة 7 ثوان قبل صب الطبقة الأخرى. وبعد إتمام صب و رص الخرسانة تمت معالجة سطح النماذج بالمالج للحصول على سطح مستو.

9- المعالجة:

بعد إتمام عملية صب النماذج الخرسانية تم تركها في جو المختبر لمدة 24 ساعة لغرض اكتمل تصلبها ، ثم تم فتح القوالب الحديدية و إخراج النماذج الخرسانية و تغطيسها في الماء في حوض المعالجة لحين إجراء الفحوصات عليها.

10-الفحوصات

10-1-فحص مقاومة الانضغاط:

استعملت ماكنة فحص نوع (ELE) ذات سعة 3000 كيلو نيوتن لفحص مقاومة الانضغاط وتم الفحص طبقا للمواصفة (B.S.1881, part (116): 1983) [13] وكانت أعمار الفحص 7، 28، 90، 180 يوم حيث تم فحص ثلاثة مكعبات لكل عمر.

10-2-فحص معايير الكسر (مقاومة الانثناء) :

استعملت ماكنة فحص نوع (ELE) ذات سعة 50 كيلو نيوتن لفحص معايير الكسر وتم الفحص طبقا للمواصفة ASTM ((192-88)) [14] . وكانت أعمار الفحص 7، 28، 90، 180 يوم حيث تم فحص ثلاثة مواشير لكل عمر وبأسلوب نقطتي التحميل لفحص معايير الكسر.

10-3-فحص الكثافة:

تم إيجاد كثافة الخرسانة بوساطة قياس وزن كل نموذج من نماذج فحص مقاومة الانضغاط والانثناء بوساطة قياس وزنه جافا في الهواء قبل الفحص وقياس إبعاده ومن ثم حجمه لايجاد الكثافة [15].

النتائج و مناقشة

1-مقاومة الانضغاط: بعد إجراء فحص الانضغاط تم التوصل إلى النتائج الموضحة الموضحة في جدول (14) أدناه:

جدول (14) : مقاومة الانضغاط للخلطات الخرسانية (بعد 28 يوم من المعالجة الاعتيادية)

الخلطة الخرسانية / الزمن بعد معالجة لمدة 28 يوم	مقاومة الانضغاط (نيوتن/ملم 2) *						
	(0) يوم	(7) أيام	(14) يوم	(28) يوم	(56) يوم	(90) يوم	(120) يوم
RIV	18.6	18.9	19.3	20.5	20.8	21.2	22.6
EIV	18.9	19.2	19.5	19.9	18.7	16.7	14.6
RIM	32.0	33.3	34.0	35.6	36.1	37.5	38.6
EIIM	32.8	32.9	33.6	34.1	34.5	34.0	33.9

*القراءات أعلاه تمثل معدل على الاقل ثلاث قراءات لنماذج الفحص

- **خرسانة خفيفة الوزن بدون ميتاكاؤلين**:

نتائج الفحص المبينة في الجدول أعلاه وشكل (1) تبين بان مقاومة الانضغاط لنماذج المعرضة لتاثير الكبريتات تزداد مع العمر لحد 28 يوم بعد غمرها بالماء الجوفي (أي عمر 56 يوم) بعدها تبدا مقاومة الانضغاط بالتناقص بينما تستمر مقاومة النماذج المعالجة في الماء العادي بالزيادة. وكان نسبة التغير بمقاومة الانضغاط للنماذج المعرضة لتاثير الكبريتات نسبة للنماذج المرجعية كالأتي: 1.6%، 1.59 %، 1.03 %، 2. 93 %-، 10.10%- ، 21.23 %-، 35.40% – للأعمار0، 7، 14، 28، 56، 90 و 120 يوم بعد فترة معالجة اعتيادية ل28 يوم .

- **خرسانة خفيفة حاوية على ميتاكاؤلين :**

نتائج الفحص المبينة في الجدول أعلاه وشكل (1) تبين بان مقاومة الانضغاط لنماذج المعرضة لتاثير الكبريتات تزداد مع العمر لحد 56 يوم بعد غمرها بالماء الجوفي (أي عمر 64 يوم) بعدها تبدا مقاومة الانضغاط بالتناقص بينما تستمر مقاومة النماذج المعالجة في الماء العادي بالزيادة. وكان نسبة التغير بمقاومة الانضغاط للنماذج المعرضة لتاثير الكبريتات نسبة للنماذج المرجعية كالأتي: 2.44%-، 1.20%-، 1.18 %-، 4.21 %-، 4.43%- ، 9.33 %-، 12.18% –للأعمار0، 7، 14، 28، 56، 90 و 120 يوم بعد فترة معالجة اعتيادية ل28 يوم .

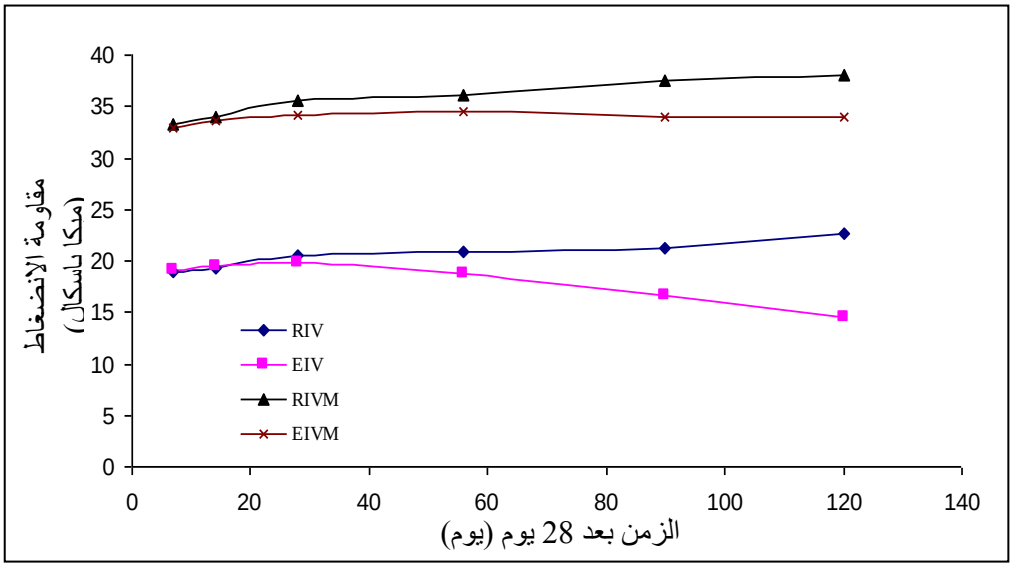

شكل (1) علاقة مقاومة الانضغاط مع الزمن

2-مقاومة الانثناء: بعد إجراء فحص الشد بالانثناء تم التوصل إلى النتائج الموضحة في جدول (15) أدناه :

جدول (15) : مقاومة الانثناء للخلطات الخرسانية

الخلطة الخرسانية / الزمن بعد معالجة لمدة 28 يوم	مقاومة الانثناء (نيوتن/ملم 2) *						
	(0) يوم	(7) أيام	(14) يوم	(28) يوم	(56) يوم	(90) يوم	(120) يوم
RIV	2.08	2.30	2.40	2.45	2.50	2.60	2.92
EIV	2.05	2.10	2.00	1.98	1.86	1.70	1.50
RIM	4.45	4.50	4.63	4.69	4.73	4.95	5.60
EIIM	4.38	4.40	4.50	4.54	4.50	4.00	3.60

*لقراءات أعلاه تمثل معدل على الأقل ثلاث قراءات لنماذج الفحص

- **خرسانة خفيفة الوزن بدون ميتاكاؤلين**:

نتائج الفحص المبينة في الجدول أعلاه وشكل (2) تبين بان مقاومة الانثناء للنماذج المعرضة لتاثير الكبريتات تزداد مع العمر لحد 7 أيام بعد غمرها بالماء الجوفي (أي عمر 56 يوم) بعدها تبدا مقاومة الانثناء بالتناقص بينما تستمر مقاومة النماذج المعالجة في الماء العادي بالزيادة. وكان نسبة التغير بمقاومة الانثناء للنماذج المعرضة لتاثير الكبريتات نسبة للنماذج المرجعية كالأتي: 1.44%-، 8.70%- ، 16.67%-، 19.18 %-، % ،% 25.60 -، 34.62 %- و% 48.63- للأعمار0، 7، 14، 28، 56، 90 و 120 يوم بعد فترة معالجة اعتيادية ل28 يوم .

- **خرسانة خفيفة حاوية على ميتاكاؤلين :**

نتائج الفحص المبينة في الجدول أعلاه وشكل (2) تبين بان مقاومة الانثناء لنماذج المعرضة لتاثير الكبريتات تزداد مع العمر لحد 28 يوم بعد غمرها بالماء الجوفي (أي عمر 64 يوم) بعدها تبدا مقاومة الانثناء بالتناقص بينما تستمر مقاومة النماذج المعالجة في الماء العادي بالزيادة. وكان نسبة التغير بمقاومة الانثناء للنماذج المعرضة لتاثير الكبريتات نسبة للنماذج المرجعية كالأتي: 1.57%-، 2.22%-، 2.80 %-، 3.20 %-، 4.86%- ، 19.20 %-، 35.71% – للأعمار0، 7، 14، 28، 56، 90 و 120 يوم بعد فترة معالجة اعتيادية ل28 يوم .

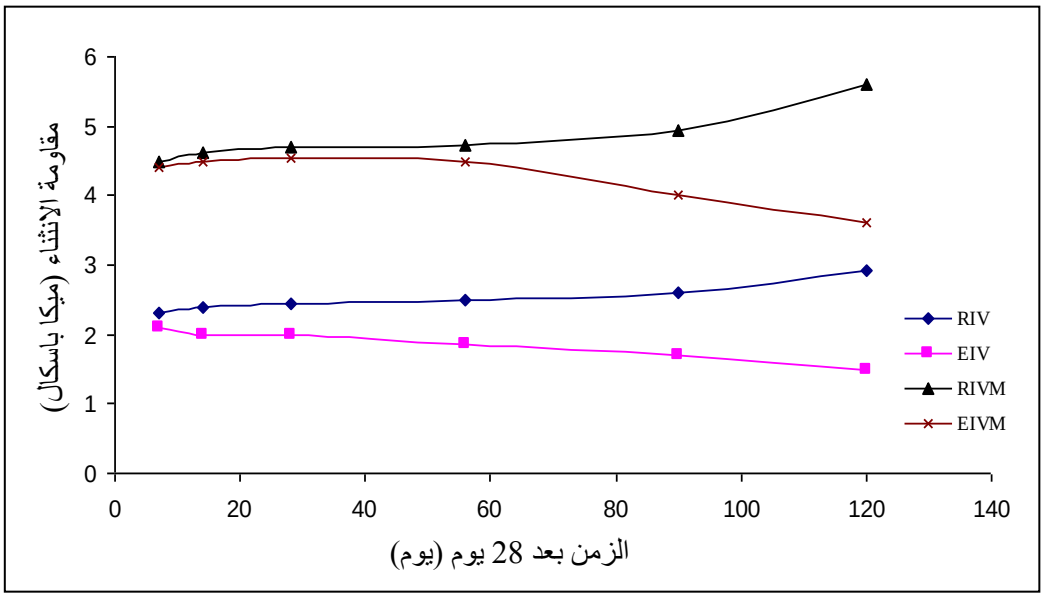

شكل (2) علاقة معايير الكسر (مقاومة الانثناء) مع الزمن

3- الكثافة: بعد إجراء فحص الكثافة تم التوصل إلى النتائج الموضحة في في جدول (16) ادناه :

جدول (16) : الكثافة للخلطات الخرسانية

الخلطة الخرسانية / الزمن بعد معالجة لمدة 28 يوم	الكثافة (كغم/م 3) *						
	(0) يوم	(7) أيام	(14) يوم	(28) يوم	(56) يوم	(90) يوم	(120) يوم
RIV	1586	1600	1625	1636	1650	1680	1730
EIV	1588	1593	1608	1618	1596	1538	1508
RIM	1870	1888	1896	1930	1973	2086	2110
EIIM	1872	1882	1893	1886	1882	1750	1677

*القراءات أعلاه تمثل معدل على الأقل ثلاث قراءات لنماذج الفحص

- **خرسانة خفيفة الوزن بدون ميتاكاؤلين**:

نتائج الفحص المبينة في الجدول أعلاه وشكل (3) تبين بان كثافة للنماذج المعرضة لتاثير الكبريتات تزداد مع العمر لحد 7 أيام بعد غمرها بالماء الجوفي (أي عمر 56 يوم) بعدها تبدا كثافة بالتناقص بينما تستمر كثافة النماذج المعالجة في الماء العادي بالزيادة. وكان نسبة التغير كثافة للنماذج المعرضة لتاثير الكبريتات نسبة للنماذج المرجعية كالأتي: 0.13%، -0.44%، -1.05% ، -1.10%، -3.27 % ، 8.45 % - و 23.04% - للأعمار 0، 7، 14، 28، 56، 90 و 120 يوم بعد فترة معالجة اعتيادية ل28 يوم .

- **خرسانة خفيفة حاوية على ميتاكاؤلين :**

نتائج الفحص المبينة في الجدول أعلاه وشكل (3) تبين بان كثافة لنماذج المعرضة لتاثير الكبريتات تزداد مع العمر لحد 28 يوم بعد غمرها بالماء الجوفي (أي عمر 64 يوم) بعدها تبدا كثافة بالتناقص بينما تستمر مقاومة النماذج المعالجة في الماء العادي بالزيادة. وكان نسبة التغير كثافة للنماذج المعرضة لتاثير الكبريتات نسبة للنماذج المرجعية كالأتي: 0.11% -0.32%، -0.74 %، -1.92 %، -4.61% ، -16.11 %، 20.52% – للأعمار 0، 7، 14، 28، 56، 90 و 120 يوم بعد فترة معالجة اعتيادية ل28 يوم .

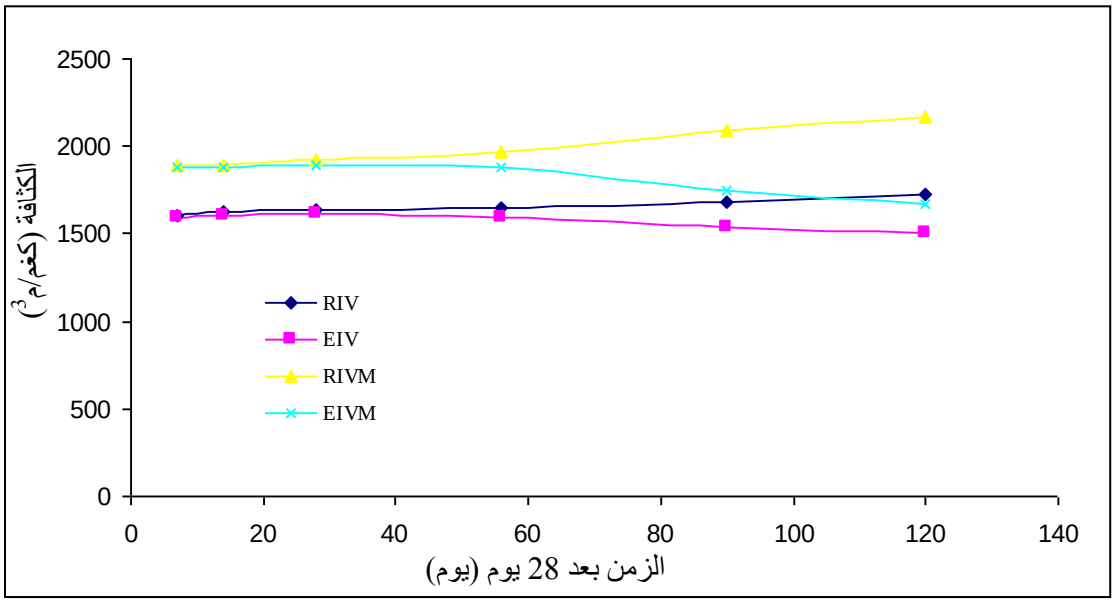

شكل (3) علاقة الكثافة مع الزمن

من النتائج الفحوصات الثلاث أعلاه نجد بان استعمال الميتاكاؤلين لا يحسن فقط من خواص الميكانيكية للخرسانة خفيفة الوزن (مقاومة الانضغاط، مقاومة الانثناء والكثافة) لكن أيضا يحسن من مقاومتها لتاثير الكبريتات الخارجي. وذلك بسبب كون الميتاكاؤلين وبسبب نعومتها العالية تعمل كمادة مالئة للفراغات إضافة الى ان السليكا والالومينيا الموجودة في الميتاكاؤلين تتفاعل مع هيدروكسيد الكالسيوم الناتج من اماهة السمنت كما هو موضح في المعادلات ادناه مما يزيد من كثافة الخرسانة ويقلل من نفاذيتها وبالتالي يحسن من مقاومتها لتاثير الكبريتات الخارجي.

$$Al_2Si_2O_5(OH_4) \xrightarrow{700-800\,^\circ C} Al_2O_3.2SiO_2 + 2H_2O \quad \ldots\ldots(1)$$

Kaolin Metakaolin

$$AS_2 + 6CH + 9H \longrightarrow C_4AH_{13} + 2\,C_3S_2H_3 \quad \ldots\ldots(2)$$

$(AS_2/CH = 0.5)$ stratlingite

$$AS_2 + 5CH + 3H \longrightarrow C_3AH_6 + 2\,C_3S_2H_3 \quad \ldots\ldots(3)$$

$(AS_2/CH = 0.6)$ hydrogarnet

$$AS_2 + 3CH + 6H \longrightarrow C_2ASH_8 + C_3S_2H_3 \quad \ldots\ldots(4)$$

$(AS_2/CH = 1.0)$ stratlingite

الاستنتاجات

1. تعرض الخرسانة خفيفة الوزن لتاثير الكبريتات يؤدي الى تاكل الخرسانة مما يسبب في نقصان في كثافة الخرسانة وتدهور مقاومة الانضغاط والانثناء مع الوقت.
2. لتاثير الكبريتات (التاثير الخارجي) يكون اكثر وضوحا في الاعمار المتاخرة
3. اضافة الميتاكاؤلين يحسن من خواص الخرسانة و أيضا يحسن من مقاومتها لتاثير الكبريتات الخارجي.

التوصيات

1. دراسة تأثير الكبريتات الداخلية على خواص الخرسانة خفيفة الوزن
2. دراسة تاثير الميتاكاؤلين على خواص الخرسانة خفيفة الوزن المتعرضة لتاثير الكبريتات الداخلي
3. استخدام مواد بوزلانية اخرى مثل سليكافيوم و دراسة تاثيرها على خواص الخرسانة خفيفة الوزن المتعرضة لتاثير الكبريتات الداخلي والخارجي.

المراجع

1. عارف سويداني، ، "*استخدام عملية الفسفتة لمعالجة مشكلة تآكل فولاذ التسليح في المنشآت الخرسانية المسلحة*"، أطروحة دكتوراه ,جامعة دمشق، **2005.**

2- Neville A. M. "*Properties of Concrete*", Long Man Group Limited, London, Fourth Edition, 2005.

3- ACI Manual of concrete practice, ACI Standard 201, 2R-92, "*Guide to durable concrete*", 1993.

4- عباس ,يحيى يونس "*آلية تغلغل الأملاح الكبريتية في الخرسانة* "رسالة ماجستير ,الجامعة التكنولوجية 2002 2 , ص1 .

5- السامرائي ,مفيد "*مقترح تحديد نسبة الأملاح في الرمل* ,"المركز الوطني للمختبرات الانشائية ,مجلة البناء الحضاري, العدد ,1 السنة الاولى ص (3-1).

6- Al-Robayi, A. H. "*Resistance of High Performance Concrete to External and Internal Sulfate Effect*", M. Sc. Thesis University of Technology, Baghdad 2005 .pp.100-102.

7- "*Economic design and construction with light weight aggregate Concrete*", EuvolightConc, Project Program of Brite 02- 1998.

8- David J , Floyd , Robert W. "*Natural aggregate in structural light weight Concrete Akers*" , Proceedings of the Session's Related to Structural Materials at Structures Congress 1989, P. 44-55.

9- المواصفة القياسية العراقية (I.O.S) رقم (5) لسنة 1984 ، *الاسمنت البورتلاندي* ، الجهاز المركزي للتقييس والسيطرة النوعية ، بغداد ، 8 صفحات.

10- المواصفة القياسية العراقية رقم (45) لسنة 1984 ، "*ركام المصادر الطبيعية المستعمل في الخرسانة والبناء*."

10- ASTM: C330–05, "*Standard Specification for Lightweight Aggregates for Structural Concrete*", Annual Book of ASTM: Standards, Vol. 04–02, 2005, pp. 187–189.

11- ASTM: C330–05, "*Standard Specification for Lightweight Aggregates for Structural Concrete*", Annual Book of ASTM: Standards, Vol. 04–02, 2005, pp. 187–189.

12- ASTM: C127–84, "*Standard Test Method for Specific Gravity and Absorption of Coarse Aggregate*", Annual Book of ASTM: Standards, Vol.04–02, 1988, pp. 64–68.

13- B.S.1881, Part 116, "*Method for Determination of Compressive Strength Concrete Cubes*", British Standard Institution, 1989, 3pp.

14- ASTM: C293–05, "Flexural *Strength of Concrete (Using Simple Beam With Center–Point Loading*", American Society of Testing and Material International, 2005.

15- ASTM: C567–00, "*Standard Test Method for Unit Weight of Structural Lightweight Concrete*", American Society of Testing and Material International, 2000.

خواص مونة الاسمنت الحاوية على غبار افران الاسمنت

أ.م.د. باسل صلاح مهدي م. اسراء يونس حردان محمد شحاذه
قسم هندسة البناء والانشاءات/ الجامعة التكنولوجية

الخلاصة

يتم في كل عام طرح الاف الاطنان من غبار افران الاسمنت كمخلفات في معامل الاسمنت العراقية حيث تتجمع بشكل تلال من المواد الملوثة للبيئة، والتي يصعب نقلها والتخلص منها بسبب نعومتها العالية، رغم كونها تشكل خسارة اقتصادية لمعامل الاسمنت حيث تحتوي على نفس المركبات للمواد الاولية للاسمنت ولكنها رغم ذلك لايعاد تدويرها في الصناعة السمنتية بسبب احتوائها على نسب عالية من القلويات والكبريتات، والتي تتأتى من المواد الاولية للاسمنت والوقود المستعمل في الحرق.

تم في هذا البحث دراسة امكانية احلال مادة غبار افران الاسمنت cement kiln dust، كجزء من وزن الاسمنت المستعمل في المونة mortar اضافة الى استعمال غبار السليكا silica fume مع الخليط الناتج لبحث تأثير ذلك على امكانية استعمال نسبة من هذه المخلفات في المواد السمنتية. وتبعا لذلك فقد تم اختيار فحص الانسياب وفحصي الثبات ومقاومة الانضغاط لدراسة تأثير هذه المخلفات على خواص المونة في الحالتين الطرية والمتصلبة على التوالي.

بينت النتائج بانه يمكن استعمال غبار افران تصنيع الاسمنت بنسبة احلال 10% من وزن الاسمنت بدون ان يؤثر ذلك سلبيا على خواص المونة المستعمل، وعدم الحاجة الى اضافة مواد بوزولانية مثل غبار السليكا الى الخليط، مما يمكن من التخلص من كميات كبيرة من هذه المخلفات الملوثة للبيئة ومن ناحية اخرى توفير فائدة اقتصادية للمشاريع الانشائية.

Properties of Cement Mortar Containing Cement Kilns Dust

Dr. B. S. Mahdi I. Younis H. M. Shehatha

Abstract

Each year, thousands of tons of cement kilns dust are extracted as by-products in Iraqi cement plants, where they accumulate in huge amounts of contaminated materials to the environment, which are difficult to transport and disposal because of their high smoothness. Although they constitute an economic loss to the cement plants because they contain the same compounds of raw materials for cement. In spite of that, they are not recycling to the cement industry because they contain high concentrations of alkalis and sulfates, which are derived from the raw materials for cement and fuel used in burning.

This research studied the possibility of substituting cement kilns dust, as part of the cement weight used in mortar, with or without addition of silica fumes, so as use certain amount of this by-product with the cementitious materials. Accordingly, the flow, soundness and compressive strength tests have been selected to study the effect of these by-products on the fresh and hardened properties of mortar.

The results showed that the cement kilns dust can be used with 10% of the weight of cement (as partial replacement) without negatively affecting the properties of mortar used. No need to add pozzolanic materials such as silica fumes to the mixture, making it possible to get rid of large quantities of these wastes contaminated the environment and on the other hand provide economic benefit to the construction projects.

1- المقدمة

يتم في كل عام طرح الاف الاطنان من غبار افران الاسمنت كمخلفات في معامل السمنت العراقية حيث تتجمع بشكل تلال من المواد الملوثة للبيئة، والتي يصعب نقلها والتخلص منها بسبب نعومتها العالية، رغم كونها تشكل خسارة اقتصادية لمعامل الاسمنت حيث تحتوي على نفس المركبات للمواد الاولية للاسمنت ولكنها رغم ذلك لايعاد تدويرها في الصناعة الاسمنتية بسبب احتوائها على نسب عالية من القلويات والكبريتات، والتي تتأتى من المواد الاولية للاسمنت والوقود المستعمل في الحرق.

يتكون غبار افران الاسمنت بشكل اساسي من المواد الاولية المغذاة الى فرن الاسمنت والتي لم يتم حرقها بشكل كامل، ولكن اعادة تدويرها مع المواد الاولية للافران قد يؤدي الى اختلال التوازن في مستوى القلويات في مواد التغذية وينتج سمنت عالي المحتوى من القلويات غير مطابق للمواصفات القياسية للسمنت الواطئ القلويات الذي يستعمل في المناطق الحاوي ركامها على سليكا فعالة قد تتفاعل مع هذه القلويات مؤدية الى اضرار للخرسانة المنتجة.

تحرى Bhatty [1-3] امكانية اضافة غبار افران الاسمنت CKD الى الاسمنت المخلوط بالرماد المتطاير fly ash وخبث الافران blast furnace slag بنسب مختلفة. حيث وجد بأن الاسمنت المخلوط مع الغبار CKD فقط اظهر انخفاضا في المقاومة، زمن التماسك، وقابلية التشغيل مقارنة بالخلطة المرجعية. وعزى انخفاض المقاومة الى وجود نسبة عالية من القلويات في الغبار. اما عند اضافة الرماد المتطاير fly ash مع الغبار فقد ادى ذلك الى انخفاض محتوى القلويات وأدى الى تحسن المقاومة حيث ان زيادة نسبة القلويات تزيد من احتمالية التفاعل القلوي مع الركام alkali – aggregate reaction والذي يمكن معالجته باضافة الرماد المتطاير او الخبث. بينما ادى اضافة الخبث الى انخفاض قابلية التشغيل ولكنه ادى الى تحسن مقاومة السمنت المخلوط نتيجة تفعيله بالمحتوى العالي للجير في الغبارCKD .

وجد Didamony وجماعته [4] بان اضافة CKD الى السمنت المخلوط الحاوي على الخبث او الخبث-غبار السليكا يفعل عملية الاماهة ويقلل تأثيرات التفاعل القلوي السليكي للركام الا ان استعمال هذا الغبار CKD يتطلب استعمال الملدنات المتفوقة معه لتقليل تأثيره السلبي على قابلية التشغيل، كما وجدوا بان [5] احلال السمنت بغبار الافران لغاية 6% لا يؤثر بشكل فعال على مقاومة الانضغاط ولكن هذه المقاومة، للإسمنت البورتلاندي الاعتيادي ولسمنت الخبث، تبدأ بالانخفاض عند زيادة نسبة الغبار عن 6%.

كما توصل الباحثين Abo-Al-Enein [6] و Mosleh [7] الى نقصان في مقاومة الانضغاط والشد عند استخدام غبار افران الاسمنت CKD مع الاسمنت البورتلاندي الاعتيادي وزيادة قليلة في هاتين الخاصيتين عند استخدام الغبار CKD مع سمنت الخبث او الاسمنت المقاوم للاملاح.

يهدف هذا البحث الى دراسة امكانية استعمال نسب مختلفة من غبار افران الاسمنت، الناتجة من احد معامل الاسمنت العراقية التي تعمل بالطريقة الرطبة، باحلاله وزنيا محل جزء من الاسمنت ودراسة ذلك على بعض خواص مونة الاسمنت cement mortar الناتجة مما يخلص البيئة العراقية من هذه المخلفات وفي نفس الوقت يوفر مردود اقتصادي جيد.

2- المواد المستعملة

تم حفظ الاولية التي شملت غبار الافران، الاسمنت، والرمل المستعملة في البحث باوعية بلاستيكية للمحافظة عليها من الرطوبة.

1.2- غبار افران الاسمنت CKD

استعمل غبار مرسبات الاسمنت من معمل سمنت الكوفة الذي ينتج الاسمنت البورتلاندي الاعتيادي بالطريقة الرطبة، ويبين الجدول (1) التحليل الكيمياوي لهذا الغبار.

جدول (1) : التحليل الكيمياوي لغبار الاسمنت

CaO	38.1
SiO_2	19.1
Al_2O_3	6.3
Fe_2O_3	2.8
MgO	1.8
SO_3	4.4
Na_2O	0.5
K_2O	4.0
L.O.I.	23.0

2.2- الاسمنت

استعمل سمنت بورتلاندي اعتيادي من معمل سمنت طاسلوجة، ويبين الجدولين (2) و (3) تركيبه الكيمياوي وخواصه الفيزيائية.

3.2- غبار السليكا

استعمل غبار السليكا غير المكثف المنتج من قبل شركة سيكا/تركيا، ويبين الجدول (4) تركيبه الكيمياوي.

4.2- الرمل

استعمل رمل منطقة الاخيضر المغربل على غربال ذو مقاس 4.75 ملم، ويبين الجدول (5) تدرج هذا الرمل.

5.2- الماء

استعمل ماء الاسالة في اعمال الخلط والمعالجة.

جدول (3) : الخواص الفيزيائية للإسمنت

الخاصية	نتيجة الفحص		حدود المواصفة العراقية IQS 5:1984
المساحة السطحية(طريقة بلين)، سم^2/غم	3520		2300 <
مقاومة الانضغاط للملاط (نت/ملم^2) بعمر	20.8	3 ايام	15 <
	26.0	7 ايام	23<
زمن التماسك (دقيقة)	141	الابتدائي	45 ≤
	320	النهائي	600 ≥
الثبات، اوتوكلاف %	0.03		0.8 >

جدول (2) : التركيب الكيمياوي للإسمنت

الاوكسيد	النسبة المئوية	حدود المواصفة العراقية IQS 5:1984
CaO	63.26	-
SiO_2	19.22	-
Al_2O_3	4.51	-
Fe_2O_3	3.34	-
MgO	2.62	5 >
SO_3	2.03	2.8 >
Insoluble Residue	0.84	1.5>
L.O.I.	3.72	4 >

جدول (4) : التركيب الكيمياوي لغبار السليكا

الاوكسيد	النسبة المئوية	حدود المواصفة الامريكية ASTM C1240-05
SiO_2	87.0	≥85%
Fe_2O_3	2.5	-
Al_2O_3	1.0	-
CaO	1.0	-
SO_3	0.5	-
K_2O+Na_2O	3.0	-
L.O.I.	2.9	-
محتوى الرطوبة	1.0	-

جدول (5) : تدرج الرمل

مقاس الغربال (المنخل)، ملم	% للمواد المارة	حدود المواصفة العراقية IQS 45:1984 (zone 3)
4.75	100	100-90
2.36	94	100-85
1.18	86	100-75
0.60	73	79-60
0.30	19	40-12
0.15	7	10-0

3- الخلطات المستعملة

تم اختيار سبعة نسب خلط لاغراض هذا المشروع، وكما مبين في الجدول (6).

جدول (6) : نسب الخلط المستخدمة

رقم الخلطة	نسبة الخلط (وزنا)				نسبة الماء/السمنت
	الاسمنت	الغبار	غبار السليكا	الرمل	
1	1	-	-	2.75	0.5
2	0.95	0.05	-	2.75	0.5
3	0.85	0.05	0.10	2.75	0.5
4	0.90	0.10	-	2.75	0.5
5	0.80	0.10	0.10	2.75	0.5
6	0.85	0.15	-	2.75	0.5
7	0.75	0.15	0.10	2.75	0.5

4- الخلط

تم استعمال خلاط من نوع (Hobart) ذو سعة (0.001 م^3)، حيث تم خلط (الاسمنت والغبار وغبار السليكا حسب النسب المبينة في الجدول رقم 6) لمدة دقيقتين لضمان الحصول على التجانس، ثم اضيف لها الرمل وخلطت لمدة دقيقتين اخريتين. بعد ذلك اضيف الماء وخلطت المواد كلها لمدة دقيقتين.

5- صب النماذج

تم ملء قوالب فحص مقاومة الانضغاط المزيتة ذات ابعاد 50*50 ملم بطبقة واحدة ورصت باستعمال المنضدة الهزازة وتم تسوية سطح القوالب بواسطة المالج، ثم غطيت بطبقة من النايلون لمدة 24 ساعة.

وضعت النماذج بعد فتحها من القوالب في الماء لحين موعد الفحص بعمر 3 و 7 أيام.

6- الفحوص المختبرية

تم خلال هذا البحث إيجاد بعض خواص مونة الاسمنت (الملاط) بالحالة الطرية والمتصلبة للخلطة المرجعية والخلطات الحاوية على غبار افران الاسمنت بدون او مع غبار السليكا.

1.6 فحص الانسياب

أجري هذا الفحص لغرض التعرف على مقدار التغير في قوام المونة نتيجة متغيرات البحث، حيث تم القيام به حسب الطريقة المحددة في المواصفة الامريكية ASTM C1437-01. التي تعرف الانسياب بالزيادة في معدل قطر قاعدة كتلة المونة كنسبة من قطر القاعدة الاصلي (100 ملم):

الانسياب= [(ق-100)/100]*100 (1)

حيث: ق= معدل قطر المونة المنتشر على القرص (ملم) مقاسا من اربعة جهات.

2.6 فحص الثبات

من الضروري ان لا يحصل تغير حجمي كبير في عجينة الاسمنت بعد تماسكها وخصوصا التمدد الذي يؤدي الى تمزق عجينة الاسمنت المتصلبة عندما تكون تحت ظروف مقيدة. وهذا التمدد قد يحصل نتيجة لتأخر او لبطئ عملية الاماهة للجير الحر الذي قد يتواجد في غبار الاسمنت المستعمل في هذا البحث والذي لايمكن تحديده بالتحليل الكيميائي نظرا لصعوبة التمييز بين CaO الحر وذلك الموجود ضمن مركبات الاسمنت.

تم اجراء هذا الفحص حسب المواصفة العراقية رقم 5 التي تشترط بان لايزيد تمدد عجينة الاسمنت المفحوص بطريقة (Le-Chatelier) عن 10 ملم وذلك لدراسة تاثير احلال الاسمنت بنسب مختلفة من غبار افران الاسمنت او احلال جزء اخر منه بغبار السليكا على ثبات الاسمنت الناتج.

3.6 مقاومة الانضغاط

تم تعيين مقاومة انضغاط الملاط بأخذ معدل ثلاثة مكعبات بأبعاد 50*50*50 ملم بعمر 3 و 7 أيام وذلك لدراسة تأثير متغيرات البحث على تحمل المونة الناتج وحسب الطريقة المتبعة في المواصفة الامريكية ASTM C109 / C109M – 11 .

7- النتائج ومناقشتها

تتضمن هذه الفقرة استعراض ومناقشة النتائج التي تم الحصول عليها من الفحوصات المختبرية.

1.7 فحص الأنسياب

يبين الجدول (7) والشكلين (1) و (2) تأثير المواد الناعمة المضافة على أنسياب المونة للخلطات السبعة المستخدمة حيث لوحظ أنه عند أضافة المواد الناعمة من غبار فرن الاسمنت وغبار السليكا يقل الأنسياب ويعود ذلك ألى زيادة المساحة السطحية والتي تؤدي ألى أمتصاص نسبة من ماء الخلط مؤدية الى انخفاض قابلية التشغيل.

جدول (7) : تأثير المواد الناعمة المضافة على أنسياب المونة

رقم الخلطة	نسبة الخلط (وزنا)				نسبة	الأنسياب
	الاسمنت	الغبار	غبار السليكا	الرمل	الماء/الاسمنت	%
1	1	-	-	2.75	0.5	156.25
2	0.95	0.05	-	2.75	0.5	155.75
3	0.85	0.05	0.10	2.75	0.5	155
4	0.90	0.1	-	2.75	0.5	152.5
5	0.80	0.10	0.10	2.75	0.5	137.5
6	0.85	0.15	-	2.75	0.5	110
7	0.75	0.15	0.10	2.75	0.5	100

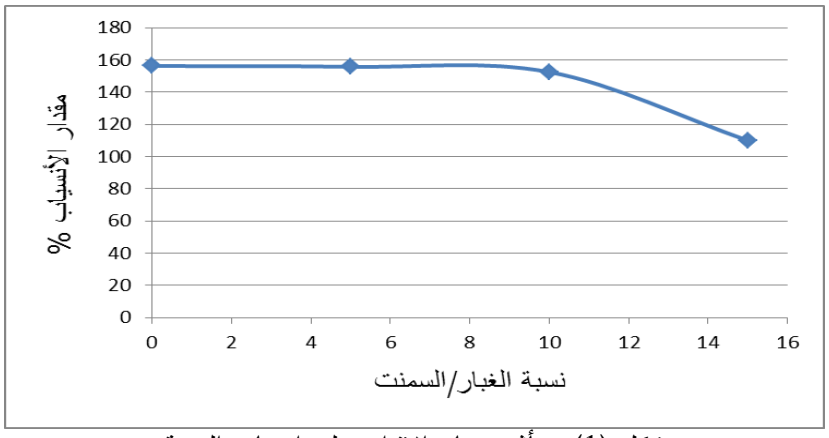

شكل (1) : تأثير غبار الافران على انسياب المونة

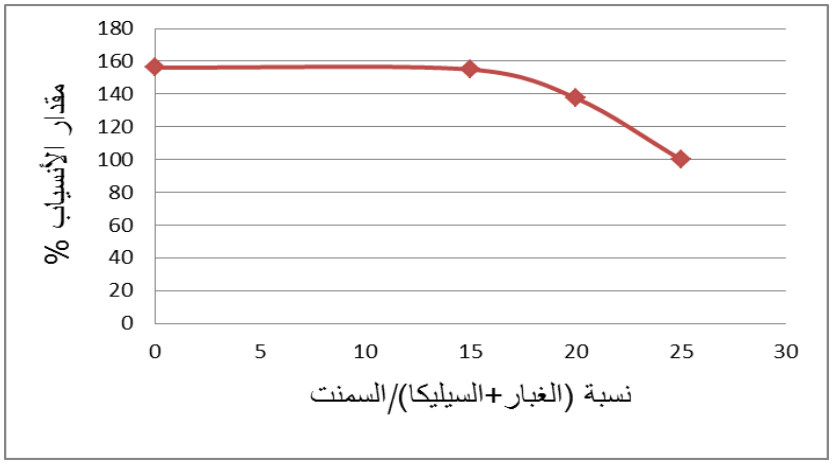

شكل (2) : تأثير اضافة غبار الافران وغبار السليكا على انسياب المونة

2.7 فحص الثبات

يبين الجدول (8) تأثير المواد الناعمة المضافة (غبار الأفران وغبار السليكا) على ثبات الاسمنت حيث يلاحظ أن القلويات الموجودة في غبار الأفران لم تؤثر على ثبات الاسمنت حتى عند استعمال نسبة غبار افران بمقدار 15% بدون او مع المادة البوزولانية. وقد يعود عدم تأثر الثبات الى أن الركام المستعمل ليس ذو فعالية سليكية عالية تؤدي الى تفاعله مع القلويات الموجودة في الغبار والتي في حالة ذلك تؤدي الى حصول نتائج تمددية للخلطات السبعة المستخدمة.

جدول (8) : تأثير المواد الناعمة المضافة على ثبات الاسمنت (حسب فحص Le-Chatelier)

رقم الخلطة	نسبة الخلط (وزنا)				نسبة الماء/الاسمنت	التمدد mm	حدود المواصفة العراقية رقم 5
	الاسمنت	الغبار	غبار السليكا	الرمل			
1	1	-	-	2.75	0.5	1	10mm≥
2	0.95	0.05	-	2.75	0.5	1	
3	0.85	0.05	0.10	2.75	0.5	1	
4	0.90	0.1	-	2.75	0.5	5	
5	0.80	0.10	0.10	2.75	0.5	5	
6	0.85	0.15	-	2.75	0.5	1	
7	0.75	0.15	0.10	2.75	0.5	1	

3.7 مقاومة الأنضغاط للمونة

يبين الجدول (9) والأشكال (3) و (4) تأثير المواد الناعمة والتي تشمل غبار افران الاسمنت وغبار السليكاعلى مقاومة انضغاط المونة بعمر 3 و7 أيام، حيث لوحظ أن اضافة غبار افران الاسمنت لغاية نسبة 10% يؤدي الى زيادة مقاومة الأنضغاط من دون اضافة ابخرة السيليكا وقد يعود ذلك الى تكثيف هيكل المونة. إن عدم تأثر مقاومة الأنضغاط عند استعمال الغبار ولغاية نسبة 10% (مع عدم استعمال غبار السليكا) يدل على عدم حصول التفاعل القلوي السليكي نتيجة لكون الركام المستعمل لايحتوي فعالية سليكية وبذلك ينتفي الغرض من استعمال غبار السليكا، كما ان نسبة اوكسيد الكالسيوم الحر (CaO) الموجودة في الغبار المضاف للمونة لم تكن بالنسبة العالية التي تؤدي الى حصول اجهادات داخلية تضعفها وكما اكد ذلك نتائج فحص الثبات اعلاه .

جدول (9) : تأثير المواد الناعمة المضافة على مقاومة الأنضغاط للمونة

رقم الخلطة	نسبة الخلط (وزنا)				نسبة الماء/الاسمنت	مقاومة الأنضغاط N/mm^2	
	الاسمنت	الغبار	غبار السليكا	الرمل		بعمر ثلاثة أيام	بعمر سبعة أيام
1	1	-	-	2.75	0.5	4.8	6.52
2	0.95	0.05	-	2.75	0.5	8.33	10.72
3	0.85	0.05	0.10	2.75	0.5	10.28	12.11
4	0.90	0.10	-	2.75	0.5	10.55	12.15
5	0.80	0.10	0.10	2.75	0.5	7.6	9.52
6	0.85	0.15	-	2.75	0.5	6.6	7.72
7	0.75	0.15	0.10	2.75	0.5	4.87	5.63

أما عند زيادة نسبة الغبار CKD عن 10% من وزن الاسمنت فقد لوحظ انخفاض المقاومة ويعود ذلك الى أن تأثير الغبار، بالنسب المبينة في هذا البحث، هو فيزياوي بشكل أساسي ويؤثر على أنخفاض قابلية التشغيل وبالتالي تكون فراغات هوائية ناتجة من عدم اكتمال الرص تقلل المقاومة وهذا دليل على أن القلويات والكبريتات واوكسيد الكالسيوم الحر

الموجودة في الغبار لاتؤثر على الخلطات عند الأضافة لغاية 10% من غبار افران الاسمنت ولكن تبدأ مقاومة الأنضغاط بالإنخفاض عند أضافة أكثر منذ 10% .

اما عند احلال 10% من الاسمنت بغبار السليكا فقد لوحظ بانه يمكن استعمال 5% فقط من غبار الاسمنت كحد اعلى (ليكون مجموع غبار الاسمنت وغبار السليكا 15%) قبل ان تنخفض المقاومة وهذا يؤكد التأثير الفيزياوي للغبار المستخدم بالنسب المبينة، على اضعاف قابلية التشغيل بحيث تؤدي الى صعوبة رص المونة وزيادة الفراغات الهوائية المسببة لانخفاض المقاومة.

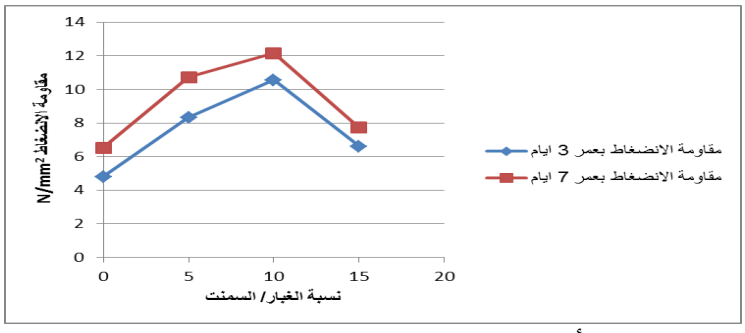

شكل (3) : تأثير غبار افران الاسمنت على مقاومة الانضغاط للمونة

شكل (4) : تأثير نسبة (غبار الاسمنت+ غبار السليكا) المضافة على مقاومة

8- الاستنتاجات

أ) أن احلال (غبار افران الاسمنت) بنسبة 10% من وزن الاسمنت المستعمل لا تؤثر على ثبات الاسمنت المقاس حسب المواصفة العراقية رقم 5 التي تشترط بأن لايزيد تمدد عجينة الاسمنت المفحوص بطريقة (Le- Chatelier) عن 10 ملم.

ب) أن تأثير احلال غبار الاسمنت يؤثر بشكل اساسي على أنسياب المونة للخلطات المستخدمة حيث يسبب انخفاض بنسبة (155.75، 152.5، و110)% عند استعمال نسبة احلال (5، 10، و15)% على التوالي من وزن الاسمنت.

ت) أن احلال غبار افران الاسمنت لغاية نسبة 10% من وزن الاسمنت يؤدي الى زيادة مقاومة الأنضغاط ولكن عند أضافة أكثر من 10% يؤدي الى أنخفاض مقاومة الأنضغاط عند عمر 7 ايام.

ث) بناءً على ما جاء في اعلاه، يمكن استعمال غبار الاسمنت بنسبة احلال 10% من وزن الاسمنت بدون ان يؤثر ذلك سلبياً على خواص المونة المستعملة، مما يمكن من التخلص من كميات كبيرة من هذه المادة الملوثة للبيئة و من ناحية أخرى توفير فائدة أقتصادية للمشاريع الأنشائية .

ج) لم يلاحظ الحاجة الى استعمال المواد البوزولانية (غبار السليكا) مع خلطات المونة المستعمل معه غبار افران الاسمنت، حيث انها ادت فقط الى انخفاض قابلية التشغيل.

9- المصادر

1- Bhatty, M.S.Y., "*Use of Cement Kiln Dust in Blended Cements*", World Cement Technology, London, U.K., Vol. 15, No. 4, 1984, pp. 126-134.

2- Bhatty, M.S.Y., "*Use of Cement Kiln Dust in Blended Cements: Alkali- Aggregate Reaction Expansion*", World Cement Technology, London, U.K., Vol. 16, No. 10, 1984, pp. 386-392.

3- Bhatty, M.S.Y., "*Properties of Blended Cement Made with Portland Cement*", Cement Kiln Dust, Fly Ash, and Slag, 8th International Congress on Chemistry of Cement, Rio de Janeiro, Brazil, Theme 3, Vol. IV, 1986, pp. 118-127.

4- El-Didamony, H., Abo-El-Enein, S.A., Ali, A.H., and El-Sokkary, T.M., " *Effect of Silica Fume on the Slag Cement Containing Wet Cement Dust*", Indian J. Eng. & Mater. Sci., Vol. 6, 1999, pp. 274-278.

5- El-Didamony, H., Abd El-Aleem, S., Abd-El-Aziz, M., and Heikal, M., "*Effect of Cement Kiln Dust Substitution on Chemical and Physical Properties and Compressive Strength of Portland and Slag Cements*", The Arabian Journal for Science and Engineering, Vol. 30, 2005, pp. 263-273.

6- Abo-El-Enein, S. A., "*Utilization of Cement Kiln Dust in Cement Industry and Building Products*", First International Symposium on the Cement Industry, Egypt, 8-10 Nov. 1997. pp. 130-141.

7- Mosleh, A. M., "*Evaluation of By-Pass Dust for the Production of Blended Cement Containing B. F. Slag*", MSc. Thesis, Institute of Environmental Studies and Research, Ain Shams University, Egypt, 1996.

Thermal Performance Of Ferrocement Eco-housing System

W. N. Al-Rifaie, Ph.D[1], L. E. Ibraheem, M.Sc[2] , H.Y. Al-Samarraie, M.Sc[3],
1 Professor Emeritus, University of Tikrit, Iraq. Email: wnrifaie@yahoo.com
2 Lecturer, University of Tikrit, Iraq.
3 Structural Engineer (SDI Company), Iraq.
Correspondance: Wail N. Al-Rifaie. Email: wnrifaie@yahoo.com

Abstract

Urban development is a key consumer of energy, a structural system based on generic services facilities is introduced by Al-Rifaie and prefabricated ferrocement cavity walls/ and roofs within the proposed system present a series of possibilities for the solution of building construction at maximum reduction of the electrical energy.
The relation between the energy required to run the building using the proposed ferrocement construction system and the use of traditional method of construction is determined

Keywords: Cooling; Eco-Housing; Energy ; Ferrocement;; Heating

ألإداء ألحراري لنظام ألمساكن أللإقتصادية الفيروسمنتية

أ.د. وائل الرفاعي ليث ابراهيم هشام السامرائي
كلية الهندسة – جامعة تكريت

الخلاصة

التنمية الحضرية تعتبر المستهلك الرئيسي للطاقة، وان النظام الهيكلي تكون جدرانه وسقوفه مجوفة وعناصره الإنشائية مسبقة الصنع و مصنعة من عنصر الفيروسمنت، قد قدم من قبل الرفاعي. أن النظام المقترح هو واحد من سلسلة من الاحتمالات لإيجاد حل للمباني لاستخدام الطاقة بحدودها الدنيا. ولقد تمت المقارنة بين النظام الإنشائي المقدم في الدراسة الحالية وبين الأنظمة الإنشائية التقليدية من حيث استخدام الطاقة.

Introduction

Urban development is a key consumer of energy, in other words, a basic product of environmental pollution and therefore, the relationship between several elements such as building materials of natural, and, manufactured building materials, and, renewable energy sources and energy sources depleted should be determined.

The majority of homes in Iraq are built using traditional masonry construction for walls. Now these days in Iraq a large number of homes with their walls are built either by concrete block or by stone constructions. Sixty years ago clay brick jack arching was the method of slabs and/ or roofs construction and since then most of homes their slabs or roofs are reinforced concrete constructions.

Ferrocement has been developed mainly during the past thirty years and yet has reached a very advanced stage in technique and design. A considerable amount of laboratory testing research and prototype constructions have been completed at the Building and Construction Engineering Department of University of Technology, Iraq for the production of ferrocement members that would be used in the roof /floor/wall of building/housing.

Building system must not only cope with strengths and flexibility requirements, but the insulation value is of high importance. In summer heat must be kept outside as much as possible. The great demands of electric power due to heating and air-conditioning systems require control to make maximum reduction of the electrical energy.

The increasing demand to low energy houses has led to the introduction of so called green houses. The basic idea of introducing green or eco-house concept is to improve the thermal performance of the building envelope to a level where the heating and/ or cooling system can be kept very simple. Green or eco-houses may then be built using the proposed ferrocement system with a well insulated.

Ferrocement[1,2,3,4] (10-50 mm thick) is a type of thin reinforced concrete with great potential, made of cement–sand mortar and reinforced with layers of fine wire meshes with or without skeletal reinforcement. Ferrocement is an excellent construction material due to its mechanical properties, and low cost, and it is considered to possess high cracking strengths. Cement mortar is a material used in construction of ferrocement which is a cement composite material made up of Portland cement, sand, water and sometimes admixtures[5-13].

It has been stated that by adjusting your home heating and cooling by just 3 degrees; turning the heat down and the cooling up, can save over 1000 pounds of CO2 emissions each year.

A structural system based on generic services facilities is introduced by Al-Rifaie and prefabricated ferrocement cavity walls and hollow roofs within the proposed system[14] present a series of possibilities for the solution of building construction at maximum reduction of the electrical energy and the modern system provide excellent thermal insulation.

Reducing the amount of energy required to run a building means reducing the emissions of carbon dioxide. The emissions of carbon dioxide depends on the fuel source for kWh. If it is wind, solar, hydroelectric or nuclear, then zero pounds of carbon dioxide are created. To estimate CO2 emissions per kWh, the U.S. average in 2005 is adopted in the present work[15]. The average is approximately 1.31 pounds of CO2 per kWh generated.

The energy required to run a building using the proposed ferrocement structural system and the use of traditional methods of construction is determined and the possibility of using the renewable energy production rather than energy depleted is presented.

The proposed modern method of eco-housing construction (ferrocement system)

A structural system (Copyright © The University of Nottingham, U.K.) for ferrocement construction based on generic services facilities is introduced.

The construction concepts as shown in Figure 1 lend themselves readily to rapid delivery and assembly of flexible accommodation where designs can be adapted to meet local requirements for both structural performance and thermal comfort as shown in the figure.

The structural part of the house consists of three basic components; the base, walls, and roof. An integral framing concept allows for overall above-ground structural integrity which considerably exceeds that of traditional methods and this minimizes the need for ground works in all. The membrane construction also enables new concepts in passive downdraught cooling to be explored where airways are incorporated within structural features as wall cavities.

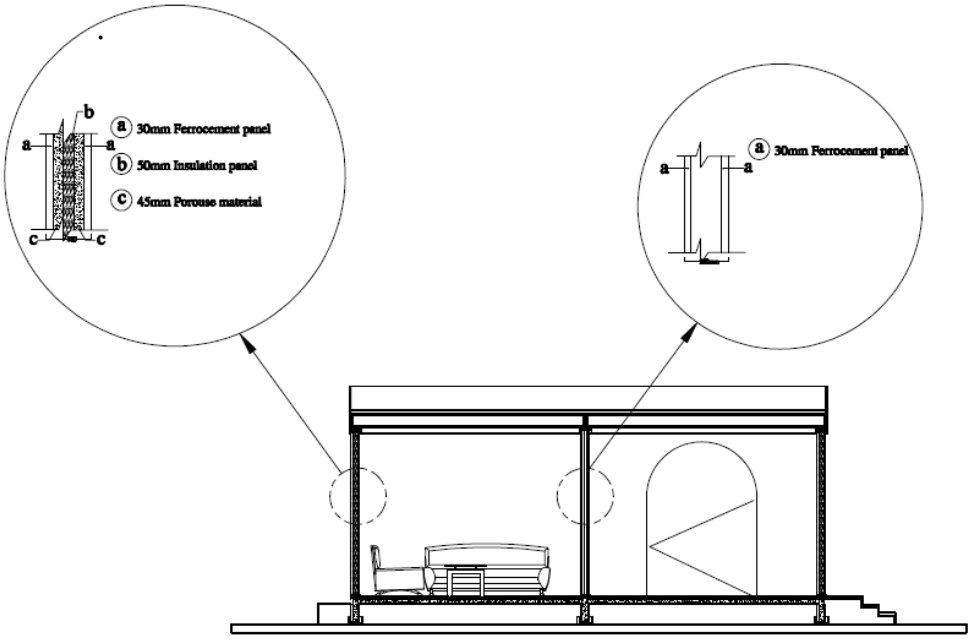

Figure (1) The proposed ferrocement system for house construction

Potential applications of the system include sustainable solutions for disaster relief and secure accommodation. The major advantages of a ferrocement construction system over current construction methods is mainly due to following perceived advantages:

1. Controlled manufacture, i.e., very high quality control.
2. Pre-Fabricated products and fast construction.
3. Reduced labour requirements and manpower can be easily trained at site.
4. Cost reduction, 15-50% cheaper than conventional techniques16.
5. Less maintenance and improved safety.
6. Reduction in dead weight, 50-75% lighter than conventional techniques16.
7. Reduced wastage.
8. Basic raw materials are available.

9. Reduced energy use for heating and cooling.
10. Ferrocement is very adequate to resist the impact, due to its higher ability of absorbing impact energy as compared with the conventional reinforced concrete, and the damage is localized at the impact zone18.
11. The ferrocement building components can withstand direct fire with a temperature values up to 756o C for a period of 2½ hours with no segregation in the surface of the elements facing the fire19.
12. Rehabilitations and strengthening of reinforced concrete elements by using ferrocement technique is very effective in increasing the cracking and ultimate loads and increasing the impact resistance[20]

Building system must not only cope with strengths and flexibility requirements, but the insulation value is of high importance. In summer heat must be kept outside as much as possible. The structural system for ferrocement construction based on generic services facilities and insulating these structures involves the application of insulation material by means of cavity wall construction which consists of two leaves (sides) of ferrocement separated by a wide space. Insulation material is used through a cavity wall. Test was carried out on a ferrocement cavity wall panel with insulation panel placed between the two leaves of the wall panel as shown in Plate (1). The obtained results as shown in Figure (2) showed that cavity wall construction consists of two leaves (sides) of ferrocement, separated by air space and the insulation panel positioned as shown gives a very good solution for insulation as shown in the figure, air is still the actual insulator, consequently reducing the demand to electrical energy.

Plate (1)

Front face 230.1^{o}C

Rear face 22^{o}C

Figure 2(a) Heating measurements of cavity ferrocement panel representing walls.

Lower face 345.1^{o}C

Upper face 28^{o}C

Figure 2(b) Heating measurements of horizontal hollow ferrocement panel representing roofs.

As stated earlier that the structural system for ferrocement construction based on generic services facilities and insulating these structures involves the application of insulation material by means of cavity wall construction which consists of two leaves (sides) of ferrocement (30 mm each) separated by a wide space and insulation material is used through a cavity wall. Test was carried out on a ferrocement cavity wall panel with insulation panel placed between the two leaves of the wall panel as shown. The obtained results showed that cavity wall construction consists of two leaves (sides) of ferrocement, separated by air space and the insulation panel positioned as shown in the figure gives a very good solution for insulation, (air is still the actual insulator), consequently reducing the demand to electrical energy. Cavity wall insulation may also be used to reduce heating/or cooling losses.

Energy assessment

In home construction there are two main areas have to be in focus: energy efficiency and construction efficiency. The present work concern with energy efficiency. In fact energy performance is highly prioritised in the development of building systems and construction productivity. The obtained results are compared with the proposed ferrocement construction method. Five kinds of traditional construction methods are:

- Method 1; 200 mm concrete block walls and 150 mm reinforced concrete slab/ roof.
- Method 2; 250 mm clay brick walls (with cement mortar) and 150 mm reinforced concrete slab/ roof.
- Method 3; 200 mm stone walls and 150 mm reinforced concrete slab/ roof.
- Method 4; 250 mm clay brick walls (with cement mortar) and 150 mm clay brick arching slab/ roof.
- Method 5; ferrocement system as in Figure (1).

It may be noted that the materials used for outer and inner wall finishing considered through the determination of heating and cooling loads are cement mortar and gypsum plastering respectively. Also, 100 mm concrete lining and 50 mm tiles with cement mortar for ground finishing and 150 mm soil and 40 mm tiles for roofing are considered in the determination of heating and cooling loads..

Residential heating and cooling load calculation requirements:

For assessing the energy efficiency of a residential house, the design temperatures, minimum and maximum, for use in performing load calculations considered in the present work are:

In winter: Indoor = 25 ^{o}C , Outdoor = 0 ^{o}C

In summer: Indoor = 23 ^{o}C , Outdoor = 57 ^{o}C

To determine the annual heating and/ or cooling energy consumption of a residential home using various traditional construction methods usually used in Iraq and most of Middle East Countries, the following formulas are used in the present investigation[16,17].

1. Heating load:

$$Q_p = U_p A_p(t_i - t_o) \quad (1)$$

Where:

Q_p = Heat Loss from the panel, Watt
A_p =Net Area (normal to heat flux direction), m^2
t_i = Indoor temperature(desired temp.), ^oC
t_o = Outdoor temperature, ^oC
U_p = Panel overall heat transfer coefficient , $U_p = 1/\sum R_{th}$, Watt/ $m^2.^oC$.
R_{th} = Thermal resistance(for each layer of panel), m^2.Co/Watt
R_{th} = L/KA
L = Panel layer thickness. m
K = Thermal conductivity (for each layer according to the material used), Watt/m. ^oC
A = Area (normal to the heat flux). m^2

2. Cooling load: (2)

$$q = U \times A \times CLTD$$

Where:

q = Heat gain (from walls and roofs), Watt
U = Wall overall heat transfer coefficient. Watt/ m^2. ^oC
A = Area (normal to the heat flux direction), m^2
CLTD (Cooling load temperature difference) , ^oC

3. Heat gains from` doors and windows (glasses)

$$\frac{q}{A} = (SC) \times (SHG)_{max} \times (CLF) \quad (3)$$

Where:

q/A: Heat gain per unit area of glass, Watt/ m^2
SC : shading coefficient.
SHG: solar heat gain.
CLF: cooling load factor.

The values of the over all heat transfer coefficient of each of the structural panel considered in the present investigation are given in Table (1).

Table (1) The determined values of heat transfer coefficient for the structural panels considered in the present investigation.

Structural member	Panel system	U_p= Heat transfer coefficient[16,17]
Wall. as mentioned above	Concrete block	5.485
	Clay brick	4.835
	Stone	3.5
	Ferrocement cavity wall with insulation panel positioned between the two ferrocement leaves.	0.22
Roof as mentioned above	Reinforced concrete	2.31
	Clay brick jack arching	2.1719
	Ferrocement channel like cross-section	0.1337

Table (2) The calculating values of heating loads

Construction system		Heating load	
Wall	Roof	kW	Ton
Concrete block	Reinforced concrete	25.17	7.157
Clay brick	Reinforced concrete	19.345	5.5
Stone	Reinforced concrete	16.45	4.677
Clay brick	Clay brick jack arching	22.75	6.47
Ferrocement cavity wall with insulation panel positioned between the two ferrocement leaves.	Ferrocement Channel like cross section	9.328	2.653

The 77 m^2 residential house shown in Figure (3) is chosen for comparison. Heating and cooling loads can be determined using a whole house approach. Using expressions 1, 2, and 3, the heating and cooling loads are calculated as given in Tables (2 and 3).

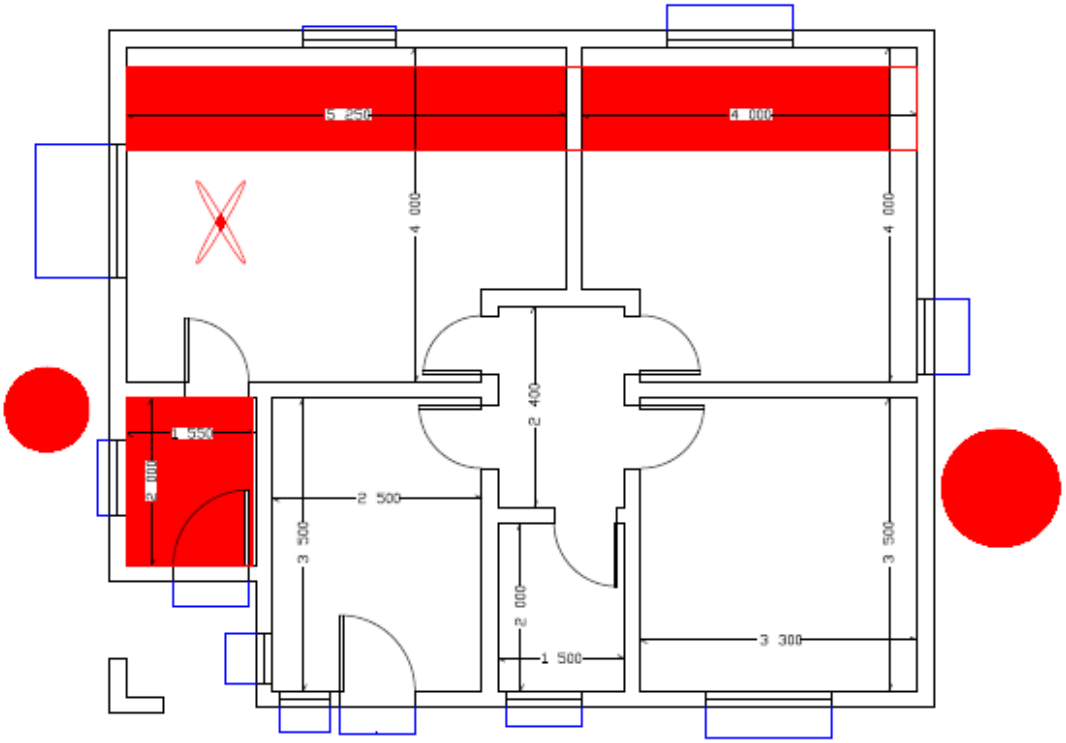

Figure (3) The 77 m^2 residential house adopted in the present work

Table (3) The calculating values of cooling loads

Construction system		Cooling load	
Wall	Roof	kW	Ton
Concrete block	Reinforced concrete	23.257	6.613
Clay brick	Reinforced concrete	21.172	6.02
Stone	Reinforced concrete	18.147	5.237
Clay brick	Clay brick jack arching	20.94	5.954
Ferrocement cavity wall with insulation panel positioned between the two ferrocement leaves.	Ferrocement Channel like cross section	8.012	2.278

It may be noted that 1 Ton of refrigeration = 3.517 kW is used `for calculating the amount of heating or cooling. It is assumed in the present work that a single home need to run 20 hours of electricity per day to cover the need for heating and cooling as given in Tables (2 and 3). To estimate carbon dioxide (CO2) emissions, the U.S. average of CO2 per kWh in 2005 which was approximately 1.31 pounds per kWh is adopted[15] to determine the emissions of CO2 per month as given in Tables (4 and 5).

Table (4) Comparison of heating load and the emission of carbon dioxide between different method of construction

Method of Construction	Heating load		Emission of CO2 Ib/month
	kW	kWh/ month	
Method 1	25.17	15102.87	17066.25
Method 2	22.98	13787.64	15580.03
Method 3	20.08	12049.19	13615.58
Method 4	22.75	13649.26	15423.67
Method 5	9.33	5597.29	6324.94

Table (5) Comparison of cooling load and the emission of carbon dioxide between different method of construction

Method of Construction	Cooling load		Emission of CO2 Ib/month
	kW	kWh/ month	
Method 1	23.26	13954.58	15768.67
Method 2	21.17	12703.67	14355.15
Method 3	18.42	11050.24	12486.78
Method 4	20.94	12563.39	14196.63
Method 5	8.01	4807.25	5432.19

It may be noted that there are some sources that generate heat inside the house have been taken into consideration such as cooker, and frozen refrigerator and sources that have been neglected such as house lighting.

Conclusions

1 High standards of energy efficient housing construction have been demonstrated in the present work. It may be seen that the modern method (ferrocement housing system) is able to produce very energy efficient dwellings. It is seen that with thermal insulation installed as part of the cavity construction panels lend to achieving high levels of thermal performance.

2 Using method 5 (ferrocement housing system), the reduction in energy consuming in heating and cooling loads in comparison with traditional methods 1, 2, 3, 4, may be summarized as: 63, 52, 44, 59% for heating and 66, 62, 56, 62% for cooling respectively.

3 Upon to what have been stated in conclusion 2, the reduction in the emission of CO2 when method 5 is used for house construction may in comparison with the traditional methods 1, 2, 3, 4 be summarized as: 63, 59, 53, 59% for heating and 65, 75, 65, 72% respectively.

References

1. IFS Committees 10, 2001"Ferrocement Model Code," Building Code Recommendations for Ferrocement (IFS 10-01).
2. ACI Publication SP.61, 1979 "Ferrocement–Materials and Applications", pp 1-195.
3. ACI committee 549, 1980, "Guide for the Design, Construction, and Repair of Ferrocement" ACI Structural Journal, May. June, pp 325-351.
4. ACI Committee 549, 1988 "State–of–the Art Report on Ferrocement", ACI Manual of Concrete Practice, part 5.
5. Al-Rifaie, W.N. "Ferrocement Wall: Penetration Testing". The Eighth International Symposium and Workshop on Ferrocement and Thin Reinforced Cement Composites, 6-8 February, 2006, Bangkok, Thailand.
6. Zaki, M. and Al-Rifaie, W.N. **,"**Design Of Ferrocement in Flexure**".** , Journal of Engineering and Technology, University Of Technology, Vol 18, No. 4, Iraq 1999.
7. Al-Rifaie, W.N. and Mahmood, N.S**,"**Finite Element Method for Non-Linear Analysis of Ferrocement Slabs and Box-Beams"**.** Proceedings of the Seventh International Symposium on Ferrocement and Thin Reinforced Cement Composites (FERRO-7), Singapore, 2001.
8. Al-Rifaie, W.N. and Mahmood, N.S,"Computational Model for Non-linear Analysis of Ferrocement Shells Using F.E.M". Journal of Ferrocement, Vol. 30, No. 1, January 2000.
9. Al-Rifaie, W.N. and Majeed, A.," Structural Behaviour of Thin Ferrocement One-Way Bending Elements*".* Journal of Ferrocement, Vol. 24, No. 2, 1994.
10. Al-Rifaie, W.N. and Abdul-Aziz, A.,**"** Thin Ferrocement Bearing Walls*".* Journal of Ferrocement, Vol. 25, No.3, 1995.
11. Al-Rifaie, W.N. and Al-Hmedawi, A.*,"* Structural Behaviour of Ferrocement Shells Roofs*".* Journal of Ferrocement, Vol. 30, No. 1, Jan. 2000.
12. Al-Rifaie, W.N. and Mnasrah, A.**"** Connection for Segmental Ferrocement, "Semi-Cylindrical Shells as a Roofing System**".** Journal of Ferrocement, Vol. 31, No.1, January 2001.

13. Al-Rifaie, W.N. and Kalaf, S.**"**Experimental Investigation of Long-Span Roofing System"**.** Proceedings of the Seventh International Symposium on Ferrocement and Thin Reinforced Cement Composites (FERRO-7), Singapore, 2001.
14. Al-Rifaie W. N., "Modern Housing System Using Ferrocement As Sustainable Construction Materials", 7th. Municipal Work, Conference & Exhibition, Kingdom of Bahrain, 24-26 April 2012.
15. http://www.epa.gov/cleanenergy/energy-resources/egrid/index.htm.
16. Jordan R.C. and Priester G.B., "Refrigeration and Air-conditioning", Prentice Hall, 1956.
17. Holman J. P., "Heat Transfer", 6th. McGraw Hill, 1986.
18. Abdul-Ameer O. A., "Ability of Ferrocement to Raise the Resistance of Reinforced Concrete Beams". M.Sc Thesis, University of Technology, 2000, Iraq.
19. Riyadh A. H. "Structural Behaviour of Ferrocement Under Direct Fire". M.Sc Thesis, University of Technology, 2005, Iraq.
20. Salah N. "Ferrocement for Structural Rehabilitation", Ph.D Thesis, University of Technology, 1998, Iraq.

Civil Engineering Department
Geotechnical and Transportation Engineering

قسم الهندسة المدنية
هندسة
الجيوتكنيك والمواصلات

قسم المدنية

فرع الجيوتكنيك

المحتويات

تسلسل	ألعنوان	رقم ألصفحة
1.	تاثير وجود التكهفات على سلوك الاسس الشريطية المسندة الى تربة النجف (حالة دراسية) سيف عكوبي \ د. حيدر عماش	1
2.	تنامي المنطقة اللدنة حول نفق في تربة تماسكية محمد فتاح قيس طه شلاش نهلة سالم	12
3.	المقاومة النوعية الجيوكهربائية التصويرية ثنائية البعد لتوصيف التربة في موقع مشروع العبيدي أ.د. حسين حميد كريم أ.م.د. محمد النعيمي وسام ماجد يعقوب محمد	34
4.	تأثير المحتوى الجبسي على خصائص منحني خاصية التربة-الماء للترب الطينية د.سهيل إدريس عبد القادر خطاب اسعد محمد أزهر مصباح العمري	53
5.	تأثير الاحمال المتكررة على قوة الشد للتربة الطينية المثبتة في مدينة الموصل د. محمد طيب حسين الليلة د. ايمن وليد الدباغ د. محمد ناظم جارو	63
6.	تأثير المواد فائقة النعومة على طاقة السطح الحرة للإسفلت الأسمنتي سعد عيسى سرسم اسراء ثامر العزاوي	73
7.	البولي أثلين واطئ الكثافة كمطور للإسفلت عبد الرحيم إبراهيم الحديدي أسامة عبدالله أمير	84
8.	دراسة خصائص حركة السابلة في منطقة المركز التجاري لبغداد سعد عيسى سرسم	92
9.	دراسة تخطيط ألتوزيع ألمروري في شبكات ألطرق ألواقعة في ألمناطق ألحضرية ألصغيرة باستخدام تقنيات نظام ألتوزيع ألجغرافي د.عبد ألخالق ما ل ألله محمد حسن ألطائي	105

S - 23

Effect of Presence of Cavity on Behavior of Strip Foundation Rested on Al-Najaf Soil as Case Study

Saif I. Akoobi
Al-Qadisiyah University
College of Engineering
Civil Engineering Dept.
saif.i.akoobi@gmail.com

Assist. Prof. Dr. Haider K. Ammash
Al-Qadisiyah University
College of Engineering
Civil Engineering Dept.
amashhk@gmail.com

Abstract

In the present study, finite element method is employed to study the effect of single cavity formed from gypsum dissolve on bearing capacity of strip foundation constructed above Al-Najaf soil. Cavity size and cavity orientation both in horizontal and vertical directions with respect to centerline of foundation were investigated. The study showed that, effect of cavity is significant and reduces the bearing capacity of soil where this reduction increases as cavity location close to the surface also it increases as cavity size increasing. It was also found that the depth beyond which the cavity effect on bearing capacity of shallow foundation diminish depend upon size of cavity while the horizontal distance beyond it the cavity effect diminish independent on cavity size. It was also observed that, three failure types are formed due to presence of cavity which are general shear failure, partial punching shear and punching shear failure.

Keywords: Al-Najaf Soil, Bearing Capacity, Cavity, Finite Element Method, Strip Foundation.

تاثير وجود التكهفات على سلوك الاسس الشريطية المسندة الى تربة النجف(حالة دراسية)

سيف عكوبي **د. حيدر عماش**

الخلاصة:

تم في هذا البحث دراسة تأثير وجود فجوة واحدة ناتجة من ذوبان الجبس على قابلية التحمل لأساس شريطي مشيد على تربة مدينة النجف بأستخدام طريقة العناصر المحددة. تم التحري عن حجم الفجوة وبعد الفجوة بألأتجاه الأفقي والعمودي عن مركز الأساس . أظهرت الدراسة أن وجود الفجوة يؤثر بصورة ملحوظة على قابلية التحمل و أن النقصان في قابلية التحمل يزداد كلما كانت الفجوة قريبة من السطح وكلما زاد حجم الفجوة. وجد أيضا أن العمق الذي بعدة يختفي تأثير الفجوة على قابلية التحمل يعتمد على حجم الفجوة بينما بعد الفجوة بالاتجاه الافقي عن مركز الاساس والذي بعدة يختفي تأثير الفجوة على قابلية التحمل لا يعتمد على حجم الفجوة. وجد ايضا ان وجود الفجوة يؤثر على نمط الفشل حيث لو حظت ثلاثة انماط فشل نتيجة لتغير حجم ومكان الفجوة بالنسبة للأساس.

كلمات مرشدة : تربة النجف، قابلية التحمل، فجوة، طريقة العناصر المحددة، أساس شريطي.

Introduction

The bearing capacity of foundation received great interest from researchers in the field of geotechnical engineering, due to the approximation found in the closed form solutions available in the time being. A well-known closed form solution proposed by Terzaghi [1] which is, in fact, an extension and improved modification of Pandtl's method, involving an approximation representing by the assumption of soil to be a plasticity problem and the application of superposition method in derivation of the equation of bearing capacity of soil at plastic state. Beside these approximations, many uncertainties may found in the field and not taken into account in Terzaghi solution. One of these uncertainties is the presence of cavities, cavities occur occasionally under foundations of structures in the areas having limestone, dolomite formations, and soil with gypseous content. Several works available in literature focused on bearing capacity of foundation above cavities, but in Iraq no research are focused on effect of cavities on bearing capacity of shallow foundations. The country has large areas contained formulation of problematic soils (e.g. Al-Najaf, Al-Mosul, and Al-Anbar areas). Wang and Hsieh [2] derived equations taking into account arching phenomenon from limit analysis for estimate ultimate strip footing pressure above void. Three failure mechanisms are considered in these equations, as shown in Figure (1). By comparing results from these equations with finite element analysis and model footing tests, Wang, et al. concluded that, collapse footing pressure equations can be formulated by means of limit analysis but formulation are very complex so that computation of collapse footing pressure requires a numerical analysis through a nonlinear programming. Azam et al. [3] performed a finite element investigation on effect of void in homogenous and stratified soil on performance of strip foundation. The soil was idealized as an elastic perfectly plastic material that obeys the yield criterion of Drucker and Prager. They noticed that, the presence of a void under the footing, void location, depth to bedrock, and layer characteristics such as layer thickness and strength ratio effect on performance of shallow foundation. Khattab and Khalil [4] carried out a parametric study on the effect of cavity on stress distribution and settlement of C-Ø soil under foundation by using 2D and 3D finite element analysis. The parameters of study were shape (i.e. Circular, Ellipse, Loaf, and Square), size, location and depth of cavity. They noticed from their investigation that shape and volume of the cavity effect noticeably on settlement and concentration of stress under the footing for the chosen cavity sections especially when the cavity is situated at a depth less than twice the width of strip foundation or 1.5 times of the width/diameter of isolated square/circular footings. Peng, et al. [5] studied cavity effect on bearing capacity of footing foundation by finite element method. They investigate in the effect of cavity location in horizontal and vertical direction with cavity size 2.0×2.0 m^2 and found that the cavity effect on bearing capacity when it found in critical depth region, which is can be define as the depth beyond it the cavity effect on bearing capacity is vanished. From their investigation, concluded that the critical depth equal to three times of foundation width in vertical direction. Kiyosumi, et al. [6] used 1-g model and limit analysis to study the bearing capacity of strip foundation on calcareous sediment rocks containing voids. They noticed three failure mechanisms for a single void (1) bearing failure without void failure; (2) bearing failure with void failure; and (3) void failure without bearing failure, depending on the location of the void as well as the size of the void.

Cavities into soil mass are widely distributed in Al-Najaf city. These cavities exist in different structures which depend on the formation origin as follows [7]:

1- Artificial cavity due to the vault (oldest) building.

2- Natural cavity due to water flowing (the gypsum dissolve) or the extinction (dry set) of Al-Najaf Sea.

Based on field observations of Al-Najaf area, the cavities formed from gypsum dissolve are uniform or irregular in shape. The range of the cross-section diameter of the cavities are from (0.5 m) to (1.5 m) [7].

The present study deals with cavities formed from gypsum dissolve due to water flowing. Finite element method was employed by using PLAXIS 2D program to investigate the effect of cavity size and cavity location in horizontal (X) direction and vertical (Y) direction on bearing capacity of strip foundation rested on Al-Najaf soil. Cavities were assumed to be as square shapes with sizes (0.5×0.5, 1.0×1.0, and 1.5×1.5) m^2 to simulate cavities formed in Al-Najaf city.

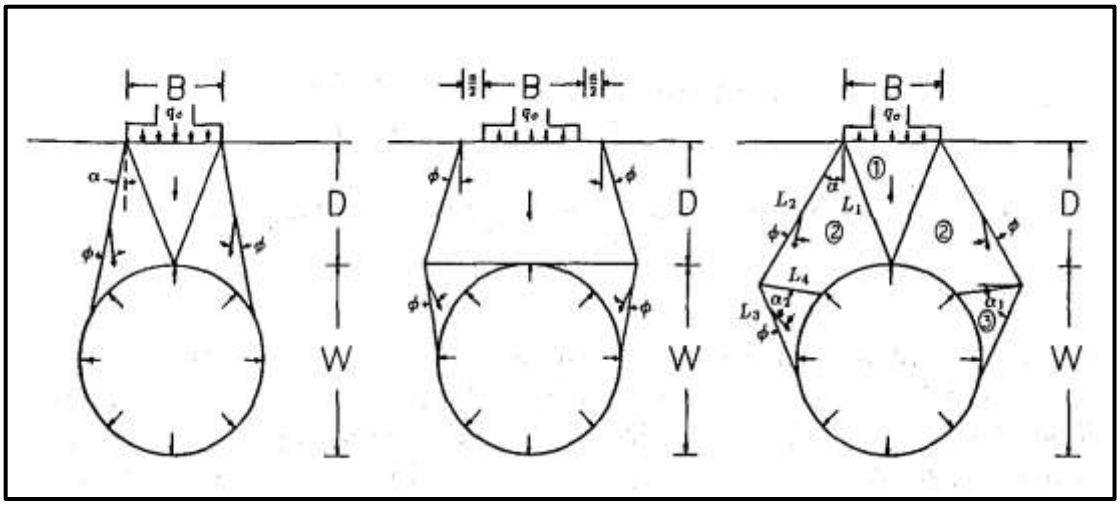

Figure (1): Failure mechanism of footing collapse[2]

Computer Program

PLAXS 2D V8.2 is a two dimensional finite element program developed mainly for dealing with soil mechanic problems and geotechnical engineering issues. The program has capability of modeling axi-symmetric and plane-strain problems, which are covering a wide range of geotechnical engineering problems. Several soil models are available in PLAXIS 2D supporting the linear elastic, elastic plastic, and elasto plastic behavior of soil. Four analyses types can be made in the program, which are plastic analysis, dynamic analysis, water flow, and c-phi reduction. The first one deals with static analysis of plane strain and axis-symmetric problems, while dynamic analysis deals with propagation of waves from machine foundation and earthquake shaking effect on soil mass. Water flow deals with flow of grounding water and consolidation phenomenon and c-phi reduction deals with calculation of factor of safety by reducing value of undrained cohesion and angle of internal friction until failure occurred. Two elements are available, which are 6-nodes and 15-nodes isoparametric triangular elements with 3 and 12 stress points respectively [8].

Validation of the Program

A validity test was conducted to check the capability of the program in estimating the stress-deformation curve for shallow foundation. The selected problem for validation from a numerical investigation carried out by Fattah, et al. [9] by SIGMA/W and SEEP/W programs

to study the behavior shallow foundation above saturated and unsaturated soil at Baghdad city. The problem involved a strip foundation with width equals to 1m constructed on saturated Bab Al- Muadham soil.

The boundaries of soil are taken as suggested by Fattah, et al. which are 20m width and 10m height.

Due to the symmetry of the problem only one half of the soil and foundation were modeled. Six-node triangular isoparametric elements with three stress points were used to develop the finite element analysis procedure. The nodal points along the centerline and those on the far right vertical boundary are assumed to move only in vertical direction, while the nodal points in the bottom of the boundary are assumed to be fixed in vertical and horizontal directions. The finite element mesh for verification problem is shown in Figure (2). The soil assumed to behave as elastic-perfectly plastic material considering Mohr-Coulomb failure criteria with properties adopted from Fattah et al. and shown in Table (1). Figure (3) shows the stress-deformation curve obtained from PLAXIS and stress-deformation curve obtained by Fattah, et al [9]. Comparison between these curves show excellent agreement are found between the two curves which support the capability of using PLAXIS program to perform numerical investigation on shallow foundation behavior. It worth mentioned here that, several trials of mesh sizes and types are used and excellent agreement is found with six-nodes elements and very fine mesh.

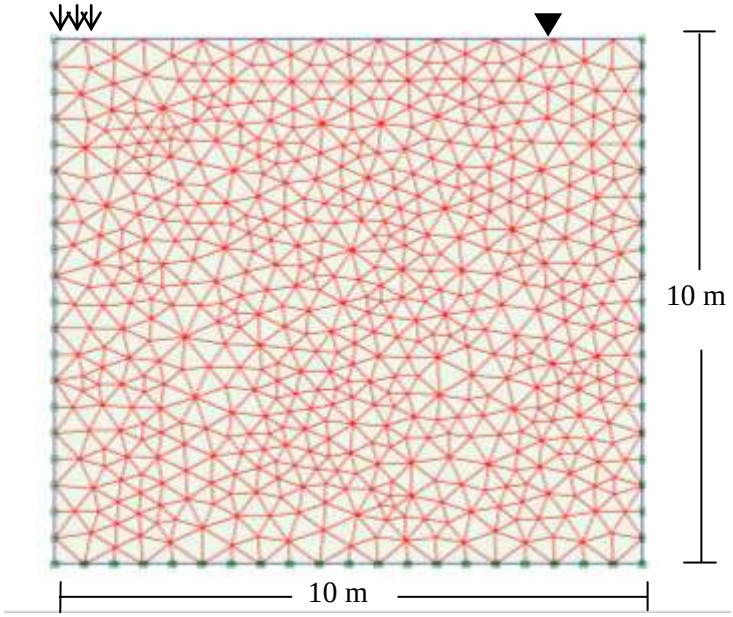

Figure (2): Finite element mesh of verification proble

Table (1): Material properties of Bab Al- Muadham soil [9]

Parameter	Value	Unit
Unit weight, γ	20.21	(kN/m^3)
Cohesion intercept, *Cu*	135	(kPa)
Poisson's ratio, υ	0.35	---
Modulus of elasticity, *E*	108000	(kPa)
Angle of internal friction, Ø	0	Degree

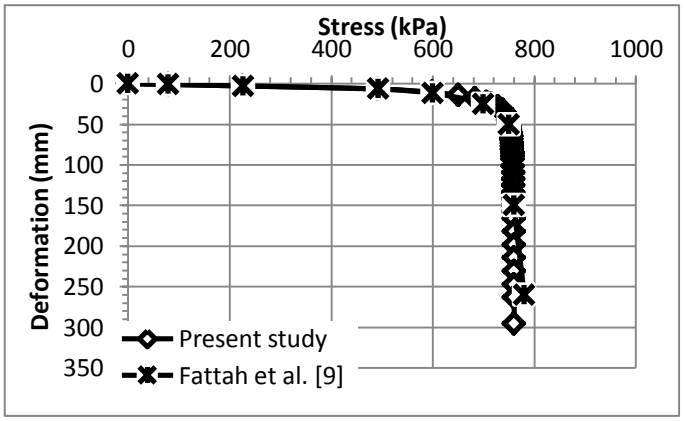

Figure (3): Comparison between stress-deformation curve obtained by Fattah et al., [9] and PLAXIS program

Finite Element Modeling and Material Properties

A flexible strip foundation with width of 3m was considered for plane strain modeling in PLAXIS 2D. The width and height of soil mass is taken equal to 30m and 20m respectively to eliminate boundary effect. Due to the symmetry of the problem only one half are considered in the finite element analysis. Six-node triangular isoparametric elements with three stress points were used to develop the finite element analysis procedure. Very fine mesh is used with total number of elements equal to 1171 elements with average area of element is 0.506 m^2 and this number varies slightly for each model. A uniformly distributed stress is placed on the flexible foundation and the settlement caused from this stress is recorded. The horizontal movement is restrained in right and left sides of boundary while horizontal and vertical movements are restrained in the bottom of the boundary. The water table is placed on the surface of the soil. The finite element mesh of the problem is shown in Figure (4).

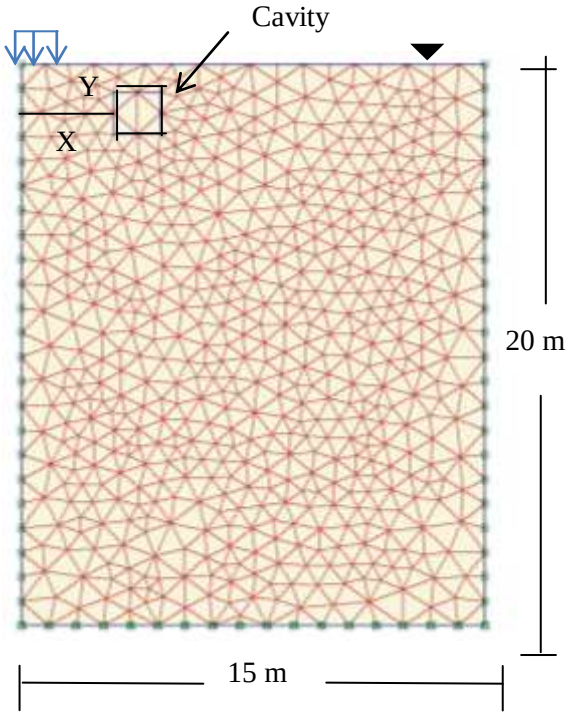

Figure (4): Finite element mesh used in the present study.

Al-Najaf gypseous soil is assumed to behave as elastic perfectly plastic with Mohr-Coulomb failure criterion. The properties of gypseous soil were adopted from Aziz [7], were evaluate it from a series of laboratory tests on undisturbed sample from Al-Jamia'a region in Al-Najaf city. Cohesion (*Cu*) and angle of internal friction (Ø) were obtained from direct shear test, while modulus of elasticity (*E*) obtained from small-scale plate loading test in laboratory. The material properties were shown in Table (2). The coefficient of at rest earth pressure (K_o) estimated by the equation given by Jacki [8]:

$$K_o = 1 - \sin Ø \qquad \ldots (1)$$

Table (2): Material properties of Al-Najaf Gypseous soil [7]

Parameter	Value	Unit
Unit weight, γ	19.4	(kN/m^3)
Cohesion intercept, *Cu*	21.0	(kPa)
Poisson's ratio, υ	0.35	---
Modulus of elasticity ,*E*	20125	(kPa)
Angle of internal friction, Ø	38.0	Degree

Results and Discussion

The load-deformation curve at center of foundation is obtained from finite element analysis of 24 models carried out during this study. From each load-deformation curve the bearing capacity is estimated. Method of Terzaghi [1] is used to estimate the bearing capacity. The method suggested that, the bearing capacity is defined as the stress required causing a deformation corresponding to 10% of the footing width. The case of strip foundation with no cavity is first modeled and analyzed, the bearing capacity is found to be equal to 233 kPa. Load-deformation curves for the cases considered in this study, as shown in Figure (5).

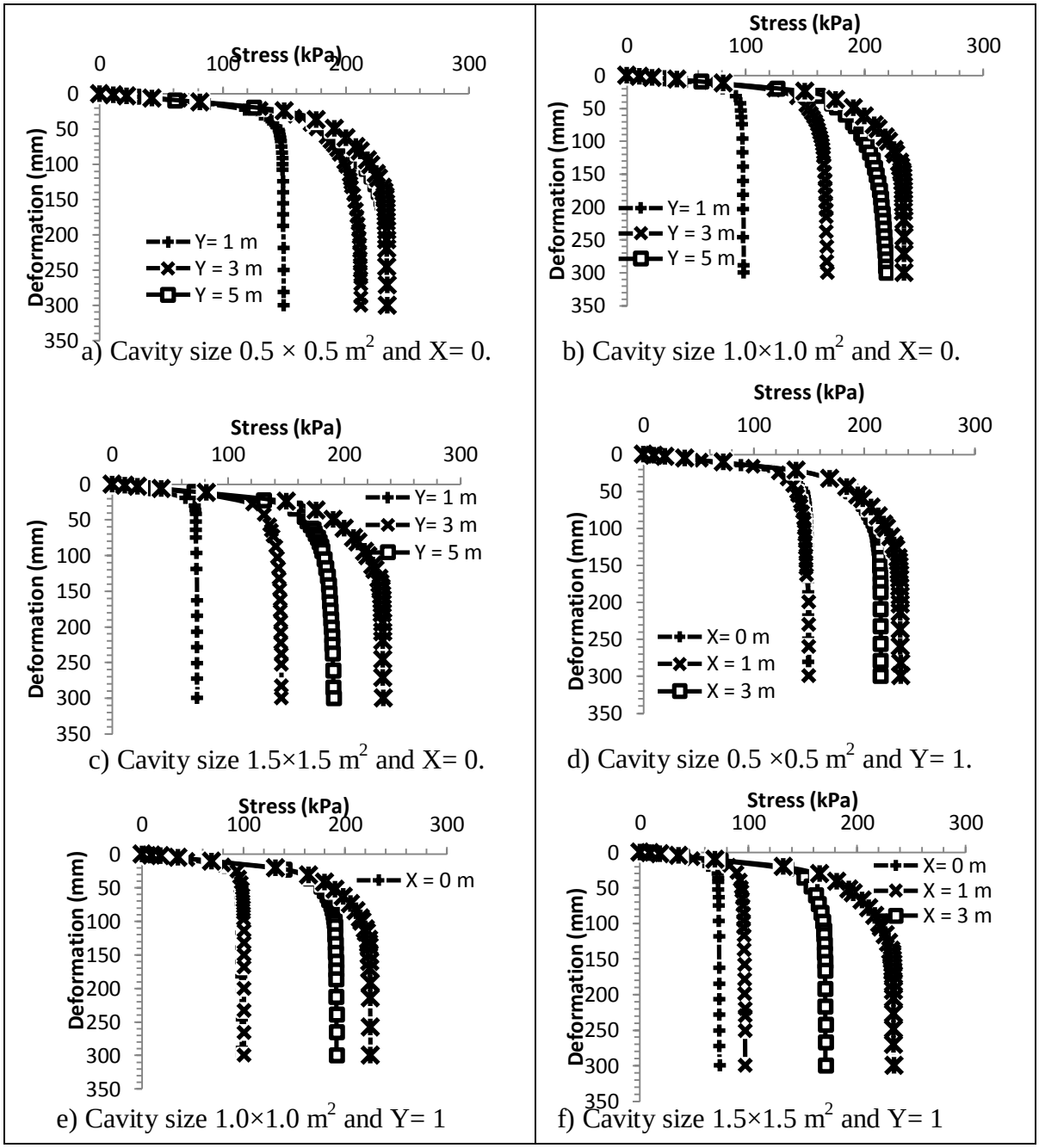

a) Cavity size 0.5 × 0.5 m^2 and X= 0.

b) Cavity size 1.0×1.0 m^2 and X= 0.

c) Cavity size 1.5×1.5 m^2 and X= 0.

d) Cavity size 0.5 ×0.5 m^2 and Y= 1.

e) Cavity size 1.0×1.0 m^2 and Y= 1

f) Cavity size 1.5×1.5 m^2 and Y= 1

Figure (5): Load-deformation curves for the cases considered in this st

Bearing Capacity Ratio (B.C.R), which is defined as the ratio of the footing ultimate bearing capacity with the presence of cavity to the footing ultimate bearing capacity without cavity, is obtained for each case to explain and discuss bearing capacity reduction due to cavity location as shown in the next sections.

Effect of Cavity Location on Bearing Capacity

To study the effect of cavity location, the relation between (B.C.R) and normalized horizontal distance between side of cavity and center of foundation (X/*B*), where B: is width of strip foundation, is drawn and shown in Figure (6-a) for different cavity sizes at depth of 1m. This Figure indicates that, the bearing capacity is significantly affect by cavity location and maximum effect on (B.C.R) occur at X/*B* = 0 with minimum reduction of bearing capacity by 36% for cavity size 0.5×0.5 m^2 and maximum reduction of bearing capacity by 69% for cavity size 1.5×1.5 m^2. It can be noticed also that, as X/*B* increase the cavity effect on bearing capacity decreases until it become insignificant at X/*B* 1.67 and this distance can be considered as critical horizontal distance beyond it there is no effect of cavity on bearing capacity of strip foundation.

Figure (6-b) shows the relation between (B.C.R) and normalized vertical distance between upper face of cavity and foundation (Y/*B*) for different cavity sizes with zero horizontal distance (i.e. X= 0). This Figure indicated that, reduction in (B.C.R) decrease as Y/*B* increase in a non-linear fashion for all cavity sizes and maximum reduction in bearing capacity reach 67 % for the case of cavity 1.5×1.5 m^2 at *Y*/*B* = 0.33. Form this Figure it can be also noticed that, for cavity size 0.5×0.5 m^2 the critical depth is reached at Y/*B* = 1.5 (i.e. 5m) while at this depth the cavity still effect on bearing capacity ratio for case of cavity sizes 1.0×1.0 m^2 and 1.5×1.5 m^2, where the reduction in bearing capacity is 11% and 21% for each size respectively and effect of these cavities diminish when reaching Y */B* = 2.3 (i.e. 6.9 m). These results are in agreement with closed form solution developed by Wang and Hsieh [2]. Also, these results are in agreement in trend with results of Peng, et al. [5], who noticed extend of critical depth to (3) times of foundation width due to cavity size 2.0×2.0 m^2.

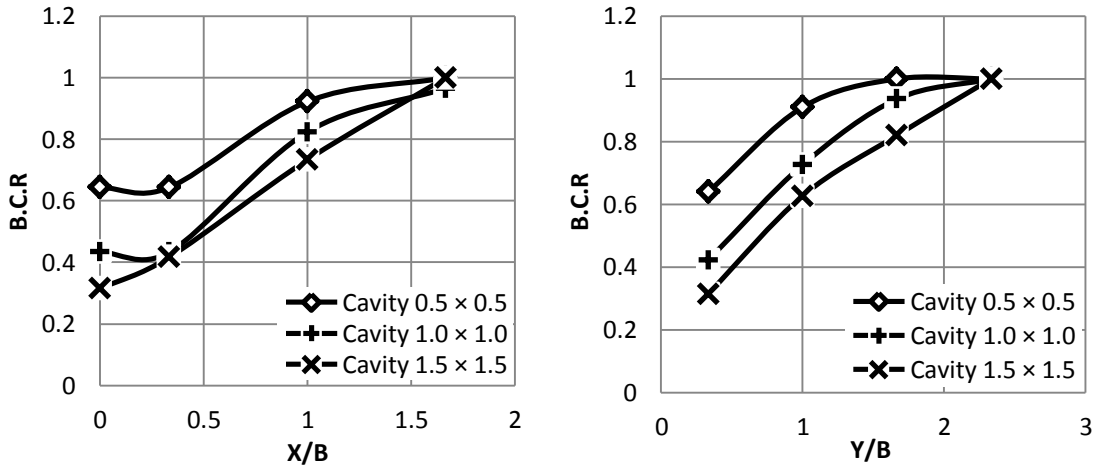

a) Y= 1 m b) X= 0 m

Figure (6): Effect of cavity location in horizontal and vertical directions on B.C.R

Effect of Cavity Size on bearing capacity

To evaluate effect of cavity size on bearing capacity, bearing capacity ratio relation with *B*/Ac, where Ac: area of cavity, is drawn and explains in Figure (7). It clearly obvious that, as cavity size increase the (B.C.R) decrease and the larger effect is for value of *Y*= 1 m and critical depth is dependent on cavity size as it shown for *B*/Ac 0.033, the critical depth is occurred at *Y*= 5m while for *B*/Ac 0.33 and 0.75 the critical depth is occurred at *Y*= 7 m.

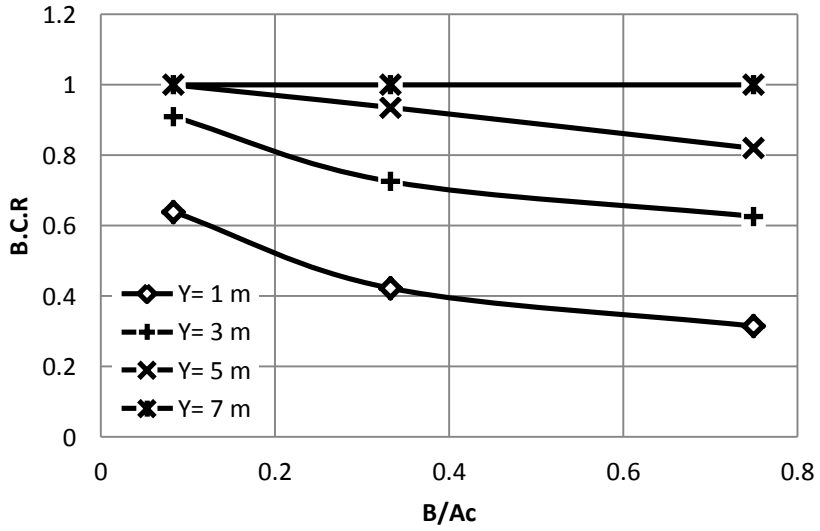

Figure (7): Effect of cavity size on B.C.R.

Failure mechanism

Presence of cavity may affect on failure mechanism of shallow foundation. In this study failure mechanism was investigated by inspection the displacement vector at ultimate stress (i.e. stress corresponding to displacement equal to 10% B). Figure (8) shows the displacement vector at ultimate state for selected cases where the cavity size and vertical depth changes. From this Figure it can be noticed that, the soil above cavity act as rigid column pushes towards the cavity and therefore the yielding developed toward cavity producing punching failure since there is no heave developed at the ground for all cases except for case of cavity size 0.5× 0.5 m and Y= 5m (Figure (8-f)). For this case, the yielding not developed toward the cavity due to small size of it and its location far away (below critical depth) from the ground surface and hence it will not affect on bearing capacity and the yielding developed below and on side of the foundation to form heave in the ground and producing general shear failure without cavity failure.

Figure (9) shows the displacement vector for some selected cases where the cavity size and location in horizontal direction changes. From this Figure it is clearly obvious that, three failure mechanisms developed depend upon size and location of cavity. In cases (a), (b) and (c) same failure mechanism discussed in Figure (8) are noticed and the yielding developed give indication about punching shear failure. In cases (e) and (f) the yielding developed towards the cavity and the type of failure is partial punching shear since there is small heave occurred except for the case (d) where the failure developed is general shear failure due to the small size of cavity (0.5×0.5 m^2) and its location beyond critical horizontal distance which make insignificant effect for it on failure mechanism.

From these observations it can be concluded that, size of cavity and its location have predominant effect on type of failure and development of displacement due to loading and three failure types can be noticed depend upon size of cavity and its location which are general shear failure, partial punching shear failure and punching shear failure.

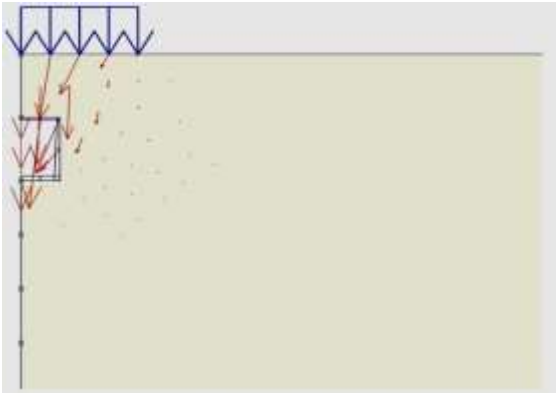

a) Cavity size 1.0×1.0 m^2, X=0.0 m and Y=1.0 m

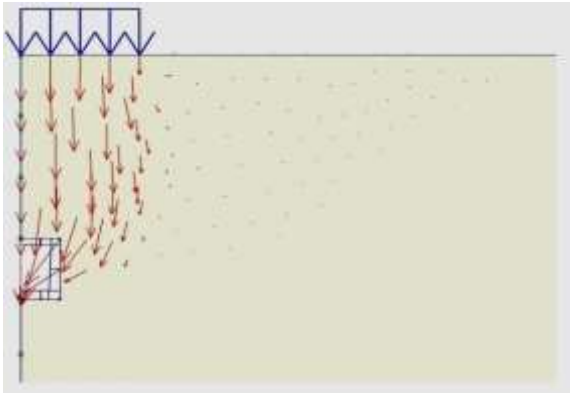

b) Cavity size 1.0×1.0 m^2, X=0.0 m and Y=3.0 m

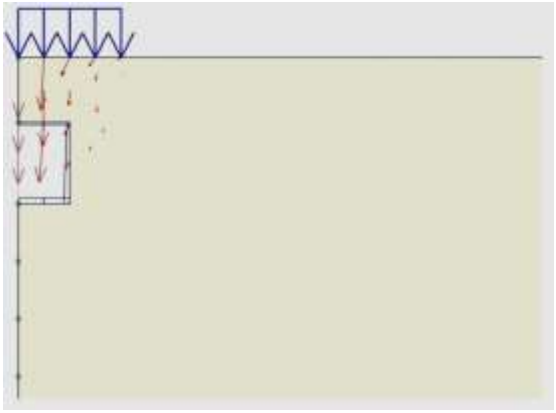

c) Cavity size 1.5×1.5 m^2, X=0.0 m and Y=1.0 m

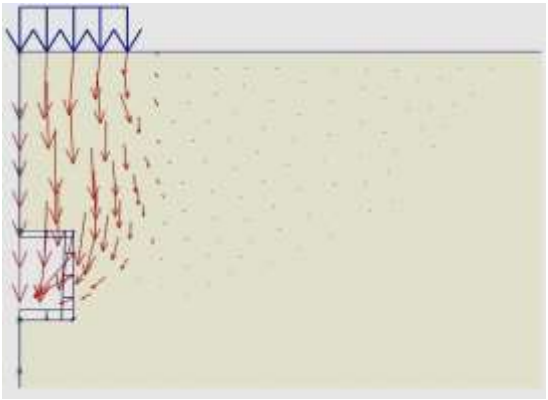

d) Cavity size 1.5×1.5 m^2, X=0.0 m and Y=3.0 m

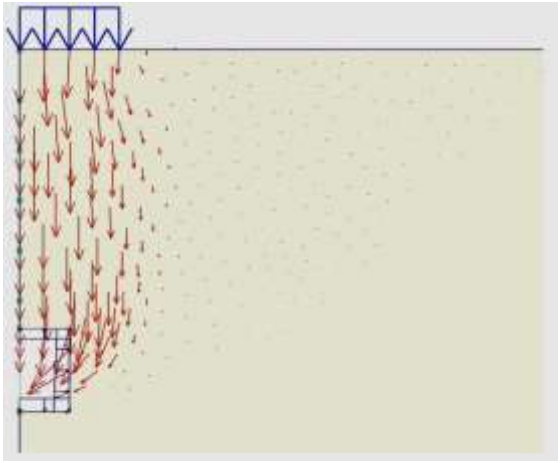

e) Cavity size 1.5×1.5 m^2, X=0.0 m and Y=5.0 m

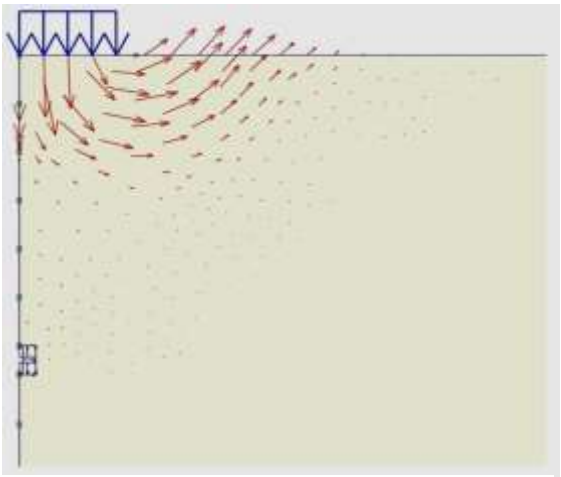

f) Cavity size 0.5×0.5 m^2, X=0.0 m and Y=5.0 m

Figure (8): Displacement vector at ultimate state for various cases

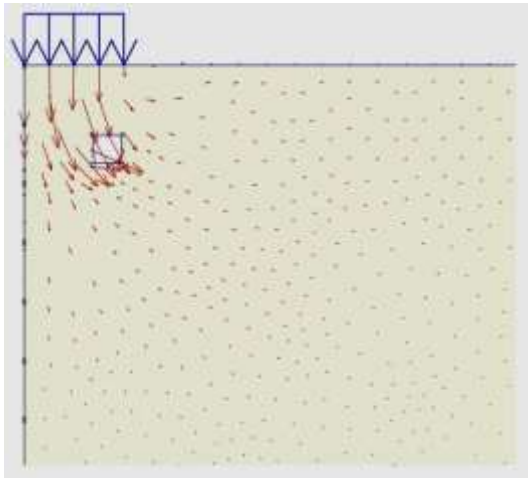

a) Cavity size 0.5×0.5 m^2, X=1.0 m and Y=1.0 m

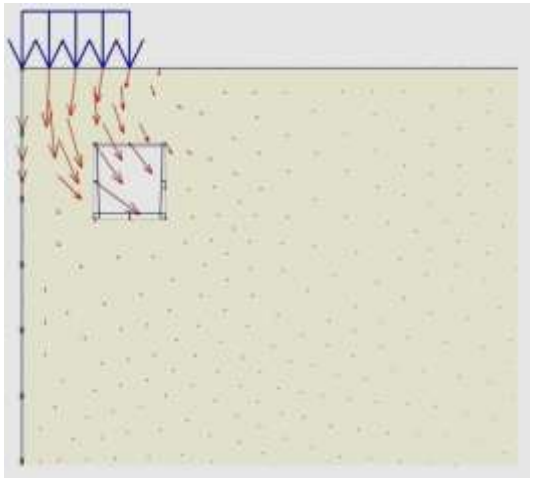

b) Cavity size 1.0×1.0 m^2, X=1.0 m and Y=1.0 m

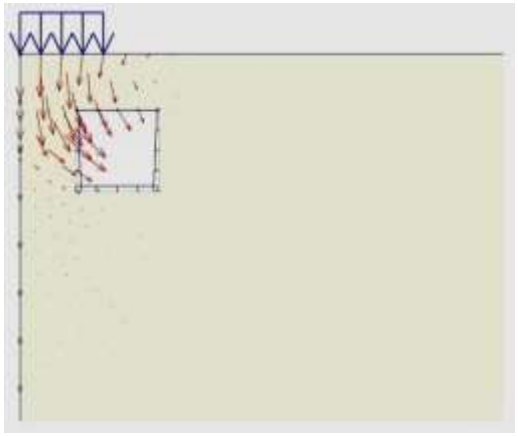

c) Cavity size 1.5×1.5 m^2, X=1.0 m and Y=1.0 m

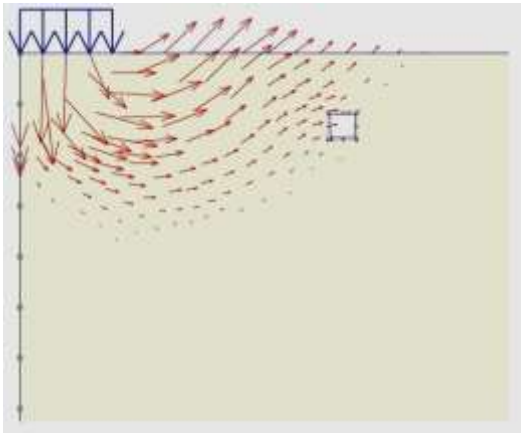

d) Cavity size 0.5×0.5 m^2, X=5.0 m and Y=1.0 m

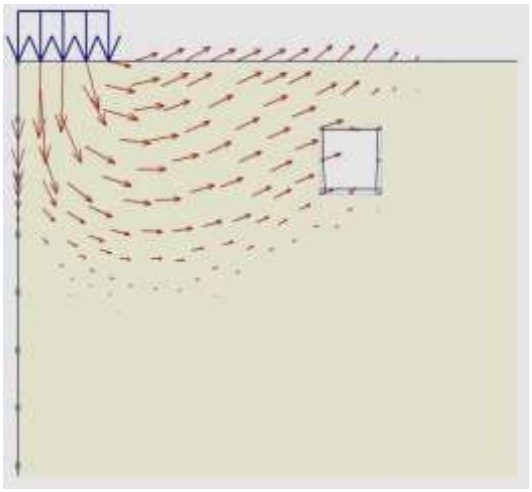

e) Cavity size 1.0×1.0 m^2, X=5.0 m and Y=1.0 m

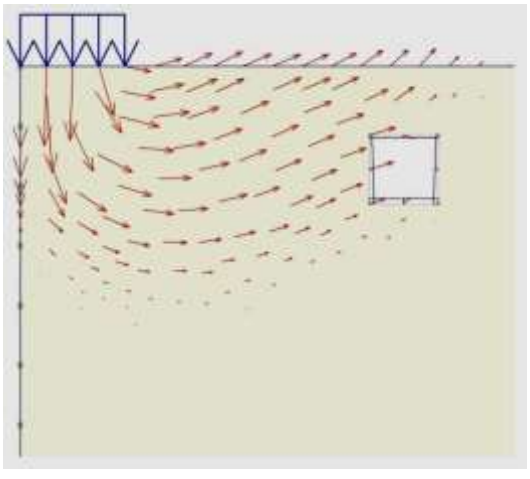

f) Cavity size 1.5×1.5 m^2, X=5.0 m and Y=1.0 m

Figure (9): Displacement vector at ultimate state for various cases

Conclusions

From the finite element investigation on behavior of strip foundation rested on Al-Najaf gypseous soil, the following conclusions can be made:

1- Presence of cavity affects strongly on failure mechanism of strip foundation and three failure types occurred due to cavity presence which are general shear failure, partial punching shear failure, and punching shear failure depend upon size and location of cavity in soil.
2- The presence of cavity reduces the bearing capacity with range of reduction between (3 % to 69 %) depends upon size and location of cavity.
3- The critical depth was found to be dependent on size of cavity and range from Y/B = 1.5 for cavity size 0.5×0.5 m^2 to Y/B = 2.33 for cavities with size 1.5×1.5 m^2 while the critical distance in X-direction was found to be approximately independent on cavity size and cavity effect diminish when it formed beyond X/B = 1.67.

References

[1] Terzaghi, k., "Theoretical Soil Mechanics", John Wily and Sons, New York, 1943,510 pp.
[2] Wang, M. C., and Hsieh, C. W., "Collapse Load of Strip Footing Above Circular Void", Journal of Geotechnical Engineering, ASCE, Vol. 133, No. 5, 1987, pp. 511-515.
[3] Azam, G., Hsieh, C. W., and Wang M. C., "Performance of Strip Footing on Stratified Soil Deposit With Void", Journal of Geotechnical Engineering, ASCE, Vol. 117, No. 5, 1991, pp. 511-515.
[4] Khattab, S. A., and Khalil, A. A., "Effect of Cavity on Stress Distribution and Settlement under Foundation", Al-Rafidain Engineering Journal, Vol. 17, No. 6, 2009, pp. 14-29. [In Arabic].
[5] Peng, F. L., Kiyosumi, M., Ohuchi M., and Kusakabe, O., "Cavity Effect on the Bearing Capacity of Footing Foundations and the Calculation Method", Under Ground Construction and Ground Movement, ASCE, GSP 155, 2006, pp. 50-57.
[6] Kiyosumi, M., Kusakabe, O., and Ohuchi, M., "Model Tests and Analyses of Bearing Capacity of Strip Footing on Stiff Ground with Voids", Journal of Geotechnical and Geoenvironmental Engineering, ASCE, Vol. 137, No. 4, 2011, pp. 363-375.
[7] Aziz, L.J., "Lateral Resistance of Single Pile Embedded in Sand with Cavities", Ph.D. Thesis, University of Technology, Iraq, 2007, 250 pp.
[8] Brinkgreve, R. B. J., "PLAXIS 2D Reference Manual Version 2", A.A. Balkema Publisher, Netherland, 2002, 180 pp.
[9] Fattah, M. Y., Ahmed, M. D., and Mohammed, H. A., "Behavior of Partially Saturated Cohesive Soil under Strip Footing", Journal of Engineering, No. 3, Vol. 19, 2013, pp. 298-311.

S - 24
Propagation of Plastic Zone around a Tunnel in Cohesive Soil

Mohammed Y. Fattah [(1)] Kais T. Shlash[(1)] Nahla M. Salim[(2)]

(1) Professor, Building and Construction Eng. Dept., University of Technology, Iraq.
(2) Assist. Professor, Building and Construction Eng. Dept., University of Technology, Iraq.

Abstract:

When a tunnel is excavated in fully saturated soil, two types of time dependent behaviours occur in the surrounding ground. The first comes from the intrinsic rate dependent characteristic of the material such as creep deformation or stress relaxation and the second is caused by the loss of apparent strength of material due to dissipation of the excessive pore water pressure in the surrounding ground. So the time dependent behaviour can be modelled using a coupled Biot consolidation finite element approach.

The finite element analyses were carried out using the modified Cam clay model for the soil. The excavation has been used together with transient effects through a fully coupled Biot formulation. The excavation technique together with Biot consolidation are implemented into finite element program named "Modf-CRISP" developed for the purpose of these analyses.

The main conclusions which can be drawn from the study are that the propagation of plastic zone will extend to the ground surface as the tunnel diameter increases and the depth of the tunnel decreases. From 64 cases studied and by using the program STATISTICA, a nonlinear estimation of the radius of plastic zone (Rp) at volume loss V_1 varying from 2% to 4% was obtained. The radius of the plastic zone increases as the volume loss increases. In reality, as soon as $\square_{max}$ reaches a certain volume loss, the lining must be applied to stop the propagation of plastic zone and control the amount of deformation caused by tunneling.

Keywords: Tunnel, cohesive soil, plastic zone, finite elements, volume loss.

تنامي المنطقة اللدنة حول نفق في تربة تماسكية

الخلاصة:

عندما يحفر نفق في تربة مشبعة كلي بالماء، يحدث نوعان من التصرف المعتمد على الزمن في التربة المحيطة: الأول يأتي من خاصية المادة الحقيقية المعتمدة على الزمن مثل تشوهات الزحف أو تراخي الاجهاد، أما الثاني فسببه فقدان المقاومة الظاهرية للمواد بسبب تصريف ضغط ماء المسام الاضافي في التربة المحيطة، و لذلك يمكن تمثيل السلوك المعتمد على الزمن للتربة بطريقة العناصر المحددة باعتماد الانضمام المزدوج حسب نظرية بيوت.

أجريت التحليلات بطريقة العناصر المحددة باستعمال نموذج كام المعدل للتربة. و قد مثلت الحفريات مع التأثيرات الزمنية من خلال التمثيل المزدوج لنظرية بيوت حيث تم تبني تقنية الحفر مع تظرية الانضمام لبيوت في برنامج العناصر المحددة المسمى "Modf-CRISP" الذي تم تطويره لهذه الدراسة.

ان أهم الاستنتاجات التي يمكن التوصل اليها من هذه الدراسة أن تنامي المنطقة اللدنة سوف يمتد الى سطح الأرض عند زيادة قطر النفق و تناقص عمقه. و من خلال 64 حالة تمت دراستها و باستعمال البرنامج STATISTICA تم الحصول على تخمين لاخطي لنصف قطر المنطقة اللدنة (Rp) عند خسارة حجمية V_1 تتراوح بين 2 و 4%. و وجد أن نصف قطر المنطقة اللدنة يزداد مع زيادة الخسارة الحجمية. و في الحقيقة، عندما تصل الازاحة $\square_{max}$ خسارة حجمية محددة، يجب أن يتم تنفيذ التبطين للنفق لوقف تنامي المنطقة اللدنة و السيطرة على التشوهات الناتجة عن حفر النفق.

Introduction:

The growth of many cities has resulted in the need for increased infrastructure. As an urban space becomes more limited, subsurface structures such as tunnels are becoming more efficient in providing the required infrastructure. In 1863, the first underground railway line was opened in London. Since then, over 100 cities worldwide have implemented underground transport systems and over 50% of them are undergoing development or expansion (Hellawell et al., 2001).

Many methods have been used to study the behaviour of soils due to tunneling. These are basically classified as experimental and theoretical approaches. The experimental approach includes model and field studies on existing tunnels while theoretical approach includes analytical and numerical solution.

The construction of a tunnel inevitably leads to a large amount of soil to be excavated than to be replaced by the volume of the tunnel. The amount of this overexcavation is quantified as the volume loss which is the ratio between the differences between volumes of excavated soil and the tunnel volume (defined by the tunnel's outer diameter) over the tunnel volume. It is a measure of the total ground disturbance that causes the settlement trough at the surface and on undrained condition (Bloodworth, 2002).

Different methods are used to calculate the volume loss. One of these methods which were adopted by Augard (1997) suggests a procedure to calculate a volume loss due to tunneling. The net volume of the surface trough is approximately equal to the volume loss at the tunnel in most ground conditions and since the ground response is at constant volume (i.e. undrained), the area below the Gaussians function is by definitions equal to 1 as it represents the probability that variable x has the value between -∞ to ∞. The volume per unit length of the surface settlement trough given as:

$$V_s = \int_{-\infty}^{\infty} \delta_v \, dx \qquad (1)$$

$$V_s = \sqrt{2\pi}\, i\, \delta_{max} \qquad (2)$$

where:
Vs: the volume of the settlement trough per unit length.

Since it is assumed that the soil deforms under a constant volume, then it can be equated to the extra amount of soil removed in excavation over that required for tunnel lining. It is common to specify this excess volume as a proportion of the theoretical tunnel volume (per unit length).

$$V_L = \frac{V_s}{V_o} x 100 \qquad (3)$$

Vo: is the volume required to construct the tunnel (per unit length).

Attewell and Selby (1989), attributed the ground losses to the following:

1. Stress relaxation that causes plastic flow of soil into the newly dug unsupported tunnel, with the consequence that slow or interrupted shield progress results in greater face take.

2. The diameter of the permanent tunnel lining is smaller than that of the shield, particularly if the shield has a bead for case of steerage.

These losses encourage radial soil movements into the tunnel void. Their study showed that the majority of tunnel in cohesive soil show settlement below 50 mm, but there are six cases of tunneling in clay soils that have resulted in large time dependent settlement of 40 mm to 250 mm. All of the cases (two in Mexico and four in the U.K.) involve tunnels having diameter of approximately 2.7 m.

It was also concluded that the long term settlements are about 2.5 times greater than the short term settlements and the width of the influence zone may also be increased by the consolidation mechanics.

Ezzeldine (1999), used the finite element analysis to study the expected ground movement due to the tunnel construction and compared it with ground control measures imposed during the construction process. The analysis was carried out at the part of line from Khalafawy to Saint- Therese station. The study was based on an available documentation related to the ground construction to emulate the most probable model to be adopted. A nonlinear stress–strain constitutive model was adopted to represent the ground surrounding the tunnel. The results were predicted in terms of the maximum displacement at the ground surface and the slope of the displacement trough. It was shown that, the settlement trough extends to about 5 diameters from the tunnel centerline and also, the maximum slope of displacement varies between (1/1500) to (1/500) and the maximum point of maximum slope takes place at about one of the diameter from the tunnel centerline.

Potts and Zdravkovic (2001), summarized a parametric study on the intermediate and long-term consolidation in London clay in terms of maximum surface settlement. The works were carried out by the Geotechnical Consulting Group in 1993. The parametric study investigated the influence of tunnel diameter, depth to tunnel axis, initial and long term pore water pressure distributions and pore water pressures boundary conditions at the tunnel. Two tunnel diameters were used 6.5 m diameter with z =15 m and 25 m and a station tunnel (diameter =12 m) with an axis depth of 25 m. The ground water was kept at a depth of 5 m below the ground surface. Two distinct pore water pressure boundary conditions were used at the tunnel perimeter during consolidation. The first one modelled a fully permeable tunnel lining using special pore water pressure boundary condition. This is due to the fact that excavation of tunnel causes suction in the surrounding ground. If zero pore water pressure conditions were prescribed at the tunnel boundary, the tunnel would in effect act as a source of water and the surrounding soil would obtain water from within the tunnel, Figure (1a). This is clearly unrealistic. While there are suctions around the tunnel, the appropriate condition at the tunnel boundary should be one of no flow Figure (1b). Once some of the suction has dissipated, by migrating of water from the surrounding ground, there are two options. In the first the tunnel lining is assumed to be impermeable and therefore the no flow condition should be maintained. This allows positive pore water pressure to build up around the tunnel. The second option is to model the lining as permeable. In this case, it is not possible to have positive pore water pressure acting on the tunnel lining.

Definition of the Basic Problem:

The present work has been carried out to study the parameters that influence the tunnel behavior during construction and after a long time.

The parametric studies in this paper investigate the influence of the following factors:

- Tunnel's diameter, D_{tunnel}.
- Depth to tunnel axis, Z_{tunnel}.

The propagation of plastic zone around the tunnel and pore water pressure were also investigated.

Figure (2) shows the geometric layout, and the soil profile used in the parametric study. The material properties for soil adopted in the analysis, are shown in Table (1). The properties were collected from reports of Baghdad Metro line in addition to those of NCCLR (1987). The modified Cam clay MCC model is used to trace the soil behavior.

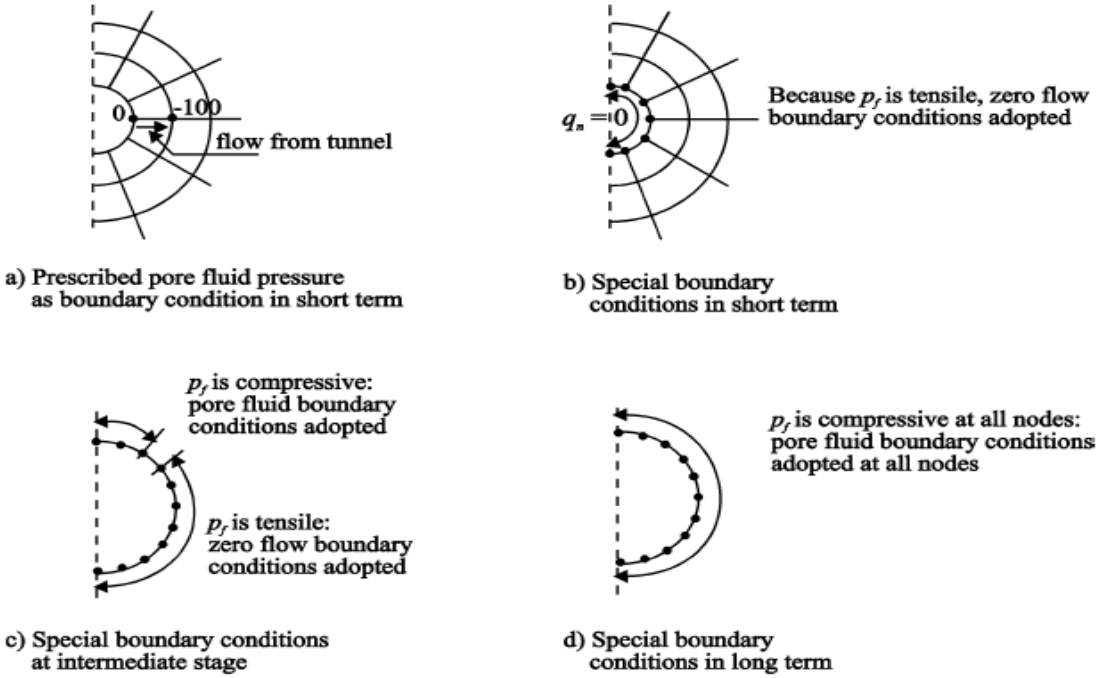

Fig. 1: Special pore pressure boundary condition for the modeling of tunnel construction (Potts and Zdravkovic, 2001).

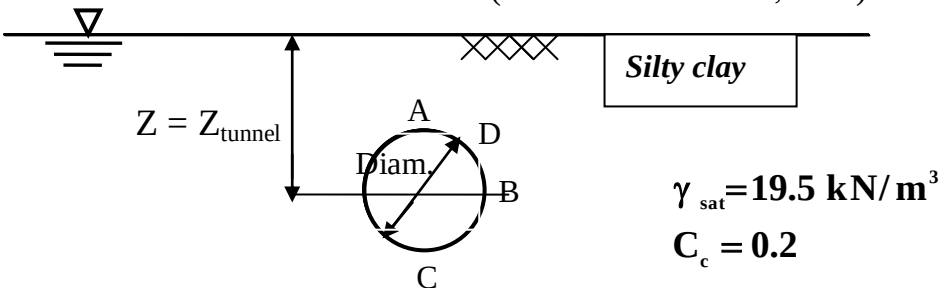

Fig. 2: Soil profile used in the parametric study.

Determination of the Elastic Young's Modulus (Es):

The methods for the determination of the elastic Young's modulus E are still very ambiguous. There are several methods used in estimation of E. In the past, these could be divided into two main groups, namely the dynamic and static Young's modulus. The researchers have in the past realized that the difference is, in fact due to the strain level dependency characteristic of the soil. Namely, the conventional static E is conventionally measured at much larger strain levels that are encountered in the dynamic measurements (Tatsuoka and Shibuya, 1992).

Therefore, in the present study, conventionally proposed empirical equation on the relation between the Young's modulus and the SPT N-value and the undrained shear strength Su, are adopted. For cohesive soil, the modulus of elasticity, E, could be obtained from simple empirical correlation between E and the undrained shear strength, Su as follows (Bowles, 1996):

For normally consolidated to lightly over consolidated clay:

E = (750 to 1200) Su (kPa) (4)

For heavily over consolidated clay:

E = (1500 to 2000) Su (kPa) (5)

where Su is the undrained shear strength.

Table 1: Soil properties used in the parametric study (Salim, 2006).

Critical State Parameters	□	*0.0866*
	□	*0.00864*
	M	*1.2*
Permeability m/ sec	K_x	$10*10^{-9}$
	k_y	$10*10^{-9}$
Modulus of elasticity (kPa)	Es	*24000*
Poisson's ratio	□	*0.3*

Note: □ = 30^o.

where: λ : the slope of the normal consolidation line,
κ : the slope of the swelling line, and
M : gradient of the critical state line.

Finite Element Discretization:

The elements used to model the plane strain problem are eight-node isoparametric solid quadrilateral elements coupled to four node fluid elements. Nodes along the horizontal plane are constrained against vertical motion, while those along the vertical plane of symmetry are constrained against horizontal motion. The pore water pressures are fixed at top of the soil in addition to the side boundaries. The ground water table is located at the ground surface.

The following supposed conditions are used:

1. The boundary condition is that there is only horizontal restriction on the left and right vertical sides, and there are both horizontal and vertical restrictions at the bottom boundary.

2. The problem boundaries are assumed to be impermeable on both vertical sides in addition to the bottom boundary. The water table is at the ground surface.

Symmetry is assumed along the tunnel vertical axis containing the crown, spring line and invert. This situation makes it possible to mesh just one half of the entire geometry. The excavation process is assumed to occur under plane strain conditions since that the effect of advancing the tunnel at the face is not considered in this analysis. In linear elastic analysis, the excavation process can be applied in a single instantaneous step. In non-linear stress-strain relationship, the program CRISP allows the effect of element removal to be spread over several increments in an "increment block". Element stiffnesses are always removed in the first increment of a block, but the associated loads are distributed over all the increments in the block. The excavation process was assumed to last for two hours per meter length and in nonlinear analysis, it was spread over fifty increments.

Finite elements for consolidation analysis:

The equations of equilibrium are:

$$\frac{\partial \sigma_X}{\partial X} + \frac{\partial \tau_{ZX}}{\partial Z} = w_x$$
$$\frac{\partial \tau_{XZ}}{\partial X} + \frac{\partial \sigma_Z}{\partial Z} = w_z \qquad (6)$$

where w_x, and w_z are the body forces per unit volume in the direction of the x and z axes, respectively. The differential equation of continuity is:

$$\frac{k_x}{\gamma_w}\cdot\frac{\partial^2 u}{\partial X^2} + \frac{k_z}{\gamma_w}\cdot\frac{\partial^2}{\partial Z^2} + \frac{\partial v}{\partial t} = 0 \qquad (7)$$

Galerkin's weighted residual method is applied to the equilibrium equations and to the continuity equation in turn. It was shown that for the equilibrium equations the resulting equations are equivalent to the principle of virtual work as shown in the following equations:

Equations (6) are multiplied by arbitrary scalar functions h and v, added together and integrated over the area of the continuum:

$$\int_A \left[h\left[\frac{\partial \sigma_x}{\partial x} + \frac{\partial \tau_{zx}}{\partial z} - wx \right] + v\left[\frac{\partial \tau_{zx}}{\partial x} + \frac{\partial \sigma_z}{\partial z} - w_z \right] \right] d(area) = 0 \qquad (8)$$

Integration of the equation by using Sienkiewicz-Green theorem will give the following equation:

Integration of the first term in equation (8) will be as follows:

$$\int_A h\frac{\partial \sigma_x}{\partial x}\partial x \partial z = -\int_A \frac{\partial h}{\partial x}\sigma_x \, dx\, dz + \int_s h\sigma_x n_x \, dS. \qquad (9)$$

So with the integration of all terms on equation (8), the principle of virtual work for a continuum is obtained:

$$\int \varepsilon^T \sigma \, d(vol) = \int d^T \pi d(area) + \int d^T w d(vol). \qquad (10)$$

Performing the same kind of operation on the continuity equation yields another "virtual principle". The first step is to multiply the continuity equation by an arbitrary scalar which can vary with x and z.

$$\int u\left[-\frac{K_x}{\gamma_w}.\frac{\partial^2 u}{\partial x^2}+\frac{k_z}{\gamma_w}.\frac{\partial^2 v}{\partial z^2}+\frac{\partial v}{\partial t}-\right]d(vol)=0 \qquad (11)$$

Sienkiewicz-Green theorem is now applied to this equation:

$$-\int_v \frac{k_x}{\gamma_w}\frac{\partial u}{\partial x}\frac{\partial u}{\partial x}+\frac{k_z}{\gamma_w}\frac{\partial u}{\partial z}\frac{\partial u}{\partial z}d(vol)-\int uv_n d(area)+\int_v u\frac{\partial v}{\partial t}d(vol)=0 \qquad (12)$$

where:

v_n : the artificial seepage velocity normal to the boundary.

When the finite element discretization is applied to the problem the displacements are assumed to vary over a finite element mesh according to:

$$d = Na \qquad (13)$$

and the excess pore pressures are assumed to vary over the same mesh according to:

$$u = Nb \qquad (14)$$

The virtual excess pore pressure is assumed to vary according to the same shape functions as the excess pore pressure:

$$\varepsilon = Ba \qquad (15)$$

and the gradient of the excess pore pressure is given by

$$\begin{Bmatrix}\frac{\partial u}{\partial x}\\ \frac{\partial u}{\partial Z}\end{Bmatrix} = Eb \qquad (16)$$

where the terms of the E matrix are obtained by differentiating N. A vector m is defined:

$$m=\begin{Bmatrix}1\\1\\0\end{Bmatrix} \qquad (17)$$

such that $\sigma = \sigma' + mu$,

and $v = m^T \varepsilon$

Substituting into equation (3.32) results in:

$$b^T\int_v \overline{N}^T m^T B\, d(vol)\,\frac{d(a)}{dt}-b^T\int_v E^T k\, E/\gamma_w d\,(vol)b = b^T\int_s \overline{N}^T v_n d(area) \qquad (18)$$

where k is a permeability matrix:

$$\begin{bmatrix}k_x & o\\ o & k_z\end{bmatrix} \qquad (19)$$

The virtual pore pressure can be cancelled from this equation, and the substitutions:

$$L = \int_v B^T m N d(vol)$$
$$\varphi = \int E^T k E / \gamma_w d(vol) \quad (20)$$

are made to obtain:

$$L^T \frac{d(a)}{dt} - \varphi b = \int_v N^T v_n d(area) \quad (21)$$

Integrate with respect to time:

$$\int_t^{t+\Delta t} L^T \frac{d(a)}{dt} dt - \varphi \int_t^{t+\Delta t} b dt = \int_t^{t+\Delta t} N^T v_n d(area) dt. \quad (22)$$

in performing this integration, the approximation is made:

$$\int_t^{t+\Delta t} \int_s N^T \; v_n d(area) dt. \quad (23)$$

In performing this integration, the approximation is made:

$$\int_t^{t+\Delta t} b dt = \{(1-\theta) b_1 + \theta b_2 \Delta t\} \quad (24)$$

where

$$b_1 = b(t)$$
$$b_2 = b(t + \Delta t)$$

The value of θ defines the way that b varies during the time interval. A similar approximation is made for integration of v_n, the equation will be:

$$L^T [a]_t^{t+\Delta t} - \varphi \{(1-\theta) b_1 + \theta b_2\} \Delta t = \int N^T \{(1-\theta) v_{n1} + \theta v_{n2}\} \Delta t \quad (25)$$

Booker and Small, (1975), consider the stability of integration schemes using different values of θ and show for stability, $\theta \geq \frac{1}{2}$. When one uses $\theta = 1$ and defining $\Delta a = a(t + \Delta t) - a(t)$ and $\Delta b = b_2 - b_1$ the equation will be:

$$L^T \Delta a - \varphi \Delta t . \Delta b = \varphi \Delta t . b_1 + \int_s N^T v_{n2} \Delta t d(area) \quad (26)$$

Using the virtual work principle for effective stresses yields:

$$\Delta \sigma = \Delta \sigma' + m \Delta u$$

Using this relation and making usual finite element substitution and therefore (noting that $\Delta u = \Delta \bar{u}$) give

$$\Delta \sigma = \Delta \sigma' + m \Delta u' \quad (27)$$

Using this relation, and making the usual finite element substitutions yield:

$$\left.\begin{aligned} \Delta\varepsilon &= B.\Delta a, \\ \overset{*}{d} &= N.a \\ \Delta\bar{u} &= \bar{N}.\Delta b \end{aligned}\right\} \quad (28)$$

to obtain

$$K\Delta a + L\Delta b = \int_s N^T \Delta T d(\text{area}) \quad (29)$$

where $K = \int B^T D B \, d(\text{vol})$ (30)

The equations can be written as (Zienkiewicz and Taylor, 2005):

$$\begin{bmatrix} K & L \\ L^T & -\varphi\Delta t \end{bmatrix} \begin{bmatrix} \Delta a \\ \Delta b \end{bmatrix} = \begin{bmatrix} \Delta r_1 \\ \Delta r_2 \end{bmatrix} \quad (31)$$

Points of Interest When Analyzing a Tunnel:

Figure (2) shows the location of points to be focused upon in the analysis:

1) The tunnel crown is the topmost point of the tunnel section (point A).
2) The spring line refers to point located at the side wall of the tunnel (point B).
3) The invert refers to the bottom of the tunnel section (point C).
4) The shoulder is referred to by point (D).

Surface Settlement due to Tunneling:

The magnitude of movements generally depends on the soil type, ground water condition, construction method, tunnel dimensions and location. Ground movements around tunnels lead to surface subsidence. The magnitude and distribution of these settlements were studied extensively by previous researchers (Clough and Shmidt, 1981, O'Reilly and New, 1982, Rankin, 1988, and Mair and Taylor, 1993).

Tunnel construction inevitably leads to displacements in the soil, and these may lead to damage to nearby structures. These ground movements are associated with two mechanisms:

a) Radial movements of the soil as a result of cutting during tunnel construction.
b) Ground movements associated with incomplete support of the tunnel face.

Effective Stress Paths around the Tunnel:

The stress paths of various points (located at the periphery of the excavation) are obtained by the finite element analysis using MCC constitutive model and are shown in Figures 3, 4 and 5.

In general, it can be noticed that:

- all effective stress paths start from the normal consolidated line.
- at the crown and invert, excavation produces a decrease in vertical stress, following an elastic unloading path up to the isotropic state where the principal directions are

inverted. Then, the vertical effective stress continues to decrease and the path reaches the critical state line (failure). After this stage, there is an increase in tangential stress (horizontal effective stress σ_x' at the crown) which causes rebound of the soil that increases the $\mathbf{P'}$ values and increase in q values takes place as shown in Figure 3.

Figure 4 shows the stress path at the spring line, the results follow the same trend of the stress path at the crown but it reaches the critical state line at $\mathbf{P'}$ = 100 kPa, which is higher than that at the crown.

Figure 5 presents the stress path below the invert for D = 7 m, and Z = 18 m. The same path as that at the crown and spring line is followed except that the initial $\mathbf{P'}$ value at the invert is higher than those for the spring line and the crown, so the stress path starts with 225 kPa and then due to unloading, $\mathbf{P'}$ is reduced while q increases and reaches the critical state line at $\mathbf{P'}$ = 130 kPa and q = 150 kPa. After the critical state, the soil exhibits a slow increase in $\mathbf{P'}$ value while q increases dramatically and reaches the yield surface.

Comparisons of stress paths at the crown, spring line and invert are presented in Figures 6, 7 and 8, respectively using D = 5 m and 7 m at a depth of Z=18 m.
Figure 7 shows that the element above the crown with D = 7 m reaches the critical state line before the element with D = 5 m, while Figure 8 shows that the element below the invert with tunnel diameter of 5 m reaches the critical state line before the element with D = 7 m.

Figure 8 shows that the diameter of the tunnel has no significant effect on the element at the spring line. Both elements for tunnel diameter = 5 m and 7 m reach the critical state line at the same time, except that the element with tunnel diameter of 7 m will be very close to the critical state line after failure while it will be far away for the element with tunnel diameter of 5 m.

Propagation of Plastic Zone due to Tunneling:

As the stresses induced by the opening exceed the yield strength of the soil, a circular yield zone of radius Rp, develops around the tunnel while the soil outside the yield zone remains elastic. The results of the propagation of plastic zone are shown through Tables 2, 3, 4 and 5.

Table 2 illustrates the state of soil elements around the tunnel reaching the yield state using different undrained shear strengths and different tunnel diameters and depths.

It can be concluded that the plastic zone can be represented by a circle bounding the tunnel with a diameter which increases as the tunnel diameter increases and as the tunnel depth decreases, (except when the tunnel diameter is 12 m, at which the propagation of plastic zone extends to the surface with the line bounding the tunnel of slope). The plastic zone diameter also increases as the tunnel depth increases. This comes from the fact that the soil elements near the tunnel reach the yield state first and then the stress will gradually transfer to the adjacent elements. Also, as the undrained shear strength is reduced, the propagation of plastic zone will extend to the surface and causes undesirable high surface subsidence.

Table 3 shows that all the values of shear strength reveal the same trend. The plastic zone is a circle bounding the tunnel and this propagation will extend to the surface as the tunnel's diameter increases (i.e D = 12 m). All the results for this case extend to the surface; while all the cases with tunnel diameter of 3 m show that the plastic zone is a circle with diameter changes depending on the depth of the tunnel and the undrained shear strength.

Deere et al. (1969) showed that the radius of the plastic region, Rp in the undrained state can be represented by the following equation.

$$R_p = \mathbf{a}\ \mathbf{exp}\left(\frac{\sigma_{v0} - p_i - S_u}{2S_u}\right) \qquad (32)$$

where

σ_{vo}: the total stress at the tunnel depth,

P_i : the total internal pressure,

a : the radius of the tunnel, and

S_u : the undrained shear strength.

Comparison of the results of the present study shown in Table 3 and the results using Deer's equation shown in Table 4, reveals that there is a good agreement when the tunnel diameter equals to 3 m and at a depth of 25 m and with Su =200 kPa. There is also good agreement at higher depths and higher tunnel diameters especially at low undrained shear strength. Both results indicate that the plastic zone extends to the surface.

Salencon (1969) showed that the radius of the plastic region, R_p in the undrained state can be represented as follows:

$$R_p = a\left\{\frac{(1-\sin\varphi)(\sigma_v + c\cot\varphi)}{p_i + c\cot\varphi}\right\}^{\frac{1}{Kp-1}} \qquad (33)$$

where

a is the radius of tunnel shaft,

σ_v is the original (pre-tunneling) stress field at the tunnel level, and

k_P is the passive earth pressure coefficient.

Table 4 shows the variation of the plastic zone using Salencon's equation. By comparing the results of the propagation of plastic zone using the finite element analysis with the results of Salencon equation, it can be noticed that there is no agreement between the results.

The conclusion is that for shallow tunnels with C/D <1.0 (C = Z-D/2), the failure envelope is cut by the surface for all values of Su and causes secondary failure at the surface, whereas for deeper tunnels, the failure envelope closes before reaching the ground surface.

From this point, the stability of the tunnel face must be based on a certain design criterion that meets the site requirements. This criterion can be based on two different concepts.

a) Yielding concept.
b) Deformation concept.

The yielding concept represents the most critical situation, where the determined support pressure can be defined as "the pressure below which deformation at the tunnel face begins to rapidly increase due to yielding".

This pressure should also ensure that the plastic region at the tunnel face does not extend to the ground surface because the yield criterion provides a critical stability condition; a safety factor must be introduced.
The other criterion is based on the deformation resulting from the yielding concept that exceeds the acceptable limits imposed by the site conditions.

Volume Loss:

The construction of a tunnel leads to a larger amount of soil to be excavated than to be replaced by the volume of the tunnel. The amount of this overexcavation is quantified by the volume loss V_1. The volume loss is a measure of the total ground disturbance. It causes the settlement trough at the surface to be in undrained condition, the volume of this settlement trough is equal to V_1.
Several relations have been proposed to estimate the V_1 from the stability ratio N (which is the ratio between the difference of the natural pressure and the pressure applied to the tunnel face). Lake et al, (1992), confirmed that if N is less than 2, the response is likely to be elastic. Between N=2 and 4, local plastic zones develop around the tunnel while between 4 and 6 plastic yielding is leading to face instability. Lake et al., (1992) summarized the relation between V_1 for London clay and the conclusion drawn is that for stability ratio of N=2 this causes the volume loss to be between (1.5%) and (3%).
In the present study, the radius of the plastic zone is studied at different values of the volume loss which can vary between 2% and 4% of the total volume of the tunnel.
In order to obtain a certain volume loss V_1, the following equation will be used (Augard, 1997):

$$V_l = \frac{Vs}{\pi \frac{D^2}{4}} \tag{34}$$

where

$$Vs = \int_{-\infty}^{+\infty} \delta v \, dx = \sqrt{2\pi}\, i\, \delta v \max \tag{35}$$

Vs: the volume of settlement trough per unit length.
D: the outer tunnel diameter.

The value of δ_{vmax} is evaluated at different values of volume loss and the radius of the plastic zone can be found. Table 5 presents some the results of the radius of plastic zone at different values of the volume loss.

Table 5 shows that the variation of the radius of the plastic zone is affected by many factors such as, the undrained shear strength, Su, and the tunnel diameter and depth. But in general, the radius of plastic zone increases as the volume loss increased. In reality, as soon as δ_{vmax} reaches a certain volume loss, the lining must be applied to stop the propagation of plastic zone and control the amount of deformation caused by tunneling.

Table 2: The radius of plastic zone that propagates around the tunnel at the end of excavation as predicted by the finite element analysis.

Diameter (m) / Depth (m)	3	5	7	12	S_u (kPa)
15	3.52	10	□ = 50°	□ = 45 °°	200
18	3.7	5.0	□ = 66°	□ = 33.7°	200
25	3.0	5.0	5.0	□ = 58.0°	200
40	3.3	4.0	7.0	□ = 65.0°	200
15	3.52	6.67	□ = 40.44°	□ = 41.0°	150
18	3.4	8.0	□ = 33.0°	□ = 35.0°	150
25	3.4	7.0	9. 0	□ = 48.0°	150
40	4.63	12.6	10	□ = 60.0°	150
15	4.66	□ = 60.0°	□ = 52.0°	□ = 41.0°	100
18	4.0	□ = 72.0°	□ = 68.0°	□ = 36.0°	100
25	5.0	7.6	12.951	□ = 51.4°	100
40	6.0	4.5	11.91	□ = 62.0°	100
15	8.0	□ = 66.5°	□ = 41°	□ = 38.2°	50
18	4.0	□ = 65.0°	□ = 69.0°	□ = 44.9°	50
25	5.0	□ = 66.5°	□ = 70.3°	□ = 48.61°	50
40	9.0	□ = 60.0°	□ = 73.92°	□ = 72.9°	50

Note: □ represents the angle between the horizontal and the line bounding the plastic zone which is in some cases extended to the surface as shown in Figure 9.

From 64 cases studies and by using the program STATISTICA, the following nonlinear estimation of Rp can be obtained:

$$Rp = 1.2 \ \frac{D}{2} \exp\ ((\frac{\gamma z}{S_u})*V_1*1.5) \qquad (36)$$

The coefficient of correlation for this equation is ($R^2 = 0.78$).

Excess Pore Water Pressure:

Figure 10 shows the variation of excess pore water pressure at the radial distance above the tunnel and with D = 7 m, Z =18 m and at different times of consolidation.

The results show that a large negative excess pore pressure occurs after excavation and during consolidation. This is a result of the unloading of the pore pressure inside the tunnel which immediately dissipates any positive excess pore pressure near the crown. Thus, the excess pore water pressure is immediately lowered to negative values after excavation and

after consolidation, but the excess pore water pressure becomes positive (compression) as the radial distance increases towards the surface of the soil, then reaches zero.
The negative excess pore pressure causes the tunnel to be in steady state after excavation, because this negative excess pore pressure produces a tension zone around the peripheries of the tunnel.
The dimensionless excess pore water pressure behind the tunnel's wall is shown in Figure 11 which shows that the region of positive pore water pressure (compression) above the crown and about one tunnel diameter from the ground surface.
This positive excess pore water pressure reaches its maximum value at the end of excavation which is about (19%) of the hydrostatic pore water pressure.This pressure causes a reduction in the effective stress and weakness in the soil.
The same result is noticed below the tunnel's invert and about one tunnel's diameter from the base; the excess pore water pressure is about (10%) of the initial hydrostatic pore pressure. In general, the positive excess pore water pressure will dissipate and produce a negative excess pore water pressure and increase in effective stress.

Table 3: The propagation of plastic zone (Rp) using Deere's equation.

Depth (m) \ Diameter (m)	3	5	7	12	S_u (kPa)
15	1.89	3.15	4.41	7.56	200
18	1.98	3.3	4.6	7.9	200
25	3.07	5.12	7.18	12.3	200
40	6.39	10.65	14.92	25.57	200
15	2.4	4.0	5.6	9.60	150
18	2.57	4.2	6.0	10.28	150
25	4.62	7.7	10.7	18.48	150
40	12.2	20.4	28.58	48.99*	150
15	3.92	6.5	9.16	15.7*	100
18	4.32	7.215	10.10	17.3*	100
25	10.4	17.35	24.29*	41.648*	100
40	44.9*	74.9*	104.8*	179.78*	100
15	16.9*	28.255*	39.5*	67.81*	50
18	20.5*	34.33*	48.0*	82.4*	50
25	19.1	198.599*	278.0*	476.6*	50
40	2220*	3700*	5181.0*	8881.7*	50

* In this case, the plastic zone is extended to the surface.

Table 4: The propagation of the plastic zone (Rp) using Salencon (1969) equation.

Diameter (m) / Depth (m)	3	5	7	12	S_u (kPa)
15	1.44	2.402	3.363	5.76	200
18	1.50	2.50	3.51	6.018	200
25	1.64	2.742	3.839	6.582	200
40	1.91	3.18	4.452	7.65	200
15	1.54	2.58	3.608	6.18	150
18	1.63	2.71	3.80	6.504	150
25	1.8	2.99	4.2	7.19	150
40	2.12	3.54	4.95	8.5	150
15	1.74	2.9	4.1	6.95	100
18	1.85	3.1	4.31	7.4	100
25	2.1	3.5	4.83	8.3	100
40	4.13	6.88	9.6	12.5	100
15	2.22	3.7	5.2	8.9	50
18	2.4	4.0	5.6	9.54	50
25	2.73	4.6	6.4	10.92	50
40	3.4	5.6	7.8	13.38	50

The maximum negative excess pore water pressure was found at the spring line and behind the wall of the excavated tunnel which reaches about (30%) of the hydrostatic pore water pressure at the end of excavation. This pressure continues to decrease reaching about (40%) of the hydrostatic pore water pressure after 10 years of consolidation. All the positive excess pore water pressures above and below the tunnel will decrease with time due to dissipation after excavation and reach zero above the crown and become negative below the invert at the end of consolidation. The excess pore water pressure above the crown decreases to a minimum value of (45%) of the initial pore water pressure and at a distance equal to 0.5 of the tunnel diameter. The excess pore water pressure starts to increase to a maximum value of about (40%) of initial pore water pressure at a distance equal to twice that of the tunnel diameter then is reduced to negative value at a distance equal to four tunnel diameters.

The consolidation causes the excess pore water pressure to reach a negative value of about (50%) of the hydrostatic pore water pressure at the tunnel's crown as shown in Figure 12 and then the excess pore water pressure increases and reaches an equilibrium value at a distance equals to four tunnel diameters. This negative excess pore water pressure near the excavated tunnel is due to immediately unloading pore water pressure inside the tunnel which dissipates the positive pore water pressure and produces negative excess pore water pressure.
The same behaviour can be noticed above the spring line as shown in Figure 13 and at the invert in Figure 14.
After 10 years of consolidation, the excess pore water pressure drops to a negative value near the tunnel wall and then increases to reach a zero value at a distance equal to 4 tunnel diameters.

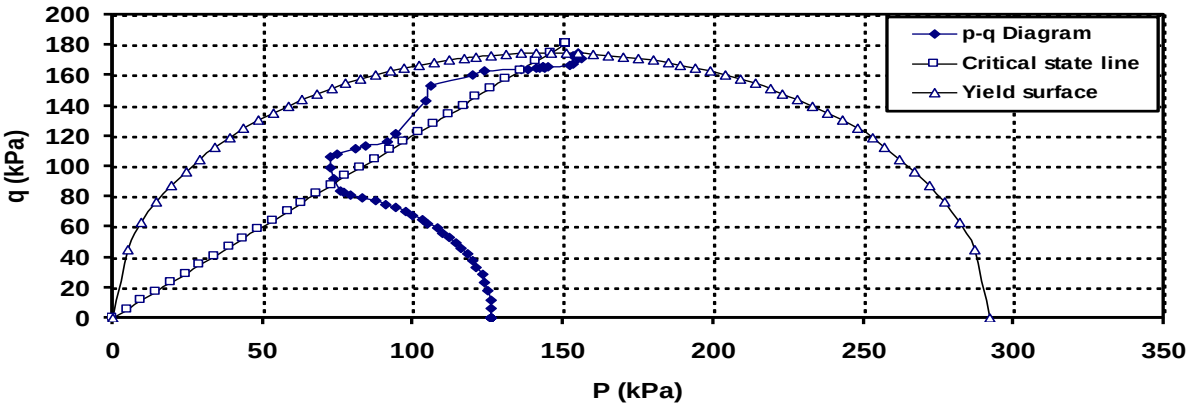

Fig. 3:Stress path at point A above the crown at the end of excavation stage (D= 7 m, Z = 18 m).

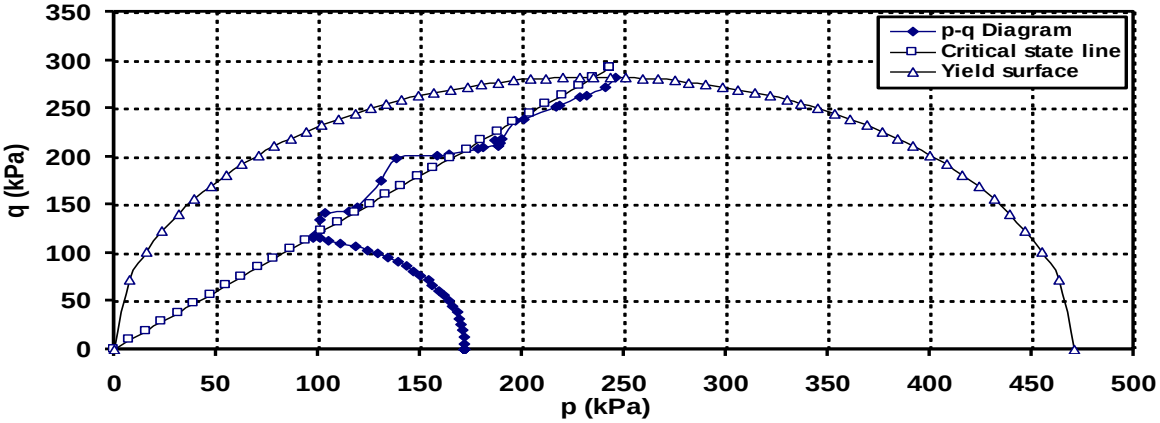

Fig. 4: Stress path at point B on the spring line at the end of excavation stage (D= 7 m, Z = 18 m).

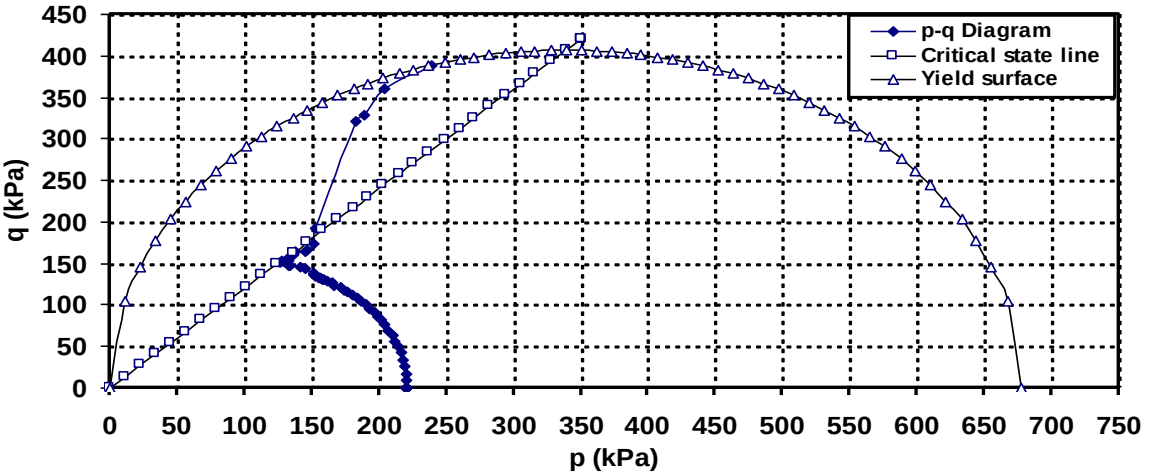

Fig. 5: Stress path at point C on the invert at the end of excavation stage (D=7 m, Z= 18 m).

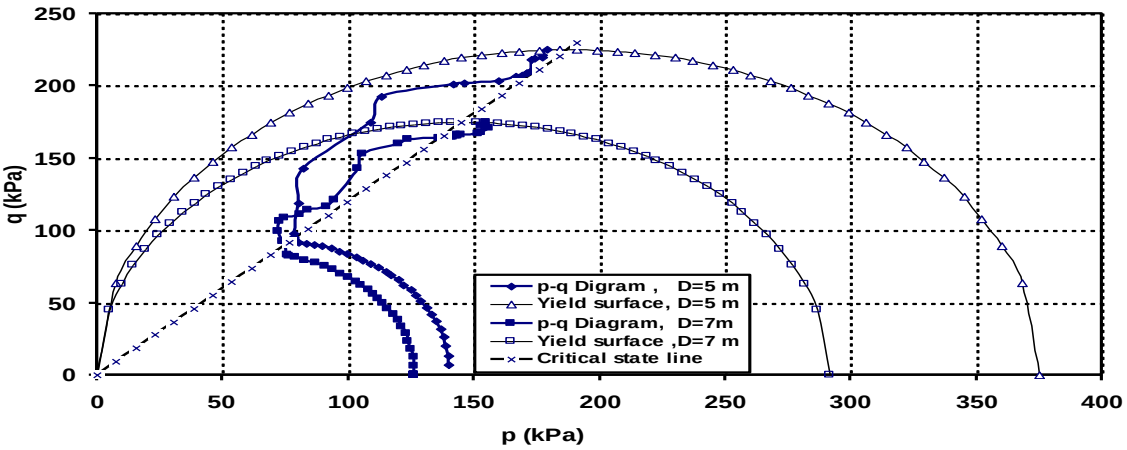

Fig. 6: Comparison of the effective stress path above the tunnel crown of two tunnels (D = 7 m and 5 m, Z = 18 m).

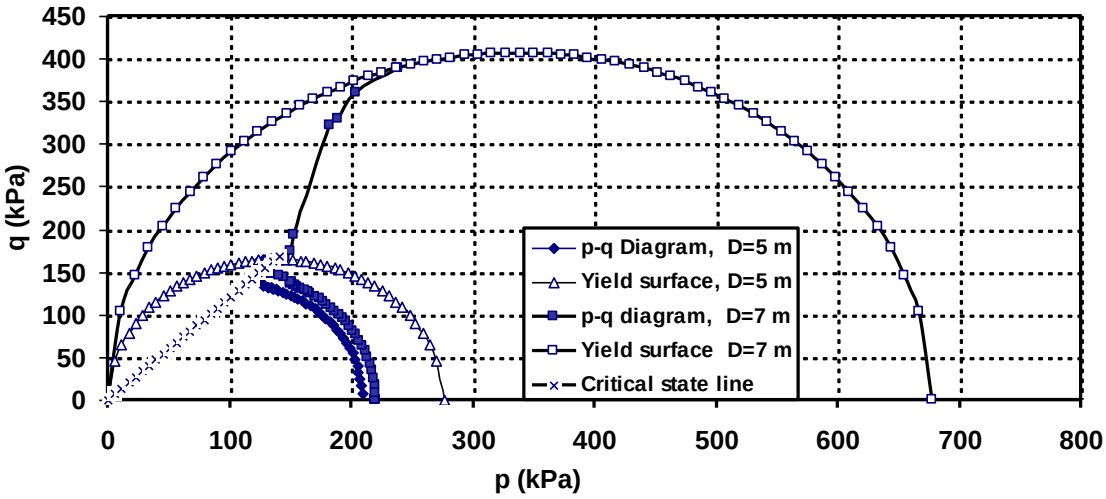

Fig. 7: Comparison of the effective stress path above the tunnel invert of two tunnels (D = 7 m and 5 m, Z= 18 m).

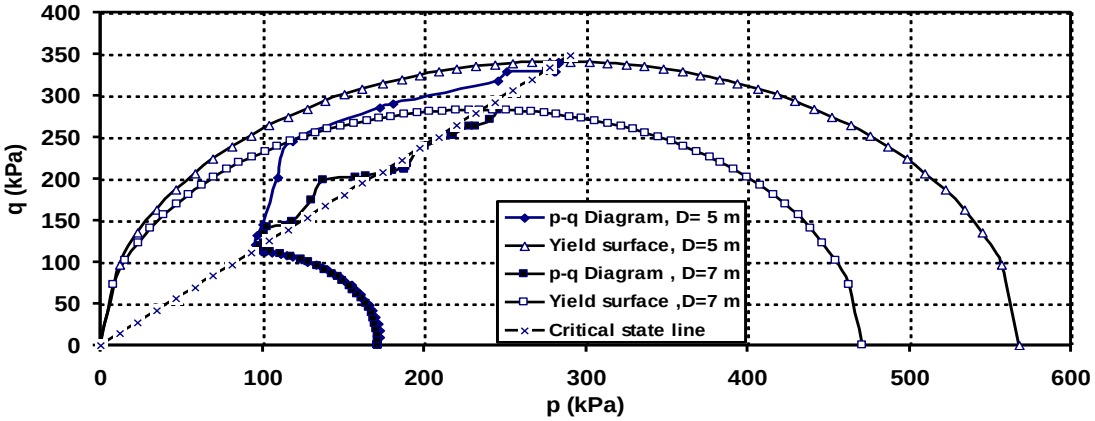

Fig. 8: Comparison of the effective stress path above the springline of two tunnels (D = 7 m and 5 m, Z = 18).

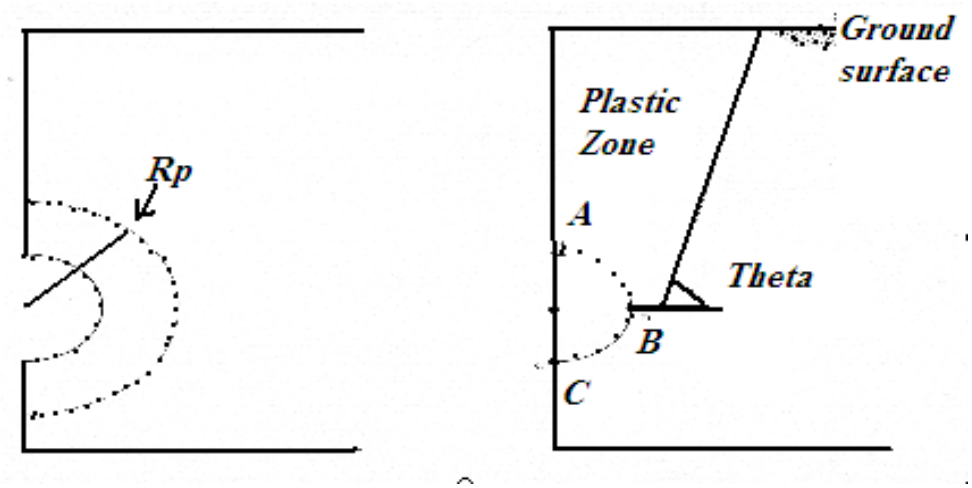

(a) (b)

Fig. 9: The propagation of the plastic zone.
(a) plastic zone bounded the tunnel
(b) plastic zone extended to the surface.

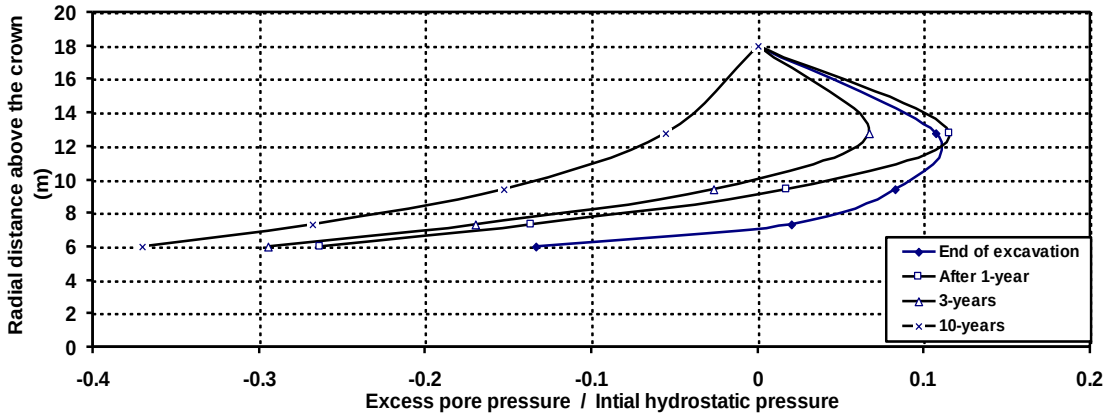

Fig. 10: Variation of the excess pore water pressure above the tunnel at different times (D = 7 m, Z = 18 m).

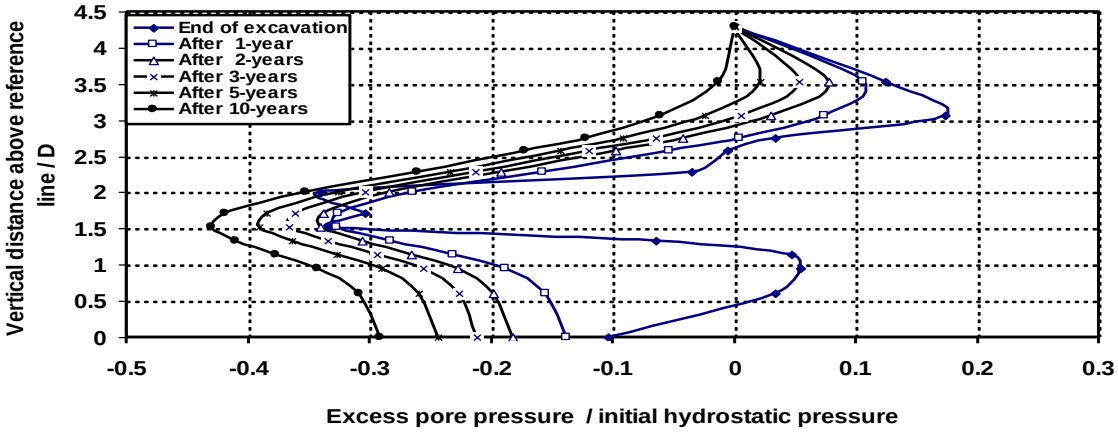

Fig. 11: Variation of the excess pore water pressure behind the tunnel at the end of excavation and during consolidation (D = 7 m, Z = 18 m).

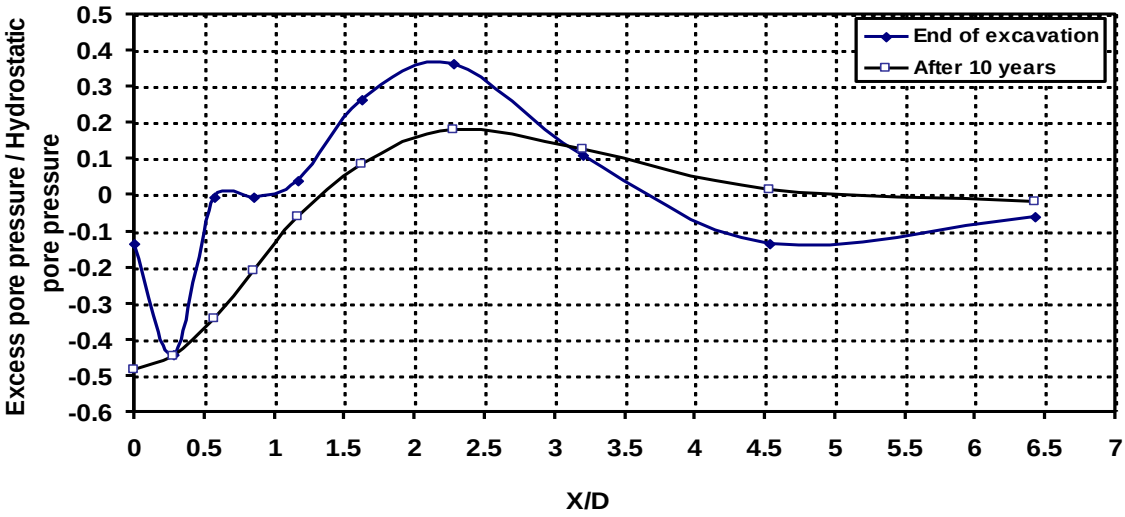

Fig. 12: Variation of the excess pore pressure above the tunnel's crown at the end of excavation and during consolidation , (D= 7 m, Z = 18 m).

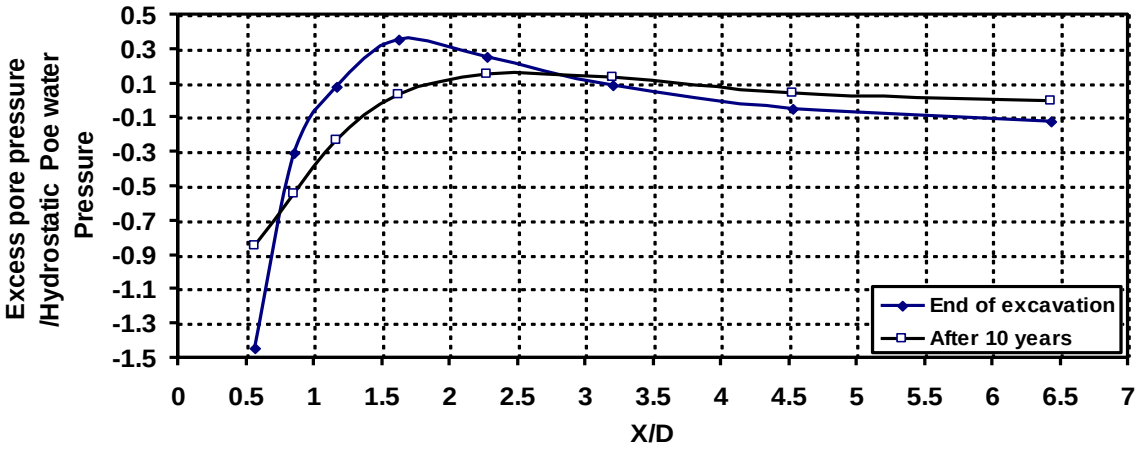

Fig. 13: Variation of the excess pore water pressure above the tunnel spring line at the end of excavation and during consolidation, (D = 7, Z= 18 m).

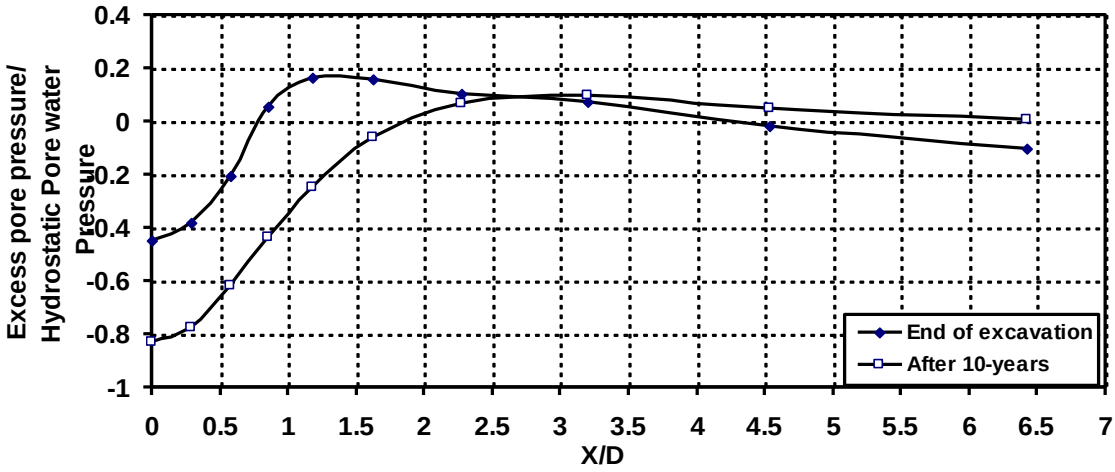

Fig. 14: Variation of the excess pore water pressure below the tunnel's invert at the end of excavation and during consolidation, (D = 7 m, Z = 18 m).

Table 5: Radius of plastic zones at different values of volume loss.

D (m)	Z (m)	Vl %	S_{max} (m)	Su (kPa)	Rp (m)
3	15	2%	-0.00750	50	2.30
3	18	2%	-0.00626	50	1.50
3	25	2%	-0.00451	50	1.50
5	15	2%	-0.02090	50	3.11
5	18	2%	-0.01740	50	3.50
5	25	2%	-0.01250	50	4.50
7	15	2%	-0.04100	50	3.99
7	18	2%	-0.03400	50	4.30
7	25	2%	-0.02450	50	6.37
3	15	3%	-0.01127	50	3.53
3	18	3%	-0.00939	50	2.42
3	25	3%	-0.00676	50	2.35
5	15	3%	-0.03100	50	3.88
5	18	3%	-0.02600	50	4.12
5	25	3%	-0.01870	50	5.17
7	15	3%	-0.06000	50	6.66
7	18	3%	-0.05100	50	5.00
7	25	3%	-0.03600	50	6.90
3	15	4%	-0.01500	50	4.10
3	18	4%	-0.01250	50	3.12
3	25	4%	-0.00900	50	3.44
5	15	4%	-0.04180	50	5.38
5	18	4%	-0.03480	50	5.20
5	25	4%	-0.02500	50	5.77
7	15	4%	-0.08200	50	6.67
7	18	4%	-0.06800	50	5.50
7	25	4%	-0.04900	50	6.50

Conclusions:

1. The propagation of plastic zone will extend to the surface as the tunnel diameter increases and the depth of the tunnel decreases. From 64 cases studied and by using the program STATISTICA, the following nonlinear estimation of the radius of plastic zone (Rp) at volume loss V_1 varying from 2% to 4% can be obtained:

$$Rp = 1.2\frac{D}{2}\,Exp\left(\left(\frac{\gamma z}{S_u}\right) * V_l * 1.5\right)$$

The radius of the plastic zone increases as the volume loss increases. In reality as soon as $\square_{max}$ reaches a certain volume loss, the lining must be applied to stop the propagation of plastic zone and control the amount of deformation caused by tunneling.

2. The element above the tunnel's crown with D = 7 m reaches the critical state line before the element with D = 5 m, while the element below the invert with tunnel diameter of 5 m reaches the critical state line before the element with D = 7 m.
3. For shallow tunnels with C/D <1.0 (C = Z-D/2), the failure envelope is cut by the surface for all values of Su and causes secondary failure at the surface, whereas for deeper tunnels, the failure envelope closes before reaching the ground surface.
4. The excess pore water pressure above the crown decreases to a minimum value of (45%) of the initial pore water pressure and at a distance equal to 0.5 of the tunnel diameter. The excess pore water pressure starts to increase to a maximum value of about (40%) of initial pore water pressure at a distance equal to twice that of the tunnel diameter then is reduced to negative value at a distance equal to four tunnel diameters.
5. After 10 years of consolidation, the excess pore water pressure drops to a negative value near the tunnel wall and then increases to reach a zero value at a distance equal to 4 tunnel diameters.

References:

- Attwell, P.B. and Selby, A.R., (1989), "Tunneling in Compressible Soils", Large Ground Movements and Structural Implications, Tunneling and Underground Space Technology, Vol. 4, printed in Great Britain.
- Augard, C. E., (1997), "Numerical Modeling of Tunneling Processes for Assessment of Damage to Building", Ph.D. thesis, University of Oxford.
- Bloodworth, A. G., (2002), "Three-Dimensional Analysis of Tunneling Effects on Structures to Develop Design Methods", Ph.D. thesis, University of Oxford.
- Booker,J.R. and Small, J.C.(1975)."An Investigation of Stability of Numerical Solutions of Biot's Equations of Consolidation", International Journal of Solids and Structures, 11 p.p. 907-917.
- Bowles, J. E., (1996), " Foundation Analysis and Design", 5th Edition, McGraw Hill.
- Clough, G.W. and Schmidt, B., (1981)." Excavation and Tunneling", Soft Clay Engineering, Chapter 8, edited by E.W. Brand and R.P. Brenner, Elsevier.
- Deere, D.U. , Peck, R. B., Mousces, J.E. and Schmidt, B.,(1969), "Design of Tunnel Lines and Support Systems", Report for U.S. Dept of Transportation, office of High speed Ground Transportation, Contract No. 3-0152.
- Ezzeldine, O.Y., (1999), "Estimation of the Surface Displacement Field due to Construction of Cairo Metro Line Elkhalafawy-Saint. Therese", Tunneling and Underground Space Technology, Vol.14, No. 3, p.p. 267-279.
- Hellawell, E. E., Hawley, A. J., Pooley, S.D., Garrod, B. and Legett, M., (2001), "Metro Under Construction around the World", Proceedings Institution of Civil Engineers, Geotechnical Engineering, vol. 149, p.p. 29-39.
- Lake, L.M., Rankin, W.J., and Hawley, J. (1992), "Prediction and Effects of Ground Movements Caused by Tunneling in Soft Ground Beneath Urban Areas. CIRIA Funders Report/ cp/5.

- Mair,R.J. and Taylor, R.N., (1993), "Prediction of Clay Behaviour around Tunnels Using Elasticity Solutions". Proceeding Predictive Soil Mechanics Worth Memorial Symposium, p.p. 449-463, Oxford.
- NCCLR (1987), National Center of Construction Laboratories and Research, Unpublished Report, Baghdad- Iraq.
- O'Reilly, M. P. and New, B. M. ,(1982), "Settlements above Tunnels in the UK-their Magnitude and Prediction", Tunneling, 82, p.p. 173-181.
- Potts, D.M. and Zdravkovic, L., (2001), "Finite Element Analysis in Geotechnical Engineering Application"' Thomas Telford, London, UK.
- Rankin, W., (1988), "Ground Movements Resulting from Urban Tunneling Prediction and Effects", Proceeding 23rd Conference of the Engineering Group of the Geological Society, London Geological Society, p.p. 79-92.
- Salim, N.M.N., (2006), "Time-Dependent Analysis of Tunnels in Clays Using the Finite Element Method", Ph.D. thesis, Building and Construction Engineering Department, University of Technology, Iraq.
- Salencon, J., (1969), "Contraction Quasi-Statique D'une Cavites Sysmetrie Spherique Ou Cylindrique Dans Un Milieu Elastoplastique", Annales Des Ponts Et Chauss, Vol. 4, pp. 231–236.
- Tatsuoka, F. and Shibuya, S. (1992), " Deformation Characteristic of Soils and Laboratory test", State of the Art Proceeding 9th Asian Regional Conference on Soil Mechanics and Foundation Engineering, Vol. 2, p.p. 101-170.
- Zienkiewicz, O. C. and Taylor, R. L., (2005), "The Finite Element Method", sixth edition

S - 25

2D GEOELECTRICAL RESISTIVITY IMAGING FOR SOIL CHARACTERIZATION AT AL-OBAIDI SITE PROJECT

Dr. Hussein H. Karim[1] Dr. Mohammed A. Al-Neami[2] and Wisam M. Y. Mohammad[3]

1. Prof.,Construction Eng. Dep. 2-Ass. Prof.,Construction Eng. Dep 3-M.Sc. Geotechincal Engineering. .University of Technology,Baghdad-Iraq.

ABSTRACT

This study deals with the integration between geotechnical investigations and 2D resistivity imaging technique which have been used in Al-Obaidi site at the Electrical Transformation Station Project in Baghdad. In this work, Wenner-Schlumberger and Wenner arrays are used as protocols chosen for this investigated study. Field work was carried along 13 spreads with length of about 130 m and the depth of investigation is around 20 m. After processing the results of the field work, data files imported from Terrameter SAS 4000 instrument to the computer and interpreted by RES2DINV software to get 2D imaging of electrical resistivity sections. These sections reflect the subsurface complexity due to sediments heterogeneity. The soil site is generally characterized by its low resistivity values which indicate that it is mostly clay to silty clay with the presence of some sand pockets. Resistivity values for both used arrays decrease with depth due to increasing soil moisture content particularly at depth 10 to 20 m. Generally, 4-7 distinct geoelectric layers have been identified representing the subsurface of the study area. High resistivity values are assigned to topsoil, medium-high resistivity values represent the upper soil layers, while lower resistivity values are indicated in the lowest soil layers. In addition, some geotechnical (physical) properties were determined from soil resistivity for each spread such as porosity, void ratio and conductivity. For groundwater, electrical conductivity, resistivity and TDS were determined.

Keywords: 2D Electrical Resistivity Imaging, Conductivity, Geoelectrical Parameters, Geotechnical Properties, Total Dissolved Solids.

المقاومة النوعية الجيوكهربائية التصويرية ثنائية البعد لتوصيف التربة في موقع مشروع العبيدي

أ.د. حسين حميد كريم أ.م.د. محمد عبد اللطيف النعيمي وسام ماجد يعقوب محمد

قسم هندسة البناء والانشاءات- الجامعة التكنولوجية

الخلاصة

تتناول هذه الدراسة التكامل ما بين التحريات الجيوتكنيكية وتقنية المقاومة النوعية الكهربائية التصويرية ثنائية البعد المستخدمة في موقع العبيدي لمشروع محطة التحويل الكهربائية في بغداد. في هذا العمل، استخدمت طريقتي فينر-شلمبرجير و فينر كترتيبات تم اختيارهما لهذه الدراسة. تم تنفيذ العمل الحقلي على طول 13 نشرة بطول حوالي 130متر بعمق تحري حوالي 20 م. بعد معالجة نتائج العمل الميداني، تم نقل ملفات البيانات من جهاز Terrameter SAS 4000 إلى جهاز الحاسبة بالأستعانة ببرنامج RES2DINV للحصول على تصوير ثنائي البعد لمقاطع المقاومة النوعية الكهربائية. تعكس هذه المقاطع مدى تعقيد ما تحت سطح الأرض نظرا لعدم تجانس الرواسب. عموما، تتميز تربة الموقع بقيم المقاومة النوعية الواطئة التي تشير الى أنها في معظمها طينية إلى طينية غرينية مع وجود بعض الجيوب الرملية. تتصف قيم المقاومة النوعية لكلا الترتيبين المستخدمين بالانخفاض مع العمق نتيجة لزيادة محتوى رطوبة التربة خاصة في العمق 10-20 م. بشكل عام، تم تحديد 4-7 طبقات جيوكهربائية مميزة تمثل ما تحت سطح منطقة الدراسة. أشارت القيم العالية للمقاومة النوعية الى التربة السطحية، وقيم المقاومة النوعية العالية - المتوسطة تمثل الطبقات العليا من التربة، بينما تشير قيم المقاومة النوعية الواطئة الى طبقات التربة السفلى. بالإضافة إلى ذلك، تم تحديد بعض الخصائص الجيوتكنيكية (الفيزيائية) في الدراسة الحالية من المقاومة النوعية للتربة ولكل مسار مثل المسامية، ونسبة الفراغات والتوصيلية الكهربائية. أما بالنسبة للمياه الجوفية، تم تحديد التوصيلية الكهربائية والمقاومة النوعية وكمية المواد الصلبة الكلية الذائبة TDS.

INTRODUCTION

Geophysical methods can he used to determine the distributions of physical properties, at depths below the ground surface that reflect the local subsurface characteristics of the materials (soil, rock or water). These methods may be used for the investigation during the reconnaissance phase of the site investigation programme since it provides a relatively rapid and cost-effective means of deriving aerially distributed information about subsurface stratification. In fact, geophysical investigation methods may be used to supplement borehole and outcrop data and to interpolate between boreholes [1].

A wide range of geophysical methods are available for subsurface investigation, for each of which there is an operative physical property to which the method is sensitive. Electrical resistivity studies in geophysics may be understood in the context of current flow through a subsurface medium consisting of layers of materials with different individual resistivities. For simplicity, the ground layers are assumed to be uniform. The resistivity (ρ) of a material is a measure of how well the material retards the flow of electrical current. In real situations the resistivity is determined by different lithologies and geological structures and so may be very inhomogeneous. This complexity is not taken into account when measuring resistivity with a four-electrode method, which assumes that the ground is uniform. The result of such a measurement is the "apparent" resistivity (ρ_a) [2, 3].

Resistivities vary tremendously from one material to another, soil materials exhibit intermediate electrical properties depending on their physical and chemical properties (texture, salinity or water content) [4]. Nowadays, electrical resistivity methods are routinely used in conjunction with boring logs for subsurface investigation [1]. In the context of soil mapping, electrical resistivity exhibits a large range of values from 1 ohm.m for saline soil to several thousands ohm.m for dry soil overlaying crystalline rocks (Fig. 1). Séger et al. (2009) [5] investigated the variation of electrical resistivity as a function of soil properties and discussed the main advantages and limits of the method to the soil properties in comparison with site investigation. Lateral changes in the subsurface resistivity will cause changes in the apparent resistivity values that might be, and frequently are, misinterpreted as changes with depth in the subsurface resistivity. In many engineering and environmental studies, the subsurface geology is very complex where the resistivity can change rapidly over short distances.

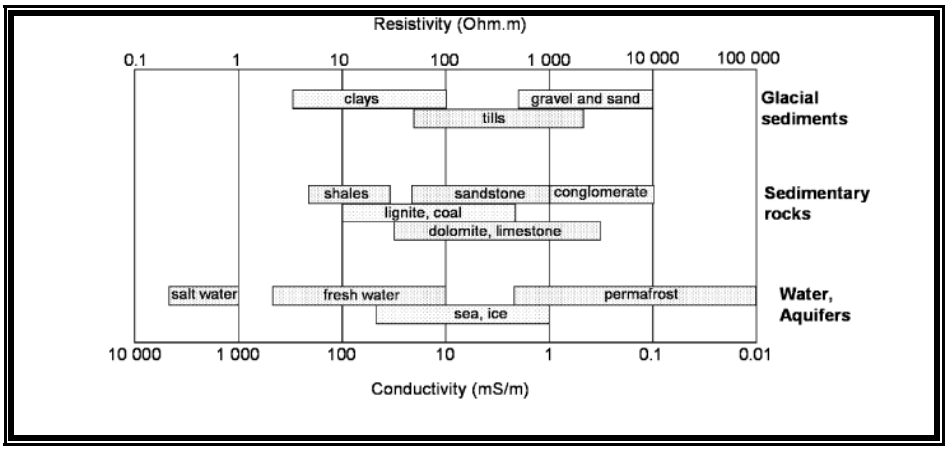

Fig. (1). Typical ranges of electrical resistivities and conductivities of earth materials [6].

The electrical conductivity is related to the particle size by the electrical charge density at the surface of the solid constituents. In clay soil, the electrical charges located at the surface of the clay particles lead to greater electrical conductivity than in coarse-textured soils because of the magnitude of the specific surface [7]. The electrical resistivity recorded by Giao et al. (2003) [8] on 25 clay samples collected worldwide ranged from 1 to 12 ohm.m [9]. Accordingly, the properties that affect the resistivity of a soil or rock include porosity, water content, composition (clay mineral and metal content), salinity of the pore water, and grain size distribution [10].

The availability of fast, inexpensive computers and the development of efficient algorithms has led to the development of electrical imaging methods. Thus the present study deals with the implementation of 2D resistivity surveying in the site investigation for monitoring the internal structure from the subsurface images since soil materials and properties are strongly correlated and can be quantified through the geoelectrical properties.

THEORETICAL BACKGROUND

There are three different models (1-, 2- and 3-D) to take resistivity measurements. Nowadays, 2-D surveys are the most practical economic compromise between obtaining very accurate results and keeping the survey costs down. Typical 1-D resistivity sounding surveys usually involve about 10 to 20 readings, while 2-D imaging surveys involve about 100 to 1000 measurements. In comparison, 3-D surveys usually involve several thousand measurements. In many geological situations, 2-D electrical imaging surveys can give useful results that are complementary to the information obtained by other geophysical method. The cost of a typical 2-D survey could be several times the cost of a 1-D sounding survey but it can give useful result as it yields a two- dimensional vertical cross-section of the "true" resistivities beneath the electrode array. Instead of deploying a single pair of current-electrodes and a single pair of potential-electrodes for 1-D survey, an array of regularly spaced electrodes linear arrangement is used for two-dimensional surveys. As in standard resistivity methods, the resolution and maximum depth of investigation depend on the separation and geometry of the electrodes [3, 11].

Two-dimensional multi-electrode arrays provide a two-dimensional vertical picture of the sounding medium. The test is accomplished by generating a current through the ground and measuring the resulting potential differences at the surface. Measured deviations from normal potentials are used as an indication of subsurface variations in electrical [12]. The current and potential electrodes are maintained at a regular fixed distance from each other and are progressively moved along a line at the soil surface. At each step, one measurement is recorded. The set of all these measurements at this first inter electrode spacing gives a profile of resistivity values. The inter-electrode spacing is increased then by a factor $n = 2$ and a second measurement line is done. This process (increasing the factor n) is repeated until the maximum spacing between electrodes is reached. One can notice that the larger the n-values, the greater the depths of investigation (Fig. 2). As the distribution of the current also depends on the resistivity contrasts of the medium, the depth of investigation deduced from the spacing is called the "pseudo-depth". The data are then arranged in a 2D "pseudo-section" plot that gives a simultaneous display of both horizontal and vertical variations in resistivity [11, 12].

There are many arrays used for resistivity imaging (RI) where each array has advantages and disadvantages depending on the nature of the study area. The most common arrays in resistivity imaging are Wenner, dipole-dipole and Wenner-Schlumberger [13, 14, 15]. Depending on the array configuration, the geometrical factor K differs, thus the array configuration has a substantial influence on the resolution, sensitivity and depth of investigation [11, 13]. Choosing the right array for the resistivity surveys is important as the geological image created by means of (RI) for the same structure will be different for each array. Moreover, choosing the array requires some considerations such as the subsurface structure, depth, vertical and horizontal change in the subsurface, and the signal strength and electric background noise [15, 16].

The Wenner electrode configuration is an array in which the four electrodes are arranged in line with equal electrode spacing (Fig. 2a). If the survey is in a noisy area and a good vertical resolution is required with a limited survey, the Werner array will be the best option [17]. While the other commonly used array is Wenner-Schlumberger array (Fig. 2b) which is hybrid between Wenner and Schlumberger arrays [18] arising out of a relatively recent work with electrical imagine surveys. If there is uncertainty whether both reasonably good horizontal and vertical resolution are required, the Wenner-Schlumberger array with overlapping data levels is the best option. This array is moderately sensitive to both horizontal and vertical structures [17, 19]. Note that the Wenner array is a special case of this array where the "**n**" factor is equals to 1. Figure 2 a and b also shows the pattern of the data points in the pseudosections for the Wenner and Wenner-Schlumberger arrays. The Wenner-Schlumberger array has a slightly better horizontal coverage compared with the Wenner array. For the Wenner array each deeper data level has 3 data points less than the previous data level, while for the Wenner- Schlumberger array there is a loss of 2 data points with each deeper data level. The horizontal data coverage is slightly wider than the Wenner array (Fig. 2a and b), but narrower than that obtained with the dipole-dipole array [19].

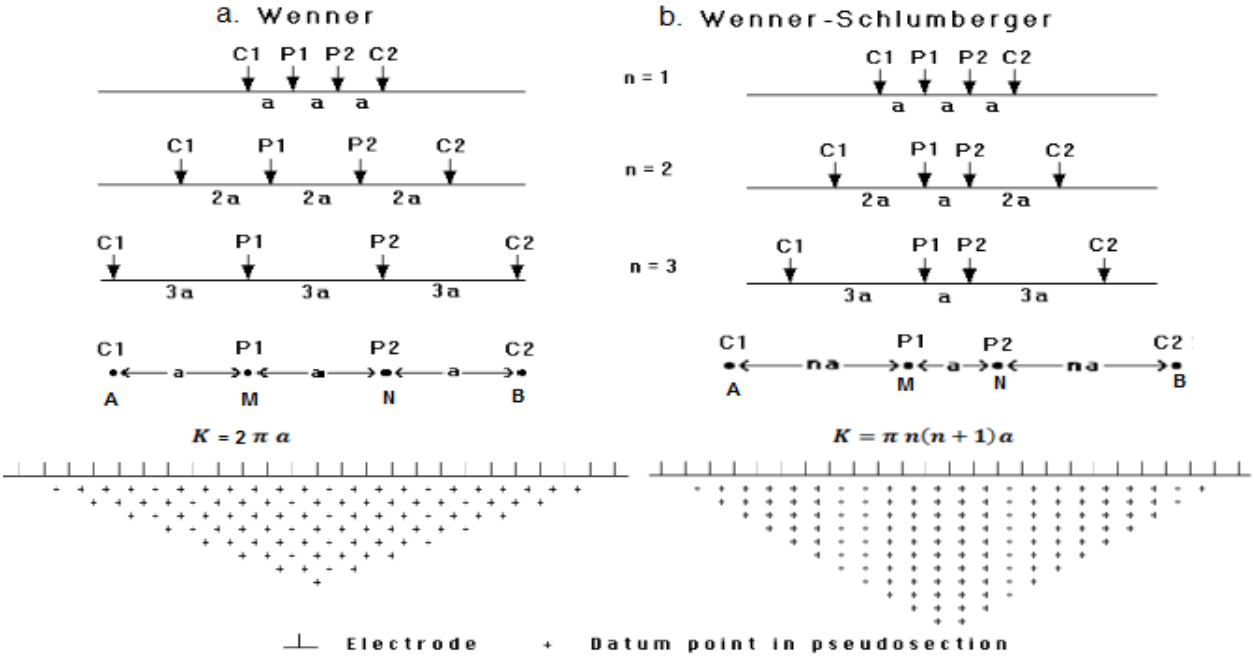

Fig. (2). A comparison of the electrode arrangement and pseudosection data pattern for the: (a) Wenner and (b) Wenner-Schlumberger arrays (Modified from Loke, 2000) [14].

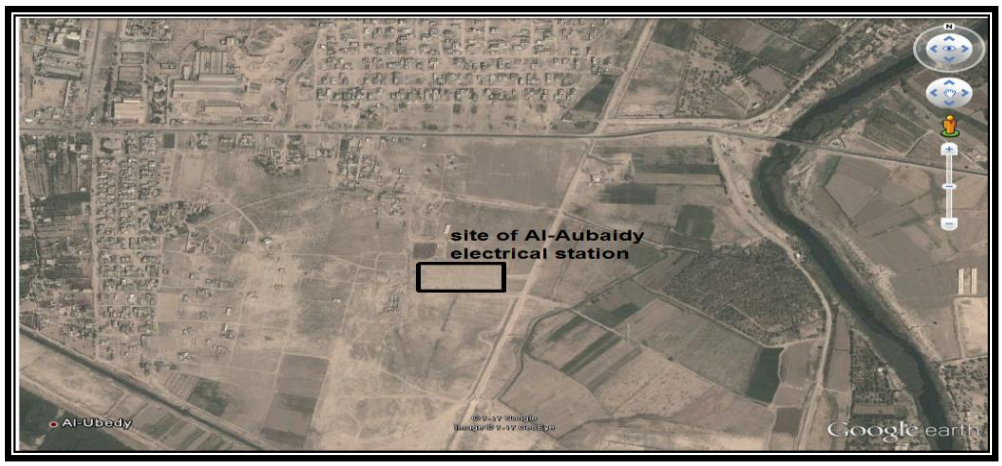

Fig. (3). Aerial photograph of Al-Obaidi electrical site

FIELD WORK AND DATA AQUISITION

The site represents a project for constructing an electrical station in Al-Obaidi area north east of Baghdad (between the old road of Baghdad- Baquba and Diyala Governorate). The station site has an area of about (300×200) m^2, with generally flat terrain. Figure 3 shows an aerial photograph for the site of Electrical Al-Obaidi Station.

In this study, measurements procedure for electrical imaging resistivity survey are taken along 13 spreads with 120-129 m in length and 3 m spacing. 4 spreads are inside the main station with 4-5 m electrode spacing due to many obstructions, whereas 9 spreads are outside the station with 3 m electrode spacing (Fig. 4). In the field, ERI survey data were acquired using Terrameter SAS 4000 system with its main components (connector system ES10-64C, electrode selector and other accessories). With this equipment, consecutive readings were taken automatically and the results averaged continuously. After finishing field measurements, the files of resistivity data must be imported from Terrameter SAS 4000 to the computer to convert them from S4K format to DAT format using SAS 4000 utilities program. The data was processed and inverted using RES2DINVsoftware. RES2DINV is a computer program that automatically determines the true resistivity model for the subsurface from the measured data. The program is also used to determine the layer parameters from the measured resistivity imaging data and to generate the inverted resistivity-depth image for each profile line.

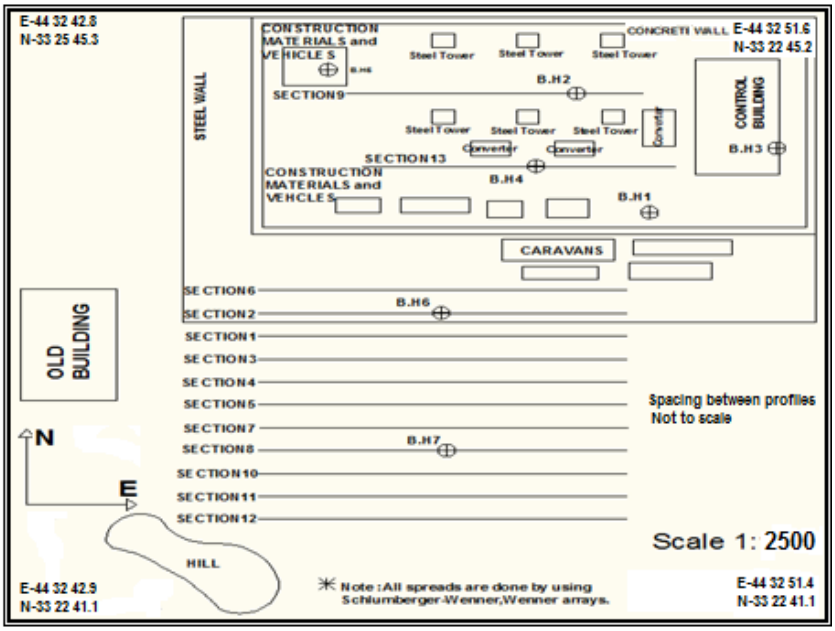

.

(a)

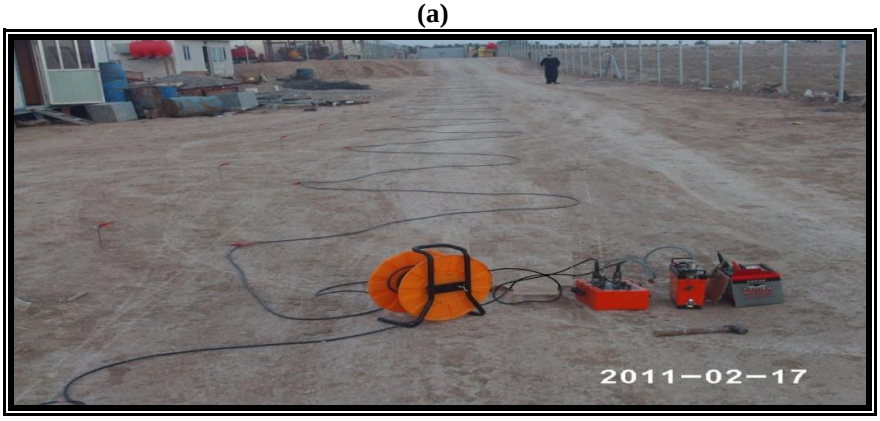

(b)

Fig. (4). (a). Site planning with resistivity imaging spreads; (b). A spread for resistivity imaging.

RESULTS AND DISCUSSION

Data Analysis

Processing and interpretations of the 2D resistivity imaging data was done using RES2DINV software and applying the Finite-Difference method to determine the soil layer parameters (resistivity and thickness of layers, or resistivity and depth to bottom of layers). The imaging sections of soil resistivity characterization for Wenner-Schlumberger and Wenner arrays are presented as shown in Figures 5a and b respectively. The recorded depth of investigation in the imaging resistivity sections is about 20 to 22 m. To emphasize the integration between the data

results obtained from resistivity images and that obtained from soil site investigation (boreholes), a correlation was made between these resistivity images and boreholes (Figs. 5 to 17).

For correlation resistivity imaging sections with boreholes, the spread 1 with borehole 6 (located at 3 m) is taken as an example. Generally, the resistivity for this section is ranging between (<1 to 30) ohm.m for Wenner-Schlumberger array. The resistivity values ranging between 2 to 5 ohm.m are common for most of the section area with lower values in the left side compared to the right one (Fig. 5a). The soil horizons are mapped as a conductive top soil (< 2 ohm.m) which may represent clayey silt, followed by an intermediate portion with a range of 2 to 15 ohm.m probably of clayey silt soils with sand. The overburden soils exhibit a pronounced thickness variation along the section. The third layer with very low resistivity (<1–2 ohm.m) may be explained as conductive clayey soil (expansive soil) near water table. The lower part of the middle of the section has lower resistivity of clayey soil (about 2 ohm.m). In addition, some anomalous areas are indicated with relatively high resistivity (27 ohm.m) in the south east part of the right half of the section which could indicate the presence of sand lens (or pockets); and the very low resistivity values (reaching 1ohm.m) which could represent conductive soil probably water logged horizon. Thus, 4 geoelectrical layers are identified in this section compared to 6 layers in borehole where the last 3 layers appear as one geoelectrical layer (2 ohm.m) as shown in Figure 5a. As a result of this correlation, it can be stated that the resistivity is inversely proportional to clay content and directly proportional to sand content and soil stiffness. Where the dark color of soil texture (as brown or grey) could be due to the increase of clay. That means the first two layers (2 to 15 ohm.m) are clayey silt soils with sand but the last four layers ($\leq$2 ohm.m) are clayey soils.

Comparing Wenner-Schlumberger and Wenner arrays (Fig. 5a and b), it can be seen that in Wenner array there is no distinct differences in resistivity on most of the section as in Wenner-Schlumberger array (with more details and difference in resistivity on the whole section). By comparison, it can be stated that Wenner-Schlumberger array is better than Wenner array for this reason. The whole section in Wenner array has resistivity ranging between around 6 to 7 ohm.m, which is slightly low with respect to the lithology. Besides, in Wenner array, the resistivity changes are sometimes limited to the upper layers without pronounced details in the lower part and with small changes (e,.g. top soil with 7 ohm.m to 5.5 ohm.m in the lower layers. For these reasons, Wenner-Schlumberger array is more representative details for than Wenner and that is shown in all Wenner sections. Figures 6 to 17 represent the rest imaging sections of soil resistivity characterization for both arrays. The correlation for the rest resistivity sections with boreholes are shown in Figures 6 to. 17.

After results analysis, characterization and correlation of resistivity imaging sections among each other (Figures 5 to17), four to seven distinct geoelectric layers have been identified representing the subsurface of the surveyed site. Besides, the site is generally characterized by its low resistivity values (1-15 ohm.m) which indicate that the soil is mostly of clayey soil. It can be also seen that the resistivity values decrease with depth due to increase in water content. For all spreads, the resistivity values are ranging from about 5–50 ohm.m. It is found that high resistivity values ($>$ 50 ohm.m) are assigned to the uppermost soil, medium–high resistivity values (15–50 ohm.m) represent the upper soil layers (approximatly above water table) and lower resistivity values (5–10 ohm.m) are assigned to layers below water table while the lowest resistivity values ($<$ 5ohm.m) are indicated at the lowest layer. The resistivity range is highly indicative of waterlogged conductive soil. It is obvious that the resistivity for both arrays also decreases with increasing stiffness of soil texture with depth and increasing soil moisture content particularly at depth 10 to 20 m. It can be stated that the analysis of the relationships between soil geotechnical properties with electrical resistivity really provides advantages for the

geotechnical engineers to solve site investigation problems and any problems related to geology efficiently and economically.

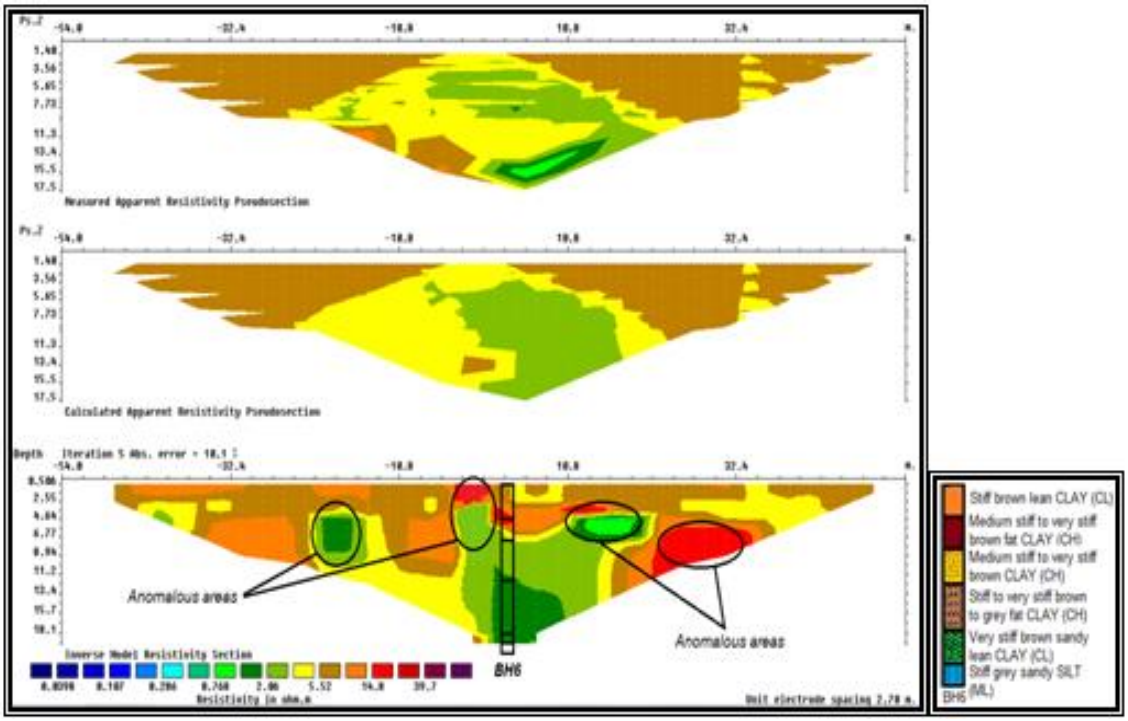

(a)

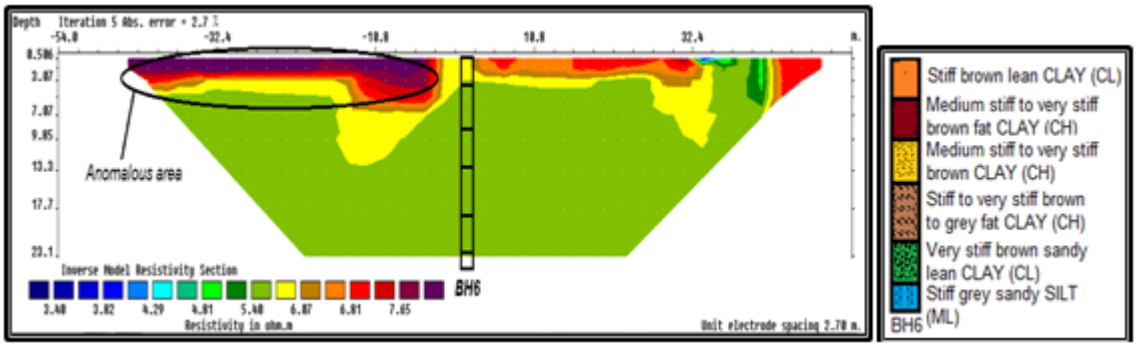

(b)

Fig. (5). Soil resistivity characterization for section 1: Wenner-Schlumberger and b) Wenner.

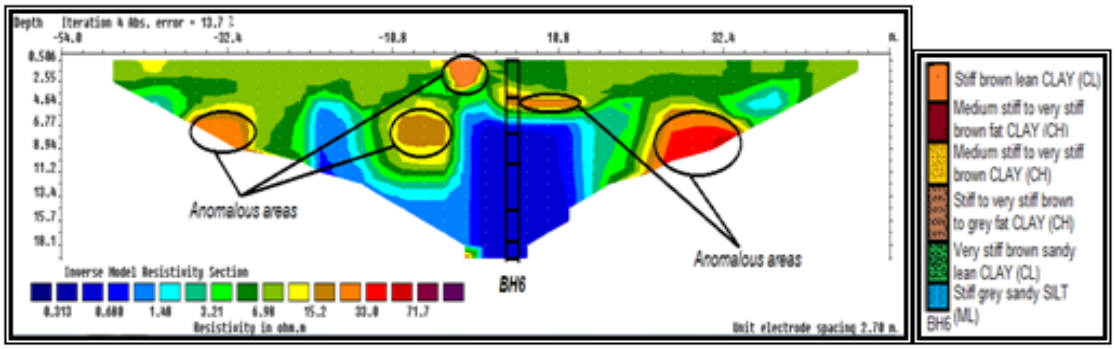

(a)

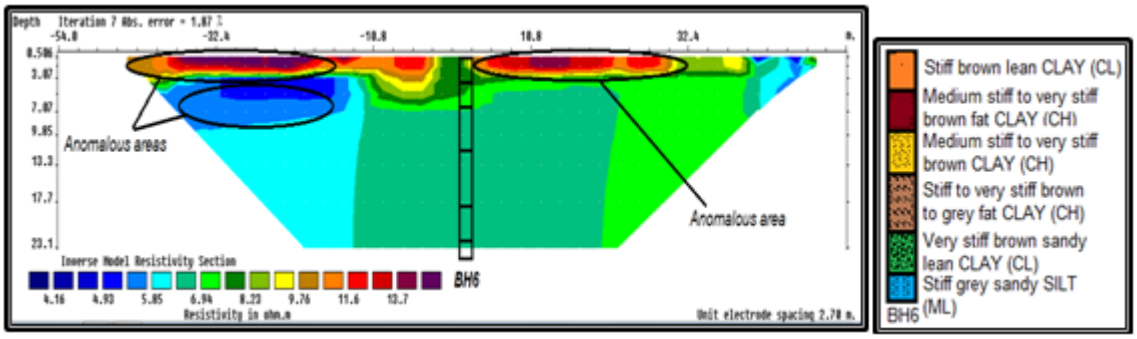

(b)

Fig. (6). Soil resistivity characterization for section 2: a)Wenner-Schlumberger and b) Wenner.

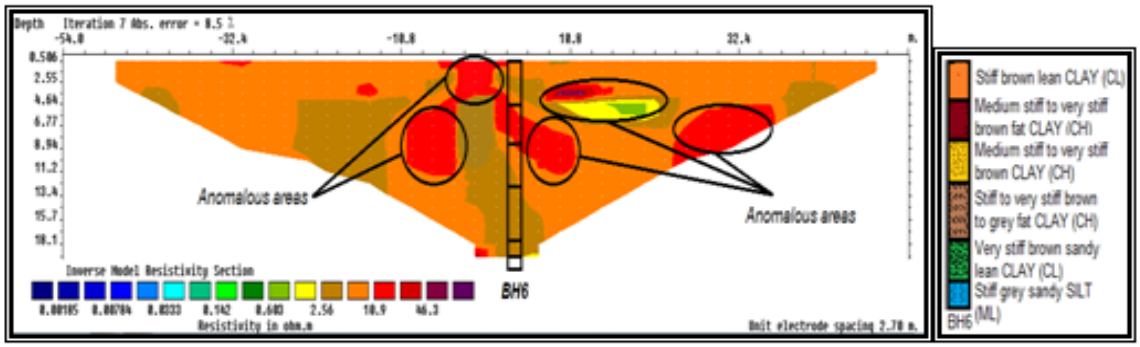

(a)

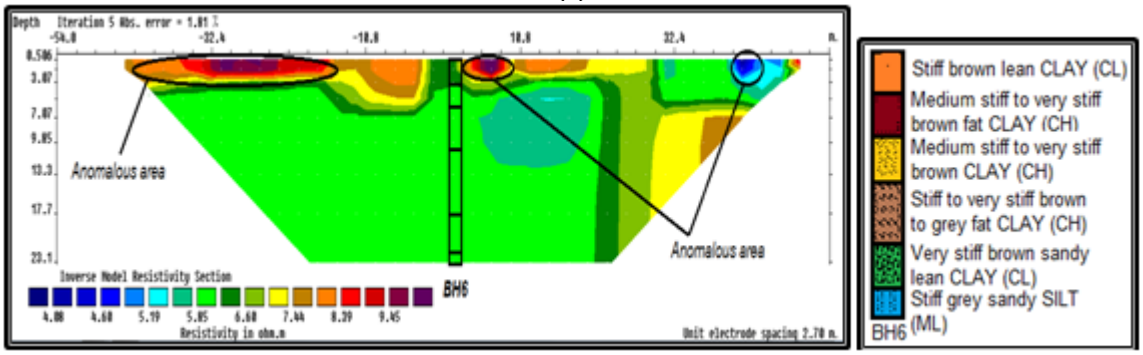

(b)

Fig. (7). Soil resistivity characterization for section 3: a) Wenner-Schlumberger and b) Wenner.

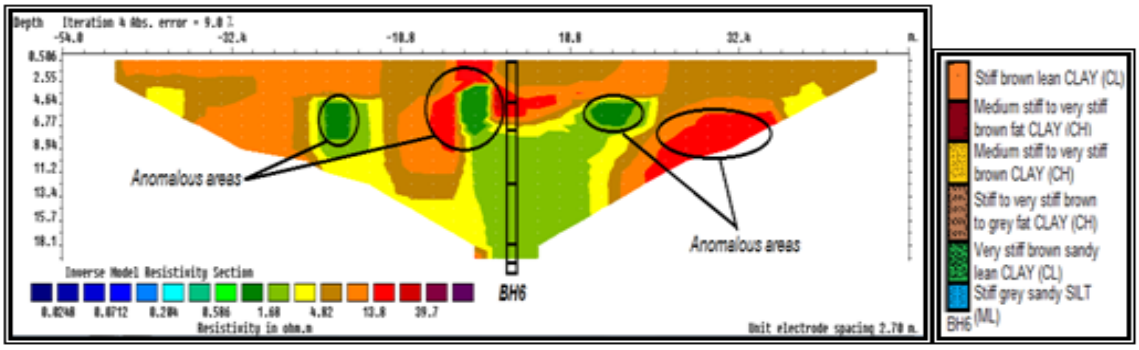

(a)

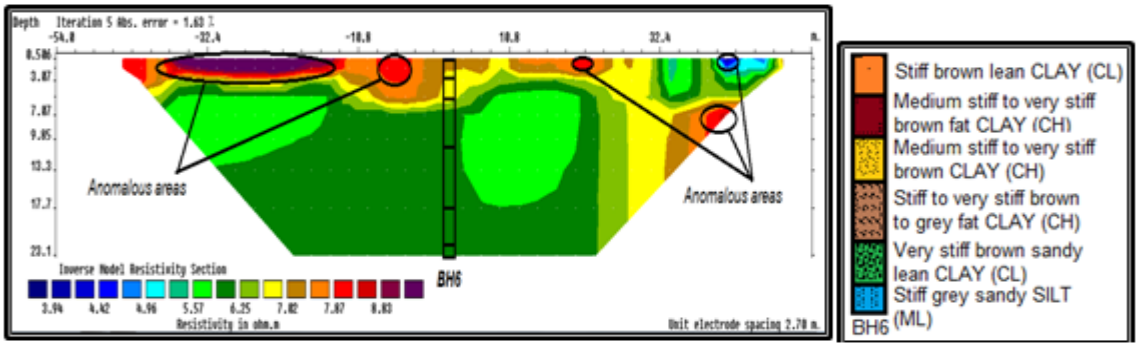

(b)

Fig. (8). Soil resistivity characterization for section 4: a) Wenner-Schlumberger and b) Wenner.

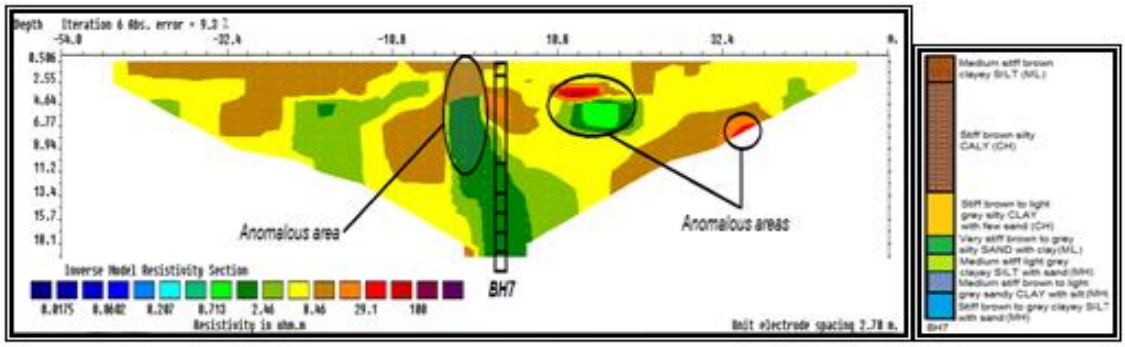

(a)

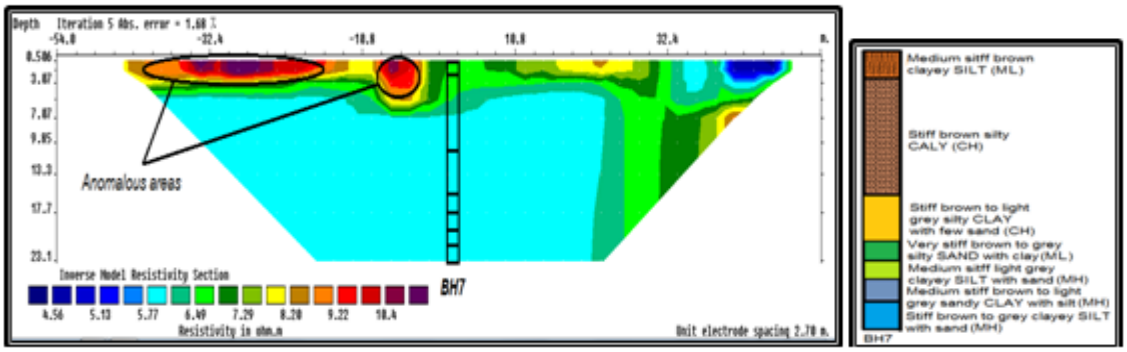

(b)

Fig. (9). Soil resistivity characterization for section 5: a) Wenner-Schlumberger and b) Wenner.

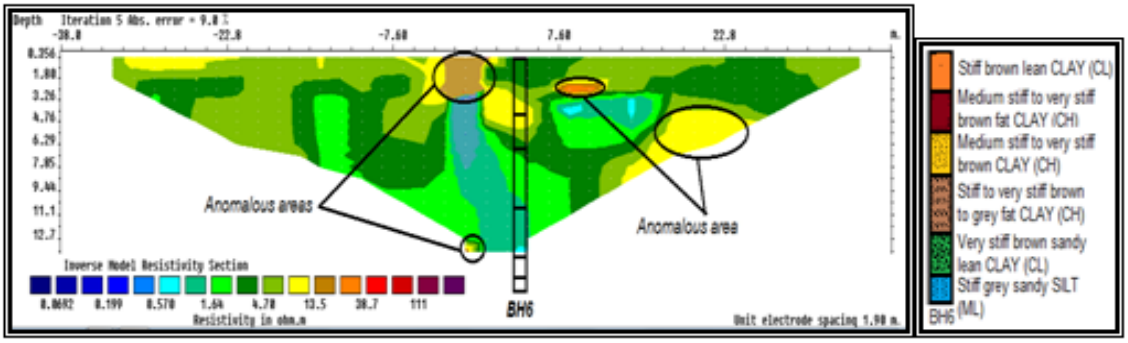

(a)

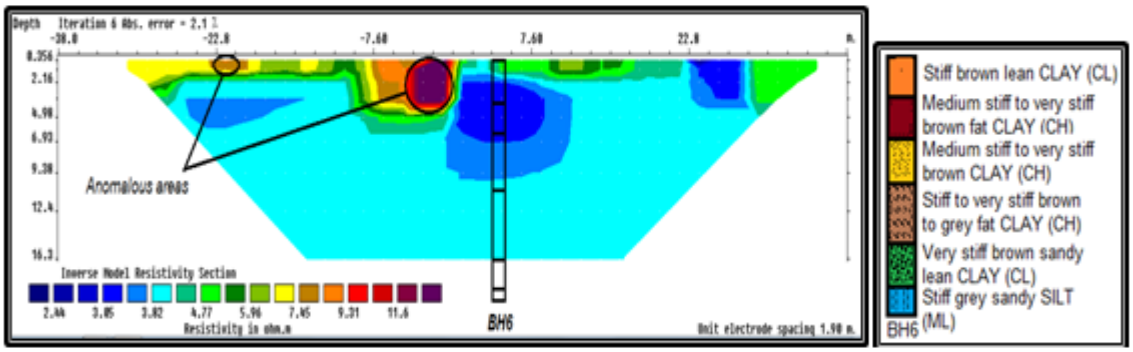

(b)

Fig. (10). Soil resistivity characterization for section 6: a) Wenner-Schlumberger and b) Wenner.

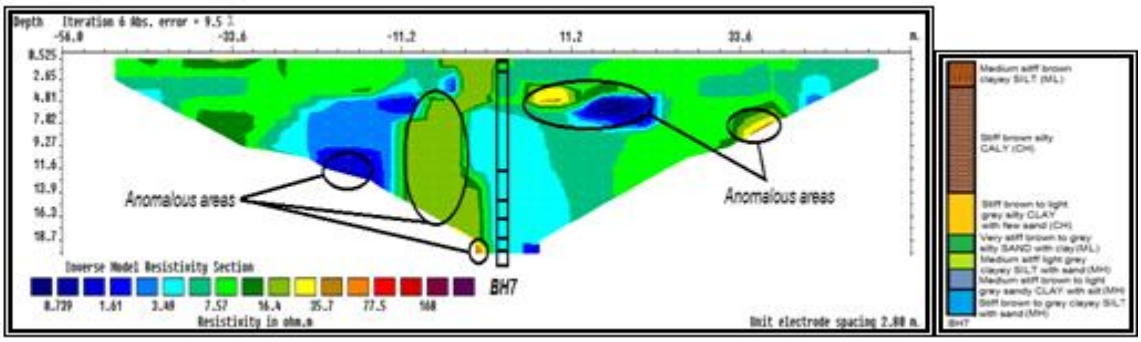

(a)

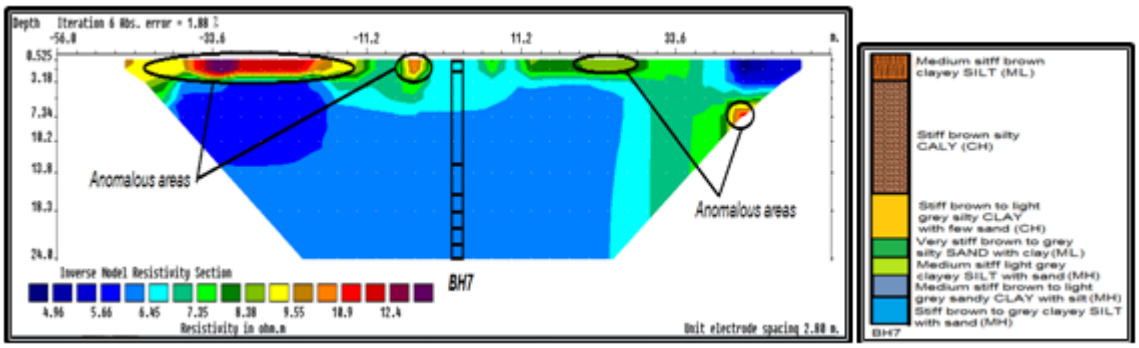

(b)

Fig. (11). Soil resistivity characterization for section 7: a) Wenner-Schlumberger and b) Wenner.

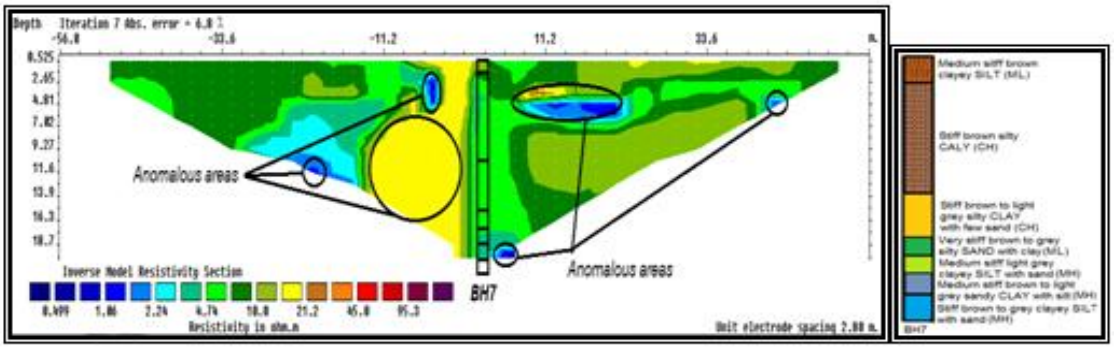

(a)

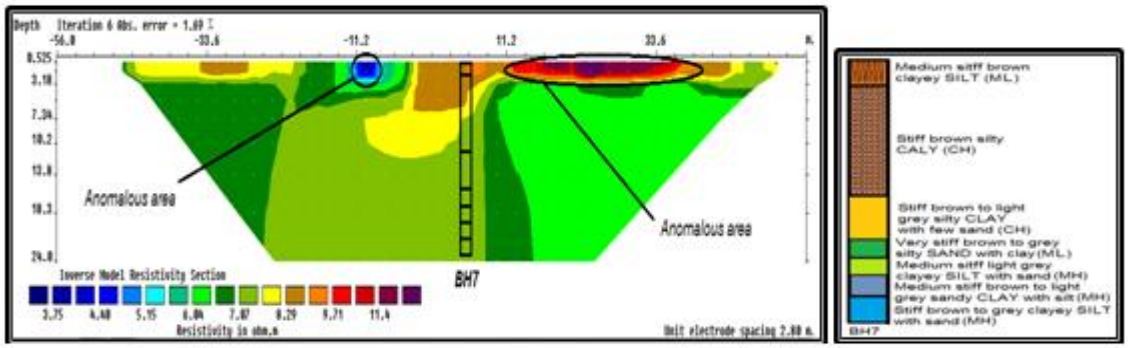

(b)

Fig. (12). Soil resistivity characterization for section 8: a) Wenner-Schlumberger and b) Wenner.

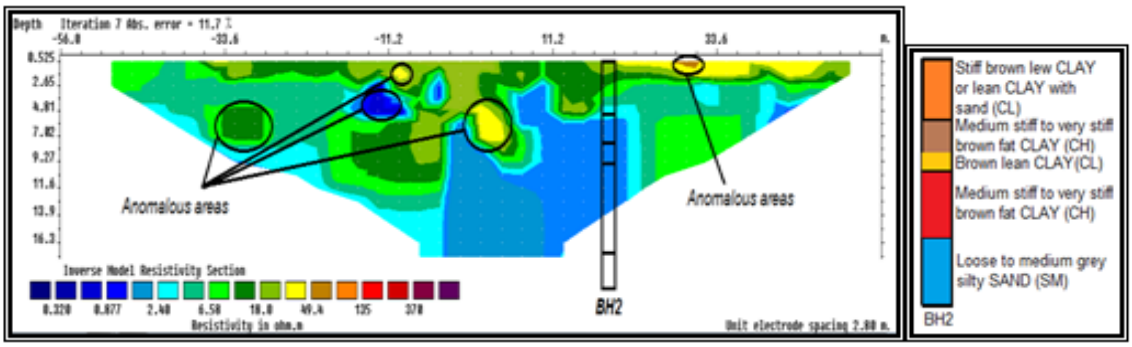

(a)

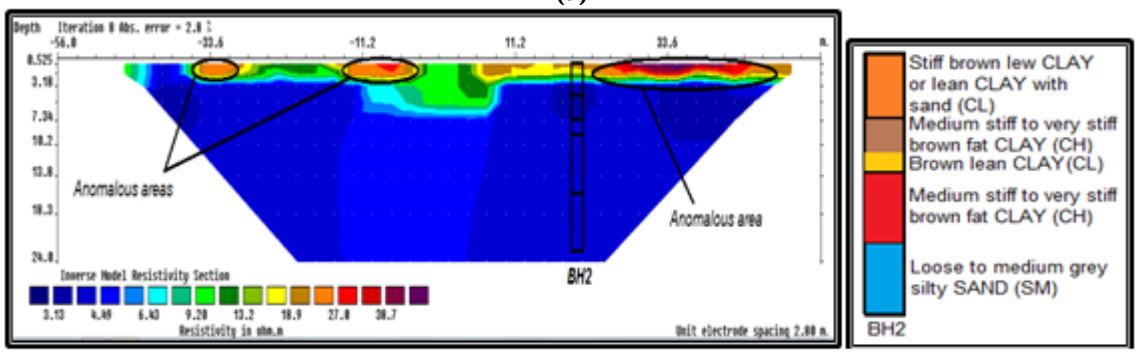

(b)

Fig. (13). Soil resistivity characterization for section 9: a) Wenner-Schlumberger and b) Wenner.

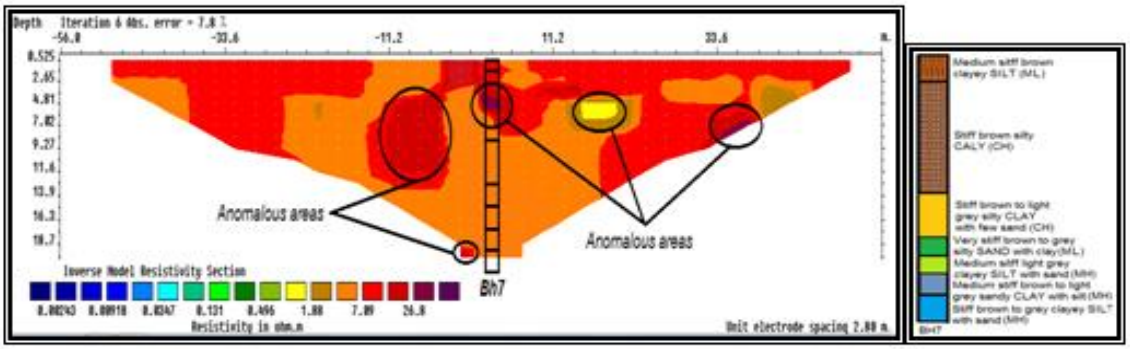

(a)

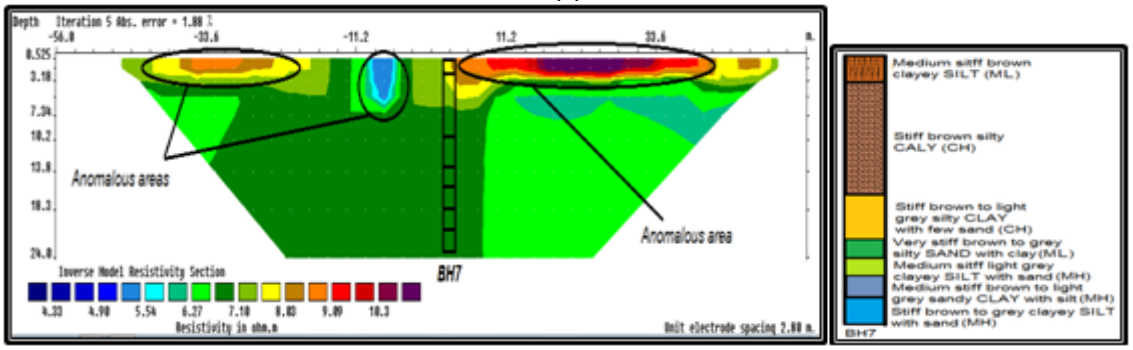

(b)

Fig. (14). Soil resistivity characterization for section 10: a) Wenner-Schlumberger and b)Wenner.

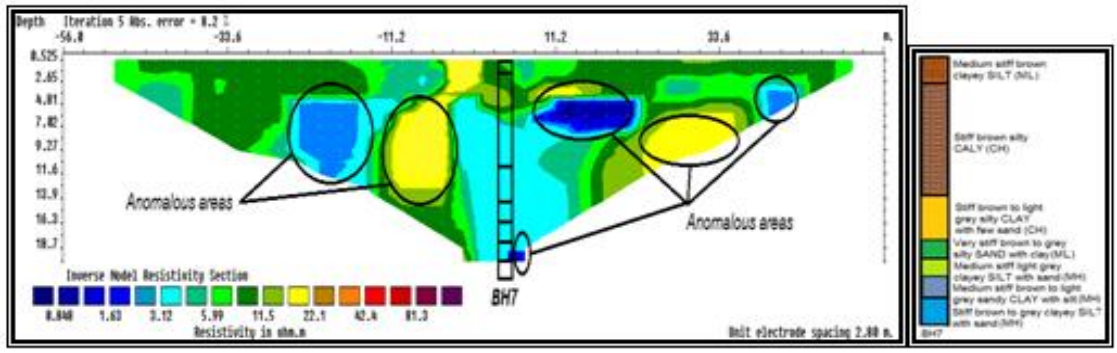

(a)

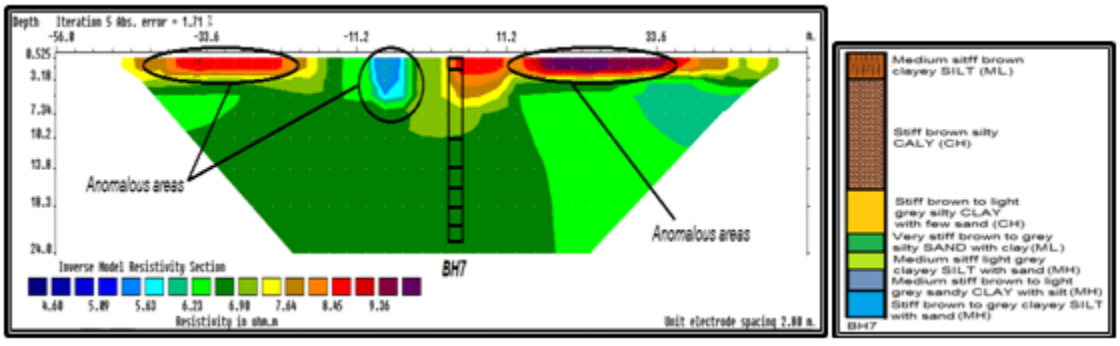

(b)

Fig. (15). Soil resistivity characterization for section 11: a) Wenner-Schlumberger and b)Wenner.

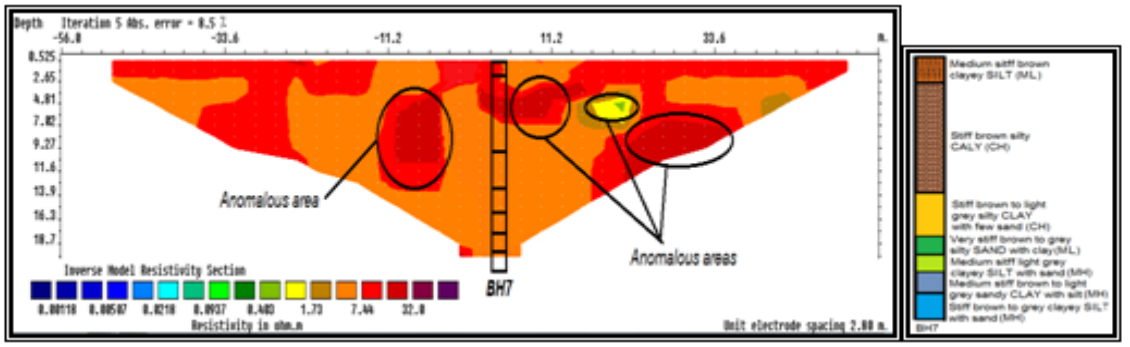

(a)

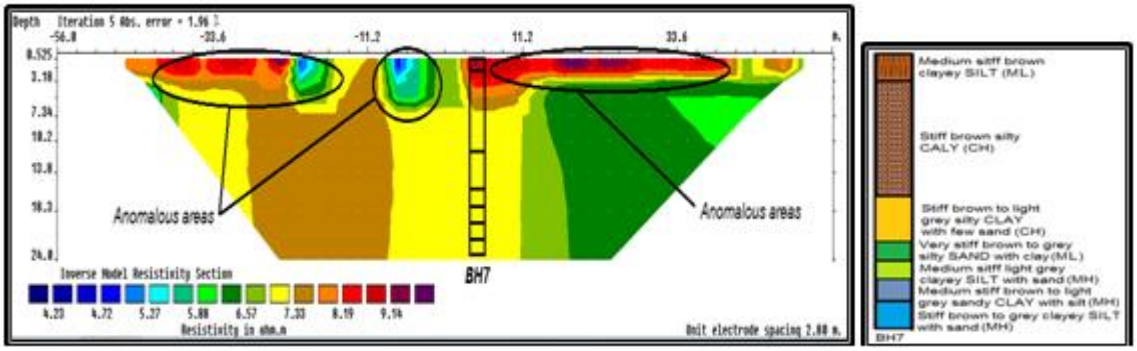

(b)

Fig. (16). Soil resistivity characterization for section 12: a) Wenner-Schlumberger and b)Wenner.

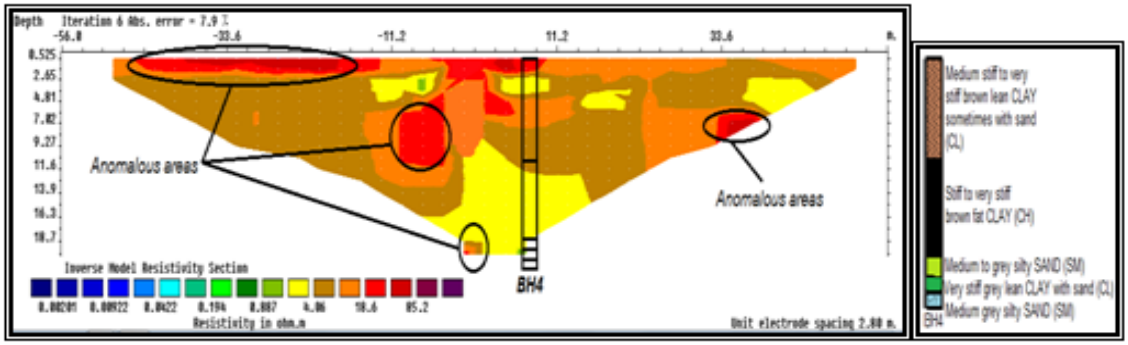

(a)

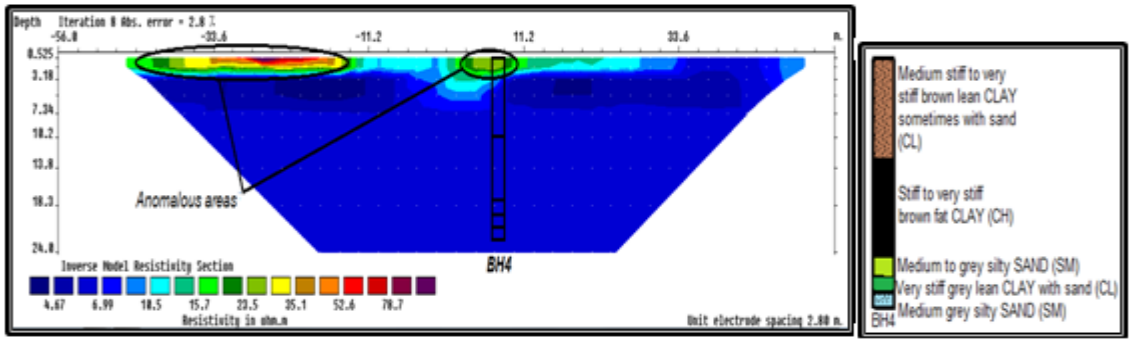

(b)

Fig. (17). Soil resistivity characterization for section 13: a) Wenner-Schlumberger and b)Wenner.

Determination of some Geotechnical (Physical) Properties from Soil Resistivity

Some geotechnical (physical) properties can be determined or estimated from soil resistivity such as porosity, void ratio conductivity, dissolved salts or solids (TDS), grain size, water content (moisture content), consistency limits (liquid limit, plastic limit and liquidity and plasticity indices) and some hydraulic parameters of groundwater strata (such as porosity, hydraulic conductivity, transmissivity, specific yield, specific retention, storage coefficient and specific capacity) [20, 21]. The variation in resistivity values is attributed to the variation in sediments type, moisture content, absence of salts (such as gypsum). Low resistivity values may be attributed to ground water (ranging around 2-3 m below NGL) or increase in moisture content or clay content. The relation between grain size composition and resistivity reflects that the decrease in resistivity with increasing fine content (clay and silt), while the increase in resistivity with increasing coarse grains (sand and gravel). Resistivity decreases with increasing L.L and P.L. as the increase in these parameters gives an indication about the increase in soil cohesion and plasticity so resistivity decreases. In this study, electrical conductivity, porosity, void ratio and TDS have been investigated for all the surveyed spreads.

Porosity

The porosity (Φ) can be determined from resistivity using Archie law (1942) [22] which is defined in the following expression:

$$F = \frac{\rho_f}{\rho_w} = a\Phi^{-m} \quad \text{or } \Phi = \sqrt[m]{\frac{a\,\rho_w}{\rho_f}} \tag{1}$$

where: F= formation factor, ρ_f = soil resistivity, ρ_w = water resistivity (it can be calculated from water conductivity E_c (from borehole if available) using the below relation [21], a and m= constants that depend on the type of soil or sediments (for the present study a = 1, m = 1.3 are taken for alluvial sediments which are the case of the studied area).

$$\rho_w = \frac{10000}{E_c} \tag{2}$$

where E_c is the electrical conductivity (μmhos/cm).

Soil and water electrical conductivity (EC)

Soil conductivity, the inverse of resistivity, can be calculated using RES2DINV program. As in resistivity imaging sections, the conductivity property can be applied and correlated with boreholes. The imaging section 1 of soil resistivity characterization for Wenner-Schlumberger array, as an example, is shown in Figure 18. As in resistivity sections, the same interpretation can be applied but in reverse. Generally, the conductivity within this section ranges between (70-900) mS/m with some heterogeneity parts, while the range (80–400) mS/m is the predominant in the whole section. As a result of the correlation of this section, the increase in conductivity represents increasing in clay contents and decreasing in sand contents. Thus the electrical conductivity for the investigated site soil along the whole spreads varies depending on the amount of moisture held by soil particles. As a guideline sands have a low conductivity (1-5 mS/m), silts have a medium conductivity (5-50 mS/m, and clays have a high conductivity (10->1000 mS/m). Consequently, EC correlates strongly to soil particle size and texture.

Accordingly, the soil site is considered to be of clayey to silty clay soil as the conductivity values are ranging between ⩾15-⩾1000 mS/m according to the above ranges and Figure 1(Grisso et al., 2009)[23].

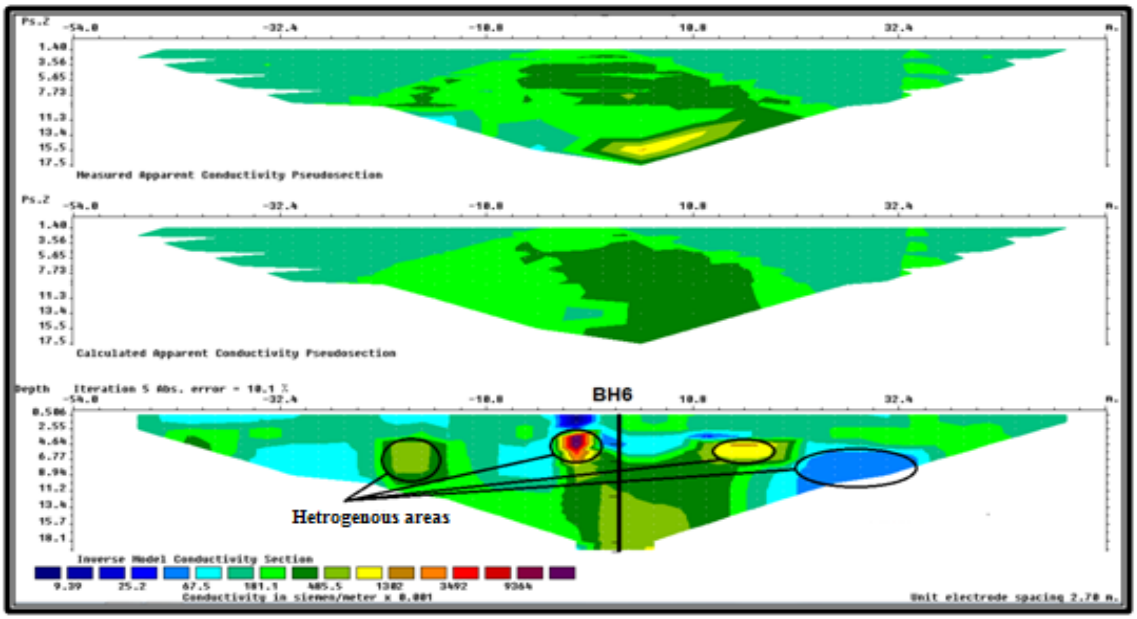

Fig. (18). Conductivity imaging section for spread no. 1 using Wenner-Schlumberger array.

For groundwater conductivity (E_c) in the studied area, it was measured to be around 300 to 400 mS/m for two tested water samples. While, water salinity= 1950 mg/ l and its pH = 7.4. By applying Eq. 2, it is found that the water resistivity for the site is between 2.5 to 3.33 ohm.m. Thus the total dissolved solids (TDS) (ppm) for groundwater can be estimated using the following relations [21]:

$$Ec\ (\mu mhos/cm) = TDS\ (ppm) * 1.54 \quad \text{or} \quad (3)$$

$$TDS\ (ppm) = Ec\ (\mu mhos/cm) * 0.64 \quad (4)$$

Accordingly, the type of water in the site is brackish as TDS values range between (1940-2560) ppm according to Todd (1980) [29] classification. Table 1 shows the summary results for the calculation of conductivity, porosity, void ratio and TDS at depth of 5-7 m for all investigated spreads.

Table (1). Summary results of some physical properties (for the depth of 5-7 m) for soil and water for the investigated spreads.

Spread No.	Soil					Water	
	Resistivity ρ_F (□□m)	Electrical Conductivity $EC\ (mS/m)$	Formation Factor ($F=\rho_F/\rho_w$)	Porosity (Φ %)	Void Ratio (e)	Resistivity ρ_w (□□m)	TDS (ppm)
1	15	66.7	4.55	31.2	0.435	3.3	1940
2	10	100	3.03	42.62	0.743	3.3	1940
3	17	58.8	5.15	28.33	0.395	3.3	1940
4	22	45.5	6.67	23.24	0.303	3.3	1940
5	25	40	10	21.06	0.267	2.5	2560
6	10	100	3.03	42.62	0.743	3.3	1940
7	8	125	2.42	50.60	1.02	2.5	2560
8	8.5	117.6	2.575	48.3	0.934	2.5	2560
9	15	66.7	4.55	31.2	0.454	3.3	1940
10	26	38.5	10.4	20.44	0.257	2.5	2560
11	12	83.3	4.8	37.04	0.588	2.5	2560
12	27	37	8.18	19.85	0.247	3.3	1940
13	16	62.5	4.85	29.7	0.422	3.3	1940

CONCLUSIONS

1. By implementing 2D resistivity imaging using Wenner-Schlumberger and Wenner arrays, it is found that Wenner-Schlumberger array is better than Wenner array as it gives greater median depth of investigation and good presentation for the subsurface both in horizontal and vertical coverage with more details.
2. The area of study is characterized by its subsurface complexity due to sediments heterogeneity as the site is generally characterized by its low resistivity values (1-15 ohm.m) which indicate that the soil is mostlyclay to silty clay with the presence of some pockets sand inter-bedded with clays.
3. In general, soil electrical resistivity in the site decreases with depth as it consists mostly of clayey soil and due to ground water effect. For conductivity, the reverse is true.
4. Electrical imaging sections reflect that the lithology of the study area is mostly of clayey soil. 4-7 distinct geoelectric layers generally represent the subsurface in the study area. High resistivity values in the topsoil, medium-high resistivity values representing the upper soil layers, while lower resistivity values are indicated in the lowest layers.
5. Some geotechnical (physical) properties were determined from soil resistivity for each spread such as porosity, void ratio and conductivity.
6. For groundwater, electrical conductivity, resistivity and TDS were determined.
7. The study concludes that the analysis of the relationships between soil geotechnical properties with electrical resistivity really provides advantages for the geotechnical engineers to solve site investigation problems and any problems related to geology efficiently and economically.

REFERENCES

[1]. Sivakugan, N., Kumar, S. K. and Das B. M *"Rock mechanis: An introduction"*, CRC Press. Taylor & Francis Group, LLC, 2013. 242 pp.

[2]. Kearey P, Brooks M, Hill I, "*An introduction to geophysical exploration",* Blackwell Science, Oxford, 2002.

[3]. Lowrie, W. *"Fundamentals of Geophysics*", Second Edition, Cambrige University Press, 2007, 381 pp.

[4]. Scollar, I., Tabbagh, A., Hesse, A. and Herzog, I., "*Archaeological Prospecting and Remote Sensing"*, 674 P., 1990. 674 pp.

[5]. Seger, M., Cousin, I. , Frison, A. , Boizard, H. and Richard, G., *" Characterisation of the structural heterogeneity of the soil tilled layer by using in situ 2D and 3D electrical resistivity measurements"*, Soil and Tillage Research, Vol. 103, Issue 2, 2009, pp. 387-398, www.ivsl.org.

[6]. Palacky, G.J., "*Clay mapping using electromagnetic methods*", First Break, Vol. 5, 1987, pp.295–306.

[7]. Fukue, M., Minatoa, T., Horibe, H. and Taya, N. (1999), "*The microstructure of clay given by resistivity measurements"*, Eng. Geol., Vol. 54, 1999, pp. 43–53.

[8]. Giao, P.H., Chung, S.G., Kim, D.Y. and Tanaka, H., "*Electrical imaging and laboratory resistivity testing for geotechnical investigation of Pusan clay deposits*", Journal of Applied Geophysics, Vol. 52, 2003, pp.157-175.

[9]. Samouelian, A., Cousin, I., Tabbagh, A., Bruand, A. and Richard, G., *"Electrical resistivity survey in soil science: a review"*, Soil Tillage Research, 2005, pp. 1 – 28.

[10]. U.S. Army Corps of Engineers, *"Geophysical exploration for engineering and environmental investigations"*, National Technical Information Service, 1995, 169 pp.

[11]. Loke M.H., "*Electrical imaging surveys for environmental and engineering studies, a practical guide to 2-D and 3-D surveys"*, Loke, www.geoelectrical.com, 2000, .57 pp.

[12]. Edwards, L.S. *"A modified pseudosection for resistivity and induced- polarization"*, Geophysics, Vol. 42, 1977, pp. 1020-1036.

[13]. Samouelian A., Cousin I., Tabbagh A., Bruand A., Richard G., *"Electrical resistivity survey in soil science: a review, soil tillage research*, 2006", pp. 173 – 193.

[14]. Loke, M. H., *"Tutorial: 2D – 3D electrical imaging surveys"*, 2004, 28 pp.

[15]. Loke, M. H., *"T Loke,utorial: 2D – 3D electrical imaging surveys"*, 2010, 110 pp., www.geoelectric.com.

[16]. ABEM Instrument AB Sweden, *"Instruction Manual Terrameter SAS 4000 / SAS 1000"*, ABEM, 2010, 136 pp.

[17]. Loke, M.H., *"Tutorial: 2-D and 3-D electrical imaging surveys*", Course Notes for USGS Workshop 2-D and 3-D Inversion and Modeling of Surface and Borehole Resistivity Data, Torrs, CT, 2001.

[18]. Pazdirek, O. and Blaha, V., *"Electrical resistivity and ground Penetrating Radar for the characterization of the internal architecture of quaternary sediments in the Midlans of Irelad"*, J. Appled Geophysics, V. 75, 2011, pp. 638-647, www.ivsl.org.

[19]. Anthony , E. "Groundwater Exploration and Management using Geophysics: Northern Region of Ghana", unpublished Ph.D Thesis, Brandenburg Technical University of Cottbus, Faculty of Environmental Sciences and Process Engineering, 2006.

[20]. Al-Nakshabandy, W. M. K., *"The relation between electrical resistivity and some geotechnical properties for soil of Samara and east Baghdad proposal electricity project"*, Unpublished M.Sc. Thesis, Baghdad University, College of Science, 2004.

[21]. Al-Rubaiay, H. J. M., *"Application of Electrical resistivity method to study hydraulic properties of Groundwater strata in Tuz Khormatu"*, Unpublished M.Sc. Thesis, 120 pp., 2004.

[22]. Archie, G.E., *"The electrical resistivity log as an aid in determining some reservoir characteristics"*. Trans. AM. Inst. Min. Metall. Pet. Eng. 146, 1942, pp. 54–62.

[23]. Grisso, R. "Bobby", Mark Alley, W.G. Wysor, David, H.,*" Soil Electrical Conductivity",* Virginia Polytechnic Institute and State University, 2009, 6 pp.

[24]. Todd, D.K, *"Ground water hydrology"*, John Wiley Inc., New-York, 1980, 336 pp.

S - 27
EFFECT OF GYPSUM CONTENT ON SOIL-WATER CHARACTERISTIC CURVE FOR CLAYEY SOILS

Suhail A. A. Khattab
Professor, Civil Engineering Department
suhailkhattab@yahoo.com

Asaad M. A. M. Al-Omari
Assistant lecturer, Civil Engineering Department
Asaad.civil@gmail.com

University of Mosul

Abstract

This research work studies the effect of the addition of varying percentage of gypsum content on the behavior of soil-water characteristic curve (SWCC) for natural clayey soils. Tests were conducted to determine SWCCs covering nearly the entire range of soil suction (100 - 10^6) kPa, for two soil samples selected from Mosul city: Al-Jammia, (soil J) and Al-Yrmook (soil Y). Results indicated that the shape mode of SWCC remained the same for all the studied cases with the occurrence of a change including an increase in the water holding capacity and air entry value due to varying initial water content. On the other hand, the effect of addition of various gypsum percent to the natural clayey soils on their SWCCs behavior was impalpable. Finally, a mathematical model for SWCC was found for all studied cases using (Fredlund & Xing, 1994) equation Model, with aid of FORTRAN program, the parameters of mathematical model were analyzed statistically, the values of R^2 ranged from (0.99868–0.99955), and SSR (1.4434–7.7205).

***Keywords**:* clayey soils, , gypsum content, soil suction, soil water characteristic curve

تأثير المحتوى الجبسي على خصائص منحني خاصية التربة-الماء للترب الطينية

د.سهيل إدريس عبد القادر خطاب
أستاذ ، قسم الهندسة المدنية-جامعة الموصل
suhailkhattab@yahoo.com

اسعد محمد أزهر مصباح العمري
مدرس مساعد، قسم الهندسة المدنية-جامعة الموصل
Asaad.civil@gmail.com

الخلاصة

يهتم هذا البحث بدراسة تصرف سلوك منحني خاصية التربة-الماء نتيجة تأثير إضافة نسب مختلفة من الجبسم للتربة الطينية. أجريت الفحوصات لنوعين من التربة الطينية لموقعين داخل مدينة الموصل (مدينة الجامعة واليرموك) وتم إيجاد المدى الكامل لاجهادات المص للتربة (100 – 10^6) كيلوباسكال.

بينت النتائج ان شكل منحني خاصية التربة-الماء لم يتغير ولكل الحالات المدروسة مع حدوث زيادة في كل من قابلية التربة للاحتفاظ بالماء وقيم دخول الهواء نتيجة تغاير المحتوى المائي الابتدائي للتربة. من الناحية الأخرى، لم يكن واضحاً تأثير إضافة نسب مختلفة من الجبسم للتربة الطينية في هذه الدراسة نسبة لتصرف وسلوك منحني خاصية التربة-الماء. كما تم استخدام برنامج بلغة فورتران لإيجاد التمثيل الرياضي لمنحني خاصية التربة-الماء وباستخدام معادلة (فردلاند واكسنك 1994)، بالإضافة إلى تحليل نتائج التمثيل الرياضي إحصائياً ووجد بان قيم معامل الارتباط تتغاير بحدود (0.9986-0.9995) وقيم مجموع المربعات المتبقية (0.1443-7.720).

1. Introduction

The case of unsaturated soil represents the general case of soils that consist of three principle phases: solid materials, water, and air. Here, it is very important to state the fourth type of interpenetrated air-water phase (contractile skin).

Soil suction stresses play one of the important roles that govern the behaviors of unsaturated soils. Soil suction represents the negative pressure applied on the soil pores-water, so the lack of water in soil pores lead to increases the soil suction, and vice versa. Generally, total suction consists of two components, matric and osmotic suctions. Matric suction represents the difference between pore-air pressure and pore-water pressure (ua - uw), while osmotic suction indicate the existence of salt solution in the soil pores-water. It is indicated that, when the value of soil suction is greater than (1500) kPa, the total and matric suctions refer nearly to the same meaning [1]. The behavior of unsaturated soil is more difficult due to the complex thermodynamics correlations for soil phases. In the past few years, intensive studies and researches were done in attempt to understand the behavior of unsaturated soil mechanics which help the geotechnical engineers to represent the original cases for soils.

There is an inverse relationship of soil suction and its water content, the curve that correlate this relationship is called the soil water characteristic curve (SWCC), or may be named: soil water retention curve. The SWCC is a continuous function that represents the soil ability to store the water in function of soil suction. It is the relationship between the amount of water in soil pores (may be expressed as gravimetric water content, volumetric water content, or degree of saturation) and soil suction. Many SWCCs could be constructed for a certain soil, depending on the initial state of soil placement and stress history. In general there are many types of SWCCs for a certain soil type and conditions with two boarder curves: drying-desorption curve, saturation is the initial state of the soil going to dryness due to suction, while wetting-adsorption curve, the dry represents the initial state of the soil. Several factors such as soil structure, initial water content, void ratio, soil type, mineralogy, and compaction method also have a potentially significant effect on features of the SWCC. Among these factors, stress history and initial water content often have the greatest effect on soil structure, which in turn dominates the nature of the soil-water characteristic curve, [2].

Locally, several researches studied some of the engineering properties for various unsaturated soils. However, insufficient research has been especially directed for understanding the behavior of unsaturated gypseous soils. Iraq is one of the areas include soils with various gypsum contents ranged between a few percent of gypsum and could reach to more than 60 [3].

2. **Mathematical Model for SWCC**:

The main goal of using the mathematical model of SWCC is to find the best fit for the experimental data. The presentation of the SWCC can be conducted using various equations proposed by: [1, 4, 5, 6], see Table (1). The experimental work done by Khattab and Al-Taie, 2005 [7] includes studying the behavior of SWCC for three clayey soils with the entire suction range. They found that the (Fredlund and Xing, 1994) model best fits the SWCCs. On the other hand, Miller et al., 2002 [8] found that all the above models, except Gardener model, provide an acceptable fit to the experimental data representing the SWCC with small suction range (100- 1000) kPa of clayey soils.

The obtained data in this experimental work were best fitted to smooth SWCC using Fredlund-Xing mathematical model, the equation parameters (a, n, m) with statistical indices (sum of square residual, SSR and correlation factor, R^2) are determined using the program

prepared by Khattab and Al-Taie, 2005 [7]. It should be noted that the continuous lines of SWCC shown in figures (2, 3, 4 and 5) represent the best fit curves using Fredlund and Xing equation, while the points represent the experimentally obtained data.

Table (1) Equations for mathematical presentation of SWCC

Author	Year	Equation	Parameters
Gardner, [4]	1958	$\Theta = \frac{1}{1+\alpha.\psi^{n}}$ $\Theta = \frac{\theta-\theta_r}{\theta_s-\theta_r}$	ψ: Soil suction. α, n: Equation parameters. θ_s: Saturation volumetric water content θ_r: Residual volumetric water content Θ: Normalized water content.
Brooks-Corney, [5]	1964	$\Theta = \left(\frac{\psi_b}{\psi}\right)^{\lambda}$	Ψ_b: Bubbling suction. ψ: Soil suction. λ: Pore size index. Θ: Normalized water content.
Van Genuchten, [6]	1980	$\Theta = \left[\frac{1}{1+(p\cdot\psi)^{n}}\right]^{m}$	p, m, n: Equation parameters. ψ: Soil suction. Θ: Normalized water content.
Fredlund-Xing, [1]	1994	$\theta(\psi,a,n,m) = C(\psi)\cdot\frac{\theta_s}{\left\{\ln\left[e+\left(\frac{\psi}{a}\right)^{n}\right]\right\}^{m}}$ $C(\psi) = \frac{-\ln\left(1+\left(\frac{\psi}{\psi_r}\right)\right)}{\ln\left[1+\left(\frac{10^{6}}{\psi_r}\right)\right]}+1$	a, m, n: Equation parameters. θ_s: Saturation volumetric water content ψ: Soil suction. ψ_r: Residual suction.

3. Testing Program

3.1 The soils

This paper presents an experimental results attained on two natural clayey soils and their mixtures with 5%, 10% and 20% gypsum content. Both natural clayey soils located in Mosul city denoted as: Al-Jammia (highly expansive clay, soil (J), obtained from the site located behind the Mosul university's stadium, and Al-Yrmook (moderate expansive clay, soil (Y), which is brought from the site located near electricity office building). Soil characterization data are presented in Table (2). According to Senthen, 1980 [9], soil (J) and soil (y) are classified as very high and moderate swelling potential respectively.

A hydrated gypsum $CaSO_4.2H_2O$, added to natural clayey soils has a purity of 91.7%, concentration and percentage of carbonate ($HCO^{-}3$, $CO^{-}3$) about 8.3 % with specific gravity of 2.3. Gypsum saturated solution with a concentration of 2.0 g/l was poured to the dry soil with adequate percentages to insure, after air drying, preparing soil with (5, 10, 20) % gypsum contents.

Table (2) Soils Characterization

Property		Soil (J)	Soil (Y)
Specific gravity		2.75	2.71
Particle size analysis	Sand (%)	5	16
	Silt (%)	51	52
	Clay (%)	44	32
Atterberg limits	LL (%)	75	45
	PL (%)	30	22
	PI (%)	45	23
Unified Soil Classification System		CH	CL
Compaction Characteristic (Standard Proctor effort)	O.M.C (%)	24	20.1
	Dry unit weight (kPa)	14.91	16.43

3.2 Sample preparation

The compacted samples were formed by mixing the dry soil (oven dry at 110 ± 10 ºC for soils J and Y) at various initial water contents and dry unit weights, see Table (3). The products were compacted into a steel mold to get samples with 3.0 cm in diameter and 1.2 cm in height. The soil samples were statically compacted with a rate of 1.0 mm/min [10], then kept under the compacted load for several minutes to avoid the rebound.

All soil samples were covered with aluminum foil, then kept in desiccators for (45-50) days (humidity control method), and (15) days (osmotic membrane method) [7]. The masses of the soil samples were measured to determine their water content using digital balance of (0.0001g) accuracy.

Table (3) Cases of studied soil samples of clayey soils treated with gypsum

Soil type	Compaction case (Standard Proctor effort)	Dry unit weight, (kN/m^3)	Water content, (%)
Natural soil (J) and treated with Gypsum content (5, 10, 20)%	Wet of optimum	14.6	28.5
	Optimum	14.9	24.0
	Dry of optimum	14.6	16.0
Natural soil (Y) and treated with Gypsum content (5, 10, 20)%	Wet of optimum	15.6	23.2
	Optimum	16.4	20.1
	Dry of optimum	15.6	16.5

3.3 Measuring SWCC

The SWCCs were found by two methods: Osmotic Membrane method, and Humidity Control Method, those methods are explained below:

- Osmotic Membrane Method: The suction values that have been obtained by this method ranged between (0 - 1500) kPa. Soil samples inside the semi impermeable membrane (which allows the moisture movement in one direction only) soaked into the closed glass bags containing the Poly-ethylene Glycol (P.E.G) solution with different concentrations to impose various values of suction. Figure (1) shows the calibration curve for the suction values versus the concentration of (P.E.G.) corresponding to (10, 200, 800) kPa have been used. An

equilibrium period of 15 days were considered [7], then the water content of the soil samples were measured after an equilibrium attained using sensitive balance of 0.0001 g accuracy.

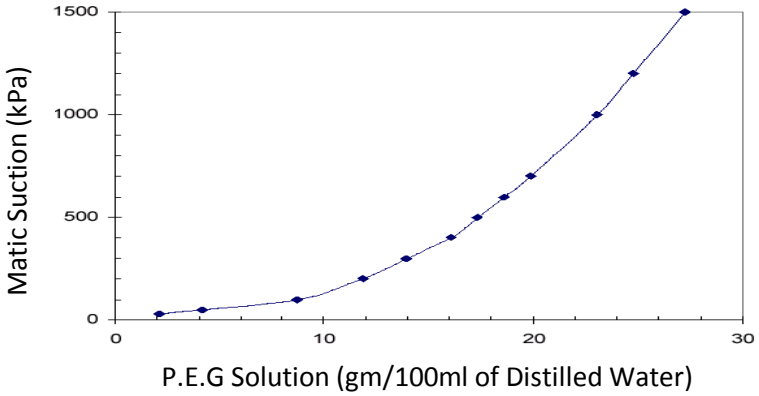

Figure (1), The calibration curve for the matric suction and P.E.G concentrations

- Humidity Control Method: The suction values obtained by this method ranged between (1600 – 1,000,000) kPa [11]. The concept of this method depends on Galvin equation derived from the law of ideal gas. The total suction in soils can be measured by calculating the partial vapor pressure of the soil water. The relationship between the partial vapor pressure of the pore-water vapor and the total suction is given as shown below, [12]:

$$h_t = -\frac{R.T}{v_{wo}.w_o}\ln\left(\frac{\bar{u}_v}{\bar{u}_{vo}}\right) \quad \text{----------} \quad (1)$$

where :

h_t : Total soil suction

R : Gas constant

T : 273.16+t, t: temperature

w_o : Specific volume of water

$\bar{u}_v$: Molecular mass of water vapor

$\bar{u}_{vo}$: Partial pressure of pore-water

v_{wo} : Saturation pressure of water vapor over a flat surface of pure water at the same temperature

$\frac{\bar{u}_v}{\bar{u}_{vo}}$: Relative humidity

$$h_t = -135022 \times \ln\frac{\bar{u}_v}{\bar{u}_{vo}} \quad \text{----------} \quad (2)$$

Using the reference temperature of 25°C, Equation 1 was summarized to the form presented in Equation 2 and the total suction can be calculated as follows, [12]:

Desiccators containing saturated salt solutions that create a particular relative humidity inside the desiccators, soil samples inside the desiccators will absorb or desorbs the moisture until the suction equilibrium is reached which is considered to be 45 days for the present study [7].

4 Results and Discussion

The effect of initial water and gypsum contents on the soil-water characteristic curves behavior for two soils type J and Y, at natural condition and treated with various gypsum percent (5, 10, and 20 %) were examined. The soil samples were prepared with initial water content and dry unit weight in three compaction conditions (dry of optimum, optimum, and wet of optimum), Table (3). The following paragraphs demonstrate the obtained results and discussions.

4.1 Effect of initial water content

Figures (2 and 3) show the Soil-water characteristic curves (SWCCs) for natural soil-J (CH), soil-Y (CL) and gypseous soils. It is clear that the SWCCs have the S-shape for the natural and gypseous soils, and the SWCC`s were arranged from soil samples compacted in the wet side then at optimum and finally at dry side along the entire soil suction range and for all the studied cases. These results could be attributed to the fact that the soil samples that are compacted at dry condition have open pore structure (i.e. relatively large air pores), while the pores of soil samples that are compacted at wet condition are discontinuous and/or closed with pores water, and hence the cohesion forces between water molecules are greater than adhesion forces between water and air. As a result the wet condition curves have higher soil-water holding capacity than curves of dry condition. These findings are similar to the results obtained by Vanapalli et al., 1998; Al-Taie, 2005; Al-Safi, 2006 [13, 14, and 15].

At high suction values the observed SWCC`s are close together with reducing volumetric water content, these observations were recognized for all the studied cases. This could be explained by the fact that any porous medium has a maximum suction related to a zero relative humidity [1]. Table (4) shows the results of mathematical model for SWCC representing with equation parameters (a, n, m) and statistical indices (SSR , R^2) for SWCCs of natural and gypseous soils (J, Y) corresponding to the effects of initial water content.

4.2 Effect of gypsum content

Statically compacted soil samples were prepared with three gypsum percentages (5, 10, and 20%) added to natural clayey soils J and Y. They were compacted in three conditions, see Table (3). Figures (4 and 5) show the SWCCs for the two natural soils J and Y with three percentage of added gypsum. The results indicate there are no logical arrangements for these curves with corresponding to gypsum content in the natural soils. This could be attributed to the effect of gypsum dissolution process, this dissolution liberalize Ca^{++} which could act as an extendable cation within the clay lattice, thus the added gypsum, after dissolution, will not act as a saline solution which lead to raising the total soil suction by increasing the osmotic suction component, but it dissolved to two components; SO_4 anions and Ca^{++} cations. It is known that the clay particle carry a net negative charge on their surface which is balanced by exchangeable cations surrounding the particles being held by electrostatic attraction. On the contrary, the results presented by Khattab and Al-Omary [16] revealed there is a significant effects on the behavior of SWCCs due to added gypsum percentages to the natural silty sand soil, they found the water holding capacity increase with added gypsum to the soil.

Table (4) shows the results of mathematical model for SWCC representing with equation parameters (a, n, m) and statistical indices (SSR , R^2) for SWCCs of natural and gypseous soils (J, Y) corresponding to the effects of gypsum content.

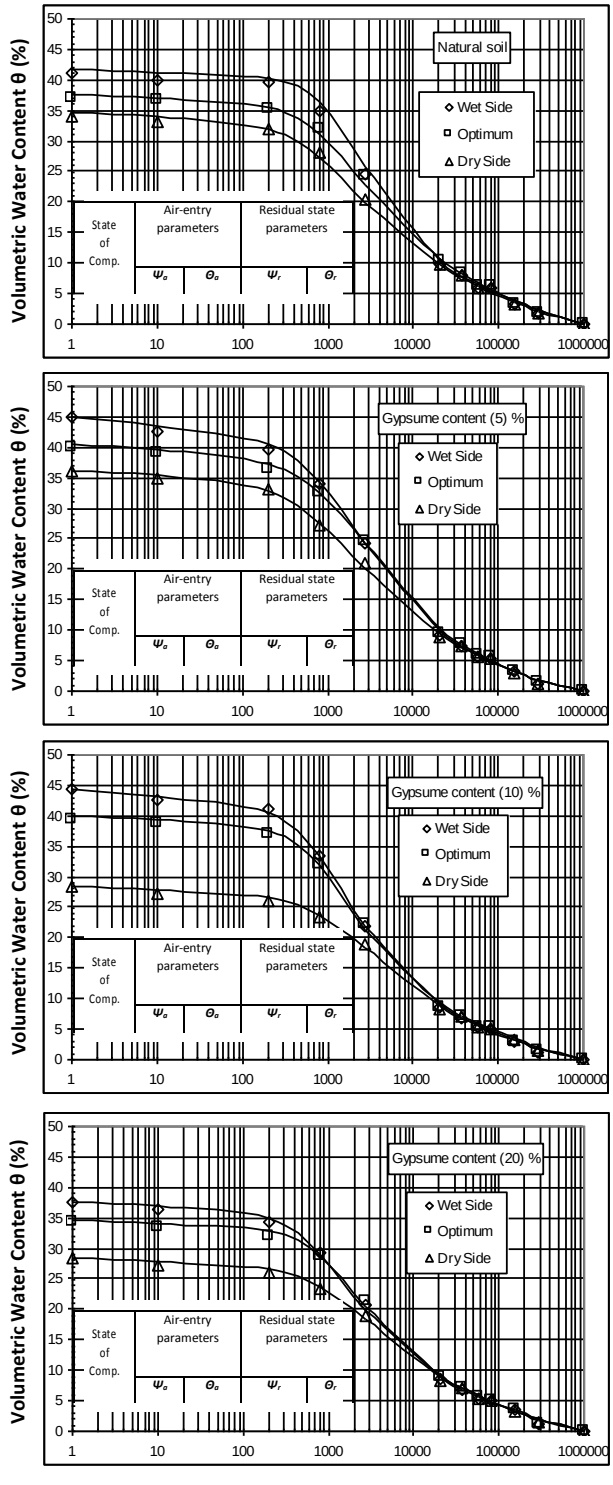

Figure (2), Soil-water characteristic curves for natural and gypseous soil-J at different initial water content

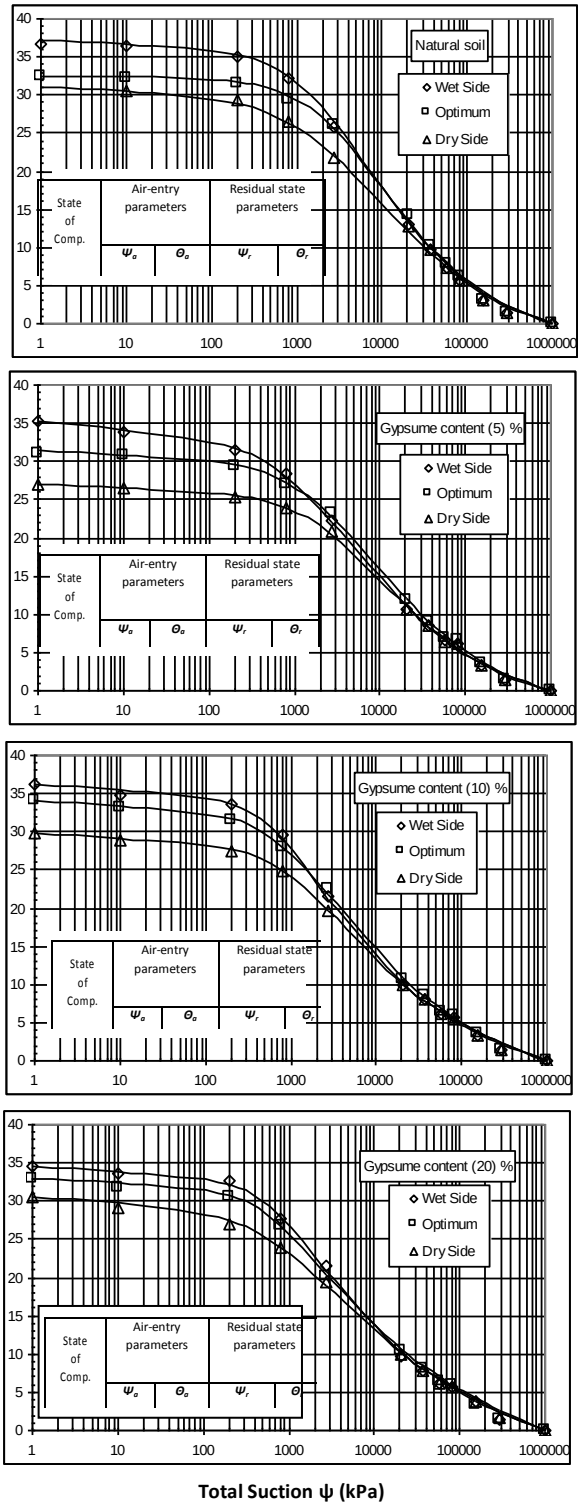

Figure (3), Soil-water characteristic curves for natural and gypseous soil-Y at different initial water content

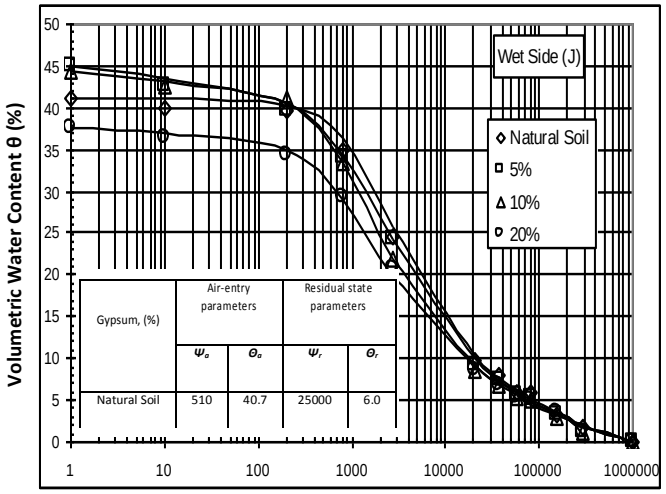

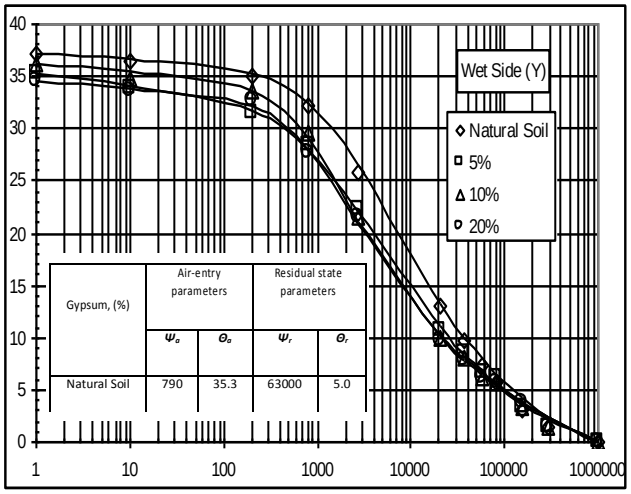

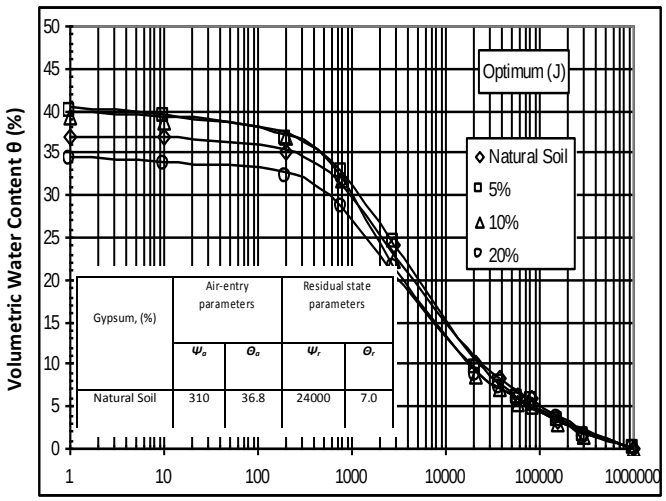

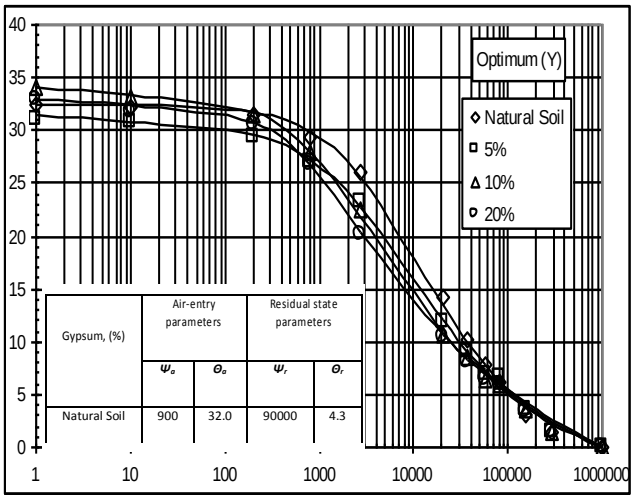

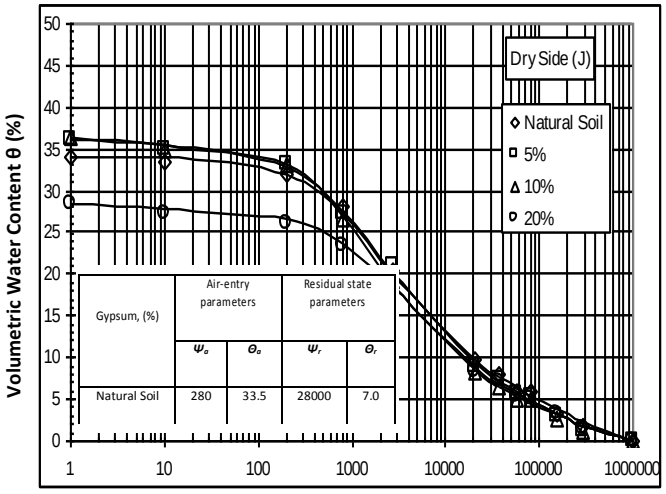

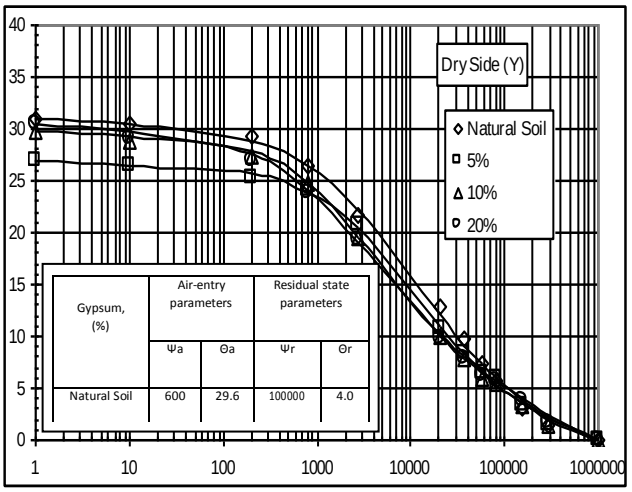

Figure (4), The SWCCs for natural soil (J) with three percentage of added gypsum

Figure (5), The SWCCs for natural soil (Y) with three percentage of added gypsum

Table (4) SWCC parameters & statistical indexes for soils J and Y related to the effect of the added gypsum

Soil type		Studied case	Equations parameters			Statistical indexes	
			a	n	m	SSR	R^2
Soil (J) Gypsum percent (%)	Natural	Wet of optimum	1479	1.5000	0.8390	6.186	0.9990
		Optimum	1256	1.1490	0.9259	4.076	0.9991
		Dry of optimum	989	1.0289	0.9419	2.609	0.9991
	5 %	Wet of optimum	1025	0.9979	1.0109	6.078	0.9990
		Optimum	1391	09239	1.0159	4.415	0.9990
		Dry of optimum	1115	0.8620	1.2120	2.984	0.9990
	10 %	Wet of optimum	855	1.2540	0.9479	2.863	0.9995
		Optimum	936	1.2950	0.9249	7.720	0.9994
		Dry of optimum	709	1.1750	0.8570	2.083	0.9992
	20 %	Wet of optimum	881	1.1710	0.9609	3.251	0.9992
		Optimum	1254	1.2000	0.9429	2.483	0.9992
		Dry of optimum	1655	0.9519	1.0410	2.703	0.9986
Soil (Y) Gypsum percent (%)	Natural	Wet of optimum	2905	0.8780	1.1420	2.049	0.9994
		Optimum	4950	0.8750	1.0830	2.276	0.9993
		Dry of optimum	3985	0.6730	1.3801	2.633	0.9987
	5 %	Wet of optimum	2185	0.8500	1.3740	2.791	0.9989
		Optimum	3843	0.7750	1.2840	2.614	0.9989
		Dry of optimum	4631	0.8290	1.2200	1.443	0.9888
	10 %	Wet of optimum	1019	1.1150	0.8710	2.716	0.9992
		Optimum	1636	0.8989	1.0680	2.358	0.9992
		Dry of optimum	1734	0.8880	1.0350	1.868	0.9991
	20 %	Wet of optimum	1169	1.0450	0.9389	3.012	0.9991
		Optimum	1123	0.9979	0.9079	3.519	0.9991
		Dry of optimum	1486	0.7629	1.1630	2.317	0.9991

5. Conclusions

The SWCCs with entire soil suction range of the natural clayey soils and with different added gypsum percent were studied, from the present study the findings can be summarized as follows:

1) The soil water characteristic curves have the same S-shape for the three cases of initial water content both for high plasticity clay (CH) and low plasticity clay (CL). The soil water characteristic curves were arranged from soil samples compacted in the wet side with high air entry value then at optimum and finally at dry side with low air entry value along the entire soil suction range and for all studied cases.
2) The shape mode of soil water characteristic curves remained the same both for high plasticity clay (CH) and low plasticity clay (CL) for all the added percentages of gypsums. There is no effect of added gypsum to the natural clayey soils on the behavior of soil water characteristic curves.
3) Finally, the mathematical equation (Fredlund & Xing 1994) was used for modeling the experimental data. The best statistical indices were obtained; the values of SSR R^2 ranged between (1.443 – 7.720) and (0.9986 – 0.9995), respectively.

References

[1] Fredlund, D.G. and Xing, A., "Equations for the soil-water characteristic curve", Canadian Geotechnical Journal, Vol. 31, No. 3, 1994, pp. 521–532.

[2] Zhou, J. and Yu, J., "Influences affecting the soil-water characteristic curve", Journal of Zhejiang University SCIENCE, Vol. 6A No. 8, 2005, pp. 797-804.

[3] Al-Qaissy, F. F., "Effect of Gypsum Content and its Migration on Compressibility and Shear Strength of the Soil", M.Sc. Thesis, University of Technology, Iraq, 1989.

[4] Gardner, W. R., "Some steady-state of the unsaturated moisture flow equation with application to evaporation from water table", Soil Science, Vol. 85, No. 3, 1958, pp. 228-232.

[5] Brooks, R. H., and Corey, A. T., "Hydraulic properties of porous medium", Colorado State University (Fort Collins), Hydrology Paper, Vol. 27, No. 3, March 1964.

[6] Van Genuchten, M. T., "A Closed form equation for predicting the hydraulic conductivity of unsaturated soils", Journal of Soil Science Society of American, Vol. 44, No. 5, 1980, pp. 892-898.

[7] Khattab, S. A. A., and AL-Taie, L. Kh. I., "Behavior of soil water characteristic curve (SWCC) for lime treated expansive soil and untreated soils from Mosul city", Proceeding of Unsaturated 2006, 4th International Conference on Unsaturated Soils, ASCE Special Publication No. 147, Vol. 2, 2005, pp. 1671-1682.

[8] Miller, C. J., Yesiller, N., Yaldo, K. and Merayyan, S., "Impact of soil type and compaction conditions on soil water characteristic" Journal of Geotechnical and Geoenvironmental Engineering, Vol. 128, No. 9, 2002, pp. 733-742.

[9] Senthen, D. R., "Characterization of expansive soils using soil suction data", Proc. of 4th Int. Conf. on Expansive Soil, Colorado, Vol. 1. 1980.

[10] Khattab, S. A. A., "Eude multi-echelles d'un sol plastique traite' a' la chaux", Ph. D. Thesis, Orleans University, France, 2002.

[11] Guillot, X., "Couplage entre propriétés microscopiques et comportment mécanique d'un matériau argileux", Ph. D. Thesis, Ecole Centrale Paris, France, 2002.

[12] Fredlund, D. G., and Rahardjo, H., "Soil mechanics for unsaturated soils", John Wily and Sons, Inc., USA, 1993.

[13] Vanapalli, S. K., Pufahl, D. E., and Fredlund, D. G., "The Effect of Stress State on the Soil Water Characteristic of a compacted Sandy-Clay Till", 51st Canadian Geotechnical Conference, Edmonton, Alberta, October 4-7, 1998, Vol. 1, pp. 87-94.

[14] AL-Taie, L. Kh. I., "Correlation between Suction and Some Engineering Properties of Lime Stabilized Clayey Soil from Mosul City", M. Sc. Thesis, Mosul University, Iraq, 2005.

[15] AL–Safi, M. K. F., "A Field-Laboratory Study of the Relationship Between (Swelling/Shrinkage) and Different Degrees of Suction of Expansive Clayey Soils Selected from Mosul City", M. Sc. Thesis. Mosul University, Iraq, 2006.

[16] Khattab, S. A. and Al-Omary A. M. A., "Effect of Disturbance and Gypsum content on Soil Water Characteristic Curve", 2nd International Conference on New Development in Soil Mechanics and Geotechnical Engineering, Near East University, Nicosia, North Cyprus, May 28-30, 2009, pp. 426-433.

Effect of Repeating Load on the Tensile Strength of Stabilized Mosul Clay

Dr. Al-Layla M.T. Professor
Dr. Al-Dabbagh A.W. Lecturer
Dr. Jaro M.N. Assist. Lecture
College of Engg. / Mosul University

Abstract

This work aims to study the tensile strength and the tensile stress-strain characteristics under the effect of the repeated loading on the lime stabilized clayey soil. The soil was treated with (2, 4 and 6%) lime, then compacted at optimum moisture content using the modified compaction effort, the stabilized samples were cured for (2) days at temperature (49^{o}C). The samples were subjected to (4) cycles of repeated loading (loading/unloading is one cycle). The applied repeated loading represented (25% and 50 %) of failure load for each group. It was found that the strength decrease (27-54%) with the cycles of loading while the strain increase. Also the tensile stress – strain curves from the repeated loading are similar to the load – deflection curves.

Key words: clayey soil treated with lime, Cycles of Loading/Unloading, Load-deflection Curves, Tensile Strength, Tensile Stress-Strain.

تأثير الاحمال المتكررة على قوة الشد للتربة الطينية المثبتة في مدينة الموصل

د. محمد طيب حسين الليلة أستاذ
د. ايمن وليد الدباغ مدرس
د. محمد ناظم جارو مدرس مساعد
كلية الهندسة/جامعة الموصل

الخلاصة

يهدف هذا البحث إلى دراسة قوة الشد وسلوكية منحنيات الإجهاد-الانفعال، تحت تأثير الأحمال المتكررة على مقاومة التربة طينية مثبتة بالنورة. تم معاملة التربة بالنورة بنسب (4,2 و 6%) عند المحتوى الرطوبي الامثل باستخدام طرقة الرص المعدلة وقد انضجت لمدة (2) يوم وبدرجة حرارة (49^{o}C). بعد الانضاج عرضت النماذج الى (4) دورات من الأحمال المتكررة (تحميل/واللاتحميل دوره واحدة) وتحت تأثير نسب مختلفة من إجهاد الفشل (50,25%) وجد أن العلاقة بين الحمل المسلط-الأود تحت تأثير الأحمال المتكررة مشابهة إلى حد كبير للعلاقة بين الإجهاد-الانفعال، وان الانفعال يزداد مع عدد الدورات بينما القوة تقل(27-54%).

Introduction

A highway pavement is a structure consists of superimposed layers whose primary function is to distribute the traffic load to the subgrade layer. This layer is subjected to repeated tensile stress due to traffic movement [1,2]. Knowing the behavior of the layer under these stresses are necessary for a proper and durable design.

The tensile strength of natural soil is much less than the compressive strength, the tensile strength can be improved by stabilizing the soil.

Jaro [3] used cement to stabilized sub-base material and he found that the tensile strength increase considerably.

Al-Layla & Al-Zubaydi [4] studied the effect of repeated loading on the lime – stabilized gypsouse soil. They found that the tensile strength decreased due to the repeated loading. They stated that the amount of reduction of tensile strength depending on the number of cycles and the values of applied load.

Al-Omary [5] investigated the tensile strength of lime stabilized cohesive soil and recommended the lime stabilization to improved the tensile strength of soil.

Al-Layla et al [6] conducted a flexural tension test on a lime stabilized cohesive soil. They found that the tensile strength increased due to the addition of lime and the improvement depend on the curing condition and the improving in compressive strength more than in tensile strength.

There are several tests used to determine the tensile strength, these tests are 1) Direct (uniaxial) tensile test 2) Indirect (brazilian) tensile test and 3) Flexure (beam) test. The flexural is recommended for the pavement design since the slab action are more probably to occur under traffic movements.

This study investigates the effect of repeated loading on the tensile strength of lime stabilized clayey soil.

Material

Soil

The soil used in this study is a clayey soil brought from Al-Hadbaa district in Mosul city. Table (1) shows some of the index properties of the soil.

Table(1) index properties of soil

Liquid limit	53
Plastic limit	29
Plasticity index	24
Specific gravity	2.72
Grain size distribution Passing No.10 (2.0mm) Passing No.40 (0.42mm) Passing No.200 (0.074mm) % of clay (0.002)	 100 92 84 42
Unified classification	CH

Lime

The lime was brought from Meshraq sulphar factory having 82% calcium hydroxide, and the chemical analysis of the used lime shown in Table (2).

Table (2) Chemical Analysis of the Lime

Composition	$Ca(OH)_2$	CaO	$CaCo_3$	Al_2O_3	Fe_2O_3	SiO_2	MgO	H_2O
Percent	71.3	6.1	6.2	0.17	0.04	11.1	4.19	0.09

Tests Procedures

Compaction test

The modified compaction test according to ASTM designation D1557-79 [7] was used for both untreated and stabilized soil with (2,4,and 6%) lime.

Flexural test

The flextural test was conducted on untreated and stabilized soil using prismatic beam (50.8 * 50.8 * 305 mm). The specimens were prepared by compacting the soil at the optimum moisture content in four layers using special square base hammer weighing (17.1)N and falling from (280)mm. The specimens were removed from the mold and wrapped with metallic paper and coated with a thin layers of wax to secure that no change in water content take place during the curing period. The curing was carried out by placing the specimens in an oven at (49 ^{o}C) for (2 days).

The specimens were tested according to British standard (B.S.1881:PART 118) [8] using two point loading technique. Figure(1) shows the sketch of specimen under loading.

Three specimens where prepared for each percentage of lime one of them was tested to failure, the others two specimens were subjected to four cycles of loading and unloading (using 25% of flextural strength for first group and 50% of flextural strength for second group). The load was applied at rate of 0.127 mm/min (0.005in/min), and the deflections at the center of the beam (top and bottom) were recorded every (30sec.) with load.

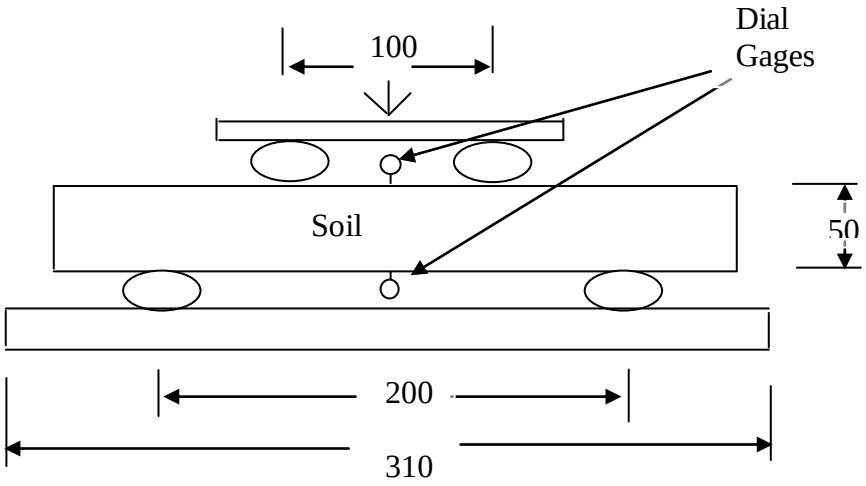

Fig.(1). The mounting of specimen (dimensions in mm)

Compression strength test

In addition to the evaluation of the flextural strength, the compression strength was determined using a portion of the beam which was free from cracks or any seen defect. This test was performed according to (ASTM D 1634-63 1997) [7].

Tensile stress analysis

The stress calculation of the beam have carried out using an elastic bending theory method [9]. This method is based on the assumptions that the plane section remain plane after bending and the modules of elasticity has the same value in tension and in compression. This mean that the stress is linearly proportion to the strain.

Duckworth [10] derived the following Equations for tensile stress (σ_t) and compressive stress (σ_c)

$$\sigma_{t,c} = \frac{6M}{bd^2} \qquad \text{----------1}$$

The Strain was found from the following Equation:-

$$\varepsilon_{t,c} = \frac{48\delta_t MC}{Pb(3L^2 - 4b^2)} \qquad \text{----------2}$$

Where :-

M=Applied bending moment
δ = Observed deflection at the center of the beam which can be obtained directly from the dial gauges fixed at top and bottom of the beam .
P=Applied load
L=Length of the beam
d=Depth of beam
b=Width of the beam
C=d/2

Results and Discussion

The compaction characteristic of the untreated and the stabilized soil with different percentages of lime is shown in fig.(2). The maximum unit weight is (18.0) kN/m^3 for untreated soil, with the addition of lime the density decrease and the optimum moisture content increase. These behavior are due to agglomeration of soil particles and the affinity of lime to water. These finding were reported by several investigators [11,12,13].

Fig.(3) shows the stress strain curves of both untreated and the stabilized soil specimens with (2,4 and 6%) lime. It can be seen that the tensile strength increases with the percent of lime up to (4) percent then decreases. Table (3) shows that the increments in the tensile strength due to addition of lime is (55,121 and 114%) for (2,4 and 6%) lime respectively. Similar results were found by Al-Layla M. T. et al [6].

The tensile strain decreases with the addition of lime, for the untreated soil the failure strain is (3.08×10^{-3}) while for (2,4 and 6%) lime, the failure strain are (2.60×10^{-3}), (2.32×10^{-3}) and (1.33×10^{-3}) respectively. The reduction in tensile strain is due to the increase in rigidity of stabilized specimens. The results show a relatively high reduction in strain for the specimens stabilized with (6%) lime. This behavior may be due to extra lime which fill the

voids between the soil particles and increased the rigidity of the specimen which caused this reduction.

Effect of repeated loading

The repeated loading reduced the tensile strength of the stabilized soil, Table(3) shows the reduction in the tensile strength when the specimen subjected to (25 and 50%) of the failure tensile strength. It is clear that when (50%) of tensile strength was used the reduction in the tensile strength were less than that of (25%) and for all percentages of lime. This behavior may be due to soil particles come more closed to each other with the increase in the value of repeated loading without breaking the bonds between the particles and this result increasing in the tensile strength. When the applied repeated loading start to break the bound between soil particles, the strength decrease with the increasing of repeated loading.

The failure tensile strain decreased with the addition of lime for the stabilized soil, while it increased with the repeated loading for (2 and 4%) lime. This behavior is due to the effect of bonds between particles which occurred as a result of stabilization. On the other hand, the strain decreased when (6%) lime was used. This is may be the result of increasing the rigidity of soil with (6%) lime more than that occurred with (2 and 4%) lime.

Table (3) Effect of lime and repeated loading on the tensile strength

Lime %	Tensile strength (kPa)	% increase of load	Load level % of final load	Tensile strength after repeated load (kPa)	% reduction
0	192.8	-	-	-	-
2	300	55	25	138	54
			50	203.2	32
4	427.2	121	25	242	43
			50	310	27
6	414	115	25	240	42
			50	284	31

Conclusions

1- The addition of lime improved the tensile strength of the clayey soil used in this study.
2- The repeated loading reduced the tensile strength and increased the failure strain up to (4%) of lime, beyond that the strain decreased.
3- The repeated loading decreased the reduction in tensile strength as the percentage of repeated loading increased from 25% to 50%.

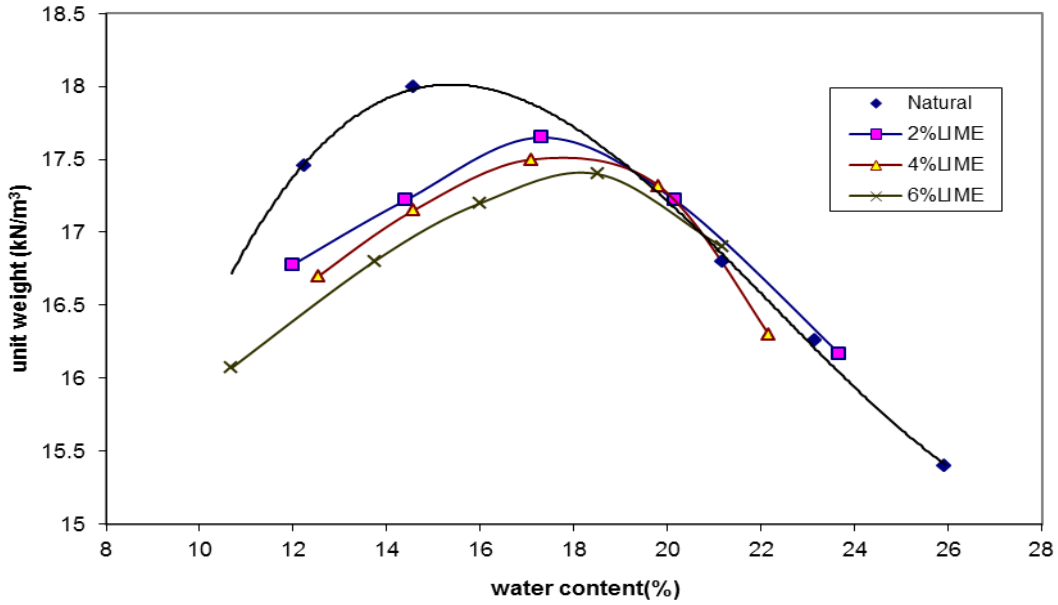

Fig.(2)Water Content Versus Unit Weight

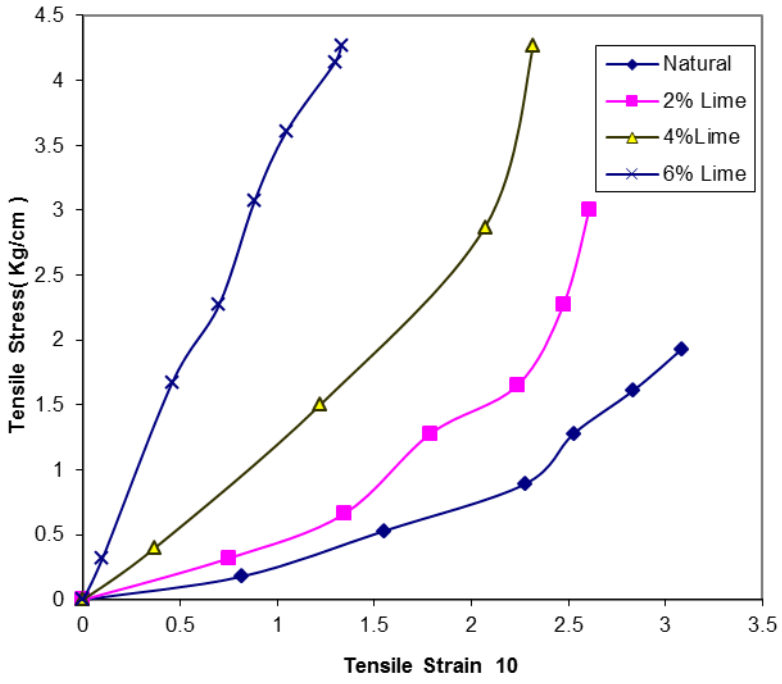

Fig.(3) Tensile Stress-Strain Curves

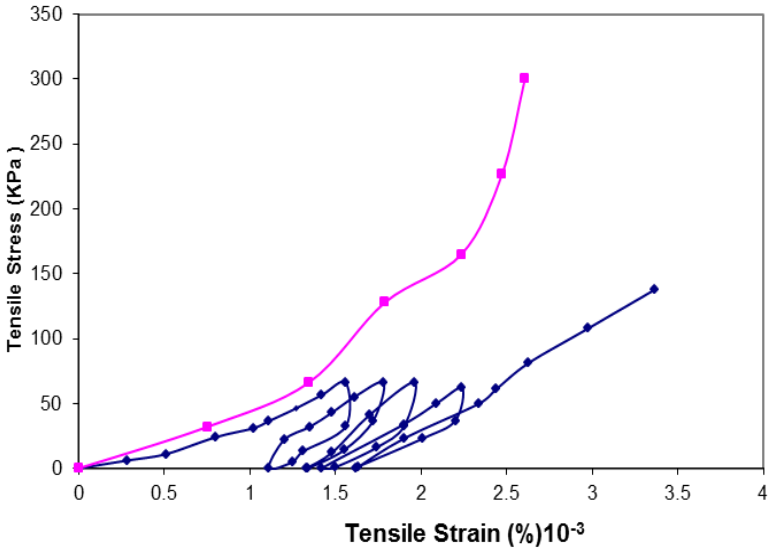

Fig. (4) Effect of Repeated Load on Tensile Strength (2% Lime 25% of theFinal Load)

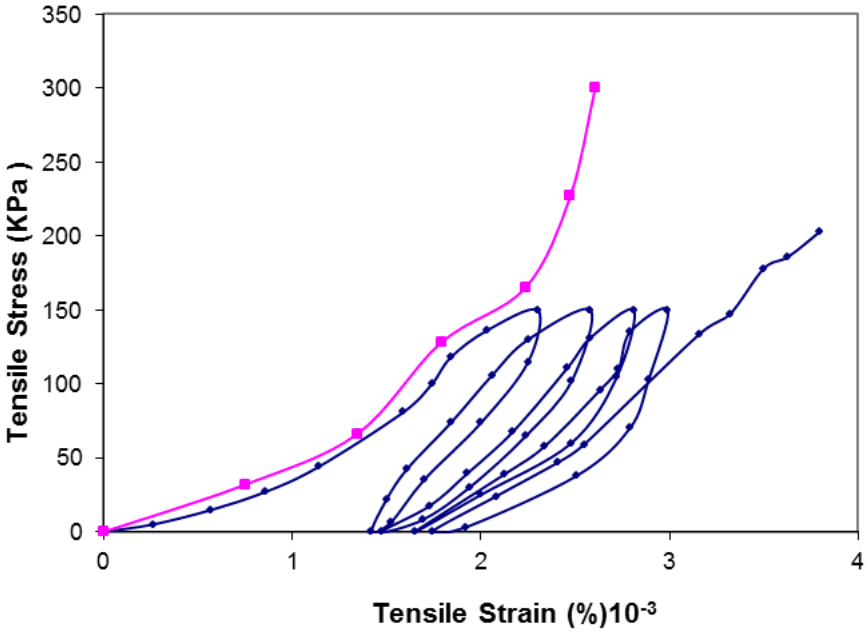

Fig.(5) Effect of Repeated Load on Tensile Strength (2% Lime 50% of the Final Load)

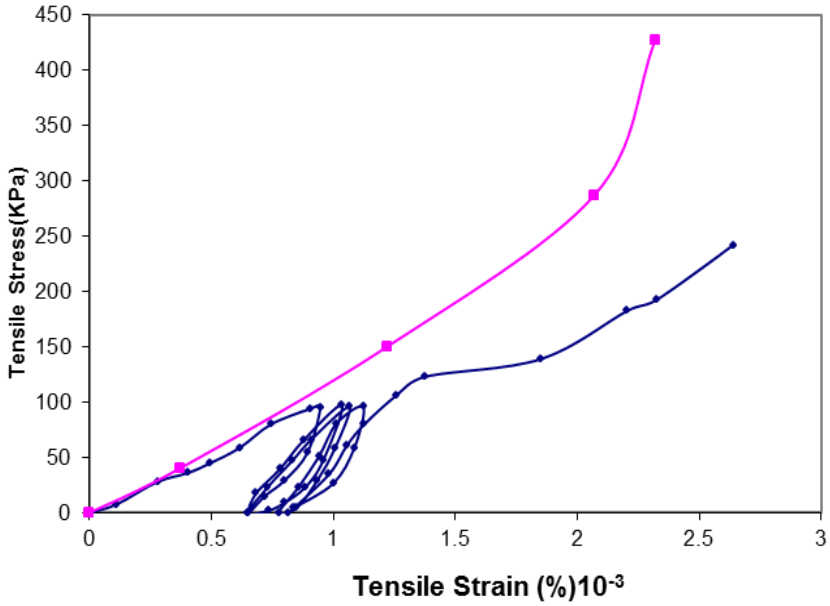

Fig. (6) Effect of Repeated Load on Tensile Strength (4% Lime 25% of the Final Load)

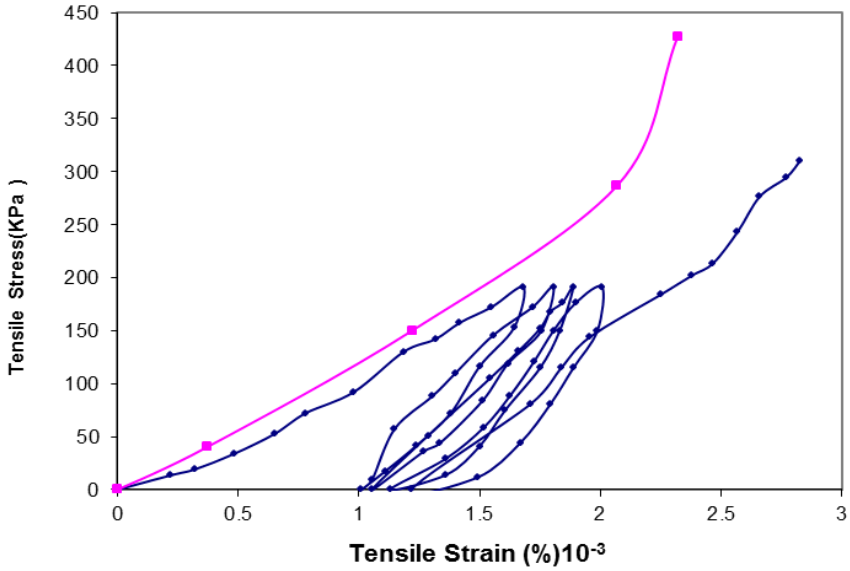

Fig.(7) Effect of Repeated Load on Tensile Strength (4% Lime 50% of the Final Load)

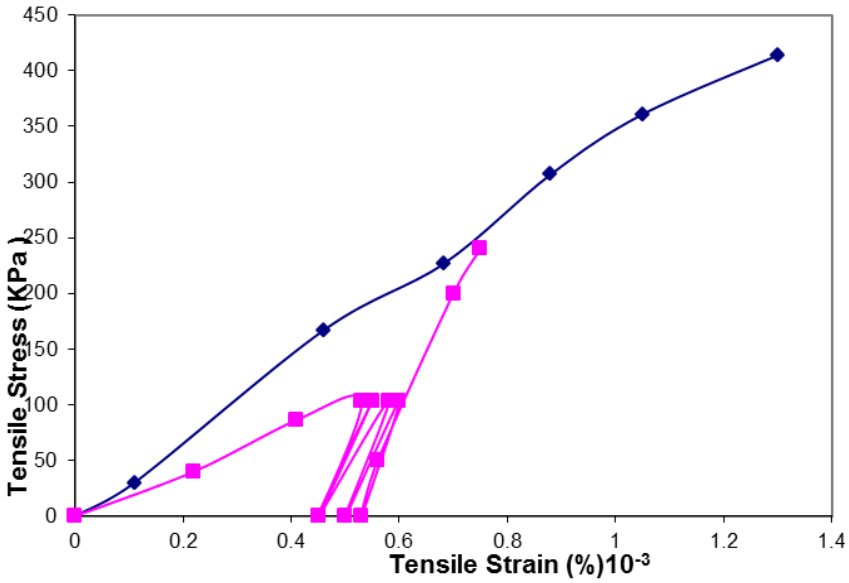

Fig.(8) Effect of Repeated Load on Tensile Strength (6% Lime 25% of the Final Load)

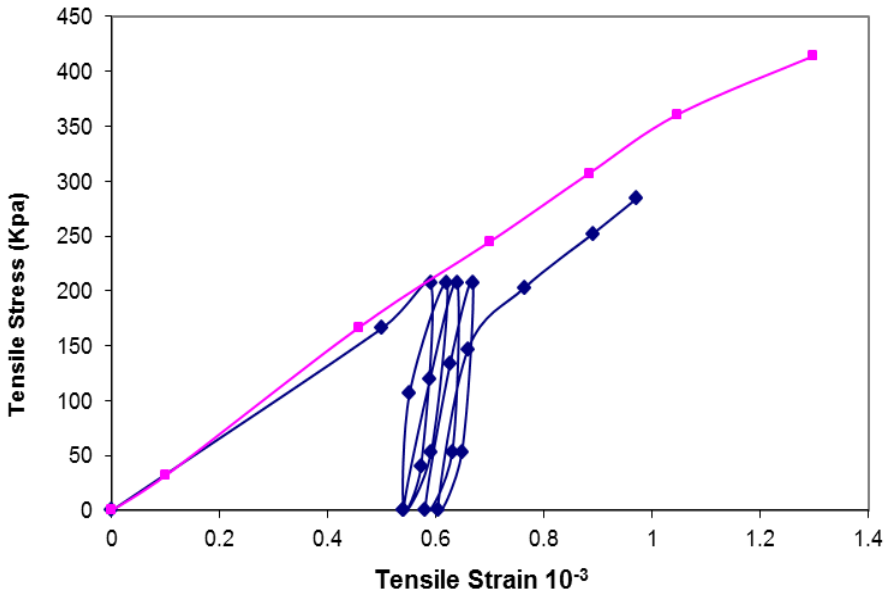

Fig.(9) Effect of Repeated Load on Tensile Strength (6%lime 50% of the Final load)

Reference

1- Al-Aboudie, N. J. S. "Soil Deformation Under Moving Load" M.Sc. Thesis, Civil Engineering Department, College of Engineering, University of Mosul, (1989).

2- Miller, G. A. Teh, S. Y. Li, D. and Zaman, M. M. "Cyclic Shear Strength of Soft Railroad Sub Grade", Journal of Geotechnical and Geoenviromental Engg., ASCE, Vol.126, No.2, PP.139-147, (2000).

3- Jaro, M. N. "Effect of Fine Material on the Tensile Strength Properties of Unstabilized and Cement-Stabilized Granular Soil", M. Sc. Thesis, Civil Engineering Department, College of Engineering, University of Mosul, (2000).

4- Al-Layla M.T., Al-Zubaydi A. H. "Behavior of Lime Stabilized Gypseous Soil Beams Under repeating Loads" the Iraqi Journal for Mechanical and Material Engineering, special issue for the papers presented in 2nd annual scientific conditions of the college of engineering, March, (2010), part (E).
5- Al-Omar, A .J .A. "Tensile Strength of Lime-Stabilized Cohesive Soil", M.Sc. Thesis, Faculty of the Graduate School, University of Texas, (1983).
6- Al-Layla M.T., Al-Dabbagh A.W., Jaro M.N. "Tensile Strength of Natural and Lime Stabilized Mosul Clay" Al-Rafidain Engineering Journal, Iraq –Mosul, Vol. 16, No.12, (2008).
7- ASTM, "American Society for Testing & Material", Vol. 04-08, (2000).
8- British Standards, " Methods of Testing Soils for Civil Engineering Purposes", 1377, (1975) .
9- Ajaz, A. and Parry, R. H. G. "Analysis of Bending Stresses in soil Beams", Journal of Geotechnical Engg., ASCE, Vol.25, No.3, (1975 b) , pp.286-291.
10- Duckworth, W.H "Precise Tensile Properties of Ceramic Bodies" American Ceramic Society, Vol.34, No.1, .(1951).
11- Diamond, S. and Kinter, E.B. "Mechanisms of Soil-Lime Stabilization" HRR Vol.92, (1965).
12- Ingles, O.G. and Metcalf, J.B. "Soil Stabilization Principles and Practice" Butterworth, (1972).
13- Mohammed, N.T. "Lime-Stabilization of Fine Grained Soil in the Vicinity of Mousl" M.Sc Thesis, University of Mosul, Engg. College, .

S - 29

تأثير المواد فائقة النعومة على طاقة السطح الحرة للإسفلت الأسمنتي

سعد عيسى سرسم اسراء ثامر العزاوي

المستخلص

تعرف طاقة السطح الحرة على انها كمية الشغل المطلوب لبناء وحدة مساحة من المادة في الفراغ، كما تعتبر طريقة مناسبة لتقدير الخراب بسبب الرطوبة للمزيج الاسفلتي. ولهذا تعتبر هذه الطريقة قادرة على تحليل تأثير المضافات على تقليل الخراب بسبب الرطوبة، وعلى خصائص الحساسية للحرارة مع استنباط مواد جديدة ذات خصائص فيزياوية وحرارية مختلفة.

في هذه الدراسة تم خلط ثلاث انواع من المواد فائقة النعومة (الرماد المتطاير، ابخرة السليكا، الفوسفات المكربن) وبنسب مئوية مختلفة مع الاسفلت السمنتي. ان الاسفلت المحسن الذي تم الحصول عليه نتيجة مثل هذا الخلط تم تعريضه لفحص قياس زاوية التلامس الثابتة والمرنة وباستخدام ثلاثة انواع من سوائل الفحص.

تم استخدام جهاز فحص صفيحة ويلملي لقياس زاوية التلامس المرنة للاسفلت المحسن باستخدام سوائل اختبار مختلفة لقياس مكونات طاقة الشد السطحية للمادة الرابطة. تم اعتماد كاميرة رقمية لتصوير سطح نقطة تلامس السائل مع الشريحة الزجاجية المغطاة بالاسفلت السمنتي. من ناحية اخرى، تم استخدام طريقة قطرة سيسل لحساب زاوية التلامس الثابتة باعتماد سوائل فحص مختلفة والمعادلات الرياضية الخاصة بالشغل في التلاصق. تم حساب ثلاثة اركان للطاقة السطحية للاسفلت. تم وضع قطرة من سائل الفحص فوق سطح مستو مغطى بالاسفلت.تنتشر هذه القطرةعلى السطح الاسفلتي وتاخذ مداها وعند ذلك يتم التقاط صورة لحد التلامس باستخدام كاميرة رقمية.

تم تحويل هذه الصور الرقمية وللطريقتين الى برنامج الحاسوب المسمى (كوميف 4.3) لتحليل الصور وايجاد الزوايا الثابتة والمرنة. تم الاستنتاج ان هذه الزوايا تكون متغيرة عند استخدام سوائل فحص مختلفة وكذلك عند استخدام مواد فائقة النعومة متعددة وبنسب مئوية مختلفة. كانت طاقة السطح الحرة للاسفلت السمني دون مضافات 30.715 أرك /سم^2 عند الفحص باستخدام صفيحة ويلملي ولكنها اظهرت زيادة بمقدار 71.3 % عند الفحص بطرقة قطرة سيسل.

Effect of Nano materials on surface free energy of asphalt cement

Saad Issa Sarsam/ Professor Esra Thamir AL-Azzawi dent

Department of civil Engineering, College of engineering/ University of Baghdad, Baghdad – IRAQ

Abstract

The surface free energy is defined as an amount of work required for creating unit area of the material in vacuum, and is considered as a suitable method for forecasting the moisture damage in asphalt mixtures. Therefore, this method seems to be capable of analyzing the effects of additives on the reduction of moisture damage, changing the temperature susceptibility characteristics, and creating new material with different physical and rheological properties.

In this study, three types of Nano materials (Fly ash, silica fumes and Phospho gypsum) were mixed in different percentages with asphalt cement. The resulted modified asphalt samples were subjected to static and dynamic contact angle measurements using three types of probe liquids.

The Wilhelmy Plate Device Method was used to measure dynamic contact angles of the modified asphalt cement with various probe liquids and determine surface free energy components of the binder. A digital camera has been implemented to capture the image that contains the contact surface of the probe liquid with a glass slide coated with asphalt cement. On the other hand, the Sessile Drop Method was used to measure static Contact angles with different probe liquids with the aid of equations of work of adhesion, to determine the three surface energy components of the asphalt binder. A probe liquid is dispensed over a smooth horizontal surface coated with asphalt binder. The drop on the asphalt binder surface expands to a point when its interfacial boundary with the binder surface just begins to expand. The image of the drop of liquid formed over the surface of the binder was captured using a digital camera.

The captured images were transferred to the image processing software (Comef. 4.3) to find both static and dynamic contact angle. It was concluded that these contact angles vary according to the type of probe liquid, and type and percentages of Nano materials added to asphalt cement. The total surface free energy of asphalt binder without additives (control) was 30.715 ergs/cm^2 using the Wilhelmy Plate,' while it shows an increase to 71.3% when using sessile drop method.

1.0 INTRODUCTION

The investigation of filler on a phenomenological basis has been a focus of researchers for many years; however, the influence and mechanisms of fine filler particles on the material behavior of asphalt are still not well understood and further research on a micro- and Nano-scale needs to be conducted.

Research work should deal with the improvement of asphalt cement by adding organic or inorganic Nano-filler and explain how should this Nano-filler be produced, processed and tested. The best methods to determine the particle size distribution below 1000 nm should also be verified. It is well known that the influence of filler particles on the binder increases with decreasing size of the filler particles. However, only rough instructions are given on the dosage such as the acceptable content of filler. Such dosage concerns mainly on overall gradation of asphalt concrete mixture, Arulraj. and Carmichael (2011).

Nano material should improve long-term performance and functional properties of the materials in a significant way without reducing the clear advantages of existing asphalt pavement materials, Partl et al (2003); Livingston (2007), which are generally recyclable and easy to repair. This is considered a very positive factor in terms of sustainability. Since the thickness of binder films between the mineral particles in a pavement is mostly in the order of a micrometer or even below, one could think of measuring properties of mixes of fillers and binders, Grove (2007); Parviz (2011). They should also fulfill ecological requirements such as low energy consumption and environmental compatibility.

The behavior of these materials deviates fundamentally from pure binders, and can be seen as the first step from the pure binder towards the composite material asphalt.

2.0 BACK GROUND

Mega quantities of asphalt material are required to spread over many thousands of kilometers all over the continents, it should always be kept in mind that Nano-particles for pavement materials must be non-hazardous, low-cost products, which are easy to handle and available in high quantities at almost any place in the world, Partl et al (2003); You et al (2011). Surface to volume ratio of Nano materials is one of the important properties of materials produced at the Nano scale. At this scale the behavior of bulk material behavior is dominant, Arabani, and Hamedi (2010); Ghasemi et al (2010).

The influence of the particle size distribution of fillers is given only little attention, in common practice, so far, in spite of the fact that there are considerable differences in the particle size distribution of different fillers, Grove (2007). The impact of three types of Nano materials on stripping potential of asphalt concrete has been investigated by Sarsam and AL-Azzawi (2013). The stripping of Nano asphalt concrete was modeled by Sarsam and AL-Azzawi (2013). Sarsam (2012) studied the improvements in Asphalt cement physical properties after it was digested with Nano materials. Nano-Filler particles are particles smaller than 0.09mm. With simple methods, like sedimentation or washing method, the grain distribution of filler between 1μm up to [0.09 mm] can be determined on a routine basis but are not commonly used in asphalt technology, Bhasin et al (2007); Cheng et al (2002).

The main objective of this research work is to verify the impact of Nano materials on the surface free energy of asphalt cement and modified asphalt.

3.0 MATERIALS PROPERTIES

3.1 Asphalt cement: penetration grades 40-50 asphalt cement, obtained from Dorah refinery, Baghdad, have been implemented in this investigation, Table 1 illustrates the measured physical properties of asphalt cement.

Table 1: Physical and rheological properties of asphalt cement

Property	Units	Specification	Results for grade (40-50)
Penetration	0.1 mm	ASTM D-5	46
Softening point	˚ C	ASTM D-36	51
Ductility	Cm	ASTM D-113	128
Specific gravity	--------	ASTM D-70	1.042
Flash point	˚ C	ASTM D- 92	310
Viscosity	Poises	ASTM D-2171	4046×10^3
Penetration index	----------	Shell nomograph	- 0.0228
Stiffness modulus	N/m^2	Shell nomograph	1.0×10^8
After thin film oven test		ASTM D- 1754	
Penetration of Residue	0.1 mm	ASTM D-5	31
Ductility	Cm	ASTM D-113	83
% loss in weight	%	SCRB- 2004	0.175

3.2 Nano materials: Three types of Nano materials have been introduced for this investigation, their properties are explained below.

3.3 Fly ash: Fly ash was obtained from local market, it was sieved, and the portion passing sieve No. 200, 75 micron was implemented in this investigation. Table 2 shows its physical properties.

Table 2: Physical properties of fly ash

Maximum Sieve size, micron	Specific gravity	Specific surface area, m^2/kg
Sieve No. 200, 75 micron (μm)	2.0	650

3.4 Silica fumes: It was manufactured by Wacker Silicon Company in Germany as fluffy powder, and obtained from local market; Table 3 shows its physical properties.

Table 3: Physical properties of Silica fumes

Maximum sieve size	PH value	Density, kg/m^3	Specific surface area, m^2/ kg
Passing 75 µm retained on 40 µm	4.5	202	200000

3.5 Phospho-gypsum: It is obtained as a waste material from the Akashat Phosphate plant. Table 4 shows its physical characteristics. On the other hand; Table 5 presents the chemical composition of the Nano materials adopted in this work.

Table 4: Physical properties of Phospho-gypsum

Maximum sieve size	Specific gravity
Passing sieve No.200, 75 µm	2.350

Table 5: Chemical composition of Nano materials used

Chemical composition, %	Fly ash	Silica fumes	Phospho-gypsum
SiO_2	61.95	99.1	0.84
Fe_2O_3	2.67	35 ppm	------
Al_2O_3	28.82	0.03	-------
CaO	0.88	0.03	33.06
MgO	0.34	52 ppm	0.56
Loss on ignition	0.86	0.70	19.11

4.0 EXPERIMENTAL PROGRAM

Asphalt cement was heated to 160 ˚ C in an automatic controlled oven, and then separated into 50 grams capacity aluminum cans. The required amount of Nano material was introduced gradually with continuous mechanical stirring. The stirring process was continued for 60 minutes at the same mixing temperature of 160 ±2 ˚ C to insure homogeneity of the mix.

Four different percentages of Nano materials have been introduced. For fly ash, the percentage starts with 3% with constant increments of 3%, While for Silica fumes and Phospho-gypsum, the percentages starts with 1% with constant increments of 1%. A glass slides of (25.4mm x76.2mm x 1mm) dimensions were heated, and then submerged into the molten asphalt binder at 160 ˚ C to a depth of approximately 15 mm, the excess binder was allowed to drain from the slide until a very thin film of binder of (0.18 to 0.35 mm) thickness, and uniform layer remains on the slide. The thickness of asphalt binder was kept uniform on both sides of the slide throughout its width.

Finished slides were stored in vertical position from the end of coated slides and placed in cork box and allowed to cool to room temperatures as shown in Figure 1. The surface free energy of the asphalt cement has been measured using three types of probe liquids recommended to be used in this test. These are water, glycerol, and Formamid. The surface energy component of a solid surface is determined by measuring its contact angles with various probe liquids. Contact angles were measured for at least three replicates with each

probe liquid for each type of asphalt binder. Two techniques have been implemented for surface free energy measurement as listed below.

4.1 Wilhelmy Plate Device Method (WPD): This method is used to measure dynamic contact angles of the asphalt binder with various probe liquids and to determine surface energy components of the binder. The glass slide coated with the asphalt binder and suspended from a microbalance is immersed slowly at a steady speed in different probe liquids. From simple force equilibrium conditions the contact angle of the probe liquid with the surface of the asphalt binder can be determined as per the procedure by Bhasin et al (2007). A photograph was captured with the aid of digital camera while the slide was in its last position in the liquid. Figure 2 shows the Wilhelmy plate Test in process. The image processing software (Comef 4.3) was used to find a dynamic contact angle. A total number of 48 slides were perpetrated and tested. Figure 3 shows a schematic diagram of the technique, while Figure 4 shows the COMEF 4.3 software desktop. Table 6 illustrates the Surface Energy Components of the Probe Liquids, Cheng et al (2002).

Figure 1: Glass slides coated with Asphalt Technique

Figure 2: The Wilhelmy plate

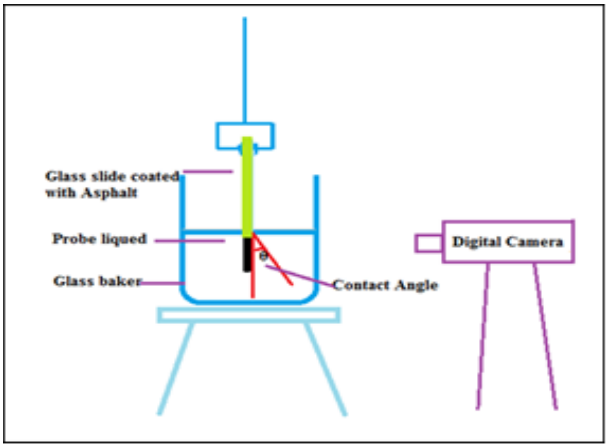

Figure 3: Schematic diagram of the Wilhelmy Technique

Figure 4: The COMEF 4.3 software desktop

4.2 Sessile Drop Method (SDM): A probe liquid is dispensed over a smooth horizontal surface coated with asphalt binder. The image of the drop of liquid formed over the surface of the binder is captured by using a digital camera. Contact angles are obtained by analyzing the image using image processing software (Comef 4.3) software. A static Contact angles measured with different probe liquids are used with equations of work of adhesion to determine the three surface energy components of the asphalt binder as per, Cheng et al (2002).

A total number of 48 slides were perpetrated for this technique. A drop with a contact angle over 90° is hydrophobic, Bhasin et al (2007). This condition is exemplified by poor wetting, poor adhesiveness and the solid surface free energy is low. A drop with a small contact angle is hydrophilic; this condition reflects better wetting, better adhesiveness, and higher surface energy. Figure 5 shows the Output of the Comef 4.3 Software for water and glycerol probe Liquids, while Figure 6 illustrates a schematic diagram of the Sessile Drop technique.

(a) **(b)**

Figure 5: Enhancements of image with different Probe Liquids, (a) water; (b) Glycerol

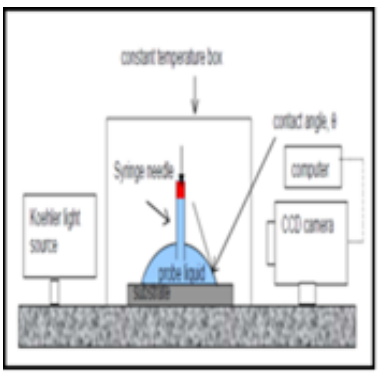

Figure 6: Schematic diagram of the Sessile drop technique

Table 6: Surface Energy Components of the Probe Liquids, NCHRP (2006)

Probe Liquid	Lifshitz-van der γ^{LW}	γ +	γ -	γ Total (ergs/cm^2)	Density g/cm^3
Water	21.80	25.5	25.50	72.80	0.997
Formamid	39.00	2.28	39.60	58.00	1.134
Glycerol	34.00	3.92	57.40	64.00	1.258

Where,
γ^{LW} = Lifshitz-van der Waals component.
γ^{+} = Lewis acid component.
γ^{-} = Lewis base component.
γ^{Total} = surface free energy (ergs/cm^2)

5.0 ANALYSIS AND DISCUSSIONS ON TEST RESULTS

5.1 EFFECT OF NANO MATERIALS ON MEASURED CONTACT ANGLE BY SESSILE DROP METHOD

Table 7 presents the average contact angle for asphalt without additives (control).The results are approximately in the range of 80.01degrees to 88.95 degrees. These results reflect better wetting and better adhesiveness and the asphalt exhibits hydrophilic behavior.
By adding different percentages of Nano materials (Fly ash, Silica fumes, Phospho-gypsum) to asphalt binder, the average contact angle was increased to the range of 91.72 to 118.01 degrees for all types of probe liquids. These results reflect poor wetting and poor adhesiveness, and the behavior changes to hydrophobic.

5.2 EFFECT OF NANO MATERIALS ON MEASURED CONTACT ANGLE BY WILHELMY PLATE METHOD

Using the Wilhelmy plate method, the contact angle for control binder is within a range from 45.86 to 56.02. This may indicate better wetting and hydrophilic behavior. When the Nano materials were introduced, test results are fluctuating and did not show any significant variations in contact angle when water was used as probe liquid. When Formamid was introduced as probe liquid, it exhibits decrease in contact angle for all percentages of Nano materials used. When Glycerol was adopted as probe liquid, it shows an increase in contact angle for most of Nano materials percentage used.

5.3 EFFECT OF NANO MATERIALS ON CALCULATED SURFACE FREE ENERGY BY SESSILE DROP AND WILHELMY PLATE METHOD

Surface free energy was determined for each type of asphalt binder based on Van Oss theory which separates the surface energy of asphalt into three components, namely, the Lifshitz-Van Der Waals component, the acid component, and the base component. Figure 7

show the variation in surface free energy of fly ash modified asphalt using the Sessile Drop method. The addition of fly ash increases the total surface free energy of the binder initially, the base component exhibit the main contribution for such changes.

Further increase in fly ash content shows lower rate of increment in surface free energy. Figure 8 shows the surface free energy of fly ash modified asphalt with Wilhelmy Plate method, similar behavior could be detected, but the total surface free energy increases as the fly ash percentages increases. Table 7 illustrates the effect of Silica fumes on surface free energy of asphalt cement. Almost similar behavior as that of fly ash could be detected for both testing methods. On the other hand, the incremental addition of Phospho-gypsum increases the total surface free energy when tested by Sessile Drop method, while it decreases when tested using Wilhelmy method.

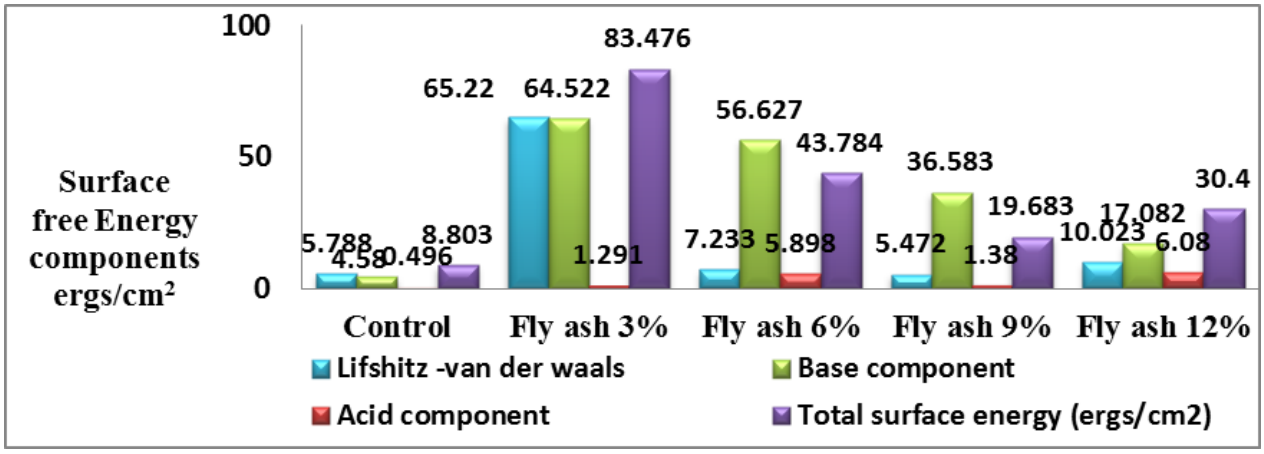

Figure 7: Effect of fly ash on surface free energy components using Sessile Drop method

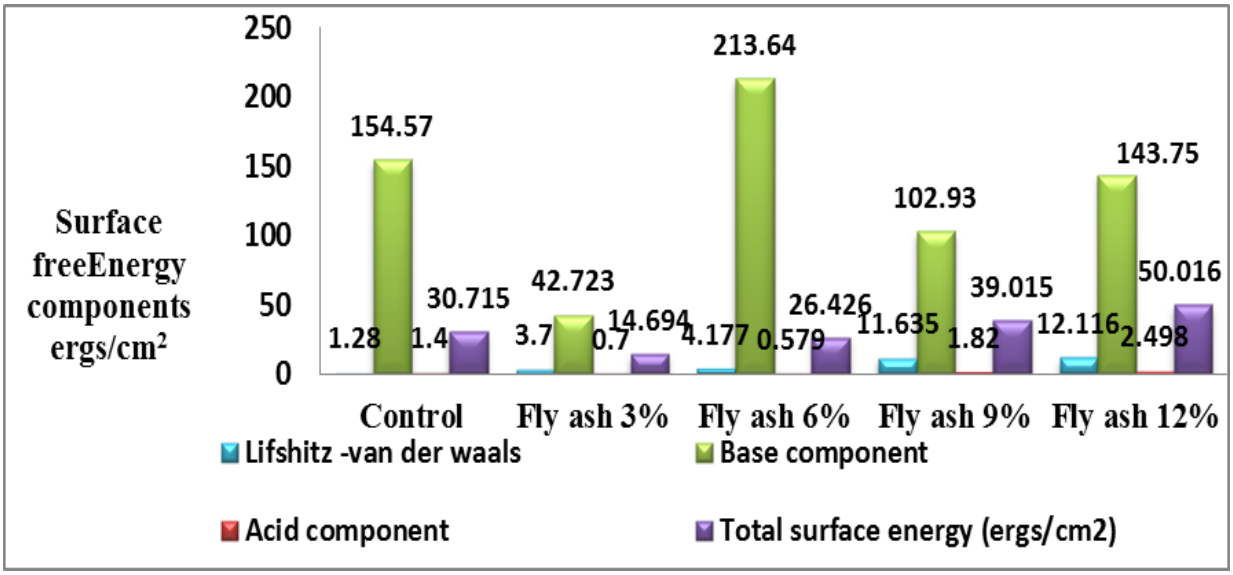

Figure 8: Effect of fly ash on surface free energy component using Wilhelmy Plate method

Table 7: Effect of Nano materials on contact angle and total surface free energy of binder

Asphalt and Nano material type	Probe liquid type	Average contact angle (°) by Sessile drop	Average contact angle (°) by Wilhelmy plate	Total surface free energy by Sessile (ergs/cm^2)	Total surface free energy by Wilhelmy (ergs/cm^2)
Control	Water	88.95	45.86		
	Formamid	80.01	56.02		
	Glycerol	83.70	46.29	8.80	30.72
3 % fly ash	Water	111.85	49.42		
	Formamid	94.98	51.00		
	Glycerol	109.93	51.01	83.47	14.69
6 % fly ash	Water	101.24	44.88		
	Formamid	95.08	49.70		
	Glycerol	92.19	49.91	43.7	26.43
9 % fly ash	Water	100.10	46.09		
	Formamid	96.85	45.23		
	Glycerol	91.72	46.84	19.68	39.01
12 % fly ash	Water	100.33	45.79		
	Formamid	104.54	49.85		
	Glycerol	94.20	49.04	30.40	50.01
1 % Silica fumes	Water	106.14	49.97		
	Formamid	100.78	50.31		
	Glycerol	102.65	48.25	29.64	65.57
2 % Silica fumes	Water	107.45	40.69		
	Formamid	101.16	49.26		
	Glycerol	92.23	50.92	27.25	34.23
3 % Silica fumes	Water	100.17	43.66		
	Formamid	107.73	48.57		
	Glycerol	96.50	43.55	18.09	38.89
4 % Silica fumes	Water	103.08	53.22		
	Formamid	108.02	49.79		
	Glycerol	107.83	52.99	17.44	72.25
1 % Phospho-gypsum	Water	117.25	45.58		
	Formamid	103.50	45.11		
	Glycerol	98.08	50.29	12.87	47.91
2 % Phospho-gypsum	Water	104.45	53.46		
	Formamid	104.48	46.35		
	Glycerol	95.69	54.20	15.54	29.58
3 % Phospho-gypsum	Water	110.66	54.22		
	Formamid	111.91	55.68		
	Glycerol	93.19	51.25	16.92	30.67
4 % Phospho-gypsum	Water	105.26	65.42		
	Formamid	118.01	52.24		
	Glycerol	108.41	45.21	22.36	19.24

6.0 CONCLUSIONS:

Based on the limitation of materials and test procedure in this work the following conclusions are drawn:

1.) When using Sessile drop method the value of total surface free energy of asphalt cement grade (40-50) was 8.8 ergs/cm^2, while when using Wilhelmy technique the value of surface free energy of asphalt cement was 30.71 ergs/cm^2.

2.) The surface free energy values as calculated by Sessile Drop method are lower than those calculated using Wilhelmy technique for asphalt cement and modified asphalt. While the contact angle values calculated by using Wilhelmy method are lower than those values calculated by using Sessile Drop method for both asphalt cement and modified asphalt when using fly ash, Silica fumes and Phospho gypsum.

3.) The addition of Nano materials to asphalt cement at different percentages causes poor wetting and poor adhesiveness, and the behavior changes from hydrophilic to hydrophobic when Sessile Drop method was adopted. The change in contact angle was fluctuating and not significant when Wilhelmy technique was adopted. .

4.) The surface free energy concept using Sessile Drop technique should be considered when the stripping of asphalt concrete is under question.

REFERENCES

1- Arulraj.P and Carmichael J. (2011)“ Effect of Nano Fly ash on Strength of Concrete” International journal of civil and structural Engineering, Volume 2, No 2, (p475-482).

2- Arabani, M. and Hamedi, Gh.(2010) “Using the Surface Free Energy Method to Evaluate the Effects of Polymeric Aggregate Treatment on Moisture Damage in Hot Mix Asphalt” (ASCE), volume No.23, issue 6, pp. (802-811).

3- Bhasin, A.; Little, D., Vasconcelos, K. and Masad, E.(2007) “Surface Free Energy to Identify Moisture Sensitivity of Materials for Asphalt Mixes”, Journal of the Transportation Research Board (TRB), volume 2001, pp. (37-45).

4- Cheng, D.; Little, D.; Lytton, R.; and Holste, J. (2002) “ Surface Free Energy Measurement of Aggregates and Its Application to Adhesion and Moisture Damage of Asphalt aggregate Systems” Journal of the Association of Asphalt Paving Technologists, Vol.71, pp.(59-88)

5- Ghasemi T., Parhizkar T.;, Ramezanianpour A.(2010) “Influence of Colloidal Nano-SiO2 Addition as Silica Fume Replacement Material in Properties of Concrete” Proceeding, Second international conference on sustainable construction materials and technologies, 28-30 June, Ancona, Italy.

6- Grove J.(2007) “New Technologies: Nanotechnology Two-lift Construction Self Compacting Concrete for Pavements, National Concrete Pavement Technology Center, SE Concrete Pavement Conference October 3.

7- Livingston R.(2007) “Nano science of Highway Construction Materials”, Office of Infrastructure R&D, Federal Highway Administration, Workshop on Nano Technology for Cement and concrete, September 5.

8- Parviz A. (2011) "Nano Materials in Asphalt and Tar" Australian Journal of Basic and Applied Sciences, 5(12): 3270-3273.
9- Partl M.; Gubler R.; Hugener M.(2003) "Nano science and technology for Asphalt pavement" Techniques report, EMPA Swiss Federal Laboratories for Materials Testing and Research, Switzerland.
10- Sarsam S. "Improving Asphalt Cement Properties by Digestion With Nano Materials" Proceedings, 2012 International Conference of Mechatronic Systems and Materials Application (ICMSMA 2012),Qingdao, China, September 8-9, 2012.
11- Sarsam S. and AL-Azzawi E. "Evaluation of Asphalt Binder Stripping using Surface Free Energy concept" Proceedings, 2nd International Conference on Applied Materials and Electronics Engineering (AMEE 2013) April 20th, 2013, Hong Kong.
12- Sarsam S. and AL-Azzawi E. "Modeling the stripping potential of asphalt concrete" Accepted for publication at ASCE Airfield & Highway Pavement Conference - Sustainable and Efficient Pavements- T&D Institute, Los Angeles, California, June 9-12, 2013.
13- You Z.: Mills-Beale J.; Foley J.; Roy S.; Odegard G.; Dai Q., Goh S. (2011) "Nano clay-modified asphalt materials: Preparation and characterization" Construction and Building Materials 25, 1072–1078.

S - 30

PLDPE AS A MODIFER FOR ASPHALT CEMENT BINDERS

Abdul-Rahim I. Al-Hadidy[1] and Usama Abdullah Amer[2]
[1,2]Lecturer, Civil Engineering Dept., Mosul Univ., Mosul, Iraq,
E-mail1, abd_et76@yahoo.com

ABSTRACT

This paper investigates the viability of using pyrolisis low density polyethylene (PLDPE) as a modifier for asphalt cement binders. Five PLDPE contents 0, 3, 6, 9 and 12% in terms of asphalt cement by weight were used. Tests including penetration, ductility, softening point, specific gravity, viscosity, stiffness, compatibility, aging properties, and temperature susceptibility were carried out in accordance with the ASTM procedure. The analyses of test results indicate that modified binders showed higher softening point, keeping the values of ductility at minimum range of specification of (100cm), caused a reduction in percent loss of weight due to heat and air (i.e. increase durability of original asphalt) and the temperature susceptibility can be reduced by the inclusion of PLDPE in the asphalt binder. In addition, the test results revealed that PLDPE is a reliable material for paving asphalt cement and being readily available can be widely used in water proofing construction materials, and this offers profound engineering and economic advantages.

KEYWORDS: Asphalt Binders, Asphalt Modifiers, Polyethylene, Polymers.

البولي أثلين واطئ الكثافة كمطور للإسفلت

عبد الرحيم إبراهيم الحديدي أسامة عبدالله أمير

الخلاصة

تتحرى هذه الدراسة عن إمكانية استخدام مادة البولي أثلين واطئ الكثافة المكسرة حراريا كمطور للإسفلت الداخل في أعمال التبليط. تم مزج خمسة نسب من هذه المادة بضمنها الإسفلت غير المعامل في تحضير النماذج الإسفلتية الجديدة. أجريت فحوصات النفاذية، الاستطالة، نقطة الليونة، الوزن النوعي، اللزوجة، الصلادة، التجانس، ثباتية الخزن، التقادم، وتأثير الحرارة على النماذج المطورة وغير المطورة بموجب المواصفات الأمريكية. أظهرت نتائج القياسات، تميز النماذج الإسفلتية المعاملة بدرجة ليونتها العالية مع امتلاكها لقابلية استطالة ضمن الحد الأدنى للمواصفات (100سم)، علما بأن الإسفلت الجديد يقلل من التأثر بالحرارة ويكون مقاوماً للظروف الجوية (زيادة ديمومة الإسفلت). إضافة إلى ذلك أظهرت النتائج إمكانية استخدام هذه المادة في إنتاج إسفلت يصلح لأعمال التسطيح وقطع النضوح .

الكلمات الدالة: الإسفلت الرابط، الإسفلت المطور، البولي أثلين، اللدائن.

INTRODUCTION

Asphalt is a viscous material that is derived from crude petroleum and is used in paving roads. Asphalt is generally understood to include asphaltenes, resins, and oils. While asphalt is primarily composed of hydrocarbon molecules (hydrogen and carbon), it also contains elements such as oxygen, nitrogen, and sulfur. Asphalt has an extremely diverse molecular structure depending on the crude source. Asphalts are thermoplastic materials—that is, they gradually liquefy when heated. Asphalts are characterized by their stiffness, consistency, or ability to flow at different temperatures [1] .

A problem with all applications that involve asphalt is the tendency for the asphalt to become brittle at low temperatures and to become soft at high temperatures. This change due to temperature is called "temperature susceptibility." Some asphalts, depending on crude oil source and refining practice are more temperature susceptible than others. Asphalt cement may be modified by the addition of components that increase the strength of the material or otherwise alter its properties. Various additives, polymers, etc., have been utilized for the purpose of improving the high and low temperature characteristics of asphalt compositions, as well as to improve their toughness and durability. Additives such as styrene based polymers, polyethylene based polymers, polychloroprene, gilsonite, various oils, and many other modifiers including tall oil have been added to asphalt to enhance various engineering properties of asphalt [1].

BACKGROUND

Asphalts with polymers from multiphase systems, which usually contain a phase rich in polymer and a phase rich in asphaltenes not absorbed by the polymer. The properties of asphalt-polymer blends depend on the concentrations and the type of polymer used. The polymer is usually loaded in concentrations of about 4-6% by weight with respect to the asphalt [2]. Higher concentrations of polymers are considered to be economically less viable and also may cause other problems related to the material properties.

Polymers used for asphalt modification can be grouped into three main categories: thermoplastic elastomers, plastomers, and reactive polymers. Thermoplastic elastomers are obviously able to confer good elastic properties on the modified binder; while plastomers and reactive polymers are added to improve rigidity and reduce deformations under load. Examples of the plastomeric types of polymers studied for asphalt modification are polyethylene (PE), ethylene-vinyl acetate (EVA), and ethylene-butyl acrylate (EBA) random copolymers [2].

The literature on asphalt modification with plastomeric polymers is quite scarce, especially with respect to rheological properties. Some preliminary data were reported in [3-10]. Al-Dubabe et al. [4] tried to evaluate the effectiveness of the polyethylene (PE)-modified asphalt. They collected asphalt binders from four refineries in Gulf countries. It was found that the softening point tend to increase with the addition of PE, which indicates improvement in resistance to deformation.

Punith and Veeraragavan [9] used reclaimed polyethylene (RPE) as an additive in asphalt concrete mixtures. They found that the performance of RPE-modified asphalt mixtures are better when compared to conventional mixtures. The rutting potential and temperature susceptibility can be reduced by the inclusion of RPE in the asphalt mixture.

Sinan and Emine [10] investigateD the possibility of using various plastic wastes containing High Density Polyethylene (HDPE) as polymer additives to asphalt concrete. The

influence of HDPE-modified binder obtained by various mixing time, mixing temperature and HDPE content on the Marshall Stability, flow and Marshall Quotient (Stability to flow ratio) were studided. The binders used in Hot Mix Asphalt (HMA) were prepared by mixing the HDPE in 4–6% and 8% (by the weight of optimum bitumen content) and AC-20 at temperatures of 145–155 and 165^{o}C and 5–15 and 30 min of mixing time. They concluded that the HDPE-modified asphalt concrete results in a considerable increase in the Marshall Stability (strength) value and a Marshall Quotient value (resistance to deformation). Four percent HDPE, 165^{o}C of mixing temperature and 30 min of mixing time were determined as optimum conditions for Marshall Stability, flow and Marshall Quotient (MQ). MQ increased 50% compared to control mix. It can be said that waste HDPE-modified bituminous binders provide better resistance against permanent deformations due to their high stability and high MQ and it contributes to recirculation of plastic wastes as well as to protection of the environment.

Mahabir and Mayajit [11] used LDPE as a modifier for asphalt paving materials. The basic properties of modified binder and mixes containing such binders were studied and compared with those of asphalt cement. It was observed that the optimum requirement of PE is 2.5%. Marshall stability, resilient modulus, fatigue life, and moisture susceptibility of mixes were improved as a result of modification of asphalt cement by reclaimed polyethylene.

Al-Hadidy and Tan [12] used low density polyethylene as a modifier for asphalt paving materials. The basic properties of modified binder and mixes containing such binders were studied and compared with those of asphalt cement. They found that modified binders showed higher softening point, keeping the values of ductility at minimum range of specification of (100+ cm), and caused a reduction in percentage loss of weight due to heat and air (i.e. increase durability of original asphalt). The results indicated that the inclusion of LDPE in SMA mixtures can satisfy the performance requirement of high-temperature and much rain zone.

OBJECTIVES OF THE PRESENT STUDY

The objectives of the present study are: (1) To determine the physiochemical properties of pyrolisis low density polyethylene -modified asphalt binder (PLDPEMAB) and compare the results with 40/50 grade asphalt cement; (2) To evaluate temperature susceptibility of PLDPEMAB and compare the results with 40/50 grade asphalt cement; (3) To determine the compatibility of polymer modified asphalt binder with PLDPE and compare the results with asphalt cement; and (4) to optimize the short-term aging performance of PLDPE MAB and compare the results with 40/50 grade asphalt cement.

SCOPE OF THE PRESENT STUDY

Laboratory studies were carried out on PLDPEMAB to evaluate engineering properties, such as penetration, ductility, softening point, loss of heat and air (aging), temperature susceptibility, and compatibility of PLDPEMAB.

The polymer modifier used in this research is plastomeric PLDPE polymer. PLDPE was chosen for the following reasons: it is suitable for Iraq continental climate; it requires a low percentage added to asphalt (5-6% wt), it has higher than 90% reliability, and costs are moderate.

EXPERIMENT

40-50 penetration grade asphalt from Baiji refinery was selected for this study. Some properties of this asphalt are listed in Table 1.

Table 1.Physicochemical properties of asphalt cement

Property	ASTM Designation No.	Test conditions & units	Result	SCRB limits [13]
Penetration	D-5	25 °C,100g,5 s,dmm	42	40-50
Softening point	D-36	R&B, °C	54	-
Ductility	D-113	25 °C, 5 cm/min, cm	150^{+}	>100
Sp. gr	D-70	25 °C/ 25 °C	1.053	-
Flash point	D-92	COC, °C	263	-
Loss on heat	D-1754	5hrs, l63 °C, %	0.25	-
Asphaltenes	D-2006	%	32.6	-

Asphalt has high asphaltene content (32.65%). This asphalt is a less compatible (gel type), and is usually considered the type, which have been used widely in the highway construction projects in Nineveh Government (400km North Baghdad Capital). Note that compatibility is a compositional property that correlates with various physical properties [14].

Asphalt has long been classified as gel or sol type. Gel-type asphalts usually exhibit pronounced non-Newtonian behavior, whereas sol-type asphalts are more Newtonian. Gel-type asphalts generally contain large amounts of asphaltenes, and sol-type asphalts are characterized by low asphaltene content. Using the classical asphalt science terminology, sol-type asphalts are more compatible, while gel-type asphalts are less compatible [14]. Less compatible (gel-type) asphalt is known to be highly susceptible to oxidative age hardening. While highly compatible (sol-type) asphalt is not susceptible to oxidative age hardening. It is anticipated that the LDPE will dissolve when interacting with asphalt.

The LDPE is by product waste material and was obtained from one private factory for bags production in Mosul city. The results of the physical and chemical properties of LDPE before and after pyrolisis processes are shown in Table 2.

Table 2.Physicochemical properties of PLDPE

Property	Result	Unit	Specifications [15-18]
Density	0.9205	gm/cm^3	0.91-0.94
Tensile strength	10.11	MN/m^2	-
Flexural modulus	0.203	GN/m^2	-
Melting point	113.2	°C	115
Chemical unit	$(-CH_2-CH_2-)_n$		
Thermal degradation temp.	406	°C	404
Price	0.05	$/kg	-

At first LDPE was subjected to thermal degradation (pyrolisis) process, mentioned by [3], after grinding to powder by means of mechanical grinding, then the asphalt was mixed with different percentages of LDPE 3, 6, 9 and 12% wt. at 160 ± 5 °C using high-speed stirrer rotating at a speed of 1750 rpm, and blending was done for a period of 3-5 minutes to obtain a homogeneity binder [9]. Four modified binders were thus produced from this asphalt. After completion, the PLDPEMB was removed from the can, divided into small pans, cooled to room temperature, sealed with aluminum foil, and stored for the following tests:

1. Rheological tests, such as penetration (ASTM D-5), ductility (ASTM D-113), softening point (ASTM D-36) . . . etc;
2. Temperature susceptibility (using equation (1) mentioned by Yang, 1993);
3. Short-term aging using the thin film oven test (TFOT) (ASTM D-1754), which simulates the aging effect of the asphalt mixtures production and construction;
4. Storage stability;
5. Compatibility test.

All tests followed the ASTM [19**]** standards.

RESULTS AND DISCISSION

Rheological Tests

The rheological properties of PLDPEMABs where evaluated and the results are presented in Table 3. The result indicates that PLDPE is effective in improving the rheological properties of asphalt cement. Examining Table 3 indicates that softening point and binder stiffness values of 6% and 9% PLDPEMAB is found to be higher by 19% and 28%, and 340% and 514% than asphalt cement, respectively, whereas the penetration value is found to be 50% and 57%% lower than asphalt cement, respectively.

In addition, it was found that PLDPE keeping the ductility values of 100+ up to 9%.

Absolute viscosity and binder stiffness of PLDPEMB as determined from shell nomograph [20] at 25 ^{o}C are summarized in Table 3. From this Table, it can be found that the absolute viscosity of 6% and 9% PLDPEMAB is found to be higher by 152% and 171%, respectively. This indicates that rutting, shoving distresses probably will be reduced in hot mix asphalt concrete mixtures.

Table 3 Rheological properties of PLDPE-asphalt binders

%PLDPE	Penetration	Ductility	Sp. gr.	Softening point °C	Viscosity 21^{o}C poise	Binder stiffness MPa
0	42	150+	1.053	54	5×0^{6}	190.7
3	24	148	1.05	61	16.49×10^{6}	246.9
6	21	141	1.045	64	22×10^{6}	481.2
9	18	127.5	1.43	69	30.7×10^{6}	517
12	16	85	1.04	71	39.6×10^{6}	587
SCRB limits	40-50	100^{+}	-	-	-	-
ASTM limits	40-50	>100	1.01-1.06	50-58	-	-

Temperature Susceptibility

The temperature susceptibility of asphalt binders is quantified by penetration index (PI). Calculated values of PI for PLDPE-modified asphalt and asphalt cement are depicts in Figure 1. A higher value of PI indicates the lower temperature susceptibility of binder. From Figure it is evident that the temperature susceptibility of PLDPEMAB is lower than asphalt cement.

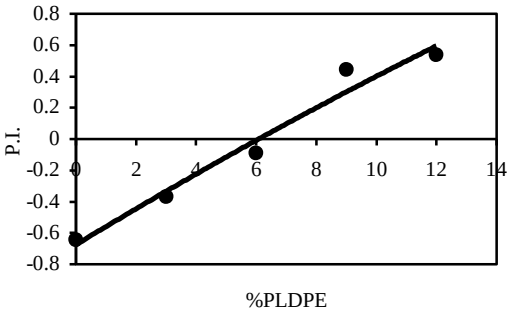

Figure 1 P.I. of PLDPEMAB

Aging Susceptibility Of PLDPEBs

Figure 2 and 3 show the ductility and softening point properties of aged PLDPE–asphalt binders.

From these Figures, it can be seen that the ductility decreases, while softening point increases, moreover the values of ductility are remain 100+ up to 9%PLDPE content.

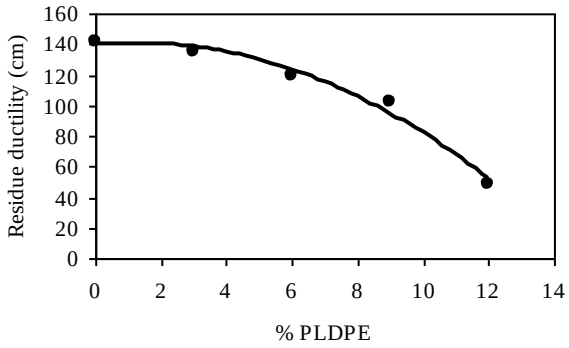

Figure 2 Residue ductility of PLDEMAB

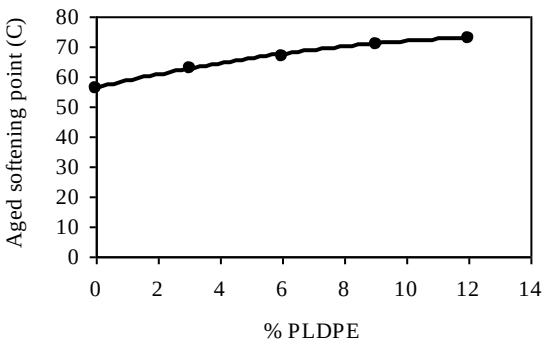

Figure 3 Aged softening point of PLDPEMAB

Figure 4 shows that the percent loss of PLDPE binders decreases as the PLDPE content increases, this is related to that the polyethylene was occupied a space of total mix, and cause reduction in asphalt volume, which leads to decrease in loss by dehydrogenation and oxidation of asphalt in the mix (i.e., durability increased slightly with the addition of PLDPE content in the mix).

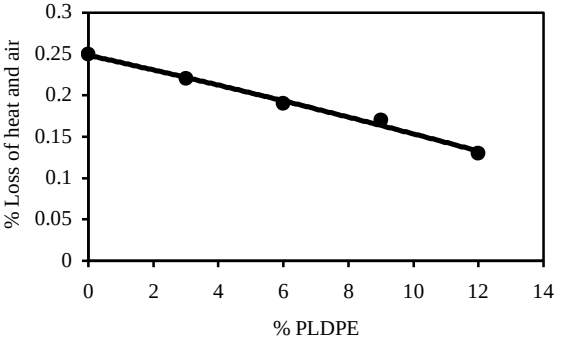

Figure 4 Percent loss of heat and air of PLDPEMAB

The hardening of modified binders was determined by the penetration of residue after exposure to heat and air. Aging was measured by aging index using the following equation:

Aging Index= (Residue penetration after aging at 25^{o}C/Original penetration at 25^{o}C). It can be seen from Figure 5 that aging index increases with increase in PLDPE content, due to the increasing in bonds between PLDPE and asphalt ,resulting in prevention of the brittleness of the resultant binder.

PLDPE/A Compatibility

The compatibility between PLDPE and asphalt was studied by passing the binder at 170°C through an ASTM 100 sieve. It was found that the binder thus prepared can be stored for future use [9] .

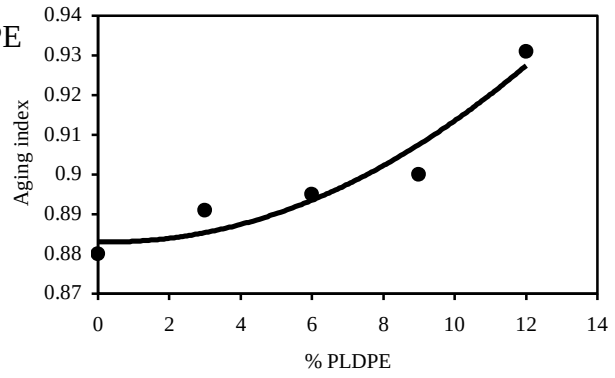

Figure 5 Aging index of PLDPEMAB

CONCLUSIONS

Based on this limited study of the utilization of PLDPE as a modifier or paving asphalt, the following findings were made:

1. Penetration at 25 °C will generally decrease as PLDPE content increases, which indicates an improved shear resistance in medium to high temperatures.
2. The addition of PLDPE kept the ductility values at a minimum range of ASTM and SCRB specifications of 100+cm up to 9% LDPE content.
3. Softening point tend to increase with the addition of PLDPE, which indicates improvement in resistance to deformation.
4. PLDPE seem to improve binder performance viscosity (stiffness). This indicates that rutting, shoving distresses probably will be reduced in hot mix asphalt concrete mixtures.
5. The percentage loss of air and heat decreases with the addition of PLDPE (i.e. the resistance of asphalt to the action of temperature and temperature changes and the action of heat increases).
6. The photomicrograph indicated that PLDPE and asphalt are compatible to an extent; and.
7. Penetration index values indicated that PLDPE reduced the temperature susceptibility of asphalt.

ACKNOWLEDGEMENTS

The authors would like to extend their appreciation to the Bituminous Laboratory/ College of Engineering/ Mosul University/ for technical assistance and the various companies that provided materials used in this study. Special thanks go to the Chairman of civil engineering department Prof. Al-Sulifany Bayar, Manager of Mosul Municipality Mr. Al-Haboo Abdul-Sattar without whom this study would not have been successful.

REFERENCES

[1] Giovanni Polacco, Jiri Stastna, Dario Biondi, Federico Antonelli, Zora Vlachovicova and Ludovit Zanzotto (2004).”Rheology of asphalts modified with glycidylmethacrylate functionalized polymers”.J.Coooid and Interface Science, 280,366-373.

[2] Al-Hadidy, AI. (2006). “Evaluation of pyrolisis polypropylene modified asphalt paving materials”, J. Al-Rafidian engineering, 14(2), 36-50.

[3] Al-Hadidy, AI, (2001). “Influence of polyethylene and sulfur wastes on characteristics of asphalt paving materials”. M.Sc. Thesis, College of Engineering, Civil Engineering Department, Al-Mustansiriyah University,Baghdad-Iraq.

[4] Al-Dubabe I.A,Al-Abdul Wahhab H.I., Asi I.M.,and Mohammed F.A.(1998).”Polymer modification of Arab asphalt”, J.Transp.Eng. 10 (3).

[5] Al-Ghannam, K.A.A, (1996). “Study on the rheological properties of asphalt, effect of modification process on the homogeneity of the system”. Ph.D. Thesis, College of Education, Chemistry Department, University of Mosul, Mosul-Iraq.

[6] Lobna A.S. (1992).”Studies of the changing of rheological properties of asphalt”.MS.C.Thesis, college of science, chemistry department, university of Mosul, Mosul-Iraq.

[7] Milkowski, W. (1985). “Catalytic modification of road asphalt by polyethylene”, J.Transportation. Engineering, 11 (1).

[8] Denning J.H.Bsc.Ph.d.Chem.MRSC and J.Garswell Bsc. (1981).”Improvement rolled asphalt surfacing by the addition of organic polymers”. Transport and Road Research Laboratory, Crowthome, Berkshire, Laboratory report 989.

[9] Punith V. S., A. Veeraragavan (2007), “Behavior of Asphalt Concrete Mixtures with Reclaimed Polyethylene as Additive”. J. Mater. Civ. Eng., 19(6), 500–507.

[10] Sinan Hınıslıoglu, Emine Agar (2004). “Use of waste high density polyethylene as bitumen modifier in asphalt concrete mix”,J. Materials Letters, 58,267-271.

[11] Mahabir Panda, Mayajit Mazumdar (2002). “Utilization of Reclaimed Polyethylene in Bituminous Paving Mixes”, J. Mater. Civ. Eng., 14(6), 527–530.

[12] Al-Hadidy AI and Tan Yi-qiu (2009). "Effect of Polyethylene on Life of Flexible Pavements". J Construction and Building Materials, Vol.23, PP 1456-1464, SCI journals.

[13] State cooperation of road and bridges (SCRB) (1999). “Hot mix asphaltic concrete pavements”. Iraqi standard specification. Ministry of Housing and construction. Department of Design and Study.

[14] Shin-Che Huang (2008). Rubber Concentrations on Rheology of Aged Asphalt Binders. J. Mater. Civ. Eng., 20(3), 221–229.

[15] Crawford, RJ, (1987). “Plastic engineering”, John Wiley & Sons, New York, 2nd edition, 22.

[16] Fredw Billmeyer, JR, (1971). “Textbook of polymer science”. John Wiley & Sons, New York, 2nd edition, 380.

[17] Jenkins, AD, (1972). “Polymeric science”. A materials science Handbook, North Holland publishing company, Amsterdam, London, Vol. 1.

[18] Mohammed, A.A, (1993). “Chemistry of polymers”. College of Education, Chemistry Department, University of Mosul, Mosul-Iraq, 166.

[19] American society for Testing and Materials (ASTM), (2000). Standard Specification, Section 4, Vol. 04-03.

[20] Yang, HH, 1993. "Pavement analysis and design", University of Kentucky, Jones Wiley and Sons, Inc. pp336,337,409,&410.

S - 31

دراسة خصائص حركة السابلة في منطقة المركز التجاري لبغداد

سعد عيسى سرسم

المستخلص

يعتبر المشي من افضل طرق التنقل في منطقة المركز التجاري ببغداد، حيث ان التوزيع المكثف لنقاط التفتيش مع اغلاق العديد من طرق الدخول الرئيسية في شبكة المواصلات وكذلك الموانع على سير المركبات وندرة مواقف المركبات قد ادى الى جعل الحركة المرورية بحالة ضعيفة الخدمية .

يلاحظ في البلدان السريعة النمو كالعراق ،ان فهم اهمية دراسة حركة السابلة ما زالت في البداية وهناك عدد محدود جدا من البيانات حول هذا النوع المهم من طرق النقل.ان معرفة خصائص السابلة يساعد بصورة كبيرة في وضع سياسات الاستخدام الحضري للارض وتوزيع اماكن الخاصة بالنقل في بغداد.ان تاثير حركة السابلة على الرصيف يمكن تصنيفه من خلال الخصائص الشخصية، هدف الرحلة، حالق الرصيف الفيزياوية، خصائص المنطقة المحيطة وتاثير الضروف المناخية.

تعرض هذه الورقة دراسة للسابلة وخصائص مسيرهم لمواقع محددة في منطقة المركز التجاري لبغداد. ان تقنية طفو السابلة قد تم اعتمادها في تحديد الاختلاف في سرعة المسير للسابلة وايجاد علاقة بين هذه السرعة وخصائص السابلة مثل الجنس والفئة العمرية وتقاليد الملبس. من جانب أخر، تم تحديد سرعة واتجاه عبور السابلة للطريق كما تم ايجاد علاقة بين خصائص السابلة وبينها. تم حساب مستوى الخدمة لكل موقع. تم الاستنتاج ان سرعة السابلة في العراق والمتمثلة ببغداد تعتبر بطيئة عند مقارنتها بالدول المتقدمة او بالدول المجاورة. اما سرعة العبور فكانت هي ايظا بطيئة عند مقارنتها بمواصفات مدونة سعة الطريق العالمية. تم الاستنتاج بوجود اختلاف حقيقي ومؤثر في سرعتي المسير والعبور للسابلة عن ماهو معروف عالميا.

Assessing Pedestrian flow characteristics at Baghdad CBD area

Saad Issa Sarsam/Professor of Transportation Engineering
Department of Civil Engineering, College of Engineering
University of Baghdad, Baghdad – Iraq

Abstract

Walking is considered as the most efficient mode of transportation at Baghdad CBD area. The heavy distributions of security check points and blockage of some major access roads at the roadway network, restrictions on vehicular movement, and scarcity of parking lots had changed the whole traffic movement to the unserviceable condition.

In rapidly developing countries like Iraq, however, the recognition of the importance of walking studies is still in its infancy; minimal data exist on this important mode of travel.

Knowledge of pedestrian characteristics could effectively assist in the optimization of policies concerning urban land use and the locational distribution of transport-related facilities in Baghdad. The influences on pedestrian movement along sidewalks can be categorized into individual attributes, the purpose of the journey, the physical nature of the sidewalk, the nature of the surrounding area, and weather effects.

In this paper, the pedestrians and their walking characteristics in specific locations at Baghdad CBD were studied. The floating pedestrian technique was implemented, and the variations in walking speed of pedestrians were related to pedestrian characteristics such as gender, age group, and clothing traditions. On the other hand, the crossing speed and the crossing direction of pedestrians were also detected, and correlated with pedestrian characteristics. The level of service was calculated for each sidewalk location. It has been found that Iraqi pedestrians walk slower than other pedestrians in the developed countries or in the region. The crossing speed was also slower than that of HCM 2000 standards. It was concluded that significant variations in crossing and walking speed among pedestrians have been noticed.

1.0 Introduction

Walking as a means of mobility has been important in each period of the human history. It is the most basic of the transport modes, the importance of walking increases as societies strive to become sustainable. Walking decreases the environmental load, and has been governed by the influence of regional culture and condition of pedestrian facilities. The movement of pedestrians in the urban environment is vital for sustaining the social and economic relationships essential to the quality of life, and is important to maintaining a healthy life. Little attention has been given to variation in users and the corresponding variation in walking or crossing speeds. Several user and environmental factors influence pedestrian speeds. Assessment of the impact of pedestrian characteristics on the walking and crossing speed was thought to be an essential issue for establishment of design standards for pedestrian facilities. As the central business district area continues to expand and traffic congestion increases, study on the attributes of pedestrian such as walking and crossing speed, gender, flow and density, need to be conducted from time to time together with the increase in population and development of one place in CBD area.

Roadways need to be designed to accommodate the needs of all road users. Roadway modifications that include widening streets, adding lanes and using traffic engineering solutions that increase vehicular efficiency can decrease pedestrian safety if not properly considered.

2.0 Background

Tsimhoni et al (2008) stated that in 2006, 4,784 pedestrians were killed in the United States, constituting about 11% of all road-traffic fatalities. In other parts of the world, pedestrians constitute even larger proportions of fatalities. For example, the percentage of pedestrian traffic accident fatalities was 18% in the European Union, 25% in China, 34% in Japan, and 48% in Delhi, India.

Many pedestrians, especially in large urban areas, violate pedestrian traffic control and place themselves at risk for collisions with motor vehicles. About one-third of fatal crashes involving pedestrians are the result of pedestrians disobeying traffic control or making misjudgments while attempting to cross a street, **US Dot. (2004).**

Tsukaguchi et al (2007) stated that their research was motivated by the need to address some of the critical issues related to pedestrian crossings. However, they concluded that pedestrian traffic is a complex phenomenon that could be approached from various academic fields. The characteristics of pedestrian behavior can be examined from a cultural perspective.

Tanaboriboon et al (1986) stated that knowledge of the characteristics of the typical Singapore pedestrian could help in optimizing land use in pedestrian design and result in more efficient and safer designs for the pedestrians.

Lam and Cheung (2000) demonstrated that it is required to conduct further study on local pedestrian characteristics in order to develop pedestrian planning standards. The walking speed and/or walking time of pedestrians are of prime importance in a study of function and design of pedestrian facilities.

Koushki and Ali (1993) studied pedestrian flow characteristics in Kuwait city and reported that favoring of automobiles as a predominant mode of travel in Kuwait City has created the greatest obstacle to the promotion of walking in city center. They observed that the pedestrian walking speeds were lower in Kuwait City center as compared to those in the United States and England but were similar to pedestrian speeds observed in Riyadh, Saudi Arabia.

Al-Masaeid et al. (1993) developed the pedestrian speed-flow relationship for the central business district (CBD) areas in Irbid, Jordan. Quadratic polynomial regression relation was found to be the best fit model.

Daamen and Hoogendorn (2003) observed that speed of pedestrians is influenced by walking characteristics such as the width, and environmental factors. The pedestrian speeds are also influenced by the type of facility. **Polus et al. (1983)** found that the average walking speed of pedestrians on sidewalks in Haifa, Israel, is 79 m/ min. In Singapore, it is observed at 74 m/ min, **Tanaboriboon et al. (1986). Koushki (1988)** found that the slowest pedestrians are in Riyadh, who walk at a speed of 65 m/ min. **Morrall et al. (1991)** found the walking speed of pedestrians at 75 m/ min in Colombo, Sri Lanka, and 84 m/ min in Calgary, Canada. They suggested that for Asian countries, such as India, Sri Lanka, and China, the pedestrian planning should be based on local pedestrian characteristics rather those from cities with dissimilar cultures. **Carey (2005)** and **Montufar et al. (2007)** found that younger pedestrians walk faster than older pedestrians and are not affected by season. **Fitzpatrick et al. (2006)** observed that the 15th percentile walking speed of younger pedestrians (1.15 m/s) is faster than that of older pedestrians of (0.92 m/s).

USDOT (2004) demonstrated that assumptions of walking speeds for signal timing may be too fast for many pedestrians to cross to the other side of the curb. Also, there appears to be a poor understanding of pedestrian signal displays by pedestrians. Pedestrian crossing signal timings may be too short to permit safe intersection crossing. Studies of pedestrian and driver reactions indicate that pedestrians generally perceive that they are visible to drivers before they are visible.

3.0 Methodology and field work

3.1 Pedestrian walking speed, volume, and density

There have been a select number of studies on pedestrian walking speeds in the past, the present investigation seeks to build upon existing research, and design an experiment to collect pedestrian walking speed data in urbanized areas in Baghdad. To conduct the speed, density and volume studies in the concentrated CBD areas, several sidewalks along the main streets were selected as the observation sites. The pedestrian volume and speed data were collected at three selected locations of Baghdad CBD area using two techniques. The first site is located in a recreational and shopping zone (AL-Mansur); the second site is a tourist zone which contains the holly shrinks, (Al-Kadimiah); while the third site is an educational zone holding colleges and scientific institutes, (Bab Al-Muadim). It was expected that sites with different land use could show different pedestrian characteristics.

The first technique adopted in the field work is by marking a longitudinal section of known length and width on the pedestrian facility and continuously recording the movement of pedestrians within this section. Pedestrians were manually timed over a measured test length of 50 meters, volume and speeds were then calculated. Random pedestrian about to enter the section was selected and tracked through the study area. The time taken by a pedestrian to traverse the test length was measured using a digital stop watch, the entry and exit times in and out of the test area was recorded. Walking speed is then derived by dividing the known length of the section by the walking time. The density was obtained by counting the number of walking pedestrians within the boundaries of the observation section site at unit time. The flow was obtained by counting the number of pedestrians passing the section entry and exit lines of the observation site within the time interval.

The second technique used by the field work is by implementation of the floating pedestrian method. A floating pedestrian was tracked when moving along the section from the start point to the exit point six times in each direction, the number of overtaking and overtaken pedestrians by the floating pedestrian was recorded, the number of pedestrian walking at opposite direction to the floating pedestrian and the time taken by the floating pedestrian to traverse the section in each direction was also recorded. Data collections were adopted for approximately 60 min during morning peak period (8.30 – 9.30 a.m.) and evening peak period (5.30 – 6:30 p.m.) on a typical two weekday of each of February and March 2013. Data were gathered, plotted, then subjected to statistical analysis using SPSS V17 software. The volume, speed, and density were calculated using the mathematical models below, **Pignataro (1973)** : **Khisty & Lall (1998).** From this data, regression models have been constructed and the predictive performances of these models were assessed. The data obtained from the field survey were examined to determine the relationships between (speed - flow), (speed - density), and (flow - density).

$V_N = (M_S + O_N - P_N) / (T_N + T_S)$ ……(1)

$V_S = (M_N + O_S - P_S) / (T_N + T_S)$ ……(2)

$T_N (av) = T_N - [(O_N - P_N)] / V_N$ ……...(3)

$T_S (av) = T_S - [(O_S - P_S)] / V_S$ ……..(4)

$S_N = L / T_N (av)$ ……...(5)

$S_S = L / T_S (av)$ ……(6)

$D = V / S$ …….....(7)

$Vu = V / We$ ……(8)

$Du = Vu / S$ ……(9)

Where: V_N; V_S represents pedestrian volume (pedestrian / Minutes) at north or south directions.
T_N ; T_S represents travel time (minutes) in each direction.
T_N (av.); T_S (av.) represents average travel time (minutes) in each direction.
M_S; M_N represents opposing pedestrian traffic count met with the floating pedestrian in each direction.
O_S; O_N represents number of pedestrians overtaking the floating pedestrian in each direction.
P_S; P_N represents number of pedestrians passed by the floating pedestrian in each direction.
S_N; SS represents the space mean speed (meter / minutes) in each direction.
L = the test section length (meters).
D = the density of pedestrian (pedestrian / meters).
V = the volume of pedestrian (pedestrian / 15 minutes).
We = Effective width of side walk section in meters.

S = pedestrian speed (meters / minutes).
Vu= unite width flow (pedestrian / 15 minutes / meter).
Du = the unit area density of pedestrian (pedestrian / meters ^{2}.

3.2 Pedestrian crossing speed and crossing direction

There is still a lack of data on the subject of Pedestrian crossing times which have a significant impact on roadway design and safety. The conflict between traffic flow and pedestrian safety can be better addressed with more information on pedestrian characteristics and crossing speeds. In order to expand on the existing information of crossing speed, a series of studies was conducted to compare with the available data. The crossing behavior of pedestrian was also studied, the time taken by various pedestrian age, gender, and clothing tradition groups to cross the carriageway was measured and the crossing speed was determined by dividing the carriageway width by the crossing time. The direction taken by the pedestrian in the crossing process (perpendicular or at an inclined positions to the traffic flow stream) was also determined for each group.

3.3 Pedestrian traffic characteristics and level of service LOS

Pedestrian volume and flow studies may be expressed in terms of volume (persons per hour), flow rate (persons per minute per meter), density (square meter per person), or walking speed (meters per minute). The aims are to conduct the speed studies in the CBD areas, and to examine the relationships of walking speed, flow and density. Modeling of pedestrian LOS can provide an insight to pedestrian facilities designs that better and more safely accommodate pedestrian mobility. Geometric and operational aspects of the sidewalks were examined by conducting a field survey. All characteristics of factors affecting LOS such as section area, clear walking area, in addition to flow rate and walking speed were collected for each sidewalk in the study area. Pedestrian LOS can be used to develop a minimum LOS standard which could prescribe the minimum acceptable LOS for the adequate accommodation of pedestrians, **Muraleetharan et al (2005); HCM (2000).** Pedestrian LOS models could also be used to support the development of pedestrian facility improvements.

4.0 Discussion of test results

4.1 Impact of gender and land use on crossing speed

The data presented in Table 1, indicates that the crossing speed of both genders is close for site three which is an educational zone (mean crossing speed is 1.44 – 1.43 m/sec. for male and female respectively). On the other hand, there is a pronounced variation in crossing speed among both genders for the other two sites. This may be attributed to the fact that most of the pedestrians at the educational zone are young.

On site two which is a tourist and religious zone, it shows the slowest crossing speed (mean crossing speed is 1.013 – 0.716 m/sec. for male and female respectively), this could be related to the presence of older aged pedestrians. On site one which is a shopping and recreational zone, male pedestrian shows the fastest crossing speed of 1.636 m/sec when compared to other sites. **AAA foundation (2010)** suggests timing for street crossing.

4.2 Impact of pedestrian gender on crossing direction

As far as the crossing direction is concerned, it could be noticed that a range of 40 – 50 % of pedestrians spend more time on the road while crossing at an angle other than the perpendicular angle to the traffic flow direction. **US.DOT (2004)** stated that crossing the street at other than perpendicular direction to traffic flow can increase the distance that one must walk to cross the street. Normally, the tendency of the pedestrian is to take the shortest course while crossing even if it involves a certain amount of risk, but as indicated by Table 1, the pedestrians were unaware of the danger of lengthy exposure to traffic movement. Such high range may also indicate lower traffic educational level; similar results were obtained by the author on a study at Mosul city, **Sarsam, (2002).**

Table: 1 Variation of average crossing speed and crossing direction with gender

Site	Mean crossing speed, Male (m/sec)	Standard deviation for Male (m/sec)	Percentage of Male crossing perpendicular to traffic flow	Mean crossing speed Female (m/sec)	Standard deviation for Female (m/sec)	Percentage of Female crossing perpendicular to traffic flow	Pedestrian Sample size of each group
Site 1	1.636	0.156	61	1.285	0.121	54	100
Site 2	1.013	0.130	48	0.716	0.092	53	120
Site 3	1.435	0.144	57	1.440	0.142	65	120

4.3 Impact of age groups and gender on crossing speed

As demonstrated in Table 2, young pedestrian of age group (15-30) are faster than elder while crossing for both genders and for all sites. Their crossing speed was in the range of 1.65 – 1.35 m/sec for male and 1.30 - 1.22 m/sec for female pedestrian. The variation of crossing speed among different sites could be attributed to the flow rate of pedestrian which is higher at site two, and to the presence of older aged pedestrian. Such finding agrees well with **Pulice (2004),** who stated that the assumptions governing the expected crossing speed have changed considerably. A standard crossing time of 1.21 m/sec was adopted to allow users to walk from the curb to the far side of the traveled way. The Traffic Engineering Handbook information as sighted in **US.DOT (2004)** suggests 0.91 to 0.99 m/sec as appropriate, while another study suggested 0.76m/sec for areas with high senior Concentrations.

Similar findings were presented by **Akcelik & Associates (2001).** Data for all sites studied in Australia indicated an average crossing speed of 1.42 m/s (in the range 1.36 to 1.52 m/s) for individual sites and periods. They stated that the crossing speed for all sites combined is very close to the general design speed of 1.2 m/s recommended by the Australian and US design guides. On the other hand, **O'Flaherty (1997)** reported the road crossing speeds at busy crossings for a mix of pedestrian age groups and found them varying in the range of 1.2–1.35 m/s.

Table: 2 Variation of crossing speed with gender and age groups

Site	Average crossing speed (m/sec)						Pedestrian sample size for each group
	Male age groups			Female age groups			
	15 - 30	31 - 46	47 - 62	15 - 30	31 – 46	47 - 62	
Site 1	1.650	1.636	1.285	1.300	1.280	1.058	100
Site 2	1.353	0.993	0.636	0.792	0.705	0.46	120
Site 3	1.354	1.311	1.138	1.261	1.342	1.220	120

4.4 Impact of gender and clothing tradition on crossing speed

The impact of clothing tradition on crossing speed is considered in this investigation. Two types of clothing styles have been considered for both genders, the typical Arabian clothing style shown in plate 1 are commonly implemented by some people while the western culture clothing style (trousers) are used by others. Table 3 demonstrates that male pedestrians have slower crossing speed of the range 1.32 – 0.93 m/sec when implementing Arabic style clothing, while male pedestrians have faster crossing speed of the range 1.680 – 1.013 m/sec when using trousers. This may be attributed to the limitations practiced in the step length which is restricted due to clothing when using the Arabic clothing tradition. When female pedestrian are considered, the variation of crossing speed among using different clothing style was not significant. This could be attributed to the slower average crossing speed range of 0.705 – 1.337 m/sec of female as compared to male. Such findings were expected by **Koushki, (1988)** in his study of pedestrian in Saudi Arabia.

Table: 3 Variation of crossing speed with gender and clothing tradition

Site	Mean crossing speed (m/sec)				Pedestrian sample size for each group
	Male pedestrian clothing style		Female pedestrian clothing style		
	Arabic style	Trousers	Arabic style	Trousers	
Site 1	1.320	1.680	0.980	1.090	100
Site 2	0.930	1.013	0.705	0.728	120
Site 3	1.279	1.321	1.337	1.264	120

4.5 Variation of walking speed with gender and land use

Table 4 illustrates the arithmetic mean walking speed of male and female pedestrians; it shows that male pedestrian walks faster than female for all of the tested sites. The shopping and recreational site exhibits almost the slowest walking speed of a range 41.28 – 36.36 m/min. for both genders. This may be attributed to the fact that people were not in hurry and move slowly to enjoy the shopping site. This was in agreement with work by **Lam and Cheung (2000)** who observed that pedestrians walking in commercial areas are faster than those in recreational areas, and the walking speed of the pedestrian depends on the surrounding environment.

a. Female style b. male style

Plate 1 Typical Arabic clothing tradition detected

It is also comparable with **Rastogi et al (2011)** statement that Land use also plays a major role in determining the walking speed of pedestrians. They found that Pedestrian speed in an educational area was 85.27 m/ min and in shopping areas 60.21 m/ min. Pedestrian at site two which is a tourist and holly shrinks site moves almost faster than those at site one with a mean speed range of 49.85 – 33.87 m/min.; it was felt that people came humble to visit the holly shrinks and are fast enough to complete the ceremony.

Table: 4 Variation of walking speed with gender and clothing tradition

Site	Mean walking speed (m/min)				Pedestrian sample size for each group
	Male pedestrian clothing style		Female pedestrian clothing style		
	Arabic style	Trousers	Arabic style	Trousers	
Site 1	41.28	38.45	37.31	36.36	60
Site 2	49.85	44.92	42.30	33.87	60
Site 3	72.79	60.78	60.33	61.73	60

At site three which is an educational zone, pedestrians are young in majority and walk faster than the other two sites as indicated by a range of 72.79 – 60.33 m/min. Such findings agrees with the study held in Singapore by **Tanaboriboon et al (1986)** which shows that the mean walking speeds of Singaporeans is 74 m/min. it also shows that the Singapore males generally walked faster than the females as their mean walking speeds are 79 m/min and 69 m/ min for males and females, respectively. The present study findings are comparable to walking speeds reported by **Laxman et al (2010)** for Philippines and the United States, **Fruin (1971),** while it is higher than that reported for China and Singapore, but slightly lower than that in Germany. The wide range of variation of mean speed between the tested sites which reflects the impact of land use was in agreement with **Finnis and Walton (2007)** in their statement that pedestrian walking speeds varied from 98 m/min to 33m/min. **Rastogi et al (2011)** tabulated a global walking speed of a range 65 – 90 m/min in their study.

The impact of clothing tradition was significant for male pedestrian; the mean speed of male pedestrian with Arabic style clothing was faster by a range of 7- 19 % when compared with that of pedestrian wearing trousers. On the other hand, such variation was not significant for female pedestrians.

4.6 Effect of age groups and clothing tradition on walking speed

As demonstrated in Tables 5 and 6, the walking speed decreases as the age group increases for both genders. The range of variation in walking speed for male pedestrians with Arabic style clothing was 47 – 77 m/ min. for young at different land use and changes to 41 – 74 m/min for adult. It decreases to 35 - 66 m/min for elder. The clothing tradition exhibits significant variation among age groups. Female pedestrian behaves similarly, although Gender was not found to be an important determinant of walking behavior. The impact of clothing style is significant especially at site three where more young pedestrians exist. These findings are in agreement with those reported by **Fruin (1971), Polus et al. (1983), Tarawneh (2001), and Montufar et al. (2007).**

Table: 5 Variation of walking speed with age group and clothing style for male pedestrian

Site	Average walking speed (m/min)						Pedestrian sample size for each group
	Male age group – (Arabic style)			Male age group – (Trousers)			
	15 - 30	31 - 46	47 - 62	15 - 30	31 – 46	47 - 62	
Site 1	47.00	41.44	35.42	45.32	40.00	30.05	60
Site 2	59.40	51.00	39.15	57.42	48.35	29.00	60
Site 3	77.73	74.64	66.00	66.12	61.08	55.14	60

Table: 6 Variation of walking speed with age group and clothing style for female pedestrian

Site	Average walking speed (m/min)						Pedestrian sample size for each group
	Female age group – (Arabic style)			Female age group – (Trousers)			
	15 - 30	31 - 46	47 - 62	15 - 30	31 - 46	47 - 62	
Site 1	42.22	39.50	30.23	40.43	38.89	29.78	60
Site 2	46.50	41.40	39.00	41.02	39.60	21.00	60
Site 3	69.57	53.34	58.08	74.91	66.00	59.28	60

4.7 Pedestrian traffic flow characteristics

Figure (1) shows the variations in walking speed when measured in the field using two different techniques; the floating pedestrian technique shows slower walking speed when compared with section technique especially at slow walking speed. However, at faster walking speed, the scatter of data was away from the trend line which could indicate weaker correlation.

Table 7 shows the variation of pedestrian flow rate and walking speed among different land uses, While Table 8 shows the level of service for each site. The flow rate of the range 103 – 156 pedestrian / 15 minutes / m is considered high when compared to other studies in Europe and United States, **Tanaboriboon et al (1986),** while it is comparable to the findings by **Sarsam (2002).**

Table: 7 Pedestrian traffic flow characteristics

Site	Unit width Flow rate (Pedestrian / 15 minutes/ m)	Mean walking Speed (meter/minute)	Standard deviation of speed (m/minute)	Density (Pedestrian /m2)	Pedestrian sample size for each age group
Site 1	133.0	38	3.4	3.51	60
Site 2	156.0	42	4.1	3.71	60
Site 3	103.6	70	6.0	1.48	60

Table: 8 Level of service parameters

Site	Sidewalk section area (m^2)	Clear walking area (m^2)	Sidewalk capacity (Pedestrian)	V/C ratio	LOS
Site 1	150	134	144.2	0.92	E
Site 2	150	100	153.8	1.01	F
Site 3	150	120	150.0	0.69	E

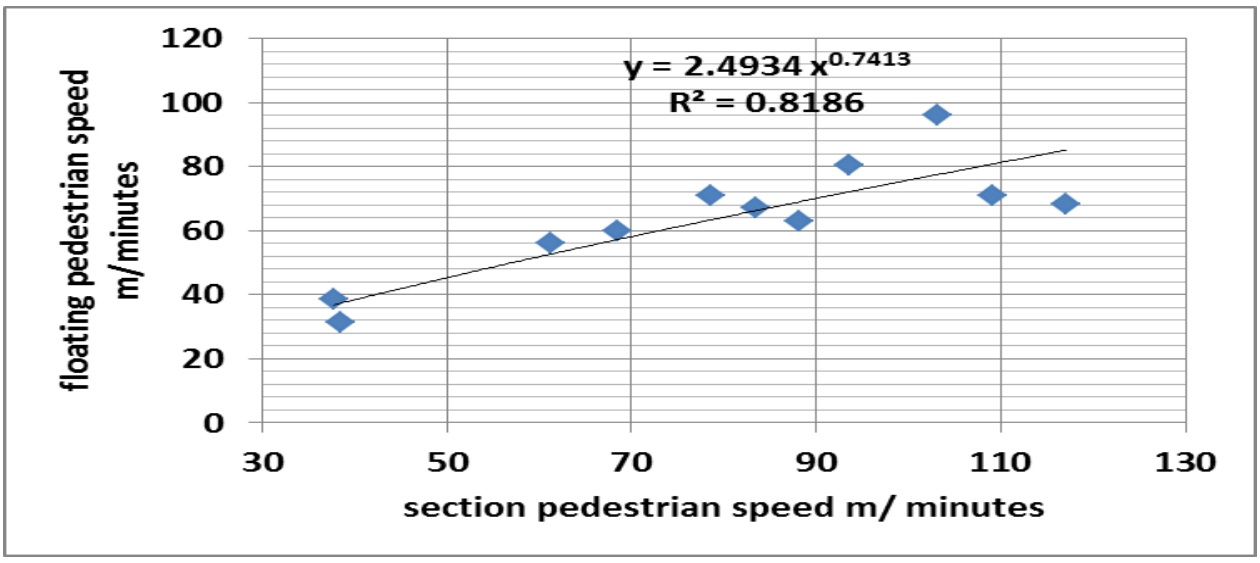

Figure: 1 Modeling the variation in walking speed using two techniques

Figure 2 presents the walking speed – Pedestrian density relationship, the mean free flow walking speed for the three sites investigated was found to be 79 m/minutes, The mean free flow walking of the Baghdad pedestrians that has been observed is comparatively slower than that of American counterpart of 85m/min, While it is faster than that of Singapore of 74 m/min. **Tanaboriboon et al (1986).** Figure 3 shows the flow rate – density relationship, it shows high coefficient of determination R^2 of 0.95. On the other hand, Figure 3 illustrates the flow rate – walking speed relationship. It shows that the maximum flow rate is within 142 pedestrian/15min./m which is further supported by the data presented in Table 7.

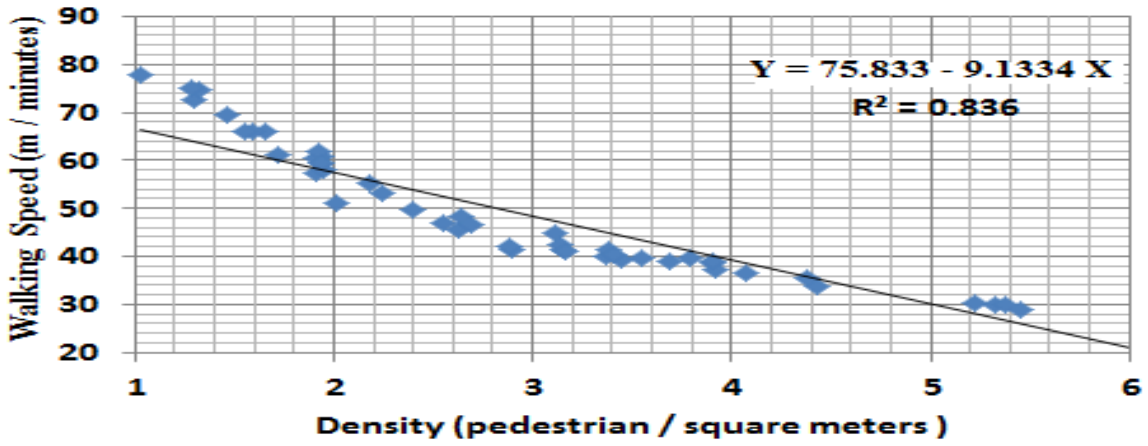

FIGURE: 2 Density – Walking speed relationship

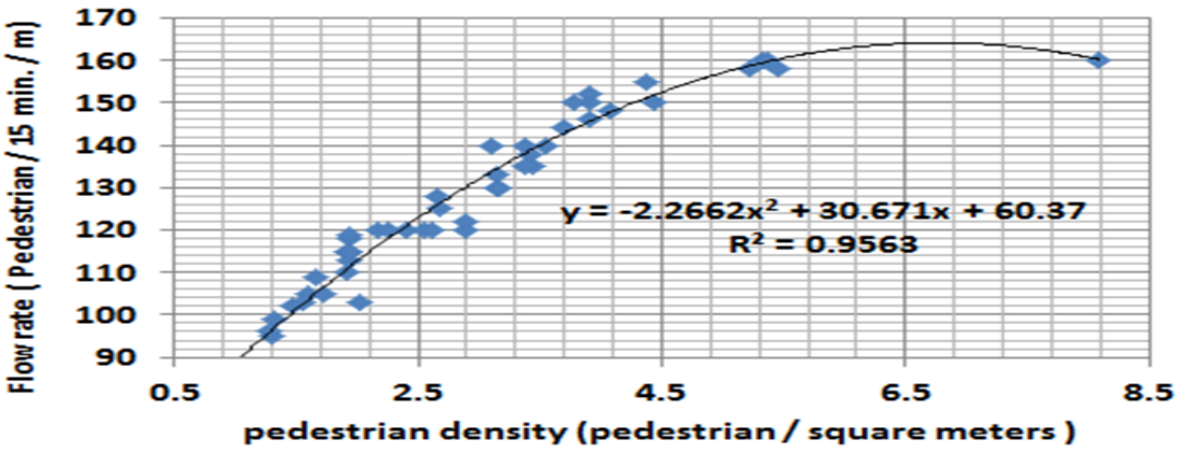

FIGURE: 3 Flow rate – density relationship

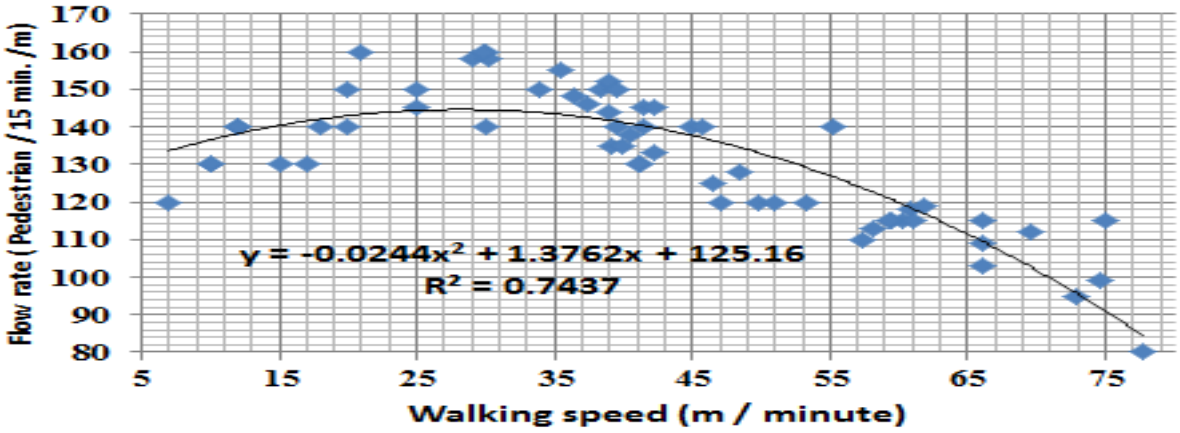

FIGURE: 4 Flow rate – walking speed relationship

5.0 Conclusions

Based on the field investigation, the following conclusions may be drawn:

1- It was found that the contributing factors of the walking speed for male and female pedestrian are clothing tradition, gender, age group.

2- Male pedestrians move faster than female pedestrians. Pedestrians in the age group of 15–30 years had the highest speed of the range 77.7 – 66.1 m/min. on the other hand; female pedestrian had the range of 74.5 – 69.9 m/min. for the same age group.

3- The clothing tradition has more impact for male pedestrian; the mean speed of male pedestrian with Arabic style clothing was faster by a range of 7- 19 % when compared with that of pedestrian wearing trousers. On the other hand, such variation has no impact for female pedestrians.

4- Male pedestrians have slower crossing speed of the range 1.32 – 0.93 m/sec when implementing Arabic style clothing, while male pedestrians have faster crossing speed of the range 1.680 – 1.013 m/sec when using trousers.
5- Female pedestrian shows the slower average crossing speed range of 0.705 – 1.337 m/sec as compared to male, while the variation of crossing speed among using different clothing style was not significant.
6- The pedestrians crossing direction was found to be in the range of 48-61 % of male crossing perpendicular to traffic flow, while the range was 53-65 % for female. This indicate that pedestrian were unaware of the danger of lengthy exposure to traffic movement. Such high range may also indicate lower traffic educational level.

6.0 Recommendations

There is a need for research into walking behavior in varied settings. Planning and implementing such facilities requires an understanding of the characteristics of pedestrian movements and their needs. It is recommended that the pedestrian planning should be based on local pedestrian characteristics rather than the pedestrian characteristics from cities with dissimilar cultures. Revising the standards and regulations, and educating the public are considered as good issues to start with.

References

1- AAA foundation for traffic safety, "Pedestrian Signal Safety for Older Persons" AAA Technical report, 2010.
2- Akcelik and association "An Investigation of Pedestrian Movement at Mid-Block Signalized Crossings" Akcelik & Associates Pty Ltd technical report, December 2001, Australia.
3- Al-Masaeid, H. R., Al-Suleiman, T. I., and Nelson, D. C. 1993. "Pedestrian speed flow relationship for central business areas in developing countries." Transp. Res. Rec., 1396, 69–74.
4- Carey, N. (2005). "Establishing pedestrian walking speeds", Portland State University, Portland, OR, 1–4.
5- Daamen, W., Hoogendoom, S.P.,(2003) Experimental research on pedestrian walking behavior. In: Proceedings of the 82nd Annual Meeting of the Transportation Research Board, Washington DC.
6- Fitzpatrick, K., Brewer, M. A., and Turner, S. (2006). "Another look at pedestrian walking speed" Transportation Research Record 1982, Transportation Research Board, Washington, DC.
7- Fruin, J. (1971) "Pedestrian planning and design" Metropolitan Association of Urban Designer and Environmental Planners, Inc., New York.
8- Fruin, J. J. (1971) "Designing for pedestrians: A level of service concept." Highway. Res. Rec., 355, 1–15.
9- Finnis K. and Walton D. "Field observations of factors influencing walking speeds" Technical report, University of Canterbury, Christchurch, New Zealand 2007.
10- Koushki, P. A. (1988). "Walking characteristics in central Riyadh, Saudi Arabia" J. Transp. Engrg., ASCE, 114(6), 735-744.
11- Koushki, P. and Ali M."An analysis of pedestrian in Kuwait" Kuwait J. Sci. Eng. 30 (1) 2003
12-Khisty C.J & Lall B.K. "Transportation Engineering- an introduction" Prentic-Hall international Inc.-Newjersy Ch. 12 -1998 (P524-540). USA.

13- Lam and Cheung "pedestrian speed/flow relationships for walking facilities in Hong Kong" Journal of Transportation Engineering, Vol. 126, No. 4, July/August, 2000.ASCE.
14- Laxman et al "Pedestrian Flow Characteristics in Mixed Traffic Conditions" Journal of Urban Planning and Development, Vol. 136, No. 1, March 1, 2010. ASCE
15-Muraleetharan T.; Hagiwara T.; Adach T.; Kagaya S. " Method to determine pedestrian level of service for crosswalks at urban intersections" Journal of the Eastern Asia Society for Transportation Studies, Vol. 6, pp. 127 - 136, 2005.
16- Montufar, M., Arango, J., Porter, M., and Nakagawa, S. (2007) "Pedestrians' normal walking speed and speed when crossing a street." Transportation Research Record 2002, Transportation Research Board, Washington, DC, 90–97.
17- Morrall, J. F., Ratnayaka, L. L., and Seneviratne, P. N. (1991). ''Comparison of central business district pedestrian characteristics in Canada and Sri Lanka.'' Transp. Res. Rec. 1294, Transportation Research Board, Washington, D.C., 57–61.
18- O'Flaherty, C. A. 1997. 'Transport planning and traffic engineering" Arnold, London.
19- Polus, A., Schofer, J. L., and Ushpiz, A. 1983. "Pedestrian flow and level of service." J. Transp. Eng., 1091, 46–56.
20- Pulice S. "Establishing Pedestrian Walking Speeds" Portland State University, ITE Student Chapter 2004.
21- Pignataro L. "Traffic Engineering theory and practice" Prentice-Hall; 1973.
22- Rastogi et al "Design Implications of Walking Speed for Pedestrian Facilities" Journal of Transportation Engineering, Vol. 137, No. 10, October 1, 2011. ©ASCE
23- Sarsam S. "Modeling pedestrian crossing and walking behavior at Mosul CBD" Proceedings, Safety on roads: 2nd international conference 21- 23 October-2002 Bahrain SORIC` 02
24- Tarawneh, M.S., 2001, "Evaluation of pedestrian speed in Jordan with investigation of some contributing factors." Journal of Safety Research 32, pp 229-236.
25- Tsukaguchi H.; Vandebona U.; Yeh K. "Comparison of attitudes toward walking in Japanese cities" Proceedings of the Eastern Asia Society for Transportation Studies, Vol.6, 2007.
26- Tanaboriboon et al "Pedestrian characteristics study in Singapore" Journal of Transportation Engineering, Vol. 112, No. 3, May, 1986. ASCE.
27- Tsimhoni O.; Kandt A.; Flannagan M. "Driver perception of potential pedestrian conflict" Report No. UMTRI-2008-46 October 2008
28- U.S. Department of Transportation, Federal Highway Administration, pedestrians, Technical report, 2004.

S - 32

Traffic Assignment Planning Study in Small Urban Areas Road Network Using GIS Technique

Dr. Abdulkhalik Malulla M. AL-Taei
Assistant Professor/Transportation Engineering
Civil Engineering Dept./College of Engineering/Mosul University

Abstract

Traffic assignment is an important, and final fourth step in the Urban Transportation Planning Process. In this study, Dohuk City road network located in CBD is selected as a study area to apply a traffic assignment algorithm developed with the assistance of GIS Software to select the shortest paths of the different tested networks selected during different strategic stages of planning. A lot of traffic stream data were collected such as, directional volumes, speeds, travel times, ideal driving legal speeds, and other network geometric characteristics such as, link length, width, and grade. Three strategic steps were selected to test the different loading alternatives on the selected road network study area. Each step included five years of traffic demand, or volume growth starting from 2012 horizon year up to 2027 goal year. During this fifteen years period, traffic demand is assumed to increase with 6 percent annually. Results obtained out of this study, were represented by different city road network plans, or scenarios representing congestion problem locations diagnosed, and the future solution plans that will be needed to solve that strategic traffic operation, and demand requirements to provide an acceptable LOS according to the requirements of the American HCM-2000. These comparisons are found serious and necessary in order to reflect the efficiency of the algorithm used as a powerful tool to solve such problems needed for any road network located in urban ,or rural city infrastructure now or in the future.

دراسة تخطيط ألتوزيع ألمروري في شبكات ألطرق ألواقعة في ألمناطق ألحضرية ألصغيرة باستخدام تقنيات نظام ألتوزيع ألجغرافي

د.عبد ألخالق ما ل ألله محمد حسن ألطائي/أستاذ مساعد / هندسة ألطرق والنقل
قسم ألهندسة ألمدنية/كلية ألهندسة/جامعة ألموصل

ألمستخلص

توزيع ألمرور يعتبر من ألخطوات ألمهمة والرابعة ألنهائية في عملية التخطيط الحضري لأية منظومة للنقل داخل ألمدن.في هذه ألدراسة تم اختيار المركز التجاري لمدينة دهوك كمنطقة دراسة من أجل تطبيق برنامج للتوزيع ألمروري تم تطويره وأعداده في هذه ألدراسة وبمساندة نظام GIS لاختيار أقصر ألمسارات لمجموعة من ألشبكات على مدار فترات إستراتيجية مختلفة من مراحل ألتخطيط. تم جمع كمية من ألبيانات ألمرورية مثل ألحجوم ألمرورية ألاتجاهية،سرعة ألمركبات،أوقات ألرحلة ،ألسرعة ألقانونية،عرض ألطريق، وميله ألطولي .كما تم اختيار ثلاثة مراحل إستراتيجية مختلفة لاختبار ألشبكة ألمحملة بألحجوم المرورية ألمختلفة وبواقع خمسة سنوات لكل فترة إستراتيجية للطلب ألمروري أبتداءأ من سنة ألدراسة2012 وحتى سنة ألهدف 2027.خلال فترة خمسة عشرة سنة ، تم افتراض أن ألطلب على المرور سيزداد بمعدل 6% سنويا .ألنتائج ألمستحصلة من هذه ألدراسة تم تمثيلها بمجموعة من ألخرائط أو ألسيناريوهات تمثل مواقع ألازدحام ألمروري ألمتوقع خلال كل فترة من ألفترات ألإستراتيجية ألمستقبلية ألمقترحة والحلول ألمناسبة لها لتوفير انسيابية ومستوى خدمة ملائمة لمستوى الخدمة أبان كل فترة مقداره LOS C وحسب توجيهات دليل ألاستيعاب ألأمريكي HCM-2000.كما تم عمل مقارنات بين خواص ألجريان ألمروري ألمتوقعة خلال كل فترة من أجل اختبار كفاءة ألبرنامج ألمعد من أجل وضع حلول منذ ألان لحل مشاكل ألازدحام في مركز مدينة دهوك حاليا ومستقبلا كما يمكن تطبيقه على شبكات ألطرق خارج ألمدن أيضا لقياس كفاءة ألأداء ألمروري فيها.

Introduction*:*

Urban transportation planning is the process that leads to decisions on transportation policies and programs. In this process, planners developed information about the impacts of implementing alternative courses of action involving transportation services, such as new highways, bus route changes, or parking restrictions. This information is used to help decision-makers in their selection of transportation policies and programs.

The forecasting process provides detailed information, such as traffic volumes, bus patronage, and turning movements, to be used by engineers and planners in their designs. A travel demand forecast might include the number of cars on a future freeway or the number of passengers on a new express bus service. It might also predict the amount of reduction in auto use that would occur in response to a new policy imposing taxes on central-area parking.

The rapid movement of people and goods is essential to economic growth in Duhok City. Funds for building and operating highway are a major fraction of expenditures for local, state, and Federal governments

Objectives *of the Study:*

The main objectives of this research work is to perform spatial and temporal analyses of traffic flow in Duhok City and to provide the following goals and objectives :

- developing and testing alternative transportation systems or projects.
- establishing short-range priorities for implementing transportation facilities.
- analyzing alternative locations for facilities.
- providing the necessary input and feedback for other planning tools.
- Providing design volumes for facility sizing; and
- Providing a new master plan for the traffic operation for the short range planning improvement policy needed for Dohuk City.

Using maps of the transportation system and a good deal of judgment, an abstract network representation of the actual transportation system could be created. Then the network is coded by transferring a map to a form that can be processed by computer programs. The coded network is evaluated in two ways: first, it is necessary to make sure that the coding was done without error; and second, the network itself is evaluated to see if it is adequately representing the transportation system included within the studied system.

The performance of road networks is a key area that transport, traffic engineers and network operators pay great attention to. The purpose of the performance of the network is to determine if the performance is meeting set strategic or operational goals.

All-or-nothing assignment:

In this method the trips from any origin zone to any destination zone are loaded onto a single, minimum cost, path between them. This model is approximate as only one path between every O-D pair is utilized even if there is another path with the same or nearly same travel cost. Also, traffic on links is assigned without consideration of whether or not there is adequate capacity or heavy congestion; travel time is a fixed input and does not vary depending on the congestion on a link. However, this model may be reasonable in sparse and uncongested networks where there are few alternative routes and they have a large difference in travel cost. This model may also be used to identify the desired path: the path which the

drivers would like to travel in the absence of congestion. In fact, this model's most important practical application is that it acts as a building block for other types of assignment techniques. It has a limitation that it ignores the fact that link travel time is a function of link volume and when there is congestion or that multiple paths are used to carry traffic.

Capacity Restraint Assignment:

The capacity restraint procedure explicitly recognizes that as traffic flow increases the speed of traffic decreases. In this procedure several assignments are made based on the "all or nothing" concept. At the end of each assignment, however, the assigned volume on each link is compared with the respective capacity and the travel time is adjusted according to a given formula. A new set of minimum time routes is computed for the next assignment. (Nicholas & Lester). The original capacity restraint procedure developed by the Bureau of Public Roads, which is documented in Traffic Assignment Manual (1964), assumed that the relationship between travel time and the volume peculiar to each link in a highway network can be expressed by the following equation:

$$T = T_0\left[1 + 0.15\left(\frac{V}{C_p}\right)^4\right] \qquad \text{.....(1)}$$

Where:
T = Travel time at which assigned volume can travel on the subject link.
T0 = Base travel time at zero volume = travel time at practical capacity x 0.87.
V = Assigned Volume
Cp = Practical capacity.

The speed-volume relationship most commonly used in computer programs was developed by the U.S. Department of Transportation, and is depicted in Figure (1).

This process may be continued for as much iteration as desired. Usually four iterations are adequate. The analyst has the choice to accept the results of any single iteration. Sometimes the link volumes obtained from all iterations are averaged to produce the final result. This procedure strives to bring the assigned volume, the capacity of a facility, and the related speed into a proper balance.

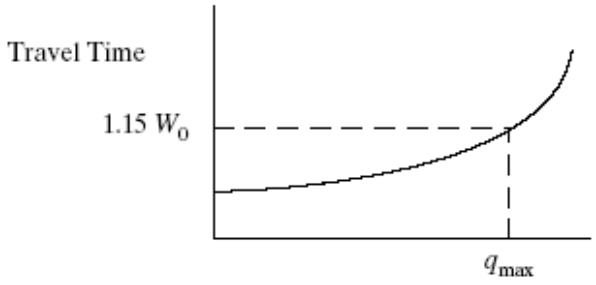

Figure(1):Travel Time Versus Vehicle Volume (Nicholas & Lester)

Study Area:

The study area that was chosen linking Baroshki District, and "Salahuddin" road toward the Dohuk Dam, and the "Gali" intersection of the North, and "Salahuddin" road to the intersection of Ahmadi Khan finished by Mirage Intersection, and the road to the Azadi Mosque, and in the south the study area surrounded with "11 September" Street, then "Shoresh" Bridge linked to the intersection of "Sulaf" overpass associated with Salahuddin

road. This study area is the heart of the Dohuk City and representing the CBD(Central Business District), were most of the commercial , social, residential, retail service, recreational, and educational activities are implemented using the road network service included in this study. This enforced vital and active zone in the city obligated the traffic related Directorates in the city to put more detailed solutions for the low level of service pronounced along the road network along the morning, and evening traffic daily service periods

The study area includes all intersections, and sections of streets linking intersections covering more than 30 cross sections of optical traffic signals. Most of the streets that connect intersections are four p lanes with median barrier of (60-150) cm; which is expected to be removed in the sections that may work as one direction only. CBD area is moving from East of the city to the West, and North to South, serve as a large segments of the city, and the many residents who are in need of movement, and mobility to their shops, stores or their study centers, etc..Duhok City, as shown in figure(2) below. Its geographical coordinates are (37°3′N 43°9′E / 37.05°N 43.15°E)

Figure(2): Google Image Showing the Boundaries of Study Area Road Network

The methodology followed in this research is shown in figure (3). First of all, the study area was identified, then collecting necessary data about study roads and intersections. In order to analyze, and display results about current traffic flow situation this data is converted to spatial data using Arc GIS 9.3 program during determination of different road classes, delay, and level of service (LOS). The collected data was then evaluated for V/C, and LOS as traffic congestion indicators. Forecasting traffic flow situation for both roads, and intersections for future have been processed ,then and finally suggesting plans scenarios with analyzing, and evaluating.

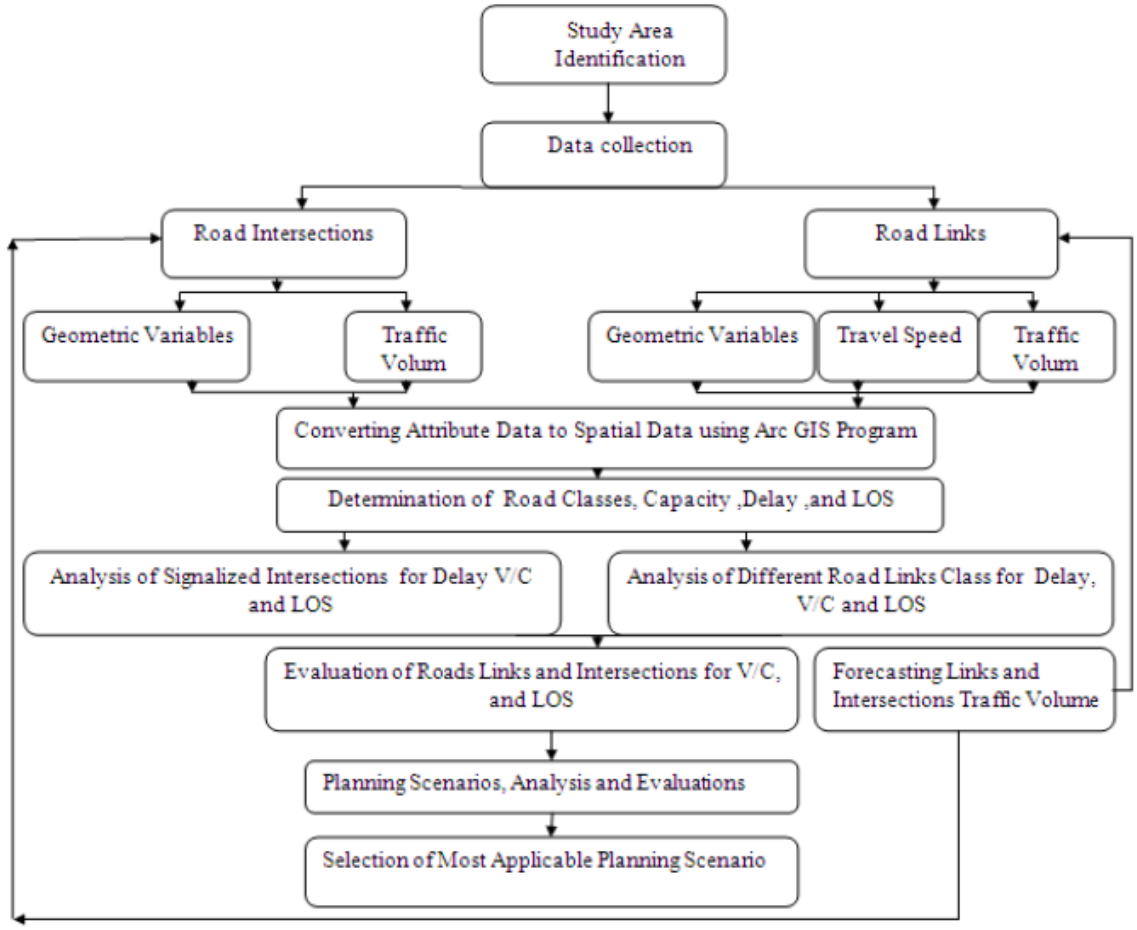

Figure (3): Methodology Flow Diagram Used in the Study

Traffic Data*:*

Data obtained from the Directorate of Traffic Dohuk Governorate shows that there is a rapid increase in the traffic volumes, as shown in the figure (4).

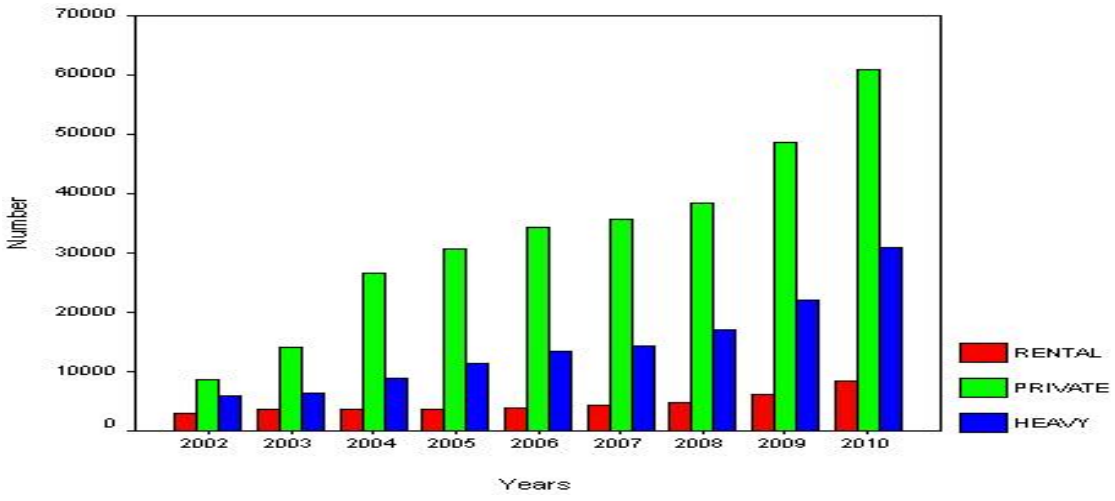

Figure (4): Number of Registered Cars in Duhok Governorate (Wahida, 2011).

The term rental cars that used in figure (4) included taxes, vans and mini buses. The heavy vehicles means those used to carry load (i.e., which carried yellow plate) even those of four wheels such as pick-ups. In considerations of increasing number of registered cars, the total number of cars are about (162,328) cars, (Directorate of Traffic Duhok Governorate, 2012), which are about (99,000) private cars, (48,000) heavy car, and (15,000) rental cars during 2012 year. In the other hand, the degree of motorization (i.e., number of cars per 1000 person) was about (100), calculated based on statistical data from Directorate of Traffic Duhok Governorate, and Directorate of Statistic/Dohuk Governorate (2012) too.

Numbers of cars were increased based on socio-economic characteristics and urban development, and they were increased randomly, with average growth rate of (25) percent from (2002 -2010) as shown in figure (4).

Duhok City Road Network and GIS Program Application:

With its extensive spatial analysis capabilities, and rich visual environment, Geographic Information Systems (GIS) can give transportation planners fast, and effective tools for analyzing travel patterns, and travel network characteristics. GIS is a powerful tool in the analysis, and design of transport routing networks. It's graphical display capabilities allow the understanding of the logic behind the routing network design. In this study, road network have to be investigated for the minimum distance path route considering all the possibilities from each of the external nodes entering the City CBD area to all other nodes exiting the same area. GIS has the capability to do this options again, and again along the different iterations repeated during the execution of this study. GIS was tried in this study to built a new planning scenarios for Dohuk City by conducting the Wardrop Theory related to Traffic Assignment of the traffic flow using city center(CBD), considering different growth periods of this flow along fifteen years of the change in that flow and deciding in the same time what are the points of congestion, and low LOS(Level of Service) , and what are the urgent needs , or planning solutions are actually needed along the strategic periods of planning considered in this study. Strategic planning periods selected in this study are five years period, during each of them complete analysis of the road network related to congestion are conducted, and solutions are decided to develop that strategy level network. Figure(5), is showing two different icons used during the road network development and assignment process to get the final shape of that network related to that level plan.GIS found to be highly realistic, and easy to treat problems like the assignment studies of this study area network. It is very well designed to put solutions to any size city road network nodes, and links and has the ability to do the job spontaneously with high level of accuracy as well. The algorithm flow chart applied in this study is shown in figure(6).

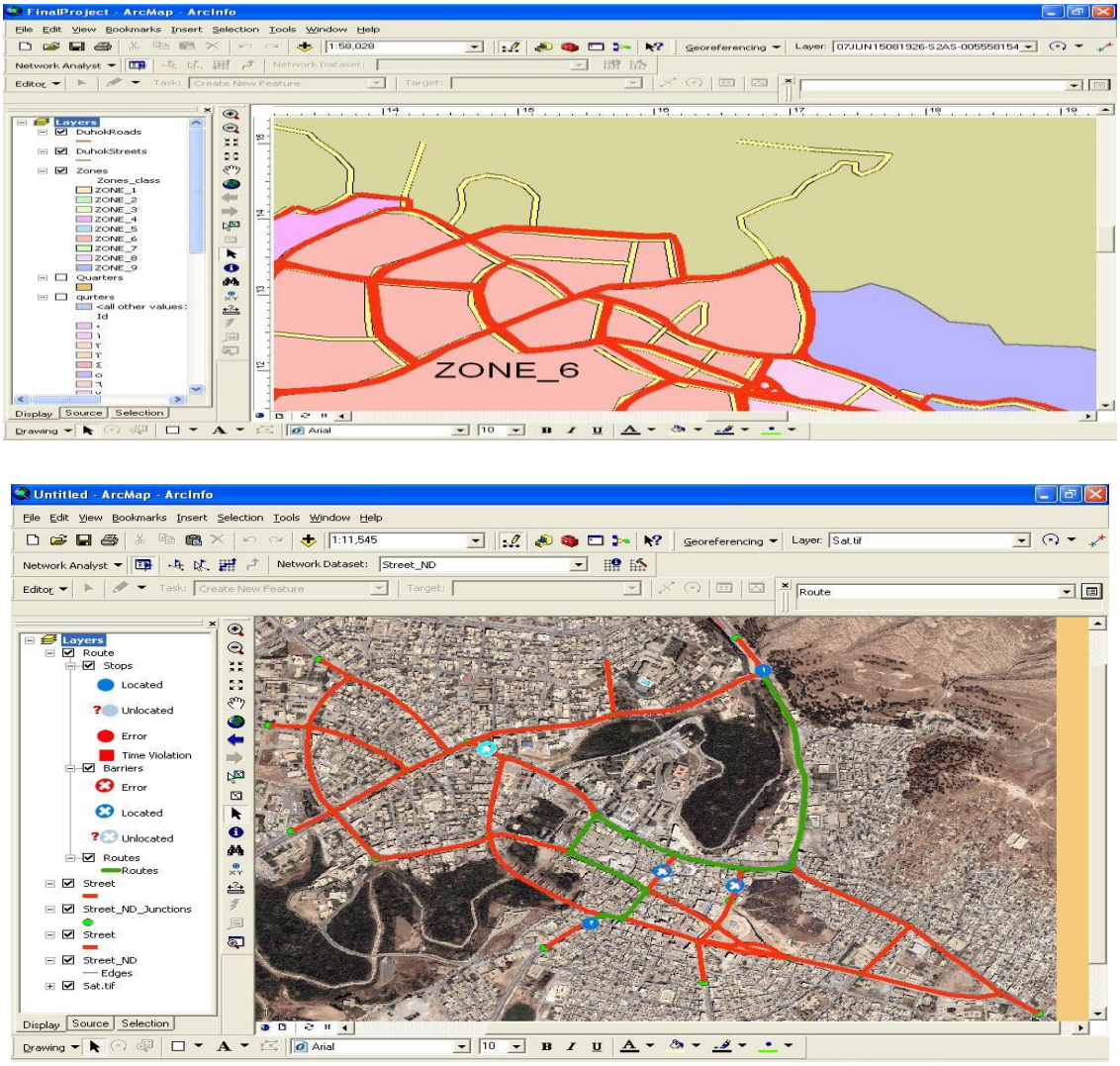

Figure (5): Two Icons Within GIS Main frame Software Selecting A Minimum Path Road Network for a Certain Node Entering Traffic Flow

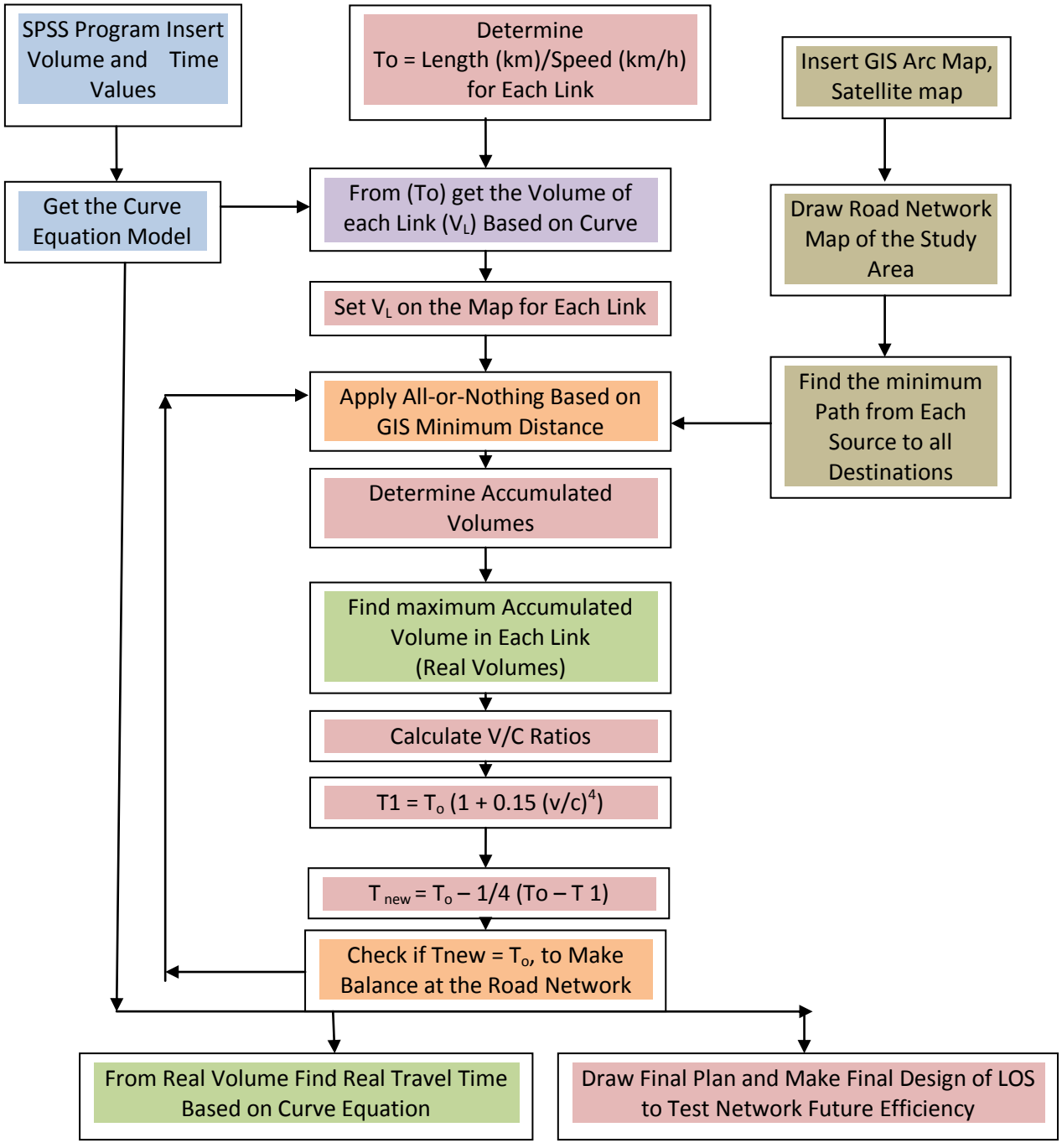

Figure (6):Proposed Traffic Road Network Assignment Analysis Algorithm Flowchart.

Surveys:

In order to perform a detailed analysis of network traffic included in the study area two main types of surveys were proposed:

1. **Engineering Surveys:** Included surveys of the intersections identify all dimensions, and measurements of the intersecting streets, as well as dimensional, geometric shapes of the streets, and the traffic direction in the intersecting approaches.
2. **Volumes, and Travel Time Surveys:** Moving Vehicle Method which included driving within the studied road network with a team of surveyors to find out the amounts of different traffic flow description parameters required for the calculations of other essential Measure of Effectiveness (Moe's). This method was followed by many researchers such as (Giglio,1978) and (Wardrop ,1969), and used in this study with the same equations for different accounts to take advantage of the data collected from the traffic surveys with at least six rounds to find out the average values of the parameters needed in the equations to find out the required directional volumes, travel times, densities, and speeds:

Coding System*:*

Road network included within the study area is coded two times, the first coding was for the nodes(i.e., intersections), as shown in figure(7), where about 30 intersections were coded by numbers. This coding is necessary in the analysis of the road network geo-referenced by GIS Software used later on to find the shortest path of moving traffic volumes from origins(i.e., study area entrances), to destinations(i.e., study area exists). Road network links were also coded for the same purpose mentioned above for the road links connecting each pair of nodes together in one ,or two directions of traffic flow to be identified later on by numbers in the GIS Package during the network analysis process. In this process , each link length was measured from geospatial dimensioning system included within the GIS Software after the identification of the network form Google Earth Program Arc Mapping System.

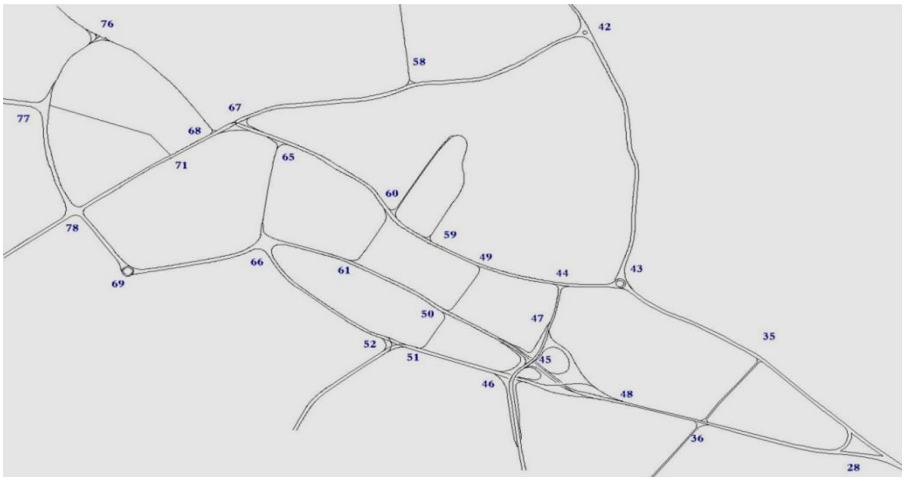

Figure(7):Node Coding for the Study Area Road Network Using Numbers

All or Nothing Assignment:

In order to apply this style of process analysis, traffic volumes should be directed inside the study area to all points or not to carry out any kind of this movement of vehicles from the source to the destination. This approach requires numbering of the nodes of the study network. Dohuk City spider road network shown in figures (7), were used in the analysis of this type of assignment study to evaluate the existing condition traffic flow service level (LOS). In order to start analysis of the road network, a statistical model relating travel time measured from the existing flow condition, and the traffic volume considered from the site surveys given was derived using SSPS Package trying different relationships considered in the package. It is a type of third degree polynomial model considered with (R) value of 0.711 and the relationship is shown in figure (8).

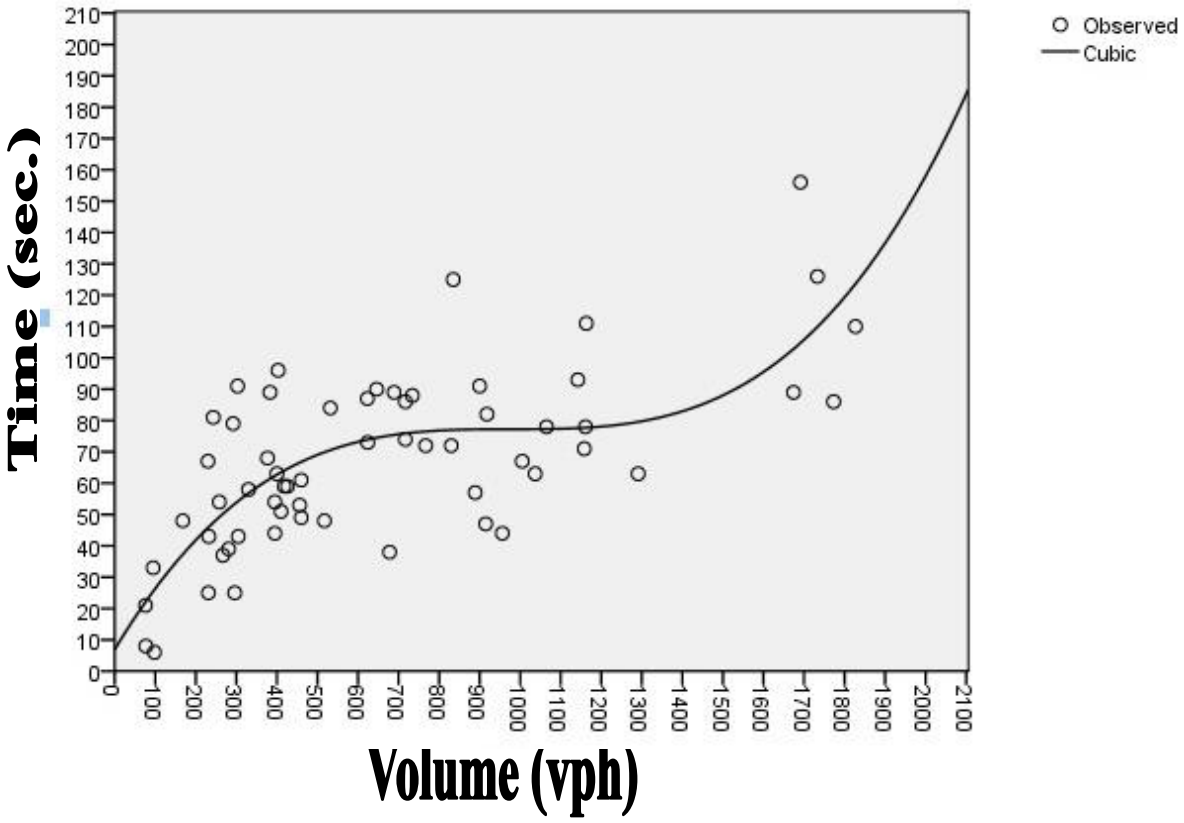

Figure (8): Time-Volume Dependent Relationship on the Existing (2012) Traffic Service Condition on Dohuk City Road Network.

$$Y = 6.903182839591902 + 0.2159153193913597\ x - 0.0002210483488709456\ x^2 + 7.544471749673656e\text{-}008\ x^3$$

Figure(9), is showing the existing Dohuk CBD network congestion condition, meanwhile figure(10) is showing the new loaded for the same network. Traffic volumes increased according to the following growth factor computation formula with growth rate assumed in this study as 6%:

Growth Factor ={$(1+r)^n$-1)/r} …….(2)

where
r = growth rate of traffic volume assumed in this study as 6% from Traffic Directorate Statistics during a long period of time,
n= number of years included within a certain strategic period of five years.

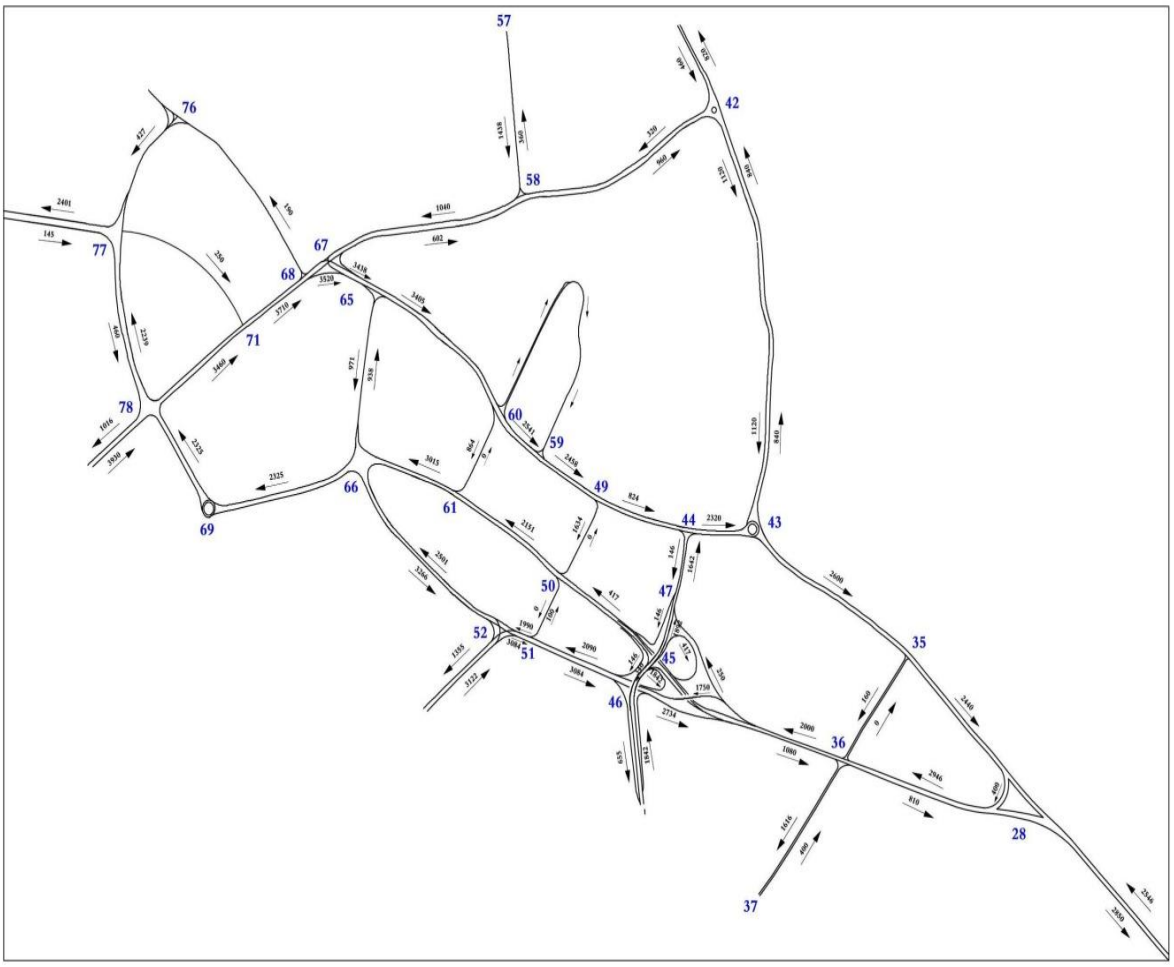

Figure(9): Study Area Map Showing Traffic Volumes (vph) on the Travel Directions for Each Link in 2012 Existing Dohuk City (CBD) Road Network.

Table (1): Travel Directional Analysis for 2012 Operation Condition from Each Node to Another Using Capacity-Restrained Method Shown on the Algorithm.

Capacity-Restrained Assignment Analysis for the Predicted 2012 Dohuk City Road Network															
From	To	L	V. link	Initial Link Time	A. Vol.	V/C	C	P50	Speed	Actual Travel Time	Delay Time	Ideal Time	LOS	Density	Cost
O.	D.	(m)	vph	Sec	vph	Ratio	PCU	km/hr	km/hr	Sec	Sec.	Sec.	Ratio	Veh./ Km	Dollar/hr
28	35	350	87	25	560	0.33	1680	50	17.75	71	46	25	C	32	$ 213.73
35	43	385	98	27	473	0.28	1680	50	20.69	67	39	28	B	23	$ 154.83
43	42	725	274	52	375	0.22	1680	50	43.50	60	8	52	B	9	$ 24.38
42	43	725	274	52	461	0.27	1680	50	39.55	66	14	52	B	12	$ 53.02
42	58	450	128	32	128	0.08	1680	50	52.26	31	0	32	A	2	0
58	42	450	128	32	551	0.33	1680	50	22.82	71	39	32	C	24	$ 177.24
58	67	410	110	29	251	0.15	1680	50	30.75	48	18	30	A	8	$ 38.65
67	58	410	110	29	238	0.14	1680	50	32.09	46	16	30	A	7	$ 32.69
68	71	125	6	9	56	0.02	2520	50	25.00	18	9	9	A	2	$ 4.20
71	78	250	50	18	50	0.02	2520	50	52.94	17	0	18	A	1	0$
77	71	300	65	21	0	0.00	1680	50	0.00	0	0	22	A	0	0 $
68	76	390	104	28	139	0.08	1680	50	43.88	32	4	28	A	3	$ 4.54
76	77	215	35	15	520	0.31	1680	50	11.06	70	55	15	C	47	$ 236.25
77	78	320	76	23	485	0.29	1680	50	16.94	68	45	23	B	29	$ 181.71
78	77	320	76	23	76	0.05	1680	50	52.36	22	0	23	A	1	0$
78	69	205	30	14	409	0.16	2520	50	11.71	63	48	15	A	35	$ 164.42
69	66	310	71	22	379	0.15	2520	50	18.30	61	39	22	A	21	$ 122.16
66	61	209	35	15	308	0.12	2520	50	13.93	54	39	15	A	22	$ 99.98
61	50	250	50	18	237	0.09	2520	50	19.57	46	28	18	A	12	$ 55.30
50	45	225	40	16	223	0.09	2520	50	18.41	44	28	16	A	12	$ 51.66
36	48	230	40	16	122	0.07	1680	50	27.60	30	13	17	A	4	$ 13.66
52	66	435	122	31	418	0.25	1680	50	24.47	64	33	31	B	17	$ 113.84
46	51	220	35	15	35	0.21	1680	50	13.42	59	43	16	B	27	$

					8										128.76
48	46	240	40	16	45	0.03	1680	50	66.46	13	0	17	A	1	0 $
28	36	380	98	27	220	0.09	2520	50	31.09	44	17	27	A	7	$ 30.51
43	44	111	3	7	267	0.11	2520	50	7.99	50	42	8	A	33	$ 93.47
44	49	190	25	13	264	0.10	2520	50	13.96	49	35	14	A	19	$ 77.70
49	59	150	10	10	239	0.09	2520	50	11.74	46	35	11	A	20	$ 70.11
59	60	110	3	7	229	0.09	2520	50	8.80	45	37	8	A	26	$ 70.76
60	65	340	82	24	226	0.09	2520	50	27.20	45	21	24	A	8	$ 38.65
65	67	90	3	6	144	0.06	2520	50	9.82	33	27	6	A	15	$ 31.82
66	52	435	122	31	159	0.09	1680	50	44.74	35	4	31	A	4	$ 4.88
44	47	100	3	7	187	0.11	1680	50	9.00	40	33	7	A	21	$ 51.11
66	65	265	55	19	296	0.35	840	50	18.00	53	34	19	C	16	$ 83.67
65	66	265	55	19	0	0.00	840	50	0.00	0	0	19	A	0	0 $
60	61	130	6	9	61	0.07	840	50	24.63	19	10	9	A	2	$ 4.90
50	49	130	6	9	0	0.00	840	50	0.00	0	0	9	A	0	0$
51	50	105	3	7	0	0.00	840	50	0.00	0	0	8	A	0	0 $
50	51	105	3	7	0	0.00	840	50	0.00	0	0	8	A	0	0$
36	35	205	30	14	530	0.63	840	50	10.54	70	55	15	D	50	$ 243.98
35	36	205	30	14	0	0.00	840	50	0.00	0	0	15	A	0	0 $
36	28	380	98	27	98	0.06	1680	50	52.62	26	0	27	A	2	0 $
48	36	230	40	16	442	0.53	840	50	12.74	65	48	17	C	35	$ 178.42
67	68	47	2	3	141	0.06	2520	50	5.13	33	30	3	A	28	$ 34.80
51	52	40	2	2	323	0.19	1680	50	2.57	56	53	3	B	126	$ 142.98
46	48	230	47	17	482	0.57	840	50	12.18	68	51	17	D	40	$ 206.62
45	48	235	40	16	183	0.22	840	50	21.69	39	22	17	B	8	$ 33.67
51	46	226	35	15	213	0.13	1680	50	18.92	43	27	16	A	11	$ 47.44
														Total	**$ 3,316.50**

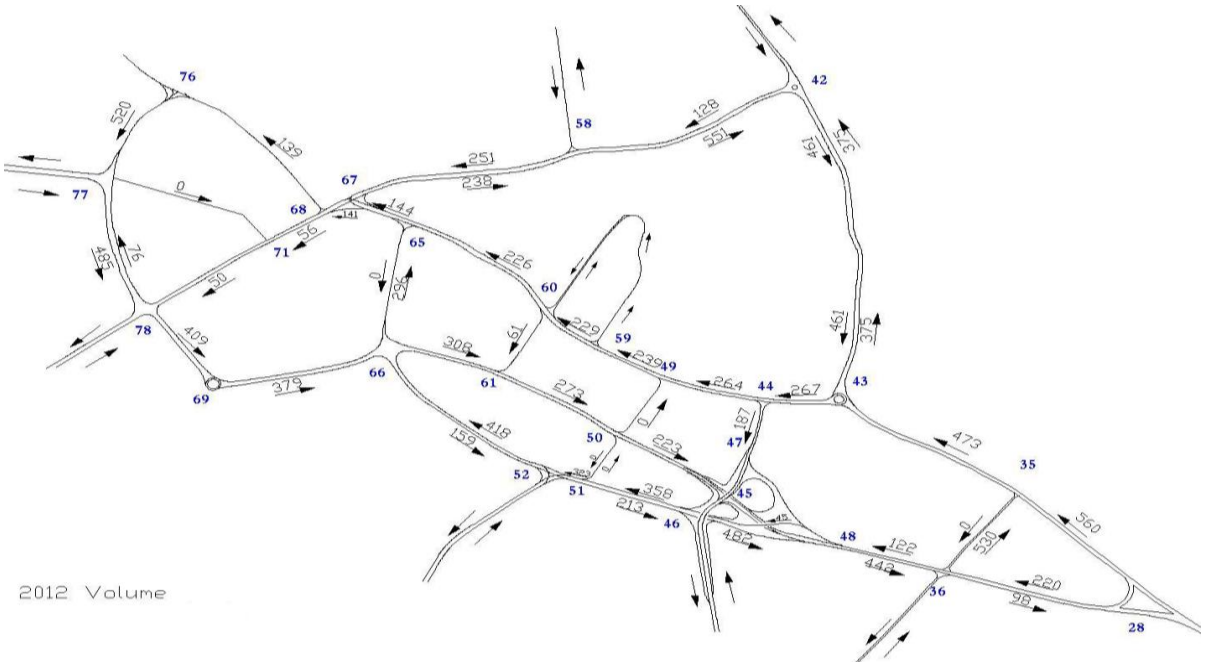

Figure (10): Study Area Map Showing Traffic Volumes (vph) on the Travel Directions for Each Link in 2012 New Loaded Dohuk City (CBD) Road Network.

Comparison Using V/C Ratio:

In 2012 existing network in many links it could be noticed that the LOS is very low for example link (36-28) in Table (3 – 1) where V/C is more than one which means that, LOS is F, but in 2012 new network the LOS in most of the links is acceptable, and there is no V/C more than one nor LOS equal to F as shown in figure(11).

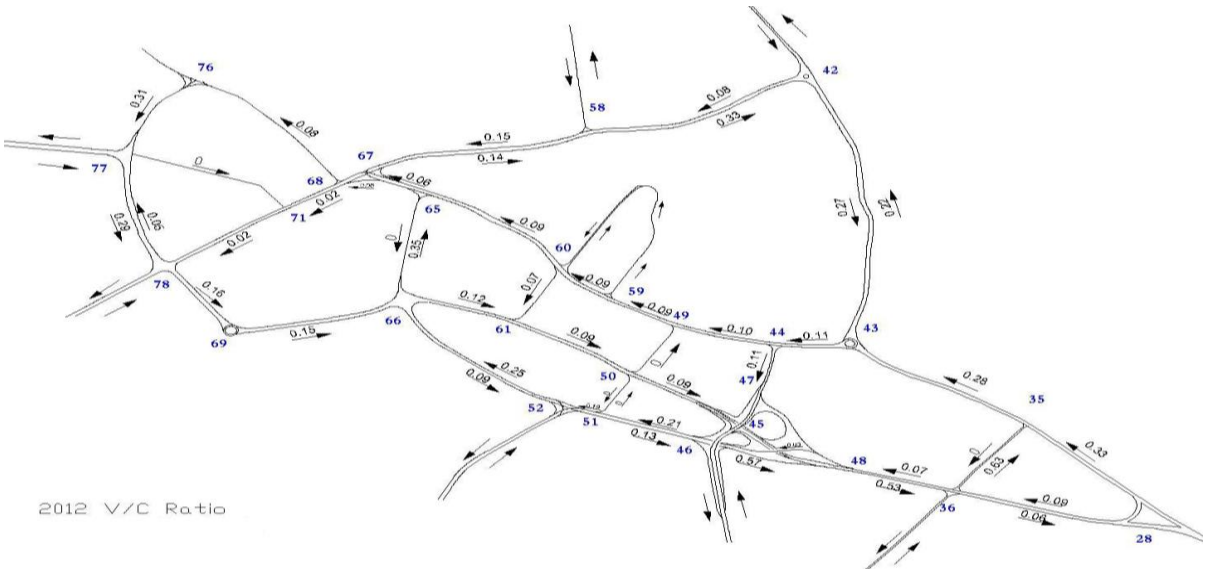

Figure(11): Study Area Map showing Volume/Capacity Ratio on the Travel Direction for Each Links in 2012 New Loaded Dohuk City (CBD) Road Network .

Comparison Using Cost:

In order to evaluate the existing road network, and the other future improvement on the road network from economic point of view, loss due to delay time difference is computed in this study in terms of money as (Time is Money), 2012 existing network the total cost determined in all links was equal to (13,750.37 $) for one hour of traffic operation during a certain work-day. Each one hour of delay time was evaluated as (Link Volume x Link Delay x 30 $/ cost of one hour of delay time) for all links, but the total cost in 2012 new network was (3,316.50 $). This means that, more than 10,000$/hr/hr, is considered as a benefit just from the delay time economic reserve due to the little improvement in the road network infrastructure development during 2012 fiscal year.

Traffic volume different parameters and Moe's where correlated using different statistical models tried by SPSS package such as the relationships shown in figures(12), and(13). Time-volume relationship is highly fitted by MMF model with correlation coefficient r of 0.999 which is more than that obtained in figure(8), as traffic flow is going to fit the road network after the first iteration of assignment.

Volume-density relationship best fitted by SSPS package is a type of Quadratic model with r value of 0.845 with standard error of estimate of 93.7 which is relatively high compared with the Time-Volume model described above as shown in figure(13) for 2012 flow condition.

Speed-Density relationship is tried by the same package and the Logarithmic model was the best fit to the data obtained during 2012 period with r value of 0.864, and standard error of estimate as 7.92, which is relatively small value describing the flow condition.

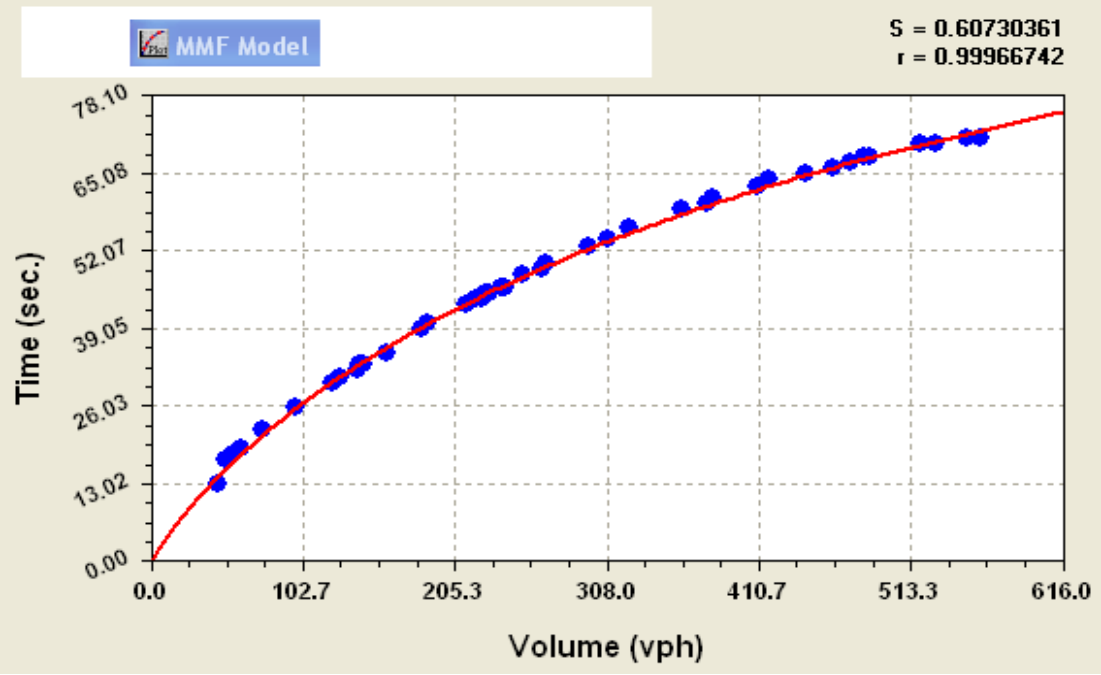

Figure (12): Volume – Time Relationship for 2012 New Plan Predicted for Dohuk City (CBD) Road Network

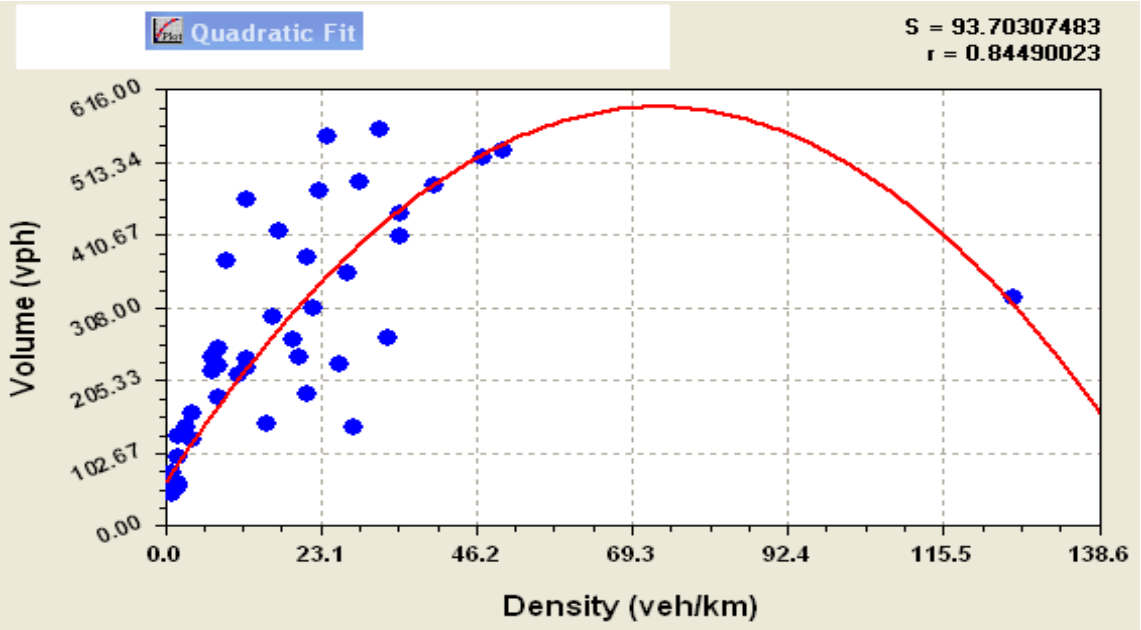

Figure(13): Density-Volume Relationship in 2012 New Plan Predicted for Dohuk City(CBD) Road Network

Comparison between 2017 New Network and 2022 New Networks:

Table (2), is representing the 2022 fiscal year predicted Moe's describing the traffic flow parameters along the 2022 year. Traffic volumes were increased during the next five years to loading again the same city road network, to test again the performance of this network, and to know what are the types of improvements needed to change the traffic performance.

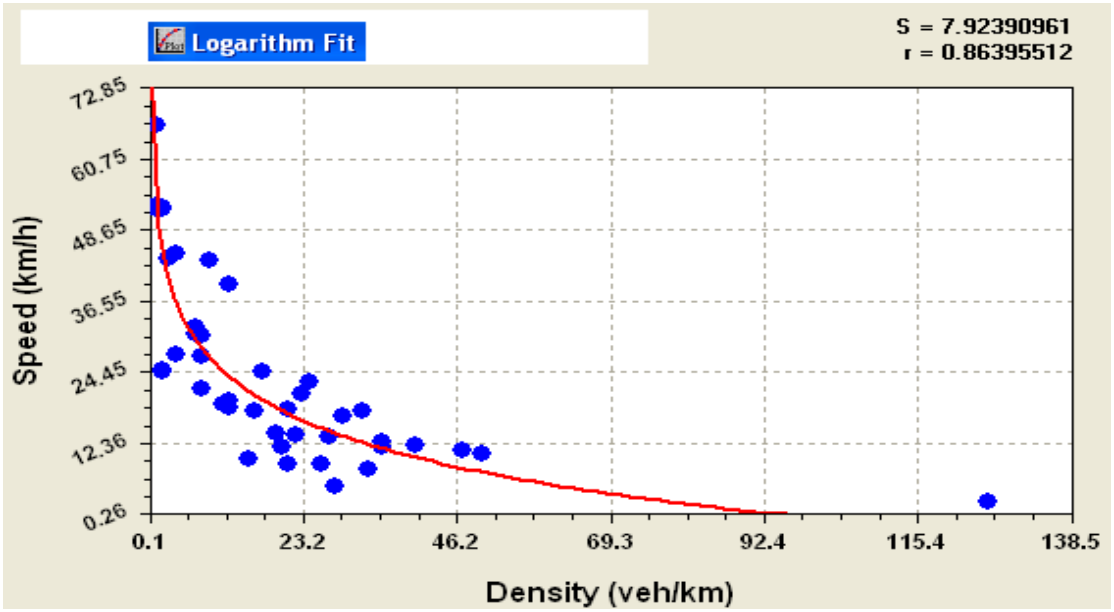

Figure (14): Density – Speed Relationship in 2012 New Plan Predicted for Dohuk City (CBD) Road Network

These parameters were useful to predict the cost of any improvement needed for the next five years (i.e., from 2022 up to 2027). Table (2), is showing the loaded 2022 traffic volume computed from the 2012 existing flows. Comparison between both 2017, and 2022 volumes is showing how much are the link load is growing, for example, link (60-65) volume became 405 vph, but it was 306 vph, ten years before capacity-restrained analysis. It means that, it will become about 33 percent more, and this will create a lot of pressure, or congestion on the same link without any widening. Fourteen links out of 49 have LOS of D to F, which indicates that, some links will need more extensive improvement during this strategic period of planning, as shown in table (2).

Table (2): Travel Direction for 2022 Improvement Map of Operation Condition form Each Node to Another Using Capacity-Restrained Method.

Capacity-Restrained Assignment Analysis for the Predicted 2022 Dohuk City Improvement Plan													
From	To	Length	Accumulate Volume	V/C	Capacity	P50	Speed	Travel Time	Delay Time	Ideal Travel Time	LOS	Density	Cost
O	D	(m)	vph	Ratio	PCU	km/hr	km/hr	Sec	Sec.	Sec.	Ratio	Veh/km	Dollar/hr
28	35	350	1003	0.60	1680	50	16.36	77	52	25	E	61	$ 432.91
35	43	385	847	0.50	1680	50	18.00	77	49	28	D	47	$ 347.86
43	42	725	672	0.40	1680	50	34.80	75	23	52	D	19	$ 127.60
42	43	725	826	0.49	1680	50	34.34	76	24	52	D	24	$ 163.74
42	58	450	229	0.14	1680	50	36.00	45	0	32	A	6	0 $
58	42	450	987	0.59	1680	50	21.04	77	45	32	D	47	$ 366.74
58	67	410	450	0.27	1680	50	22.36	66	36	30	B	20	$ 136.65
67	58	410	426	0.25	1680	50	23.06	64	34	30	B	18	$ 122.47
68	71	125	100	0.04	2520	50	17.31	26	17	9	A	6	$ 14.21
71	78	250	90	0.04	2520	50	37.50	24	0	18	A	2	0 $
77	71	300	0	0.00	1680	50	0.00	0	0	22	A	0	0 $
68	76	390	249	0.15	1680	50	29.25	48	20	28	A	9	$ 41.32
76	77	215	931	0.55	1680	50	10.05	77	62	15	D	93	$ 477.42
77	78	320	869	0.52	1680	50	14.96	77	54	23	D	58	$ 390.56
78	77	320	136	0.08	1680	50	36.00	32	0	23	A	4	0 $
78	69	205	732	0.29	2520	50	9.71	76	61	15	C	75	$ 373.80
69	66	310	679	0.27	2520	50	14.88	75	53	22	C	46	$ 297.96
66	61	209	552	0.22	2520	50	10.60	71	56	15	D	52	$ 257.18
61	50	250	424	0.17	2520	50	14.06	64	46	18	B	30	$ 162.70
50	45	225	399	0.16	2520	50	13.06	62	46	16	B	31	$ 152.42
36	48	230	218	0.13	1680	50	18.82	44	27	17	A	12	$ 49.96
52	66	435	749	0.45	1680	50	20.61	76	45	31	D	36	$ 278.72
46	51	220	641	0.38	1680	50	10.70	74	58	16	C	60	$ 310.73
48	46	240	81	0.05	1680	50	39.27	22	0	17	A	2	0 $
28	36	380	394	0.16	2520	50	22.06	62	35	27	A	18	$ 113.73
43	44	111	478	0.19	2520	50	5.96	67	59	8	B	80	$ 235.13
44	49	190	473	0.19	2520	50	10.21	67	53	14	B	46	$ 210.07

49	59	150	428	0.17	2520	50	8.44	64	53	11	B	51	$ 189.75
59	60	110	410	0.16	2520	50	6.29	63	55	8	A	65	$ 188.24
60	65	340	405	0.16	2520	50	19.43	63	39	24	A	21	$ 129.92
65	67	90	258	0.10	2520	50	6.61	49	43	6	A	39	$ 91.38
66	52	435	285	0.17	1680	50	30.12	52	21	31	B	9	$ 49.07
44	47	100	335	0.20	1680	50	6.32	57	50	7	B	53	$ 138.98
66	65	265	530	0.63	840	50	13.63	70	51	19	E	39	$ 224.94
65	66	265	0	0.00	840	50	0.00	0	0	19	A	0	$
60	61	130	109	0.13	840	50	17.33	27	18	9	A	6	$ 16.06
50	49	130	0	0.00	840	50	0.00	0	0	9	A	0	0 $
51	50	105	0	0.00	840	50	0.00	0	0	8	A	0	0 $
50	51	105	0	0.00	840	50	0.00	0	0	8	A	0	$
36	35	205	949	0.56	1680	50	9.58	77	62	15	D	99	$ 492.29
35	36	205	0	0.00	840	50	0.00	0	0	15	A	0	$
36	28	380	176	0.10	1680	50	36.00	38	0	27	A	5	$
48	36	230	792	0.47	1680	50	10.89	76	59	17	D	73	$ 392.08
67	68	47	253	0.10	2520	50	3.53	48	45	3	A	72	$ 93.88
51	52	40	578	0.34	1680	50	2.00	72	69	3	C	289	$ 333.18
46	48	230	863	0.51	1680	50	10.75	77	60	17	D	80	$ 434.76
45	48	235	328	0.39	840	50	15.11	56	39	17	D	22	$ 106.73
51	46	226	381	0.23	1680	50	13.34	61	45	16	B	29	$ 142.18
												Total	$ 8,087.32

Figure (15), is showing the time-volume variation curve for the predicted 2022 new plan year. The function was a 3rd degree polynomial curve with high correlation coefficient r of 0.999, ,, and low standard mean of error S of 0.244 , as found from the best model prediction package. This result is similar to the function used in the initial iteration at 2012 year when the algorithm started to analyze the road network with the aid of GIS to start computing the minimum path trees, or trimming of the trees from the beginning of the analysis.

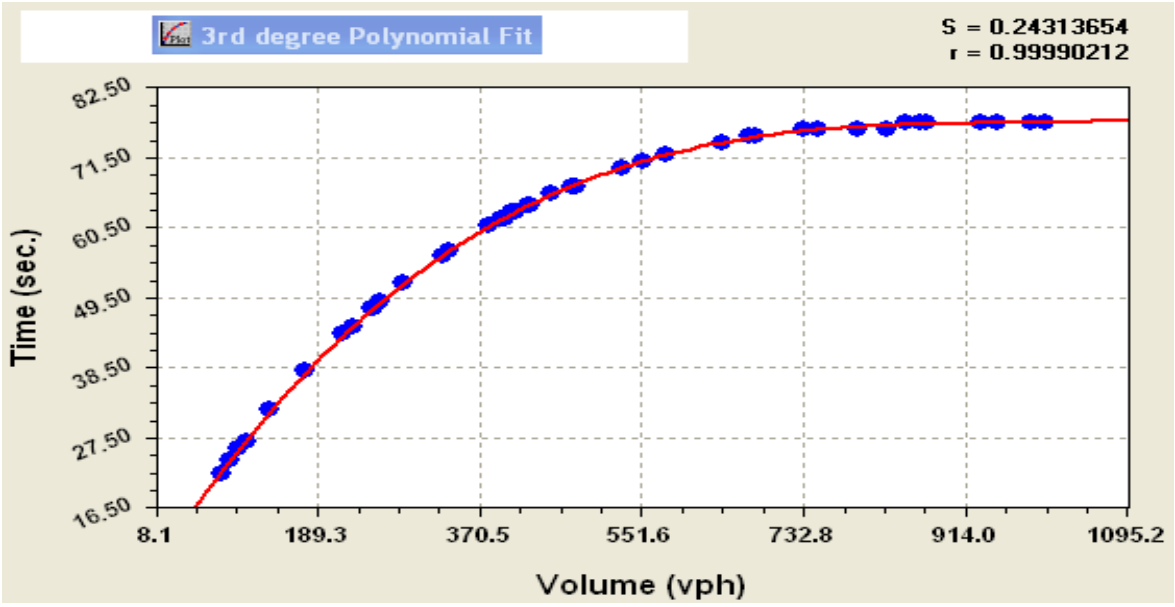

Figure (15): Volume – Time Relationship in 2022 New Loaded Dohuk City (CBD) Road Network.

Comparison of 2027 Improved Road Networks:

The fourth stage in this study was how to test the traffic operation, and performance for a second strategic planning period about how the new predicted (2022-2027) road network will work. A detailed 2027 road network analysis was implemented in order to test the 2027 loaded network using the same assignment process with the same algorithm developed in this study with the assistance of the GIS technique in order to select the shortest distance path along the new 2027 network plan. Table (3), is showing the full analysis of the predicted traffic flow matrix for the 2027 new loading plan condition with the main Moe's found important to describe , and test the new plan. Table(3), is showing the full analysis, and the predicted traffic flow matrix for the 2027 improved loading plan from the 2022 future plan after the execution of the Capacity-Restrained Method on the 2027 plan after traffic growth from 2022 up to 2027 fiscal year to improve some of the congested links on this final 2027 plan. A new matrix shown in Table (3), is showing this process with a new set of Moe's listed down to describe the new traffic operation condition, and a full analysis discussion of the new Moe's analysis is shown below:

Table (3): Travel Direction for 2027 Operation Condition form Each Node to Another Using Capacity Restrained Method Using New Loaded Dohuk City (CBD) Road Network.

Capacity-Restrained Assignment Analysis for the Predicted 2027 Dohuk City Improvement Plan													
From	To	Length	Accumulate Volume	V/C	Capacity	P50	Speed	Travel Time	Delay Time	Ideal Travel Time	LOS	Density	Cost
O	D	(m)	vph	Ratio	PCU	km/hr	km/hr	Sec	Sec.	Sec.	Ratio	Veh/km	Dollar/hr
28	35	350	1342	0.80	1680	50	15.75	80	55	25	E	85	$ 612.88
35	43	385	1134	0.67	1680	50	18.00	77	49	28	D	63	$ 465.52
43	42	725	899	0.53	1680	50	33.90	77	25	52	D	27	$ 185.73
42	43	725	1105	0.66	1680	50	33.90	77	25	52	D	33	$ 228.33
42	58	450	307	0.18	1680	50	30.00	54	0	32	A	10	$
58	42	450	1321	0.79	1680	50	20.25	80	48	32	E	65	$ 523.80
58	67	410	602	0.36	1680	50	20.22	73	43	30	C	30	$ 217.96
67	58	410	570	0.34	1680	50	20.50	72	42	30	C	28	$ 201.91
68	71	125	134	0.05	2520	50	14.06	32	23	9	A	10	$ 25.72
71	78	250	120	0.05	2520	50	31.03	29	0	18	A	4	0 $
77	71	300	0	0.00	1680	50	0.00	0	0	22	A	0	0 $
68	76	390	333	0.20	1680	50	24.63	57	29	28	B	14	$ 80.28
76	77	215	1246	0.74	1680	50	9.92	78	63	15	D	126	$ 649.28
77	78	320	1162	0.69	1680	50	14.96	77	54	23	D	78	$ 522.66
78	77	320	182	0.11	1680	50	29.54	39	0	23	A	6	0 $
78	69	205	980	0.39	2520	50	9.58	77	62	15	C	102	$ 508.39
69	66	310	908	0.36	2520	50	14.49	77	55	22	C	63	$ 413.88
66	61	209	738	0.29	2520	50	9.90	76	61	15	B	75	$ 374.93
61	50	250	568	0.23	2520	50	12.50	72	54	18	B	45	$ 255.59
50	45	225	534	0.21	2520	50	11.57	70	54	16	B	46	$ 239.60
36	48	230	292	0.17	1680	50	15.92	52	35	17	B	18	$ 86.35
52	66	435	1002	0.60	1680	50	20.34	77	46	31	E	49	$ 381.34
46	51	220	858	0.51	1680	50	10.29	77	61	16	D	83	$ 437.28
48	46	240	108	0.06	1680	50	32.00	27	0	17	A	3	0 $
28	36	380	527	0.21	2520	50	19.54	70	43	27	B	27	$ 187.35

43	44	111	640	0.25	2520	50	5.40	74	66	8	B	118	$ 351.98
44	49	190	633	0.25	2520	50	9.24	74	60	14	B	68	$ 318.03
49	59	150	573	0.23	2520	50	7.50	72	61	11	B	76	$ 292.12
59	60	110	549	0.22	2520	50	5.58	71	63	8	B	98	$ 288.49
60	65	340	542	0.21	2520	50	17.24	71	47	24	B	31	$ 209.97
65	67	90	345	0.14	2520	50	5.59	58	52	6	A	62	$ 148.16
66	52	435	381	0.23	1680	50	25.67	61	30	31	B	15	$ 94.25
44	47	100	448	0.27	1680	50	5.45	66	59	7	B	82	$ 219.60
66	65	265	709	0.84	840	50	12.72	75	56	19	E	56	$ 330.57
65	66	265	0	0.00	840	50	0.00	0	0	19	A	0	0 $
60	61	130	146	0.17	840	50	14.18	33	24	9	A	10	$ 28.80
50	49	130	0	0.00	840	50	0.00	0	0	9	A	0	0 $
51	50	105	0	0.00	840	50	0.00	0	0	8	A	0	0 $
50	51	105	0	0.00	840	50	0.00	0	0	8	A	0	0 $
36	35	205	1270	0.76	1680	50	9.34	79	64	15	D	136	$ 679.97
35	36	205	0	0.00	840	50	0.00	0	0	15	A	0	0 $
36	28	380	235	0.14	1680	50	29.74	46	0	27	A	8	0 $
48	36	230	1059	0.63	1680	50	10.75	77	60	17	D	99	$ 533.52
67	68	47	338	0.13	2520	50	2.97	57	54	3	A	114	$ 150.98
51	52	40	774	0.46	1680	50	1.89	76	73	3	D	409	$ 471.68
46	48	230	1155	0.69	1680	50	10.75	77	60	17	D	107	$ 581.81
45	48	235	439	0.52	840	50	13.02	65	48	17	D	34	$ 175.72
51	46	226	510	0.30	1680	50	11.79	69	53	16	C	43	$ 224.30
												Total	$11,698.72

Figure(16), is showing the traffic volume loaded road network after growing the volume to 2017 future year after complete network assignment using the newly designed algorithm. This result is supported by the GIS Software to show the best orientation of the road network links with acceptable V/C ratio and LOS expected and to best future plan the studied road network.

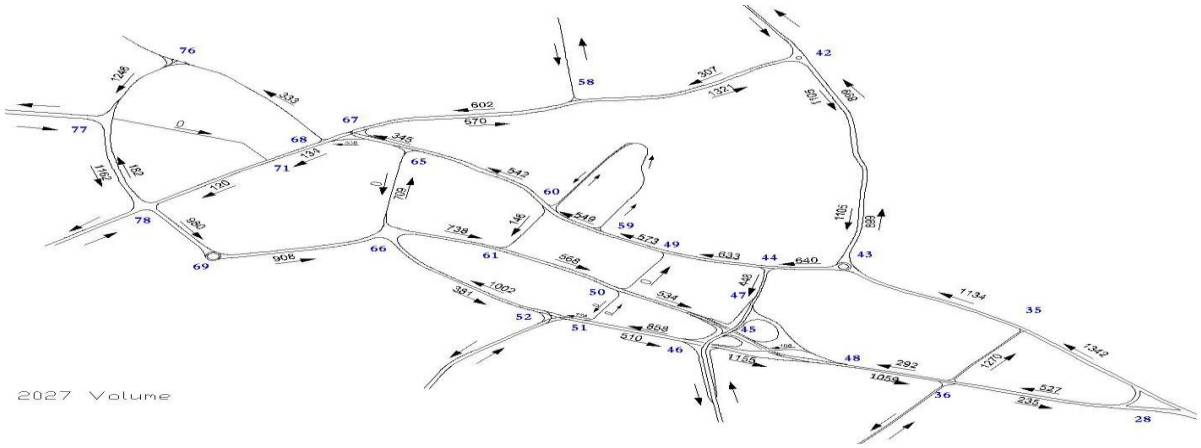

Figure(16): Study Area Map showing the Traffic Volumes (vph.) on the Travel Direction for Each Links in 2027 New Loaded Dohuk City (CBD) Road Network

Conclusions*:*

According to the methodology of the research work followed in this study, and the time limitations to perform the main stages included in it, the following conclusions could be drawn out:

1. V/C Ratio**:** In 2012 existing network in many tracks the level of service is very low for example link (36-28) where the v/c is more than one which means LOS is F, but in 2012 new network the level of service in most tracks is good, and there is no v/c more than one nor LOS equal to F..
2. Average Travel Speed: In 2012 existing network the speed is relatively slow, and the average speed in all links is about 17 km/h, but in existing 2012 new network the average speed is about 30 km/hr, and in some links the speed is reaching (50-60km/h).

3- Travel Cost: In 2012 existing network the total cost in all links is 13,750.37 dollar for one hour in a day. Each one hour of delay time is evaluated as (Link Volume x Link Delay x 30 $/ cost of one hour of delay time) for all links, but the total cost in 2012 new network is 3,316.50 dollar.. In 2022 new network the total cost is (8,087.32 dollar). In 2027 new network the total cost became (11,698.72 dollar) only,

4- GIS (Geographic Information System) proved to be very effective tool to put a direct, and perfect solution to the road networks inside, or outside cities from the traffic congestion solution point of view. It is found to reduce time, and effort during the analysis, especially at the capacity-restrained assignment process. It can be used to address the objectives of finding the optimum route between any given origin, and destination,

5- New plan of 2012 traffic operation solution could be implemented after changing traffic flow directions within the CBD road network,

6- Future plan for 2017 strategic year is the execution of the Capacity-Restrained Method on the plan to improve some of the congested links on this final plan.

7- Future plan for 2022 strategic year using Capacity-Restrained Method on the same plan need more extensive improvement during this strategic period of planning.

8- Improved loading of 2027 plan derived from the 2022 plan after the execution of the Capacity-Restrained Method is concluded to improve some of the congested links on this final 2027 plan .

9- The algorithm proposed, and developed in this study for the application to solve the road network assignment problems has a programming given structure. Some of the programming systems, and languages included within this algorithm are Java Programming contributed with other complicated statistical and mathematical functions represented by the well known GIS to reach the final decision, and

10- Minimum path assignment solutions resulted in this study are completely decided to satisfy the road user desire to reach his/or her destination comfortably with high degree of convenience..

Recommendations:

1. The algorithm could be designed to solve a traffic assignment problems depending upon minimum travel time, or maximum travel speed,
2. This methodology proposed in this study could be applied on any network with any size of number of lanes, or nodes,

3. This study should be taken under option for the future urban transportation planning process for Duhok City to develop the future road network after any desired strategic period of time,
4. This algorithm could be used to test the master plan prepared for the infrastructure of any proposed future city road network, and
5. The same methodology could be applied on Dohuk City road network infrastructure to test the traffic safety, noise, and air pollution problems needed for the sustainability of the city driving environment.

References:

-Giglio, D., & Minciardi, D. (2008)." *Optimization of Traffic Flows in Congested Metropolitan Areas*". Proceedings of the 11th International IEEE Conference on Intelligent Transportation Systems Beijing, China.

-Google earth, et al. (2010). Duhok, Iraq.

-Haixiang, Yang, Qingquan & Yonghui, (2010). *"A Spatial Analysis Approach for Describing Spatial Pattern of Urban Traffic State"*. Annual Conference on Intelligent Transportation Systems Madeira Island, Portugal, *13th International IEEE*

-Transportation Research Board "*Highway Capacity Manual (2000)* ". Washington, DC.

-LIU Li-xin, (2008). "*Optimization of Traffic Flow in a Road Network*". Automobile and Traffic college, Qingdao Technological University, Qingdao, Shandong, 266520, P. R. China.

-Maerivoet, S. and B. De Moor (2005). "*Traffic Flow Theory*." Physics/0507126.

-Moshe E. Ben-Akiva, Song Gao, Zheng Wei, and Yang Wen. (2010). "*A Dynamic Traffic Assignment Model for Highly Congested Urban Networks*". Journal homepage: www.elsevier.com/locate/trc.

-Nicholas J. Garber & Lester A. Hoel. (2009)."*Traffic and Highway Engineering*". *Forth Edition University of Virginia.*

-Wahida Mustafa Omer. (2011). "*Spatial Analysis of Traffic Congestion in Duhok City Urban Roads Network Using GIS Technology*". *University of Duhok, School of Planning.*

-*Weisbord, G., D. Vary et al. (2003). "Measuring Economic Costs of Urban Traffic Congestion to Business."* Journal of the Transportation Research Board, 1839(-1): 98 – 106.

-*Pires.H.A.,"The Development of a Trip Assignment Algorithm to Improve Traffic Flow in Dohuk City"*, M.sc, Thesis ,Institute of Higher Planning, Dohuk University, June, 2013.

-Directorate of Traffic Dohuk Governorate, 2012 ,Traffic Data Statistics.